sensors

Special Issue Reprint

Novel Sensor Technologies for Civil Infrastructure Monitoring

Edited by
Chengyu Hong

mdpi.com/journal/sensors

MDPI

Novel Sensor Technologies for Civil Infrastructure Monitoring

Novel Sensor Technologies for Civil Infrastructure Monitoring

Guest Editor

Chengyu Hong

MDPI

Basel • Beijing • Wuhan • Barcelona • Belgrade • Novi Sad • Cluj • Manchester

Guest Editor
Chengyu Hong
College of Civil and
Transportation Engineering
Shenzhen University
Shenzhen
China

Editorial Office
MDPI AG
Grosspeteranlage 5
4052 Basel, Switzerland

This is a reprint of the Special Issue, published open access by the journal *Sensors* (ISSN 1424-8220), freely accessible at: https://www.mdpi.com/journal/sensors/special_issues/226F9YENS8.

For citation purposes, cite each article independently as indicated on the article page online and as indicated below:

Lastname, A.A.; Lastname, B.B. Article Title. *Journal Name* **Year**, *Volume Number*, Page Range.

ISBN 978-3-7258-9141-2 (Hbk)
ISBN 978-3-7258-9142-9 (PDF)
https://doi.org/10.3390/books978-3-7258-9142-9

© 2026 by the authors. Articles in this reprint are Open Access and distributed under the Creative Commons Attribution (CC BY) license. The reprint as a whole is distributed by MDPI under the terms and conditions of the Creative Commons Attribution-NonCommercial-NoDerivs (CC BY-NC-ND) license (https://creativecommons.org/licenses/by-nc-nd/4.0/).

Contents

About the Editor . . . . . **vii**

Alemdar Bayraktar, Mehmet Akköse, Carlos E. Ventura, Tony Y. Yang and Emin Hökelekli
Onsite Seismic Monitoring Behavior of Undamaged Dams During the 2023 Kahramanmaraş Earthquakes (M7.7 and M7.6)
Reprinted from: *Sensors* **2024**, *24*, 6856, https://doi.org/10.3390/s24216856 . . . . . **1**

Ioannis Karampinis, Martha Karabini, Theodoros Rousakis, Lazaros Iliadis and Athanasios Karabinis
Analytical Equations for the Prediction of the Failure Mode of Reinforced Concrete Beam–Column Joints Based on Interpretable Machine Learning and SHAP Values
Reprinted from: *Sensors* **2024**, *24*, 7955, https://doi.org/10.3390/s24247955 . . . . . **27**

Chengyu Hong, Chengkai Xu, Weibin Chen, Jianwei Liu and Junkun Tan
Monitoring Excavation- Induced Deformation of a Secant Pile Wall Using Distributed Fiber Optic Sensors
Reprinted from: *Sensors* **2025**, *25*, 254, https://doi.org/10.3390/s25010254 . . . . . **42**

Omar A. Kamel, Ahmed A. Abouhussien, Assem A. A. Hassan and Basem H. AbdelAleem
An Evaluation of the Acoustic Activity Emitted in Fiber-Reinforced Concrete Under Flexure at Low Temperature
Reprinted from: *Sensors* **2025**, *25*, 2703, https://doi.org/10.3390/s25092703 . . . . . **64**

Grzegorz Marek Kacprzak and Semachew Molla Kassa
Assessment of the Interaction of the Combined Piled Raft Foundation Elements Based on Long-Term Measurements
Reprinted from: *Sensors* **2025**, *25*, 3460, https://doi.org/10.3390/s25113460 . . . . . **84**

Dawid Piotrowski, Marcin Jasiński, Artur Nowoświat, Piotr Łaziński and Stefan Pradelok
The Performance of an ML-Based Weigh-in-Motion System in the Context of a Network Arch Bridge Structural Specificity
Reprinted from: *Sensors* **2025**, *25*, 4547, https://doi.org/10.3390/s25154547 . . . . . **120**

Linsheng Huo, Liukun Zhao, Aocheng Hu, Fanwei Meng and Hongnan Li
Digital Image Correlation-Based Bolt Preload Monitoring
Reprinted from: *Sensors* **2026**, *26*, 913, https://doi.org/10.3390/s26030913 . . . . . **149**

Giorgio S. Senesi, Olga De Pascale, Ignazio Allegretta, Roberto Terzano and Bruno Marangoni
Machine Learning-Enhanced Evaluation of Handheld Laser-Induced Breakdown Spectroscopy (LIBS) Analytical Performance for Multi-Element Analysis of Rock Samples
Reprinted from: *Sensors* **2026**, *26*, 1076, https://doi.org/10.3390/s26031076 . . . . . **168**

Ante Marendić, Dubravko Gajski, Ivan Duvnjak and Ana Kosor
Experimental Accuracy Evaluation of UAV-Based Homography for Static and Dynamic Displacement Monitoring of Structures
Reprinted from: *Sensors* **2026**, *26*, 1593, https://doi.org/10.3390/s26051593 . . . . . **190**

Weibin Chen, Zhijie Peng, Xiangsheng Chen, Linshuang Zhao, Tao Xu, Qiang Li, et al.
Concrete Crack Detection and Classification Methods Based on Machine Vision and Deep Learning
Reprinted from: *Sensors* **2026**, *26*, 2381, https://doi.org/10.3390/s26082381 . . . . . **214**

Han Liu, Israel Sousa, Shelby E. Doyle, Antonella D'Alessandro, Filippo Ubertini and Simon Laflamme
Piezoresistive Sensing Performance of Smart Layer in Multi-Material 3D-Printed Reinforced Cementitious Beams
Reprinted from: *Sensors* **2026**, *26*, 3204, https://doi.org/10.3390/s26103204 . . . . . **244**

About the Editor

Chengyu Hong

Chengyu Hong is a Distinguished Research Fellow and doctoral supervisor at Shenzhen University. He serves as Director of the Geotechnical and Underground Engineering Laboratory, and Deputy Director of the Smart Infrastructure Center in the Future Underground City Research Institute, College of Civil and Transportation Engineering. He received his Ph.D. in geotechnical engineering from The Hong Kong Polytechnic University. His research focuses on advanced sensing technologies, intelligent infrastructure monitoring, AI and big-data analytics for geotechnical engineering, and geotechnical digital twin systems. He has presided over multiple national-provincial projects including the NSFC Youth Fund, General Program, High-Speed Railway Joint Fund, and national key R&D program subjects, together with over 20 industrial collaborative projects, with total research funding exceeding 27 million RMB in the recent five years. He has published more than 150 SCI papers, over 90 as the first/corresponding SCI author, and authored two monographs. He holds more than 20 Chinese and US invention patents, and has won multiple major awards including Gold and Silver Medals at the Geneva International Invention Exhibition, and first-rank-principal-awarded Provincial Science and Technology Progress Prizes.

sensors

MDPI

Article

Onsite Seismic Monitoring Behavior of Undamaged Dams During the 2023 Kahramanmaraş Earthquakes (M7.7 and M7.6)

Alemdar Bayraktar [1,*], Mehmet Akköse [1], Carlos E. Ventura [2], Tony Y. Yang [2] and Emin Hökelekli [3]

[1] Civil Engineering Department, Karadeniz Technical University, Trabzon 61080, Türkiye
[2] Civil Engineering Department, University of British Columbia, Vancouver, BC V6T 1Z4, Canada; ventura@civil.ubc.ca (C.E.V.)
[3] Civil Engineering Department, Bartın University, Bartın 74100, Türkiye
* Correspondence: alemdarbayraktar@gmail.com

Abstract: On 6 February 2023, two major earthquakes struck Türkiye, with their epicenters in the Pazarcık (M7.7; focal depth: 8.6 km) and Elbistan (M7.6; focal depth: 7 km) districts of Kahramanmaraş city. Most of the dams in the earthquake region remained structurally safe and stable. However, 17 dams in Türkiye and 1 dam in Syria were damaged during the 2023 Kahramanmaraş earthquakes. The main objective of this study was to better understand the real seismic behaviors of the dams during the two mainshocks and significant aftershocks. An earthfill dam, a concrete-faced rockfill dam (CFRD), and a roller-compacted concrete (RCC) dam constructed in the disaster area were selected to identify the real seismic behaviors of different types of dams during strong earthquakes. Acceleration records measured at the crest, right and left abutments, and foundations of the selected dams during the 2023 Kahramanmaraş earthquakes were taken into account to determine the real seismic behavior of the dams before, during, and after the earthquakes. The results of this investigation provide valuable insights into the real seismic behaviors of different types of dams in the vicinity of fault lines during strong earthquakes.

Keywords: earthfill dam; concrete-faced rockfill dam; roller-compacted concrete dam; monitored seismic behavior; seismic monitoring; 2023 Kahramanmaraş earthquakes

1. Introduction

Dams are typically designed, constructed, operated, maintained, and monitored by skilled engineers, making them generally resistant to earthquake effects. However, strong earthquakes can still cause damage to dams [1–16]. The extent of damage to dams during earthquakes is influenced by several factors, including their typology, geometry, construction materials, foundation stratigraphy, and unique design features, as well as the presence of a reservoir and the dam's past loading history. Additionally, earthquake characteristics—such as magnitude, epicentral distance, depth, and proximity to fault lines—can significantly affect the level of damage [12–14,17,18].

Despite advancements in seismic analysis of dams, accurately predicting their behavior during strong ground shaking remains challenging. This is primarily due to the difficulties in modeling the inelastic response of dams, limited information on the spatial variability of ground motion, and other contributing factors. However, seismic instrumentation and monitoring systems allow for real-time observation of dam behavior and structural safety before, during, and after earthquakes. These systems help identify critical dynamic properties of dams, such as internal damping, amplification of ground motion from the foundation or abutments to the crest, wave propagation within the structure, differential movement between abutments, and natural frequencies along with mode shapes.

Several studies have been conducted on the behavior of dams during earthquakes. Seed et al. [10], Tani [11–13], and Tani and Nakashima [14] investigated the behavior of large fill

dams during seismic events. Pells and Fell [19] reported on the damages and cracking observed in embankment dams due to earthquakes. Matsumoto [20] and Matsumoto et al. [21] assessed the impact of seismic activity on dam safety in Japan. Zhang [22] evaluated the behavior of dams and hydropower structures during the Wenchuan earthquake, which occurred on 12 May 2008, with a magnitude of 8.0 and a focal depth of 15 km in the Wenchuan-Beichuan Longmenshan Fault belt in Sichuan Province. Researchers also analyzed the seismic damage and behavior of earth and concrete-faced rockfill dams during this earthquake [3,23]. Additionally, USCOLD [15] prepared a report on the observed behavior of dams during earthquakes, and Gordan et al. [6] reviewed the dynamic behavior of earth dams and embankments during seismic events.

On 6 February 2023, two powerful earthquakes struck Türkiye, with epicenters in the Pazarcık (M7.7, focal depth: 8.6 km) and Elbistan (M7.6, focal depth: 7 km) districts of Kahramanmaraş, occurring at 04:17 and 13:24 local time, respectively [24]. Later, on 20 February 2023, another earthquake with a magnitude of M6.4 hit Yayladağ, Hatay, at 20:04 local time. These seismic events caused extensive damage to buildings across 11 provinces and severely impacted engineering structures, including dams, bridges, tunnels, and more [2,24–31].

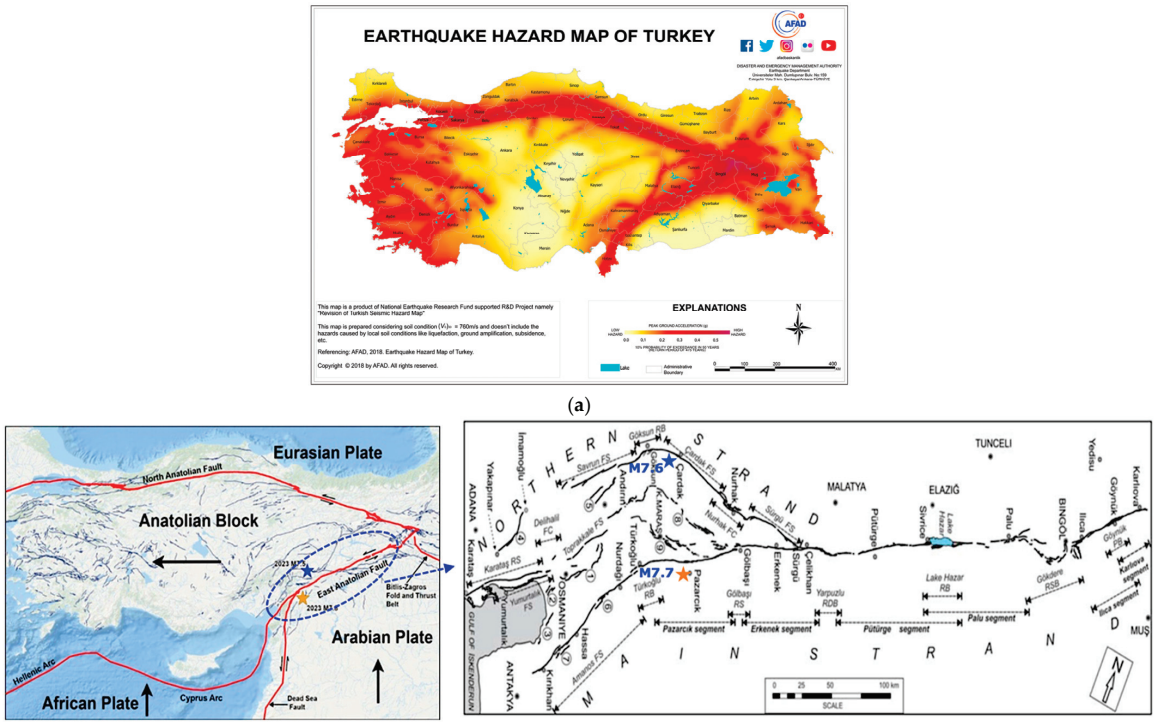
This paper aims to assess the actual seismic behavior of dams located in the earthquake-affected region during the two main shocks and significant aftershocks of the 6 February 2023 Kahramanmaraş earthquakes in Türkiye. The study begins with an overview of the region's major active faults, seismic activity in Türkiye, and the specific characteristics of the 6 February 2023 earthquakes. It also provides details on the damaged dams, which include zoned earthfill dams, earth core rockfill dams, earth core sand gravel dams, earthfill dams, and concrete-faced rockfill dams. Subsequently, the seismic behavior of an earthfill dam, a concrete-faced rockfill dam (CFRD), and a roller-compacted concrete (RCC) dam in the earthquake region is evaluated separately, examining their behavior before, during, and after the 2023 Kahramanmaraş earthquakes.

2. 6 February 2023 Kahramanmaraş, Türkiye, Earthquakes

Türkiye is located in one of the most seismically active regions in the world. The major active faults and the earthquake hazard map of Türkiye published in 2018 are shown in Figure 1. It can be seen from Figure 1 that Türkiye lies on the Anatolian plate and is surrounded by the Arabian, the African, and the Eurasian plates. The tectonic deformation of Türkiye is largely accommodated by two major active faults, including the East Anatolian Fault (EAF) and the North Anatolian Fault (NAF). The fault mechanism of the EAF zone, which is about 450 km long, is the NE-trending left-lateral strike-slip fault system that lies between Karlıova and Hatay [32,33]. The EAF zone extends to the left-lateral strike-slip Dead Sea Fault Zone in the south [34].

On 6 February 2023, at 04:17 a.m. local time (01:17 GMT), with a moment magnitude of M7.7 (Mercalli intensity scale: XI), the Pazarcık (Kahramanmaraş) earthquake occurred on the EAF zone. The epicenter of the Pazarcık (Kahramanmaraş) earthquake was located at 37.288° N, 37.043° E and approximately 40 km north-west of Gaziantep, and 33 km south-east of Kahramanmaraş, with a focal depth of 8.6 km [24]. Approximately 10 min after the mainshock on 6 February 2023, at 04:28 a.m. local time (01:28 GMT), with a moment magnitude of M6.6, a strong aftershock at Nurdağı (Gaziantep) occurred on the EAF zone. The epicenter of the aftershock was located at 37.304° N, 36.92° E and approximately 82 km south-west of Gaziantep city, and 51 km south-west of Kahramanmaraş city, with a focal depth of 6.2 km. Following the first two events, approximately 9 h later, at 13:24 p.m. local time (10:24 GMT), an M7.6 earthquake at Elbistan (Kahramanmaraş) shook the region again. The epicenter of the second mainshock was located at 38.089°N, 37.239° E, approximately 98 km north-west of Adıyaman city, and 62 km north-east of Kahramanmaraş city, with a focal depth of 7.0 km. The Elbistan (Kahramanmaraş) earthquake (M7.6; Mercalli intensity scale: X) occurred along the Çardak-Sürgü fault segment, which is a part of the EAF zone [24]. In addition, on 20 February 2023 at 20:04 local time (17:04 GMT), a large M6.4

earthquake struck Yayladağ, Hatay, within the East Anatolian Fault (EAF) zone, with coordinates N36.037°, E36.021° and a focal depth of 21.73 km [24].

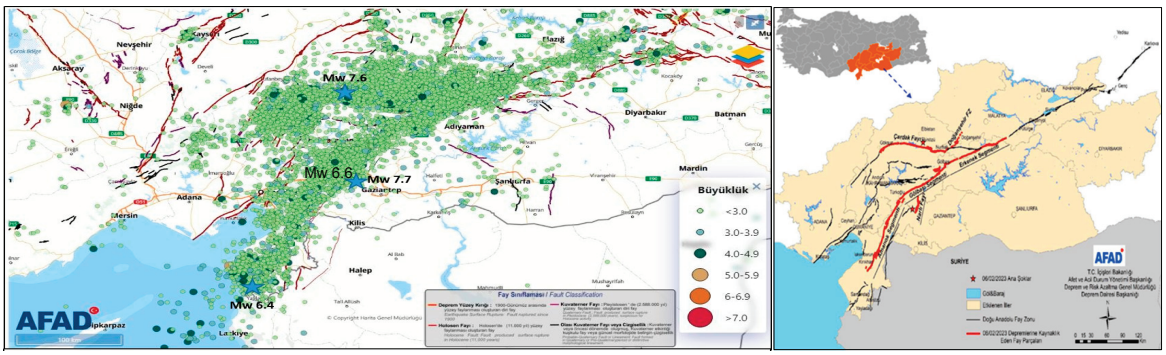


(**a**)

(**b**)

Figure 1. The earthquake hazard map (**a**), and main active faults of Türkiye and the East Anatolian Fault (EAF) system (**b**) [31,35,36].

Figure 2 displays the locations of the epicenters of the mainshocks and aftershocks, and the fault lines and the affected area. A total number of 38,000 aftershocks were recorded in the region between February 6 and 6 May 2023 within a 200 km epicenter distance. In total, 579 of these aftershocks had magnitudes exceeding M4.0 [1]. These earthquakes, all of which are unprecedented in recent history in terms of magnitude and coverage, caused major devastation in a total of 11 provinces. The total population of the 11 provinces affected by the earthquake was registered as 14,013,196 persons in 2022 and the total number of buildings in the region was close to 2.6 million [30].

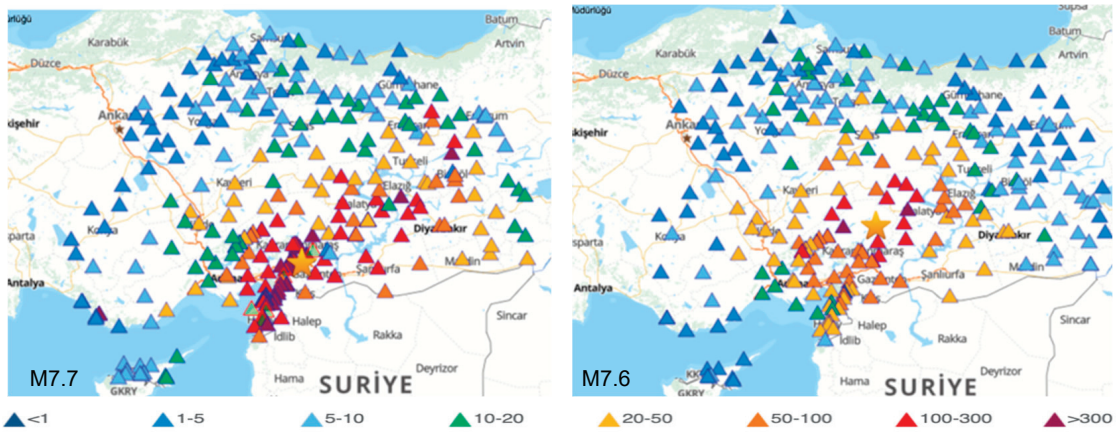


(**a**) (**b**)

Figure 2. The epicenters of the mainshocks and aftershocks of the February 2023 Kahramanmaraş and Hatay earthquakes (**a**), and the affected region (**b**) [24].

The strong ground motion data of the 6 February 2023 Kahramanmaraş earthquakes were recorded by the Turkish Accelerometric Database and Analysis System (TADAS)

(https://tadas.afad.gov.tr, accessed on 1 August 2024), which is operated by AFAD (Disaster and Emergency Management Presidency) by using more than 800 strong motion stations in Türkiye and Cyprus [35]. The peak ground acceleration (PGA) distributions, indicated by the triangles, recorded at the stations for M7.7 and M7.6 are shown in Figure 3. The peak ground acceleration (PGA), peak ground velocity (PGV) and peak ground displacement (PGD) of the first mainshock (M7.7) were reported as 1372.07 cm/s^2 (E-W) (TK3135, Repi = 142.15 km), 186.78 cm/s (N-S) (TK3123, Repi = 143.00 km) and 661.90 cm (U-D) (TK0720, Repi = 428.19 km). The PGA, PGV and PGD of the second mainshock (M7.6) were reported as 635.45 cm/s^2 (N-S) (TK4612, Repi= 66.68 km), 170.79 cm/s (N-S) (TK4612 Repi = 66.68 km) and 614.52 cm (U-D) (TK0720, Repi = 472.58 km) [35].



(**a**) (**b**)

Figure 3. The peak ground accelerations (units in cm/s^2) of 6 February 2023 Kahramanmaraş, Türkiye, earthquakes: M7.7 (**a**) and M7.6 (**b**) [35].

3. Seismic Behaviors of Dams During the 2023 Kahramanmaras Earthquakes

Türkiye presents a challenging tectonic and geological environment for the construction of safe dams. Many dams in Türkiye are located in close proximity to active faults, and some have been built directly across them. There are 140 dams used for irrigation, drinking water, flood control, and electricity generation in the region near the epicenter and fault ruptures of the 2023 Kahramanmaraş earthquakes. This region contains 19% of the total number of dams and 39% of Türkiye's installed hydraulic capacity [30].

Despite such a high acceleration, most of the dams remained in a structurally safe and stable condition in the earthquake-affected region. Seventeen dams in Türkiye and one dam in Syria were damaged during the 6 February 2023 Kahramanmaraş earthquakes [30]. The estimated damage cost for the seventeen dams was USD 141.8 million [30]. The characteristics, locations and damage levels of the damaged dams are presented in Table 1. The types of damaged dams include zoned earthfill, earth core rockfill, earth core sand gravel, earthfill and concrete-faced rockfill dams. Although the dams in the earthquake-affected region were exposed to two major earthquakes and many aftershocks, the dams experienced minor to major cracks. Nevertheless, they did not fail to retain water and resulted in no uncontrolled release of water from the reservoir.

The horizontal acceleration values at the crest levels of the damaged dams were approximately calculated to be four times greater than at the dam foundation [2]. Longitudinal cracks were observed at the crests and upstream faces of the dams, with their length and depth increasing significantly through the dam crest. The width of the longitudinal cracks at the dam crest was also considerably large. In addition to dam damages in Türkiye, the Medanki dam in Afrin (Syria) was damaged due to the 2023 Kahramanmaraş earthquakes. It is an earthfill dam, and its high and crest length are 75 m and 980 m, respectively. It is located near the south-east border of Türkiye. Cracks occurred along the dam crest; however, there was no water leakage after the earthquakes [2].

Table 1. Main characteristics of the damaged dams during the 6 February 2023 Kahramanmaraş earthquakes [2,26,30].

Name	Location	Type *	Constr. Year	Crest Length (m)	Height from Foundation (m)	Damage Level
Aslantaş	Osmaniye	ZED	1984	566.0	95.0	Minor cracks along the crest
Kalecik	Osmaniye	ECRD	1985	194.6	80.0	Moderate cracks along the crest
Yarseli	Hatay	ECSGD	1989	960.0	43.5	Moderate cracks along the crest
Bahçe Arıklıkaş	Osmaniye	ED	2000	355.0	25.0	Major cracks along the crest
Samandağ Karamanlı	Hatay	ED	2005	406.0	26.0	Minor cracks along the crest
Hassa Demrek	Hatay	ED	2006	503.0	26.0	Minor cracks along the crest
Büyük Karaçay	Hatay	CFRD	2017	415.1	105.0	Minor cracks along the crest
Kırıkhan Kutlusoğuksu	Hatay	ECRD	2017	419.1	40.0	Major cracks along the crest
Reyhanlı	Hatay	ED	2020	9271.0	28.2	Major cracks along the crest
Sürgü	Malatya	ECRD	1969	736.0	57.0	Moderate cracks along the crest
Sultansuyu	Malatya	ECSGD	1992	721.3	60.0	Major cracks along the crest
Çetintepe	Adıyaman	ECRD	2022	780.0	116.0	Moderate cracks along the crest
Kartalkaya	Kahramanmaraş	ZED	1972	205.0	57.0	Major cracks along the crest
Kılavuzlu	Kahramanmaraş	ECSGD	2014	556.0	61.0	Moderate cracks along the crest
Islahiye Bayraktepe	Gaziantep	ECSGD	2017	233.5	41.0	Minor cracks along the crest
Nurdağı Hamidiye	Gaziantep	ECRD	2018	182.0	29.0	Moderate cracks along the crest
Yukarı Afrin	Kilis	ECSGD	2015	720.2	60.0	Minor cracks along the crest

* ZED: zoned earthfill dam, ECRD: earth core rockfill dam, ECSGD: earth core sand gravel dam, ED: earthfill dam, CFRD: concrete-faced rockfill dam.

The monitoring data for the damaged dams shown in Table 1 were not recorded by AFAD [35] during the February 2023 Kahramanmaraş earthquakes. However, monitoring data were obtained from the undamaged dams in the earthquake-affected region during the February 2023 Kahramanmaraş earthquakes. An earthfill dam, a concrete-faced rockfill dam (CFRD), and a roller-compacted concrete (RCC) dam constructed in the earthquake-prone region were selected to assess the real seismic behavior of different types of dams during strong earthquakes in this study. The real seismic behaviors of these three selected dams, which are the Tahtaköprü Dam, Kavşak Bendi Dam and Feke II Dam, are individually evaluated and discussed in detail below. SARA ACEBOX accelerometers were installed at the aforementioned dams to record the necessary data after the completion of construction [35]. The collected data, sampled at 100 Hz, underwent filtering and baseline correction procedures. A Butterworth filter was applied with low and high cut-off frequencies set at 0.025 Hz and 40.0 Hz, respectively.

3.1. Behavior of Earthfill Dams

The Tahtaköprü Dam was selected to evaluate the monitored seismic behavior of earthfill dams during the 6 February 2023 Kahramanmaraş earthquakes. The dam is located approximately 15 km northeast of Hassa District in Hatay Province, near the Syrian border. It was constructed on the Karasu Stream between 1967 and 1975 for irrigation purposes for the type of an earthfill dam. Elevation works were conducted on the dam body between 2017 and 2019, resulting in an increase in the crest level from 407.50 m to 416.50 m [36]. The Tahtaköprü Dam has a height of 55.5 m from the foundation, a crest length of 401.03 m, and a crest width of 10 m. According to the Türkiye Earthquake Hazard Map published in 2018 [35], the maximum ground motion acceleration (PGA) values at Tahtaköprü Dam location for the 475- and 2475-year return periods are 0.465 g and 0.858 g, respectively. According to ICOLD, the 475-year return period corresponds to the Safety Evaluation Earthquake (SEE), while the 2475-year return period corresponds to the Maximum Credible Earthquake (MEC). The dam was designed to withstand 0.25 g [37].

Some views from the crest, upstream and downstream faces, and spillway of the Tahtaköprü dam after the 2023 Kahramanmaraş earthquakes are shown in Figure 4. The strong ground motion accelerometer stations with three components were installed at the dam crest (TK2716), right abutment (TK2715) and left abutment (TK2717) of the dam on 4 April 2021. Figure 5 displays the epicenters of the 2023 Kahramanmaraş earthquakes and the accelerometer station locations. The left (TK2715) and right (TK2717) abutment stations

were located on the bedrock. Elevations of TK2715, TK2716 and TK2717 stations were 431.0 m, 415.0 m and 419.0 m, respectively [35].



Figure 4. Views from Tahtaköprü dam after the 2023 Kahramanmaraş earthquakes.



Figure 5. The locations of the main (M7.7) and aftershock (M6.6) epicenters and the Tahtaköprü Dam accelerometer stations.

The acceleration data recorded on the Tahtaköprü dam crest and its abutments were obtained for the M4.4, M7.7, and M6.6 earthquakes. On 27 January 2023, at 16:12, an earthquake with a magnitude of M4.4 occurred, which preceded the M7.7 and M6.6 earthquakes on 6 February 2023. The earthquake (M4.4) had a depth of 18.35 km and an epicenter distance of 135.08 km from the dam. During the M4.4 earthquake, acceleration graphs recorded in the E-W, N-S, and U (vertical) directions at the crest station (TK2716) are plotted in Figure 6. For this earthquake, the maximum accelerations measured in the crest in the E-W, N-S, and U (vertical) directions are 0.68 cm/s^2, 0.91 cm/s^2, and 0.57 cm/s^2, respectively. When evaluating the acceleration records of the M4.4 earthquake in Figure 6, the dominant periods of the dam before the February 2023 Kahramanmaraş earthquakes were

calculated as 0.59 s, 0.62 s, and 0.37 s for the E-W (in the dam axis or cross-valley), N-S (in the stream or upstream/downstream direction), and U (vertical) components, respectively. The dominant period corresponds to the largest amplitude value in the Fourier transform of the crest acceleration data.

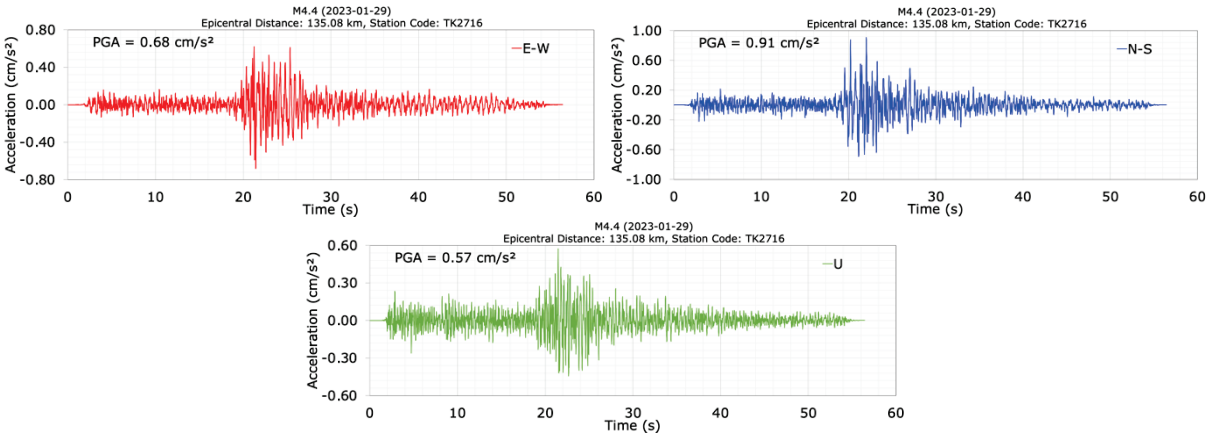


Figure 6. Acceleration time histories at the dam crest station (TK2716) during the M4.4 earthquake.

Acceleration measurements during the 6 February 2023 Kahramanmaraş earthquakes were taken at three locations, the dam crest (TK2716), the right abutment (TK2715), and the left abutment (TK2717), for both the mainshock (M7.7) and the aftershock (M6.6) earthquakes. The M6.6 aftershock occurred approximately 10 min after the M7.7 mainshock. The distances of stations TK2715, TK2716, and TK2717 from the epicenter of the M7.7 mainshock earthquake are 57.62 km, 57.38 km, and 57.34 km, respectively, while the distances from the epicenter of the M6.6 aftershock earthquake are 54.05 km, 53.84 km, and 53.85 km [35]. The epicenters of both earthquakes are very close to each other. Figure 7 shows the locations of the dam and the active faults, named as the East Anatolian Fault (EAF) and the Dead Sea Fault (DSF). The EAF and DSF faults are located within approximately 13 km and 1 km from the dam site, respectively. The 6 February 2023 Kahramanmaraş earthquakes occurred along the East Anatolian Fault (EAF).

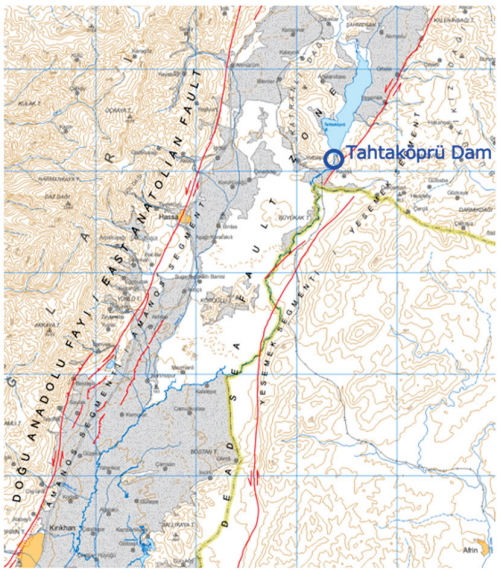
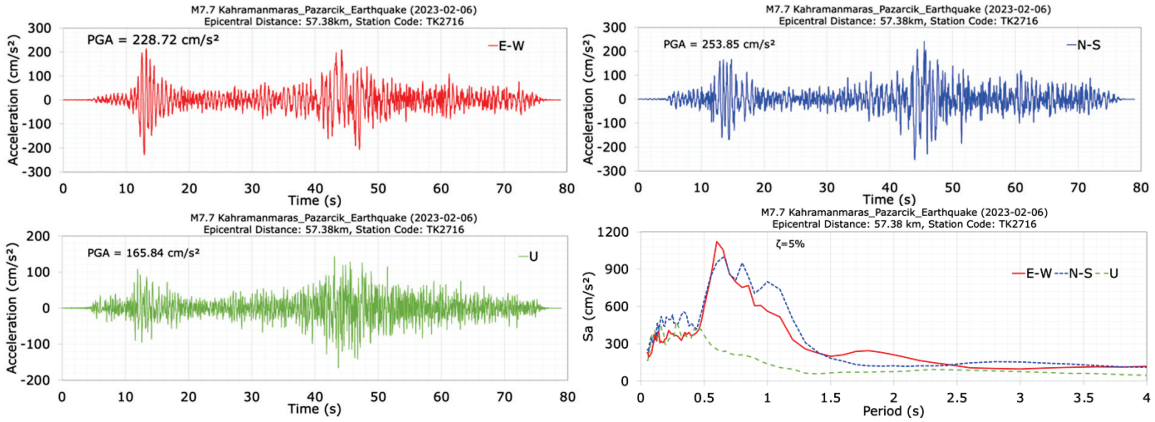


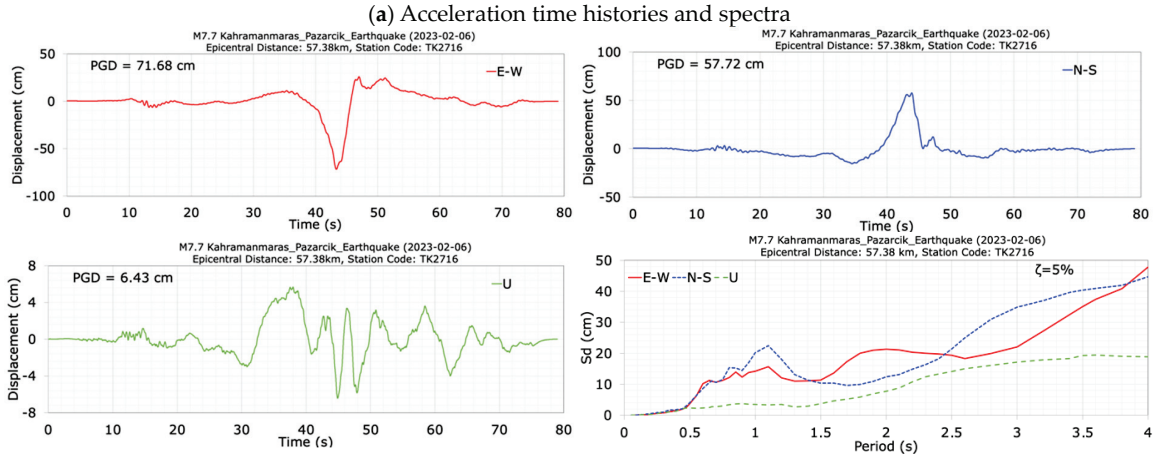
Figure 7. The location of Tahtaköprü Dam as well as the EAF and DSF faults [33].

Figure 8 displays the time histories and spectra of the accelerations and displacements in the dam axis (E-W), stream (N-S), and vertical (U) directions during the mainshock (M7.7) at the crest station (TK2716). The duration of the records is approximately 80 s. It

can be seen from Figure 8 that the seismometer at the crest station (TK2716) recorded peak accelerations of 228.72 cm/s^2 in the dam axis (E-W), 253.85 cm/s^2 in the stream (N-S), and 165.84 cm/s^2 in the vertical (U) directions. The largest crest acceleration occurred in the stream (N-S) direction. Furthermore, Figure 8 demonstrates that the acceleration response spectra values at the crest station (TK2716), with a 5% damping ratio, peak in the period range of 0.5 s to 1.5 s. Two significant pulses of the M7.7 strong earthquake motion can also be observed in all the acceleration time histories recorded at the crest (Figure 8). After the M7.7 mainshock, the dominant periods of the dam in the dam axis (E-W), stream (N-S) and vertical (U) directions were calculated as 0.61 s, 0.83 s and 0.49 s, respectively. The damping ratios for the chosen dams were determined using the Logarithmic Decrement Method, taking into account the maximum acceleration components measured at the dam crest. For the Tahtaköprü earthfill dam, the damping ratios were calculated as 6.70% for the M7.7 earthquake's N-S component and 10.69% for the M6.6 aftershock's E-W component, based on PGA data.



(**a**) Acceleration time histories and spectra



(**b**) Displacement time histories and spectra

Figure 8. Acceleration (**a**) and displacement (**b**) time histories and spectra at the crest station (TK2716) during the M7.7 earthquake.

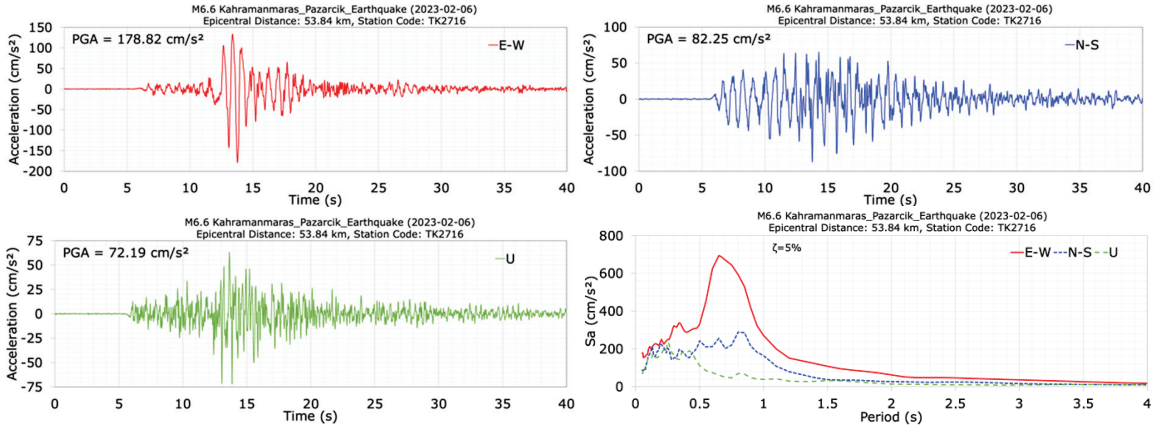
The peak displacements at the dam crest in the dam axis (E-W), stream (N-S) and vertical (U) directions are 71.68 cm, 57.72 cm and 6.43 cm, respectively, for the M7.7 earthquake. Although significant horizontal crest displacements were obtained from the accelerations recorded at the crest during the main earthquake (M7.7), during the observational inspections, no permanent deformations or cracks were found in the dam crest, body or foundation, and no water leakage was observed downstream (see Figure 4). It can be stated that the absence of permanent deformations in embankment dams, despite large horizontal displacements during the earthquake, can be attributed to the elastic behavior of materials, effective damping mechanisms, temporary nature of seismic forces,

compaction and redistribution of materials, and the dam's geometric configuration. The effects of these factors can be explained as follows. (1) Elastic behavior of materials: The materials used in embankment dams, such as compacted soil and rock fill, exhibit significant elastic behavior under dynamic loading. During an earthquake, the dam materials can deform elastically, absorbing and then releasing the seismic energy without undergoing permanent deformation. This elastic response is typically reversible, meaning that once the seismic forces subside, the materials return to their original state. (2) Damping mechanisms: Embankment dams have inherent damping mechanisms that dissipate the seismic energy. These mechanisms include internal friction within the dam materials, energy absorption by the foundation, and interaction with the surrounding environment. Effective damping reduces the impact of transient seismic forces, helping to prevent permanent displacements. (3) Temporary deformations: The recorded horizontal displacements during an earthquake are often temporary and can be largely attributed to the inertial forces acting on the dam. These forces cause the dam to move back and forth, resulting in significant but temporary displacements. Once the earthquake ends, the inertial forces cease, allowing the dam to settle back to its original position. (4) Compaction and redistribution of materials: During seismic shaking, the granular materials in the dam body can undergo compaction and slight rearrangement. This process can improve the overall stability and density of the dam, reducing the likelihood of permanent deformations. The materials may become more tightly packed, increasing their resistance to future seismic events. (5) Geometric configuration: The design and geometric configuration of embankment dams play a crucial role in their seismic behavior. Properly designed slopes, adequate freeboard, and well-compacted materials enhance the dam's ability to withstand large displacements without experiencing permanent damage. These factors collectively ensure that the dam can absorb and dissipate seismic energy without sustaining long-term damage, maintaining its structural integrity and safety.

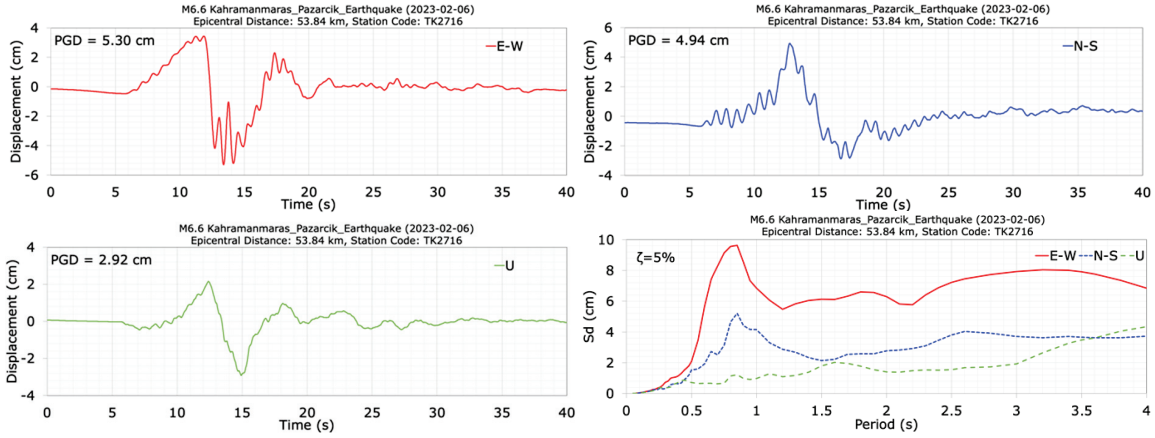
After the main shock earthquake (M7.7), an aftershock earthquake with a magnitude of M6.6 and almost the same epicenter distance occurred approximately 10 min later. The acceleration and displacement time histories and spectra at the crest station (TK2716) during the aftershock (M6.6) earthquake in the dam axis (E-W), stream (N-S), and vertical (U) directions are presented in Figure 9. The total duration of the records is approximately 40 s. It can be seen from Figure 9 that the seismometer at the crest station (TK2716) recorded peak accelerations of 178.82 cm/s^2 in the dam axis direction (E-W), 82.25 cm/s^2 in the stream direction (N-S), and 72.19 cm/s^2 in the vertical direction (U). The largest crest acceleration occurred in the dam axis (E-W) direction. The values of horizontal acceleration response spectra calculated for a 5% damping ratio at the crest station have effective values in the period range of 0.5 s to 1.0 s. The obtained peak displacements at the crest point in the E-W, N-S and U directions are 5.30 cm, 4.94 cm and 2.92 cm, respectively. Following the M6.6 aftershock earthquake, the dominant periods of the dam were calculated as 0.73 s in the dam axis (E-W), 0.76 s in the stream (N-S), and 0.41 s in the vertical (U) directions, respectively.

Figure 10 displays the variations in the dominant periods of the dam in the dam axis (E-W), stream (N-S), and vertical (U) directions for the M4.4, M7.7, and M6.6 earthquakes. It can be seen from Figure 10 that the dominant periods of the dam in the dam axis (E-W), stream (N-S) and vertical (U) directions show a noticeable change before, during, and after the mainshock (M7.7). The dominant periods of the dam following the mainshock (M7.7) and aftershock (M6.6) were found to be longer compared to the initial earthquake (M4.4) that occurred before the February 2023 earthquakes. The recorded dominant periods of the Tahtaköprü earthfill dam, with a crest length-to-height ratio of 7.23, during the M4.4, M7.7, and M6.6 earthquakes in the dam axis (E-W), stream (N-S), and vertical (U) directions range from 0.59 s to 0.61 s, 0.62 s to 0.83 s, and 0.37 s to 0.41 s, respectively. The increases in the dam-dominant period in the stream direction (N-S) for the M7.7 and M6.6 earthquakes are 25.30% and 18.42%, respectively. The dominant periods in the dam axis (E-W) direction increased by 3.28% and 19.18% for the main (M7.7) and aftershock (M6.6), respectively, while those in the vertical (U) direction increased by 24.49% and 9.76%, respectively. The

dam exhibited changes in its dominant periods when subjected to the pre-shock, main shock, and aftershock, but no damage was observed. This situation can be attributed to the elastic behavior of the materials, the effective damping mechanisms, the temporary nature of the seismic forces, changes in the frequency content of the of the input ground motions, the compaction and redistribution of the materials, and the geometric configuration of the dam.



(**a**) Acceleration time histories and spectra



(**b**) Displacement time histories and spectra

Figure 9. Acceleration (**a**) and displacement (**b**) times histories and spectra at the crest station (TK2716) during the M6.6 earthquake.

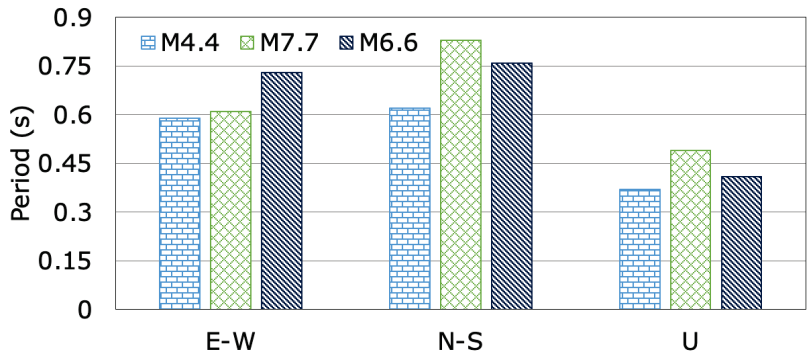
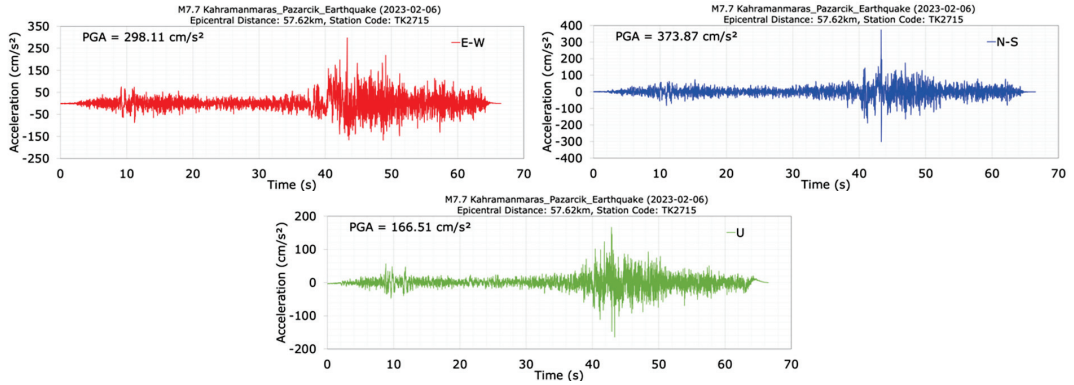


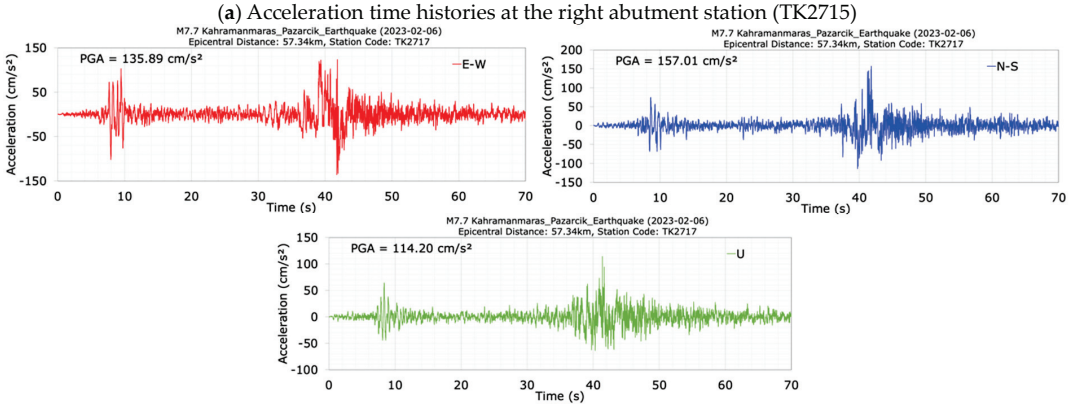
Figure 10. The changes in dominant periods of Tahtaköprü Dam during the M4.4, M7.7, and M6.6 earthquakes.

The acceleration records measured during the M7.7 mainshock earthquake on the right (TK2715) and left (TK2717) abutments of the dam are depicted in Figure 11. The maximum accelerations in the dam axis (E-W), stream (N-S), and vertical (U) directions recorded at the

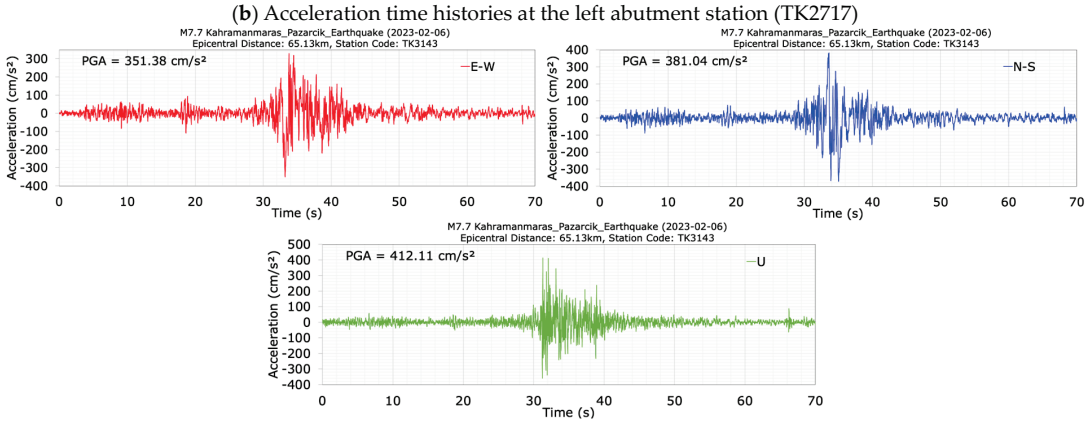
crest (TK2716), the left (TK2717) and right (TK2715) abutments, the magnification ratios of the acceleration components relative to each other, and the acceleration magnifications at the crest relative to the right and left abutments are summarized in Table 2. A peak horizontal acceleration of 373.87 cm/s^2 was recorded in the stream (N-S) direction on bedrock at the right abutment (TK2715) that is 16.0 m above the dam crest, while a peak horizontal acceleration of 157.01 cm/s^2 was measured in the stream (N-S) direction on bedrock at the left abutment (TK2717) that is 4.0 m above the dam crest. The maximum acceleration ratios between the N-S and E-W components (N-S/E-W) recorded at the crest, left and right abutments were calculated as 1.11, 1.16, and 1.25, respectively. The maximum N-S/E-W increase ratio obtained at the right abutment was 1.25. The maximum U/E-W and U/N-S acceleration ratios occurred at the left abutment, with values of 0.84 and 0.73, respectively.



(**a**) Acceleration time histories at the right abutment station (TK2715)



(**b**) Acceleration time histories at the left abutment station (TK2717)



(**c**) Acceleration time histories recorded at the TK3143 station

Figure 11. Acceleration time histories recorded at the right abutment station (TK2715) (**a**), the left abutment station (TK2717) (**b**), and at the TK3143 station during the mainshock (M7.7).

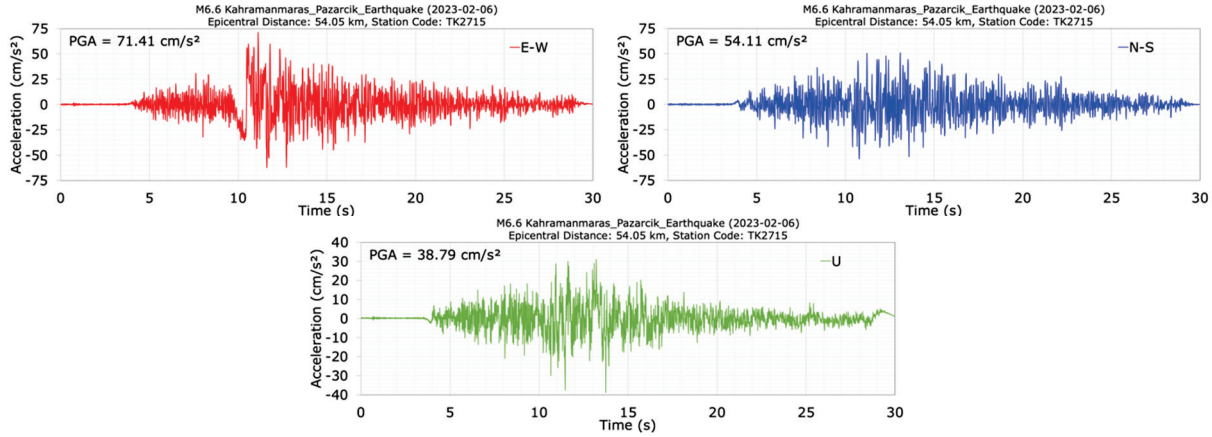
Table 2. Comparison of the peak ground accelerations and the ratios recorded at dam crest, left and right abutments for the M7.7 mainshock.

Location	Peak Ground Acceleration (cm/s^2)									
	E-W	N-S	U	Ratio						
				N-S/E-W	U/E-W	U/N-S	Crest/LA		Crest/RA	LA/RA
Crest	228.72	253.85	165.84	1.11	0.73	0.65	E-W	1.68	0.77	0.46
Left Abut. (LA)	135.89	157.01	114.20	1.16	0.84	0.73	N-S	1.62	0.68	0.42
Right Abut. (RA)	298.11	373.87	166.51	1.25	0.56	0.45	U	1.45	0.99	0.69

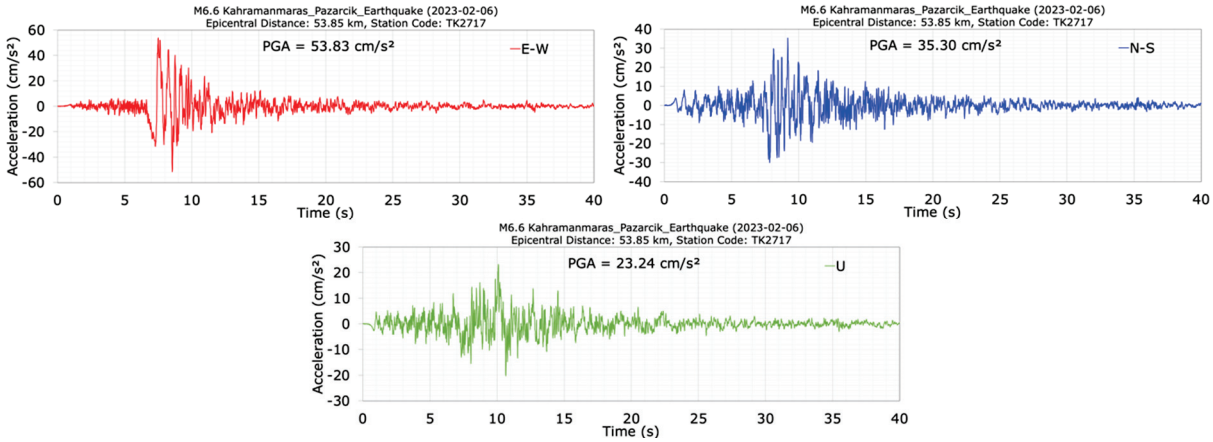
The maximum increase ratios (Crest/LA) from the left abutment (LA) to the crest are 1.62, 1.68 and 1.45 in the stream direction (N-S), dam axis (E-W) and vertical (U) directions, respectively. The ratios (Crest/RA) from the right abutment (RA) to the crest in the same direction are 0.68, 0.77 and 0.99, respectively. The crest acceleration ratios at the left abutment are larger than the right abutment. The maximum amplification at the dam crest occurred in the dam axis (E-W) direction, with a value of 1.68. For the M7.7 earthquake, an increase in crest accelerations can be observed in comparison to the accelerations on the left abutment, while a decrease in crest accelerations can be observed in comparison to the accelerations on the right abutment. The ratios between left (LA) and right (RA) abutment accelerations (LA/RA) in the stream (N-S), dam axis (E-W), and vertical (U) directions are 0.42, 0.46, and 0.69, respectively. For the M7.7 earthquake, the accelerations recorded at the right abutment of the dam are greater than those recorded at the left abutment.

The acceleration data recorded at the TK3143 station, located 11.9 km west of the Tahtaköprü dam, during the first M7.7 mainshock are shown in Figure 11c. This station, with an epicentral distance of 65.13 km, is located on moderately stiff ground with a shear wave velocity (Vs30) of 444 m/s [35]. The epicenter distances of the right and left abutments of the dam are 57.62 km and 57.32 km, respectively. From Figure 11c, it can be observed that the maximum accelerations recorded at the TK3143 station during the M7.7 earthquake in the E-W, N-S and vertical directions are 351.38 cm/s^2, 381.04 cm/s^2 and 412.11 cm/s^2, respectively. The acceleration values recorded at the left and right abutments of the dam during the same earthquake were 135.89 cm/s^2, 157.01 cm/s^2, 114.20 cm/s^2; 298.11 cm/s^2, 373.87 cm/s^2, and 166.51 cm/s^2 for the E-W, N-S, and vertical components, respectively. The acceleration values at TK3143 are higher compared to those at the dam abutments. Furthermore, the frequency content of the acceleration records at the dam abutments differs from that of the TK3143 station data. This indicates that local ground conditions play a significant role in the intensity and frequency components of seismic waves.

The acceleration records at the right (TK2715) and left (TK 2717) abutments of the dam during the M6.6 aftershock earthquake are plotted in Figure 12. Table 3 summarizes the maximum acceleration ratios measured in the dam axis (E-W), stream (N-S), and vertical (U) directions at the crest (TK2716), left (TK2717), and right (TK2715) abutments for the M6.6 aftershock. During the M6.6 aftershock earthquake, peak accelerations in the E-W, N-S, and vertical (U) directions were recorded at the crest (TK2716) as 178.82 cm/s^2, 82.25 cm/s^2, and 72.19 cm/s^2, respectively. The maximum acceleration ratios between the horizontal components (N-S/E-W) measured at the crest, the left and right abutments are 0.46, 0.66, and 0.76, respectively. The maximum acceleration ratio between the U and E-W components (U/E-W) was 0.54 at the right abutment while the maximum acceleration ratio between the U and N-S components (U/N-S) was calculated as 0.88 at the crest.



(**a**) Acceleration time histories at the right abutment station (TK2715)



(**b**) Acceleration time histories at the left abutment station (TK2717)

Figure 12. Acceleration time histories recorded at the right (TK2715) (**a**) and the left (TK2717) (**b**) abutment stations during the aftershock (M6.6).

Table 3. Comparison of peak ground accelerations and the ratios recorded at dam crest, left and right abutments for the M6.6 aftershock.

Location	Peak Ground Acceleration (cm/s^2)									
	E-W	N-S	U	Ratio						
				N-S/E-W	U/E-W	U/N-S	Crest/LA		Crest/RA	LA/RA
Crest	178.82	82.25	72.19	0.46	0.40	0.88	E-W	3.32	2.50	0.75
Left Abut. (LA)	53.83	35.30	23.24	0.66	0.43	0.66	N-S	2.33	1.52	0.65
Right Abut. (RA)	71.41	54.11	38.79	0.76	0.54	0.72	U	3.11	1.86	0.60

The crest acceleration amplification ratios (Crest/LA) relative to those recorded at the left abutment in the E-W, N-S, and U (vertical) directions are 3.32, 2.33, and 3.11, respectively. However, the crest acceleration amplification ratios (Crest/RA) relative to those recorded at the right abutment in the dam axis (E-W), stream (N-S), and vertical (U) directions are 2.50, 1.52, and 1.86, respectively. Significant increases in crest accelerations compared to the left and right abutment accelerations were observed during the M6.6 aftershock earthquake. The maximum crest acceleration amplification ratio during the M6.6 aftershock was calculated as 3.32 in the cross-canyon direction (E-W). The acceleration ratios (LA/RA) between the left abutment and the right abutment in the stream (N-S), dam axis (E-W) and vertical (U) directions were recorded as 0.65, 0.75 and 0.60, respectively. The accelerations recorded at the right abutment of the dam during the M6.6 aftershock also exceed those recorded at the left abutment. It is thought that the reason why the accelerations at the right abutment station, which is 12 m above the left abutment station

point, are greater than those at the left abutment station is due to the difference in elevation and soil properties as well as the topographic amplification in the canyon.

Upon comparing Tables 2 and 3, it becomes evident that the PGAs recorded at the right abutment during the M7.7 mainshock have the highest values, while the PGAs at the crest during the M6.6 aftershock exhibit the largest values. An analysis of Figure 11a reveals spikes in both the E-W and N-S directions at the right abutment during the M7.7 earthquake. If the spikes in the E-W and N-S acceleration records shown in Figure 11a are excluded, the PGA values measured at the right abutment for the E-W and N-S components during the M7.7 earthquake are 218.42 cm/s^2 and 189.72 cm/s^2, respectively. Not considering the spikes in the acceleration records at the right abutment during the M7.7 earthquake reveals higher horizontal PGA values recorded at the dam crest when compared to the right abutment, similar to the situation during the M6.6 earthquake.

3.2. Behavior of Concrete-Faced Rockfill Dams (CFRDs)

The Kavşak Bendi Dam was chosen to assess the real seismic behavior of concrete-faced rockfill dams during the 6 February 2023 earthquakes. This dam is a concrete-faced rockfill dam (CFRD) constructed for the purpose of energy production between the years 2009–2014 on Seyhan River in the Kozan District of Adana Province, Türkiye. The current dam has a height of 88 m from the foundation, 73 m from the thalweg, a crest length of 186 m, a crest width of 8 m, and a crest elevation of 323 m. According to the Türkiye Earthquake Hazard Map published in 2018 [35], the PGA values for the 475 and 2475-year return periods at the location of Kavşak Bendi Dam are calculated as 0.239 g and 0.493 g, respectively. The strong ground motion accelerometers with three components were installed at the dam crest (TK0140) and the right abutment bedrock (TK0141) of the dam on 29 December 2022. Figure 13 shows a view of the dam, the locations of the dam accelerometers, and the epicenters of the first (M7.7) and the second (M7.6) mainshocks of the 6 February 2023 Kahramanmaras earthquakes. Elevations of the TK0140 and TK0141 stations are 322.0 m and 312.0 m, respectively [35].

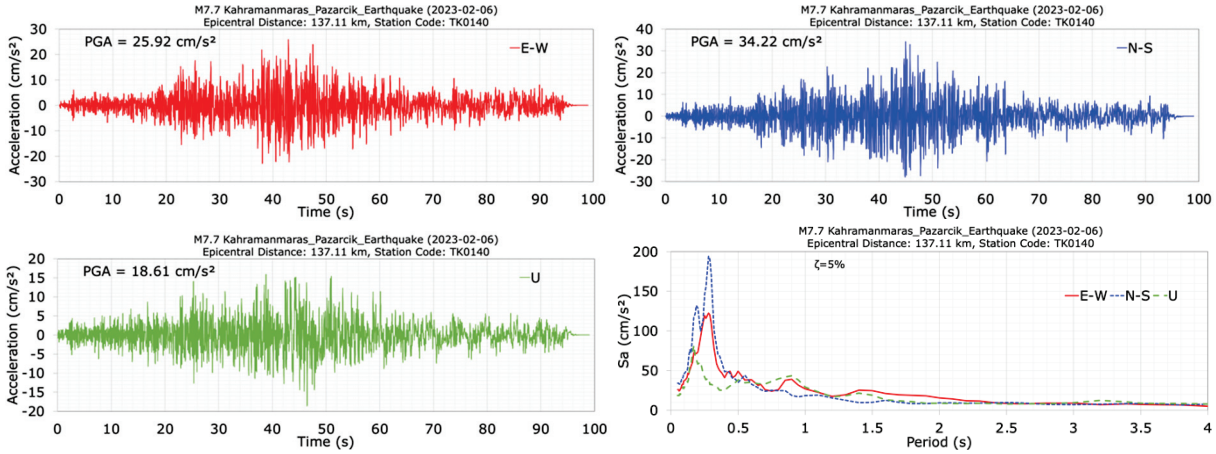


Figure 13. The locations of the first (M7.7) and the second main shock (M7.6) epicenters and the Kavşak Bendi dam accelerometer stations.

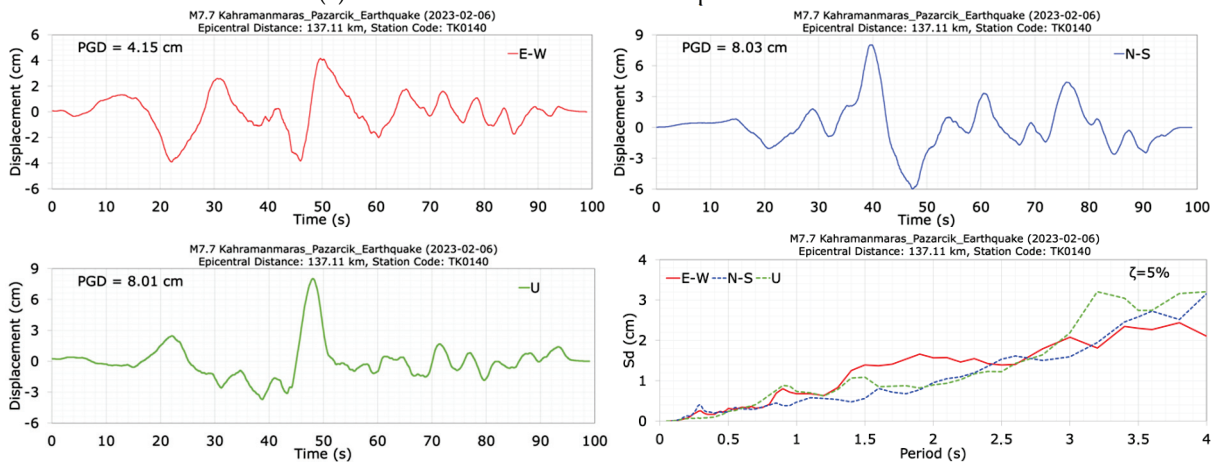
Prior to the Kahramanmaraş earthquakes on 6 February 2023, no earthquake was recorded by the sensors at the Kavşak Bendi Dam (AFAD, 2023b). Therefore, the dominant period of the dam could not be determined before the 6 February 2023 Kahramanmaraş earthquakes. However, accelerations were recorded at the dam crest (TK0140) and right abutment (TK0141) stations for the first (M7.7) and the second (M7.6) mainshocks of the 6 February 2023 Kahramanmaras earthquakes. TK0140 and TK0141 stations were located at distances of 137.11 km and 137.23 km, respectively, from the epicenter of the first mainshock (M7.7) earthquake, and at distances of 161.17 km and 161.28 km, respectively, from the epicenter of the second mainshock (M7.6) earthquake [35].

The acceleration and the displacement time histories and spectra at the dam crest station (TK0140) in the E-W (along dam axis), N-S (along the stream) and U (vertical)

directions of the mainshock (M7.7) are shown in Figure 14. The duration of the acceleration records is approximately 100 s. It can be seen from Figure 14 that the seismometer at the dam crest station (TK0140) recorded peak accelerations of 25.92 cm/s^2 in the dam axis (E-W), 34.22 cm/s^2 in the stream (N-S), and 18.61 cm/s^2 in the vertical (U) directions. The largest crest acceleration occurred in the stream (N-S) direction. Additionally, Figure 14 shows that the values of acceleration response spectra calculated for a 5% damping ratio at the dam crest station have high values between the period range of 0.1 s to 0.5 s. The peak displacements at the crest point in the dam axis (E-W), stream (N-S) and vertical (U) directions are 4.15 cm, 8.03 cm and 8.01 cm for the M7.7 earthquake, respectively. Following the first mainshock (M7.7), the dominant periods of the dam in the dam axis (E-W), stream (N-S) and vertical (U) directions were calculated as 0.25 s, 0.27 s, and 0.17 s, respectively.



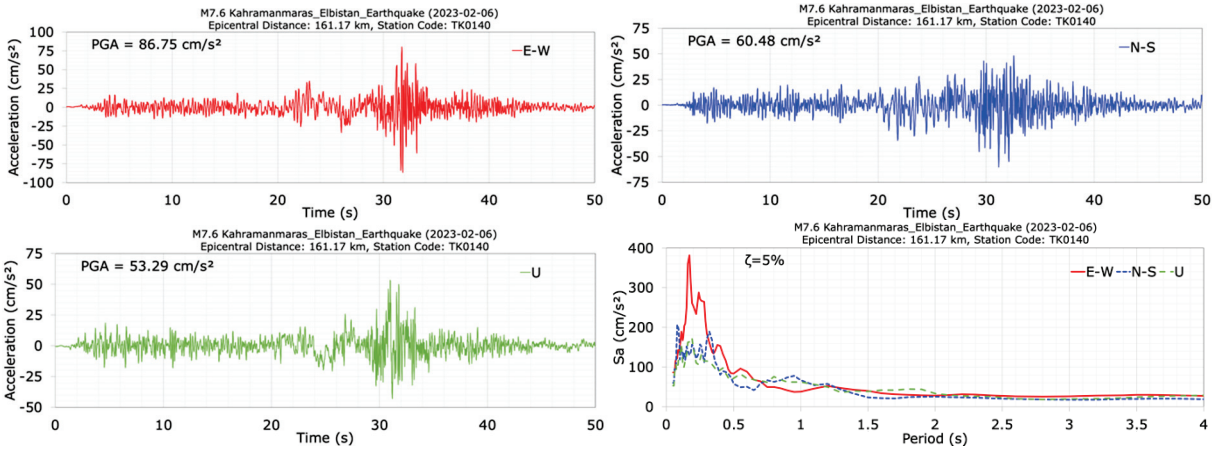
(**a**) Acceleration time histories and spectra



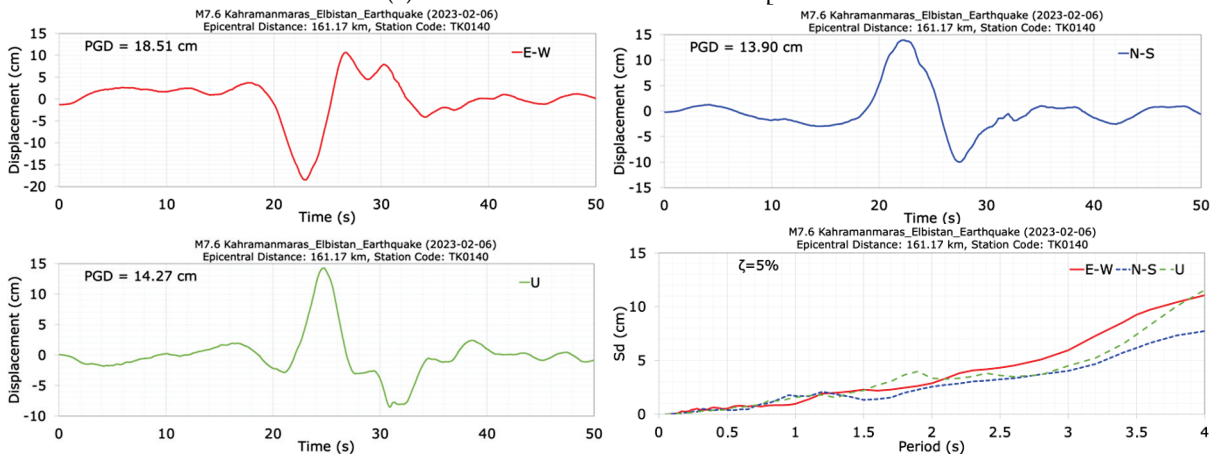
(**b**) Displacement time histories and spectra

Figure 14. Acceleration (**a**) and displacement (**b**) time histories and spectra at the dam crest station (TK0140) during the M7.7 earthquake.

The acceleration and displacement time histories and spectra at the dam crest station (TK0140) in the E-W, N-S and vertical (U) directions of the second mainshock (M7.6) are shown in Figure 15. The duration of the records is 50 s. The seismometer at the dam crest station (TK0140) measured peak accelerations of 86.75 cm/s^2 in the dam axis (E-W), 60.48 cm/s^2 in the stream (N-S), and 53.29 cm/s^2 in the vertical (U) directions. The largest crest acceleration of 86.75 cm/s^2 was recorded in the dam axis (E-W) direction. For the N-S component of the M7.7 earthquake and the E-W component of the M7.6 earthquake, the calculated damping ratios at the dam crest of the Kavşak Bendi cocrete-faced rockfill dam are 4.26% and 7.98%, respectively, based on PGA data.



(**a**) Acceleration time histories and spectra



(**b**) Displacement time histories and spectra

Figure 15. Acceleration (**a**) and displacement (**b**) time histories and spectra at the dam crest station (TK0140) during the M7.6 earthquake.

The horizontal acceleration response spectra calculated for a 5% damping ratio show large values between the period range of 0.1 s to 0.5 s. The obtained peak displacements for the crest point in the dam axis (E-W), stream (N-S) and vertical (U) directions are 18.51 cm, 13.90 cm and 14.27 cm, respectively. After the second mainshock earthquake with a magnitude of M7.6, which occurred 9 h after the first mainshock (M7.7), the dominant periods of the dam were calculated as 0.27 s in the dam axis (E-W), 0.30 s in the stream (N-S), and 0.20 s in the vertical (U) directions.

The changes in the dominant periods of the dam, calculated from the analysis of accelerations measured at the crest station (TK0140) following the M7.7 and M7.6 mainshocks, are illustrated in Figure 16 for the dam axis (E-W), stream (N-S), and vertical (U) directions. The recorded dominant periods of the Kavşak Bendi concrete-faced rockfill dam, with a crest length-to-height ratio of 3.67, during the M7.7 and M7.6 earthquakes in the dam axis (E-W), stream (N-S), and vertical (U) directions range from 0.25 s to 0.27 s, 0.27 s to 0.30 s, and 0.17 s to 0.20 s, respectively. The dominant periods of the dam in the stream (N-S), dam axis (E-W) and vertical (U) directions show a slight change during the two mainshocks. The dominant periods of the dam due to the second mainshock (M7.6) lengthened according to the earthquake (M7.7). The increase ratios of the dominant periods in the dam axis (E-W), stream (N-S) and vertical (U) directions during the second mainshock (M7.6) are 7.41%, 10.0% and 15.0%, respectively. The accelerations of the M7.6 earthquake recorded on the dam crest are larger than the accelerations of the M7.7 earthquake. It was observed that the periods of the dam increase with increasing the earthquake acceleration values. The M7.7

and M7.6 earthquakes did not result in any visible seismic damage, crack, or deformation to the Kavşak Bendi dam body or the site (Figure 13).

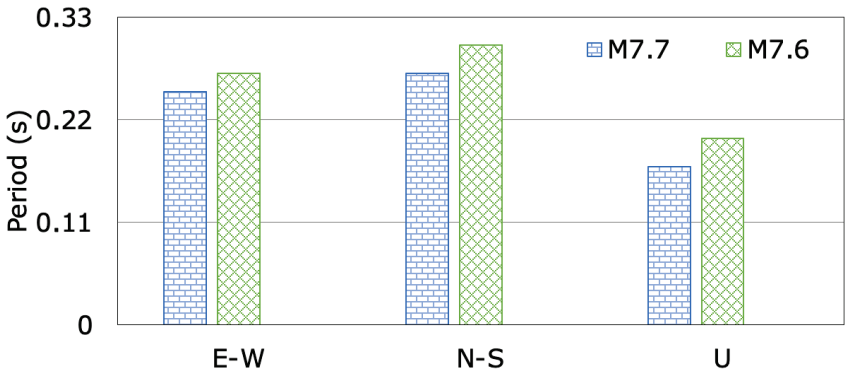


Figure 16. The changes in dominant periods of Kavşak Bendi Dam during the M7.7 and M7.6 earthquakes.

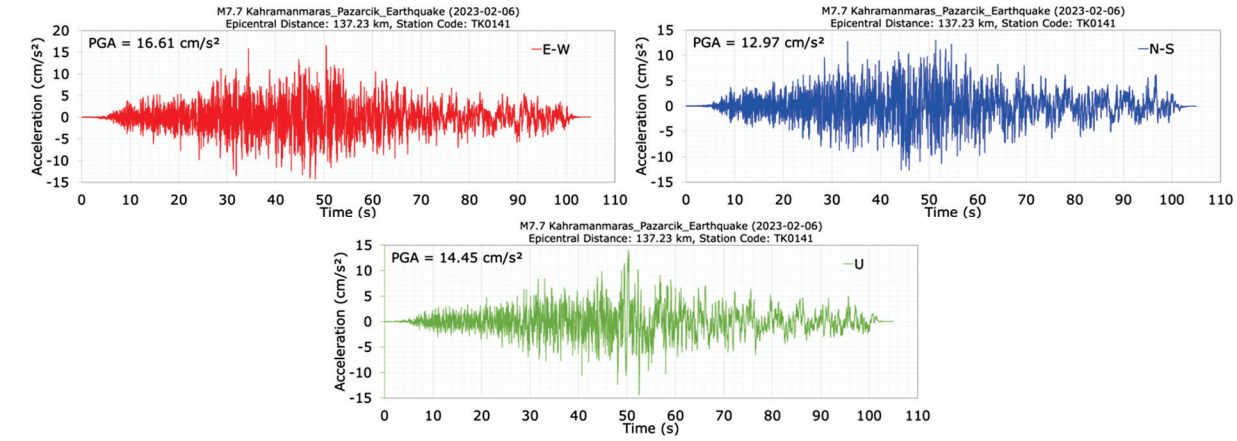
The acceleration records measured at the right abutment (TK0141) of the dam during the M7.7 and M7.6 mainshocks are plotted in Figure 17. Table 4 summarizes the maximum accelerations recorded at both the dam crest (TK0140) and the right abutment (TK0141) stations, and the crest amplification ratios relative to the right abutment in the E-W, N-S, and vertical (U) directions. The right abutment station (TK0141) is located 10.0 m below the dam crest station (TK0140). For the M7.7 earthquake, the acceleration amplification ratios at the dam crest relative to the right abutment are calculated as 1.56, 2.64 and 1.29 for the dam axis (E-W), stream (N-S), and vertical (U) directions. However, during the M7.6 earthquake, the acceleration amplification ratios at the dam crest relative to the right abutment for the E-W, N-S, and U components are 0.45, 0.78, and 0.71, respectively. The maximum crest acceleration amplification ratios for the M7.7 and M7.6 earthquakes in the N-S direction are 2.64 and 0.78, respectively. During the M7.7 earthquake, there are significant increases in crest accelerations relative to the right abutment for all acceleration components, whereas the M7.6 earthquake results in significant decreases in crest accelerations relative to the right abutment. This is thought to be due to spikes in the acceleration records of the M7.6 earthquake.

Table 4. Comparison of the peak ground accelerations recorded at dam crest (TK0140) and right abutment (TK0141) stations for the M7.7 and M7.6 earthquakes.

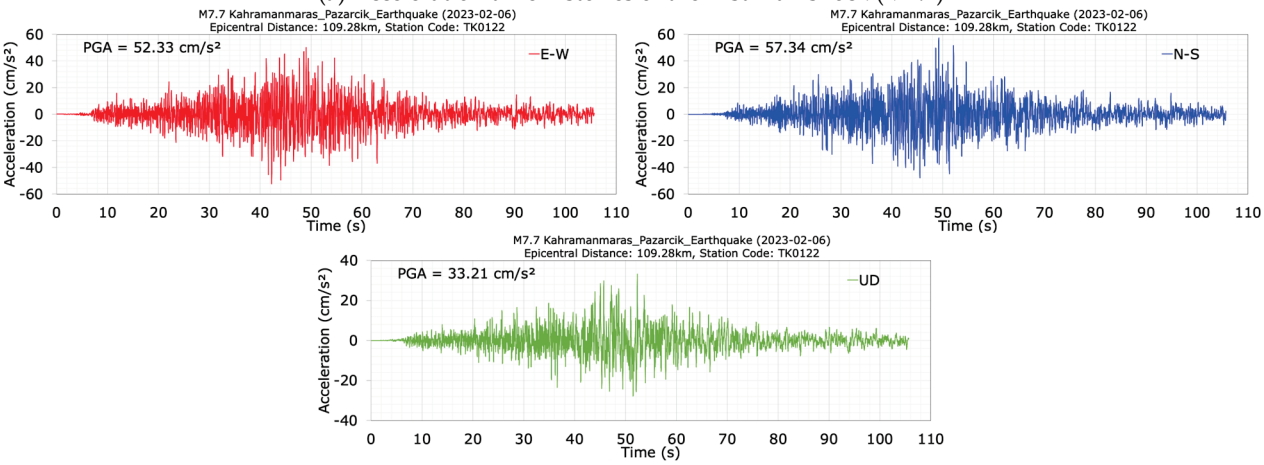
Location	Peak Ground Acceleration (cm/s^2)					
	E-W		N-S		U	
	M7.7	M7.6	M7.7	M7.6	M7.7	M7.6
Crest	25.92	86.75	34.22	60.48	18.61	53.29
Right Abut. (RA)	16.61	191.35	12.97	77.99	14.45	74.93
Ratio of Crest/RA	1.56	0.45	2.64	0.78	1.29	0.71

The acceleration data recorded at the TK0122 station, located 29.33 km south-east of the Kavşak Bendi dam, during the M7.7 mainshock are illustrated in Figure 17b. This station, situated on moderately stiff ground with a shear wave velocity (Vs30) of 501 m/s, is at an epicentral distance of 109.28 km. The right abutment of the dam is 137.23 km from the M7.7 earthquake epicenter. As shown in Figure 17b, the maximum accelerations recorded at the TK0122 station during the M7.7 earthquake in the E-W, N-S, and vertical directions are 52.33 cm/s^2, 57.34 cm/s^2, and 33.21 cm/s^2, respectively. In contrast, the recorded acceleration values at the right abutment of the dam during the same event are 16.61 cm/s^2, 12.97 cm/s^2, and 14.45 cm/s^2 for the E-W, N-S, and vertical (U) components, respectively. Although the acceleration values at TK0122 are higher than those at the dam

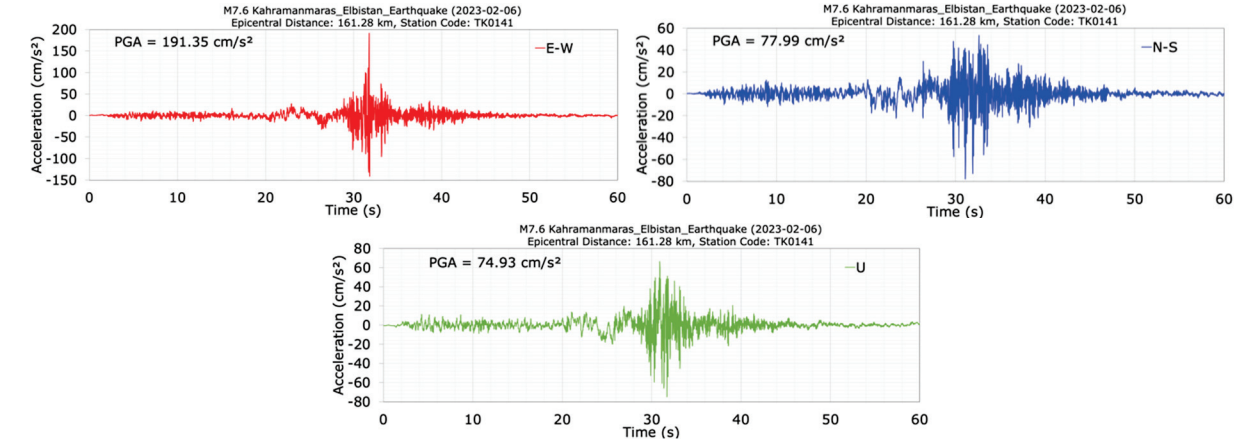
abutment, the frequency content of the acceleration records at the dam abutments is similar to that of the TK0122 station data.



(**a**) Acceleration time histories of the first mainshock (M7.7)



(**b**) Acceleration time histories recorded at the TK0122 station



(c) Acceleration time histories of the second mainshock (M7.6)

Figure 17. Acceleration time histories at the right abutment station (TK0141) (**a**) and TK0122 station (**b**) during the first (M7.7), and the second (M7.6) (**c**) mainshocks.

3.3. Behavior of Roller-Compacted Concrete Dams (RCCs)

Feke II Dam, located on Göksu River in the Feke District of Adana Province, Türkiye, was constructed between 2009 and 2011 years for the purpose of energy production, using the roller-compacted concrete construction method. The dam's height from the foundation is 71.0 m, and its crest length is 256.50 m. According to the Türkiye Earthquake Hazard Map published in 2018 [35], the peak ground acceleration (PGA) values of the Feke II Dam

location are calculated as 0.254 g and 0.516 g for the 475 and 2475-year return periods, respectively. The strong ground motion accelerometers with the three components were installed at the dam crest (TK0133) and foundation (TK0134) of Feke II Dam on 25 October 2021. Figure 18 provides a view of the dam and the locations of the epicenters of the M7.7 and M7.6 earthquakes, as well as the accelerometer positions. The TK0134 station was situated on the bedrock. The elevation of the dam's thalweg is 485 m, while the elevations of TK0133 and TK0134 stations are 546 m and 494.0 m, respectively [35].

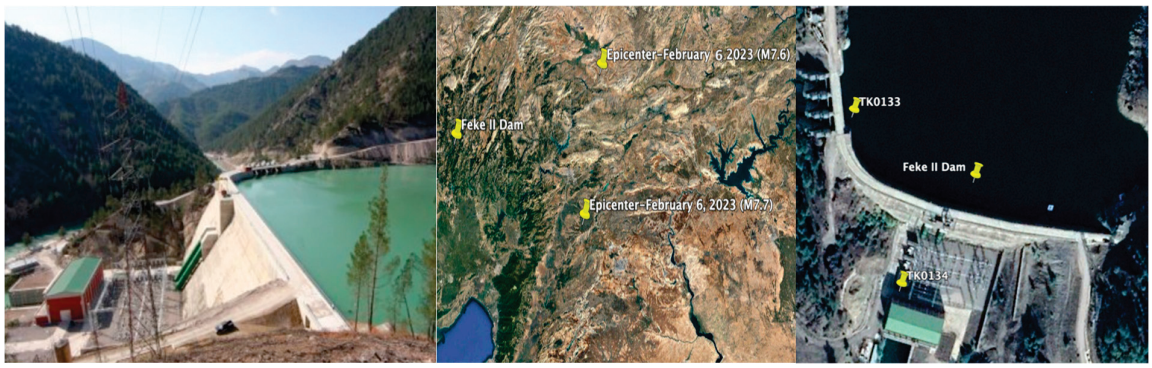


Figure 18. The locations of the first (M7.7) and the second main shock (M7.6) epicenters and the Feke II dam accelerometer stations.

Prior to the 2023 Kahramanmaraş earthquakes, an earthquake was recorded at the dam on 20 October 2022, at 11:34 am, with a magnitude of M4.5, a depth of 7.64 km, and an epicenter distance of 123.02 km. Acceleration time histories measured in the E-W (dam axis), N-S (stream), and vertical (U) directions at the crest station (TK0133) during the M4.5 earthquake are depicted in Figure 19. The maximum accelerations measured at the dam crest during the M4.5 earthquake are 0.59 cm/s^2, 0.45 cm/s^2, and 0.34 cm/s^2 for the E-W, N-S, and U directions, respectively. When evaluating the acceleration records in Figure 19, the dominant periods of the dam before the Kahramanmaraş earthquakes on 6 February 2023 are calculated as 0.48 s, 0.33 s, and 0.30 s, respectively, for the E-W (dam axis), N-S (stream), and vertical (U) directions.

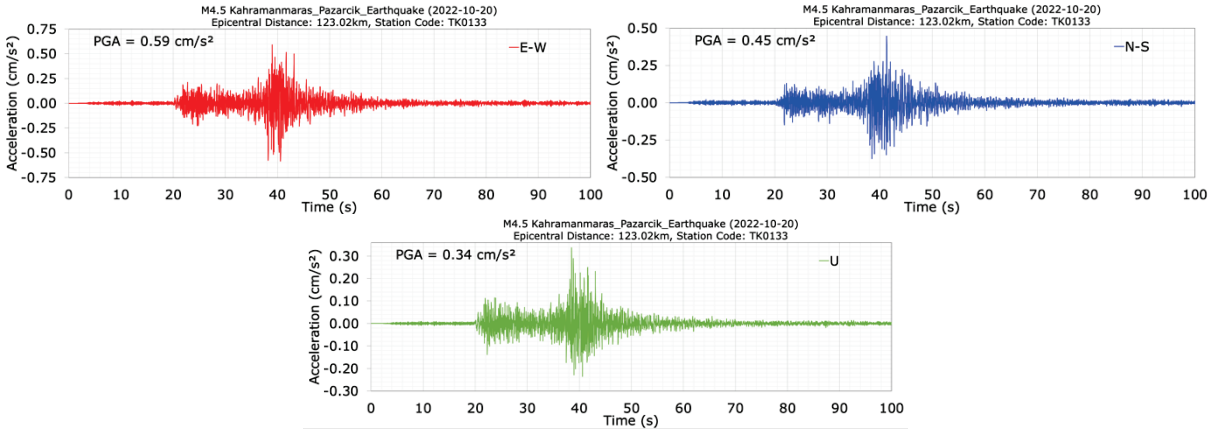
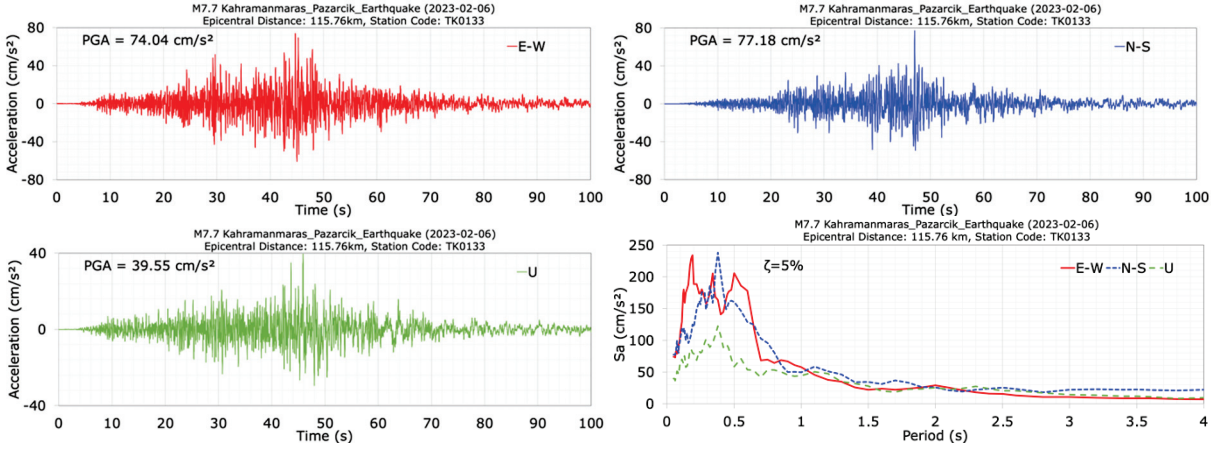


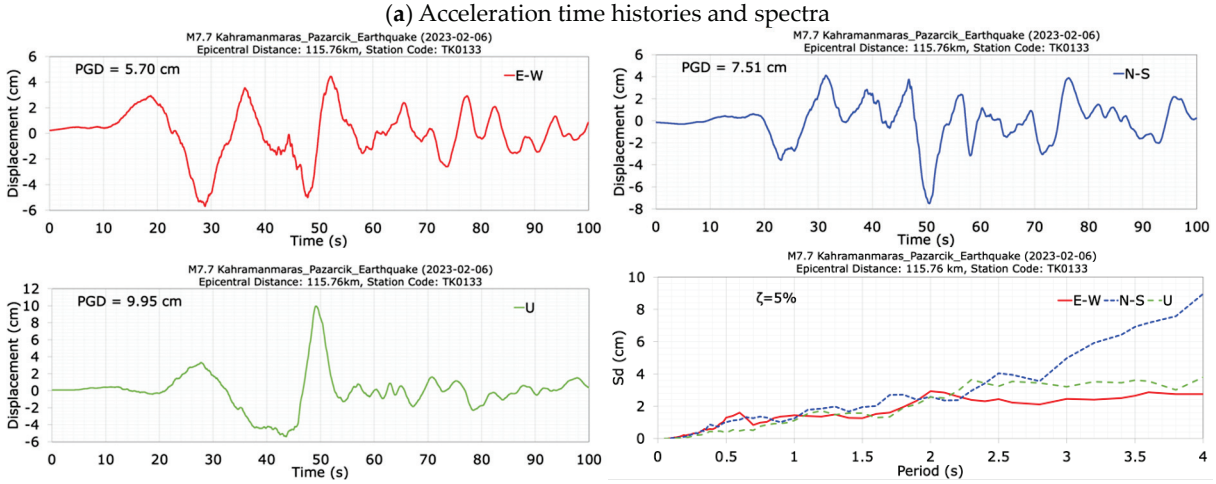
Figure 19. Acceleration time histories at the dam crest station (TK0133) during the M4.5 earthquake.

The accelerations of the 6 February 2023 Kahramanmaras earthquakes were recorded at the dam crest (TK0133) and foundation (TK0134) stations for the first (M7.7) and the second (M7.6) mainshocks. The TK0133 and TK0134 stations are located at distances of 115.76 km and 115.66 km from the epicenter of the first mainshock (M7.7), and at distances of 126.52 km and 126.52 km, respectively, from the epicenter of the second mainshock (M7.6) [35]. The acceleration and displacement time histories and spectra at the crest station

(TK0133) in the E-W (dam axis), N-S (stream), and vertical (U) directions are displayed in Figure 20 for the first mainshock (M7.7). The duration of the record is approximately 100 s. It can be seen from Figure 20 that the seismometer at the dam crest station (TK0133) measured peak accelerations of 74.04 cm/s^2 in the dam axis (E-W), 77.18 cm/s^2 in the stream (N-S), and 39.55 cm/s^2 in the vertical (U) directions. The largest crest acceleration occurred in the stream (N-S) direction. Additionally, Figure 20 shows that the values of acceleration response spectra calculated for a 5% damping ratio at the dam crest station (TK0133) have high values between the period range of 0.1 s to 0.75 s. The peak displacements at the crest point in the dam axis (E-W), stream (N-S) and vertical (U) directions are 5.70 cm, 7.51 cm and 9.95 cm for the M7.7 earthquake. Following the first mainshock earthquake of M7.7, the dominant periods of the dam were calculated as 0.41 s in the dam axis (E-W), 0.50 s in the stream (N-S), and 0.38 s in the vertical (U) directions.



(**a**) Acceleration time histories and spectra

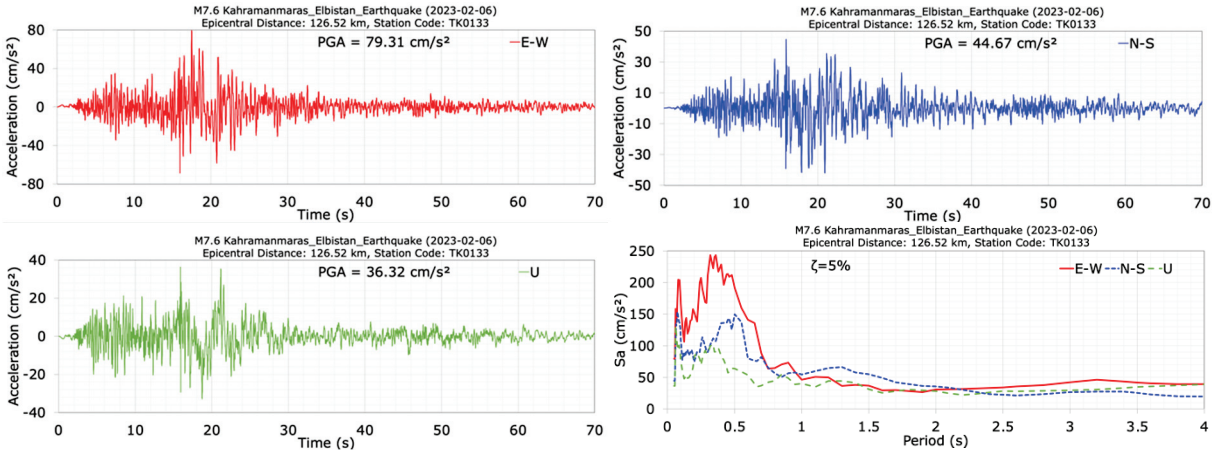


(**b**) Displacement time histories and spectra

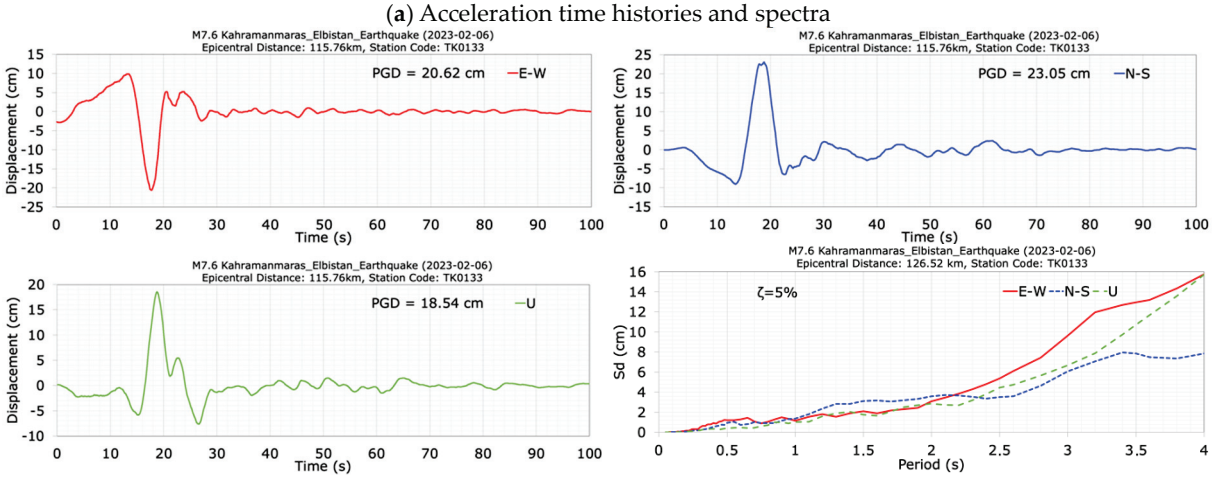
Figure 20. Acceleration (**a**) and displacement (**b**) time histories and spectra at the dam crest station (TK0133) during the M7.7 earthquake.

The acceleration and displacement time histories recorded at the dam crest station (TK0133) in the E-W (along the dam axis), N-S (along the stream) and vertical (U) directions are shown in Figure 21 for the second mainshock earthquake (M7.6). The duration of the records is approximately 70 s. The peak accelerations of 79.31 cm/s^2 in the dam axis direction (E-W), 44.67 cm/s^2 in the stream (N-S), and 36.32 cm/s^2 in the vertical (U) directions were measured at the dam crest station (TK0133). The largest crest acceleration occurred in the dam axis (E-W) direction. The damping ratios calculated for the M7.7 earthquake's N-S component and the M7.6 earthquake's E-W component, taking into account the maximum acceleration components recorded at the crest of the Feke II RCC

dam, are 3.47% and 7.06%, respectively. The values of horizontal acceleration response spectra calculated for a 5% damping ratio at the dam crest station (TK0133) have effective values between the period range of 0.1 s to 0.75 s. The obtained peak displacements for the crest point in the E-W (dam axis), N-S (stream) and vertical (U) directions are 20.62 cm, 23.05 cm and 18.54 cm, respectively. After the second mainshock (M7.6), which occurred 9 h after the first mainshock (M7.7), the dominant periods of the dam in the dam axis (E-W), stream (N-S), and vertical (U) directions are calculated as 0.40 s, 0.40 s, 0.33 s, respectively.



(**a**) Acceleration time histories and spectra



(**b**) Displacement time histories and spectra

Figure 21. Acceleration (**a**) and displacement (**b**) time histories and spectra at the dam crest station (TK0133) during the M7.6 earthquake.

The changes in the dam dominant periods in the dam axis (E-W), stream (N-S), and vertical (U) directions, calculated from the evaluation of acceleration records measured at the dam crest station (TK0133) for the M4.5, M7.7 and M7.6 earthquakes, are illustrated in Figure 22. The recorded dominant periods of the Feke II roller-compacted concrete dam, with a crest length-to-height ratio of 3.61, during the M4.5, M7.7 and M7.6 earthquakes in the dam axis (E-W), stream (N-S), and vertical (U) directions range from 0.48 s to 0.41 s, 0.33 s to 0.40 s, and 0.30 s to 0.33 s, respectively. It can be seen from Figure 22 that the dominant periods of the dam in the dam axis (E-W), stream (N-S), and vertical (U) directions show a noticeable change before, during, and after the mainshocks. During the first (M7.7) and second (M7.6) mainshocks, the dominant periods in the stream (N-S) and vertical (U) directions lengthened according to the earthquake (M4.5). The increases in the dominant periods in the stream direction (N-S) for the M7.7 and M7.6 earthquakes are 34% and 17.5%, respectively. While the dominant periods in the dam axis (E-W) decrease by 17.07% and 20.0%, those in the vertical (U) direction increase by 21.05% and 9.09% after the first (M7.7) and second (M7.6) mainshocks. The first (M7.7) and the second (M7.6) mainshock

earthquakes did not cause any visible seismic damage, cracks or deformation to the dam body or the site (Figure 18).

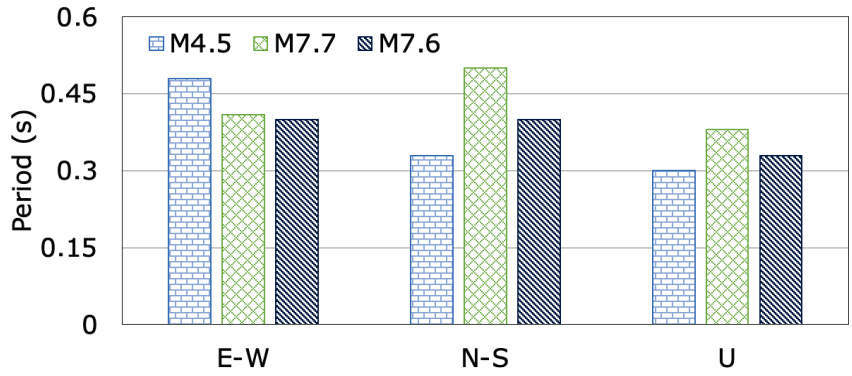


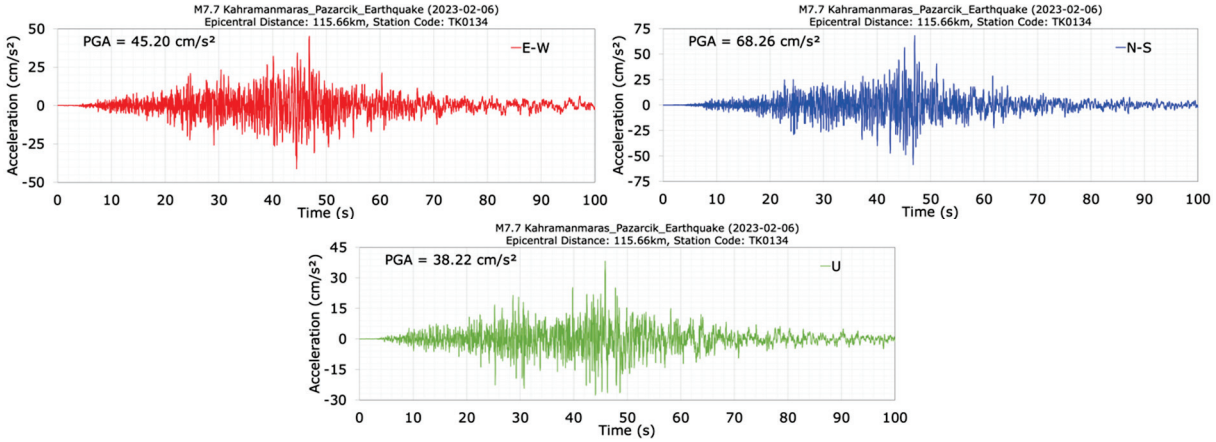
Figure 22. The changes in dominant periods of Feke II Dam during the M4.5, M7.7 and M7.6 earthquakes.

The acceleration time histories measured at the foundation of the dam (TK0134) during the M7.7 and M7.6 mainshock earthquakes are depicted in Figure 23. Maximum accelerations measured at the dam crest (TK0133) and the foundation (TK0134) stations, and crest amplification ratios relative to the foundation in the E-W, N-S, and vertical (U) directions are summarized in Table 5. The station at the foundation (TK0134) was located 52.0 m below the dam crest station (TK0133). For the M7.7 earthquake, the crest acceleration amplification ratios relative to the foundation in the E-W (dam axis), N-S (stream), and U (vertical) directions were calculated as 1.64, 1.13, and 1.03, respectively. The corresponding acceleration amplification ratios in the E-W, N-S, and vertical directions were 1.71, 0.85, and 1.02 for the M7.6 earthquake. During the M7.7 earthquake, an increase in crest accelerations relative to the foundation was observed for all acceleration components. For the M7.6 earthquake, an increase in crest accelerations relative to the foundation was observed in the E-W (dam axis) and vertical (U) directions, while a decrease was observed in the N-S (stream) direction. The maximum crest acceleration amplification ratios for the M7.7 and M7.6 earthquakes were calculated in the N-S (stream) direction as 1.13 and 0.85, respectively.

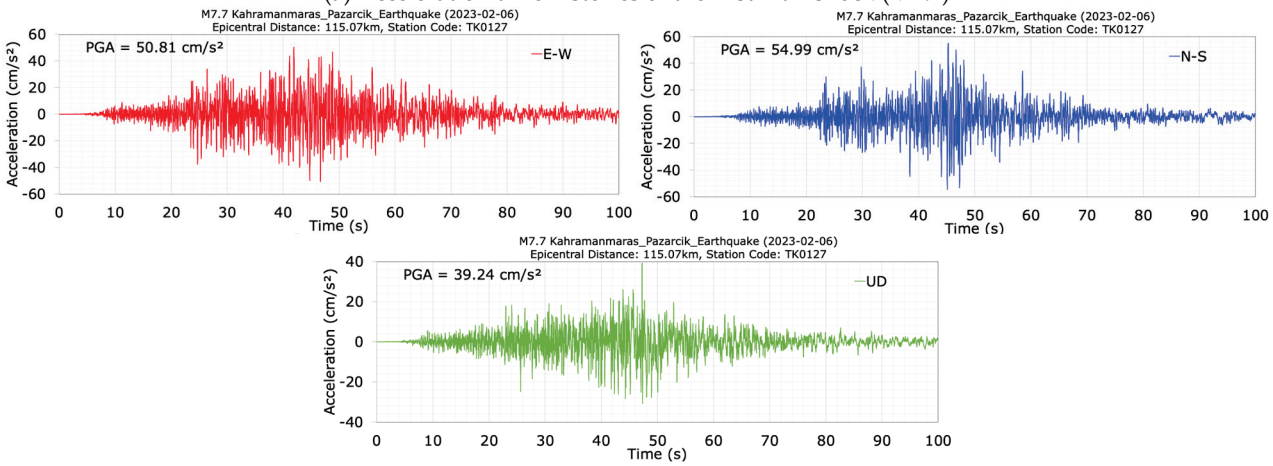
Table 5. Comparison of peak ground accelerations recorded at the dam crest (TK0133) and foundation (TK0134) stations for the M7.7 and M7.6 earthquakes.

Location	Peak Ground Acceleration (cm/s^2)					
	E-W		N-S		U	
	M7.7	M7.6	M7.7	M7.6	M7.7	M7.6
Crest	74.04	79.31	77.18	44.67	39.55	36.32
Foundation	45.20	46.50	68.26	52.74	38.22	35.52
Ratio of Crest/Foundation	1.64	1.71	1.13	0.85	1.03	1.02

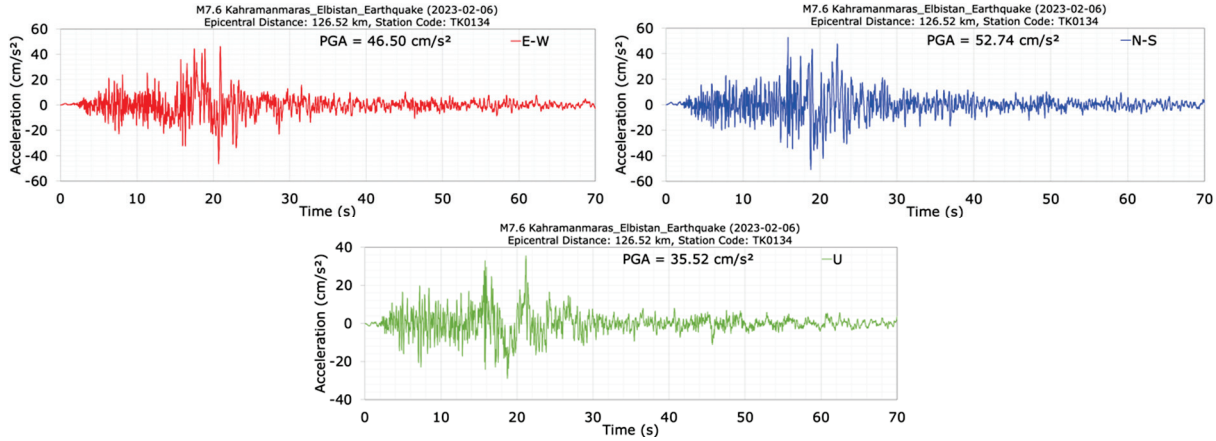
The acceleration data recorded at the TK0127 station, located 9.44 km northeast of the Feke II dam during the M7.7 mainshock, is shown in Figure 23b. This station, situated on moderately stiff ground with a shear wave velocity (Vs30) of 583 m/s, is 115.07 km from the earthquake epicenter. The right foundation of the dam is located 115.66 km from the M7.7 epicenter. As seen in Figure 23b, the maximum accelerations recorded at the TK0127 station during the M7.7 earthquake in the E-W, N-S, and vertical directions are 50.81 cm/s^2, 54.99 cm/s^2, and 35.52 cm/s^2, respectively. In comparison, the acceleration values recorded at the right abutment of the dam during the same event are 45.20 cm/s^2, 68.26 cm/s^2, and 38.22 cm/s^2 for the E-W, N-S, and vertical (U) components, respectively. The acceleration values at TK0127 are comparable to those at the dam foundation. Additionally, the frequency content of the acceleration records at the dam foundation is similar to that of the TK0127 station data.



(**a**) Acceleration time histories of the first mainshock (M7.7)



(**b**) Acceleration time histories recorded at the TK0127 station



(**c**) Acceleration time histories of the second mainshock (M7.6)

Figure 23. Acceleration time histories at the foundation station (TK0134) (**a**) and TK0127 station (**b**) during the first (M7.7) and the second (M7.6) (**c**) mainshocks.

4. Conclusions

The seismic behavior of undamaged earthfill, concrete-faced rockfill (CFRD), and roller-compacted concrete (RCC) dams subjected to the 6 February 2023 Kahramanmaraş earthquakes in Türkiye was evaluated and discussed in this paper. This evaluation considers the acceleration data recorded at the dam crests, abutments and foundations during the pre-shock (M4.4), main shocks (M7.7 and M7.6), and aftershock (M6.6). The findings are outlined as follows:

- The M7.7 and M7.6 mainshocks, along with the M6.6 aftershock, did not cause any visible seismic damage, cracks, or permanent deformations to the Tahtaköprü earthfill, Kavşak Bendi concrete-faced rockfill or Feke II roller-compacted concrete dam dams.
- The dominant periods of the Tahtaköprü earthfill, Kavşak Bendi concrete-faced rockfill, and Feke II roller-compacted concrete dams in the stream, dam axis, and vertical directions generally increased by different ratios following the two main shocks (M7.7 and M7.6) and the aftershock (M6.6).
- The maximum damping ratios for the Tahtaköprü earthfill, Kavşak Bendi concrete-faced rockfill, and Feke II RCC dams during the earthquakes were 10.69%, 7.98% and 7.06%, respectively.
- The Tahtaköprü earthfill dam experienced significant horizontal crest displacements during the first main shock (M7.7). However, no permanent deformation was observed at the dam crest or the body. This can be attributed to the elastic behavior of materials, effective damping mechanisms, temporary nature of seismic forces, compaction and redistribution of materials, and the dam's geometric configuration.
- The acceleration amplification ratios at the crest of the Tahtaköprü earthfill, Kavşak Bendi concrete-faced rockfill and Feke II RCC dams in the stream, dam axis, and vertical directions generally increased in varying amounts relative to the abutments and foundation following the two mainshocks (M7.7 and M7.6) and the aftershock (M6.6).
- The right and left abutments of the Tahtaköprü earthfill, Kavşak Bendi concrete-faced rockfill and Feke II RCC dams exhibited significantly different behaviors during the two mainshocks (M7.7 and M7.6) and the aftershock (M6.6).
- The acceleration time histories recorded at the crests of the dams exhibit distinct frequency content compared to those from the abutments and foundation.
- The 3D numerical models of the Tahtaköprü earthfill, Kavşak Bendi concrete-faced rockfill and Feke II RCC dams can be calibrated using the data and findings in this study, and the earthquake safety of the dams can be determined for different earthquake scenarios that may occur in the future and necessary repair and strengthening measures can be taken.

Author Contributions: Conceptualization, A.B., M.A., C.E.V., T.Y.Y. and E.H.; Methodology, A.B., M.A., C.E.V., T.Y.Y. and E.H.; Software, A.B.; Validation, A.B., M.A., C.E.V., T.Y.Y. and E.H.; Formal analysis, A.B.; Investigation, A.B., M.A., C.E.V., T.Y.Y. and E.H.; Data curation, A.B., M.A., C.E.V., T.Y.Y. and E.H.; Writing—original draft, A.B., M.A., C.E.V., T.Y.Y. and E.H.; Writing—review & editing, A.B., M.A., C.E.V., T.Y.Y. and E.H.; Visualization, A.B., M.A., C.E.V., T.Y.Y. and E.H. All authors have read and agreed to the published version of the manuscript.

Funding: This research received no external funding.

Data Availability Statement: The datasets generated during and/or analyzed during the current study are available from the corresponding author on reasonable request.

Acknowledgments: The authors would like to express sincere thanks to the General Directorate of State Hydraulic Works (DSI) and Disaster and Emergency Management Authority (AFAD).

Conflicts of Interest: The authors declare no conflicts of interest.

References

1. Bayraktar, A.; Kartal, M.E. Linear and nonlinear response of concrete slab on CFR dam during earthquake. *Soil Dyn. Earthq. Eng.* **2010**, *30*, 990–1003. [CrossRef]
2. Bayraktar, A.; Ventura, C.E.; Yang, T.Y.; Hökelekli, E.; Taş, Y. Observed damage behavior of earth dams during the Kahramanmaraş, Turkey, earthquakes (M = 7.7, M = 7.6) of February 6, 2023. *Geotech. Geol. Eng.* **2024**, TDMSK-127. Available online: https://www.tdmd.org.tr/TR,84/bildiriler.html (accessed on 23 September 2024). [CrossRef]
3. Chen, G.; Jin, D.; Mao, J.; Gao, H.; Wang, Z.; Jin, L.; Li, Y.; Li, X. Seismic damage and behavior analysis of earth dams during the 2008 Wenchuan earthquake, China. *Eng. Geol.* **2014**, *180*, 99–129. [CrossRef]
4. Gazetas, G. Seismic response of earth dams: Some recent developments. *Soil Dyn. Earthq. Eng.* **1987**, *6*, 1–47. [CrossRef]
5. Gazetas, G. Seismic analysis and design of rockfill dams: State-of-the-art. *Soil Dyn. Earthq. Eng.* **1992**, *11*, 27–61. [CrossRef]

6. Gordan, B.; Raja, M.A.; Armaghani, D.J.; Adnan, A. Review on dynamic behaviour of earth dam and embankment during an earthquake. *Geotech. Geol. Eng.* **2022**, *40*, 3–33. [CrossRef]
7. ICOLD. *Dam Failures Statistical Analysis*; Bulletin 99; International Commission on Large Dams (ICOLD): Paris, France, 1995.
8. Okamoto, S. *Introduction to Earthquake Engineering*; University of Tokyo Press: Tokyo, Japan, 1973.
9. Sasaki, T. *Analysis of Acceleration Data of Dams Collected by JCOLD*; Tentative Report, Seismic Aspects of Dam Design; ICOLD: Stavanger, Norway, 2015.
10. Seed, H.B.; Makdisi, F.I.; De Alba, P. *The Performance of Earth Dams During Earthquakes*; Report No. UCB/EERC-77/20; University of California, Berkeley: Berkeley, CA, USA, 1977.
11. Tani, S. Damage to earth dams. *Spec. Issue Soils Found.* **1996**, *36*, 263–272. [CrossRef] [PubMed]
12. Tani, S. Behavior of large fill dams during earthquake and earthquake damage. *Soil Dyn. Earthq. Eng.* **2000**, *20*, 223–229. [CrossRef]
13. Tani, S. Earthquake damage to fill dams in Japan. *Jpn. Agric. Res. Q.* **2000**, *34*, 39–48. Available online: https://www.jircas.go.jp/sites/default/files/publication/jarq/34-1-039-048_0.pdf (accessed on 1 August 2024).
14. Tani, S.; Nakashima, M. Earthquake damage to earth dams in Japan-maximum epicentral distance to cause damage as a function of magnitude. *Soil Dyn. Earthq. Eng.* **1999**, *18*, 593–602. [CrossRef]
15. USCOLD. *Observed Performance of Dams during Earthquakes*; United States Committee on Large Dams: Denver, CO, USA, 2000.
16. Zhang, L.; Peng, M.; Chang, D.; Xu, Y. *Dam Failure Mechanisms and Risk Assessment*; John Wiley & Sons: Singapore, 2016.
17. Costigliola, R.M.; Mancuso, C.; Pagano, L.; Silvestri, F. Prediction of permanent settlements of an upstream faced earth dam. *Comput. Geotech.* **2022**, *144*, 104594. [CrossRef]
18. Sica, S.; Russo, A.D. Seismic response of large earth dams in near-source areas. *Comput. Geotech.* **2021**, *132*, 103807. [CrossRef]
19. Pells, S.; Fell, R. *Damage and Cracking of Embankment Dams by Earthquake and the Implications for Internal Erosion and Piping*; UNICIV Report No. R-408; The University of New South Wales: Sydney, Australia, 2002; ISBN 85841 375 2.
20. Matsumoto, N. The recent earthquakes and dam safety in Japan: Analysis of observed seismic data. In Proceedings of the ICOLD Europe 2010, Innsbruck, Austria, 22–23 September 2010; Available online: https://www.ancold.org.au/wp-content/uploads/2014/09/Recent-earthquakes-and-dam-safety-in-Japan.pdf (accessed on 1 August 2024).
21. Matsumoto, N.; Sasaki, T.; Sato, N. Effects of the 2011 Tohoku Earthquake on dams (1)-Characteristics of ground motion. *J. Jpn. Soc. Dam Eng.* **2012**, *22*, 28–36. [CrossRef]
22. Zhang, C. The performance of dams during the Wenchuan 5-12 earthquake and lessons learned from the event. *J. F Earthq. Tsunami* **2011**, *5*, 309–327. [CrossRef]
23. Zou, D.; Xu, B.; Kong, X.; Liu, H.; Zhou, Y. Numerical simulation of the seismic response of the Zipingpu concrete face rockfill dam during the Wenchuan earthquake based on a generalized plasticity model. *Comput. Geotech.* **2013**, *49*, 111–122. [CrossRef]
24. AFAD. *February 06, 2023 Kahramanmaraş (Pazarcık and Elbistan) Earthquakes Field Study Preliminary Assessment Report*; Disaster and Emergency Management Presidency (AFAD): Ankara, Türkiye, 2023. Available online: https://deprem.afad.gov.tr/assets/pdf/Arazi_Onrapor_28022023_surum1_revize.pdf (accessed on 1 August 2024). (In Turkish)
25. BDG. *Preliminary Assessments on the Effects of 6 February 2023 Pazarcik (Mw 7.7) and Elbistan (Mw7.6) Earthquakes on Dams in the Region and Possible Problems That Occur in the Future*; Dam Safety Association: Ankara, Türkiye, 2023; Available online: https://www.barajguvenligi.com/sayfa/23/iki-buyuk-depremin-barajlar-uzerindeki-etkisini-degerlendiren-on-rapor (accessed on 1 August 2024). (In Turkish)
26. Çetin, K.Ö.; Ilgaç, M. *Reconnaissance Report on February 6, 2023 Kahramanmaraş-Pazarcık (Mw = 7.7) and Elbistan (Mw = 7.6) Earthquakes*; Türkiye Earthquake Reconnaissance and Research Alliance: Ankara, Türkiye, 2023.
27. EERI. *2023 Türkiye Earthquake Sequence Joint Preliminary Virtual Reconnaissance Report (PVRR)*; NHERI Design Safe Project ID: PRJ-3824; EERI: Oakland, CA, USA, 2023.
28. Erdik, M.; Tümsa MB, D.; Pınar, A.; Altunel, E.; Zülfikar, A.C. A Preliminary Report on the February 6, 2023 Earthquakes in Türkiye. *Temblor*, 24 February 2023. [CrossRef]
29. Hancılar, U.; Şeşetyan, K.; Çaktı, E.; Şafak, E.; Yenihayat, N.; Malcıoğlu, F.S.; Dönmez, K.; Tetik, T.; Süleyman, H. *Kahramanmaraş-Gaziantep Türkiye M7.7 Earthquake, 6 February 2023 (04:17 GMT+03:00) Strong Ground Motion and Building Damage Estimations Preliminary Report (v6)*; Boğaziçi University: Istanbul, Türkiye, 2023.
30. SBB. *2023 Kahramanmaraş and Hatay Earthquakes Report*; Presidency of Strategy and Budget: Ankara, Türkiye, 2023. Available online: https://www.sbb.gov.tr/wp-content/uploads/2023/03/2023-Kahramanmaras-and-Hatay-Earthquakes-Report.pdf (accessed on 1 August 2024).
31. USGS. *The 2023 Kahramanmaraş, Turkey, Earthquake Sequence*; United States Geological Survey: Reston, VA, USA, 2024. Available online: https://earthquake.usgs.gov/storymap/index-turkey2023.html (accessed on 1 August 2024).
32. Balkaya, M.; Ozden, S.; Akyüz, H.S. Morphometric and Morphotectonic characteristics of Sürgü and Çardak Faults (East Anatolian Fault Zone). *J. Adv. Res. Nat. Appl. Sci.* **2021**, *7*, 375–392. [CrossRef]
33. MTA. *Türkiye Active Fault Maps*; General Directorate of Mineral Research and Exploration (MTA): Ankara, Türkiye, 2023. (In Turkish)
34. Karabacak, V.; Altunel, E.; Meghraoui, M.; Akyüz, H.S. Field evidences from northern Dead Sea Fault Zone (South Turkey): New findings for the initiation age and slip rate. *Tectonophysics* **2010**, *480*, 172–182. [CrossRef]
35. AFAD. *Disaster and Emergency Management Presidency (AFAD), Ankara, Türkiye, 2023*. Available online: https://deprem.afad.gov.tr/home-page (accessed on 1 August 2024).

36. Duman, T.Y.; Emre, Ö. The East Anatolian Fault: Geometry, segmentation and jog characteristics. *Geol. Soc. Lond. Spec. Publ.* **2013**, *372*, 495–529. [CrossRef]
37. Aydın, S.; Karabulut, İ.; Er, Y. Tahtaköprü Dam upgrade and evaluation of dynamic performance. In Proceedings of the 3rd Turkey Earthquake Engineering and Seismology Conference, Dokuz Eylül Üniversitesi, İzmir, Türkiye, 14–16 October 2015; Available online: https://www.tdmd.org.tr/pdf/pdf2015/TDMSK_127.pdf (accessed on 1 August 2024). (In Turkish).

Disclaimer/Publisher's Note: The statements, opinions and data contained in all publications are solely those of the individual author(s) and contributor(s) and not of MDPI and/or the editor(s). MDPI and/or the editor(s) disclaim responsibility for any injury to people or property resulting from any ideas, methods, instructions or products referred to in the content.

sensors

MDPI

Article

Analytical Equations for the Prediction of the Failure Mode of Reinforced Concrete Beam–Column Joints Based on Interpretable Machine Learning and SHAP Values

Ioannis Karampinis [1], Martha Karabini [2], Theodoros Rousakis [2], Lazaros Iliadis [1] and Athanasios Karabinis [2,*]

[1] Laboratory of Mathematics and Informatics (ISCE), Department of Civil Engineering, Democritus University of Thrace, 67100 Xanthi, Greece; ikarampi@civil.duth.gr (I.K.); liliadis@civil.duth.gr (L.I.)

[2] Laboratory of Reinforced Concrete and Seismic Design, Department of Civil Engineering, Democritus University of Thrace, 67100 Xanthi, Greece; mkarampi@civil.duth.gr (M.K.); trousak@civil.duth.gr (T.R.)

* Correspondence: akarabin@civil.duth.gr

Abstract: One of the most critical components of reinforced concrete structures are beam–column joint systems, which greatly affect the overall behavior of a structure during a major seismic event. According to modern design codes, if the system fails, it should fail due to the flexural yielding of the beam and not due to the shear failure of the joint. Thus, a reliable tool is required for the prediction of the failure mode of the joints in a preexisting population of structures. In the present paper, a novel methodology for the derivation of analytical equations for this task is presented. The formulation is based on SHapley Additive exPlanations values, which are commonly employed as an explainability tool in machine learning. Instead, in the present paper, they were also utilized as a transformed target variable to which the analytical curves were fitted, which approximated the predictions of an underlying machine learning model. A dataset comprising 478 experimental results was utilized and the eXtreme Gradient Boosting algorithm was initially fitted. This achieved an overall accuracy of ≈84%. The derived analytical equations achieved an accuracy of ≈78%. The corresponding metrics of precision, recall, and the F1-score ranged from ≈76% to ≈80% and were close across the two modes, indicating an unbiased model.

Keywords: reinforced concrete; beam–column joints; failure mode prediction; machine learning; SHAP; analytical equations

1. Introduction

One of the most critical aspects that affect the overall behavior of a reinforced concrete (RC) structure during a major seismic event pertains to the mechanical behavior of its beam–column joints [1]. Joints support adjacent beams and slabs and, thus, their failure can lead to structural destabilization and part of the structure collapsing, potentially endangering human lives [2]. This mechanical behavior is largely described by two distinct and complementary aspects. On the one hand, the total strength of the joint provides a quantification of the capacity of the system in terms of shear forces. On the other hand, the qualitative behavior of the joint in terms of its failure mode can be an even more important factor in terms of the overall safety of the system and the amount of seismic energy it can absorb.

Qualitatively, there are two primary failure modes that an RC beam–column joint system can exhibit [3]. In the first one, the longitudinal reinforcement bars in the adjacent beam are the first to reach their yield capacity. However, the system maintains its stability and, furthermore, due to a phenomenon known as hardening [4], the beam can absorb further amounts of seismic energy until either the reinforcement bars or the concrete fail [2]. In the second case, the joint fails due to shear prior to the beam reaching the aforementioned yielding point. This failure mode is fundamentally different from the

previous one. Contrary to the ductile, yielding failure mode caused by bending, the joint failure due to shear is sudden, brittle, and leads to the destabilization of the system. In addition, no further amounts of energy can be absorbed.

To this end, modern design codes [5–7] are often grounded in the so-called principle of ductility, mandating that, if failure is to occur, the first failure mode is to be preferred. Thus, given the large number of existing RC structures, the prediction of the failure modes of their joints is crucial. If a structure does not abide by the standards imposed by modern design codes, preventative steps might be required [8,9]. Thus, significant research efforts have been dedicated to this task, both from a theoretical and an experimental perspective [10–13].

From a different perspective, the proliferation of machine learning (ML) methodologies has allowed for the implementation of powerful ML algorithms in many engineering challenges, producing state-of-the-art results [14,15]. Specifically for the task of RC beam–column joint failure mode prediction, several researchers have previously examined the problem from different perspectives.

In particular, Kotsovou et al. [16] utilized artificial neural networks (ANNs) to estimate the total strength of exterior joints and predict their failure mode. Similarly, Suwal and Guner also employed ANN algorithms in their work [17]. However, contrary to [16], they worked on a more extensive dataset, which included interior joints as well. Mangathalu and Jeon [18] experimented with various ML algorithms to predict both the strength of a joint as well as its failure mode. This included the implementation of so-called intrinsically explainable models [19], such as LASSO logistic regression, which also produced analytical expressions. However, the results presented therein were unbalanced, as the model was greatly skewed in favor of one of the failure modes. Marie et al. [20] employed several algorithms, including support vector machines (SVMs), ordinary least squares (OLS), and non-parametric kernel regression, to estimate joints' ultimate bearing capacity. Lastly, Gao and Lin [21] utilized models such as k-nearest neighbors (k-NN), eXtreme Gradient Boosting (XGBoost), ANNs, and random forest to predict an RC beam–column joint failure mode. They also utilized the SHapley Additive exPlanations (SHAP values) explainability algorithm to quantify the overall significance of each of their considered input features in the model predictions.

The research presented herein exhibits notable novel elements. A novel methodology for the derivation of analytical equations for the prediction of the RC joint failure mode is presented. The methodology is based on a recently developed modeling approach [22], which utilizes SHAP values as a basis to form simplified analytical expressions that approximate the predictions of the underlying ML model. SHAP is a feature attribution algorithm. This means that the predictions of the underlying model are decomposed into terms corresponding to the contribution of each individual feature. Thus, it is often employed to quantify the magnitude of the total effect of each feature in an outcome [21]. In the work presented herein, SHAP values were not only employed to gauge the importance of each feature, i.e., to identify which features should be utilized in a potential analytical expression. Rather, SHAP values themselves formed the basis of these analytical expressions.

Therefore, the methodology presented herein offers several distinct advantages in comparison to the currently established literature, such as the LASSO logistic regression mentioned above. Firstly, feature selection was carried out in an informed manner, utilizing SHAP, and components were added to the resulting equations incrementally. Secondly, this allowed for the tradeoff between model complexity and accuracy to be tuned, depending on the specific application at hand. Thirdly, the form of the terms corresponding to each individual feature were adjusted independently. In addition, this was not carried out blindly, but rather in an informed manner, guided by the form of the respective SHAP scatter plots, as it is shown in Section 3.2. Finally, so-called precision–recall (P-R) curves were employed to demonstrate how the resulting equations could be further fine-tuned, depending on the requirements of the application at hand.

2. Materials and Methods

2.1. Dataset Overview and Feature Engineering

The dataset that was employed in the present study comprised experimental measurements of reinforced concrete beam–column joints. A total of 486 specimens were contained in the dataset, which were originally collected by Suwal and Guner [17] from 153 studies previously published in the literature. The experiments pertained to the cyclic loading of beam–column joint systems until failure occurred, mimicking their behavior during a significant seismic event. In all cases, the applied load at the moment of failure was measured using appropriately placed sensors. In addition, the failure mode of each specimen was also recorded. Thus, each input vector in the original dataset was described by the following 14 attributes [17]:

1. The joint type: This categorical variable described whether the joint was "interior", i.e., beams are attached on two opposing sides, or "exterior".
2. f_c: The compressive strength of the concrete, measured in MPa.
3. ρ_{jt}: The amount of transverse reinforcement, i.e., stirrups, in the joint, expressed as a percentage of its area.
4. f_{yjt}: The yield strength of the stirrups in the joint, measured in MPa.
5. ρ_b, ρ_c: The amount of longitudinal reinforcement in the beam and column, respectively, expressed as a percentage of the respective cross-sectional areas.
6. f_{yb}, f_{yc}: The yield strength of the longitudinal reinforcement in the beam and column, respectively, measured in MPa.
7. h_b, h_c, b_b, b_c: The height (h) and width (b) of the beam and column, respectively, measured in mm.
8. ALF: The axial load factor, i.e., the axial load applied to the column normalized to the respective compressive strength f_c.
9. The failure mode: This was the dependent variable in the present study and took two distinct values. Specifically, the value "Joint Shear" ("JS") corresponded to cases where the joint failed suddenly in a brittle, shear manner and the beam had not yet reached its yield capacity. Accordingly, the value "Beam Yield-Joint Shear" ("BY-JS") pertained to specimens wherein the ductile flexural yielding of the beam reinforcement preceded the brittle shear failure of the joint [3].

As was stated in the Introduction, the aim of the present study was to obtain simple, analytical expressions to predict the failure mode of the joints based on the independent variables/features. Thus, the input features were critical to the proposed formulation and, to this end, a procedure known as feature engineering [23] was performed on the original dataset. It should be highlighted that feature engineering is more general and more involved than preprocessing a dataset. Indeed, preprocessing steps often include the appropriate scaling of the features [24], removing outliers, or imputing missing values [25]. On the other hand, feature engineering can also include the generation of new features from existing ones, which can be more appropriate for specific modeling purposes.

To this end, in the present study, each reinforcement percentage ρ_x was multiplied by the respective yield stress f_x. This resulted in three new features, denoted by ρf_x, where $x =$ "yjt", "yb", and "yc" for the joint, beam, and column, respectively. Furthermore, the heights of the beam and column where combined into a single feature by obtaining the ratio h_b/h_c. Thus, the original set of 13 independent variables was reduced to only 7. Finally, in 8 out of 486 instances (1.65%) the compressive strength of the concrete was over 100 MPa. These are considered extreme values for this feature [5] and, thus, this small subsample was removed from the dataset.

Figure 1 shows the distribution of the attributes that were included in the final dataset after feature engineering. It can be observed that approximately 53.35% of specimens belonged to the failure mode "JS" and the remaining 46.65% belonged to "BY-JS". A large gap between the two would indicate the presence of what is known as the class imbalance problem [26,27]. This can lead to the degradation of the performance of any ML model, and

specialized techniques exist in the literature to address it [28,29]. However, in the present study, the distribution of the failure modes was balanced and, thus, the implementation of such techniques was not necessitated. Finally, Figure 2 presents an indicative RC beam–column joint, as well as the two considered failure modes, for illustration.

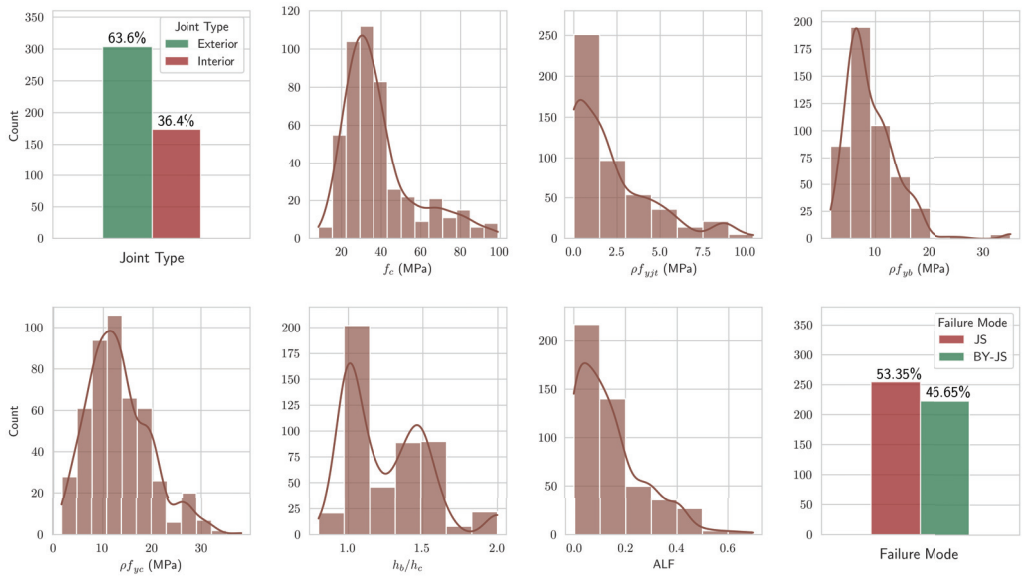


Figure 1. The distribution of the input features and the failure mode in the final dataset, after feature engineering.

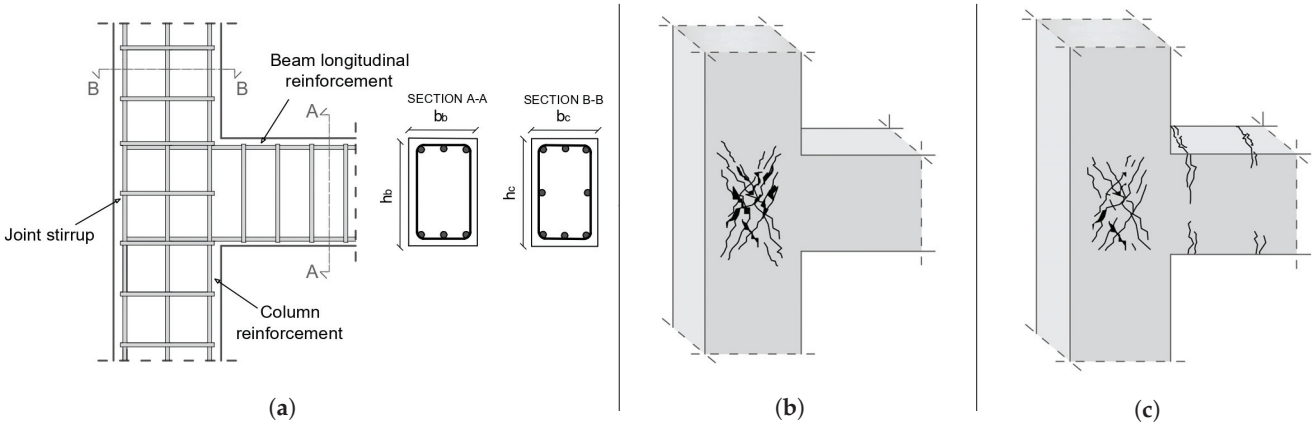


Figure 2. (**a**) Indicative beam–column joint, (**b**) JS failure mode, and (**c**) BY-JS failure mode.

2.2. Machine Learning Modeling

There are a large number of readily available classification algorithms that can be implemented for the task of the prediction of the failure mode of joints [30,31]. However, as was previously mentioned, the goal of the present study was not to exhaustively search the many available algorithms to identify the best possible machine learning model. Rather, the aim was to utilize the predictions of one such model, in conjunction with the SHAP values explainability technique, as a basis to produce simplified, analytical equations for the prediction of the failure mode. As is shown in the following, the SHAP values approximate the behavior of the underlying ML model. Given that they were fundamental to the proposed formulation, their reliability had to be ensured and thus, it was important for the underlying ML model to obtain a sufficiently high accuracy. To this end, there exist many readily available classification algorithms in the literature.

In the present study, the so-called eXtreme Gradient Boosting (XGBoost) [32] algorithm was employed, which has been successfully utilized in similar studies [2,21]. The funda-

mental idea of this algorithm is to combine a group of so-called "weak learners" (usually decision trees) in a powerful ensemble model via an iterative procedure called boosting [33]. Thus, the final model takes the form of the following Equation (1) [32,33]:

$$f(\boldsymbol{x}) = \sum_{m=1}^{N_E} \lambda_m f_m(\boldsymbol{x}; \boldsymbol{\theta}_m) \tag{1}$$

In the above equation, f_m are the base models of the ensemble, $\boldsymbol{\theta_m}$ and λ_m are the learned model parameters as well as the respective weights, and N_E is the maximum number of base models in the ensemble and is one of the user-defined hyperparameters. In the present study, a maximum number of $N_E = 10$ trees were employed, each with a maximum depth of 3 and a maximum number of leaves equal to 5. These were selected using a trial-and-error approach, in order to obtain a sufficiently high accuracy without overfitting.

In addition to XGBoost being a very powerful algorithm, it offers several advantages in comparison to other popular classification algorithms, such as artificial neural networks (ANNs) or support vector machines (SVMs). Firstly, as a tree-based algorithm, XGBoost is not susceptible to features whose ranges have different orders of magnitude, which is why no feature scaling was performed as part of the preprocessing presented in the previous section. Secondly, the tree-based nature of XGBoost offers significant computational gains. On the one hand, the ML models themselves are faster to train. On the other hand, the computation of the SHAP values, which generally can be a slow process, can be efficiently carried out using the dedicated TreeSHAP algorithm [34].

2.3. Shapley Additive Explanations (SHAP Values)

SHapley Additive exPlanations (SHAP values) [35] belong to the class of the so-called machine learning interpretability methodologies [36], which aim to explain and analyze how complex ML models arrive at their predictions. In addition, SHAP values belong to the subclass of the so-called additive feature attribution methods [35]. Fundamentally, this means that the underlying trained ML model f is locally (at each input vector $\boldsymbol{x}$) approximated by a linear function g, which is given by the following Equation (2) [35]:

$$g(\boldsymbol{x}') = \phi_0 + \sum_{i=1}^{k} \phi_i x_i' \tag{2}$$

In the above equation, k is the number of input variables, ϕ_i are the corresponding SHAP values, ϕ_0 is the average prediction of the model, and $\boldsymbol{x}' \in \{0,1\}^k$ is the so-called "simplified input" [35] and shows whether the value of each particular feature is missing or not in the input vector $\boldsymbol{x}$. The above condition is known as local accuracy [35] and ensures that the sum of the SHAP values is close to the predictions of the underlying ML model. Thus, if this model has a sufficiently high accuracy, the sum of the SHAP values will, in turn, approximate the real target variable in the dataset.

Lundberg and Su-In, who introduced SHAP values in their seminal paper [35], based the computation of these coefficients, ϕ_i, on so-called Shapley regression values. These coefficients were introduced by Lloyd Shapley in the framework of cooperative game theory [37]. Intuitively, the aim is to divide the "score" from a "game" fairly amongst the "players", according to each "player's" contribution. Formally, and following the original notation in [35], let $F = \{1, 2, ..., k\}$ denote the set of all the independent variables/features in the dataset and let $S \subseteq F$ be a subset, called a "coalition" [38]. Then, the coefficients ϕ_i are given by the following Equation (3) [35]:

$$\phi_i = \sum_{S \subseteq F \setminus \{i\}} \frac{|S|!(|F| - |S| - 1)!}{|F|!} \Big(f_{S \cup \{i\}}(\boldsymbol{x}_{S \cup \{i\}}) - f_S(\boldsymbol{x}_s) \Big). \tag{3}$$

Thus, conceptually, SHAP values are obtained as a result of a weighted averaging over all feature coalitions of the difference between the model predictions with and without the inclusion of the feature i.

In a binary classification setting utilizing XGBoost, as is the case in the present study, SHAP values decompose the so-called log-odds, or logits [34]. Specifically, one of the failure modes is designated as the generic "positive" class, while the other becomes the "negative" class. The log-odds are then given by the following equation [39]:

$$\ln\left(\frac{p}{1-p}\right) \tag{4}$$

In the above equation, p denotes the probability that a given input vector belongs to the "positive" class. In the present study, the failure mode "JS" was designated as the positive class and "BY-JS" as the "negative" one.

3. Results

In this section, the main results and findings of the present study are presented. As was previously mentioned, the ultimate goal of the proposed formulation was to derive simplified, analytical expressions for the prediction of the failure mode. This was carried out by unraveling the predictions of a fully trained ML classifier via the SHAP values explainability methodology, which was presented in the previous section. Subsequently, these SHAP values were used as a basis for the derivation of the final analytical equations.

As was mentioned, the underlying ML classifier needed to exhibit a high enough accuracy, in order to ensure the reliability of the SHAP values and, ultimately, of the analytical equations. To this end, the rest of this section is organized as follows. Firstly, Section 3.1 briefly presents the results of the XGBoost classifier presented in Section 2.2. Similar results have been analyzed in the literature [2,21]. However, they serve as the basis for the subsequent derivation of the analytical equations, which is the main novelty of the present study. This procedure is presented in Section 3.2, along with the corresponding classification metrics from the derived equations.

3.1. XGBoost Classification Results

To measure the performance of the binary classification model, several well-known metrics were employed. Specifically, we utilized the so-called precision, recall, F1-score, and overall accuracy. In a binary classification framework, these are given by the following equations [40]:

$$\text{Precision} = \frac{\text{TP}}{\text{TP} + \text{FP}} \tag{5}$$

$$\text{Recall} = \frac{\text{TP}}{\text{TP} + \text{FN}} \tag{6}$$

$$\text{F1-Score} = 2\frac{\text{Precision} \cdot \text{Recall}}{\text{Precision} + \text{Recall}} \tag{7}$$

$$\text{Accuracy} = \frac{\text{TP} + \text{TN}}{\text{TP} + \text{TN} + \text{FP} + \text{FN}} \tag{8}$$

In the above equations, TP (true positive) denotes the number of input vectors that belong to the generic "positive" class (in this case, the failure mode "JS") and are correctly assigned to it by the classifier, TN (true negative) denotes the number of input vectors that belong to the generic "negative" class (in this case, the failure mode "BY-JS") and are correctly classified, while FP (false positive) and FN (false negative) denote the input vectors that the model incorrectly assigns to the respective failure modes. It should be highlighted that the first three metrics are defined for each failure mode separately, while accuracy is an overall metric.

In order to obtain the performance metrics, a so-called k-fold cross-validation scheme was employed [41]. This procedure started by splitting the dataset into k parts. Subsequently, the algorithm iterated over these partitions and, at each iteration, it utilized the $k-1$ parts of the dataset for training, while the remaining part was used to gauge the performance of the trained model on "unseen" data. The final classification metrics were obtained as the averages of the respective metrics of each fold.

This procedure greatly reduced the variance of the obtained classification metrics, which can occur due the randomness of the train/test split. Thus, the reliability and robustness of the obtained results was increased. In the present study, $k = 10$ folds were employed. Furthermore, it should be highlighted that the cross-validation scheme was stratified [41]. This means that each train/test subset had approximately the same proportion of exterior/interior nodes and failure modes and these proportions were approximately the same as those in the original dataset.

Following the above, Figure 3 presents the cross-validated classification metrics obtained from the XGBoost classifier described in Section 2.2. As can be readily observed, the average classification accuracy using the test dataset was high, approximately 84%. The respective classification metrics of the two failure modes were relatively close to each other, indicating a model that was not skewed towards one of the two modes. This was also supported by the fact that the precision, recall, and F1-score were all relatively close to each other and to the overall accuracy.

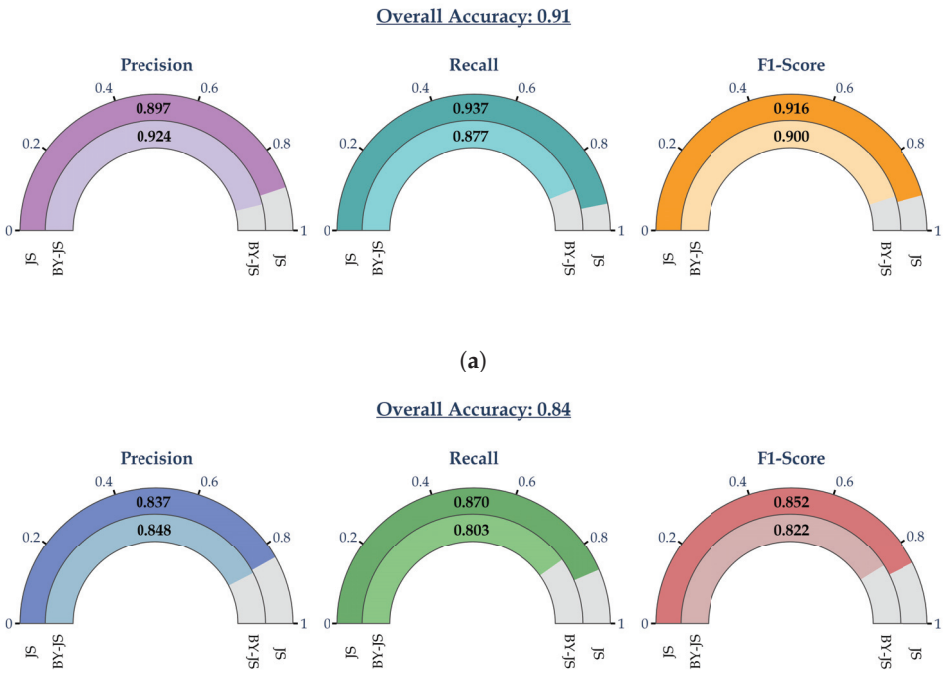


Figure 3. Classification metrics of XGBoost classifier obtained via 10-fold cross-validation. (**a**) Train dataset and (**b**) Test dataset.

3.2. Derivation of Analytical Equations

In this section, the main results and findings of the present study are presented. These pertain to the derivation of simplified, analytical equations for the rapid and efficient determination of the failure mode of reinforced concrete beam–column joints. These equations are based on the SHAP values presented in Section 2.3, and they can be constructed by sequentially and incrementally adding more terms to achieve the desired tradeoff between complexity and accuracy [22].

To this end, the first step in the proposed methodology pertained to the computation of the SHAP values, ϕ_i, for each input vector. These were computed separately for the train and test parts of each fold in the 10-fold cross-validation scheme. This facilitated the training of the analytical equations in a similar manner to the underlying ML model. Subsequently, the SHAP values were aggregated and normalized to produce a single quantifier for the overall effect of each feature on the model's predictions. Specifically, these aggregated values were obtained as follows [42]:

$$\bar{\phi}_j = \frac{\phi'_j}{\sum_{m=1}^{k} \phi'_k}, \quad \phi'_j = \frac{1}{n} \sum_{i=1}^{n} |\phi_{ij}| \tag{9}$$

In the above equation, $|\phi_{ij}|$ denotes the SHAP value corresponding to the feature j computed for the input vector i, n is the total number of such input vectors in the dataset, and k is the total number of independent variables/features. Due to the above normalization, the extracted coefficients could be interpreted as the percentage of the average influence of each feature on the model's predictions. The coefficients $\bar{\phi}_j$ were computed for each fold in the 10-fold cross-validation and their average was obtained. The results are shown in Figure 4.

It can be readily observed that the two most important numerical features were found to be f_c, with an average importance of approximately 22.3%, and ρf_{yb}, with an average importance of approximately 22.9%. The ratio of the height of the beam to the height of the column also had a relatively high importance, while the importance of the axial load factor was found to be relatively small.

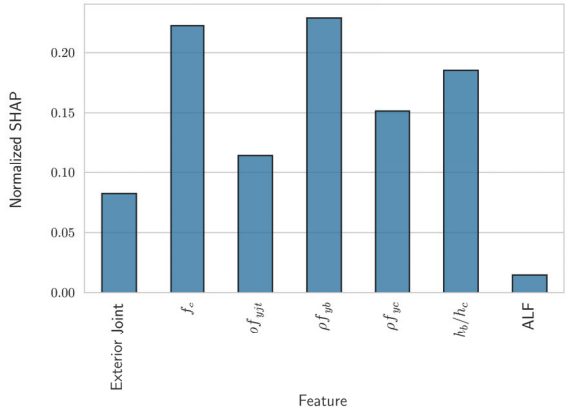


Figure 4. Cross-validated normalized SHAP values, $\bar{\phi}_j$, as in Equation (9).

As was previously discussed, the fundamental idea of the proposed methodology was to fit simplified, analytical equations to the SHAP values of each feature. These values were additive and, according to the local accuracy condition shown in Equation (2), their sum approximated the true predictions of the ML model. Thus, as was discussed in Section 2.3 and Equations (3) and (4), they approximated the logit of the probability that a given input vector belonged to the failure mode "JS".

Figure 5 presents the scatter plots of the SHAP values for the two most important features as identified in Figure 4, namely ρf_{yb} and f_c. The analytical equations that corresponded to the contribution of each feature were derived based on these scatter plots. For example, the SHAP values of ρf_{yb} could be approximated by a square root function, a logarithm, or a parabola. Similarly, the SHAP values of f_c could be approximated by a function of the form $1/x$ or an exponential.

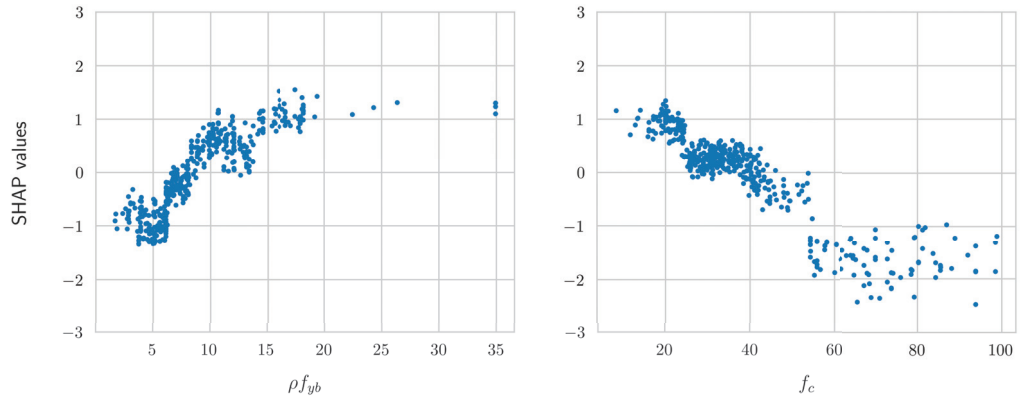


Figure 5. Scatter plots of the SHAP values of the two most significant numerical features, namely ρf_b and f_c.

In the present study, we experimented with a wide array of possible analytical functions for each feature, including polynomials of various degrees, and the aforementioned roots, logarithms, and inverses. For each feature, the form of the analytical equation that resulted in the highest accuracy was selected. The final coefficients in each case were computed by averaging the coefficients that were computed for each fold in the 10-fold cross-validation process. Figure 6 shows the scatter plots of the SHAP values of the features that were employed in the final equations, as well as the best-fitted curves that resulted from the cross-validation process. It also displays the envelope of each fitted curve, i.e., the minimums and maximums across the 10 folds. It can be readily observed that the coefficients of the fitted curves did not exhibit a huge variation across each fold, as the respective bands of the envelopes are not very large. In any case, as was previously mentioned, the 10-fold cross-validation procedure reduced the variance of the coefficients that were obtained for each particular dataset.

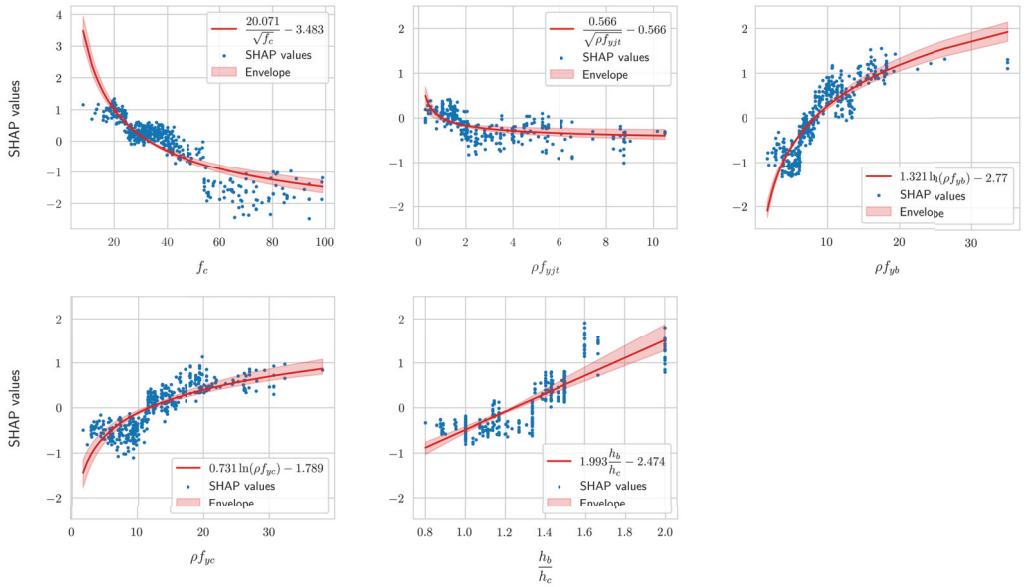


Figure 6. Scatter plots of the SHAP values of the numerical features that were employed, along with the best-fitted cross-validated curves. The envelope corresponds to the minimum and maximum values across the 10 folds.

The curves presented above are in qualitative agreement with the currently established literature with regards to the behavior of reinforced concrete beam–column joints. For example, increasing the compressive strength of the concrete and the amount or strength

of the stirrups in the joint decreases the log-odds that the given joint/input vector will exhibit the "JS" failure mode, i.e., that it will belong to the "positive" class. Additionally, increasing the amount of reinforcement in the beam or its strength results in a beam with increased strength compared to the joint, thus increasing the likelihood that the "JS" failure mode will occur. A similar observation holds for increasing the ratio of the height of the beam, compared to the height of the column. It should be noted that there is a correlation between the height of each bar in Figure 4 and the range of the respective SHAP values in the above figure. Furthermore, the variations in these values, as seen, for example, in the subplot for f_c, can be further analyzed using SHAP interaction values [34]. However, due to the excellent results achieved herein, this added complexity was not deemed justifiable. Before the final forms of the derived analytical expressions are presented, two additional points should be highlighted.

In addition, as can be observed from Figure 5, the expression for the contribution of ρf_{yjt} was not valid if $\rho f_{yjt} = 0$, i.e., if the joint had no stirrups. For those cases, the SHAP values of this feature ranged from approximately 0.36 to 0.505. Therefore, its contribution could be adequately captured using a single value, the mean. In this case, the average across the 10 folds was approximately equal to 0.429, with a standard deviation of approximately 0.055. Furthermore, as can be seen from Equation (2), in order for the condition of local accuracy to be valid, the constant ϕ_0 had to be added. This corresponded to the mean model prediction. In our case, this had an average value of approximately 0.156 across the 10 folds and a standard deviation of approximately 0.0067. It should be reiterated that these values correspond to the log-odds, as defined in Equation (4), that a given input vector/joint belonged to the failure mode "JS". Thus, if the inverse sigmoid transformation is employed to solve for the actual probability p, we obtain

$$p = \frac{1}{1 + e^{-0.156}} \approx 0.5389.$$

This means that, on average, the model predicted a 53.89% probability for the "JS" failure mode, which was close to the distribution of the original dataset, as shown in the last subplot of Figure 1. Following the above, the final derived analytical equations for the prediction of the failure mode took the following forms. Specifically, for joints with stirrups, i.e., wherein $\rho f_{yjt} > 0$, we have

$$\frac{20.071}{\sqrt{f_c}} + 1.321 \ln \rho f_{yb} + 0.731 \ln \rho f_{yc} + 1.993 \frac{h_b}{h_c} + \frac{0.566}{\sqrt{\rho f_{yjt}}} - 10.926, \tag{10}$$

while for joints without stirrups, i.e., wherein $\rho f_{yjt} = 0$, we have

$$\frac{20.071}{\sqrt{f_c}} + 1.321 \ln \rho f_{yb} + 0.731 \ln \rho f_{yc} + 1.993 \frac{h_b}{h_c} - 9.931 \tag{11}$$

The above equations were utilized to predict the failure mode of a joint as follows. First, the geometric and mechanical characteristics of the beam, column, and joint were obtained. These included their dimensions as well as the amount and strength of the reinforcement bars. Subsequently, Equations (10) and (11) were utilized. If the resulting quantity was $\geq$0, then the corresponding probability was $\geq$0.5. Thus, the joint under consideration was predicted to belong in the "JS" failure mode. Otherwise, it was assigned to "BY-JS".

Table 1 shows the respective average classification metrics obtained via the 10-fold cross-validation procedure. For each fold, the classification metrics derived from the corresponding analytical equation were computed separately using the respective training and test subsets. The respective standard deviations are also presented. Finally, Figure 7 displays the classification metrics of the final model, i.e., wherein the formulas in Equations (10) and (11) were employed.

Table 1. Cross-validated classification metrics of fitted analytical curves of each fold.

	Training Set		Testing Set	
	BY-JS	**JS**	**BY-JS**	**JS**
Precision	0.7697 ± 0.016	0.7932 ± 0.010	0.7749 ± 0.071	0.7847 ± 0.056
Recall	0.7613 ± 0.014	0.8004 ± 0.018	0.7447 ± 0.080	0.8072 ± 0.071
F1-Score	0.7653 ± 0.011	0.7967 ± 0.012	0.7575 ± 0.065	0.7944 ± 0.054
Accuracy	0.7822 ± 0.011		0.7781 ± 0.057	

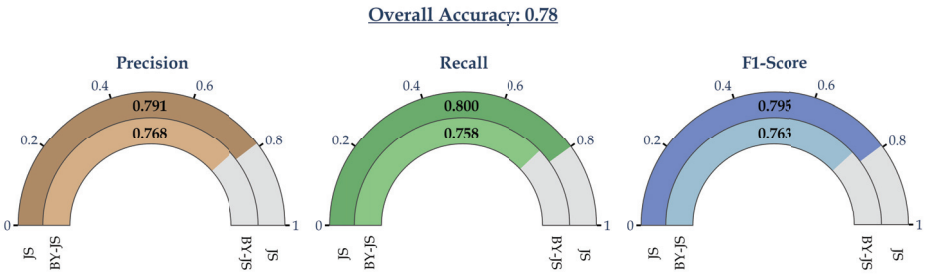


Figure 7. The classification metrics of the entire dataset of the final fitted Equations (10) and (11) using the cross-validated coefficients.

As can be readily observed from Table 1, the average classification metrics between the training and test datasets were close to each other. This indicates that the fitted analytical equations did not overfit. This can be attributed to the fact that relatively simple terms were selected for the analytical equation of each feature, as shown in Figure 6. In addition, as was mentioned in Section 2.2, the employed cross-validation scheme was stratified, which means that each train/test subset had approximately the same proportion of exterior/interior nodes and failure modes, and these proportions were approximately the same as those in the original dataset. This meant that the training and test subsets were balanced, which could also contribute to reducing overfitting.

Similarly, from Figure 7, it can be readily observed that the final simplified equations achieved high classification metrics in both failure modes. For the failure mode "JS", the precision, recall, and F1-score were all very close to each other and approximately equal to 80%. This demonstrated the very good ability of the analytical equations to detect this failure mode, which, as was mentioned, was the most severe and potentially damaging one. Similarly, the precision, recall, and F1-score for the "BY-JS" failure mode were also very close to each other, ranging from approximately 76–77%. These metrics were approximately 2.3–4.4% lower than the corresponding ones of the "JS" failure mode. If these differences were large, then the derived model would be considered biased towards the failure mode with the highest metrics. However, in this case, the respective differences were very small and the derived model was balanced between the two modes. Finally, it should be highlighted that the obtained overall accuracy was also high, approximately equal to 78%. All the aforementioned metrics, including the overall accuracy, were relatively close to the respective metrics obtained by the underlying XGBoost model. Thus, the derived Formulas (10) and (11) could be employed confidently, without a substantial performance degradation, compared to the underlying fully trained ML model.

The above results pertained to the "balanced" classifier obtained in Equations (10) and (11). The classification threshold for the "JS" failure mode was set at $p \geq 0.5$ or, equivalently, $\ln\left(\frac{p}{1-p}\right) \geq 0$. However, it is often the case, especially in engineering applications, that "erring on the side of safety" is preferred. For example, it could be required that a higher recall is obtained for the "JS" failure mode, the most dangerous and potentially damaging one. This would lead to more "JS" specimens being identified, although the corresponding precision index would be lower. This is due to the well-known precision–recall tradeoff [43,44]. This tradeoff can be visualized via so-called precision–recall (P-R) curves [45,46]. Similar to ROC curves [47,48], the area under the curve (AUC) of P-R curves gives a quantification of

their overall performance. The baseline in this case is the simple "majority classifier", i.e., a model that constantly assigns the input vectors to the class with the most input vectors in the training dataset.

Following the above, Figure 8 shows the precision–recall curve of the "JS" failure mode, computed via the analytical Equations (10) and (11). The top-right corner corresponds to the "perfect classifier", and the closer the P-R curve is to it, the better its overall performance was.

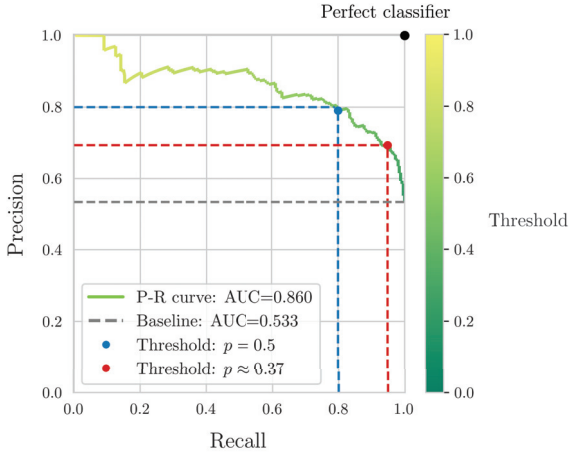


Figure 8. Precision-Recall curve for the classifier obtained via the analytical Equations (10) and (11).

Firstly, it can be readily observed that as the threshold for p decreased, more input vectors were assigned to the "JS" failure mode. Thus, the recall index of this mode increased, while, conversely, the precision index decreased. The threshold $p = 0.5$ was a balanced one, with the precision and recall very close to each other and close to 80%. We also identified the p threshold for a recall of ≈95%, which is a commonly employed engineering standard. In this case, $p \approx 0.37$ and the precision was reduced to ≈69%, while the overall accuracy of the classifier was reduced from ≈78% to ≈75%.

4. Summary and Conclusions

The mechanical behavior of reinforced concrete beam–column joints during a major seismic event is one of the most critical aspects that affect the overall behavior of a structure. Qualitatively, modern design codes dictate that, if failure is to occur, the flexural yielding of the beam, which is a ductile failure mode, should be the first to occur ("BY-JS" failure mode) and not the brittle shear failure of the joint ("JS" failure mode). Thus, the rapid and reliable estimation of the joint failure mode is one of the most crucial engineering problems faced by modern societies.

In this regard, machine learning classification algorithms have a demonstrated capability to produce state-of-the-art results in similar engineering challenges. However, they often suffer from a lack of transparency, as their predictions cannot be easily understood. Furthermore, ML algorithms are hard to incorporate into adopted engineering practice and design codes, which necessitate the existence of simplified analytical formulas in order to make predictions.

Thus, in the framework of the present research effort, a methodology for the derivation of simplified analytical equations for the prediction of the failure mode of reinforced concrete beam–column joints is presented. The proposed formulation aimed to create a link between the proven ability of ML algorithms to produce state-of-the-art results and the aforementioned need for simplified analytical expressions.

To this end, an underlying ML model was employed for the classification task, i.e., for the prediction of the probability corresponding to each failure mode. Subsequently, the SHAP values explainability technique was utilized to decompose these predictions into components pertaining to each individual feature. As Equation (9) and Figure 4 demonstrate, this allowed for the quantification of the overall influence of each feature on the

outcome. Guided by this feature-importance hierarchy, the most important features' SHAP values were utilized as a basis for the derivation of the simplified analytical expressions. The proposed methodology offered several distinct advantages.

Firstly, the derived equations were derived in an informed manner, wherein more terms could be added or removed independently to achieve the desired tradeoff between complexity and accuracy, guided by the feature-importance hierarchy presented in Figure 4. This was also facilitated by individually adjusting the form of the analytical equation that was fitted to each feature's SHAP values, guided by the form of the corresponding SHAP scatter plots, as shown in Figure 5.

Secondly, as is shown in Equation (2), the SHAP values approximated the behavior of the underlying ML model. Thus, the derived equations could achieve comparable levels of performance, as demonstrated in Figures 3b and 7. Indeed, the XGBoost classification model achieved an overall accuracy of approximately 84%. It corresponding precision, recall, and F1-score for the "JS" failure mode ranged from approximately 83.7 to 87%. Accordingly, the overall classification accuracy for the derived Equations (10) and (11) was approximately 78% and the corresponding classification metrics ranged from 79.1 to 80%.

Finally, it should be noted that the obtained classification metrics of the analytical equations were balanced between the two failure modes. Indeed, as is shown in Figure 7, the respective differences ranged from approximately 2.3 to 4.4%. However, as is demonstrated by Figure 8, the derived equations could easily be modified to achieve a different metric balance, for example, to obtain a higher recall index for the "JS" failure mode.

Overall, the results presented herein are promising, as they demonstrate the potential for the derivation of analytical expressions with a comparable accuracy to fully trained ML models. Even though the examined application pertained to the prediction of the RC joint failure mode, the results presented here encourage the application of the examined methodology to similar complex and impactful engineering challenges. Finally, even though the derived equations are based on a dataset consisting of 478 RC joint experimental results, they can be continuously updated as more data are incorporated, potentially leading to new insights into the behavior of RC beam–column joints.

Author Contributions: Conceptualization, I.K., M.K., T.R., L.I. and A.K.; methodology, I.K., M.K., T.R., L.I. and A.K.; software, I.K., M.K., T.R., L.I. and A.K.; validation, I.K., M.K., T.R., L.I. and A.K.; formal analysis, I.K. and M.K.; investigation, I.K., M.K., T.R., L.I. and A.K.; resources, M.K., T.R. and L.I.; data curation, I.K., M.K., T.R., L.I. and A.K.; writing—original draft preparation, I.K. and M.K.; writing—review and editing, T.R., L.I. and A.K.; visualization, I.K. and M.K.; supervision T.R., L.I. and A.K. All authors have read and agreed to the published version of the manuscript.

Funding: This research received no external funding.

Institutional Review Board Statement: Not applicable.

Informed Consent Statement: Not applicable.

Data Availability Statement: The data that support the findings of this study are available upon reasonable request.

Conflicts of Interest: The authors declare no conflicts of interest.

Abbreviations

The following abbreviations are used in this manuscript:

RC	Reinforced concrete
ML	Machine learning
ANN	Artifical neural network
SHAP	SHapley Additive exPlanations
k-NN	*k*-nearest neighbors
SVM	Support vector machine
OLS	Ordinary least squares

XGBoost	eXtreme Gradient Boosting
P-R	Precision–recall
AUC	Area under the curve

References

1. Najafgholipour, M.; Dehghan, S.; Dooshabi, A.; Niroomandi, A. Finite element analysis of reinforced concrete beam-column connections with governing joint shear failure mode. *Lat. Am. J. Solids Struct.* **2017**, *14*, 1200–1225. [CrossRef]
2. Karabini, M.; Karampinis, I.; Rousakis, T.; Iliadis, L.; Karabinis, A. Machine Learning Ensemble Methodologies for the Prediction of the Failure Mode of Reinforced Concrete Beam–Column Joints. *Information* **2024**, *15*, 647. [CrossRef]
3. Kuang, J.; Wong, H. Behaviour of Non-seismically Detailed Beam-column Joints under Simulated Seismic Loading: A Critical Review. In Proceedings of the Fib Symposium on Concrete Structures: The Challenge of Creativity, Avignon, France, 26–28 April 2004.
4. Braga, F.; Caprili, S.; Gigliotti, R.; Salvatore, W. Hardening slip model for reinforcing steel bars. *Earthq. Struct.* **2015**, *9*, 503–539. [CrossRef]
5. *Recommendations for Design of Beam-Column Connections in Monolithic Reinforced Concrete Structures (ACI 352R-02)*; Technical Report; American Concrete Institute: Indianapolis, IN, USA, 2002.
6. *Retrofitting of Concrete Structures by Externally Bonded FRPs with Emphasis on Seismic Applications (FIB-35)*; Technical Report; The International Federation for Structural Concrete: Lausanne, Switzerland, 2002.
7. *EN 1992 Eurocode 2 Part 1-1*; General Rules and Rules for Buildings. Technical Report; European Committee for Standardization: Brussels, Belgium, 2004.
8. Karayannis, C.G.; Sirkelis, G.M. Strengthening and rehabilitation of RC beam–column joints using carbon-FRP jacketing and epoxy resin injection. *Earthq. Eng. Struct. Dyn.* **2008**, *37*, 769–790. [CrossRef]
9. Tsonos, A.; Stylianidis, K. Pre-seismic and post-seismic strengthening of reinforced concrete structural subassemblages using composite materials (FRP). In Proceedings of the 13th Hellenic Concrete Conference, Rethymno, Greece, 25–27 October 1999; Volume 1, pp. 455–466.
10. Park, R.; Paulay, T. *Reinforced Concrete Structures*; John Wiley & Sons: Hoboken, NJ, USA, 1991.
11. Tsonos, A.G. Cyclic load behaviour of reinforced concrete beam-column subassemblages of modern structures. *WIT Trans. Built Environ.* **2005**, *81*, 11.
12. Antonopoulos, C.P.; Triantafillou, T.C. Experimental investigation of FRP-strengthened RC beam-column joints. *J. Compos. Constr.* **2003**, *7*, 39–49. [CrossRef]
13. Nikolić, Ž.; Živaljić, N.; Smoljanović, H.; Balić, I. Numerical modelling of reinforced-concrete structures under seismic loading based on the finite element method with discrete inter-element cracks. *Earthq. Eng. Struct. Dyn.* **2017**, *46*, 159–178. [CrossRef]
14. Thai, H.T. Machine learning for structural engineering: A state-of-the-art review. *Structures* **2022**, *38*, 448–491. [CrossRef]
15. Kaveh, A. Applications of Artificial Neural Networks and Machine Learning in Civil Engineering. *Stud. Comput. Intell.* **2024**, *1168*, 472.
16. Kotsovou, G.M.; Cotsovos, D.M.; Lagaros, N.D. Assessment of RC exterior beam-column Joints based on artificial neural networks and other methods. *Eng. Struct.* **2017**, *144*, 1–18. [CrossRef]
17. Suwal, N.; Guner, S. Plastic hinge modeling of reinforced concrete Beam-Column joints using artificial neural networks. *Eng. Struct.* **2024**, *298*, 117012. [CrossRef]
18. Mangalathu, S.; Jeon, J.S. Classification of failure mode and prediction of shear strength for reinforced concrete beam-column joints using machine learning techniques. *Eng. Struct.* **2018**, *160*, 85–94. [CrossRef]
19. Oviedo, F.; Ferres, J.L.; Buonassisi, T.; Butler, K.T. Interpretable and explainable machine learning for materials science and chemistry. *Accounts Mater. Res.* **2022**, *3*, 597–607. [CrossRef]
20. Marie, H.S.; Abu El-hassan, K.; Almetwally, E.M.; El-Mandouh, M.A. Joint shear strength prediction of beam-column connections using machine learning via experimental results. *Case Stud. Constr. Mater.* **2022**, *17*, e01463. [CrossRef]
21. Gao, X.; Lin, C. Prediction model of the failure mode of beam-column joints using machine learning methods. *Eng. Fail. Anal.* **2021**, *120*, 105072. [CrossRef]
22. Karampinis, I.; Morfidis, K.; Iliadis, L. Derivation of Analytical Equations for the Fundamental Period of Framed Structures Using Machine Learning and SHAP Values. *Appl. Sci.* **2024**, *14*, 9072. [CrossRef]
23. Verdonck, T.; Baesens, B.; Óskarsdóttir, M.; vanden Broucke, S. Special issue on feature engineering editorial. *Mach. Learn.* **2024**, *113*, 3917–3928. [CrossRef]
24. Ahsan, M.M.; Mahmud, M.P.; Saha, P.K.; Gupta, K.D.; Siddique, Z. Effect of data scaling methods on machine learning algorithms and model performance. *Technologies* **2021**, *9*, 52. [CrossRef]
25. Lee, H.; Yun, S. Strategies for Imputing Missing Values and Removing Outliers in the Dataset for Machine Learning-Based Construction Cost Prediction. *Buildings* **2024**, *14*, 933. [CrossRef]
26. Ghosh, K.; Bellinger, C.; Corizzo, R.; Branco, P.; Krawczyk, B.; Japkowicz, N. The class imbalance problem in deep learning. *Mach. Learn.* **2024**, *113*, 4845–4901. [CrossRef]
27. Kumar, P.; Bhatnagar, R.; Gaur, K.; Bhatnagar, A. Classification of imbalanced data: Review of methods and applications. *IOP Conf. Ser. Mater. Sci. Eng.* **2021**, *1099*, 012077. [CrossRef]

28. Wongvorachan, T.; He, S.; Bulut, O. A comparison of undersampling, oversampling, and SMOTE methods for dealing with imbalanced classification in educational data mining. *Information* **2023**, *14*, 54. [CrossRef]
29. Jeong, D.H.; Kim, S.E.; Choi, W.H.; Ahn, S.H. A comparative study on the influence of undersampling and oversampling techniques for the classification of physical activities using an imbalanced accelerometer dataset. *Healthcare* **2022**, *10*, 1255. [CrossRef] [PubMed]
30. Sen, P.C.; Hajra, M.; Ghosh, M. Supervised classification algorithms in machine learning: A survey and review. In *Emerging Technology in Modelling and Graphics: Proceedings of the IEM Graph 2018*; Springer: Singapore, 2020; pp. 99–111.
31. Kotsiantis, S.B.; Zaharakis, I.D.; Pintelas, P.E. Machine learning: A review of classification and combining techniques. *Artif. Intell. Rev.* **2006**, *26*, 159–190. [CrossRef]
32. Chen, T.; Guestrin, C. Xgboost: A scalable tree boosting system. In Proceedings of the 22nd ACM SIGKDD International Conference on Knowledge Discovery and Data Mining, San Francisco, CA, USA, 13–17 August 2016; pp. 785–794.
33. Friedman, J.H. Greedy function approximation: A gradient boosting machine. *Ann. Stat.* **2001**, *29*, 1189–1232. [CrossRef]
34. Lundberg, S.M.; Erion, G.; Chen, H.; DeGrave, A.; Prutkin, J.M.; Nair, B.; Katz, R.; Himmelfarb, J.; Bansal, N.; Lee, S.I. From local explanations to global understanding with explainable AI for trees. *Nat. Mach. Intell.* **2020**, *2*, 56–67. [CrossRef]
35. Lundberg, S.; Su-In, L. A unified approach to interpreting model predictions. *arXiv* **2017**, arXiv:1705.07874.
36. Linardatos, P.; Papastefanopoulos, V.; Kotsiantis, S. Explainable AI: A review of machine learning interpretability methods. *Entropy* **2020**, *23*, 18. [CrossRef] [PubMed]
37. Shapley, L. *Notes on the n-Person Game-II: The Value of an n-Person Game*; RAND Corporation: Santa Monica, CA, USA, 1951.
38. Aas, K.; Jullum, M.; Løland, A. Explaining individual predictions when features are dependent: More accurate approximations to Shapley values. *Artif. Intell.* **2021**, *298*, 103502. [CrossRef]
39. Norton, E.C.; Dowd, B.E. Log odds and the interpretation of logit models. *Health Serv. Res.* **2018**, *53*, 859–878. [CrossRef] [PubMed]
40. Raschka, S. An overview of general performance metrics of binary classifier systems. *arXiv* **2014**, arXiv:1410.5330.
41. Allgaier, J.; Pryss, R. Cross-Validation Visualized: A Narrative Guide to Advanced Methods. *Mach. Learn. Knowl. Extr.* **2024**, *6*, 1378–1388. [CrossRef]
42. Karampinis, I.; Iliadis, L.; Karabinis, A. Rapid Visual Screening Feature Importance for Seismic Vulnerability Ranking via Machine Learning and SHAP Values. *Appl. Sci.* **2024**, *14*, 2609. [CrossRef]
43. Buckland, M.; Gey, F. The relationship between recall and precision. *J. Am. Soc. Inf. Sci.* **1994**, *45*, 12–19. [CrossRef]
44. Gordon, M.; Kochen, M. Recall-precision trade-off: A derivation. *J. Am. Soc. Inf. Sci.* **1989**, *40*, 145–151. [CrossRef]
45. Sofaer, H.R.; Hoeting, J.A.; Jarnevich, C.S. The area under the precision-recall curve as a performance metric for rare binary events. *Methods Ecol. Evol.* **2019**, *10*, 565–577. [CrossRef]
46. Miao, J.; Zhu, W. Precision-recall curve (PRC) classification trees. *Evol. Intell.* **2022**, *15*, 1545–1569. [CrossRef]
47. Fan, J.; Upadhye, S.; Worster, A. Understanding receiver operating characteristic (ROC) curves. *Can. J. Emerg. Med.* **2006**, *8*, 19–20. [CrossRef]
48. Yang, S.; Berdine, G. The receiver operating characteristic (ROC) curve. *Southwest Respir. Crit. Care Chronicles* **2017**, *5*, 34–36. [CrossRef]

Disclaimer/Publisher's Note: The statements, opinions and data contained in all publications are solely those of the individual author(s) and contributor(s) and not of MDPI and/or the editor(s). MDPI and/or the editor(s) disclaim responsibility for any injury to people or property resulting from any ideas, methods, instructions or products referred to in the content.

sensors

MDPI

Article

Monitoring Excavation-Induced Deformation of a Secant Pile Wall Using Distributed Fiber Optic Sensors

Chengyu Hong [1,2], Chengkai Xu [3,*], Weibin Chen [2], Jianwei Liu [1] and Junkun Tan [1]

[1] China Railway Seventh Group Co., Ltd., Zhengzhou 450016, China; cyhong@szu.edu.cn (C.H.); liujianwei79@163.com (J.L.); tanjunkunde@126.com (J.T.)
[2] College of Civil and Transportation Engineering, Shenzhen University, Shenzhen 518060, China; jerrychenweibin@163.com
[3] Department of Civil and Environmental Engineering, The Hong Kong Polytechnic University, Hung Hom, Kowloon, Hong Kong, China
* Correspondence: xu.chengkai@outlook.com

Abstract: This paper investigates the use of the BOTDA (Brillouin Optical Time-Domain Analysis) technology to monitor a large-scale bored pile wall in the field. Distributed fiber optic sensors (DFOSs) were deployed to measure internal temperature and strain changes during cement grouting, hardening, and excavation-induced deformation of a secant pile wall. The study details the geological conditions and DFOS installation process. During grouting, the temperature increased by approximately 69 °C due to cement hydration 30 min post-grouting, while the strain decreased by 0.5% on average due to cement slurry shrinkage. During excavation, the temperature changes were minimal, but the excavation depth significantly influenced the strain distribution, with continuous compressive deformation observed in two monitored boreholes. Two analytical methods, the numerical integration method (NIM) and the finite difference method (FDM), were used to calculate the lateral pile displacement based on the monitored strain data. The results were compared with previous monitoring data, showing that the lateral displacement of the pile was minimal after excavation and was attributed to the high stiffness of the secant pile wall. This study demonstrates the effectiveness of DFOSs and BOTDA technology for monitoring complex pile wall behaviors during construction.

Keywords: BOTDA; distributed fiber optic sensors; bored pile wall; excavation

1. Introduction

In geological and geotechnical engineering, the excavation of cutting slopes disturbs the initial state of equilibrium of the soil mass and may lead to slope failure in the field [1–4]. In recent years, there have been slope failures triggered by a combination of excavation, continuous rainfall, and complex engineering geological conditions [5–8]. The retaining structures used to stabilize a soil mass include different types such as geosynthetic-reinforced soil walls [9], sheet pile retaining walls [10–12], prestressed anchor retaining walls [13], and bored pile retaining walls [14–17]. Among all these retaining structures, bored pile retaining walls have been demonstrated to be among the most effective structures for maintaining the overall integrity of slopes [14]. The excavation process has a significant influence on the stability of a soil mass, and a study on the mechanical performance of retaining structures during excavation is essentially required for rational field design and construction.

A variety of sensors have been developed for monitoring strain/stress distribution. To realize continuous measurements in space of the strain/stress characteristics of piles in

large-scale geostructures, distributed fiber optic sensors (DFOSs) based on Brillouin Optical Time-Domain Analysis (BOTDA) or Brillouin Optical Frequency-Domain Reflectometry (BOFDR) have been used. For analyzing the end-bearing and skin friction behaviors and the deformation characteristic of piles utilizing DFOSs, a wide range of studies [18–32] were performed. However, these studies primarily focused on pile performance under loading conditions, paying limited attention to the strain and temperature variations during the cement grouting and hardening stages, as well as to the subsequent excavation process—factors that are critical for understanding the long-term stability of retaining walls. In addition, to evaluate the behavior of piles as retaining structures, DFOSs were utilized to obtain the full-length deformation along the pile depth produced by lateral soil movements, which was then used to calculate the lateral deflection of the piles based on numerical and analytical methods [16,17,33,34]. The lateral movement/displacement/deflection of piles can also be defined by the term "horizontal displacement", which results from excavation or loading along one side of a pile wall. Nevertheless, most previous studies primarily focused on the introduction of new sensing technologies for monitoring the behavior of bored pile retaining walls [16], the effect of the excavation process on pile performance [16,17], and the performance of secant piled walls [33,34]. It could be concluded from the literature that, based on distributed BOTDA sensors, investigations on the assessment of full-length strain along bored pile retaining walls during the cement grouting and hardening processes are scarce. Furthermore, the analytical methods for the calculation of lateral pile movement have not been systematically discussed yet.

The traditional methods of monitoring DFOSs frequently necessitate lengthy periods of manual data reading in the field, and the effects of construction disturbances on the construction sites can cause DFOSs to receive high levels of noise, which leads to errors in the subsequent results and is an inherent challenge when DFOSs are used for construction monitoring. Recent advances in artificial intelligence provide opportunities to address such challenges in the field of DFOSs. Various machine learning techniques have been devised to improve the performance of DFOSs [35]. In addition, convolutional neural network models or algorithms, including the translation mean method [36], the Savitzky–Golay method [34,36,37], the percentile-filter method [36], and the Ransac algorithm [28], have been developed to perform real-time data denoising in BOTDA [38] and to accelerate the data processing efficiency of BOTDA [39]. A review of these methods will be useful in denoising the signals of DFOSs in investigations.

This study presents an investigation of the field monitoring of a bored pile wall subjected to excavation using DFOSs. An introduction of the BOTDA technique is first presented, and the sensors for field monitoring were calibrated. After geological investigations, these DFOSs were employed to measure the internal temperature and strain distribution profile of bored piles in the cement grouting, hardening, and excavation processes. Based on the measured strain distribution along the pile depth, lateral displacement was calculated by two analytical methods, and previous studies were also compared with the current study for a validation analysis. This study is innovative in systematically integrating the DFOS and BOTDA technologies to monitor the combined effects of cement grouting, hardening, and excavation-induced deformation, providing high-resolution, real-time strain and temperature profiles. Furthermore, by introducing two analytical methods to compute the lateral pile displacement, this research offers a robust alternative to traditional techniques, addressing critical gaps in understanding pile behavior during construction.

2. Brillouin Optical Time-Domain Analysis (BOTDA) Technique

The real-time monitoring of strain and temperature changes throughout the entire length of an optical fiber can be achieved through various DFOS techniques, including

Optical Frequency-Domain Reflectometry (OFDR), Brillouin Optical Time-Domain Analysis (BOTDA), and Brillouin Optical Tim- Domain Reflectometry (BOTDR). Each of these techniques has unique advantages and limitations, making them suitable for different applications in monitoring large-scale piles during construction. BOTDA relies on the Brillouin interaction between a pulsed pump wave and a counter-propagating probe wave, where a local acoustic wave is formed at the intersection point and detected. However, this technique can fail if the optical fiber cable is disconnected due to harsh field conditions [40]. In such cases, the BOTDR technique can be used instead. In contrast to BOTDA, just a pulsed pump is delivered into the tested fiber from one side in BOTDR measurements. Since the time-resolved probe signal is back-reflected owing to spontaneous Brillouin scattering as opposed to stimulated Brillouin scattering, the signal strength is much lower than that obtained with BOTDA. The spatial resolution of BOTDA and BOTDR is often lower than that of OFDR (which is, e.g., ±1 cm in the sensing range of 50–70 m for Luna OBR 4600), and the OFDR technique can detect smaller changes in pile deformation [41,42]. However, this high resolution may also make OFDR more susceptible to the measurement noise caused by environmental factors, such as temperature fluctuations or mechanical vibrations, particularly in dynamic environments like construction sites. Additionally, the cost of the equipment and the complexity of data interpretation can be higher for OFDR than for the BOTDA and BOTDR systems, which are often more cost-effective for long-range and large-scale monitoring applications.

In the present study, BOTDA was used for measurements of both strain and temperature. The principle of the BOTDA technique is based on the stimulated Brillouin scattering (SBS) effect, as shown in Figure 1. A pump light pulse and a continuous spectrum are input into the two ends of a single fiber-optic sensor, and continuous light is amplified due to the Brillouin effect when the frequency difference between the two different light signals matches the Brillouin frequency shift. The axial strains and temperatures of fiber optic sensors can be directly measured on the basis of their linear relationship with the Brillouin light scattering (BLS) frequency change in the optical fiber. This linear relationship proposed by Horiguch et al. [43] can be written as:

$$v_B(\varepsilon, T) = v_B(\varepsilon_0, T_0) + \frac{\partial v_B(\varepsilon, T)}{\partial \varepsilon} \times (\varepsilon - \varepsilon_0) + \frac{\partial v_B(\varepsilon, T)}{\partial T} \times (T - T_0) \quad (1)$$

where $v_B(\varepsilon_0, T_0)$ and $v_B(\varepsilon, T)$ are the frequency shift of Brillouin scattered light before and after the test, and ε_0 and ε are the axial strain at a certain spatial resolution of the optical fiber sensor before and after the test, respectively. T_0 and T are the surrounding temperature before and after the test. $\frac{\partial v_B(\varepsilon,T)}{\partial \varepsilon}$ and $\frac{\partial v_B(\varepsilon,T)}{\partial T}$ are the calibrated strain coefficient and calibrated temperature coefficient.

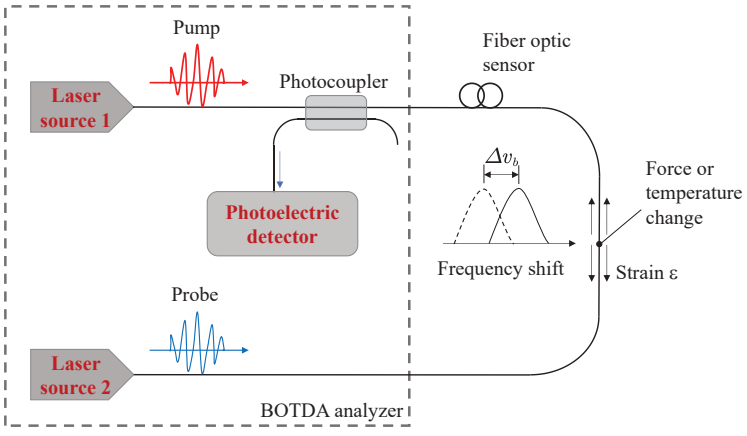


Figure 1. Stimulated Brillouin scattering (SBS) principle.

The field monitoring test utilized a DiTeSt SN0050 Dual Reading Unit data logger manufactured by Omnisens (Switzerland) [44], which has a sampling resolution of 0.2 m and a spatial resolution of 0.5 m. The measurement accuracy of the strain and temperature measurements was at a level of ± 5 με and ± 0.2 °C, respectively [16]. The frequency step was set to 2 MHz, and the reading interval was 2 ns during the measurement. In the field, a single measurement took an average of 87 s, and the signal from each fiber was read twice to minimize random errors. The BOTDA settings information is summarized in Table 1.

Table 1. Parameter setting of BOTDA data logger.

Equipment Parameter	Parameter Setting
Sampling resolution	0.2 m
Spatial resolution	0.5 m
Reading interval	2 ns
Frequency step	2 MHz
Sensor line length	300 m

3. Laboratory Calibrations

In this study, two kinds of easy-bending single-mode fibers (SMFs) were adopted for the strain and temperature measurements. Figure 2a shows the structure of a bare FOS for the strain measurement of piles. The external diameter of the strain sensor was 0.9 mm. The SMF for strain measurement not only provides improved performances with extremely low fiber attenuation at wavelengths ranging from 1260 nm to 1625 nm, but also has excellent bending resistance because it was manufactured by a plasma-activated chemical technique. To improve the fiber's longevity, the SMF was coated with two layers of UV-cured acrylic including a silica clad and a PVC buffer coating. An armored optical cable was used not only for signal transmission but also for temperature monitoring, as shown in Figure 2b. This temperature sensor cable mainly includes a 0.9 mm tight-buffer fiber (for temperature monitoring), a flexible metal tube, an aramid yarn, and an external jacket (3 mm). The SMF for the temperature sensor is loosely placed into a hollow steel tube. The inner fiber is loose and shielded by the metal tube, allowing it to be solely exposed to temperature changes. As mentioned by Soga and Luo [41], there is a large space for movement between the metal tube and the fiber because the 0.9 mm tight-buffer fiber is loose inside the metal tube. Therefore, it can be seen that the strain information is not transmitted through the metal housing to the internal fibers. In summary, the fiber has a high strain sensitivity and can withstand extreme environmental conditions.

A series of laboratory calibration experiments were carried out by exerting varied strains on a specified length of the SMF. Figure 2c shows an overall view of the setup of the calibration test. The SMF cable was mounted on a calibration platform and twisted into six loops between two high-precision micro-displacement platforms with a diameter of 40 mm and a spacing of 350 mm, whereas one of the micro-displacement platforms was coupled with a linear variable differential transformer (LVDT) with measurement accuracy of 0.01 mm to control the applied strain and to verify the calculated strain. As shown in Figure 3a, the Brillouin frequency shift had a highly linear relationship with the applied strain (interval of 500 micro strains), and we could obtain the strain coefficient of 0.04715 MHz/με through this relationship. The calibration result for the temperature is shown in Figure 3b, which also shows a clear linear relationship between Brillouin frequency shift and temperature. Based on the obtained strain coefficient, the calculated strain was verified by the measured strain by the LVDT. As shown in Figure 3c, the calculated strain agreed well with the measured strain. In this study, the structure of the fiber optic cables used in the calibration tests was the same as that of the inner bare

fiber optic cable for field monitoring applications, except for one external PVC protection layer. Based on previous literature reporting that the strain transfer coefficients from the monitored substrates to fiber optic sensors are mostly between 0.95 and 0.99, it appears that almost all strains of substrates can be transferred to inner bare fiber optic strain sensors [45–47]. In addition, the fiber optic was placed in a sonic tube commonly used in cast-in-place piles and grouted into an integrated section by cement [48]. Similar to the situation in this study, where a dual-layer-coating fiber embedded in cement withstood a uniform strain field, 95% of the solid strain could be developed in the fiber beyond 55 mm, and 99% of the strain could be developed over 84 mm from both ends of the cable [47]. Therefore, the influence of the external protective layer on the strain transfer coefficient for transfer between the monitored substrate and the fiber optic sensor was limited (less than 5%).

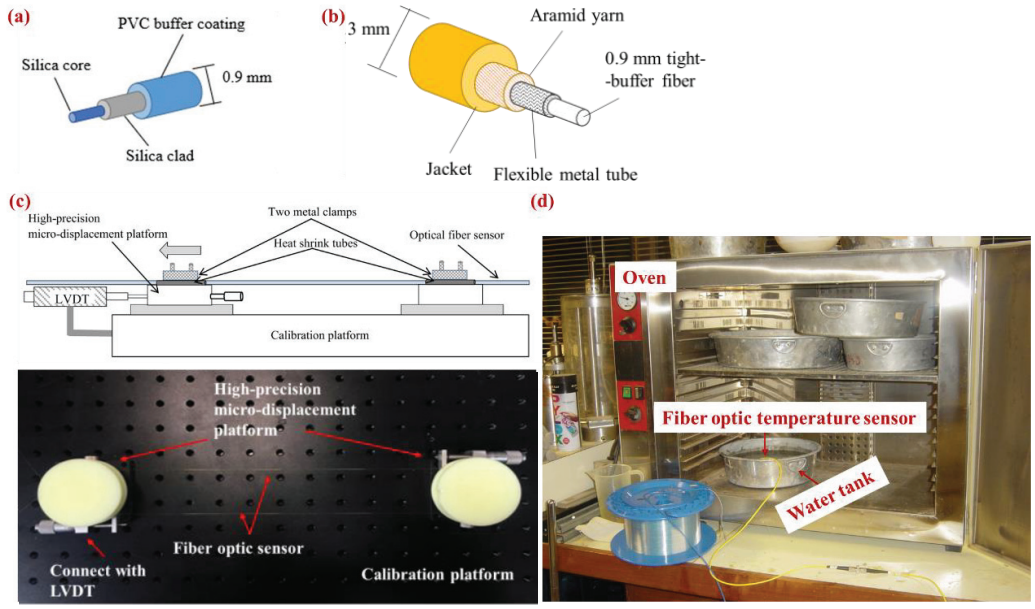


Figure 2. Calibration test: (**a**) structure of bare FOS for strain measurement, (**b**) temperature compensation fiber, (**c**) overall view of strain calibration setup, and (**d**) overall view of temperature calibration setup.

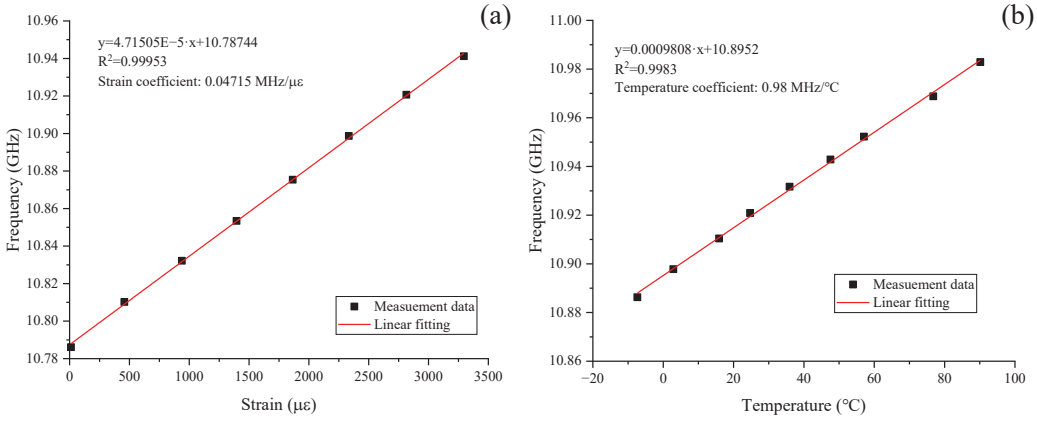


Figure 3. *Cont.*

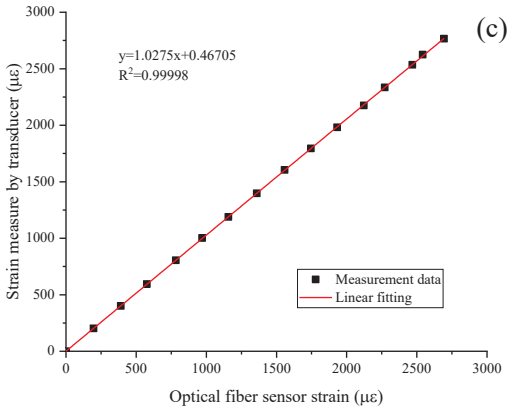


Figure 3. Calibration results of the DFOS: (**a**) calibration results of the DFOS for strain measurement, (**b**) calibration results of the DFOS for temperature measurement, and (**c**) comparison of strain measured by LVDT and DFOS.

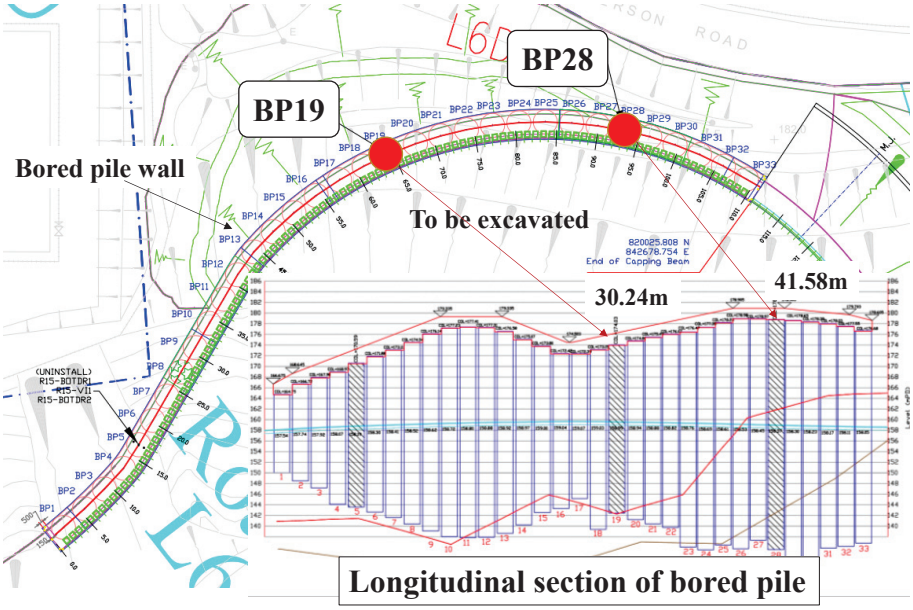
4. Engineering Geological Condition and Field Monitoring

4.1. Engineering Geological Condition

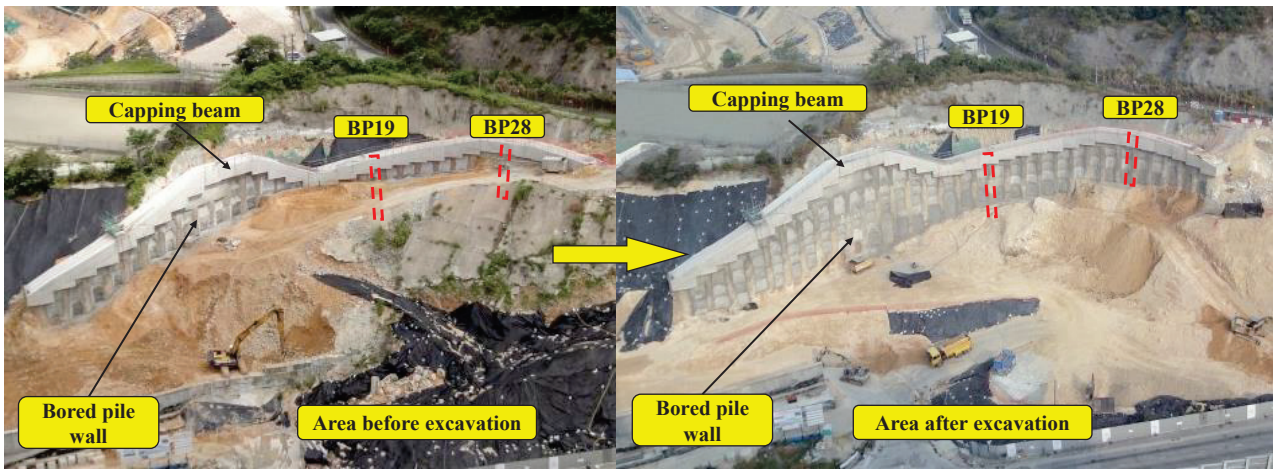
It is necessary to conduct engineering geological investigations, which are fundamental for the selection of construction sites and the reinforcement design for slopes subject to excavation investigations. The monitoring project was located at Anderson Road in Sai Kung District, east coast of Hong Kong. This district is a seaside region known for its landscape, little settlements, and beautiful seascapes. A traffic road was constructed at the bottom of the soil slope, and the upslope was a service reservoir facility. A secant pile wall was constructed to stabilize this soil slope, which was subjected to multi-stage excavations. This retaining wall includes 33 bored piles, reaching 3.0 m in diameter for each pile. A capping beam with dimensions of 2.0 m in height and 3.0 m in width was constructed to connect all bored piles. A schematic view of the secant pile wall is shown in Figure 4a. Photos of the site in this study before and after slope excavation are shown in Figure 4b,c.

According to the geological survey report, the geological profile around the secant pile wall is shown in Figure 5a, with a 36.5 m thick layer of completely decomposed granite (CDG) covering moderately to slightly decomposed granite (M/SDG). Some physical properties of CDG are summarized in Table 2. The slope surface was inclined at 30° with respect to the horizontal. It should be noted that the heterogeneity of the CDG layer, including local fractures and variations in material properties, may influence the performance of DFOSs. For example, localized discontinuities or weak zones within the soil could lead to irregular signal fluctuations or noise in the strain measurements. To mitigate these potential impacts, we optimized the sensor layout and employed advanced data processing techniques. Two bored piles (BP19 and BP28) with length of 30.24 m and 41.58 m (as shown in Figure 4) were mounted with DFOSs in this study to investigate the mechanical behavior of piles subjected to excavation. In each monitoring pile, two prefabricated holes were reserved for steel tubes for the installation of DFOSs, as illustrated in Figure 5b. A total of four SMF cables, including two temperature-monitoring cables and two strain-monitoring cables, were installed in two opposite holes, perpendicularly to the direction of the excavation face of the secant pile wall, as shown in Figure 5c. The temperature-monitoring fibers were installed within rigid sleeves, allowing them to slide freely and remain unaffected by strain, ensuring that their signals only reflected temperature variations. The strain-monitoring fibers, on the other hand, were bonded to the structure and thus subjected to both strain and temperature effects. By using the temperature data from the temperature-monitoring fibers for compensation, the temperature effects on the strain-monitoring fibers were removed, isolating the strain-induced signal. The distance between the two opposite holes was 2100

mm. This configuration was carefully designed to capture both tensile and compressive strains along the pile depth induced by the excavation, as well as to monitor temperature variations during cement grouting and hardening. The placement of the holes perpendicularly to the excavation face allowed the sensors to effectively measure the bending behavior of the pile under asymmetric soil pressure and excavation-induced deformation. Additionally, embedding the cables in opposite holes ensured symmetrical monitoring, minimizing potential measurement errors caused by construction disturbances or uneven loading conditions. Furthermore, this layout was determined based on the pile diameter, as the installation of too many sensors could result in mutual interference, reducing the measurement accuracy. Temperature sensors and strain sensors were installed in close proximity to enable temperature compensation for the strain measurements, thereby improving the reliability and precision of the strain data. This balanced approach ensured sufficient data resolution while avoiding overcrowding of the sensors, addressing both technical constraints and monitoring objectives.



(a)



(b) (c)

Figure 4. Overall view of the field site: (**a**) schematic view of the locations of the instrumented piles, (**b**) photo of the site before excavation, and (**c**) photo of the site after excavation.

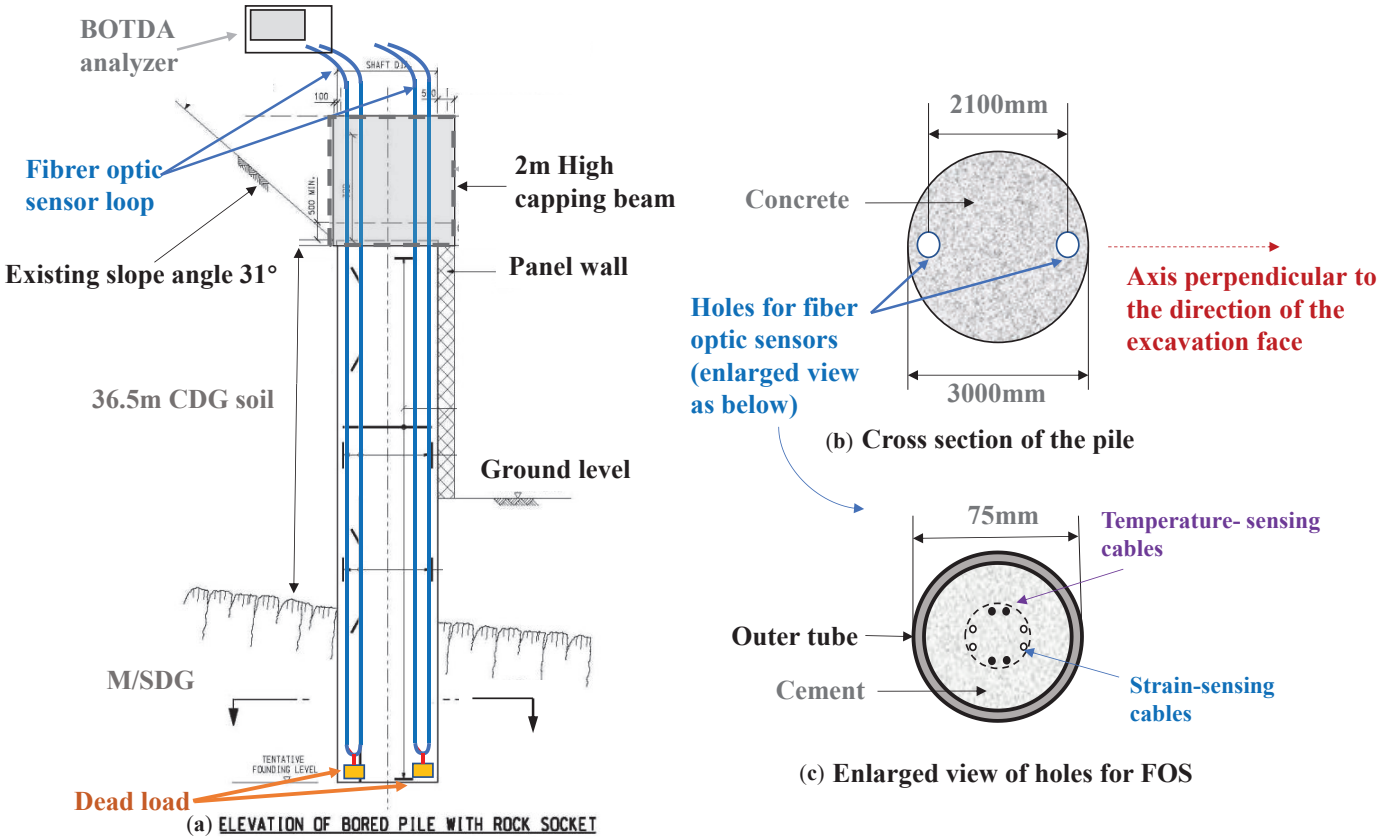


Figure 5. Schematics of geological profile and DFOS layout scheme: (**a**) overview of field monitoring, (**b**) cross section of a pile, and (**c**) detailed location of FOS.

Table 2. Physical parameters of CDG.

Specific Gravity	Dry Density (g/cm^3)	Plastic Limit (%)	Liquid Limit (%)	Cohesion (kPa)	Friction Angle (°)
2.6	1.75	22.7	32.8	26	34

4.2. Field Monitoring

Some details of the field installation of the DFOSs in this case are shown in Figure 6. When designing the spacing of the two fiber optic sensors, in order to sufficiently measure the strain when the pile is bending, the measurement points must be symmetrically arranged at a certain distance from the center of the pile. This is because it is difficult to ensure uniformity of the concrete–soil contact interface when a bored pile is introduced, and the steel reinforcement placed in the pile may lead to an uneven strain distribution in the pile. Therefore, the design of the monitoring system was based on the expected maximum horizontal displacement of 20–60 mm prior to construction and the average Young's modulus $E_0 = 28 \times 106$ kPa of the bored pile. At a spacing of 2100 mm (as shown in Figure 5b), the maximum strain was between 0.3 and 0.6%, which falls within the practical range for fiber optic strain monitoring that has an upper strain limit of approximately 3–5% [49]. Figure 6a shows that the central section of each SMF cable was suspended by a dead load, which kept the cable vertical and confirmed the bottom location of the cables when reading the sensing data. Each DFOS cable was connected in a measurement loop and placed into the reserved tubes, as shown Figure 6b. Imai et al. [50] agreed that it is feasible and advantageous to install DFOSs inside the structural components, for example,

by embedding them inside the concrete, which has numerous advantages. Likewise, the DFOSs were embedded inside the structural components, as shown in Figure 6c.

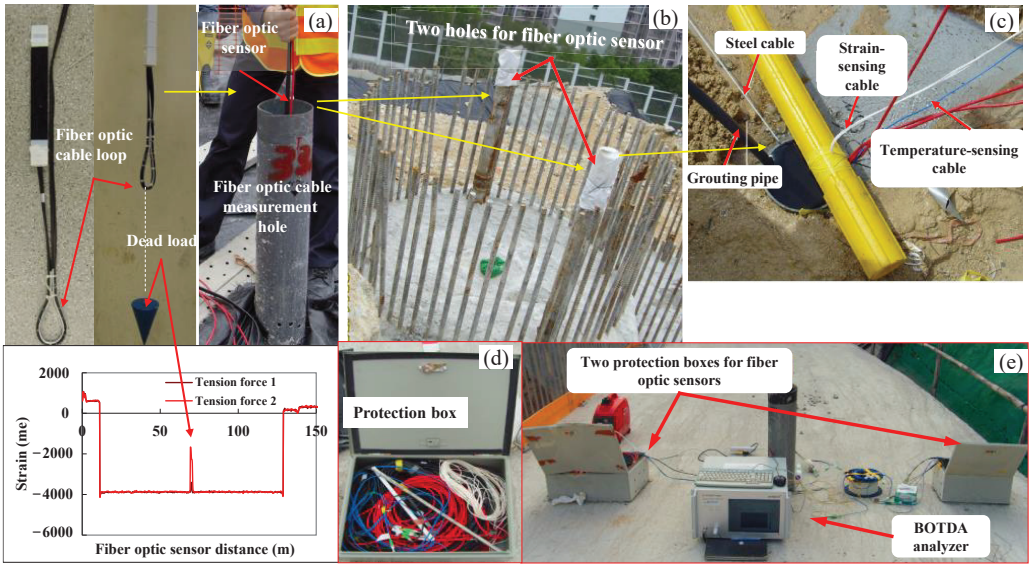


Figure 6. Field installation and monitoring of the DFOSs with the BOTDA sensing technology: (**a**) central section of each SMF cable suspended by a dead load, (**b**) location of the reserved tubes, (**c**) installations of all cables, (**d**) protection box for the pile embedded with DFOSs, and (**e**) field work of data collection and reading using the BOTDA analyzer.

It is worth noting that the whole monitoring hole was filled with cement grout, which ensured that all fiber optic sensors successfully reflected the pile wall deformation after the cement hardened [47,48]. Figure 6d shows two protection boxes for the placement of DFOSs. Figure 6e illustrates the setup of data collection from fiber optic sensors using the BOTDA analyzer. According to Kechavarz, et al. [51], it is also crucial to have some prior knowledge of the size of the minimum strain that has to be recorded and to make sure that it is much larger than the measurement performance in order to improve the performance of the developed system in the field load test. For a secant pile wall, the initial maximum axial strain can be estimated with prior knowledge of the applied force and pile diameter.

5. Monitoring Results and Analysis

5.1. Data Reading and Processing

Figure 7 illustrates the initial frequency distributions for stain monitoring and temperature monitoring of the pile BP28. The measured data can be separated into two symmetrical measurement sections from pile head to pile toe, representing a loop of the sensor cable along the pile depth. The obtained initial frequency distributions showed substantial fluctuations. Previous research has shown that the data analysis of distributed strain/temperature measurements obtained in the field has always been complex due to unavoidable measurement errors produced by the complex strain input as well as the analyzer's performance restrictions [52,53]. To make an accurate judgment on the deformation of a pile, it is necessary to analyze the original data and undertake smoothing analysis using scientific procedures. Various scientific approaches, at present, have been used to process the original signal, including the translation mean method [36], the Savitzky–Golay method [34,36,37], the percentile-filter method [36], and the Ransac algorithm [28]. Rolling filtering is a technique for eliminating noise from measurement data [52]. As the BOTDA analyzer evaluates a weighted average of strain across space, the Savitzky–Golay filter [54] was considered for noise reduction. This method fits a polynomial to a local subset of

data points within a defined window, minimizing the least-squares error. The filter parameters, including the polynomial order and the window size, significantly influence the results. Larger window sizes result in excessive smoothing and loss of detail, while higher polynomial orders introduce oscillations that are not representative of the physical strain distribution. A second-order polynomial with a window size of 15 was selected after testing different parameter combinations on a subset of the data. This configuration has been shown in prior research to effectively reduce noise while maintaining the physical characteristics of distributed strain and temperature profiles [34,36].

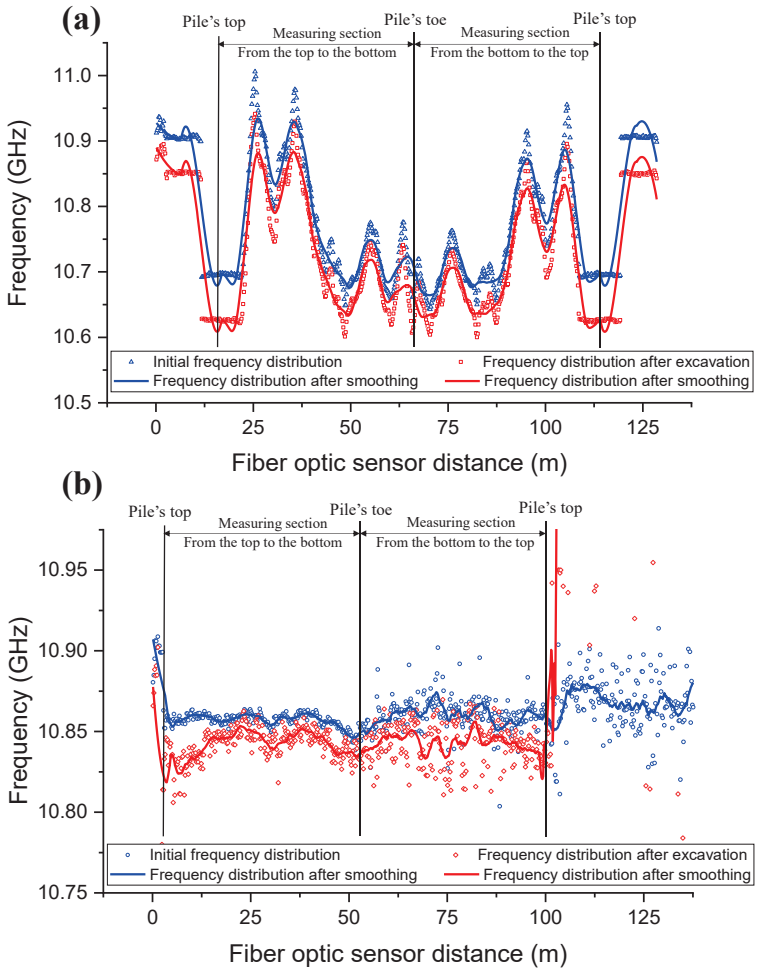


Figure 7. Initial and smoothed frequency distributions along the DFOS for (**a**) stain monitoring in pile BP28 and (**b**) temperature monitoring in pile BP28.

The comparisons between the original frequency distributions and the smoothed distributions are also presented in Figure 7. It is clear that the fluctuation amplitudes of the raw distributions are reduced, and all curves become smoother as a result of the filtering of unnecessary noise and surrounding interferences. In addition to the introduction of a smoothing analysis, the two symmetrical measurement sections were averaged. The smoothed and averaged frequency distributions can be used to compute both strain and temperature distributions using previous calibrated coefficients, as described in Section 3. Both smoothed and averaged strain distributions (pure strain change) were obtained considering the measured temperature distribution using the fiber optic sensors. The temperature difference between the two measurements was calculated and compensated in relation to the strain value by the temperature compensation factor of 18.793 $\mu\varepsilon/^{\circ}C$ provided by Omnisens, Switzerland [44].

5.2. Effect of Grouting and Cement Hardening

In the grouting process, it is inevitable that the flow of cement slurry will affect the position of the FOS cables, causing errors in the measured data masking the real effects of the cement slurry. Therefore, first, sensor data were collected immediately once grouting was completed, and a second data collection was conducted over the complete grouting of 30 min. The strain and temperature distributions obtained in the two data collections for BP19 are shown in Figure 8. It can be seen that the temperature increased in a range from 63 to 73 °C (about 69 °C on average), while the obtained shrinkage strain was within the range of 0.2–0.6% (around 0.5% on average) 30 min after grouting was completed. The temperature fluctuated with the pile depth, approximately ranging from −5 °C to +5 °C. Similar fluctuations occurred in some previous studies [24,55]. It was inferred that this fluctuation was mainly caused by the following factors: (1) the buried piles were surrounded by CDG and M/SDG, or the CDG stratum was heterogeneous (as shown in Figure 5a); (2) there might be unavoidable cracks or defects within the pile after construction. The crack theory is based on the concept that cracks are essentially structural discontinuities that may alter the stress and strain distribution inside a material. The existence of fractures may lead to localized stress concentrations, which in turn might cause fluctuations in the strain signals [56]; (3) construction disturbances on construction sites can cause DFOSs to receive amounts of noise that can lead to errors in the subsequent results. During the grouting process, the heat emitted by the cement hydration reaction rapidly leads to a temperature rise in the cement slurry, but rapidly dissipates in the following half hour. Such a high hydration temperature (60–80 °C) was also reported by Fellenius et al. [57]. The strain change mainly resulted from the shrinkage deformation of the cement slurry in the process of the hydration reaction. The cement slurry at the pile tip started the hydration reaction earlier, since cement grouting was conducted from the pile tip to the top. As a result, the shrinkage degree at the bottom was relatively smaller than at other positions. It may be worth noting that the uncorrelation between temperature and strain in this study (as shown in the following Figure 8) was proved by a Spearman's correlation coefficient ρ of −0.083, which is larger than −0.4. Kowalczyk et al. [58] assumed that two variables are correlated only when ρ is in a range from −1 to −0.4 and from 0.4 to 1, indicating that the presented temperature sensor is insensitive to strain.

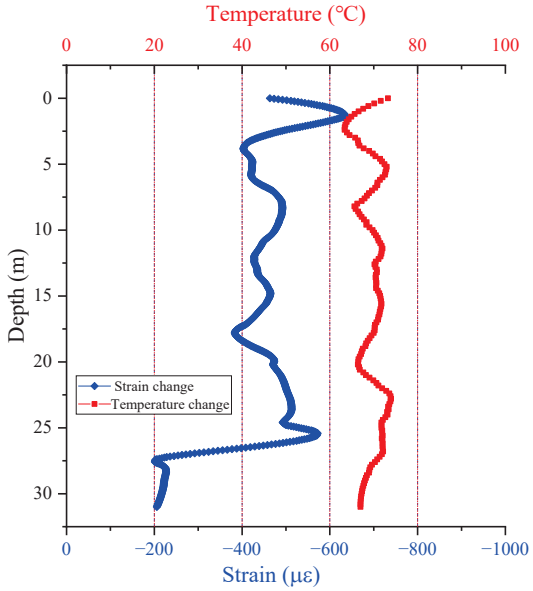


Figure 8. Changes in strain and temperature in two data collections (once grouting was completed and over the complete grouting of 30 min) along the length of BP19.

The temperature distribution profile of BP19 measured after cement hardening (April 14) was used as the baseline, and the temperature change along the pile, measured from March 10 (after grouting, before the initial setting time of the cement) to May 5, is plotted in Figure 9. As shown in Figure 9, the average temperature measured on the day of grouting was higher than that measured one month later, in the range from 27 °C to 54 °C (38.5 °C in average), which was due to the heat concentration and dissipation caused by the hydration reaction of the cement grout. After the initial setting time of the cement grout, the measured temperature profile varied within a limited range (from −5 to 5 °C), indicating that the hydration reaction was completed after March 29. This observed temperature variation with the pile depth was mainly attributed to a temperature change in the surrounding environment.

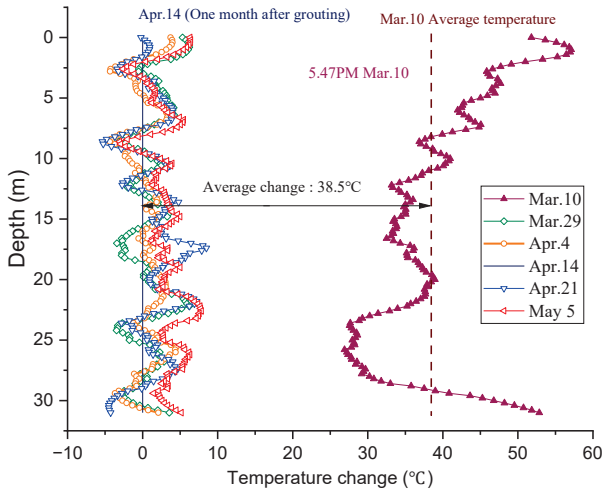


Figure 9. Average temperature profile measured from March 10 (after grouting, before initial setting time of cement) to May 5 along pile BP19.

Before and after cement hardening, the strain and temperature distributions in two boreholes of BP28 were measured to evaluate the effect of the hardening process on the pile performance, as shown in Figure 10. It is seen in Figure 10a,b that an obvious strain reduction before and after hardening was clearly observed. Both strain distributions measured at deeper positions close to the pile tip were relatively lower than the strain at lower positions. The strain distributions inside two capping beams were similar, presenting consistent variation trends as time elapsed. The temperature distribution showed a slight change after the hardening of the cement grout, as shown in Figure 10b,c. The temperatures measured at the pile tips were both around 2.5 °C lower than at the pile head.

5.3. Effect of the Excavation Progress

Both initial temperature and strain distributions before the excavation were used as reference baselines to investigate the influence of different excavation stages on the deformation characteristics of the pile. Figure 11 depicts the strain distribution profiles in the two opposite boreholes of BP19 and the corresponding excavation depths at different excavation stages (From September 22 to December 29). Compressive strain distributions inside the two boreholes were clearly observed and presented a significant increment in magnitude as the excavation progressed. The excavation depth had a significant influence on the strain distribution profiles of pile BP19. The strain distribution inside the borehole close to the excavation area (within a range from −450 με to 0 με, as shown in Figure 11b) was higher than that inside the borehole away from the excavation area (within a range from −380 με to 0 με, as shown in Figure 11a). The magnitude of the compressive (negative)

strain increased as the excavation depth increased, and the maximum negative strain moved downward as the excavation progressed from 4 m to 13 m.

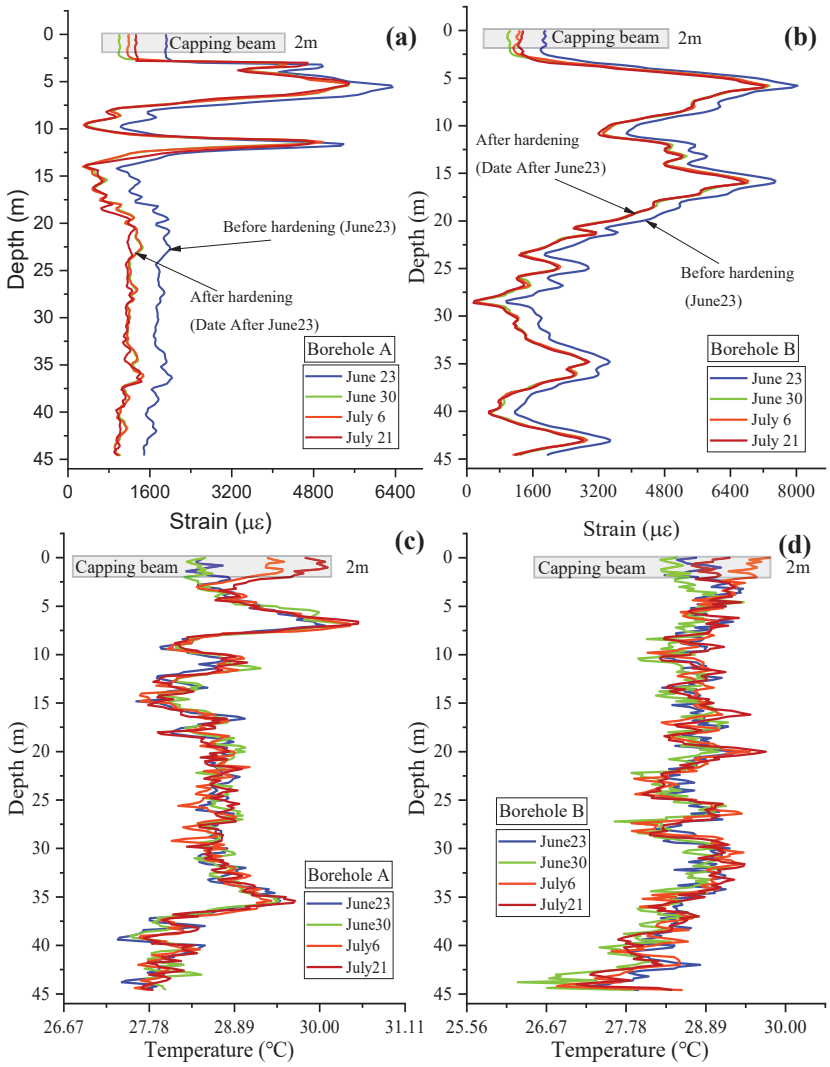


Figure 10. Strain and temperature distributions in two boreholes of BP28 before and after hardening of cement grout: (**a**) strain profile of borehole A, (**b**) strain profile of borehole B, (**c**) temperature profile of borehole A, and (**d**) temperature profile of borehole B.

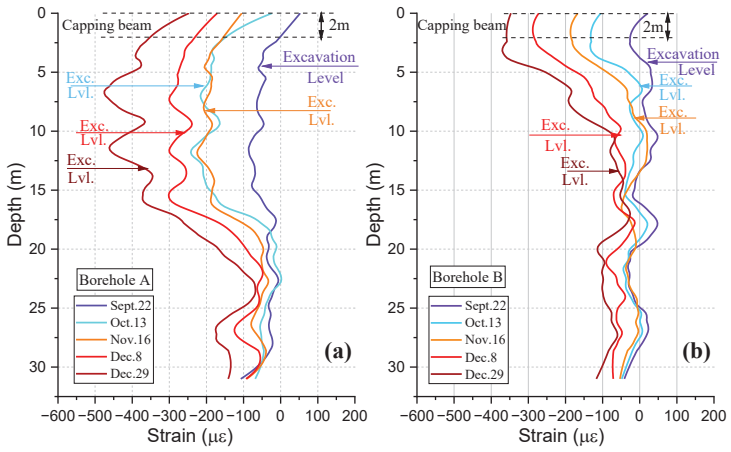


Figure 11. Measured strain profiles along pile BP19 at different excavation stages for (**a**) borehole A and (**b**) borehole B.

Figure 12a–e depict the strain profile distributions inside two opposite boreholes of BP19 at different excavation dates or excavation levels (excavation depths). The obtained averaged strain clearly indicates that the bored pile was under substantial compression. The larger compressive strain at borehole A (close to the excavation area) indicates that the pile moved toward the excavation face. All curves for the strain inside the two boreholes intersect at the bottom of the capping beam (2 m underground), revealing that the capping beam constrained the pile movement during the excavation.

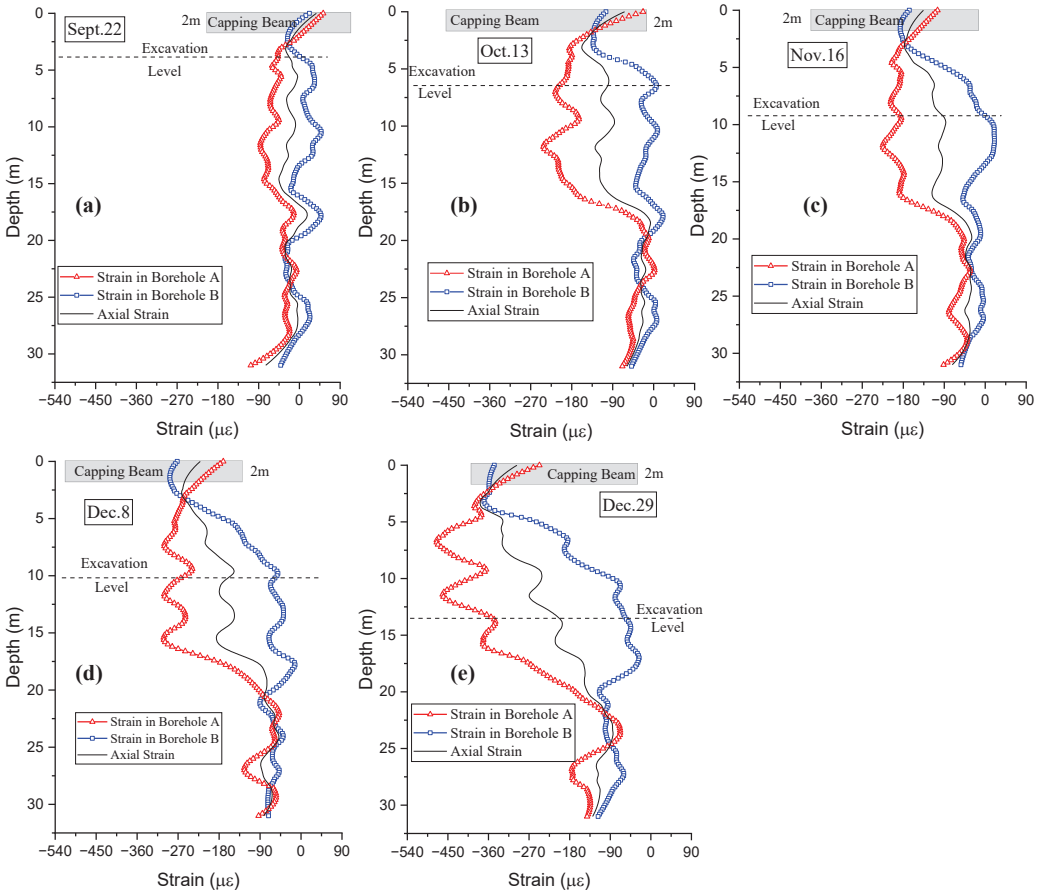


Figure 12. Comparison among strain distributions in two boreholes of BP 19 and their average strain distributions at different excavation levels: (**a**) September 22nd; (**b**) October 13th; (**c**) November 16th; (**d**) December 8th; (**e**) December 29th.

6. Analytical Methods for the Calculation of the Lateral Pile Movement

It is essential to investigate the lateral deflection of piles caused by soil excavation and the location of the maximum lateral deflection. In field monitoring, the conventional point inclinometer was popular and extensively applied to measure lateral displacement [16,33,37,59–61]. Alternatively, based on the strain distribution observed with DFOSs, two numerical approaches, including the finite difference method (FDM) and the numerical integration method (NIM), were successfully used to compute lateral displacement against pile depth [16,62]. The NIM is a popular method to obtain the deflection $y(z)$ of piles with the assumption that strain distribution along the longitudinal direction of a pile is linear, as shown in Figure 13. This assumption aligns with the basic beam theory, and the relationship between curvature and strain is expressed as:

$$y''(z) = k = \frac{M}{EI} \tag{2}$$

$$\frac{M}{EI} \times \frac{D}{2} = \frac{\varepsilon_t - \varepsilon_c}{2} \tag{3}$$

where M, E, and I are bending moment, elastic modulus, and moment of inertia of the cross section of a pile, respectively; k is the curvature coefficient; D is the distance between two opposite fiber optic sensors; and ε_t and ε_c represent the tensile and the compressive strain, respectively. Combing Equations (2) and (3) yields:

$$y(z) = \frac{1}{D}\iint (\varepsilon_t - \varepsilon_c) dz dz \tag{4}$$

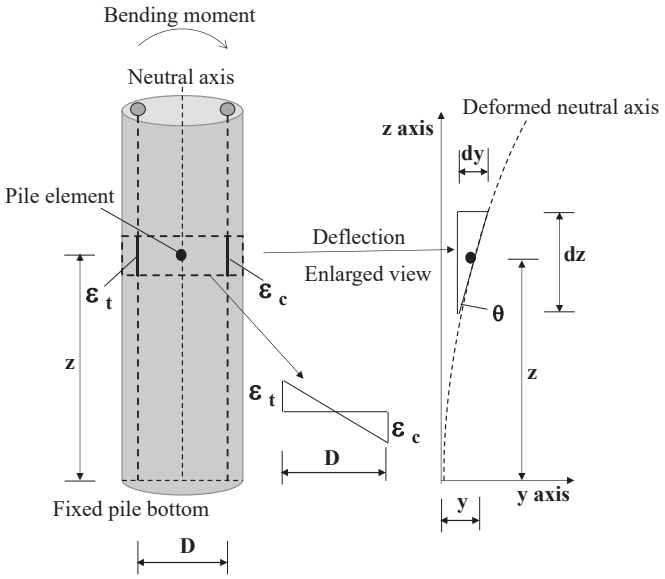


Figure 13. Schematics of deflection calculation for beam element.

To calculate the standard deviation of the displacement using the NIM, we need to integrate the square of the strain differences over the length of a pile. For the 95% confidence interval, the accuracy of the displacement is approximately calculated as 0.155 mm.

The FDM discretizes the governing equations of the basic beam theory into a finite difference form, allowing the curvature and displacement to be calculated iteratively over small segments of the pile. It is assumed that a continuous beam is separated into several tiny elements, and the interval between adjacent elements is assumed to be h. The first derivatives of y at the locations $z - h$, z, and h are obtained as follows:

$$\mathrm{y}'(z) = \frac{1}{h}[y(z+h) - y(z)] \tag{5}$$

$$y\mathrm{y}'(z-h) = \frac{1}{h}[y(z) - y(z-h)] \tag{6}$$

where $\mathrm{y}'(z)$ and $\mathrm{y}'(z-h)$ are the slopes of the deflection of the pile depth from z to $z+h$ and from $z-h$ to z, respectively. The second-order derivative can be obtained as shown below:

$$\begin{aligned} \mathrm{y}''(z) &= \tfrac{1}{h}\left\{\tfrac{1}{h}[y(z+h) - y(z)] - \tfrac{1}{h}[y(z) - y(z-h)]\right\} \\ &= \tfrac{1}{h^2}[y(z+h) - 2y(z) + y(z-h)] \end{aligned} \tag{7}$$

To calculate the overall pile deformation from discrete strain measurements distributed along the pile length based on the elasticity theory, it is assumed that the pile deflection is small and the strain distribution along pile section is linear. This assumption was also made

in previous studies [34,63,64]. According to the basic beam theory, we can use Equations (2) and (3) combined with Equation (7) to obtain the lateral displacement of the pile:

$$yy(z+2h) - 2y(z+h) + y(z) = \frac{h^2}{D}(\varepsilon_t - \varepsilon_c) \tag{8}$$

Equation (8) can be solved by the given boundary conditions. In this study, the monitored pile was inserted into slightly decomposed granite; so, the pile tip could be considered as a fixed end.

Figure 14 shows the lateral displacement distributions calculated by both NIM and FDM at five different excavation stages. The two lateral displacement distributions along the pile depth at different excavation levels calculated by NIM and FDM were consistent, with a maximum difference of less than 3% being obtained at the pile head. The lateral displacement increased from the pile tip to the pile head, approaching a maximum level at the pile head. The maximum lateral displacement increased as the excavation work proceeded. In addition, within a 95% confidence interval, the true value of displacement was within ±0.155 mm of the calculated result.

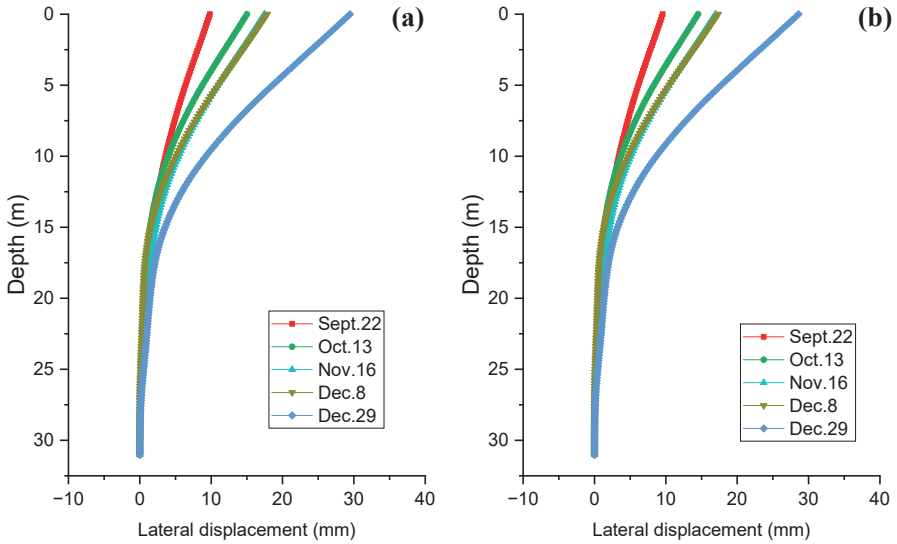


Figure 14. Comparison between the lateral displacements calculated by (**a**) NIM and (**b**) FDM.

7. Discussion

To further verify the calculated lateral displacement based on NIM and FDM, some relevant studies [65–72] were selected for comparison. Figure 15 shows the maximum lateral displacement against the excavation depth from the present study and some previous studies. The maximum displacement of the presented secant pile wall obtained by NIM and FDM increased as the excavation depth rose, which is consistent with the curve trends observed in previous studies. The ratio of the maximum displacement to the excavation depth in the present study was around 0.2%, which is relatively low compared to the values obtained in previous studies. This difference may be attributed to the fact that the maximum deflection is also influenced by retaining stiffness, soil strength, water level change, and construction methods. To objectively discuss the relationship between maximum lateral displacement and excavation depth, Spearman's correlation coefficient ρ was also used to evaluate the strength and direction of the monotonic association between maximum lateral deflection and excavation depth. In this study, the calculated ρ between maximum lateral deflection and excavation depth equaled 0.423, which is larger than 0.4 (as mentioned in Section 5.2). This fact reconfirmed that the maximum displacement had a positive correlation with the excavation depth.

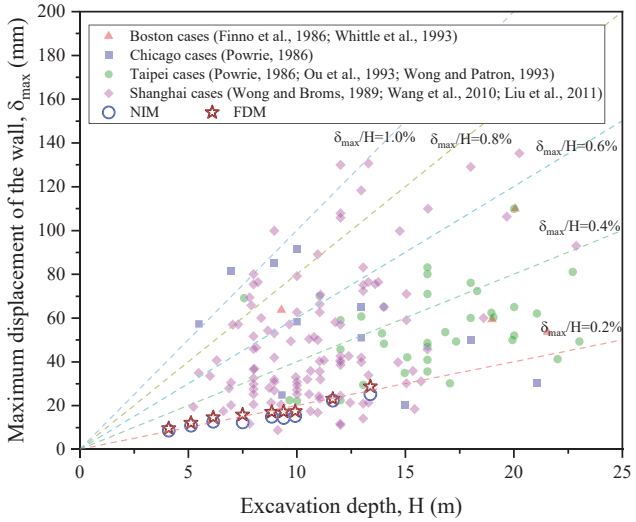


Figure 15. Comparison of maximum lateral deflection versus excavation depth between the current study and previous studies [65–72].

Figure 16 presents the locations of the maximum wall displacement against the excavation depth from the present study and previous studies [71,73]. The previous studies were divided into three groups according to the type of the retaining walls (including compound deep soil mixing walls, diaphragm walls, and contiguous pile walls). In most previous studies, the maximum deflections were present when the ratio of L_w/H was within the range of 0.5–2.0. The ratio of L_w/H in the present study was limited (less than 0.1), indicating that the stiffness of the secant pile wall was high, and the influence of the excavation work on the pile movement was ignorable.

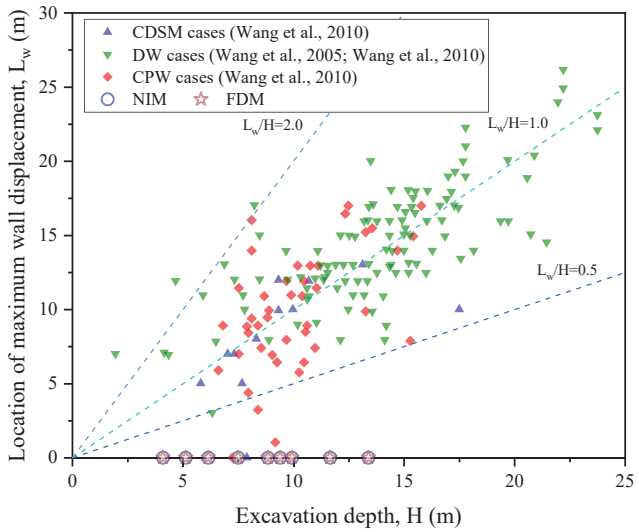


Figure 16. Comparison of the locations of maximum wall displacement versus excavation depth between the current study and previous studies [71,73].

However, the deformation behavior of a pile during excavation is governed by the soil–structure interactions, which are influenced by the excavation depth, the soil properties, and the pile characteristics. As the excavation depth increases, the removal of lateral soil support induces stress release and lateral soil movements, which impose bending moments and shear forces on the pile. The pile resists these movements through its stiffness and embedment depth, which results in a coupled soil–pile response. The results presented in this study, which analyzed the effect of excavation depth on pile deformation, are consistent

with these soil–structure interaction mechanisms. As the excavation depth increased, the lateral soil movements became more pronounced, exerting greater forces on the pile and resulting in larger displacements.

Moreover, compared to traditional monitoring methods (e.g., inclinometers, strain gauges, extensometers), DFOSs offer distributed measurements with high spatial resolution (millimeters to centimeters), enabling the detection of localized strain or deformation patterns that may be missed by discrete sensors. While traditional methods provide higher point-specific accuracy, their limited spatial coverage can overlook subtle changes along the structure. In terms of cost and deployment, the DFOS systems require higher initial expenses due to the need of specialized equipment and fiber installation but become more economical and efficient for large-scale or long-term monitoring, as one fiber can replace hundreds of discrete sensors. In contrast, the traditional techniques are more suitable for small-scale applications but become labor-intensive and costly when dense monitoring networks are required. These characteristics make DFOSs particularly advantageous for large-scale geotechnical and structural health monitoring projects.

8. Conclusions

This study presents an investigation of the field monitoring of a bored pile wall using DFOSs. Both grouting and excavation phases of the secant pile wall were considered in this monitoring study. Our conclusions and findings are as follows:

(1) The internal temperature increased by about 69 °C on average due to the cement hydration reaction inside the measurement borehole (30 min after cement grouting was completed) and a corresponding shrinkage strain of 0.5% on average was measured, due to the hardening effect of the cement slurry;

(2) The excavation depth had a significant influence on the strain distribution inside two boreholes in the monitored pile. A compressive strain distribution (inside the two opposite boreholes) of the monitored secant pile was clearly observed and increased substantially as the excavation progressed. The capping beam mounted at the pile heads exerted a substantial restrain on the induced deformation, decreasing the pile movement towards the excavation area;

(3) The displacement distribution of the pile wall was computed by both NIM and FDM. The calculated maximum displacement of the presented secant pile wall increased as the excavation depth rose, which was consistent with the curve trends observed in previous studies and was also reconfirmed by the fact that the calculated ρ between maximum lateral deflection and excavation depth equaled 0.423. A comparative study indicated that the lateral displacement of the presented pile was limited after excavation due to the high stiffness of the secant pile wall.

The use of the DFOS technology demonstrated its potential to provide high-resolution, distributed-strain data, enabling a more precise monitoring of pile behavior during construction. This will enhance the ability to assess structural performance in real time, contributing to safer and more efficient construction practices, particularly in urban excavation projects where deformation control is critical. The results also reinforce the suitability of secant pile walls as retaining structures requiring minimal deformation, offering valuable guidance for future designs. This work opens several avenues for future research. Investigating the behavior of secant pile walls in different soil types or under varying loading scenarios could expand the applicability of these findings. The long-term monitoring of pile walls under operational conditions will provide insights into their performance over time, including creep effects and cyclic loading behavior. Additionally, integrating DFOS data in advanced numerical models could improve the accuracy of soil–structure interaction predictions. Future research should also explore the application of DFOSs in other retaining

structures and their potential for real-time monitoring and automated decision-making during construction.

Author Contributions: Conceptualization, C.H. and W.C.; methodology, C.H. and J.L.; software, C.X.; writing—original draft preparation, C.X.; writing—review and editing, W.C. and J.T.; All authors have read and agreed to the published version of the manuscript.

Funding: This research received no external funding.

Institutional Review Board Statement: Not applicable.

Informed Consent Statement: Not applicable.

Data Availability Statement: The data that support the findings of this study are available upon reasonable request.

Conflicts of Interest: Author C.H. was employed by the company China Railway Seventh Group Co., Ltd. and Shenzhen University. J.L. and J.T. was employed by the company China Railway Seventh Group Co., Ltd. The remaining authors declare that the research was conducted in the absence of any commercial or financial relationships that could be construed as a potential conflict of interest.

References

1. Oh, S.; Lu, N. Slope stability analysis under unsaturated conditions: Case studies of rainfall-induced failure of cut slopes. *Eng. Geol.* **2015**, *184*, 96–103. [CrossRef]
2. Song, Y.-S.; Hong, W.-P.; Woo, K.-S. Behavior and analysis of stabilizing piles installed in a cut slope during heavy rainfall. *Eng. Geol.* **2012**, *129*, 56–67. [CrossRef]
3. Xu, D.-S.; Yin, J.-H. Analysis of excavation induced stress distributions of GFRP anchors in a soil slope using distributed fiber optic sensors. *Eng. Geol.* **2016**, *213*, 55–63. [CrossRef]
4. Li, R.; Hu, X.; Chen, F.; Wang, X.; Xiong, H.; Wu, H. A systematic framework for DEM study of realistic gravel-sand mixture from particle recognition to macro-and micro-mechanical analysis. *Transp. Geotech.* **2022**, *34*, 100693. [CrossRef]
5. Zhi, M.; Shang, Y.; Zhao, Y.; Lü, Q.; Sun, H. Investigation and monitoring on a rainfall-induced deep-seated landslide. *Arab. J. Geosci.* **2016**, *9*, 182. [CrossRef]
6. Lin, F.; Wu, L.; Huang, R.; Zhang, H. Formation and characteristics of the Xiaoba landslide in Fuquan, Guizhou, China. *Landslides* **2018**, *15*, 669–681. [CrossRef]
7. Wang, J.-J.; Liang, Y.; Zhang, H.-P.; Wu, Y.; Lin, X. A loess landslide induced by excavation and rainfall. *Landslides* **2014**, *11*, 141–152. [CrossRef]
8. Tang, Z.-Q.; Yin, Z.-Y.; Jin, Y.-F.; Zhou, X.-W. A novel mesoscale modelling method for steel fibre-reinforced concrete with the combined finite-discrete element method. *Cem. Concr. Compos.* **2024**, *149*, 105479. [CrossRef]
9. Mirmoradi, S.; Ehrlich, M. Effects of facing, reinforcement stiffness, toe resistance, and height on reinforced walls. *Geotext. Geomembr.* **2017**, *45*, 67–76. [CrossRef]
10. Endley, S.N.; Dunlap, W.A.; Knuckey, D.M.; Sreerama, K. Performance of an Anchored Sheet-Pile Wall. In *Geotechnical Measurements: Lab and Field*; ASCE Library: Reston, VA, USA, 2000; pp. 179–197.
11. Prästings, A.; Larsson, S.; Müller, R. Multivariate approach in reliability-based design of a sheet pile wall. *Transp. Geotech.* **2016**, *7*, 1–12. [CrossRef]
12. Day, R.; Potts, D. Modelling sheet pile retaining walls. *Comput. Geotech.* **1993**, *15*, 125–143. [CrossRef]
13. Ye, S.; Fang, G.; Zhu, Y. Model establishment and response analysis of slope reinforced by frame with prestressed anchors under seismic considering the prestress. *Soil Dyn. Earthq. Eng.* **2019**, *122*, 228–234. [CrossRef]
14. Zhang, C.; Lijun, S.; Weizhi, C.; Jiang, G. Full-scale performance testing of bored piles with retaining walls in high cutting slope. *Transp. Geotech.* **2021**, *29*, 100563. [CrossRef]
15. Adam, D.; Markiewicz, R.; Pulko, B.; Popović, Z.; Logar, J. Piles as retaining structures in slopes–Case histories. *Piles Retaining Struct.* **2017**, *2*, 3–15.
16. Xu, D.-S.; Yin, J.-H.; Liu, H.-B. A new measurement approach for deflection monitoring of large-scale bored piles using distributed fiber sensing technology. *Measurement* **2018**, *117*, 444–454. [CrossRef]
17. Pei, H.; Yin, J.; Wang, Z. Monitoring and analysis of cast-in-place concrete bored piles adjacent to deep excavation by using BOTDA sensing technology. *J. Mod. Opt.* **2019**, *66*, 703–709. [CrossRef]
18. Glisic, B.; Inaudi, D.; Nan, C. Pile monitoring with fiber optic sensors during axial compression, pullout, and flexure tests. *Transp. Res. Rec.* **2002**, *1808*, 11–20. [CrossRef]

19. Seo, H. Monitoring of CFA pile test using three dimensional laser scanning and distributed fiber optic sensors. *Opt. Lasers Eng.* **2020**, *130*, 106089. [CrossRef]
20. Ruidong, L.; Yin, Z.-Y.; Shaoheng, H. 3D Reconstruction of Arbitrary Granular Media Utilizing Vision Foundation Model. *Appl. Soft Comput.* **2024**, *169*, 112599.
21. Wang, P.; Yin, Z.Y.; Hicher, P.Y.; Cui, Y.J. Micro-mechanical analysis of one-dimensional compression of clay with DEM. *Int. J. Numer. Anal. Methods Geomech.* **2023**, *47*, 2706–2724. [CrossRef]
22. Hong, C.-Y.; Zhang, Y.-F.; Li, G.-W.; Zhang, M.-X.; Liu, Z.-X. Recent progress of using Brillouin distributed fiber optic sensors for geotechnical health monitoring. *Sens. Actuators A Phys.* **2017**, *258*, 131–145. [CrossRef]
23. Bersan, S.; Bergamo, O.; Palmieri, L.; Schenato, L.; Simonini, P. Distributed strain measurements in a CFA pile using high spatial resolution fibre optic sensors. *Eng. Struct.* **2018**, *160*, 554–565. [CrossRef]
24. De Battista, N.; Kechavarzi, C.; Soga, K. Distributed fiber optic sensors for monitoring reinforced concrete piles using Brillouin scattering. In Proceedings of the Sixth European Workshop on Optical Fibre Sensors, Limerick, Ireland, 30 May 2016; p. 99160U.
25. Monsberger, C.M.; Lienhart, W.; Hayden, M. Distributed fiber optic sensing along driven ductile piles: Design, sensor installation and monitoring benefits. *J. Civ. Struct. Health Monit.* **2020**, *10*, 627–637. [CrossRef]
26. Hong, C.-Y.; Zhang, Y.-F.; Liu, L.-Q. Application of distributed optical fiber sensor for monitoring the mechanical performance of a driven pile. *Measurement* **2016**, *88*, 186–193. [CrossRef]
27. Zheng, X.; Shi, B.; Zhu, H.-H.; Zhang, C.-C.; Wang, X.; Sun, M.-Y. Performance monitoring of offshore PHC pipe pile using BOFDA-based distributed fiber optic sensing system. *Geomech. Eng.* **2021**, *24*, 337–348.
28. Sun, Y.; Li, X.; Ren, C.; Xu, H.; Han, A. Distributed fiber optic sensing and data processing of axial loaded precast piles. *IEEE Access* **2020**, *8*, 169136–169145. [CrossRef]
29. Tang, Z.-Q.; Zhou, X.-W.; Jin, Y.-F.; Yin, Z.-Y.; Zhang, Q. A novel coupled bES-FEM formulation with SUPG stabilization for thermo-hydro-mechanical analysis in saturated porous media. *Comput. Geotech.* **2024**, *173*, 106454. [CrossRef]
30. Li, R.; Zhang, P.; Yin, Z.Y.; Sheil, B. Enhanced Hybrid Algorithms for Segmentation and Reconstruction of Granular Grains From X-Ray Micro Computed-Tomography Images. *Int. J. Numer. Anal. Methods Geomech.* **2024**, *48*, 4206–4220. [CrossRef]
31. Wang, P.; Xu, C.; Yin, Z.-Y.; Song, S.-X.; Xu, C.; Dai, S. A DEM-based Generic Modeling Framework for Hydrate-Bearing Sediments. *Comput. Geotech.* **2024**, *171*, 106287. [CrossRef]
32. Lu, Y.; Shi, B.; Wei, G.; Chen, S.; Zhang, D. Application of a distributed optical fiber sensing technique in monitoring the stress of precast piles. *Smart Mater. Struct.* **2012**, *21*, 115011. [CrossRef]
33. Mohamad, H.; Soga, K.; Pellew, A.; Bennett, P.J. Performance monitoring of a secant-piled wall using distributed fiber optic strain sensing. *J. Geotech. Geoenviron. Eng.* **2011**, *137*, 1236–1243. [CrossRef]
34. Mohamad, H.; Bennett, P.J.; Soga, K.; Klar, A.; Pellow, A. Distributed optical fiber strain sensing in a secant piled wall. In Proceedings of the 7th FMGM 2007: Field Measurements in Geomechanics, Boston, MA, USA, 24–28 September 2007; pp. 1–12.
35. Venketeswaran, A.; Lalam, N.; Wuenschell, J.; Ohodnicki, P.R., Jr.; Badar, M.; Chen, K.P.; Lu, P.; Duan, Y.; Chorpening, B.; Buric, M. Recent advances in machine learning for fiber optic sensor applications. *Adv. Intell. Syst.* **2022**, *4*, 2100067. [CrossRef]
36. Gao, L.; Han, C.; Xu, Z.; Jin, Y.; Yan, J. Experimental study on deformation monitoring of bored pile based on BOTDR. *Appl. Sci.* **2019**, *9*, 2435. [CrossRef]
37. Klar, A.; Bennett, P.J.; Soga, K.; Mair, R.J.; Tester, P.; Fernie, R.; St John, H.D.; Torp-Peterson, G. Distributed strain measurement for pile foundations. *Proc. Inst. Civ. Eng. Geotech. Eng.* **2006**, *159*, 135–144. [CrossRef]
38. Wu, H.; Wan, Y.; Tang, M.; Chen, Y.; Zhao, C.; Liao, R.; Chang, Y.; Fu, S.; Shum, P.P.; Liu, D. Real-time denoising of Brillouin optical time domain analyzer with high data fidelity using convolutional neural networks. *J. Light. Technol.* **2018**, *37*, 2648–2653. [CrossRef]
39. Yan, M.; Tan, X.; Mahjoubi, S.; Bao, Y. Strain transfer effect on measurements with distributed fiber optic sensors. *Autom. Constr.* **2022**, *139*, 104262. [CrossRef]
40. Bao, X.; Zhou, Z.; Wang, Y. Distributed time-domain sensors based on Brillouin scattering and FWM enhanced SBS for temperature, strain and acoustic wave detection. *PhotoniX* **2021**, *2*, 14. [CrossRef] [PubMed]
41. Soga, K.; Luo, L. Distributed fiber optics sensors for civil engineering infrastructure sensing. *J. Struct. Integr. Maint.* **2018**, *3*, 1–21. [CrossRef]
42. Gao, L.; Gong, Y.; Liu, H.; Ji, B.; Xuan, Y.; Ma, Y. Experiment and numerical study on deformation measurement of cast-in-place concrete large-diameter pipe pile using optical frequency domain reflectometer technology. *Appl. Sci.* **2018**, *8*, 1450. [CrossRef]
43. Horiguchi, T.; Kurashima, T.; Tateda, M. Tensile strain dependence of Brillouin frequency shift in silica optical fibers. *IEEE Photonics Technol. Lett.* **1989**, *1*, 107–108. [CrossRef]
44. Omnisens S.A. *User Manual (UM-018) for Omnisens, DITEST STA-R*; Omnisens S.A.: Morges, Switzerland, 2009.

45. Han, H.-M.; Shi, B.; Zhang, L.; Wei, G.-Q.; Chen, Q. Error analysis and experimental research of joint fiber-optic displacement sensor based on shear lag model. *Measurement* **2021**, *186*, 110106. [CrossRef]
46. Mahjoubi, S.; Tan, X.; Bao, Y. Inverse analysis of strain distributions sensed by distributed fiber optic sensors subject to strain transfer. *Mech. Syst. Signal Process.* **2022**, *166*, 108474. [CrossRef]
47. Tan, X.; Bao, Y.; Zhang, Q.; Nassif, H.; Chen, G. Strain transfer effect in distributed fiber optic sensors under an arbitrary field. *Autom. Constr.* **2021**, *124*, 103597. [CrossRef]
48. Habel, W.; Hofmann, D.; Hillemeier, B. Deformation measurements of mortars at early ages and of large concrete components on site by means of embedded fiber-optic microstrain sensors. *Cem. Concr. Compos.* **1997**, *19*, 81–102. [CrossRef]
49. Silva-López, M.; Fender, A.; MacPherson, W.N.; Barton, J.S.; Jones, J.D.; Zhao, D.; Dobb, H.; Webb, D.J.; Zhang, L.; Bennion, I. Strain and temperature sensitivity of a single-mode polymer optical fiber. *Opt. Lett.* **2005**, *30*, 3129–3131. [CrossRef]
50. Imai, M.; Igarashi, Y.; Shibata, M.; Miura, S. Experimental study on strain and deformation monitoring of asphalt structures using embedded fiber optic sensor. *J. Civ. Struct. Health Monit.* **2014**, *4*, 209–220. [CrossRef]
51. Kechavarzi, C.; Pelecanos, L.; de Battista, N.; Soga, K. Distributed fibre optic sensing for monitoring reinforced concrete piles. *Geotech. Eng. J. SEAGS AGSSEA* **2019**, *50*, 43–51.
52. Mei, Y. Error Analysis for Distributed Fibre Optic Sensing Technology Based on Brillouin Scattering. Ph.D. Thesis, University of Cambridge, Cambridge, UK, 2018.
53. Liu, X. Characterization of Brillouin Scattering Spectrum in LEAF Fiber. Master's Thesis, University of Ottawa, Ottawa, ON, Canada, 2011.
54. Savitzky, A.; Golay, M.J. Smoothing and differentiation of data by simplified least squares procedures. *Anal. Chem.* **1964**, *36*, 1627–1639. [CrossRef]
55. De Battista, N.; Kechavarzi, C.; Seo, H.; Soga, K.; Pennington, S. Distributed fibre optic sensors for measuring strain and temperature of cast-in-situ concrete test piles. In *Transforming the Future of Infrastructure Through Smarter Information: Proceedings of the International Conference on Smart Infrastructure and Construction, Virtual, 27–29 June 2016*; ICE Publishing: London, UK; pp. 21–26.
56. Mao, J.; Chen, J.; Cui, L.; Jin, W.; Xu, C.; He, Y. Monitoring the corrosion process of reinforced concrete using BOTDA and FBG sensors. *Sensors* **2015**, *15*, 8866–8883. [CrossRef] [PubMed]
57. Fellenius, B.H.; Kim, S.-R.; Chung, S.-G. Long-term monitoring of strain in instrumented piles. *J. Geotech. Geoenviron. Eng.* **2009**, *135*, 1583–1595. [CrossRef]
58. Kowalczyk, T.; Pleszczynska, E.; Ruland, F. *Grade Models and Methods for Data Analysis: With Applications for the Analysis of Data Populations*; Springer Science & Business Media: Berlin, Germany, 2004; Volume 151.
59. Tan, Y.; Wang, D. Characteristics of a large-scale deep foundation pit excavated by the central-island technique in Shanghai soft clay. II: Top-down construction of the peripheral rectangular pit. *J. Geotech. Geoenviron. Eng.* **2013**, *139*, 1894–1910. [CrossRef]
60. Xu, D.-S.; Yin, J.-H.; Cao, Z.-Z.; Wang, Y.-L.; Zhu, H.-H.; Pei, H.-F. A new flexible FBG sensing beam for measuring dynamic lateral displacements of soil in a shaking table test. *Measurement* **2013**, *46*, 200–209. [CrossRef]
61. Sivaraman, S.; Muthukkumaran, K. Non-linear performance analysis of free headed piles in consolidating soil subjected to lateral loads. *Eng. Sci. Technol. Int. J.* **2021**, *24*, 449–457. [CrossRef]
62. Hong, C.-Y.; Zhang, Y.-F.; Zhang, M.-X.; Leung, L.M.G.; Liu, L.-Q. Application of FBG sensors for geotechnical health monitoring, a review of sensor design, implementation methods and packaging techniques. *Sens. Actuators A Phys.* **2016**, *244*, 184–197. [CrossRef]
63. Ding, Y.; Wang, P.; Yu, S. A new method for deformation monitoring on H-pile in SMW based on BOTDA. *Measurement* **2015**, *70*, 156–168. [CrossRef]
64. Pelecanos, L.; Soga, K.; Elshafie, M.Z.; de Battista, N.; Kechavarzi, C.; Gue, C.Y.; Ouyang, Y.; Seo, H.-J. Distributed fiber optic sensing of axially loaded bored piles. *J. Geotech. Geoenviron. Eng.* **2018**, *144*, 04017122. [CrossRef]
65. Finno, R.J.; Schubert, W.R. Clay liner compatibility in waste disposal practice. *J. Environ. Eng.* **1986**, *112*, 1070–1084. [CrossRef]
66. Whittle, A.J.; Hashash, Y.M.; Whitman, R.V. Analysis of deep excavation in Boston. *J. Geotech. Eng.* **1993**, *119*, 69–90. [CrossRef]
67. Powrie, W. The Behaviour of Diaphragm Walls in Clay. Ph.D. Thesis, University of Cambridge, Cambridge, UK, 1986.
68. Ou, C.-Y.; Hsieh, P.-G.; Chiou, D.-C. Characteristics of ground surface settlement during excavation. *Can. Geotech. J.* **1993**, *30*, 758–767. [CrossRef]
69. Wong, L.; Patron, B. Settlements induced by deep excavations in Taipei. In Proceedings of the 11th Southeast Asian Geotechnical Conference, Singapore, 4–8 May 1993; pp. 787–791.
70. Wong, K.S.; Broms, B.B. Lateral wall deflections of braced excavations in clay. *J. Geotech. Eng.* **1989**, *115*, 853–870. [CrossRef]
71. Wang, J.; Xu, Z.; Wang, W. Wall and ground movements due to deep excavations in Shanghai soft soils. *J. Geotech. Geoenviron. Eng.* **2010**, *136*, 985–994. [CrossRef]

72. Liu, G.B.; Jiang, R.J.; Ng, C.W.; Hong, Y. Deformation characteristics of a 38 m deep excavation in soft clay. *Can. Geotech. J.* **2011**, *48*, 1817–1828. [CrossRef]
73. Wang, Z.W.; Ng, C.W.; Liu, G.B. Characteristics of wall deflections and ground surface settlements in Shanghai. *Can. Geotech. J.* **2005**, *42*, 1243–1254. [CrossRef]

Disclaimer/Publisher's Note: The statements, opinions and data contained in all publications are solely those of the individual author(s) and contributor(s) and not of MDPI and/or the editor(s). MDPI and/or the editor(s) disclaim responsibility for any injury to people or property resulting from any ideas, methods, instructions or products referred to in the content.

sensors

MDPI

Article

An Evaluation of the Acoustic Activity Emitted in Fiber-Reinforced Concrete Under Flexure at Low Temperature

Omar A. Kamel [1], Ahmed A. Abouhussien [1,*], Assem A. A. Hassan [2] and Basem H. AbdelAleem [3]

[1] Kinectrics Inc., 393 University Ave, Toronto, ON M5G 1E6, Canada; oalaaeldein@mun.ca
[2] Department of Civil Engineering, Faculty of Engineering and Applied Science, Memorial University of Newfoundland, St. John's, NL A1B 3X5, Canada; ahassan@mun.ca
[3] Faculty of Engineering, Cairo University, Cairo University Rd, Oula 3725121, Egypt; bhaa18@mun.ca
* Correspondence: aabouhussien@mun.ca

Abstract: This study investigated the changes in the acoustic emission (AE) activity emitted in fiber-reinforced concrete (FRC) under flexure at two temperatures (25 °C and −20 °C). Seven concrete mixtures were developed with different water-binder ratios (w/b) (0.4 and 0.55), different fiber materials (steel fiber (SF) and synthetic polypropylene fiber (Syn-PF)), different fiber lengths (19 mm and 38 mm), and various Syn-PF contents (0%, 0.2%, and 1%). Prisms with dimensions of 100 × 100 × 400 mm from each mixture underwent a four-point monotonic flexure load while collecting the emitted acoustic waves via attached AE sensors. AE parameter-based analyses, including *b*-value, improved *b*-value (*Ib*-value), intensity, and rise time/average signal amplitude (RA) analyses, were performed using the raw AE data to highlight the change in the AE activity associated with different stages of damage (micro- and macro-cracking). The results showed that the number of hits, average frequency, cumulative signal strength (CSS), and energy were higher for the waves released at −20 °C compared to those obtained at 25 °C. The onset of the first visible micro- and macro-cracks was noticed to be associated with a significant spike in CSS, historic index (*H (t)*), severity (S_r) curves, a noticeable dip in the *b*-value curve, and a compression in bellows/fluctuations of the *Ib*-value curve for both testing temperatures. In addition, time and load thresholds of micro- and macro-cracks increased when samples were cooled down and tested at −20 °C, especially in the mixtures with higher w/b, longer fibers, and lower fiber content. This improvement in mechanical performance and cracking threshold limits was associated with higher AE activity in terms of an overall increase in CSS, S_r, and *H (t)* values and an overall reduction in *b*-values. In addition, varying the concrete mixture design parameters, including the w/b ratio as well as fiber type, content, and length, showed a significant impact on the flexural behavior and the AE activity of the tested mixtures at both temperatures (25 °C and −20 °C). Intensity and RA analysis parameters allowed the development of two charts to characterize the detected AE events, whether associated with micro- and macro-cracks considering the temperature effect.

Keywords: fiber-reinforced concrete; passive acoustic emission analysis; four-point flexural test; crack classification; cold temperatures

1. Introduction

The properties of materials generally (specifically concrete) change drastically when the temperature drops from ambient to subnormal temperatures [1,2]. Previous studies reported an increase in flexure strength, elastic stiffness, and compressive strength at low temperatures [3,4]. Despite the aforementioned beneficial effects, concrete is shown to be

more brittle [4,5]. Sloan [6] studied the seismic behavior of reinforced concrete members at low temperatures and reported that decreasing temperature to −40 °C led to a sudden failure once they reached the maximum compressive strength indicating a brittle failure. Various solutions were proposed to improve concrete's brittle behavior, especially at low temperatures. One of the most effective approaches is designing concrete with randomly dispersed discontinuous fibers [7,8].

By including fibers, concrete's intrinsic flaws, such as poor post-cracking ductility, low tensile strength, and low deformation capacity can be controlled [9,10]. Hence, cementitious materials will be damaged by numerous narrow cracks, thereby reducing the risk of catastrophic failure [11–13]. Ismail and Hassan [14] investigated the effect of including various lengths and contents of steel fibers on the mechanical properties and impact resistance of rubberized concrete mixtures. The results revealed that increasing steel fiber content up to 1% increased the compressive strength, splitting tensile strength, flexure strength, and impact resistance by 1.07, 1.93, 1.75, and 4 times, respectively, to that of a control mixture without fiber. The mechanical behavior of fiber-reinforced concrete (FRC) is dependent on a number of factors, including the water-binder (w/b) ratio and fiber type, volume fraction, length, strength, and stiffness [15–17].

Among several techniques used to assess the concrete's performance, an acoustic emission (AE) analysis is a real-time non-invasive technique that has been used by many researchers in FRC applications [18–23]. AE refers to sound waves produced when a material undergoes cracking. The characteristics of the generated AE wave (e.g., counts, the number of hits, amplitudes, rise time, duration, frequency, signal strength, and energy) are proportional to the size of crack growth, which can provide valuable information regarding cracking levels [24–26]. An AE analysis can take the form of parameter-based or waveform-based AE approaches. A waveform-based AE analysis can offer more information than a parameter-based analysis regarding source identification and signal characterization [27], yet a parameter-based analysis, such as *b*-value, improved *b*-value (*Ib*-value), intensity, and rise time/average signal amplitude (RA) analysis approaches, may provide quantitative results that can be used to evaluate the extent of damage in concrete structures.

The *b*-value and intensity analyses performed by Abouhussien and Hassan [18] on the AE signal amplitudes emitted under flexure in fiber-reinforced self-consolidated concrete allowed for the early detection of two stages of damage (micro- and macro-cracking) prior to failure. In addition, analyzing the change in RA values and average frequency (AF) allowed Aggelis, Soulioti [20] to highlight the effect of chemically treated and untreated steel fibers on the fracture mechanism of FRC under four-point flexure tests. An RA analysis allowed Liu, Li [28] to monitor the mechanical performance of crumb rubber basalt fiber-reinforced concrete under a three-point flexure test.

Concrete mixtures with different microstructures and mechanical properties produce different types of acoustic activity when they undergo cracking [29]. Consequently, factors that affect concrete microstructure, such as cold temperatures, are anticipated to change the behavior of AE waves emitted in concrete mixtures and should be investigated. The sensitivity of the AE monitoring technique to the changes in the concrete microstructure was examined in this study. Whilst the behavior of AE waves emitted in FRC under flexure at ambient room temperature is well documented [18], the literature lacks information regarding the change in acoustic activity at subfreezing temperatures. The ultimate goal of this study is to fill this gap and to assess the effect of different w/b and fiber types, lengths, and contents on AE wave propagation at low temperatures reaching −20 °C. The selected low temperature value of −20 °C considered in this study was based on the average operating temperatures during the winter months in North America. Furthermore,

the study aims to develop criteria to characterize the micro- or macro-cracking stages considering the temperature effect and the aforementioned mixture design variables.

2. Research Significance

AE waves accompanying the nucleation of concrete cracks can provide valuable information about the damage if properly collected and analyzed. Any change in transfer medium microstructure caused by factors such as the concrete type and the exposure to cold temperature can affect the behavior of AE waves. As a result, this study investigates the behavior of the AE waves emitted in FRC under flexure at low temperature. In addition, this paper studied the effect of varying the w/b, fiber materials (steel or synthetic polypropylene), fiber contents (0%, 0.2%, and 1%) and fiber lengths (19 mm and 38 mm), and testing temperatures (−20 °C and 25 °C) on the behavior of the AE waves. This study also developed classification charts based on intensity and RA analysis parameters that consider temperature effect to evaluate the cracking behavior of FRC. This study is anticipated to enrich the integration of the AE analysis method as a non-destructive technique for FRC in cold regions.

3. Experimental Program

3.1. Concrete Mixture Development

The trail mixture stage targeted a class of SCC mixtures having a slump flow diameter of 700 ± 50 mm, meeting the SCC conformity criteria given by the EFNARC (2005) [30]. Several trial mixtures were performed to determine the minimum w/b, total binder content, optimum type and content of supplementary cementing materials (fly ash (FA) or metakaolin (MK)), and the type and content of fibers required to develop mixtures M1, M6, and M7, meeting the acceptable fresh properties limits of SCC according to the EFNARC (2005) [30] without overdosing the high-range water-reducing admixtures (HRWRAs). Meanwhile, mixtures M2–M5 were adopted from a previous study performed by the authors [23]. The optimum results of the seven concrete mixtures are listed in Table 1. Since the characteristics of the acoustic waves are related to the mechanical properties and microstructure of the damage source [29], two non-fibrous SCC mixtures (M1 and M2) were developed with different w/b (0.55 and 0.4, respectively) to investigate the effect of turning a high amount of water into ice on the behavior of the acoustic waves when samples are cooled down and tested at −20 °C. The variation in the w/b ratios is expected to have an impact on the microstructure of concrete and the overall flexural behavior of concrete at low temperatures.

Table 1. Concrete mixtures composition.

Mixture No.	Mixture Type	Cement (kg/m^3)	MK (kg/m^3)	FA (kg/m^3)	C/F	W/B	C.A. (kg/m^3)	F.A. (kg/m^3)	Water Content (kg/m^3)	V_f %	HRWRA (kg/m^3)
M1	M500-0.55w/b	500	-	-	0.7	0.55	606.15	865.83	275	-	1.43
M2	M500-0.4w/b	500	-	-	0.7	0.4	686.57	981.21	200	-	2.17
M3	M550-control	275	110	165	0.7	0.4	619.67	885.84	220	-	3.51
M4	M550-SynF19	275	110	165	0.7	0.4	619.67	885.84	220	0.2	4.42
M5	M550-SynF38	275	110	165	0.7	0.4	619.67	885.84	220	0.2	4.69
M6	M550-1%SynF38	275	110	165	0.7	0.4	619.67	885.84	220	1	5.76
M7	M550-SF35	275	110	165	0.7	0.4	619.67	885.84	220	0.2	4.66

Note: 1 kg/m^3 = 0.06243 lb/ft^3.

Mixture designation was as follows:

- M500-0.55 w/b means a concrete mixture with a binder content of 500 kg/m^3 and 0.55 water–binder ratio.
- M550-SynF38 means a concrete mixture with a binder content of 550 kg/m^3 and reinforced with synthetic fibers 38 mm in length.

In addition, five concrete mixtures (M3–M7) with 550 kg/m^3 binder content were developed as follows: control non-fibrous SCC mixture (M3); two SCC mixtures with 0.2% Syn-PF but different lengths (19 mm and 38 mm) (M4 and M5, respectively); one SCC mixture reinforced with 0.2 SF (35 mm) (M6); and one SCC mixture with 1% Syn-PF 38 mm length (see Figure 1). These mixtures are aimed at evaluating the effect of changing the mixture design parameters of concrete on the flexural behavior and the corresponding AE response. The geometrical and mechanical characteristics of these fibers are described in Table 2. Fibers were selected based on their commercial availability. Two percentages of fibers (0.2% and 1%) were selected in this investigation to study the effect of the increased activity of fibers' pull-out and breakage on the AE activity. In the SCC mixtures, 0.2% was found to be the maximum possible dosage of fibers that satisfied the requirements of fresh properties for SCC [30], while the 1% fibers in normal vibrated concrete (M7) was the maximum percentage of fibers that ensured a homogeneous mixture with no fiber balling [31].



(**a**) (**b**)

Figure 1. Pictures of the fibers used: (**a**) 38 mm polypropylene synthetic fibers, (**b**) 35 mm single hooked-end steel fibers.

Table 2. Typical features of steel and polypropylene fibers.

Fiber Type	Material	Length (mm)	Diameter (mm)	Specific Gravity	Tensile Strength (MPa)	Fiber's Shape
SF-35	Steel	35	0.55	7.85	1150	single hooked-end
SynF-19	polypropylene	19	0.66	0.91	300	straight
SynF-38	polypropylene	38	0.64	0.91	515	straight

Notes: 1 mm = 0.039 in.; 1 MPa = 145 psi.

3.2. Material Properties

General-use Canadian Portland cement (type GU) was used in all mixtures, which was in compliance with ASTM Type I [32], and had a specific gravity of 3.15. Fly ash (FA) and metakaolin (MK) were used as supplementary cementing materials to enhance the mixture suspension. FA and MK had specific gravity of 2.5 and 2.38, respectively. The physical and chemical properties of all cementitious materials are listed in Tables 3 and 4. Both coarse

aggregate (C.A.) and fine aggregate (F.A.) used in this investigation had a specific gravity of 2.6 and water absorption of 1%. The coarse-to-fine aggregate ratio was taken at 0.7 in all mixtures to achieve acceptable fresh properties of the SCC mixtures. The W/B ratio was kept constant at 0.4 in all mixtures except for mixture M2, where a W/B of 0.55 was used to study the effect of higher W/B (that will turn into ice after freezing) on the flexure performance and the characteristics of the AE waves at −20 °C. To obtain successful SCC mixtures (in terms of fresh properties), a high-range water-reducing admixture (HRWRA) was added to all SCC mixtures to achieve the desired slump flow of 700 ± 50 mm, as per ASTM C C1611 [33]. The HRWRA used was similar to that described in ASTM Type F [34] and had a specific gravity of 1.2 and a pH level of 9.5.

Table 3. Chemical composition of all cementitious materials used in mass percent (%).

Chemical Properties F%	Cement	MK	Fly Ash
SiO_2	19.63	51–53	51
Al_2O_3	5.48	42–44	23
Fe_2O_3	2.37	<2.2	12
FeO	--	--	--
TiO_2	--	<3.0	--
C	--	--	--
Cr_2O_3	--	--	--
MnO	--	--	--
P_2O_5	--	<0.21	--
SrO	--	--	--
BaO	--	--	--
SO4	--	<0.5	--
CaO	62.43	<0.2	5
MgO	2.47	<0.1	--
Na_2O	--	<0.05	--
C_3S	52.33	--	--
C_2S	16.82	--	--
C_3A	10.51	--	--
C_4AF	7.23	--	--
K_2O	--	<0.40	--
L.O.I	2.04	<0.50	--

Table 4. Physical properties of all cementitious materials used.

	Cement	MK	Fly Ash
Specific Gravity	3.15	2.5	2.38
Blaine Fineness (m^2/kg)	410	19,000	420

3.3. Specimen Details and Preparation

To perform compressive strength according to ASTM C39 [24] and flexure test according to ASTM C78 [25], six cylinders (100 mm diameter and 200 mm height) and four prisms (100 × 100 × 400 mm) were cast from each mixture (see Figure 2). Samples were kept at ambient room temperature for 24 h before demolding. Then, the samples were de-molded and kept in a moist curing room at 25 °C for 28 days to reach the target strength. The moist curing room was used to maintain relative humidity in the range of 80% to 85% throughout the curing period. After reaching maturity, samples were divided into two groups. Each group consisted of three cylinders and two prisms. For each mixture, one group was tested at room temperature (25 °C), and the other group was kept in a freezer for 48 h to reach a steady-state temperature of −20 °C before testing [26].

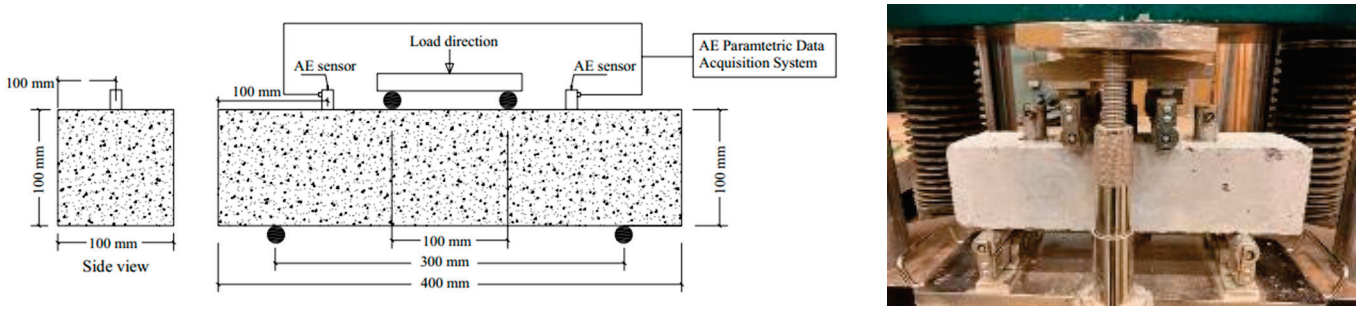


Figure 2. Four-point load flexure setup, AE sensors' locations and samples' positioning.

3.4. Four-Point Flexure Load Setup

A Tinius Olsen universal hydraulic machine was used to perform the four-point flexure test, as shown in Figure 2. The machine conducted the test on a deflection control mode at a constant displacement rate of 0.2 mm/min until failure according to ASTM C78 [25]. The load resisted by the specimens with time was recorded with the aid of a data-acquisition system.

3.5. AE Monitoring Setup

All prisms were tested under ongoing AE monitoring throughout the flexure test via the two attached AE sensors shown in Figure 2. Those piezoelectric sensors had an integral preamplifier model R6I-AST [27]. This type was suitable for the test due to its high sensitivity and low resonant frequency (55 kHz), which made it more convenient to monitor failures in many previous applications, such as metals, fiber-reinforced polymers, and concrete structures [6,27,28]. The two sensors were attached to the surface of each prism using a two-part epoxy adhesive. The exact locations of the sensors are shown in Figure 2. The attached sensors were connected to cables leading to a four-channel AE data acquisition system and AEwin signal processing software (AEwin for USBTM software, Version E3.32) provided by the manufacturer (Mistras Group) [29], which was used to record the signals emitted throughout the tests.

4. AE Data Filtering

4.1. Amplitude-Duration AE Data Filtering

To eliminate noise data and vast wave reflections within the boundaries of samples, the data acquisition system had built-in analog and digital filters, as shown in Table 5.

Table 5. Settings of the AE acquisition system.

AE Setup Parameters	Values
Threshold	40 dB_{AE}
Sample rate	1 MSPS
Pre-trigger	256 µs
Length	1k points
Preamp gain	40 dB
Preamp voltage	28
Analog filter	1–50 kHz
Digital filter	100–400 kHz
Peak definition	200 µs
Hit definition time	800 µs
Hit lockout time	1000 µs
Maximum duration	1000 µs

4.2. Post-Testing Amplitude-Duration AE Data Filters

Moreover, an amplitude-duration-based filter (Swansong II filter) was applied post-testing on the data collected during the four-point flexure test, as can be seen in Table 6. This filter is based on the concept that the real high-amplitude AE signals are typically associated with long values of signal duration and vice versa. The limits of this filter were identified by means of the visual inspection of the resulting AE signals, as can be seen in Table 5. This filter was effective in isolating the noise resulting from the contact between loading heads and specimens, and it was successfully adapted in many previous AE-based studies [6,31,35].

Table 6. Acceptance limits for AE amplitude-duration filter.

Amplitude Range (dB)	Duration (μs)		Amplitude Range (dB)	Duration (μs)	
	Lower	Upper		Lower	Upper
$40 \leq A < 45$	0	400	$60 \leq A < 65$	300	1000
$45 \leq A < 48$	0	500	$65 \leq A < 70$	500	2000
$48 \leq A < 52$	0	600	$70 \leq A < 80$	1000	4000
$52 \leq A < 56$	0	700	$80 \leq A < 90$	2000	7000
$56 \leq A < 60$	100	800	$90 \leq A < 100$	3000	10,000

5. AE Analysis Methods

In the parameter-based approach, any signal is reduced to a few sets of parameters, and the evolution of these parameters with time or any external parameter (e.g., the applied load or crack width development) is investigated to establish a specific correlation that might exist between damage progression and the investigated AE parameters. This paper adopted a set of parameter-based analyses as follows:

5.1. b-Value Method

The *b*-value analysis method was first used in seismic waves generated by earthquakes and has been recognized extensively by seismologists for quantifying seismicity [35,36]. AE waves are similar to seismic waves, and the *b*-value method can also be applied to the AE field. The Gutenberg–Richter (GR) law [37] of seismicity can be modified for the AE analysis as follows:

$$b = (a - \log N_A)/\log A_{dB} \quad (1)$$

where N_A is the number of AE events with amplitudes greater than A_{dB} precedent to a specific event, A_{dB} is the peak amplitude of the AE event in decibels, a is the intercept along the log N-axis, and b is the slope of the regression line, also called the *b*-value of these AE events. From Equation (1), a bigger *b*-value can be obtained when micro-cracks begin to form. In contrast, a smaller *b*-value can be obtained when macro-cracks develop.

5.2. Ib-Value Method

Shiotani et al. [38] proposed the improved *b*-value (*Ib*-value) method after it had been applied successfully to geotechnical and concrete materials [39,40]. The *Ib*-value has been defined by utilizing statistical values of AE events, and it can be calculated as follows:

$$Ib = \frac{\log N(\mu - \alpha\sigma) - \log N(\mu + \Psi\sigma)}{(\alpha + \Psi)\sigma} \quad (2)$$

Ib-value is usually calculated for a group of events, where μ and σ are the mean values and standard deviation of the amplitude distribution of the AE event group, respectively, and α and Ψ are user-defined constants, which would represent the coefficients of the lower and upper limits of the amplitude. It is understood that the *Ib*-value is a transient

feature that is updated with each new hit recorded during the fracture process. It should be sensitive enough to even small fracturing events, so the population N is usually set to 100 recent hits [41].

5.3. AE Signal Intensity Analysis

The damage of concrete structures can be characterized using the intensity analysis of the AE signals. Intensity analysis involves the plot of historical index (HI) and log severity (log S_r), both of which are based on the AE signal strength [42]. AE signal strength takes the amplitude and duration into account, so it is the most effective parameter to determine the trend of the AE data [43].

HI measures changes in the signal strength throughout the loading process. HI at a specific time ($H(t)$) is calculated using the following equation [44]:

$$H(t) = \frac{N}{N-K} \frac{\sum_{i=K+1}^{N} S_{oi}}{\sum_{i=1}^{N} S_{oi}} \quad (3)$$

where N is the number of hits up to time t, S_{oi} is the signal strength of the specific event, and K is an empirical parameter that depends on the number N and can be calculated as shown in Table 7. HI can be used to highlight the change curve in the cumulative signal strength versus time. This method can determine the onset of new damages for the specimen or structure.

Table 7. The K-parameter used to calculate the $H(t)$ for concrete structures.

Number of Hits, N	≤50	51–200	201–500	≥501
K	0	N-30	0.85N	N-75
J	0	50	50	50

The severity index (S_r) is defined as the average signal strength for the J hits that have the largest numerical value of signal strength [45]. It can be calculated using Equation (4):

$$S_r = \sum_{i=1}^{J} \frac{S_{oi}}{J} \quad (4)$$

where S_{oi} is the signal strength of a specific event and J is an empirical constant related to the material for concrete structures, as shown in Table 7. Therefore, S_r refers to the average strength of the 50 signals with the largest peak amplitudes of signal strength.

5.4. Average Frequency (AF) Versus Rise Time/Amplitude (RA) Analysis

According to RILEM [46], the average frequency (AF) is defined as the number of counts in a hit divided by the duration of the signal, and RA-value is calculated from the rise time divided by the amplitude. The AF is measured in kHz, while the value of RA is measured in μs/V. The two parameters can be calculated based on the following equations:

$$\text{AF} = \text{AE ringdown counts/duration time} \quad (5)$$

$$\text{RA} = \text{the rise time/amplitude} \quad (6)$$

Based on the relationship between the AF and RA value established by Ohtsu et al. [47], the cracks can be classified into tensile cracks and shear cracks (Figure 3). A shear crack has occurred when the AE signal has high RA and low AF values. Meanwhile, tensile cracks have occurred when the AE signal has low RA and high AF values [43]. See Table 8.

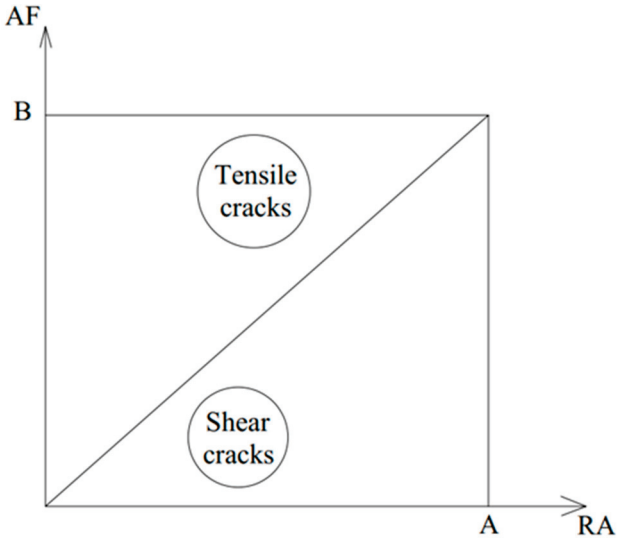


Figure 3. Typical crack classification based on the relationship between the AF and RA values [47].

Table 8. Examples of M-values obtained in concrete-based specimens tested under a four-point flexure test.

Authors	Mixture Type	Dimensions (mm)	Loading Type	Max RA (ms/V)	Max A-FRQ (kHz)	M (s/V/kHz)
Soulioti, Barkoula [48]	Steel-fiber-reinforced concrete (SFRC)	100 × 100 × 100	Monotonic	6	65	0.09
Aggelis [49]	Plain concrete	100 × 100 × 400	Monotonic	15	550	0.027
Shahidan, Bunnori [50]	Steel-reinforced concrete (RC)	150 × 250 × 1900	Cyclic	150	150	1
Behnia, Chai [51]	RC, SFRC, polypropylene FRC	200 × 250 × 2500	Cyclic	5×10^{-3}	400	12.5×10^{-6}
Prem and Murthy [52]	RC	100 × 200 × 1500	Monotonic	200	200	1

6. Results and Discussion

Table 9 lists the compressive and flexure strength for all mixtures at both temperatures (25 °C and −20 °C). The onset times and loads of both micro- and macro-cracking stages that were noticed visually and detected by the AE analysis are listed in Tables 10 and 11. All the results are discussed in further details in the following sections.

Table 9. A summary of test results of the developed mixtures, tested at 25 °C and −20 °C.

Mixture No.	Mixture Type	Testing Temperature	Compressive Strength (MPa)	Maximum Flexure Load (KN)	Flexure Strength (MPa)
M1	M500-0.55w/b	25 °C	61.16	23.64	10.64
		−20 °C	76.68	32.75	14.74
M2	M500-0.4w/b	25 °C	66.79	27.35	12.31
		−20 °C	79.18	34.61	15.57
M3	M550-control	25 °C	74.12	31.14	14.01
		−20 °C	89.91	39.85	17.93
M4	M550-SynF19	25 °C	78.63	32.97	14.84
		−20 °C	90.77	43.19	18.54
M5	M550-SynF38	25 °C	76.16	33.76	15.19
		−20 °C	88.28	43.34	19.05
M6	M550-1%SynF38	25 °C	51.75	30.89	13.90
		−20 °C	63.67	37.19	16.74
M7	M550-SF35	25 °C	78.74	35.64	16.04
		−20 °C	89.59	44.73	19.68

Table 10. AE parameters collected at the first visible micro-crack onset at 25 °C and −20 °C.

Mixture No.	Mixture Type	Testing Temperature	Signal Amplitude (dB)		Number of Hits		CSS (pV.s) × 10^6		*H (t)*		$S_r \times 10^4$ (mV.s)		*B*-Value		First Micro-Crack Load (KN)	First Micro-Crack Time (s)	
			CH-1	CH-2	CH-1	CH-2	CH-1	CH-2	CH-1	CH-2	CH-1	CH-2	CH-1	CH-2		AE Analysis	Visually Noticed
M1	M500-0.55w/b	25 °C	81	83	89	76	1.77	1.69	1.77	1.66	4.32	4.22	3.43	3.64	3.76	61	63
		−20 °C	80	81	106	98	1.98	1.83	1.93	1.84	4.53	4.36	2.86	2.97	4.11	79	80
M2	M500-0.4w/b	25 °C	79	81	112	121	2.05	1.99	2.05	1.98	4.59	4.65	3.23	3.08	4.26	84	86
		−20 °C	80	82	124	132	2.16	2.24	2.19	2.13	4.72	4.76	2.57	2.75	4.89	94	94
M3	M550-control	25 °C	79	80	132	139	2.28	2.21	2.25	2.32	4.81	4.79	2.32	2.19	5.33	89	90
		−20 °C	81	79	146	163	2.49	2.55	2.36	2.77	4.96	4.88	2.04	2.13	5.81	103	105
M4	M550-SynF19	25 °C	83	81	178	183	2.76	2.83	2.47	2.41	5.07	5.13	0.71	0.80	6.92	114	121
		−20 °C	84	82	191	203	2.99	3.01	2.57	3.04	5.25	5.41	0.46	0.51	7.21	131	135
M5	M550-SynF38	25 °C	80	81	155	163	2.48	2.55	2.29	2.39	4.81	4.91	1.49	1.56	5.89	97	104
		−20 °C	82	79	169	174	2.63	2.51	2.43	2.66	4.96	5.05	1.84	1.71	6.23	112	117
M6	M550-1%SynF38	25 °C	84	83	184	192	2.69	2.73	2.59	2.65	4.97	5.03	1.55	1.63	6.34	109	118
		−20 °C	81	80	183	201	2.81	2.88	2.77	2.89	5.07	5.18	1.31	1.22	6.69	123	131
M7	M550-SF35	25 °C	80	81	203	209	3.09	3.16	2.94	3.03	5.29	5.33	0.53	0.67	7.64	179	187
		−20 °C	82	80	217	226	3.21	3.24	3.07	3.21	5.41	5.52	0.31	0.44	8.13	207	212

Table 11. AE parameters collected at the onset of the macro-cracking stage at 25 °C and −20 °C.

Mixture No.	Mixture Type	Testing Temperature	Signal Amplitude (dB)		Number of Hits		CSS (pV.s) × 10^4		*H (t)*		S_r (mV.s)		*B*-Value		Macro Crack Load (KN)	Macro Crack Time (s)
			CH-1	CH-2	CH-1	CH-2	CH-1	CH-2	CH-1	CH-2	CH-1	CH-2	CH-1	CH-2		
M1	M500-0.55w/b	25 °C	79	81	1424	1389	3.95×10^7	3.73×10^7	4.51	4.22	5.91×10^5	5.85×10^5	3.92	2.17	23.64	206
		−20 °C	81	83	1651	1589	4.19×10^7	4.02×10^7	5.03	4.89	6.27×10^5	6.13×10^5	3.19	3.31	32.75	248
M2	M500-0.4w/b	25 °C	80	79	1756	1813	4.56×10^7	4.37×10^7	5.24	5.33	6.68×10^5	6.51×10^5	2.97	3.04	27.35	251
		−20 °C	82	83	1844	1901	4.78×10^7	4.69×10^7	5.76	5.83	7.29×10^5	7.18×10^5	2.72	2.81	34.61	263
M3	M550-control	25 °C	81	84	1969	2006	4.88×10^7	4.93×10^7	5.91	5.79	7.46×10^5	7.39×10^5	2.46	2.55	31.14	277
		−20 °C	79	82	2034	2103	5.16×10^7	5.27×10^7	6.15	6.37	7.67×10^5	7.55×10^5	1.94	2.03	39.85	286
M4	M550-SynF19	25 °C	81	83	2307	2341	5.39×10^7	5.46×10^7	8.04	8.33	7.88×10^5	7.73×10^5	0.86	0.99	32.97	306
		−20 °C	83	81	2463	2391	5.62×10^7	5.68×10^7	8.38	9.12	8.09×10^5	7.91×10^5	0.23	0.29	43.19	327
M5	M550-SynF38	25 °C	79	81	2068	2034	4.96×10^7	4.88×10^7	6.89	7.04	7.13×10^5	7.34×10^5	1.76	1.86	33.76	281
		−20 °C	82	79	2109	2141	5.29×10^7	5.41×10^7	7.46	7.66	7.72×10^5	8.03×10^5	1.13	1.08	42.34	309
M6	M550-1%SynF38	25 °C	81	82	2237	2209	5.16×10^7	5.09×10^7	7.32	7.68	8.65×10^5	8.86×10^5	0.89	0.94	30.89	266
		−20 °C	80	83	2343	2296	5.33×10^7	5.43×10^7	7.91	8.12	9.23×10^5	9.41×10^5	0.66	0.59	37.19	294
M7	M550-SF35	25 °C	79	81	2591	2678	5.89×10^7	5.77×10^7	9.11	9.73	11.21×10^5	11.37×10^5	0.37	0.41	35.64	394
		−20 °C	83	81	2719	2788	6.13×10^7	6.33×10^7	9.87	10.13	12.05×10^5	11.86×10^5	0.18	0.23	44.73	434

6.1. Micro- and Macro-Crack Stages' Onset Indicators in Terms of AE Analysis Parameters

The variation in the AE waves' parameters collected by the monitoring setup, such as number of hits, CSS, signal amplitudes, and the results of the various parameter-based AE analyses, were related to the visually noticed micro- and macro-cracks. Figure 4 shows the variation of the AE activity parameters emitted during the flexure test by sensor-2 for sample-1 of mixture M550-SynF19 when tested at −20 °C along with flexure load-time curve applied during the test. The comparison between the applied load and the corresponding AE parameters shown in Figure 4 indicated that the studied AE parameters are sensitive to the cracking behavior of the tested specimen throughout the test till failure. An overall increase was noticed in the values of the number of hits, CSS, and S_r indicating an increased AE activities due to the initiation of micro-cracks and propagation of macro-cracks. On the other hand, the values of the *H (t)*, *b*-value, and *Ib*-value fluctuated throughout the test time as the AE activities were increased since these parameters are more sensitive to the extent of damage compared with the number of hits, CSS, and S_r. As shown in Figure 4a, the number of hits curve followed and overall increasing pattern with no noticeable changes along with the flexure test. Hence, the change in the number of hits cannot be used as a cracking onset indicator. Meanwhile, there was a noticeable spike in CSS, S_r, and *H (t)* curves after 132 s, and this spike was recorded 3 s before visually noticing the first micro-crack. In addition,

the *b*-value curve kept fluctuating with a decreasing pattern, and there was a noticeable dip at the same detected time (132 s). In addition, the *Ib*-value curve kept fluctuating with no noticeable pattern change prior to the micro-crack onset stage.

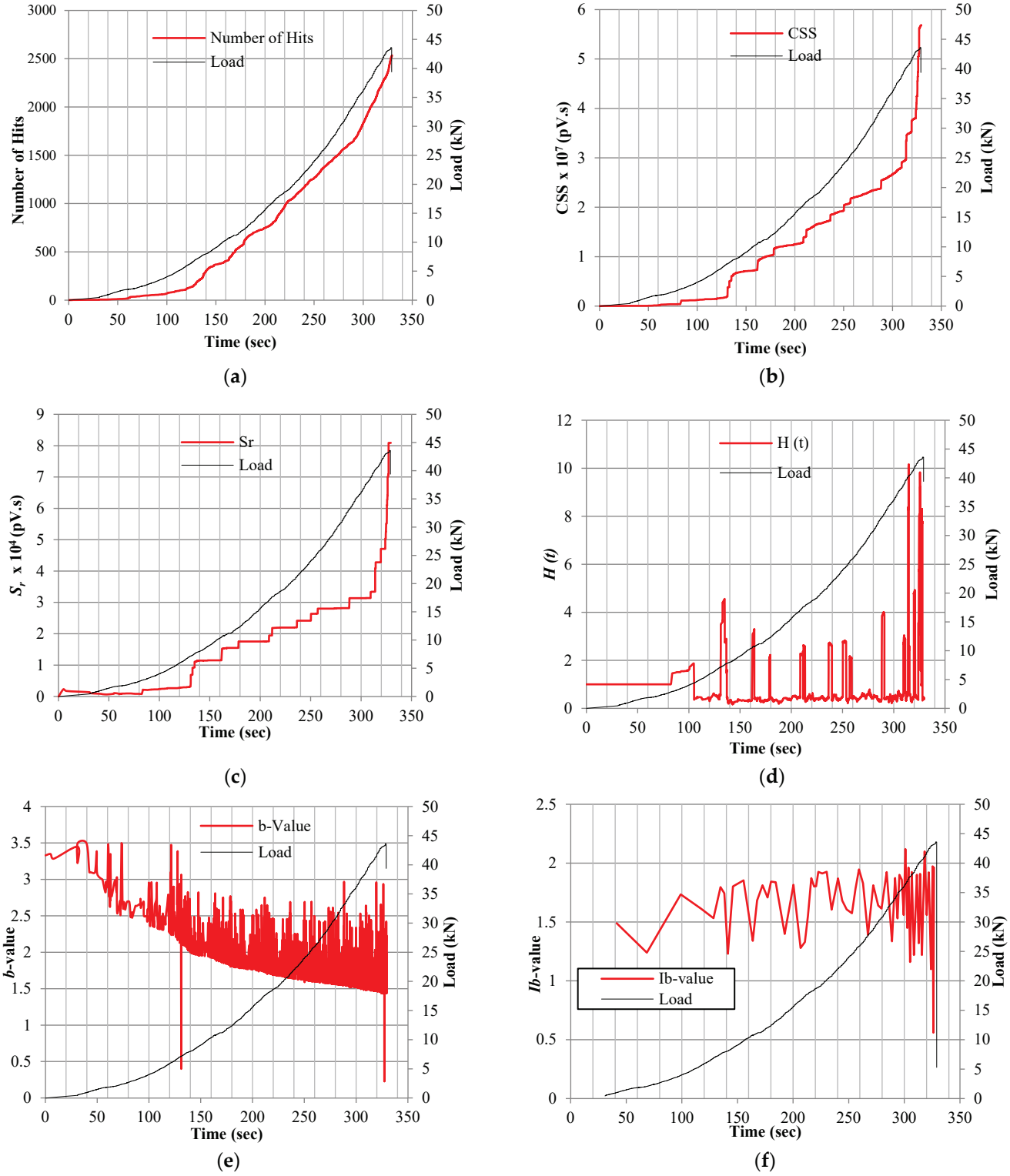


Figure 4. The change in AE parameters throughout flexure test versus applied load on sensor-2 sample-1 mixture M550-SynF19 tested at −20 °C: (**a**) number of hits, (**b**) CSS, (**c**) S_r, (**d**) *H (t)*, (**e**) *b*-value, and (**f**) *Ib*-value.

Previous researchers related the sharp variations in the CSS, S_r, *H (t)*, *b*-value, and *Ib*-value curves to different damage mechanisms [29,38,41,52]. In particular, a previous

study mentioned that the formation of the first micro-crack was accompanied by the first slope change in the S_r curve versus time and the first drastic dip in *b*-value and *Ib*-value curves versus time [34]. It should be highlighted that the AE waves' parameter analysis allowed for the detection of micro-crack onset earlier than the visual inspection, as shown in Table 10. On average, at −20 °C, the AE monitoring detected the micro-cracks 2 secs earlier for mixture M500-0.55w/b, 2 secs earlier for mixture M500-0.4w/b, 1 sec earlier for mixture M500-control, 7 secs earlier for mixture M550-SynF19, 5 secs earlier for mixture M550-SynF38, 9 secs earlier for mixture M550-1%SynF38, and 8 secs earlier for mixture M550-SF35. This earlier alarm could be due to the formation of invisible micro-cracks inside the tested samples; meanwhile, the visual inspection can only detect the micro-cracks developed on the surface.

Similarly, as shown in Figure 4b–d, a sharp spike in CSS, *H (t)*, and S_r curves was noticed after approximately 324 s when the sample reached a load of 43.45 KN before failure. In addition, a significant dip in the *b*-value coincided with the formation of a visually noticeable macro-crack near the midspan of the tested sample after the previously mentioned time (324 s). In addition, the bellows of the *Ib*-value curve fluctuations became closer and higher prior to failure (macro-crack onset). It should be mentioned that almost all other tested samples failed after showing similar AE change patterns before failure. The higher values of the AE events recorded at this stage can be attributed to the further propagation of micro-cracks, which eventually led to the creation of micro-cracks. Therefore, monitoring previously mentioned AE waves' parameters can be considered as indicators to the onset of micro- and macro-cracking stages.

6.2. Cold Temperature Effect on AE Activity Parameters

Overall, the mechanical performance of the tested concrete mixtures in terms of compressive and flexural strength was enhanced and the micro- and macro-crack load and time threshold increased along with decreasing the samples' temperature to −20 °C (see Tables 9–11). The AE monitoring setup detected the onset of micro-cracks when the loads reached approximately 27–36% and 33–41% of the failure loads when samples were tested at 25 °C and −20 °C, respectively. The results of the first cracking loads, failure loads, and the corresponding studied AE parameters at both the times of micro- and macro-cracking detection for all tested samples are summarized in Tables 10 and 11.

For instance, mixture M4 reached an average compressive strength of 78.63 MPa and an average flexure strength of 14.84 MPa when samples were tested at 25 °C. Both values increased by 15.4% and 24.9% when samples were cooled down and tested at −20 °C. The same mixture witnessed the formation of the first micro-crack at 7.41 KN when tested under flexure at −20 °C, and this value was 7% higher than that at 25 °C. This enhancement in mechanical performance and cracking threshold limits reflected on an overall increase in the associated CSS, S_r, and *H (t)* values and an overall decrease in *b*-values as listed in Tables 10 and 11.

For instance, the AE parameters associated with the onset of the first detected micro-crack for mixture M4 (as shown in Table 10) witnessed an average increase of 21.8% in the cumulative number of hits, 27.6% in CSS, 38.6% in *H (t)*, and 9.4% in S_r and an average decrease of 36.3% in *b*-values as a result of cooling down samples from 25 °C to −20 °C. The same pattern was noticed until the onset of the macro-cracking stage for the same mixture, as shown in Table 11. For instance, till the onset of the first macro-crack, there was an average increase of 11.2% in the cumulative number of hits, 8% in CSS, 11.9% in *H (t)*, and 18.3% in S_r and an average decrease of 61% in *b*-values when testing samples at −20 °C compared to 25 °C. This pattern in the collected AE parameters is attributed to the increase in flexure resistance that made the mixtures resist higher loads at −20 °C.

6.3. Effect of W/C Ratio on the Behavior of AE Waves Emitted at −20 °C

Concrete mixtures with different microstructures generate different acoustic activity when they undergo cracking. Hence, mixtures M1 and M2 with different w/b (0.55 and 0.4, respectively) were included to evaluate the effect of changing the microstructure due to turning a huge amount of water into ice at −20 °C. Increasing the w/b was found to significantly decrease compressive strength, flexure strength, the load and time threshold of the micro-and macro-cracks' onset, and the total AE activity recorded till the first micro-crack and till failure (which means less crack formation) when the samples were tested at 25 °C. Meanwhile, this reduction effect in structural performance and AE activity was not such noticeable when tests were performed at −20 °C.

For instance, increasing the w/b from 0.4 (M2) to 0.55 (M1) was a companied by a reduction of 9.2% in compressive strength at 25 °C compared to only 3.3% at −20 °C, and by 15.7% in flexure strength at 25 °C compared to only 5.6% at −20 °C (see Table 9). In addition, there was a decrease by 13.3% in micro-crack onset load at 25 °C compared to 9.1% at −20 °C, and the first micro-crack formation took 23 s less at 25 °C (for M1 compared to M2) compared to only 15 s less at −20 °C (refer to Table 10). Furthermore, till the detection of the first micro-crack, increasing the w/b from 0.4 (M2) to 0.55 (M1) resulted in a decrease of 37.2% and 25.7% in the collected number of hits, 15.1% and 13.8 in the CSS, 15.1% and 13.8 in the *H (t)*, and 15.1% and 13.8 in the S_r at 25 °C and −20 °C, respectively. This reduction in the total collected AE activity and micro-crack onset load and time could be attributed to the reduction in the structural performance along with increasing w/b, which did not allow many cracks to appear.

6.4. Effect of Adding Fibers on the Behavior of AE Waves Emitted at −20 °C

To evaluate AE monitoring sensitivity to fiber pullout and breakage inside concrete mixtures, a non-fibrous control mixture (M3) and another four fibrous mixtures with different fiber lengths, types, and contents (M4–M7) were developed and tested. Overall, there was an enhancement in the flexural performance along with adding different types of fibers accompanied by an increase in the AE activity regardless of samples' temperature during the test. For instance, compared to mixture M3, adding 0.2% of 19 mm synthetic polypropylene fibers increased the flexure strength by 5.6% when samples were tested at −20 (see Table 9) and an increase of 24% in the number of hits, 28.1% in CSS, 9.8% in *H (t)*, and 7.1% in S_r for the total AE events recorded till the onset of the first micro-crack (as shown in Table 10).

This behavior could be attributed to the extra flexural strength added via including fibers and the mixtures that allowed more time and resistance for crack formation. In addition, fiber breakage and slippage could have caused extra acoustic activity that was recorded by the AE sensors. It is worth highlighting that for mixture M7 with 1% synthetic polypropylene fibers, there was a post macro-cracking load resistance and softening behavior, as shown in Figure 5. During that stage, the monitoring system recorded a high AE activity that could be caused by fiber pullout and breakage that may have induced extra acoustic waves. For instance, as shown in Figure 5, sample-2 in mixture M7 tested at 25 °C reached 16.7 KN till the first macro-crack and there was a slight drop in the resistance till the fibers started to hold back the load by itself and reached 17.1 KN, then shifted to the softening phenomenon. After reaching the macro-cracking load (16.7 kN) the total collected number of hits increased from 1938 to 9815, CSS increased from 4×10^7 to 14.93 mV.s, *H (t)* kept fluctuating with an overall increasing pattern, and S_r increased from 3×10^5 to 16.93×10^5 mV.s.

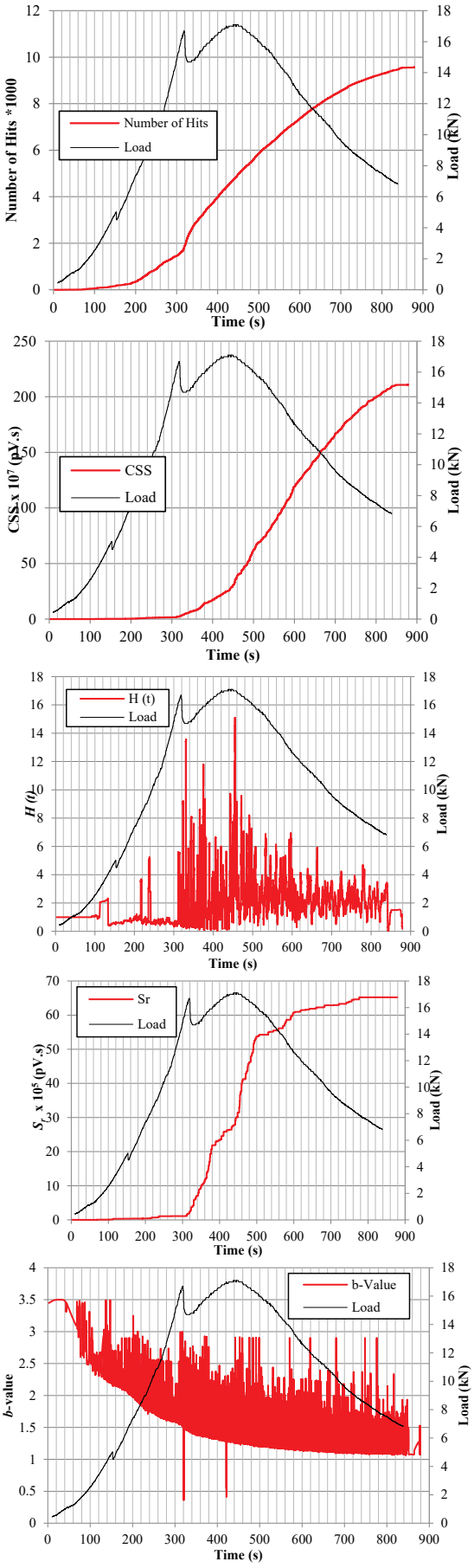


Figure 5. Flexure loading test along with AE parameter data, which were recorded by sensor-2 for sample-2 mixture M550-1%SynF38 tested at 25 °C.

6.5. Effect of Fiber Type on the Flexural Performance and Behavior of AE Waves at −20 °C

Two different materials of fibers were included in the study: polypropylene synthetic in mixture M5 and steel in mixture M7. The steel fibers were supported to be more beneficial terms of enhancing flexure resistance with much more noticeable AE activity over polypropylene synthetic fiber mixtures at both temperature conditions. For instance, mixture M7 witnessed the onset of the first detected micro-crack after 207 s at load 8.13 KN compared to 112 s at load 6.23 KN for mixture M5 at 25 °C, as shown in Table 10. In addition, till the onset of the first micro-crack in mixture M7, the total collected AE parameters were 28.2% more number of hits, 23.9% more CSS, 26.8% more *H (t)* values, 8.6% more S_r values, and 57% more in *b*-values in mixture M7 compared to M5 when both were tested at 25 °C. The increased AE activity could be attributed to the enhancement in the flexural performance.

It is worth noting that there was not any noticeable pattern in changing the values of wave signal's amplitude along with changing fiber materials in both temperatures (25 °C and −20 °C), which eliminates any potential attenuation effect that could be proposed specifically in the case of polypropylene fibers considering its acoustic absorption capacity as a material. For instance, till the onset of first micro-crack, the wave signal amplitude detected by both channels was 80 and 81 dB in mixture M5 and 80 and 81 in mixture M7 when both were tested at 25 °C, as shown in Table 10.

6.6. Effect of Fiber Content on the Behavior of AE Waves Emitted at −20 °C

Fibers are mainly added to concrete mixtures to make it damaged by many narrow cracks, hence eliminating the undesired catastrophic failure. Hence, high acoustic activity is anticipated to be recorded during the flexure test. As a result, mixture M6 was included with 1% polypropylene synthetic fibers compared to only 0.2% fiber content at mixture M5 to monitor the AE activity, specifically the signal amplitudes values at both temperatures conditions. As shown in Table 11, although increasing the fiber content should increase the flexure performance, reaching such a high fiber content of 1% was found to decrease the flexure performance at both temperatures. For instance, the first macro-crack was detected at 37.19 KN after 294 s in mixture M6 compared to 42.34 KN after 304 s in mixture M5 when both were tested at −20 °C. Along with the reduction in flexure performance when increasing fiber dosage, the AE activity increased and mixture M6 experienced total hits of 2296; CSS of 5.43×10^7 pV.s; and *H (t)* of 8.12, S_r of 9.41×10^5 mV.s, which were more than the AE data recorded for mixture M5 that were total hits of 2141, CSS of 5.37×10^7 pV.s, *H (t)* of 7.66, and S_r of 8.03×10^5 mV.s.

These results could be attributed to the fact that increasing the fiber content over a certain value will not make a homogeneous mixture. Hence, the structural performance will degrade. In addition, the extra dosage of fibers will yield more acoustic activity due to the increased breakage and pull-out activity. These results support the conclusion that AE monitoring could be considered as a crack monitoring tool but not a structural performance evaluation tool. This conclusion matches the fact that the collected signals are related to the cracking activity of a certain mixture.

6.7. Effect of Fiber Length on the Behavior of AE Waves Emitted at −20 °C

Fiber length affects the failure mode in FRC mixtures. For instance, shorter fibers are anticipated to be subjected to pull-out. Meanwhile, longer fibers are anticipated to be broken. Hence, two FRC mixtures (M4 and M5) with two different Syn-P lengths, 19 mm and 38 mm, respectively, were included to investigate if there was any difference in the behavior of the acoustic activity developed in both mixtures. As shown in Table 9, mixture M5 with longer fibers showed a better flexural resistance with a delayed first visible

micro-crack at both temperatures. Meanwhile, there was a lower AE activity detected in mixture M5 till failure. For instance, mixture M5 witnessed 19.05 MPa flexural strength and 6.23 MPa micro-crack threshold, which were 3% and 15.6%, respectively, higher than that of mixture M4 at −20 °C. In addition, mixture M5 witnessed 11.7% less number of hits, 5% less CSS, 19.1% less *H (t)* values, 2% less S_r values, and 73.1% higher *b*-values than mixture M4 till failure at −20 °C (see Tables 9–11). The increased AE activity detected in mixture M4 could be attributed to the increased fiber pull-out occurrence due to the insufficient length of fibers. Meanwhile, mixture M5 has fibers with enough development length that they developed less acoustic activity. This observation confirms the conclusion that the AE technique is a non-destructive structural health monitoring technique, not a structural performance evaluation tool.

6.8. Classifying Micro- or Macro-Cracking Levels

6.8.1. AE Intensity Analysis Parameter-Based Chart

Upon the results of the previous sections, intensity analysis parameters (*H (t)* and S_r) were found to change along with crack progression. Hence, analyzing the variation of the values of both parameters was investigated in this study to classify the AE detected hits, whether associated with micro- or macro-cracks. The average intensity analysis parameters were taken from the two sensors, plotted on the chart shown in Figure 6, and correlated to the counterpart cracking level. Surprisingly, the dots plotted in the chart (Figure 6) clustered in two zones according to the cracking stage that they were recorded in. The values of *H (t)* and S_r were found to have specific ranges depending on the crack source type. For instance, the ranges of the values of *H (t)* and S_r were 1.37–2.55 and 2.89–4.61 × 10^4 (pV.s), respectively, for the AE events that were detected during the micro-cracking stage (Table 10). Meanwhile, these ranges were 1.83–3.73 and 5.61–8.55 × 10^4 (mV.s) for *H (t)* and S_r, respectively, at the macro-cracking stage (Table 11). The chart in Figure 6 can further be used to estimate the cracking stage in a specific flexure test using the AE monitoring outputs. For instance, if the *H (t)* and S_r values of a specific AE event were found to be 3.5 and 7.0 × 10^4 (pV.s), respectively, then macro-cracks are anticipated at the time these signals were recorded. This chart has the potential to be a step on the way to develop cracking level classification criteria based on the AE intensity analysis parameters.

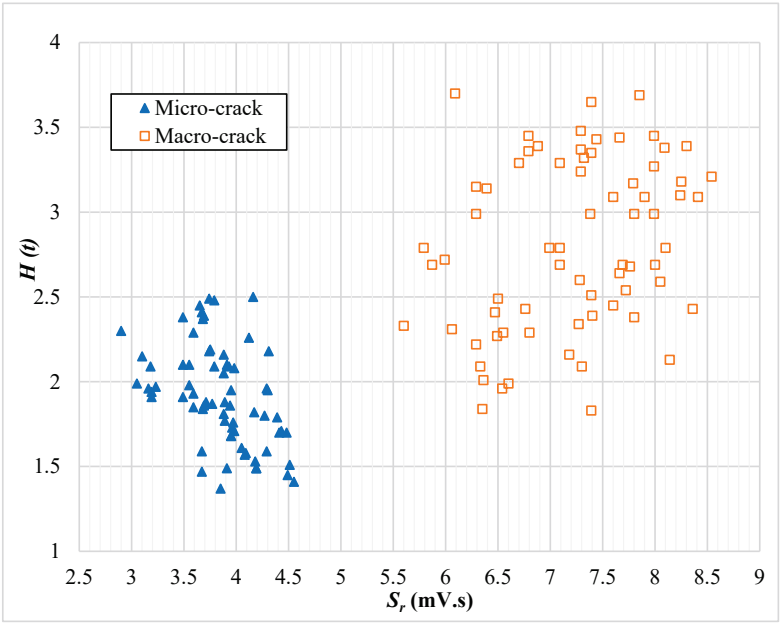


Figure 6. Crack level classification chart based on intensity analysis parameters.

6.8.2. RA Analysis-Based Chart

The RA analysis was mainly used in previous studies to classify the cracks developed during flexure tests into shear or tensile cracks. Upon identifying the AE events collected during the flexure tests, whether they were associated with micro- or macro-cracks, a trial was made to utilize the RA analysis to characterize the AE hits also. Alternatively, Figure 7 shows the values of RA vs. AF for all tested mixtures to find a specific pattern for micro- and macro-crack-related hits. It can be observed from Figure 7 that micro-crack events have relatively higher AF values and lower RA values. Meanwhile, macro-crack events have relatively higher RA values and lower AF values. In both charts, both point clusters were separated by a straight line (diagonal threshold) with a slope value "M" that was determined as indicated in Section 5. The M-values were 1.94×10^{-3} s/V/kHz. These results confirmed the effectiveness of the RA vs. AF analysis for classifying the crack level in all samples regardless of the mixture type or testing temperature. It should be kept in mind that the obtained M-values are exclusively related to these mixtures, loading type, and loading configuration.

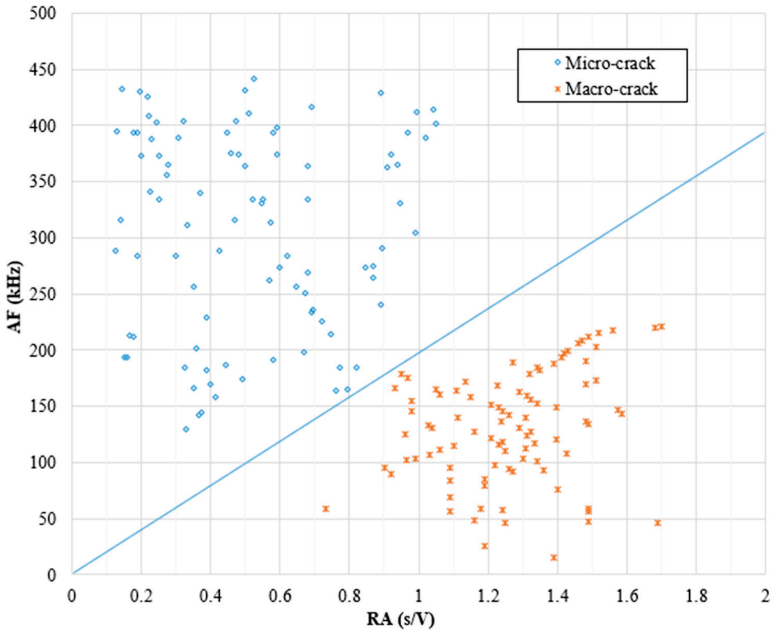


Figure 7. Crack level classification chart based on results of RA and AF analysis.

7. Conclusions

This study investigated the properties of the acoustic emission waves accompanying cracking events in FRC mixtures under flexure at different temperatures (25 °C and −20 °C) along with visual inspection results. Three parameter-based AE analysis were implemented to develop a criterion regarding the pattern of the AE waves emitted during flexure test along with crack formation. The following findings were reached based on the current study:

The four AE parameter-based analyses utilized in this study were intensity, RA, *b*-value, and *Ib*-value analyses, which have the potential to highlight the cracking activity in the listed FRC mixtures at room and subfreezing temperatures (25 °C and −20 °C).

1. The initiation of micro- and macro-cracking coincided with a significant jump in the CSS, $H(t)$, and S_r curves and an extreme dip in the *b*-value curve, while the bellows of the *Ib*-value curve fluctuation became noticeably concentrated only prior to macro-crack onset with no specific pattern change prior to micro-crack initiation.

2. Flexural performance was enhanced, and time and load thresholds of micro- and macro-cracks increased when the samples were cooled down and tested at −20 °C, significantly in mixtures with higher W/B, longer fibers, and lower fiber content. This improvement was also associated with higher AE activity in the form of increased CSS, S_r, and *H (t)* values and lower *b*-values.
3. The AE activity monitoring and analysis detected the onset of micro-cracks when the loads reached approximately 27–36% and 33–41% of the failure loads when samples were tested at 25 °C and −20 °C, respectively.
4. Changing the concrete mixture design parameters, including the w/b ratio as well as fiber type, content, and length, resulted in a noticeable effect on the flexural behavior and the AE activity of the tested mixtures at both temperatures (25 °C and −20 °C).
5. The intensity analysis parameters (*H (t)*, and S_r) were found to have specific ranges according to the associated crack type. Subsequently, a micro- and macro-crack classification chart was developed and presented to characterize the crack type based on the values of the *H (t)* and S_r for the accompanying AE event.
6. Micro-crack events were found to have relatively higher AF values and lower RA values. Meanwhile, macro-crack events have relatively higher RA values and lower AF values. Consequently, an RA analysis-based chart was developed and presented to classify the recorded AE events whether correlated with micro- or macro-crack activity in the tested specimens. A diagonal line with a slope M = 194.44 × 10^{-3} kHz/s/V was found to split the AE events based on the values of RA and AF.
7. The micro- and macro-crack classification charts developed can be used to evaluate the flexural behavior of FRC at low temperatures within the range of the studied parameters in this study. Future research is needed to refine and assess the effectiveness of the developed charts in the assessment of actual concrete structures exposed to cold temperatures and monitored with AE sensors.

Author Contributions: Conceptualization, A.A.A. and A.A.A.H.; Methodology, O.A.K.; Validation, A.A.A.; Formal analysis, O.A.K.; Investigation, O.A.K., A.A.A. and B.H.A.; Resources, A.A.A.H.; Data curation, O.A.K.; Writing—original draft, O.A.K.; Writing—review & editing, A.A.A., A.A.A.H. and B.H.A.; Supervision, A.A.A., A.A.A.H. and B.H.A.; Project administration, A.A.A.H. and B.H.A.; Funding acquisition, A.A.A.H. All authors have read and agreed to the published version of the manuscript.

Funding: This research received no external funding.

Institutional Review Board Statement: Not applicable.

Informed Consent Statement: Not applicable.

Data Availability Statement: No new data were created or analyzed in this study. Data sharing is not applicable to this article.

Conflicts of Interest: Authors Omar A. Kamel and Ahmed A. Abouhussien were employed by the Kinectrics Inc. company. The remaining authors declare that the research was conducted in the absence of any commercial or financial relationships that could be construed as a potential conflict of interest.

References

1. Lee, G.; Shih, T.; Chang, K.-C. Mechanical properties of concrete at low temperature. *J. Cold Reg. Eng.* **1988**, *2*, 13–24. [CrossRef]
2. Gardner, D.R.; Lark, R.J.; Barr, B. Effect of conditioning temperature on the strength and permeability of normal-and high-strength concrete. *Cem. Concr. Res.* **2005**, *35*, 1400–1406. [CrossRef]
3. Yap, S.P.; Bu, C.H.; Alengaram, U.J.; Mo, K.H.; Jumaat, M.Z. Flexural toughness characteristics of steel–polypropylene hybrid fibre-reinforced oil palm shell concrete. *Mater. Des.* **2014**, *57*, 652–659. [CrossRef]

4. Kim, M.-J.; Kim, S.; Lee, S.K.; Kim, J.H.; Lee, K.; Yoo, D.Y. Mechanical properties of ultra-high-performance fiber-reinforced concrete at cryogenic temperatures. *Constr. Build. Mater.* **2017**, *157*, 498–508. [CrossRef]
5. Rostasy, F.; Wiedemann, G. Strength, deformation and thermal strains of concrete at cryogenic conditions. In Proceedings of the First International Conference on Cryogenic Concrete, Newcastle upon Tyne, UK, 27–31 March 1981.
6. Sloan, J.E. The Seismic Behavior of Reinforced Concrete Members at Low Temperatures. Master's Thesis, North Carolina State University, Raleigh, NC, USA, 2005.
7. Bandelt, M.J.; Billington, S.L. Bond behavior of steel reinforcement in high-performance fiber-reinforced cementitious composite flexural members. *Mater. Struct.* **2016**, *49*, 71–86. [CrossRef]
8. Gesoglu, M.; Güneyisi, E.; Muhyaddin, G.F.; Asaad, D.S. Strain hardening ultra-high performance fiber reinforced cementitious composites: Effect of fiber type and concentration. *Compos. Part B Eng.* **2016**, *103*, 74–83. [CrossRef]
9. Brandt, A.M. Fibre reinforced cement-based (FRC) composites after over 40 years of development in building and civil engineering. *Compos. Struct.* **2008**, *86*, 3–9. [CrossRef]
10. Soufeiani, L.; Raman, S.N.; Jumaat, M.Z.B.; Alengaram, U.J.; Ghadyani, G.; Mendis, P. Influences of the volume fraction and shape of steel fibers on fiber-reinforced concrete subjected to dynamic loading—A review. *Eng. Struct.* **2016**, *124*, 405–417. [CrossRef]
11. Park, S.H.; Kim, D.J.; Ryu, G.S.; Koh, K.T. Tensile behavior of Ultra High Performance Hybrid Fiber Reinforced Concrete. *Cem. Concr. Compos.* **2012**, *34*, 172–184. [CrossRef]
12. Farhat, F.A.; Nicolaides, D.; Kanellopoulos, A.; Karihaloo, B.L. High performance fibre-reinforced cementitious composite (CARDIFRC)—Performance and application to retrofitting. *Eng. Fract. Mech.* **2007**, *74*, 151–167. [CrossRef]
13. Kim, M.K.; Kim, D.J.; An, Y.-K. Electro-mechanical self-sensing response of ultra-high-performance fiber-reinforced concrete in tension. *Compos. Part B Eng.* **2018**, *134*, 254–264. [CrossRef]
14. Ismail, M.K.; Hassan, A.A. Impact resistance and mechanical properties of self-consolidating rubberized concrete reinforced with steel fibers. *J. Mater. Civ. Eng.* **2017**, *29*, 04016193. [CrossRef]
15. Choumanidis, D.; Badogiannis, E.; Nomikos, P.; Sofianos, A. The effect of different fibres on the flexural behaviour of concrete exposed to normal and elevated temperatures. *Constr. Build. Mater.* **2016**, *129*, 266–277. [CrossRef]
16. Swamy, R.N.; Mangat, P.S. Influence of fiber geometry on the properties of steel fiber reinforced concrete. *Cem. Concr. Res.* **1974**, *4*, 451–465. [CrossRef]
17. Lee, J.-H. Influence of concrete strength combined with fiber content in the residual flexural strengths of fiber reinforced concrete. *Compos. Struct.* **2017**, *168*, 216–225. [CrossRef]
18. Abouhussien, A.A.; Hassan, A.A. Crack Growth Monitoring in Fiber-Reinforced Self-Consolidating Concrete via Acoustic Emission. *ACI Mater. J.* **2019**, *116*, 181–191. [CrossRef]
19. Abouhussien, A.A.; Hassan, A.A.A. Assessment of Crack Development in Engineered Cementitious Composites Based on Analysis of Acoustic Emissions. *J. Mater. Civ. Eng.* **2019**, *31*, 04019078. [CrossRef]
20. Aggelis, D.G.; Soulioti, D.V.; Barkoula, N.M.; Paipetis, A.S.; Matikas, T.E. Influence of fiber chemical coating on the acoustic emission behavior of steel fiber reinforced concrete. *Cem. Concr. Compos.* **2012**, *34*, 62–67. [CrossRef]
21. Aggelis, D.G.; Soulioti, D.V.; Gatselou, E.A.; Barkoula, N.M.; Matikas, T.E. Monitoring of the mechanical behavior of concrete with chemically treated steel fibers by acoustic emission. *Constr. Build. Mater.* **2013**, *48*, 1255–1260. [CrossRef]
22. Li, G.; Zhang, L.; Zhao, F.; Tang, J. Acoustic Emission Characteristics and Damage Mechanisms Investigation of Basalt Fiber Concrete with Recycled Aggregate. *Materials* **2020**, *13*, 4009. [CrossRef]
23. Ridgley, K.E.; Abouhussien, A.A.; Hassan, A.A.; Colbourne, B. Assessing abrasion performance of self-consolidating concrete containing synthetic fibers using acoustic emission analysis. *Mater. Struct.* **2018**, *51*, 119. [CrossRef]
24. Ohtsu, M. Acoustic emission characteristics in concrete and diagnostic applications. *J. Acoust. Emiss.* **1987**, *6*, 99–108.
25. Colombo, I.S.; Main, I.; Forde, M. Assessing damage of reinforced concrete beam using "b-value" analysis of acoustic emission signals. *J. Mater. Civ. Eng.* **2003**, *15*, 280–286. [CrossRef]
26. Rao, M.V.; Lakshmi, K.P.; Rao, G.N.; Vijayakumar, K.; Udayakumar, S. Precursory microcracking and brittle failure of Latur basalt and migmatite gneiss under compressive loading. *Curr. Sci.* **2011**, *101*, 1053–1059.
27. Abouhussien, A.A.; Hassan, A.A.A. Acoustic emission monitoring for bond integrity evaluation of reinforced concrete under pull-out tests. *Adv. Struct. Eng.* **2017**, *20*, 1390–1405. [CrossRef]
28. Liu, H.; Li, W.; Luo, G.; Liu, S.; Lyu, X. Mechanical properties and fracture behavior of crumb rubber basalt fiber concrete based on acoustic emission technology. *Sensors* **2020**, *20*, 3513. [CrossRef]
29. Pollock, A.A. Material Brittleness and the energetics of acoustic emission. In *Experimental Mechanics on Emerging Energy Systems and Materials, Proceedings of the 2010 Annual Conference on Experimental and Applied Mechanics, Indianapolis, IN, USA, 7–10 June 2010*; Springer: Berlin/Heidelberg, Germany, 2011; Volume 5.
30. BIBM; CEMBUREAU; ERMCO; EFCA; EFNARC. *The European Guidelines for Self-Compacting Concrete*; International Bureau for Precast Concrete (BIBM): Brussels, Belgium, 2005.

31. AbdelAleem, B.H.; Ismail, M.K.; Hassan, A.A. Properties of self-consolidating rubberised concrete reinforced with synthetic fibres. *Mag. Concr. Res.* **2017**, *69*, 526–540. [CrossRef]
32. *C150, A*; Standard Specification for Portland Cement. ASTM international: Conshohocken, PA, USA, 2012.
33. *C1611/C1611M, A.*; Standard Test Method for Slump Flow of Self-Consolidating Concrete. ASTM International: Conshohocken, PA, USA, 2009.
34. *C494-13, A*; Standard Specification for Chemical Admixtures for Concrete. ASTM International: Conshohocken, PA, USA, 2013.
35. Han, Q.; Carpinteri, A.; Lacidogna, G.; Xu, J. Fractal analysis and yule statistics for seismic prediction based on 2009 L'Aquila earthquake in Italy. *Arab. J. Geosci.* **2015**, *8*, 2457–2465. [CrossRef]
36. Smith, W.D. The b-value as an earthquake precursor. *Nature* **1981**, *289*, 136–139. [CrossRef]
37. Gutenberg, B.; Richter, C.F. Frequency of earthquakes in California. *Bull. Seismol. Soc. Am.* **1944**, *34*, 185–188. [CrossRef]
38. Shiotani, T. Application of the AE Improved b-Value to Quantiative Evaluation of Fracture Process in Concrete-Materials. *J. Acoust. Emiss.* **2001**, *19*, 118–133.
39. Shiotani, T. Evaluation of progressive failure using AE sources and improved b-value on slope model tests. *Prog. Acoust. Emiss. VII JSNDI* **1994**, 529–534.
40. Shiotani, T.; Ohtsu, M. *Prediction of Slope Failure Based on AE Activity*; ASTM Special Technical Publication; ASTM International: Conshohocken, PA, USA, 1999; Volume 1353, pp. 156–174.
41. Aggelis, D.G.; Soulioti, D.V.; Sapouridis, N.; Barkoula, N.M.; Paipetis, A.S.; Matikas, T.E. Acoustic emission characterization of steel fibre reinforced concrete during bending. In *Nondestructive Characterization for Composite Materials, Aerospace Engineering, Civil Infrastructure, and Homeland Security 2010*; SPIE: Bellingham, WA, USA, 2010.
42. Chotickai, P. Acoustic Emission Monitoring of Prestressed Bridge Girders with Premature Concrete Deterioration. Master's Thesis, University of Texas at Austin, Austin, TX, USA, 2001.
43. Noorsuhada, M. An overview on fatigue damage assessment of reinforced concrete structures with the aid of acoustic emission technique. *Constr. Build. Mater.* **2016**, *112*, 424–439. [CrossRef]
44. Di Benedetti, M.; Nanni, A. Acoustic emission intensity analysis for in situ evaluation of reinforced concrete slabs. *J. Mater. Civ. Eng.* **2014**, *26*, 6–13. [CrossRef]
45. Fowler, T.J.; Blessing, J.A.; Conlisk, P.J.; Swanson, T.L. The MONPAC system. *J. Acoust. Emiss.* **1989**, *8*, 1–8.
46. Ohtsu, M. Recommendation of RILEM TC 212-ACD: Acoustic emission and related NDE techniques for crack detection and damage evaluation in concrete: Measurement method for acoustic emission signals in concrete. *Mater. Struct.* **2010**, *43*, 1177–1181.
47. Ohtsu, M.; Isoda, T.; Tomoda, Y. Acoustic emission techniques standardized for concrete structures. *J. Acoust. Emiss.* **2007**, *25*, 21–32.
48. Soulioti, D.; Barkoula, N.M.; Paipetis, A.; Matikas, T.E.; Shiotani, T.; Aggelis, D.G. Acoustic emission behavior of steel fibre reinforced concrete under bending. *Constr. Build. Mater.* **2009**, *23*, 3532–3536. [CrossRef]
49. Aggelis, D.G. Classification of cracking mode in concrete by acoustic emission parameters. *Mech. Res. Commun.* **2011**, *38*, 153–157. [CrossRef]
50. Shahidan, S.; Bunnori, N.M.; Mohd, S.; Nor, N.M.; Johari, M.A.M. Analysis of the AE signals parameter at the critical area on the concrete beam. In Proceedings of the 2012 IEEE Symposium on Industrial Electronics and Applications, Bandung, Indonesia, 23–26 September 2012.
51. Behnia, A.; Chai, H.K.; Yorikawa, M.; Momoki, S.; Terazawa, M.; Shiotani, T. Integrated non-destructive assessment of concrete structures under flexure by acoustic emission and travel time tomography. *Constr. Build. Mater.* **2014**, *67*, 202–215. [CrossRef]
52. Prem, P.R.; Murthy, A.R. Acoustic emission and flexural behaviour of RC beams strengthened with UHPC overlay. *Constr. Build. Mater.* **2016**, *123*, 481–492. [CrossRef]

Disclaimer/Publisher's Note: The statements, opinions and data contained in all publications are solely those of the individual author(s) and contributor(s) and not of MDPI and/or the editor(s). MDPI and/or the editor(s) disclaim responsibility for any injury to people or property resulting from any ideas, methods, instructions or products referred to in the content.

sensors

MDPI

Article

Assessment of the Interaction of the Combined Piled Raft Foundation Elements Based on Long-Term Measurements

Grzegorz Marek Kacprzak [1,*] and Semachew Molla Kassa [2]

[1] Faculty of Civil Engineering, Warsaw University of Technology, 00-637 Warsaw, Poland
[2] College of Engineering and Technology, Wachemo University, Hossana P.O. Box 667, Ethiopia; smakmolla23@gmail.com
* Correspondence: grzegorz.kacprzak@pw.edu.pl; Tel.: +48-668-402-343

Highlights:

What are the main findings?

- FEM analysis enables us to complete the missing readings from sensors that are not correctly functioning, leading to conclusion that the CPRF column in the range of small settlements (a few millimeter level) is characterized by lower "stiffness" than that of a single column, while with larger settlements (0.06D), the increase in load-bearing capacity and stiffness of the CPRF column in comparison to a single column is observed.
- In the analyzed CPRF, the CMC columns carry 75% of the total load.

What is the implication of the main finding?

- The need to carry out measurements with ongoing comparison to the results of FEM analysis—the current calibration of the digital twin system for assessing the work of the foundation.
- Optimized design of CPRF elements—the possibility to draw in weaker soil beneath the foundation.

Abstract: Understanding the complex phenomena of interactions between the elements of a combined piled raft foundation (CPRF) is essential for the proper design of such foundations. To evaluate the effects of mutual influence among the CPRF's elements, a series of long-term measurements of selected physical quantities related to the performance of the foundation were conducted on a building with a frame structure, stiffening walls, and monolithic technology, consisting of seven aboveground stories and one underground story. The analysis distinguishes the real deformations resulting from temperature changes and from stress strains resulting from load changes. The two types of deformations were subjected to further interpretation of only changes in the stress and strain over time. Changes in stress values in the subsoil, as well as strain measurements in the vertical direction of concrete columns, were recorded to assess the load distribution between the CPRF's components. The numerical analysis results obtained for a fragment of the monitored foundation were compared with actual measurement results to verify the numerical model of interaction between the structure and the soil. Field monitoring and FEA methods were used to compare the long-term deformation analysis, and they helped to minimize the monitoring time. This comparison also served to supplement and simultaneously expand the dataset of test results on a real-world scale.

Keywords: combined pile raft foundation; long-term in situ measurements; FEM analysis; sensors

1. Introduction

Gotman N.Z. and Gotman A.L. [1] analyzed the interaction between piles, soil, and slabs in a combined piled raft foundation in cohesive soils, focusing on changes in axial forces within the piles. Measurements of axial force changes were taken using strain-gauge-equipped force meters placed at the base and head of 9.0 m long piles, as well as at two cross-sections located at depths of 4 m and 7 m below the pile head. The study considered three configurations: piles working individually, piles in a group, and piles in a combined piled raft foundation. Their findings showed that in a combined piled raft foundation, pile–pile interaction causes the mobilization of friction on the pile side only in the lower portion—between 25% and 33% of the total pile length measured from the bottom. This contrasts with piles working alone, where friction is mobilized along the entire pile length from top to bottom.

Oliver Reuil and Mark F. Randolph [2] studied the behavior of the combined piled raft foundation of the Westend Duo building in Frankfurt, which was founded on Frankfurt clay. The foundation slab covered an area of 4100 m^2, and monitoring included measurements of axial forces in three piles, stress on the ground beneath the slab using five pressure sensors, groundwater pore pressure using five sensors, and settlement at 23 points using geodetic surveying. The authors reported that the maximum settlement of the slab, 4.7 cm, did not exceed the estimated value of 7.2 cm. Preliminary analyses had indicated that the piles would absorb approximately 40% of the total load (αFPP = 40%).

Kharichkin [3] focused on measuring vertical forces in piles to evaluate their role as "reducers" of settlement in a raft footing under a residential building in Moscow. The building consisted of two sections, one 70 m tall (22 stories) and the other 90 m tall (30 stories), with a total foundation area of 3000 m^2. Each section was supported by driven prefabricated piles spaced at 0.9 × 0.9 m and 1.05 × 1.05 m, respectively, with lengths of approximately 14 m and cross-sectional dimensions of 0.3 × 0.3 m. Six piles were equipped with SVD-100 force sensors welded to steel plates at the pile heads to measure forces. Results indicated that corner piles experienced forces of 345 kN, which were 1.9 times greater than piles along the edge of the slab and 2.3 times greater than piles located within the slab's plan. Settlements were measured as 18.6 mm for the lower building and 21.0 mm for the taller building [4].

Ryuuichi Sonoda [5] analyzed a building in Port Island, Kobe City, founded on a pile–slab foundation. The seven-story steel-frame building, with dimensions of 35.25 × 55.80 m^2 in plan, was supported by a 0.4 m thick slab and 2.4 m high foundation beams resting on 93 prestressed high-strength concrete piles (PHC) with a diameter of 0.65 m and a length of 12 m. One pile was equipped with deformation sensors at depths of 4.4 m, 8.4 m, and 11.4 m. The monitoring system also included 12 benchmarks for geodetic settlement measurements and a point for measuring pore water pressure in the ground. The forces measured in the piles after construction closely matched numerical predictions. The safety of different structures is monitored using a field monitoring system and another monitoring system [6].

In Frankfurt am Main, Katzenbach [7] carried out automatic measurements of piles and subsoil for high-rise buildings founded on combined piled raft foundations in Frankfurt clay during the 1990s and subsequent years. These measurements verified the numerically estimated load distribution between piles and subsoil under foundation slabs. One notable

example is the Messeturm building, which is 256 m tall and founded on a square plan of 58.8 m × 58.8 m. Its foundation consists of a 6.0 m thick slab in the central area, tapering to 3.0 m at the edges, supported by 64 bored piles with diameters of 1.3 m and lengths ranging from 26.9 m to 34.5 m, spaced 3.5 to 6.0 diameters apart. The 256 m high Messeturm building, on a square plan of 58.8 m × 58.8 m, founded on a 6.0 m thick slab in the central prt, decreasing to 3.0 m at the edges, and on 64 piles of 1.3 m in diameter and lengths ranging from 26.9 m to 34.5 m, spaced 3.5 to 6.0 diameters, was described in detail by Sommer et al. [8], Sommer [9], El-Mossallamy and Franke [10], and Tamaro [11]. Monitoring included geodetic measurements of settlements and tilts, ground settlement at various depths using extensometers, ground stresses under the slab using pressure sensors, and axial force distribution along piles using deformation measurements at six points. These observations revealed that 55% of the load was carried by the piles, while 45% was borne by the ground under the foundation slab. Additionally, friction mobilized by the piles varied with depth, ranging from 25 to 70 kPa at depths up to 15 m below the slab base and increasing to 110 kPa for inner piles and 160 kPa for outer piles at greater depths. Katzenbach found that piles in combined piled raft foundations mobilized significantly greater friction compared to piles working individually.

Similar monitoring was conducted for the Messe Torhaus building in Frankfurt am Main, which is approximately 130 m tall (30 floors). The building was supported by two independent slabs, each resting on 42 bored piles with a diameter of 0.9 m and a length of 20 m, spaced 3–3.5 diameters apart. Measurements showed that 80% of the load was carried by the piles, while 20% was borne by the subsoil under the slab. The ground's load contribution originated primarily from the self-weight of the foundation slab [12,13].

Katzenbach also analyzed the DG-Bank building (Westendstrasse 1 in Frankfurt am Main), which is 208 m tall with 53 floors. The foundation consisted of a 3.0–4.5 m thick slab covering an area of 2940 m^2, supported by 40 bored piles with diameters of 1.3 m and lengths of 30 m. Measurements indicated that half of the load was carried by the ground under the foundation slab. Further studies by Katzenbach examined load distribution between piles and subsoil for other buildings founded on Frankfurt clay, including the Taunustor-Japan Centre (40% piles), Forum-Kastor and Pollux (35–40% piles), Congress Centre Messe Frankfurt (40% piles), Main Tower (85% piles), Eurotheum (30% piles), and Commerzbank (96% piles).

This work's original contribution is to assess the long-term measurements of CPRF deformations using fieldwork measurements (sensors) and finite element methods (ZSoil version 2011) software.

The main objective of this study is to assess the interaction of elements constituting the combined piled raft foundation of an eight-story monolithic reinforced concrete building. A measurement system was designed and implemented for the first time in Poland. The system includes a method for measuring stress changes in the ground under the foundation slab and deformation measurements of foundation columns to estimate theoretical force changes at three depths.

2. Materials and Methods

2.1. Soil and Water Conditions

The analyzed building is located within a deep Carpathian foreland filled with Miocene sediments. In the ceiling of Miocene clays, which were not drilled directly under the building, an erosion incision was eroded and filled with silty periglacial formations several to a dozen or so meters thick. These formations were formed mainly in silty clays, silt, and fine and silty sands covered from the ground surface with fluvioglacial sands. Within the sandy-silt intercalations in Miocene formations, at a depth of 10 to 25 m below ground

level, a Tertiary aquifer was drilled and taken in the area by drilled wells. Hydrated sand lenses were found with groundwater under low hydraulic tension within the periglacial deposits. Groundwater was observed in the near-surface layer of fluvioglacial sands during drilling.

Based on the research results, two essential geotechnical layers can be distinguished in the subsoil under the building, as shown in Figure 1. The first one is a layer of Quaternary Pleistocene silty periglacial formations, developed in the form of silty clays, silt, sandy silt, and less frequently clays, silty clays, sporadically sandy clays, and clayey sands, in a plastic and soft-plastic state with a liquidity index of IL = 0.4–0.55. Below are silty and fine sands, constituting the interbedding of Miocene clays in a compacted state, with a density index of approximately ID = 0.7–0.8. The red dot indicates the vertical profile of the soil corresponding to the boherholes.

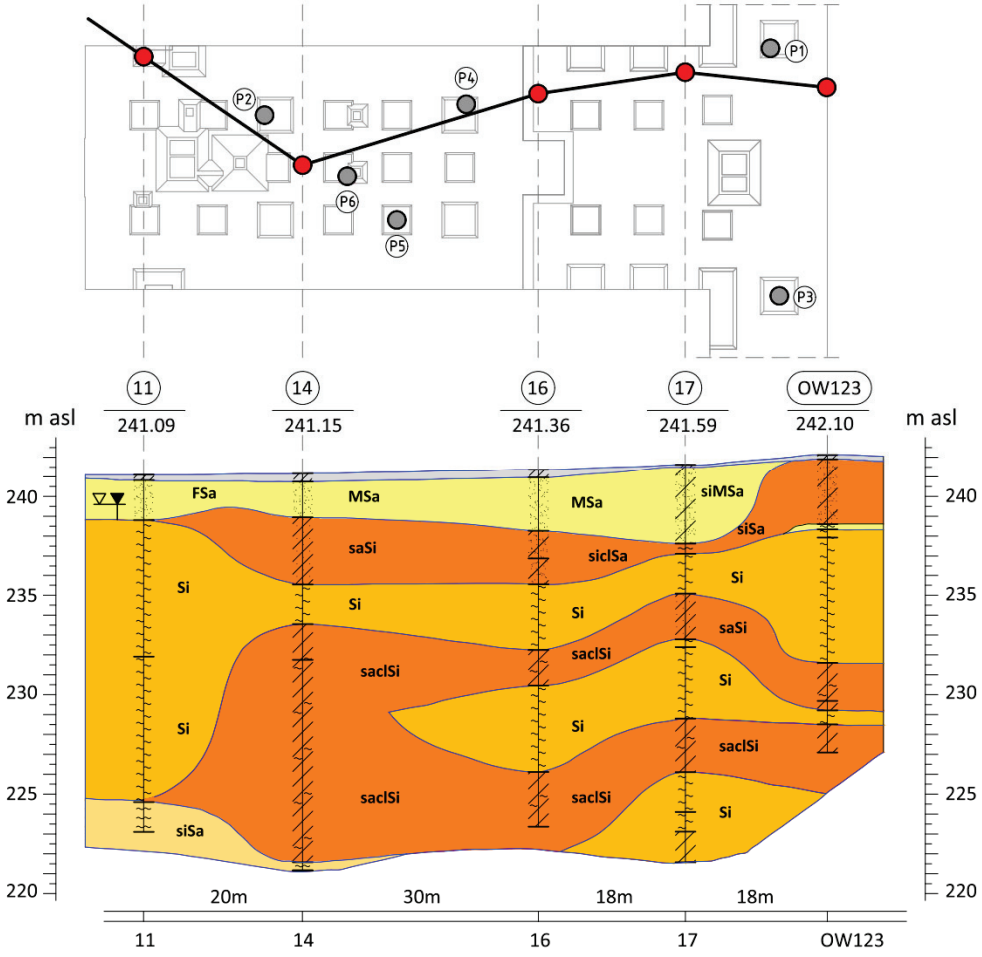


Figure 1. Geological engineering cross-section of the ground beneath the analyzed building. The location of the tested concrete columns (P1 to P6) was marked [14].

The ground conditions in the vicinity of columns P1–P6 (see Figure 1) were detailed by adding the results from the closest CPT—Figure 2 for P1, from the dilatometric test (Figure 3 for column P3) and Figure 4 (for P1 to P6). The resistance of the CPT recorded at the level of 2.0–5.0 MPa confirms the state of silty soils that was macroscopically recognized and presented in the geological engineering cross-section (Figure 1) (by PN-B-04452: IL = 0.21 for qc = 5.0 MPa, IL = 0.51 for qc = 2.0 MPa).

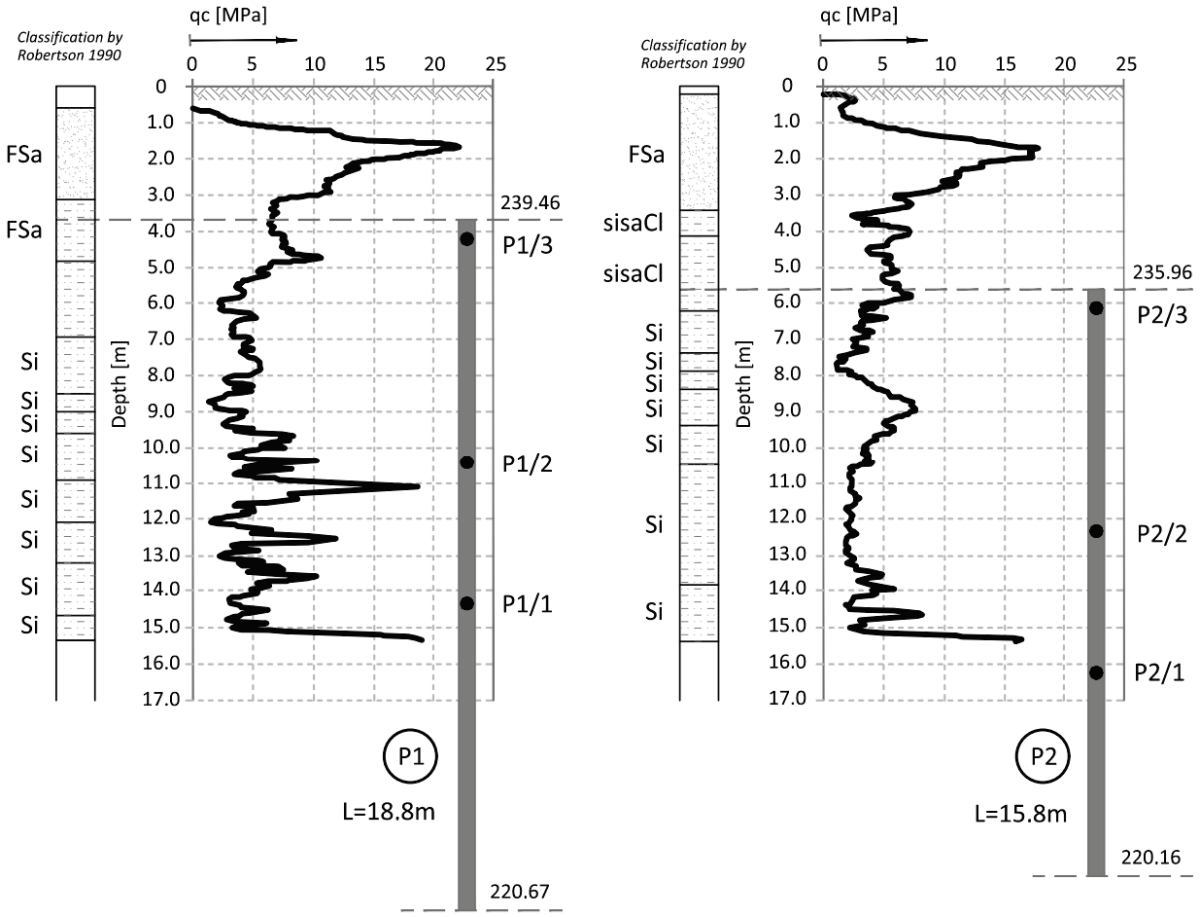


Figure 2. CPT probing in the vicinity of columns P1 and P2 [15].

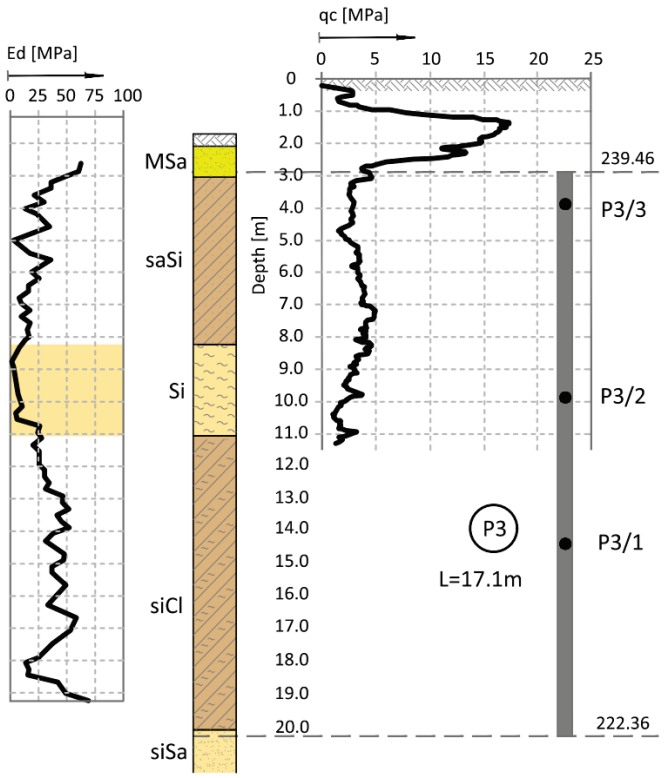


Figure 3. DMT probing (Ed module value) and CPT probing in the vicinity of column P3 [14,15].

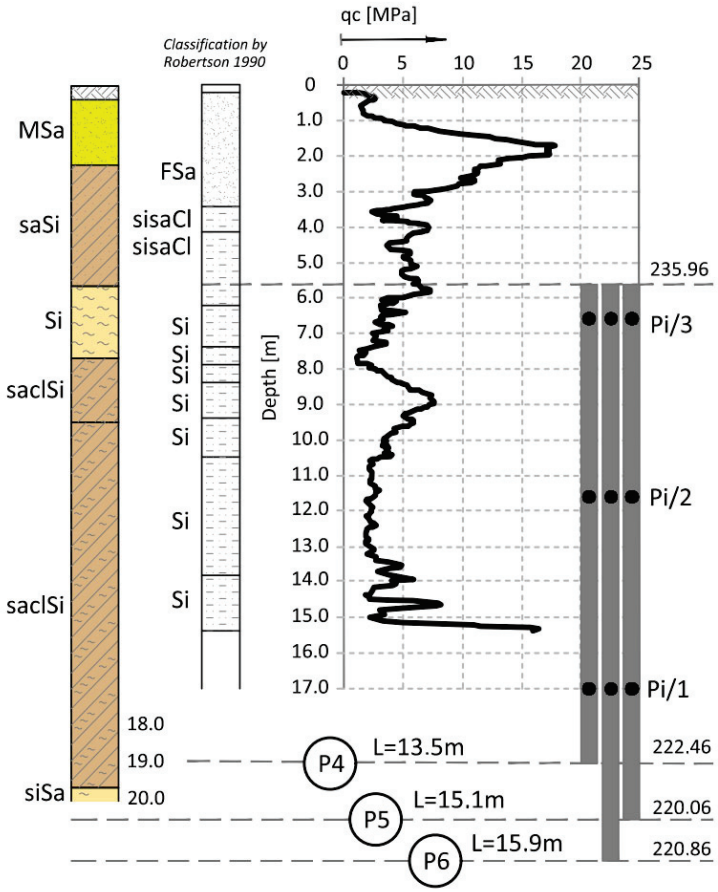


Figure 4. CPT probing in the vicinity of columns P4, P5, and P6 [15].

2.2. Building Structure

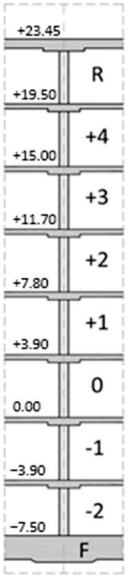
The analyzed building has the shape of a cuboid with a rectangular base with dimensions of 26.90 m × 84.20 m.

The building has a height of 32.6 m from the foundation level, consisting of seven aboveground floors and one underground floor located in the "deeper" section. The facility was designed using monolithic construction technology as a skeleton structure with stiffening walls. The building is founded 4.50 m below ground level on a foundation slab that is 0.80 m thick, with localized thickening to 1.0–1.2 m under the pillars. Table 1 provides the start dates for the individual concreting stages as well as the indicative layout of the floors in the analyzed building. To limit vertical displacements of the structure, localized deep-ground reinforcement was implemented in the area where pillars and walls meet the foundation slab. This reinforcement was carried out using CMC concrete displacement columns (Les Colonnes à Module Contrôlé), which have a diameter of 0.40 m. The columns were embedded into the load-bearing soil, consisting of silty sands, to a depth of at least 1.0 m. The total length of the CMC columns ranged from 8.4 m to 19.3 m. For further analysis, the foundation system consisting of the CMC columns and the soil beneath the slab was modeled and analyzed as a combined piled raft foundation (CRPF).

The monitored building is part of the newly constructed hospital in Kraków-Prokocim, which consists of a total of twenty facilities, including nine hospital buildings with a combined total area of 150,000 m^2 and a volume of 500,000 m^3. The construction was completed within 4.5 years. The analyzed building was monitored for almost 800 days (which corresponds to approximately 80% of the total planned load (excluding variable load from crowds). The shell stage of the building was completed after approximately 200 days, reaching 50% of the total planned load (see Table 1).

Table 1. Concreting schedule by the construction journal records and an indicative layout of the floors in the analyzed building.

Time [Days]	Start of Concreting	Time Between Stages	% of Total Load	Stage
	18 March 2016	0	0.00	Foundation slab
	24 April 2016	39	0.11	–2
0	20 May 2016	24	0.16	Kick-off automatic measurements
0	20 May 2016	0	0.16	–1
38	27 June 2016	38	0.21	0
67	26 July 2016	29	0.26	+1
95	23 August 2016	28	0.31	+2
117	14 September 2016	22	0.35	+3
132	29 October 2016	15	0.40	+4
160	27 October 2016	28	0.45	Roof (R)
201	24 November 2016	41	0.50	Contractual completion of the shell stage



2.3. Measurements of Deformation of CMC Concrete Displacement Columns

The measurements included six CMC concrete displacement columns, where longitudinal deformations were measured at three depths. Each column, located beneath the recesses of the foundation slab, has a diameter of 0.40 m and extends several meters in length. The columns were embedded through layers of weak-bearing silt and dust and rested in a layer of sand, penetrating the sand layer to a depth of at least 1.0 m. The locations of the measured columns and the adopted nomenclature are illustrated in Figure 5. In the subsequent sections of the paper, the axial force variation was analyzed for all columns (from P1 to P6). Additionally, a stress distribution analysis was performed for the slab–subgrade–column system near column P1 [16], focusing on the distribution of load transfer between the structure, the soil beneath the foundation slab, and the concrete column(s).

2.3.1. Measuring Sensors

The system was constructed using Geokon model 4800 wire pressure sensors, which have a measurement range of 170 kPa. These sensors consist of two stainless steel sheets welded together around their perimeter, with a narrow gap between them filled with hydraulic fluid [17,18]. External loads applied to the sensor surface result in changes in the volume of the chamber, causing the fluid to move into or out of the pressure transducer. This movement alters the length of the string connected to the steel membrane that is in contact with the fluid, thereby changing the string's natural frequency [19–21]. Assuming the hydraulic fluid is incompressible, the difference in the frequency of the string vibrations can be translated into changes in pressure [22,23]. Integration with a temperature sensor enables thermal compensation for the sensor readings, ensuring accuracy across varying temperatures. Using individual calibration cards, calculations are performed to determine changes in vertical stresses in the ground beneath the foundation slab, expressed directly in kPa [24,25]. Figure 6 illustrates the construction details of the measuring device, while its basic technical data are provided in Table 2.

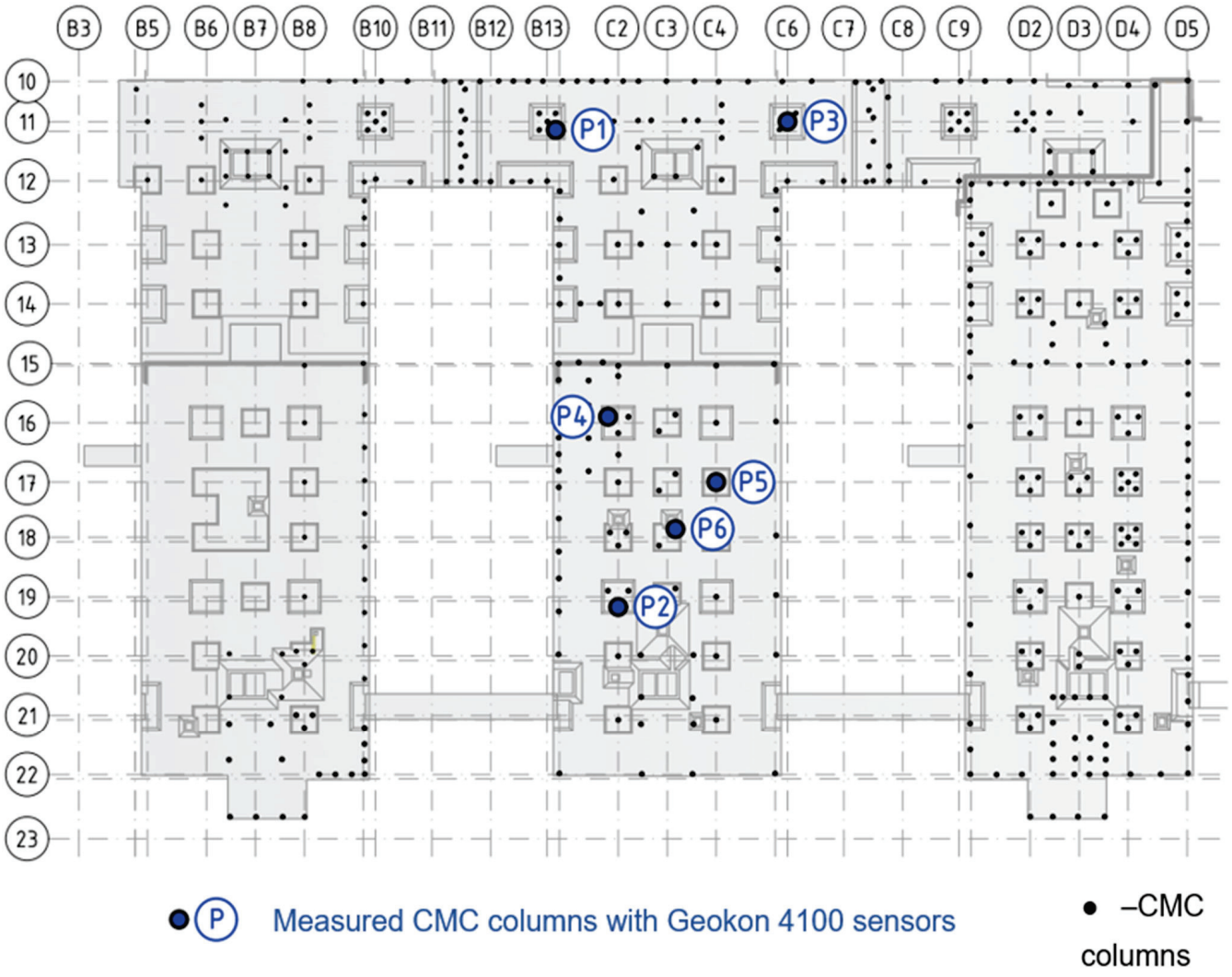


Figure 5. Location and marking of measured concrete columns (P1–P6).

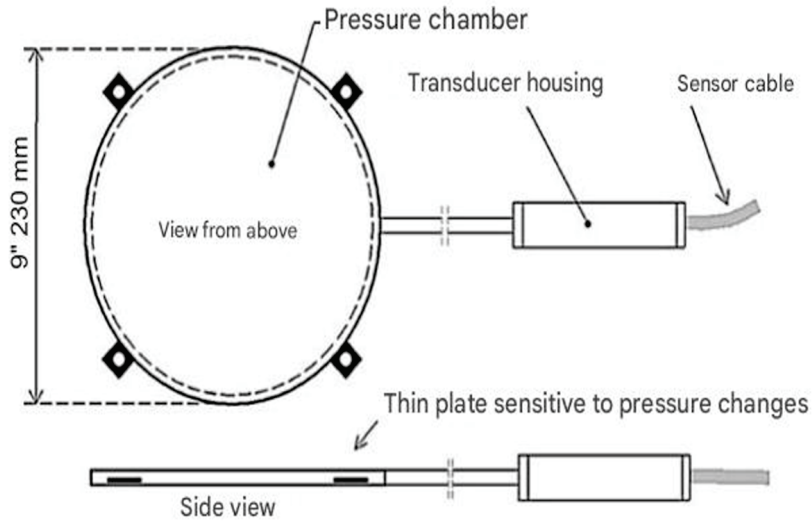


Figure 6. Construction of a string pressure transducer.

Table 2. Technical parameters of the Geokon 4800 pressure sensor.

Transducer Type	**String**
Measurement range	170 kPa
Overload	150% range
Resolution	±0.025% of the range
Accuracy	±0.1% of the range
Linearity	<0.5% of the range
Chamber dimensions	6 mm × 230 mm
Transducer dimensions	150 mm × 25 mm
Material	Stainless steel
Temperature range	−20 to +80 °C

2.3.2. Installation Method

The pressure transducers were installed in the ground beneath the leveling concrete. Prior to installation, the mounting locations were carefully prepared: the ground was excavated to a depth of approximately 0.10 m, and the shape of the recess was adjusted to match the dimensions of the sensor, as shown in Figure 7. Each transducer was placed inside a polypropylene woven bag filled with sand. This procedure was designed to eliminate point interactions and ensure uniform pressure transfer from the foundation slab to the sensor.



Figure 7. View of the recess prepared for the installation of the pressure transducer.

2.4. Measurements of Stresses in the Ground Under the Foundation Slab

To estimate changes in stress values in the ground at the contact point with the foundation slab caused by the varying self-weight of the building during construction, three wire pressure transducers (measured in kPa) were installed in the equalization chamber [26]. One of the sensors was placed in the depression near the measured concrete column (S8), while the other two were positioned as follows: one in the middle of the distance between the edges of adjacent depressions (S7), and the other in the middle of the distance between the edge of the depression and the nearest concrete column (S9), as shown in Figure 8.

2.4.1. Method of Measuring Deformations

In each of the measured concrete columns, string sensors were installed at three different depths to measure the vertical deformation of the shafts (expressed in microstrain [με]). These sensors enabled the observation of changes in force distribution along the column due to variations (or consistency) in the applied load [27].

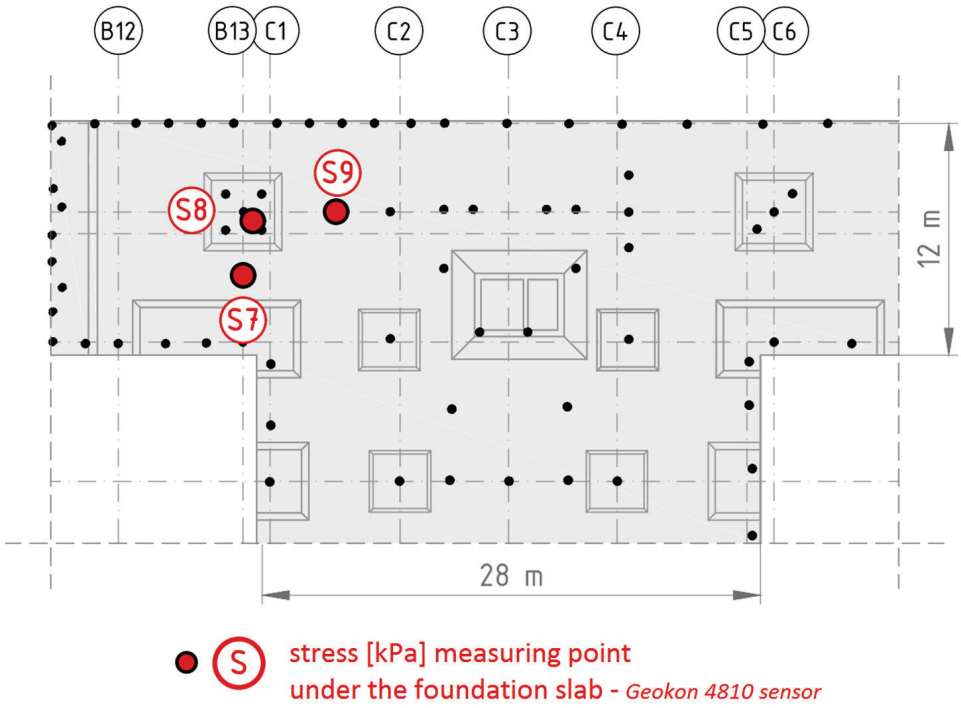


Figure 8. Location and names of stress measurement points in the ground under the foundation slab.

Steel profiles were embedded within the analyzed columns, and Geokon model 4100 (Geokon, Inc., Lebanon, NH, USA), wire strain gauges were heated and attached to the profiles at three designated locations. Figure 9 provides a visual representation of the measuring device, while its basic technical data are summarized in Table 3.



Figure 9. Geokon 4100 string strain sensor.

Table 3. Technical parameters of the Geokon 4100 strain sensor.

Sensor type	**String**
Measurement range	9000 με
Resolution	0.4 με
Accuracy	±0.1% of range
Linearity	<0.5% of range
Temperature range	20 to +80 °C
Active sensor length	51 mm

The sensors are enclosed within steel protective housings, as shown in Figure 10, to prevent damage during installation. These housings are specifically designed to minimize resistance from the concrete mix during the pressing or vibrating of the steel profiles, as illustrated in Figures 10–13.

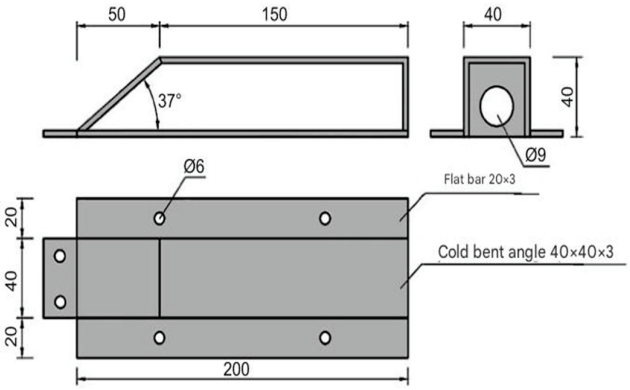


Figure 10. Construction of protective casings.

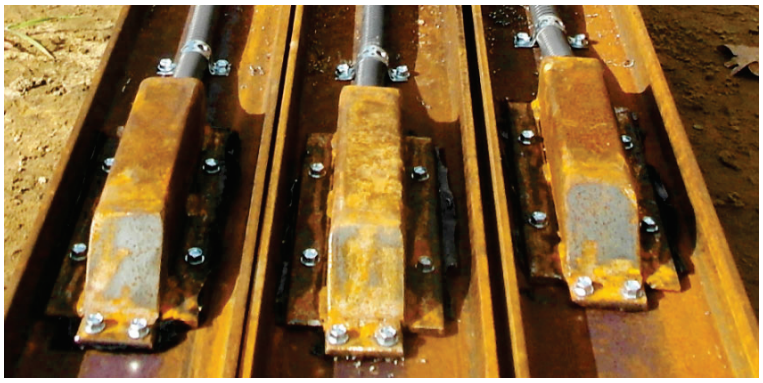


Figure 11. Protective casings installed on IPE120 profiles.



Figure 12. Protective casings installed on RO pipes $2'' \times 2.9$.



Figure 13. View of steel profiles with sensors during the insertion into the concrete mix.

Columns P1 and P2 were equipped with steel pipes measuring approximately 50 mm in diameter, with a wall thickness of 2.9 mm and a length of 15.2 m. The locations of the sensors along the length of the profile are shown in Figure 14. After subjecting these columns to test loads, the upper part of the profile, approximately 1.8 m in length, was cut off to align with the upper surface of the base concrete [28].

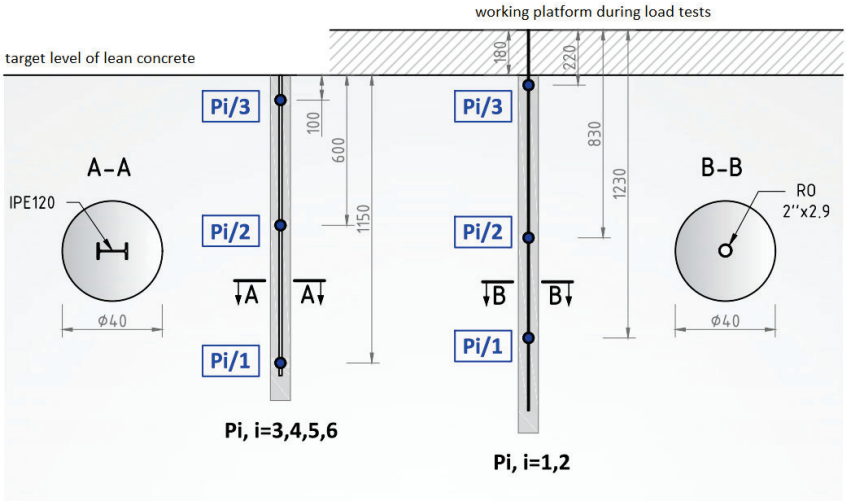


Figure 14. The method of installing deformation sensors and the adopted numbering.

Columns P3, P4, P5, and P6, on the other hand, were equipped with IPE120 steel I-beams (TD Slavsant, Kyiv, Ukraine), each 12.0 m long. Figure 14 also illustrates the sensor placements along the length of these profiles.

2.4.2. Assessment of Compressive Forces in CMC Columns

The determination of compressive forces in columns based on deformation measurements was carried out based on physical laws relating stress to deformation. For the purposes of this study, it was assumed that the dependency is linear, where Ncol is the normal force of the column, Acs is cross-sectional area of the column, Ecm is the elastic modulus of the sandstone aggregate, ε is the change in deformation measured by the sensor, and σ is the stress.

$$\sigma = E_{cm}\varepsilon \quad (1)$$

The value of the modulus of elasticity, *E*, was adopted based on the PN-EN 1992-1-1:2008 standard Eurocode 2—Design of concrete structures—Part 1-1: General rules and rules for buildings [29] for concrete class C25/30, reducing it by 30% due to the use of sandstone aggregate: Ecm = 21.7 GPa.

It was assumed that there is full adhesion between the steel profile and the concrete, ensuring the compatibility of deformations. The transformed cross-sectional areas *Acs* were determined for columns with an IPE120 profile and a tubular profile, taking into account the ratio of the modulus of elasticity of steel Est = 200 GPa and concrete Ecm = 21.7 GPa.

The value of the force Ncol in the column at various depths was determined using the formula

$$\mathrm{N_{col}} = \mathrm{A_{cs}E_{cm}}\varepsilon \quad (2)$$

where ε is the change in deformation measured by the sensor, taking into account the correction related to different thermal expansion coefficients of steel and concrete, which corresponds to the stresses in the structural element, excluding free thermal deformations (as further explained in the text).

It should be noted that the values of the forces were determined under the assumption of constant stiffness in compression of the column along its length (AcsEcm = const). This means that the assumption was made that along the length of the column, there are no disturbances causing a change in the column's diameter (Acs = const) or a change in the elastic properties of the column concrete (Ecm = const).

Based on the above detailed introduction and the field tests incorporated in this section, we have provided the complete workflow in this paper, as shown in Figure 15.

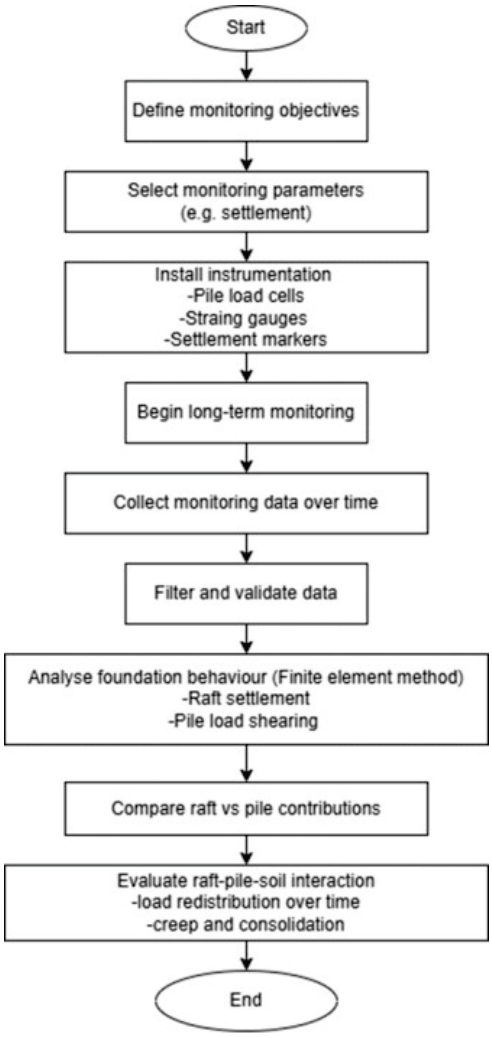


Figure 15. Flowchart of the study.

3. Results and Discussion

3.1. Take-Off Measurements of Column Deformation

Take-off measurements ("zero measurements") for the deformation sensors installed in the columns were taken immediately after their completion, i.e., on 12 October 2015. The readings of the sensors in columns P1 and P2 were also read during the test load. The detailed procedure is shown in Section 3.2.

Automatic measurements were started on 20 May 2016. In Figures 16 and 17, the recorded strain values from this period are presented in relation to the assumed take-off measurements from 12 October 2015. The dotted lines in Figures 16 and 17 were introduced only to increase the figures' readability because the intermediate periods' strain functions are unknown.

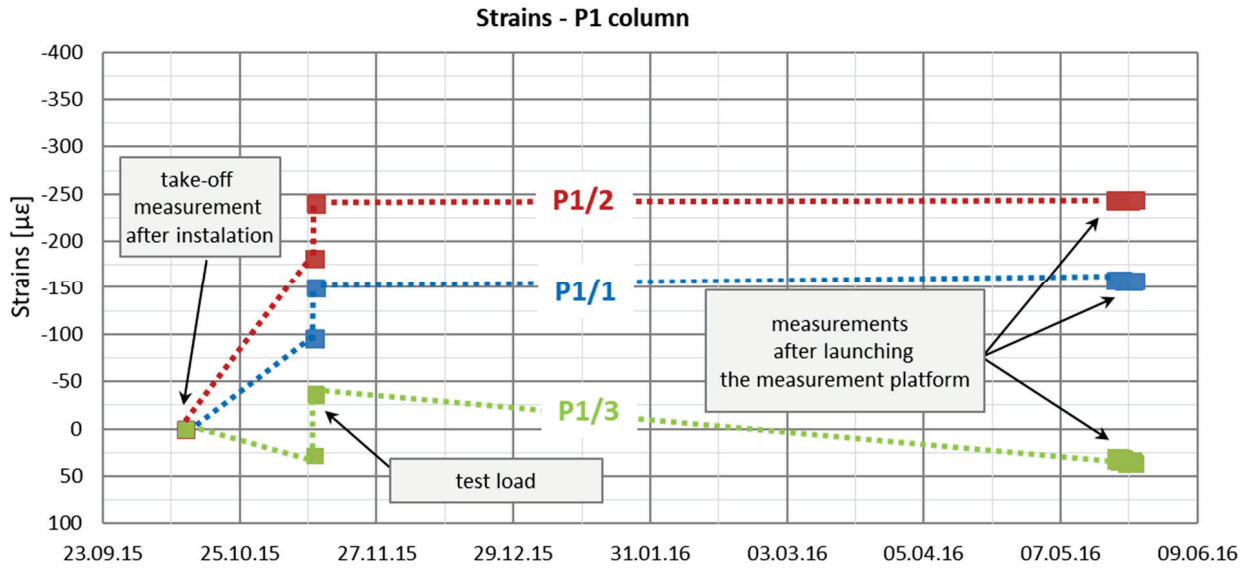


Figure 16. Strain graphs of the P1 column in the period from the take-off measurements to the start of automatic measurements.

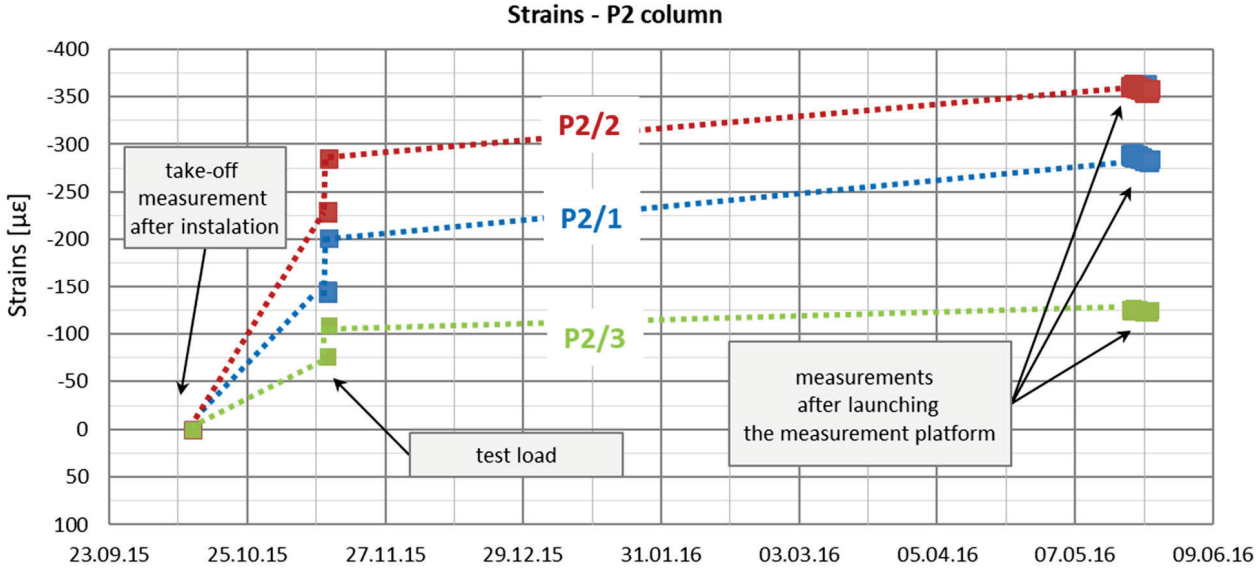


Figure 17. Strain graphs of the P2 column in the period from the take-off measurements to the start of automatic measurements.

Temperature was measured at every step and was taken into account when determining e(s)—stress and strain values–as part of the true stresses (line 462). It cannot be clearly determined whether the first measurement, taken on 12 October 2015, reflects the temperature increase due to the heat of hydration or the cooling phase of the concrete. Comparing the measured temperatures of 20.3 °C, 18.4 °C, and 20.7 °C recorded on 12 October 2015, in sensors P1/1, P1/2, and P1/3, respectively, with the values recorded a month later—11.2 °C, 11.4 °C, and 11.7 °C—it can be observed that the temperature of the concrete decreased along the entire length of the column. On 20 May 2016, the temperature stabilized across all sensors at 9.9 °C, 9.0 °C, and 11.6 °C and remained exactly the same one year later. In column P2, a temperature decrease over time was observed in all sensors. The recorded values for sensors P2/1, P2/2, and P2/3 were, respectively, 15.7 °C, 16.4 °C, and 15.5 °C on 12 October 2015; 10.2 °C, 10.2 °C, and 10.1 °C on 12 November 2015; and 9.2 °C, 8.9 °C,

and 10.9 °C on 20 May 2016. Finally, it should be concluded that the concrete temperature measurements indicate a cooling trend over time.

Based on the graphs of deformations measured in columns P1 and P2 at three depths (Figures 16 and 17), from their installation on 12 October 2015 until the activation of automatic measurements on 20 May 2016, three distinct phases can be identified. The first phase corresponds to changes in deformation due to the maturation of the concrete mix. The second phase is associated with deformation changes resulting from the application and removal of the test load. The third phase covers the waiting period for the initiation of automatic measurements during the building's construction, reflecting an increase in load due to the building's own weight.

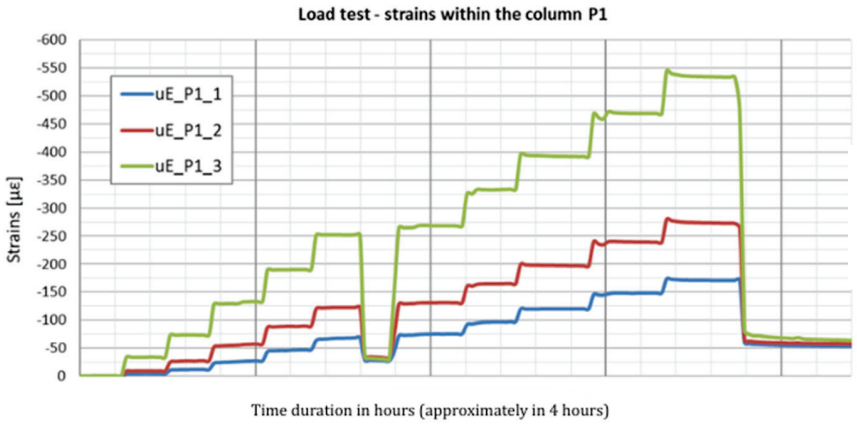
In the first phase, column shortening was observed in all sensors except P1_3, most likely caused by temperature changes following the release of heat during cement hydration, along with concrete shrinkage. Shrinkage occurs due to structural changes in the cement paste caused by physicochemical processes of water loss during concrete setting and hardening. It is assumed that shrinkage was facilitated by the soil's moisture content of 25%. In contrast, sensor P1_3, located near the column head, exhibited an opposite trend: swelling, likely caused by the presence of water in the upper soil layers during the setting of the concrete mix. Column shortening may also have resulted from the load imposed by the concrete mix itself. However, since column deformations were measured at only two points in time (at the start of the concrete setting process and at the onset of the test load), it is not possible to fully or accurately interpret the processes occurring in the column during the initial 30 days after its installation in the ground.

The strain graphs for both columns during the load tests are presented in Figures 18a and 19a. In this analysis, the zero strain reading corresponds to the measurement taken prior to the application of the test load. The recorded strain values reflect only the changes resulting from the variation in the load applied to the column head.

During the second phase, corresponding to the test load, column shaft shortening was observed (Figure 19), accompanied by a residual force remaining in the column shaft after unloading. Based on deformation measurements, it can be concluded that the residual force in column P1 is greater than that in column P2. Comparing these observations with the axial force changes along the column during the test load (Figure 20), these conclusions appear well founded. The performance of the side surface of column P1 is better compared to column P2, which ultimately results in the mobilization of greater force during the test load and, consequently, a higher residual force in column P1.

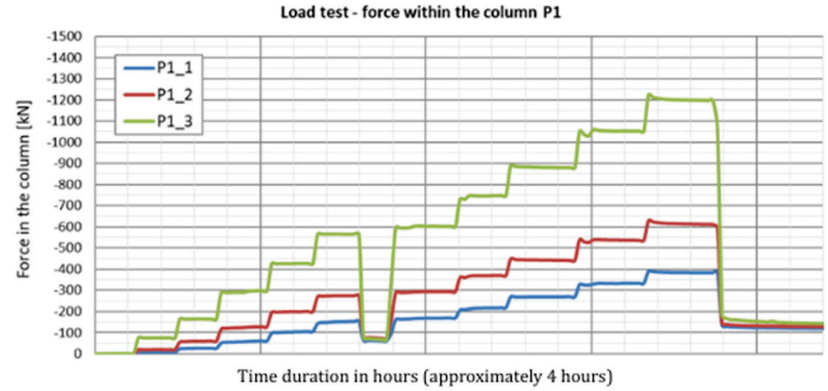
In column P2 (Figure 20b), during the first stage of loading, the force estimated from the measurement with sensor P2_3 was only slightly higher than the force estimated using sensor P2_2. After the fifth stage and unloading of the column, the force at point P2_2 was higher than that at point P2_3 during the subsequent loading step. Although a measurement error cannot be ruled out, the author believes that this axial force distribution could indicate narrowing in the vicinity of sensor P2_2. It may also suggest the absence of friction mobilization on the column side up to the depth at which the P2_2 sensor was located.

In the third and final phase, a phenomenon similar to that observed in the first phase is evident. Measurements from all sensors, except P1_3, indicate column shortening, while sensor P1_3 shows column lengthening. As in the first phase, this can be attributed to the presence of water in the substrate, which causes soil swelling—a phenomenon observed exclusively in the upper part of the column.



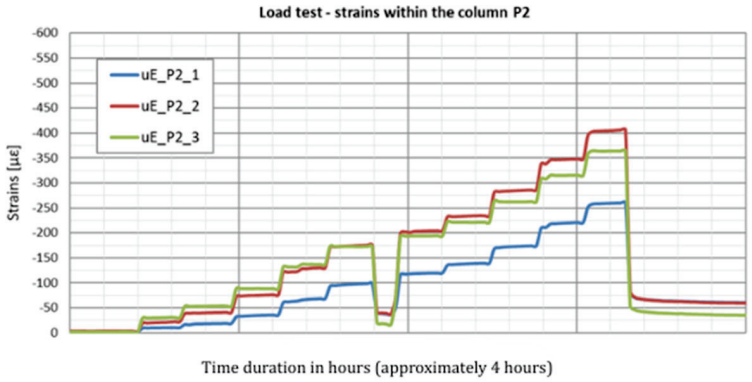
Permanent strains after test load

(**a**)



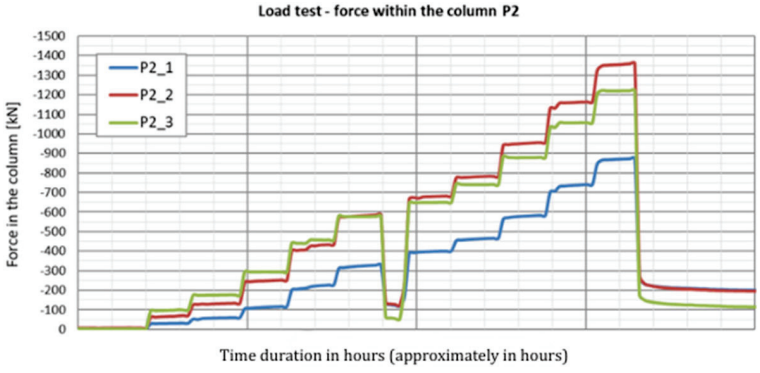
(**b**)

Figure 18. (**a**) Deformation of column P1 and (**b**) axial force in column P1 during the load test.



Permanent strains after test load

(**a**)



(**b**)

Figure 19. (**a**) Deformation of column P2 and (**b**) axial force in column P2 during the load test.

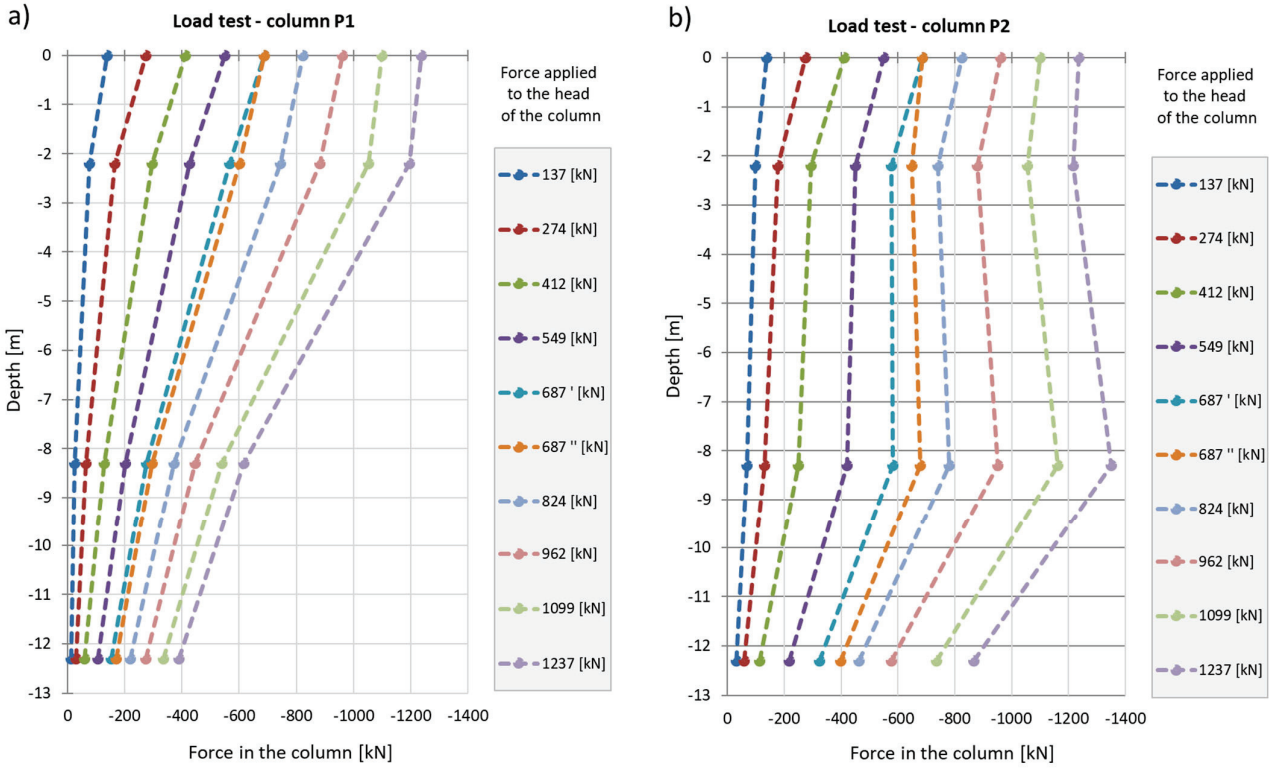


Figure 20. Graphs of the force distribution along columns (**a**) P1 and (**b**) P2 during the test load. Graphs were made based on the strain readings.

3.2. Load Test of Columns P1 and P2

Test Procedure

The tests were conducted from 4 November to 17 November 2015.

The test loading was performed in accordance with PN-83/B-02482 regarding the bearing capacity of piles and pile foundations [30].

To conduct the tests for six columns, a structure composed of a main beam (2×IPE550) with a length of 8 m and two secondary beams (2×HEB300) with a length of 4 m was used. The connection between the secondary beams and the anchoring piles was made by welding, as specified in the design documentation (PW).

The load application was performed using a setup consisting of (a) one hydraulic cylinder (serial number 1) with a nominal force of 2000 kN, and an electric-powered hydraulic pump with a pressure gauge; (b) the monitoring of the column displacement using three dial gauges with a range of 50 mm and a readout accuracy of 0.01 mm; (c) a precision leveling method for controlling the displacement of the anchoring columns.

The test loads were performed in two stages:

Stage 1:

The load was incrementally increased until reaching a force approximately equal to the calculated design load (Q).

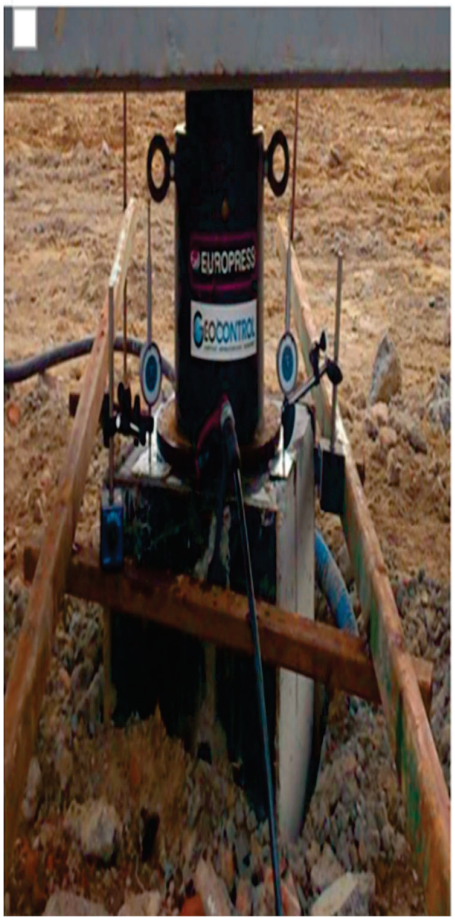
After reaching the force close to the calculated design load (Q), the column was unloaded to zero, and the permanent deformation was stabilized for 10 min.

Stage 2:

Following the reinforcement designer's suggestion, the column was loaded to a force equal to 200% of the calculated design load. The column was then unloaded, and after 10 min, the permanent deformation was recorded. The image in the Tables 4 and 5 are used to measure the displacement. The data are shown in Tables 4 and 5.

Table 4. Load test results for P1.

Stage	Force (kN)	Pressure (MPa)	Time (min)	Readings (mm)		Average (mm)	Increment (ds) (mm)		Settlement (mm)
0	0.00	0.0	---	45.00	45.00	45.00	45.00	0.00	--
1	137	50.0	10	44.70	44.75	44.72	44.72	0.28	0.28
2	274	50.0	10	44.67	44.73	44.69	44.70	0.03	0.03
3	412	100.0	10	44.30	44.38	44.25	44.31	0.39	0.69
4	274	100.0	10	44.29	44.37	44.24	44.30	0.01	0.70
5	412	150.0	10	43.73	43.87	43.62	43.74	0.56	1.26
6	412	150.0	10	43.70	43.85	43.69	43.71	0.03	1.29
7	549	200.0	10	43.00	43.26	42.86	43.04	0.67	1.96
8	687	200.0	10	42.99	43.26	42.84	43.03	0.01	1.97
9	687	250.0	10	42.13	42.55	42.00	42.23	0.80	2.77
10	687	250.0	10	42.11	42.54	41.98	42.21	0.02	2.79
11	0	0.0	10	44.18	44.33	44.08	44.20	−1.99	0.80
12	687	250.0	10	41.86	42.35	41.70	41.97	2.23	3.03
13	687	250.0	10	41.76	42.26	41.60	41.87	0.09	3.13
14	687	250.0	10	41.75	42.24	41.58	41.86	0.02	3.14
15	824	300.0	10	40.76	41.76	40.63	40.95	0.91	4.05
16	824	300.0	10	40.76	41.45	40.60	40.94	0.01	4.06
17	962	350.0	10	39.56	40.56	39.48	39.87	1.07	5.13
18	962	350.0	10	39.46	40.46	39.38	39.77	0.10	5.23
19	962	350.0	10	39.46	40.45	39.35	39.75	0.01	5.25
20	1099	400.0	10	37.80	39.22	37.72	38.25	1.51	6.75
21	1099	400.0	10	37.72	39.18	37.65	38.18	0.06	6.82
22	1099	400.0	10	37.67	39.13	37.60	38.13	0.05	6.87
23	1237	450.0	10	35.77	37.80	35.58	36.38	1.75	8.62
24	1237	450.0	10	35.64	37.69	35.44	36.26	0.13	8.74
25	1237	450.0	10	35.59	37.65	35.39	36.21	0.05	8.79
26	0	0.0	10	36.30	38.77	34.95	36.67	−0.46	8.33



Columns P1 and P2 were subjected to a test load, among other things, to verify the correct operation of the measuring devices installed inside the columns. Load tests were also conducted to obtain the load–settlement relationship for the columns, which is necessary for the proper design of the building's foundation. A force was applied to the column heads, with the value increasing in ten stages. After the fifth stage, the columns were unloaded.

After the fifth stage, the reason for the unloading is to evaluate elastic recovery, calibrating measuring devices.

Regarding the results shown in Figure 21, during the mid-test unloading, the settlement of P1 is recovered similarly to P2, whereas the same does not occur at the end of the test.

When comparing the final deformation results recorded in columns P1 and P2, they are of the same order, i.e., approximately 50 microstrains. A different behavior was observed in Figure 21—after removing the load, there was no recovery of vertical deformation measured at the head of column P1. To clarify the matter, the results of all six load tests were compared. For columns numbered 50 (in axis D4/20), 126 (in axis D2/14), 329 (P2), 255 (P1), 434 (in axis D8/21), and 411 (in axis B8/16), the recovery of vertical deformation

(the difference in settlement between the last load and unload step) is as follows: −4.60 mm, −3.82 mm, −6.71 mm, −0.46 mm, −5.06 mm, and −3.99 mm, respectively.

Table 5. Load test results for P2.

Stages	Force (kN)	Pressure (MPa)	Time (min)	Readings (mm)		Average (mm)	Increment (ds) (mm)		Settlement (mm)
0	0.00	0.0	---	35.00	35.00	35.00	35.00	0.00	---
1	137	50.0	10	34.73	34.68	34.65	34.69	0.31	0.31
2	137	50.0	10	34.72	34.67	34.65	34.68	0.01	0.32
3	274	100.0	10	34.39	34.37	34.39	34.38	0.30	0.62
4	274	100.0	10	34.39	34.37	34.39	33.38	0.00	0.62
5	412	150.0	10	33.86	33.80	33.82	33.83	0.56	1.17
6	412	150.0	10	33.83	33.78	33.79	32.80	0.03	1.20
7	549	200.0	10	32.99	32.90	32.87	32.92	0.88	2.08
8	549	200.0	10	32.99	32.88	33.83	32.90	0.02	2.10
9	687	250.0	10	32.24	32.04	32.01	32.10	0.80	2.90
10	687	250.0	10	32.21	32.02	31.98	32.07	0.03	2.93
11	0	0.0	10	34.56	34.51	34.51	34.53	−2.46	0.47
13	687	250.0	10	31.66	31.52	31.56	31.58	2.95	3.42
14	687	250.0	10	31.64	31.50	31.54	31.56	0.02	3.44
15	824	300.0	10	31.07	30.90	31.94	30.97	0.59	4.03
16	824	300.0	10	31.06	30.89	30.93	30.96	0.01	4.04
17	962	350.0	10	30.06	29.80	29.78	29.88	1.08	5.12
18	962	350.0	10	30.03	29.76	29.75	29.85	0.03	5.15
19	1099	400.0	10	28.67	28.30	28.20	28.39	1.46	6.61
20	1099	400.0	10	28.64	28.29	28.18	28.37	0.02	6.63
21	1237	450.0	10	27.43	26.01	26.74	26.73	1.64	8.27
22	1237	450.0	10	27.40	25.99	26.71	26.70	0.03	8.30
23	0	0.0	10	33.53	33.39	33.32	33.41	−6.71	1.59



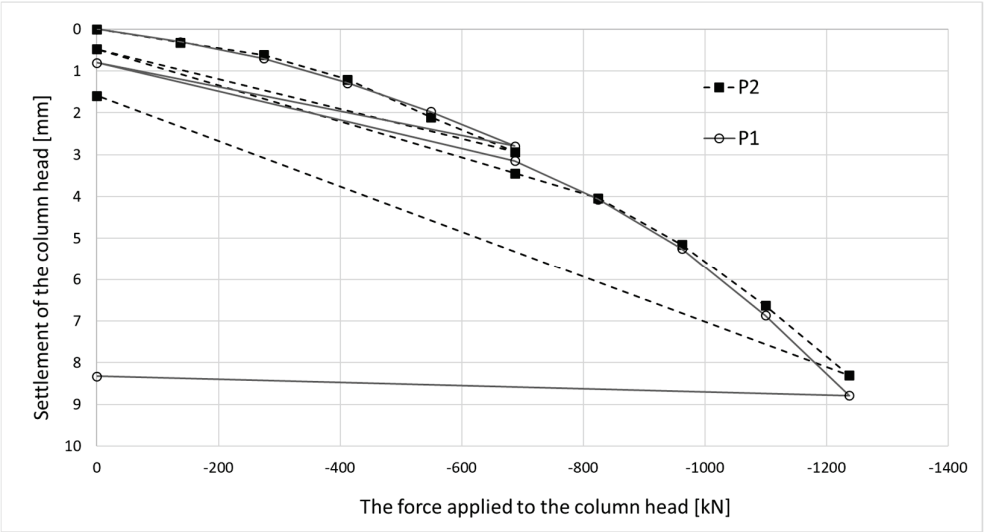


Figure 21. The load–settlement relationship for the head for columns P1 and P2 (load test results).

Clearly, the measurement in column P1 differs from the other five, which indicates a high probability of an error in reading the vertical deformation.

In column P1, the distribution of the axial force corresponded to typical column operation. Specifically, the estimated force values at all stages of the test load were highest for the sensor located at the highest point (P1_3), where the observed values were close to the force applied to the head at each stage of the load. The lowest force values were recorded by the sensor at the deepest point (P1_1). This response indicates good cooperation between the column side and the ground, as well as good quality of the column shaft.

When comparing these conclusions with the results of the CPT probing, it is important to note that the soil surrounding the P1 and P2 columns, at the location of the P1_2 and P2_2 sensors, exhibits significantly different cone resistance qc. For column P1, the resistance is approximately twice as high as that for column P2 (over 5 MPa for column P1 compared to 2.5 MPa for column P2, on average). The higher force values at the mid-height of column P1, compared to the upper part after the fifth stage and unloading, may also suggest variable values of the modulus of elasticity of the hardened concrete along the column.

Despite the differing behavior of the side surfaces and bases of columns P1 and P2, the load–settlement relationship determined for their heads is very similar (Figure 21). This indicates that, from the perspective of the structure's overall behavior, the columns perform almost identically within the analyzed load range.

The conclusions from the axial force distribution interpretation along the shafts of columns P1 and P2 for different load steps can be compared to the findings resulting from the load–settlement relationship for their heads (Figure 21). After the final unloading for P1, practically no change in the head elevation was observed, while the head of column P2 moved upwards after the load was removed. The share of plastic deformation of the soil along and under column P2 is relatively small. Column P2 deforms elastically without the cooperation of the side surface (lack of lateral constraints). In the case of column P1, the side surface works much better, which is manifested by a practically complete reduction in the column head displacement upwards because the side surface counteracts the column from rising.

The maximum force applied to the heads of columns P1 and P2 of 1200 kN causes an estimated elastic shortening of column P1 by about 8.3 mm (assuming the modulus of elasticity for the concrete column E = 21.7 GPa, diameter D = 0.40 m and length L = 18.8 m) and of column P2 by about 7.0 mm (assuming the same value of the modulus and diameter and length L = 15.8 m). The values estimated in this way are close to the values of the settlements of the heads of columns P1 and P2 measured during the test load (Figure 21). The estimated elastic shortening of column P1 observed on the load–settlement graph, taking into account good ground conditions around the column, may indicate the mobilization of friction along the entire length of the column, which results in a decrease in the axial force in the column. As shown in Figure 21, column P2 shortens elastically by about 6.0 mm. Permanent deformations of the substrate amount to about 2.0 mm. The extension (with excellent approximation) of the last linear section of the axial force dependence over depth for column P1 (Figure 22a) shows that the side surface transfers almost the entire force value applied to the column head, with practically no work performed by the column base. It follows from Figure 22b that different substrate–column interaction processes accompany the work performed by column P2. The agreement of the estimated and observed elastic deformations confirms the above interpretation of the axial force variation with depth, where the side layer does not cooperate with the ground in the first eight meters, both under load and during unloading. The return of elastic deformation of the column shaft is noticeable in the absence of resistance of the side layer. The work of the lower part of the column, for a depth greater than 8.0 m, causes the mobilization of friction at the column–ground interface and/or a slight settlement of the base, resulting in plastic deformation of the ground.

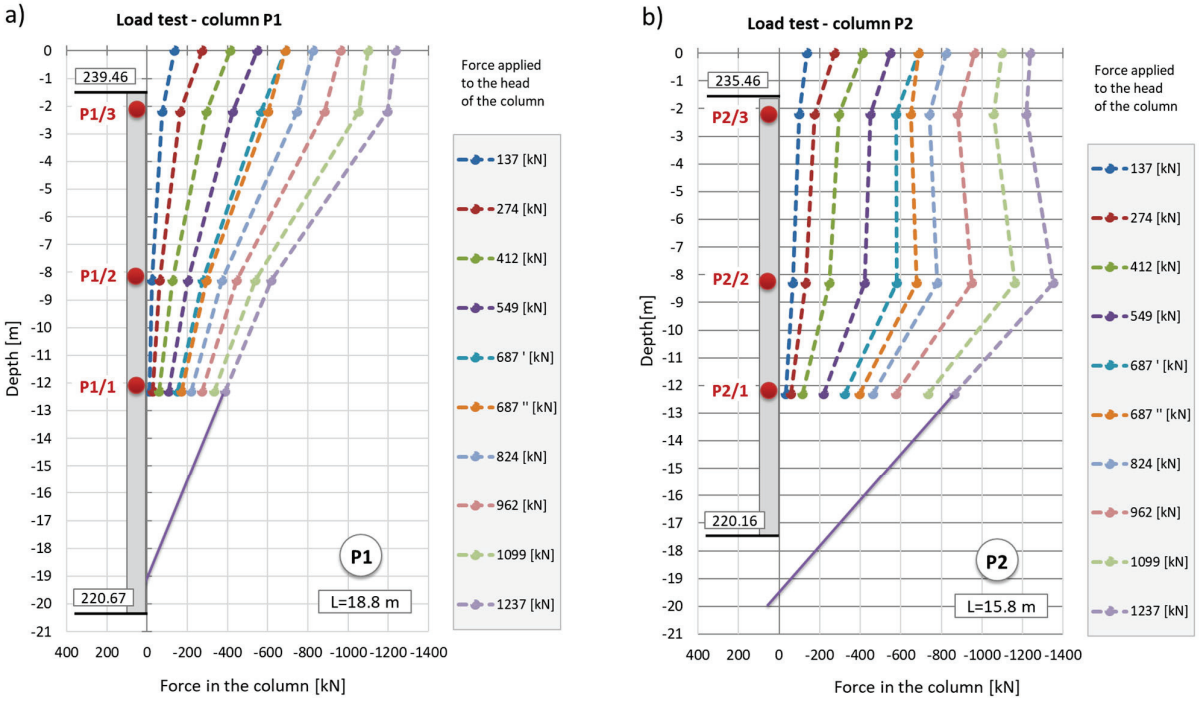


Figure 22. Hypothetical extension of the force distribution diagram along columns (**a**) P1 and (**b**) P2 during the test load.

3.3. The Influence of Temperature Changes on the Measurement of Column Deformations

Sensors Pi_3 were installed at the point of the greatest temperature and atmospheric pressure fluctuation. For example, Figure 23 shows a graph of temperature changes as a function of time measured by sensor P1_3, placed in column P1. The graph shows that the temperature of the concrete near the head changes significantly and directly affects the values of deformations and, therefore, the estimated values of the axial force in the column.

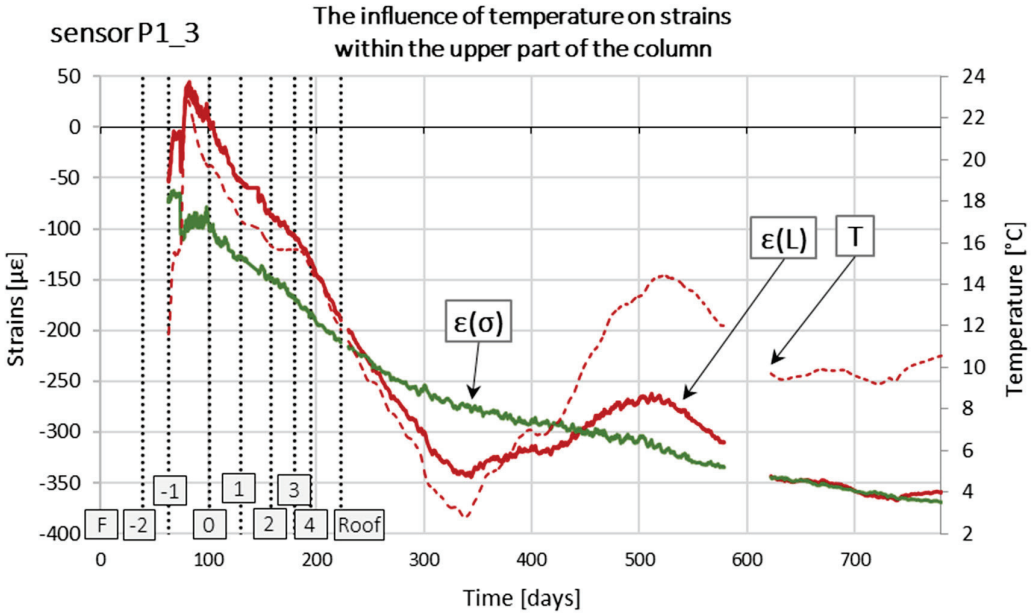


Figure 23. Influence of temperature on the determined strain values. Designations: ε(L)—real strains; ε(σ)—stress strains.

Analyzing the actual deformations of concrete in a simplified way, we can distinguish free deformations, deformations resulting in the formation of stresses, and creep and shrinkage deformations. Neglecting rheological phenomena due to the relatively short measurement period, we can assume that the actual deformations (L) are the sum of deformations caused by the impact of temperature and deformations resulting from mechanical impacts, which generate stresses in whole or in part. In other words, these are such deformations that could be determined at the measuring point based on the measurement of the change in the base length made using an external measuring device, e.g., a caliper. Stress strains are theoretical strains that, using Hooke's law, correspond to the values of stresses at the measuring point. Mechanical and non-mechanical interactions can cause them. For example, in a wholly restrained beam element, its length does not change due to temperature, and therefore, no strains occur. Using the temperature measurement, however, we can determine the theoretical value of the strains that would occur if the element were free to change length. Temperature changes in a restrained beam generate stresses that do not cause strains.

In the analyzed case, based on measurements with wire sensors, the actual strains $\varepsilon(L)$ were determined, and then stress strains $\varepsilon(\sigma)$ were separated from them (Figure 23). In the further part of the work, only the changes in stress strains $\varepsilon(\sigma)$ over time will be analyzed.

3.4. Distribution of Force on the Elements of the Combined Piled Raft Foundation

The stress (pressure) change in the subsoil under the foundation slab was analyzed as a function of time (Figure 24). As mentioned earlier, the string pressure transducers were located in such a way as to enable the determination of the part of the foundation slab through which the load is transferred to the subsoil from the point support of the column type. One of the stress sensors was installed in a depression in the vicinity of the measured concrete column (S8), while the other two were in the middle of the spans, between the adjacent depressions (S7), and between the depression and the subsequent columns (S9)—compare. The measurements were designed to provide the information necessary to determine the vertical load distribution between the subsoil under the foundation slab and the concrete columns.

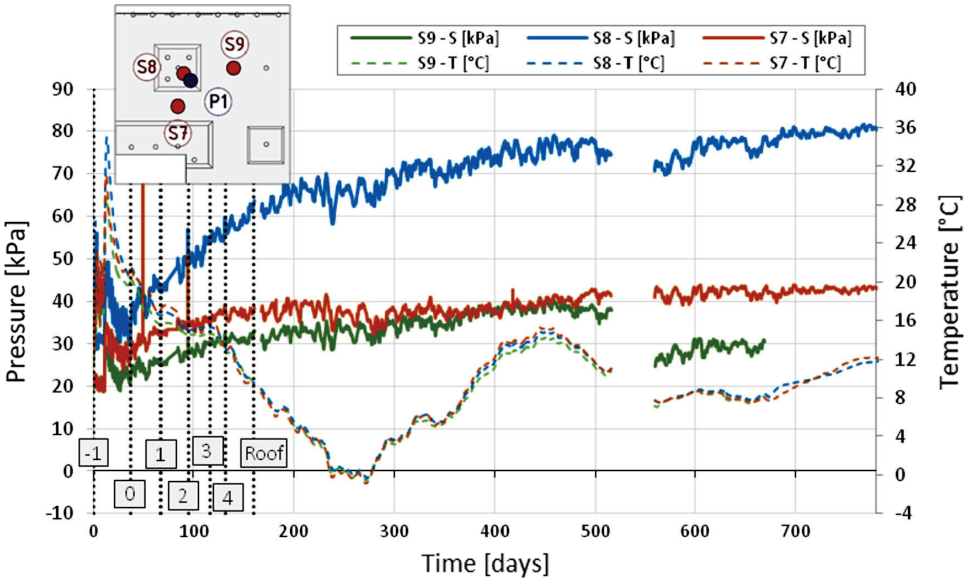


Figure 24. Change in the stress value in the ground under the foundation slab as a function of time for selected locations, taking into account the correction resulting from the stresses existing in the ground at the moment of starting the measurement.

The automatic measurement system was launched on 20 May 2016 at 16% of the construction progress about the shell of the entire building (compare Table 1), i.e., after the foundation slab and the ceiling above story—two were completed in the part between axes C1-C5/15′-22′ and after concreting the foundation slab between axes B12-C7/10-15 (in the measurement area). In connection with the above, a correction was introduced to the stress measurement, consisting of taking into account the initial stress resulting from the thickness of the slab, i.e., 30 kPa for sensor S8 in the recess and 20 kPa for the two remaining sensors S7 and S9.

Based on the stress measurements in the subsoil under the foundation slab outside the recess (sensors S7 and S9), assuming for analysis the stress value from measurements taken between day 400 and 500, i.e., approx. 40 kPa, it can be hypothesized that the soil, apart from the foundation slab's dead weight, transfers the load from the aboveground part of the structure at a level of approximately 20 kPa. The area of the slab within the column, where the recess of the foundation slab with an area of 3.5 m × 3.5 m is located, transfers to the ground a load that is more than twice as high, i.e., the stresses measured in the ground are on the order of 80 kPa, of which 30 kPa is the dead weight of the foundation slab, and 50 kPa is the load transferred by the column to the foundation.

To determine the load distribution on the subgrade and concrete columns, a comparison was made of the stress values transferred to the subgrade by the aboveground part of the structure (Figure 24) and the forces mobilized in the concrete columns (from Figure 25) with the total value of the force transferred by the column to the foundation slab. This force was estimated by the structural designer at the level of $F_{c,d}$ = 10,125 kN based on the analysis of the FEM model of the aboveground part of the structure. Assuming the average load factor at the level of 1.2 (static and strength calculations were carried out based on the PN-B standard package), the average value of the force in the column can be estimated as Fc,k = 8438 kN. The additional load on the ground beyond the slab depth, which was measured as 20 kPa in the area of 7.75 m × 10.30 m − 3.5 m × 3.5 m = 67.6 m^2, allows us to estimate the value of the force taken up by the ground under the slab at the level of Fr2,k = 1352 kN. The additional load on the ground under the slab recess, determined based on the measured stress of 50 kPa in the area of 3.5 × 3.5 = 12.3 m^2, gives the force value Fr1,k = 613 kN. In total, the plate transfers a force of $F_{r,k}$ = 1965 kN to the subgrade. The value of the axial force estimated after 788 days based on the measurement of concrete deformations with the P1_3 sensor located near the head of the P1 column is $F_{p,k}$ = 869 kN. Considering the actual distribution of seven columns within the recess (Figure 25), it can be assumed that the total load taken by the group of columns is Fpg7,k = 7 × 869 kN = 6083 kN. The sum of the values of the force taken by the ground Fr,k = 1965 kN and the columns Fpg7,k = 6083 kN is Fc′,k = 8048 kN is very close to the force value specified by the structural designer, i.e., 8438 kN. The difference is about 4.8%. Finally, it can be assumed that in the analyzed plate–pile system, the subsoil takes over Fr,k/Fc′,k = 1965/8048 = 24.4% of the total load transferred to the foundation from the column and the Fpg7,k/Fc′,k column = 6083/8048 = 75.6% of this load. The lack of results observable between days 520 and 560 of monitoring is due to a break in data readings caused by the service provider, which resulted from the expiration of the initial monitoring service agreement. Once a new contract was signed, the readings were resumed. This is a limitation of the study. P1 to P6 is the column load with respective sensors to measure the displacement.

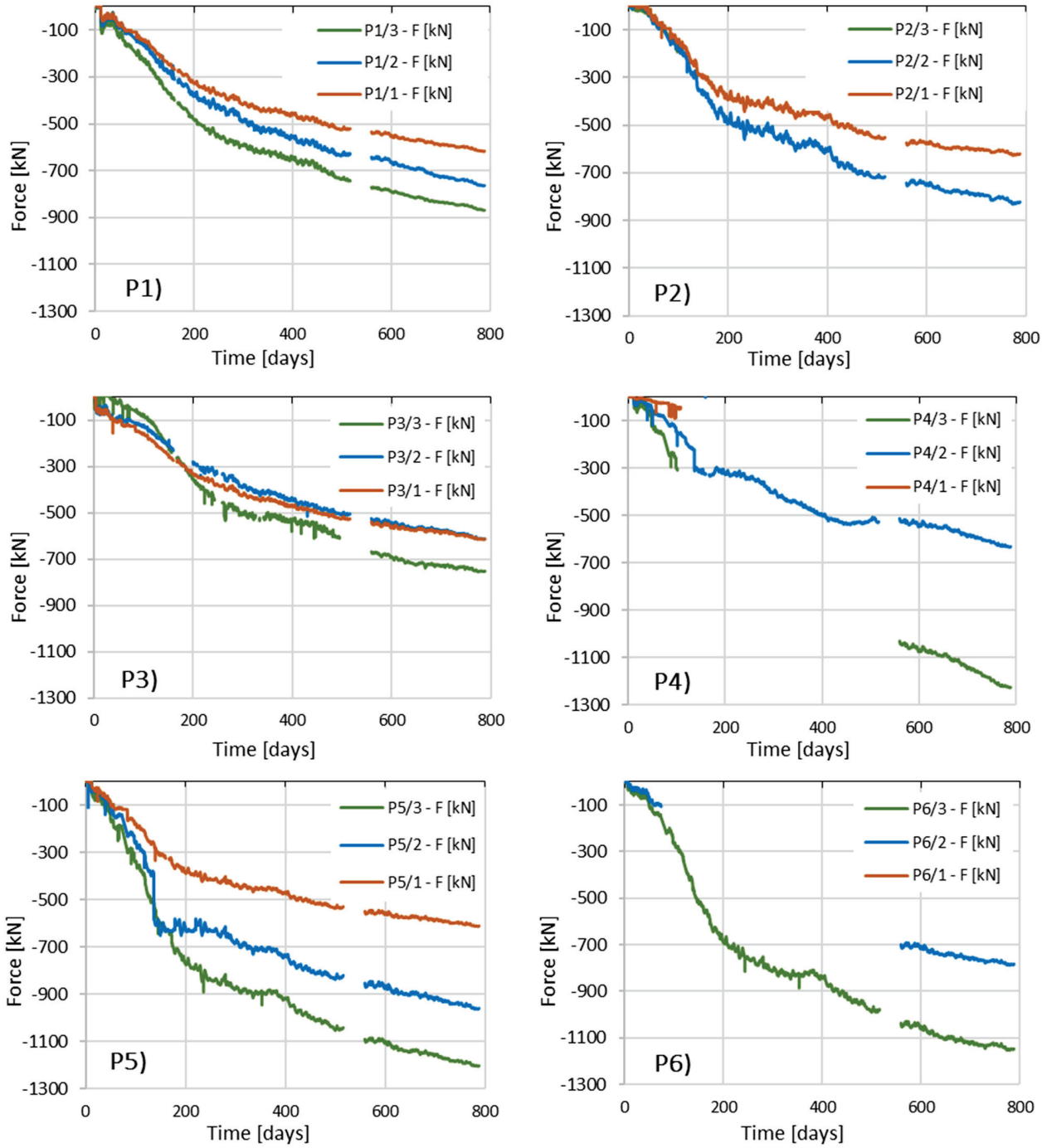


Figure 25. Change in the estimated value of the axial force as a function of time based on the measurement of concrete deformations.

3.5. Analysis of the Behavior of Columns as a CPRF Element

Figure 25 shows the changes in the values of axial forces in columns P1 and P2 as a function of time, estimated based on deformation measurements using sensors placed along the tested columns.

After about 100 days of observation in column P2, sensor P2_3, which is located in the vicinity of the column head, no correct readings were observed.

During the measurements of deformations in column P4, 120 days after their commencement, the lack of correct readings was found in two sensors: the lowest (P4_1) and the highest located (P4_3) sensor. The fault caused by the broken wiring was removed in sensor P4_3 after 560 days.

During the installation of the measuring system in column P6, the repeated lifting and pressing of the steel I-beam into the concrete mix damaged the cable of the lowest-located sensor P6_1.

After approximately 70 days of readings in column P6, the middle sensor of column P6_2 was not receiving correct readings. The sensor was restored to working order after 560 days.

For all columns, after the conventional date of completion of the shell stage of the structure, i.e., after 201 days from the start of automatic measurements, a uniform increase in deformations was observed in all sensors installed in a given column.

A different issue is the absence of results for sensors numbered P2/3 and P6/1, which were damaged, for example, during installation. Yet, another issue concerns the lack of readings in sensors numbered P4/3 and P3/2, where it should be noted that due to excessive stretching or shortening of the string in the sensor—i.e., going beyond the measurement range—the sensors did not provide valid data within the expected range of strain/force. Such results were deliberately removed from the force vs. time chart. Once the readings returned to the valid measurement range, the data were again included in the chart.

Generally, it can be assessed that in column P3, friction along the side surface is mobilized the least. The force diagrams in the upper part of the column show similar values, while they overlap in the lower part. Column P1 behaves similarly, but the decrease in axial force with depth is more pronounced here, which may indicate better mobilization of friction. Column P2 shows better cooperation with the soil medium.

Columns P5, P6, and P4 observe the highest values of the estimated axial forces, which indicates that these columns operate very effectively.

The analysis of the change in the axial force value as a function of time (Figure 25) over 788 days allowed for the following conclusions to be drawn:

Column P1 (No. 257)

Column P1 works in a group of five or seven columns if we consider the additional two anchor columns made to carry out the test (Figure 26) at a spacing of 1.4 m (approx. 3.5D). Considering the anchor columns, column P1 works as a middle column.

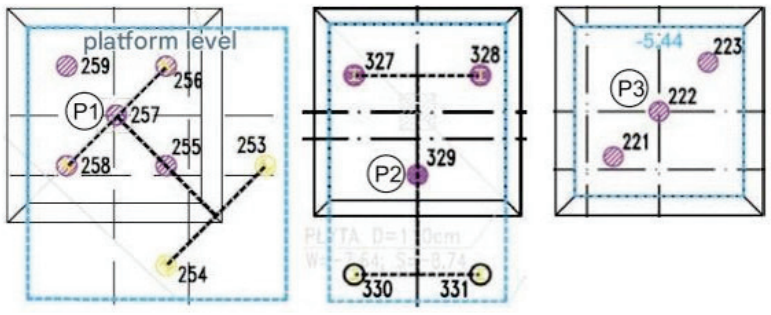


Figure 26. Column arrangement around columns P1, P2, and P3.

Figure 27 compares the distribution of the axial force along column P1 for the last reading taken into account in this analysis, i.e., after 788 days from the start of measurements on 20 May 2016, with the change in the value of the axial force from the test load of the column. The course of the axial force along the column for the last reading leads to the conclusion that the side surface of the column in the plate–pile system works more weakly than in the single-layer system. The value of the axial force along the length of the column in the plate–pile system decreases slightly, i.e., by approx. 230 kN over the measured length of 10 m, in contrast to a single column, where the decrease in the force value along the length is apparent. The reduction in the contribution of the CPRF column sidewall to the load

transfer is compensated by better mobilization of force in the lower unmeasured part of the column with a length of 8.8 m, including the base. This can be explained by increased friction on the sidewall in the lower part of the column and/or increased mobilization of the soil resistance under the column base.

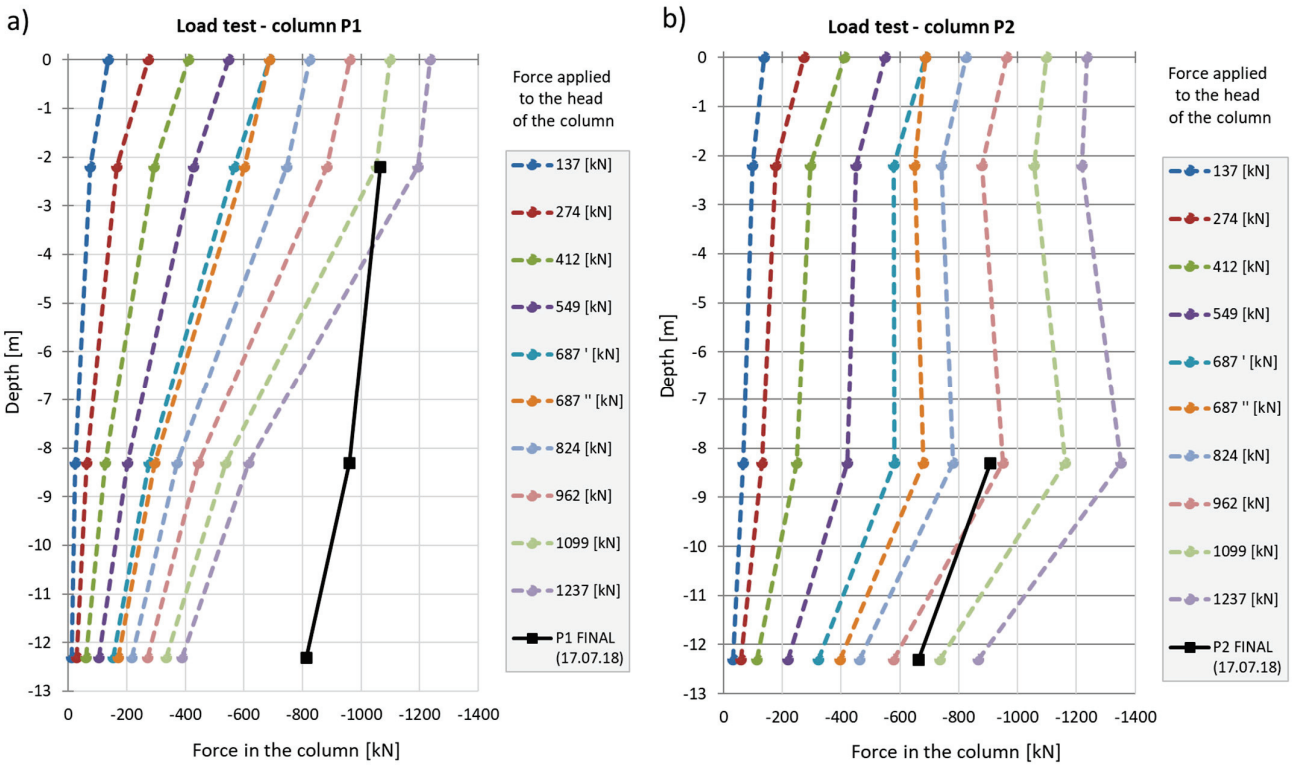


Figure 27. Distribution of force along columns (**a**) P1 and (**b**) P2 during the test load and for the last reading during the construction of the building (solid black line).

The observations led to the conclusion that the statement about the existence of the so-called "dead zone" that typically occurs at small axle spacing between columns of 3D should be considered correct. This situation can be explained by the limitation of friction mobilization on the side due to the reduction in the relative displacement of the upper section of the column with respect to the surrounding soil. As a result of the pressure of the slab on the columns and the ground, the columns and the surrounding soil under the slab are subject to identical displacement. This interpretation is consistent with the conclusions presented in regarding the interactions between piles and the interactions between piles and the slab, according to which the friction on the side of the pile/column in the combined piled raft foundation is mobilized only in its lower part, i.e., on 1/3 to $\frac{1}{4}$ of the total pile length, i.e., 6.3 m in the case of our tests. In their work [31,32] indicated that the shaft friction distributions they presented for small center-to-center spacings, i.e., 3D, suggest that for a small range of settlements (0.03D), the raft in a piled-raft foundation negatively influences the distribution of unit shaft friction along the pile in the zone directly beneath the raft (up to 6 m, or 1/5 L for a central pile, and up to 25 m, or 0.83L for corner and edge piles). For greater settlements (0.10D), the behavior of the piles in a group and in the piled-raft foundation is very similar, although the performance of the central pile in the piled-raft foundation is noticeably better. The reduction in shaft friction mobilization directly beneath the raft results from the lack of relative displacement between the pile shaft and the surrounding soil.

Column P2 (No. 329)

The P2 column works in a five-column arrangement (after considering the additional two anchor columns), with a spacing of 2.30 m (approx. 5.85D).

The P2 column should be defined as the middle one in the column arrangement. Considering the column spacing close to 6D, according to the conclusions from the numerical analysis [10], it should be expected that the P2 column will work similarly to a single column.

Later in the work, a more extensive analysis for column P2 was performed, supplementing the field measurements with the results of numerical analysis.

Column P3 (No. 222)

The P3 column works in a three-column arrangement (Figure 26) as a middle column with a spacing of 1.43 m (3.6D).

As stated above, in column P3, friction along the side surface is mobilized the least in comparison to other columns. Very similar force values in three sensors, practically throughout the entire measurement period, indicate that the column load of 750 kN is transferred to a small extent by the first measured section of the column (approx. 130 kN) and, above all, by the lower, unmeasured part of the column, i.e., the side surface together with the base. Relating these observations to Kazenbach's conclusions [7] from the monitoring of piles under the Commerzbank Tower building in Frankfurt, it can be assumed that columns embedded in load-bearing sands underlying much weaker dust mobilize a high value of friction on the side surface.

Columns P4, P5 and P6

It is assumed that columns P4, P5 and P6 operate in similar ground conditions and under similar load conditions. Column P5 operates in a single-column configuration, column P6 in a two-column configuration (spacing 2.83 m), and column P4 in a three-column configuration (spacing 2.33 m), as shown in Figure 28.

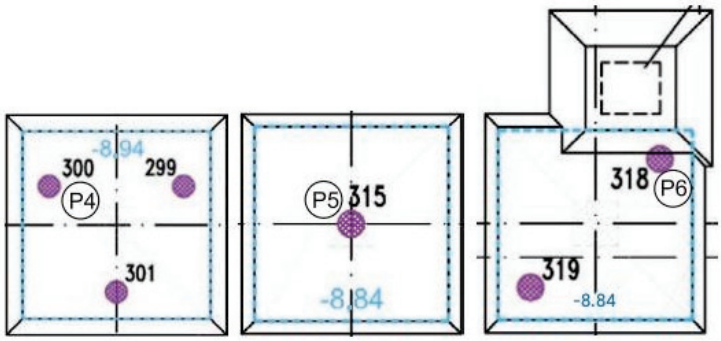


Figure 28. Arrangement of columns around columns P4 (No. 300), P5 (No. 315), and P6 (No. 318).

From the direct readings, the full distribution of force values along the length of column P5 can be estimated. In columns P4 and P6, although time-limited, reading is possible at the middle sensor (P4_2 and P6_2) and at the column head (P4_3 and P6_3).

Comparing the readings from the highest positioned sensors (Pi_3) in all three columns, it can be concluded that the force values on the last day of measurement are very similar to each other (1227 kN, 1203 kN, and 1148 kN for columns P4, P5, and P6, respectively).

Comparing the axial force drop on the upper measured section of the three columns, between sensors Pi_3 and Pi_2, it can be observed that the column side surface P4 works best, then P6 and P5, with the axial force decreasing by 595 kN, 362 kN and 243 kN, respectively.

To sum up, based on the distribution of estimated axial force values along the length of the column on the last day of measurement, based on the change of the axial force value with depth, it can be concluded that the behavior of columns P1, P2 and P3 is similar to the behavior of typical middle (inner) piles in a plate–pile system. Columns P1, P2 and P3 are

located inside the group of columns. The small differences in the interpreted force values indicate poor side surface performance. The reduction in the side surface friction observed at the top of the columns indicates the existence of a "dead zone".

Based on the measurements carried out, the behavior of columns P4, P5 and P6 can, with high probability, be compared to the behavior of typical columns' corners/edges in the spacing of the order of 6D. Columns P4, P5 and P6 were located on the edge of the column group. The mobilization of friction on the side surface along the entire length of the column results in a significant decrease in the axial force along the column.

3.6. Detailed Analysis of the P2 Column Based on Field Measurements and FEM Calculations (ZSoil)

Based on the measurement of the actual deformations of concrete columns, a part was distinguished as stress, and then the axial force values were derived. This approach was particularly important for the sensors closest to the heads, where the most significant temperature changes were observed. In the case of columns P2 and P4, it was impossible to measure the strain in the column just below the foundation slab after 100 and 120 days, respectively.

Hence, to determine the course of the change of the axial force in the column head during P2, as a supplement to the readings from the P2_3 sensor during the field tests, a numerical analysis was carried out using the finite element method in the ZSoil program. The analysis also verified the possibility of using alternative tools to determine the values of axial forces in the column caused only by changes in load without the influence of temperature. The column choice resulted from possibly calibrating the model based on the load–settlement relationship from the test load. Moreover, thanks to the geodetic monitoring of the foundation slab settlements on the benchmark located directly above the P2 column, it was possible to obtain the information needed to compare the work of the combined piled raft foundation column with the column working independently.

3.6.1. FEM Model

The FEM model [33,34] was limited to a detailed analysis of the part of the structure located between the B12-C7/10-15 axes (red contour) with column P2, taking into account the influence of the part located between the C1-C5/15′-22′ axes and the parts of the neighboring buildings with uniformly distributed load shown in Figure 29. The model considered the point average load from the most unfavorable combination of loads from all stories of the analyzed building acting on the foundation slab (from ARSA to Zsoil). The load in the form of concentrated forces was applied to the foundation slab at the locations of columns and walls. The model reproduced the actual arrangement of columns with their lengths from the as-built documentation. The columns were modeled as piles (beams) with a D = 0.40 m diameter. To stiffen the structure, all stories were taken into account in the FEM model.

In order to model the subsoil, the constitutive soil model HSs (hardening soil model with small stiffness [35]) was used, for which the parameters were selected based on the available results of field and laboratory tests (Table 6).

The parameters adopted for the constitutive model of the subsoil medium were verified by comparing the load–settlement relationship for column P2 during the test load (Figure 30) and the settlement of the foundation slab located between axes B12-C7/10-15 of the building part (Figure 31).

Comparing the results of field tests and numerical simulations, a relatively good convergence with the results of the test load of column P2 can be observed (Figure 30). The numerically estimated settlement of the foundation slab compared to the geodetic measurements indicates a two- or three-fold overestimation of the results (Figure 31A,C),

assuming the full load of the building. Assuming that 60% of the target weight of the building is applied to the foundation slab, the subsoil settles quite similarly to reality (Figure 31A,B). It is worth noting that the geodetic measurement on 12 June 2018 did not show any differences (except for the R11_H benchmark, where the change was 1 mm) compared to the measurement from 30 January 2017, i.e., from the 254th day from the start of automatic measurements. Based on the assumptions made at the beginning of the introduction, on the 201st day from the launch of the measuring platform, the progress of work on the building structure was approximately 50%.

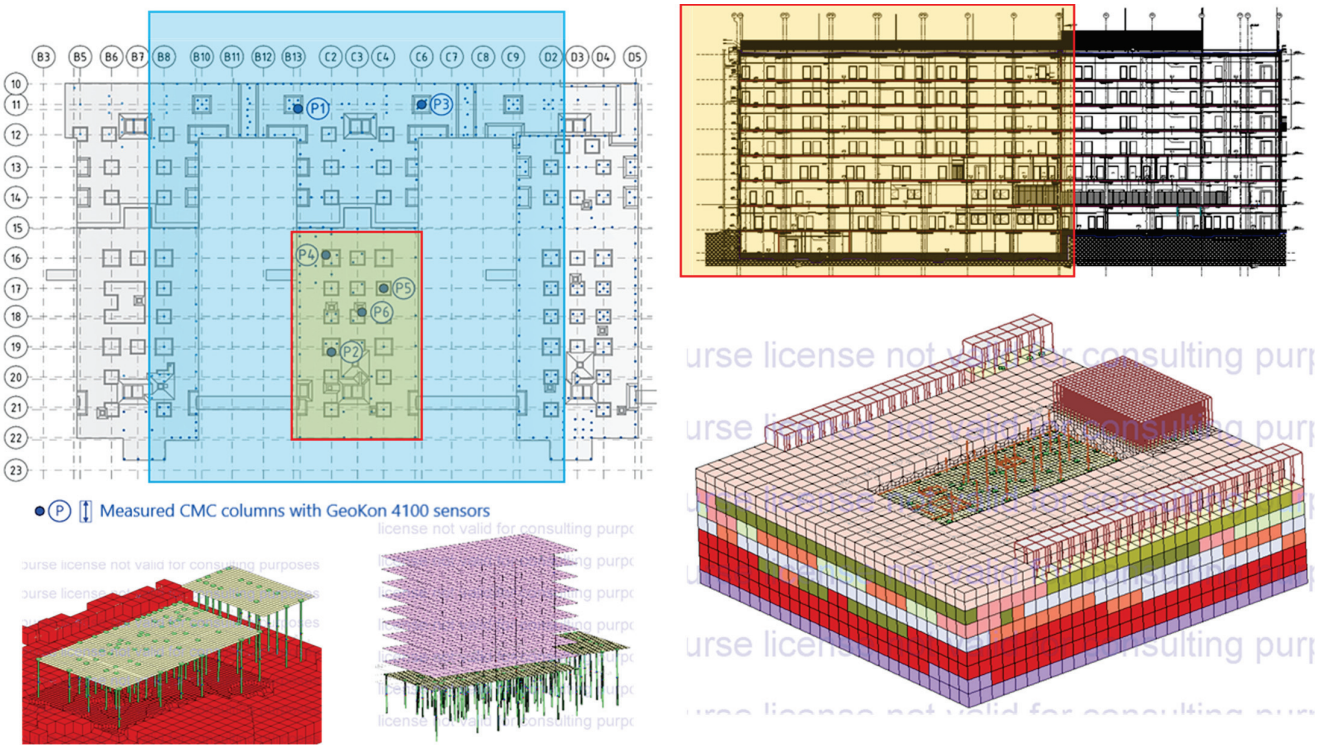


Figure 29. FEM model (ZSoil) of the selected part of the building.

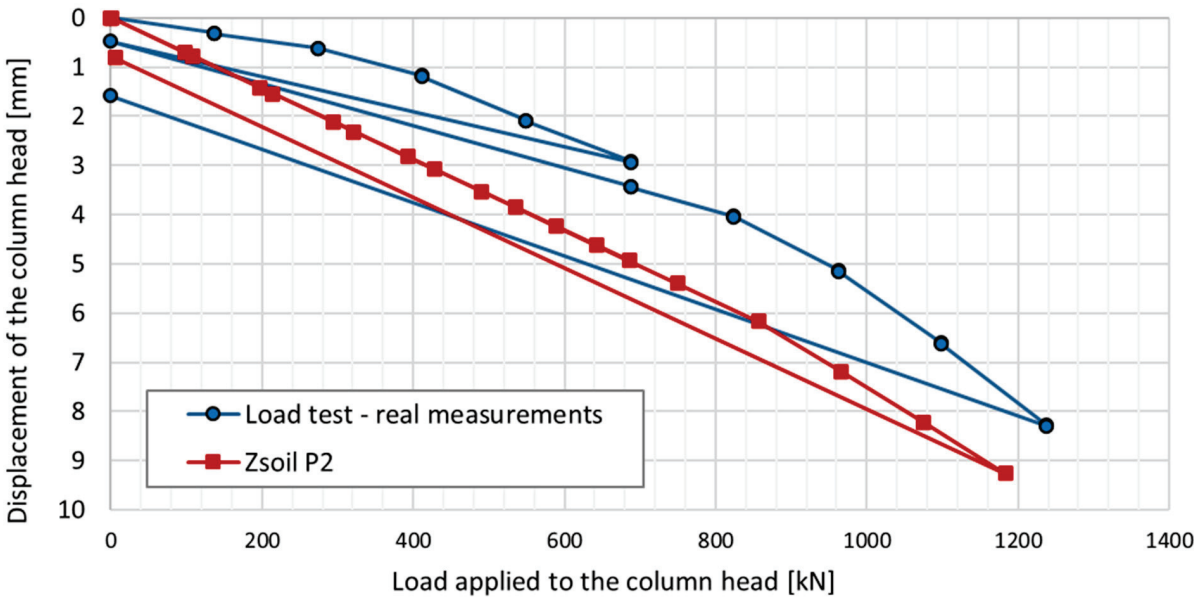
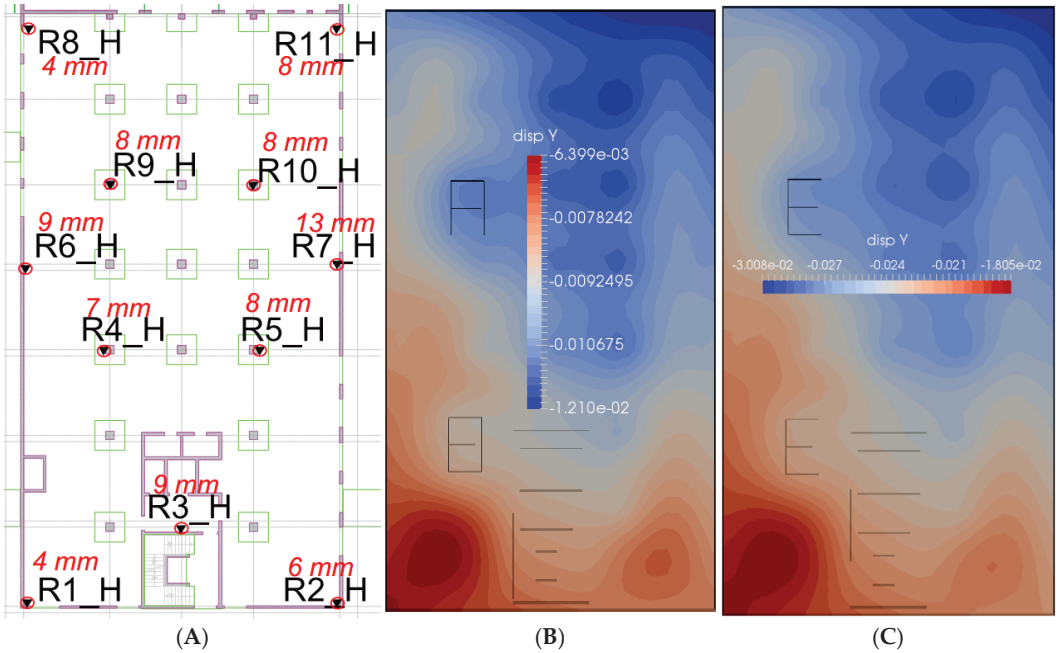


Figure 30. Load–settlement relationship of the P2 column head. Comparison of actual measurements with FEM simulation (ZSoil P2).

Table 6. Parameters of the HSs model of the subsoil.

	Soil Layer								
Parameter	**IIb**	**IIIb**	**IVa**	**IVb**	**IVc**	**IVd**	**Va**	**VI**	**W**
E_0^{ref} (kPa)	408,000	276,000	312,000	120,000	252,000	336,000	168,000	516,000	500,000
$\gamma_{0.7}$ ($\times 10^4$)	1.61	2.28	1.63	1.68	2.14	1.82	4.50	1.43	1.43
E_{ur}^{ref} (kPa)	90,000	60,000	75,000	20,000	50,000	70,000	32,000	110,000	110,000
E_{50}^{ref} (kPa)	27,000	16,000	25,000	6000	13,000	22,000	10,000	35,000	35,000
σ^{ref} (kPa)	80	99	86.8	59.4	104.5	110.5	135	112.5	100
m (-)	0.5	0.6	0.5	0.55	0.6	0.6	0.75	0.5	0.5
v_{ur} (-)	0.2	0.2	0.2	0.2	0.2	0.2	0.2	0.2	0.2
R_f (-)	0.9	0.9	0.9	0.9	0.9	0.9	0.9	0.9	0.9
C' (kPa)	0	2	0	0.5	4	5	6.5	0	0
φ' (°)	39	35	36	32	34	36	23	41	41
ψ (°)	7	6	5	2	6	2	0	10	10
e_{max} (-)	0.85	1.2	0.85	2.2	1.4	1.2	2.0	0.85	0.85
f_t (kPa)	0	0	0	0	0	0	0	0	0
D (-)	0.25	0.25	0.25	0.25	0.25	0.25	0.25	0.25	0.25
E_{oed}^{ref} (kPa)	27,000	16,000	25,000	6000	13,000	70,000	10,000	35,000	35,000
σ_{oed}^{ref} (kPa)	216.2	232.4	266.3	126.3	237.0	268.3	221.0	331.0	294.1
K_0^{NC} (-)	0.37	0.426	0.41	0.47	0.44	0.41	0.61	0.34	0.34
q^{POP} (kPa)	200	200	200	200	200	200	200	200	30
K_0^{SR} (-)	0.37	0.426	0.41	0.47	0.44	0.41	0.61	0.34	0.34
K_0 (-)	2	1.5	0.78	0.9	0.95	0.85	1.5	0.75	0.5



(**A**) (**B**) (**C**)

Figure 31. Comparison of the foundation slab settlements based on the results of (**A**) geodetic monitoring (last measurement from 12 June 2018, identical as on 30 January 2017) and FEM analysis (ZSoil) (**B**) for 60% load and (**C**) for 100% load.

3.6.2. Analysis of Results

The analysis of the changes in the value of the axial force as a function of time for the measured columns showed that this course is bilinear. In the conventional time of 200 days, the increase in the axial force for all correctly functioning sensors is more significant than for later measurements. Geodetic measurements of the foundation slab settlements over time confirmed these observations.

For deformation measurements taken after day 201, i.e., for the finishing phase of the building, taking into account the estimated change in the force values determined based on the measurements with individual sensors (P2_2 and P2_1), it was estimated that the finishing works, which translated into a further increase in load, progressed at a rate of 0.04% per day. Hence, for further analysis, the steps of 55%, 60%, 70% and 80% of the total load were conventionally assumed as 325, 450, 700, and 949 days from the start of automatic measurements on 20 May 2016.

The FEM analysis in ZSoil was performed assuming the nodal load from ARSA, as a result in the form of reactions from rigid supports, on which the entire structure of the building was based, including the foundation slab. This situation resulted in the inability in ZSoil to take into account the direct transfer of the load from the foundation slab's own weight to the subsoil. Therefore, the values of axial forces in the numerically modeled columns were corrected by the value of the foundation slab's weight.

Considering that automatic measurements began after the foundation slab and the ceiling above the "−2" level were completed, the modification of axial forces also included the ceiling weight. In total, according to Table 1, the values of axial forces, estimated numerically at each load step, were reduced by the value of forces generated for 16% of the full load. In accordance with the records from the construction journal regarding the commencement of concreting of individual levels of the building, for each characteristic load step, the corrected value of axial force at the depth corresponding to the location of sensors P2_3, P2_2, and P2_1 was read from the ZSoil program and compared with the force values from the column deformation measurements (Figure 32). Additionally, the values of axial force at a depth of 14.48 m estimated in ZSoil were plotted with the label ZSoil P2/0.

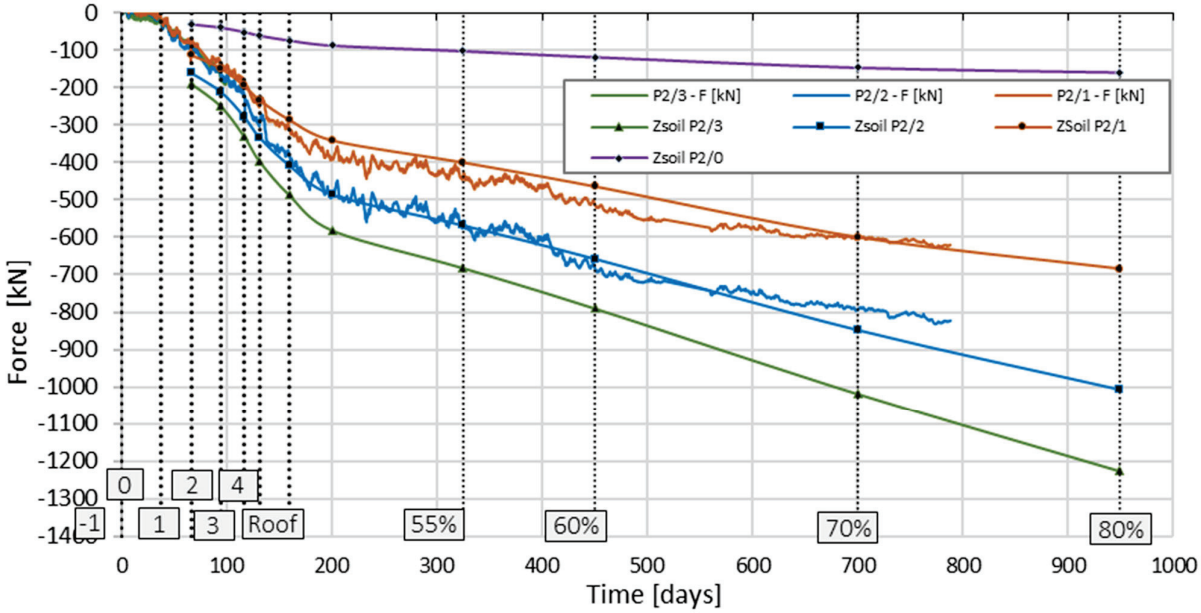


Figure 32. Change in axial force values as a function of time in column P2 for three depths. Force values were estimated from field tests and read after correction from the FEM model (ZSoil).

Comparative analysis of the results indicates a good convergence of the force values in sensors P2_2 and P2_1, especially in the last three steps of the construction implementation phase and at the building completion stage. After exceeding the conventional step of 70% of the building load, the force values from field measurements stabilized, while the forces from the numerical analysis continued to increase. Similarly to the observations from the building settlements, which stabilized and did not change the settlements estimated numerically for the 60% load step, a further increase in the axial force resulting from the FEM analysis can be considered unjustified.

This is most likely because the load values from the most unfavorable combination were used in the numerical analysis and were overestimated compared to the actual values. The numerically determined value of force as a function of time in the P2_3 sensor, located in the vicinity of the column head, allowed for a comparison of the behavior of a single column with the behavior of a column of a combined piled raft foundation. Figure 33 shows the course of the load settlement relationship of the column head. The actual measurement of the foundation slab settlement in the benchmark located directly above the P2 column was compared with the value of force in the P2_3 sensor read from the FEM model. Scholars monitor structures using field monitoring systems and finite element methods [36–38]. These methods help to minimize structural risks in buildings and large bridges [39–41].

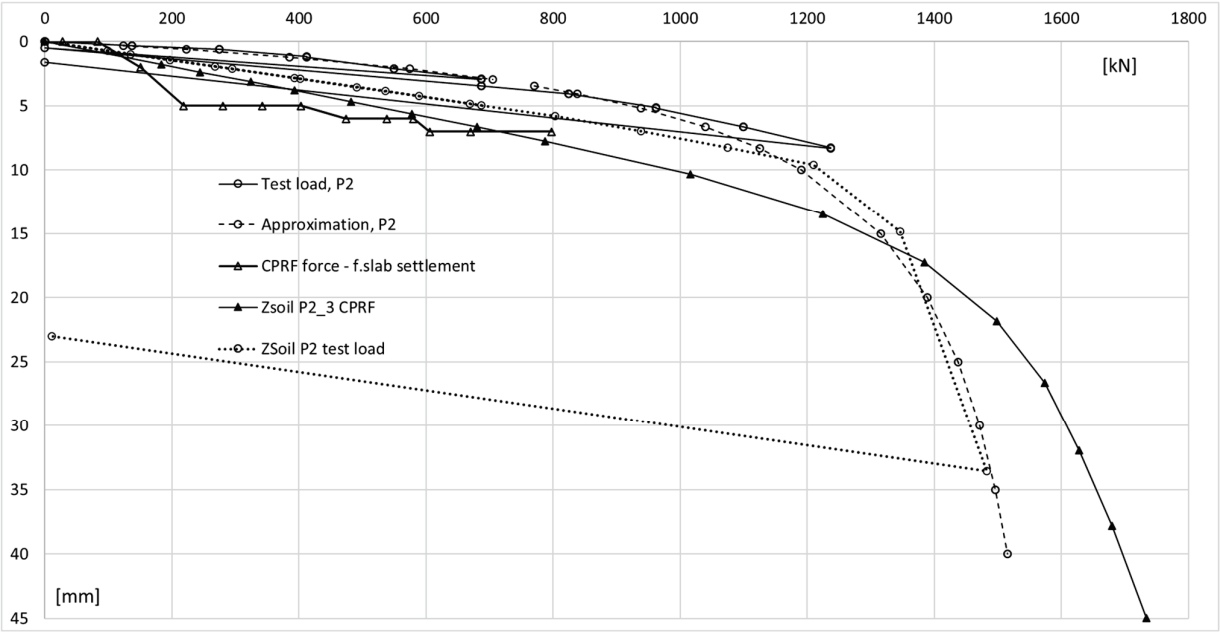


Figure 33. Load–settlement relationship of the P2 column head (for a column working alone vs. for a column in a slab–pile foundation). Actual measurements from the column test (continuous line, empty circle marker); FEM simulation of the test (ZSoil Test Load P2, dotted line).

The hyperbolic curve approximated of actual measurements of the test (dashed line). CPRF force vs. plate settlement and column working in CPRF show force readings from FEM analysis after axial force correction vs. plate settlement above column P2 and results from FEM analysis with axial force correction (ZSoil—P2_3 CPRF).

Based on the comparison of the load–settlement (Ns) curve for a single column from the test load with the Ns curve for a column with a combined piled raft foundation, it can be concluded that the CPRF column, in the range of small deformations of the soil medium (correspondingly, the settlement of the column head at the level of several millimeters), is characterized by lower stiffness, i.e., it settles more than an independent column at a similar load value.

Considering the ongoing development of construction works, determining the force–time course in the P2_3 sensor, located near the column head and at an additional depth of 14.48 m, made it possible to supplement the actual measurements and compare the axial force distribution along the length of the combined piled raft foundation column with the force distribution measured in a single column during test loads (Figure 34).

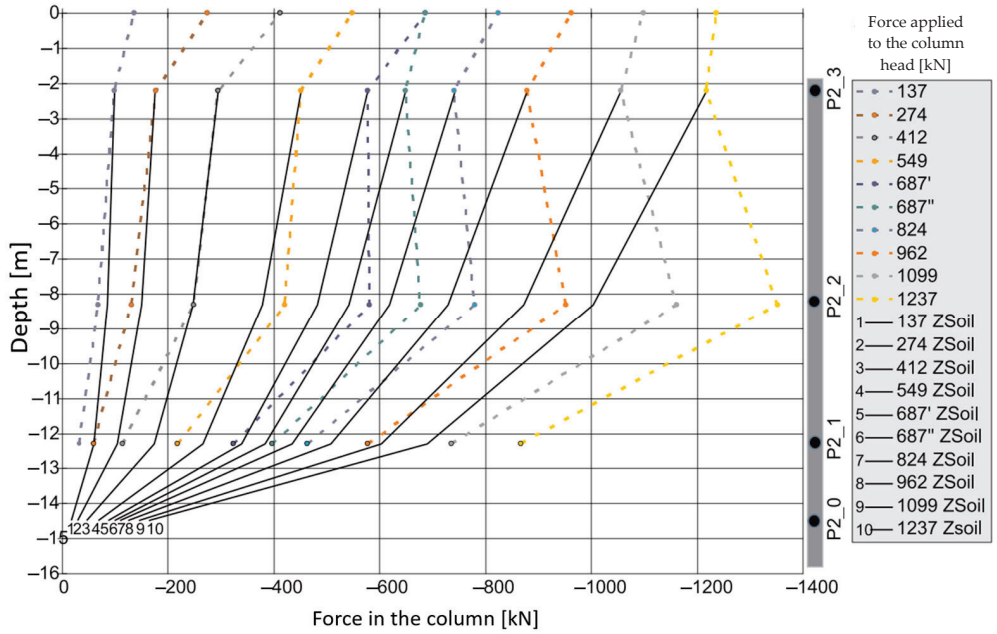


Figure 34. Distribution of force along column P2 during test load (actual results) and during the construction of the building based on the FEM analysis (ZSoil).

Based on the linear approximation of the numerically estimated values in ZSoil, the force values in sensors P2_2, P2_1, and P2_0 were determined for the force value read in sensor P2_3 from the test load. The compiled information made it possible to draw the following conclusions:

- For the first three load steps (137 kN, 274 kN, 412 kN), the value of the axial force in the FPP column is reduced to a lesser extent compared to the single column, which can be interpreted as a weaker mobilization of friction on the side surface of the column.
- For subsequent load steps, we observe different behavior of the CPRF column—a more significant decrease in the axial force along the length of the CPRF column indicates a more significant mobilization of friction on the side surface than in the case of a single column.
- The involvement of the side surface in the cooperation in the ground with relatively low mechanical parameters in the CPRF sub-plate zone, compared to the lack of mobilization of friction on the side surface of the column working independently, can be explained by the increase in vertical normal stresses in the soil medium around the column, caused by the pressure of the foundation slab.

4. Conclusions

The measurement system, consisting of a setup for monitoring stress changes in the soil beneath the building's slab, as well as a system for measuring deformation of concrete columns, was presented. It can be considered a significant contribution to the development of knowledge regarding the interaction between the elements of a combined piled–raft foundation.

In the analysis, actual deformations resulting from temperature changes were separated from stress-induced deformations arising from changes in load, and only stress-induced deformation changes over time were further interpreted.

Using measurements of soil stresses and forces in the columns, the distribution of load between the subsoil and the concrete columns was estimated, indicating that in the analyzed piled-raft system, the columns bear 75% of the total load from the pillar. The analysis of changes in axial force values in six columns over time showed that after exceeding the conventional date marking the completion of the raw structural state, i.e., approximately 201 days after the start of automatic measurements, the increase in force in all sensors for a selected column occurred proportionally. Among the examined columns, the following behaviors were observed:

- Typical behavior for middle columns with small changes in axial force measured along the column, indicating weak lateral skin friction and simultaneously suggesting the existence of a "dead zone".
- Typical behavior for corner/boundary columns with spacing on the order of 6D, with the ability to mobilize friction along the entire length of the column, ultimately resulting in a distinct decrease in axial force at depth.

Based on finite element analysis (FEA) in ZSoil, missing readings at the head and base of one of the columns were supplemented, while simultaneously comparing these readings with those from other correctly functioning sensors. Comparing the behavior of an individual column with the behavior of the piled-raft foundation column, it was deduced that the piled-raft column, within the range of small settlements (several millimeters), exhibits lower "stiffness" than a single column. However, with larger settlements (0.06D), an increase in load-bearing capacity and stiffness of the piled-raft foundation column was observed, in line with conclusions from archival analyses.

Author Contributions: Conceptualizations, G.M.K.; Data curation, G.M.K.; Formal analysis, G.M.K.; Investigation, G.M.K.; Methodology, G.M.K.; Software, G.M.K.; Supervision, G.M.K.; Validation, G.M.K.; Visualization, G.M.K.; Writing—original draft, G.M.K. and S.M.K.; and Writing—review and editing, G.M.K. and S.M.K. All authors have read and agreed to the published version of the manuscript.

Funding: This paper was co-financed under the research grant of the Warsaw University of Technology supporting the scientific activity in the discipline of Civil Engineering, Geodesy and Transport.

Institutional Review Board Statement: Not applicable.

Informed Consent Statement: Not applicable.

Data Availability Statement: The data are provided by the corresponding author.

Conflicts of Interest: The authors declare that there are no conflicts of interest.

References

1. Gotman, N.Z.; Gotman, A.L. A contribution to the piled raft foundation design. *Darmstadt Geotech.* **2009**, *18*, 91–99.
2. Reuil, O.; Randolph, M.F. Optimized design of combined pile raft foundations. *Darmstadt Geotech.* **2009**, *18*, 149–169.
3. Kharichkin, A.; Bezvolev, S. Soil-pile interaction in pile foundation and pile reactions monitoring. *Darmstadt Geotech.* **2009**, *18*, 243–255.
4. Kharichkin, A.; Godzikovsky, V.A.; Antonov, V.D. Patent for SVD-100 Pile. Dynamometer. Patent RU 69241 U1, 10 July 2006.
5. Sonoda, R.; Kitiyodom, P. Post-analyses of settlements of piled raft foundation in a reclaimed ground. *Darmstadt Geotech.* **2009**, *18*, 289–306.
6. Yang, D.; Xiao, W.; You, H. Wind-induced fatigue life prediction of bridge hangers considering the effect of wind direction. *Eng. Struct.* **2025**, *327*, 119–523.

7. Katzenbach, R.; Moorman, C. Piled raft foundation projects in Germany. In *Design Applications of Raft Foundations*; Hemsley, J.A., Ed.; Thomas Telford Publishing: London, UK, 2000; pp. 323–391.
8. Sommer, H.; DeBenedittis, D. Messe Turm, foundations for the tallest building in Europe. In Proceedings of the 4th DFI Conference, Stresa, Italy, 7–12 April 1991; pp. 139–145.
9. Sommer, H. Development of locked stresses and negative shaft resistance at the piled raft foundation—Messeturm Frankfurt/Main. In *Deep Foundations on Bored and Auger Piles*; Van Impe, W.F., Ed.; A.A Balkema: Rotterdam, The Netherlands, 1993; pp. 347–349.
10. El-Mossallamy, Y.F.E. *Piled Rafts: Numerical Modeling to Simulate the Behavior of Piled Raft Foundations*; Selbstverlag der Autoren; Darmstadt Institute of Geotechnics: Darmstadt, Germany, 1997.
11. Tamaro, G.J. Foundation engineers: Why do we need them? In *Martin S. Kapp Lecture*; ASCE: New York, NY, USA, 1996.
12. Kamiński, K.; Nowicki, P. Designing Compressed Reinforcement Cross-Sections by Curvature and Nominal Stiffness Methods. *Appl. Mech. Mater.* **2016**, *797*, 69–78. [CrossRef]
13. Bednarski, Ł.; Sienko, R. Measurements of structure deformations using wire sensors. *Inżynieria I Bud.* **2013**, *11*, 615–619.
14. *Additional Geotechnical Studies for the Construction of the PROKOCIM University Hospital Building at Jakubowskiego and Kostaneckiego Streets in Kraków*; Geocontrol Design and Research Institute Sp. z o.o.: Kraków, Poland, 2015.
15. Geoteko Ltd. *Geological and Engineering Documentation for the Concept of the New Seat of the PROKOCIM University Hospital at Jakubowskiego and Kostaneckiego Streets in Kraków*; Geoteko Ltd.: Kraków, Poland, 2007.
16. Sieńko, R.; Bednarski, L.; Howiacki, T. About distributed internal and surface strain measurements within prestressed concrete truck scale platforms. *IOP Conf. Ser. Mater. Sci. Eng.* **2019**, *471*, 52074. [CrossRef]
17. Siwowski, T.; Rajchel, M.; Sienko, R.; Bednarski, L. Smart monitoring of the FRP composite bridge with distributed fibre optic sensors. In Proceedings of the 9th International Conference on Fibre-Reinforced Polymer (FRP) Composites in Civil Engineering (CICE 2018), Paris, France, 7–19 July 2018; Springer Nature: Paris, France, 2018; pp. 17–19.
18. Mardanshahi, A.; Sreekumar, A.; Yang, X.; Barman, S.K.; Chronopoulos, D. Sensing Techniques for Structural Health Monitoring: A State-of-the-Art Review on Performance Criteria and New-Generation Technologies. *Sensors* **2025**, *25*, 1424. [CrossRef]
19. Sieńko, R.; Bednarski, Ł.; Kanty, P.; Howiacki, T. Application of Distributed Optical Fibre Sensor For Strain and Temperature Monitoring within Continuous Flight Auger Columns. *IOP Conf. Ser. Earth Environ. Sci.* **2019**, *221*, 12006. [CrossRef]
20. Pozo, F.; Tibaduiza, D.A.; Vidal, Y. Sensors for structural health monitoring and condition monitoring. *Multidiscip. Digit. Publ. Inst.* **2021**, *21*, 1558. [CrossRef] [PubMed]
21. Wu, T.; Liu, G.; Fu, S.; Xing, F. Recent progress of fiber-optic sensors for the structural health monitoring of civil infrastructure. *Sensors* **2020**, *20*, 4517. [CrossRef] [PubMed]
22. Zhu, R.; Zhou, F.; Wan, Z.; Deng, S.; Dong, X.; Zhou, Z.; Xing, W. Improving the Performance of Piled Raft Foundations Using Deformation Adjustors: A Case Study. *Buildings* **2022**, *12*, 1903. [CrossRef]
23. Capozzoli, L.; Fornasari, G.; Giampaolo, V.; De Martino, G.; Rizzo, E. Multi-Sensors Geophysical Monitoring for Reinforced Concrete Engineering Structures: A Laboratory Test. *Sensors* **2021**, *21*, 5565. [CrossRef]
24. Bednarski, Ł.; Sieńko, R.; Grygierek, M.; Howiacki, T. New distributed fibre optic 3D Sensor with thermal self-compensation system: Design, research and field proof application inside geotechnical structure. *Sensors* **2021**, *21*, 5089. [CrossRef]
25. Wang, D.; Yang, X.; Zhang, S.; Chen, C.; Zhao, Y. Long-Term Bearing Capacity of Concrete Pile Composite Foundation under Composite Salt Erosion. *Buildings* **2024**, *14*, 289. [CrossRef]
26. Buda-Ożóg, L.; Zięba, J.; Sieńkowska, K.; Nykiel, D.; Zuziak, K.; Sieńko, R.; Bednarski, Ł. Distributed fibre optic sensing: Reinforcement yielding strains and crack detection in concrete slab during column failure simulation. *Measurement* **2022**, *195*, 111192. [CrossRef]
27. Bednarz, B.; Popielski, P.; Sieńko, R.; Howiacki, T.; Bednarski, Ł. Distributed fibre optic sensing (DFOS) for deformation assessment of composite collectors and pipelines. *Sensors* **2021**, *21*, 5904. [CrossRef]
28. Howiacki, T.; Sieńko, R.; Zuziak, K. Distributed strain, settlement and temperature sensing in geotechnical earth embankments. In *Geotechnical Engineering Challenges to Meet Current and Emerging Needs of Society*; CRC Press: Boca Raton, FL, USA, 2024; pp. 1457–1462.
29. *PN-EN 1992-1-1:2008 Eurocode 2*; Design of Concrete Structures—Part 1-1: General Rules and Rules for Buildings. Polish Committee for Standardization: Warsaw, Poland, 2008.
30. *PN-83/B-02482*; Building Foundations. Load-Bearing Capacity of Piles and Pile Foundations. Polish Committee for Standardization: Warsaw, Poland, 1984.
31. Hanisch, J.; Katzenbach, R.; Konig, G. *Kombinierte Pfahl-Plattengrundungen*; Ernst and Sohn: Berlin, Germany, 2002.
32. Kacprzak, G.; Biss, M. *FEM Analysis (ZSoil) of the Displacement Columns of the Slab-Pile Foundation of Building H of the University Hospital Collegium Medicum in Krakow*; Warbud SA Warsaw: Warszawa, Poland, 2017.
33. Biss, M. Calculation of Settlements of Buildings Using FEM. Master's Thesis, Warsaw University of Technology, Warszawa, Poland, 2017.

34. Truty, A. Hardening soil model with same strain stiffness. In *Technical Report*; Zace Services Ltd.: Lausanne, Switzerland, 2008.
35. Daopei, Z.; Siyuan, T.; Haocheng, Y.; Zhangli, W. A Feasibility Study on Monitoring Pile-Soil Bonding Condition Using Piezoceramic Transducer and Horizontal Impact. *J. Sens.* **2021**, *2021*, 5575854.
36. Irfan, J.; Irshad, A.; Wali, U.; Mahmood, A.; Mohanad, M.; Ali, M. Experimental Study on Lateral and Vertical Capacity of Piled Raft and Pile Group System in Sandy Soil. *Appl. Sci.* **2022**, *12*, 8853.
37. Oday, A.A.; Jaffar, A.K.; Al-abboodi, I. Assessment of Settlement Behaviour of Reinforced Concrete Slab Foundation Under Full Load Test. *Int. J. GEOMATE* **2025**, *28*, 117–124.
38. Qibiao, W.; Jie, L.; Tao, F.; Shaohua, Y. Database Analysis of Long-Term Settlement Behavior of Pile Foundations in Shanghai Soft Coastal Clays. *Buildings* **2024**, *14*, 3334. [CrossRef]
39. Peng, Z.; Kuihua, W. Development of a smart axial strain sensor for static load testing of foundation piles. *MATEC Web Conf.* **2018**, *232*, 4018.
40. Dongning, L.; Deshan, M.; Dong, S.; Shaohua, R.; Wenbin, W.; Chengyu, H. Monitoring Axial Force Development in a Super-Long Pile during Construction Using BOFDA and Data Interpretation Approaches: A Case Study. *Buildings* **2022**, *12*, 1462. [CrossRef]
41. Ashutosh, K.; Sonu, K. Settlement-Based Load-Bearing in a Combined Pile–Raft Foundation. *Geotech. Geol. Eng.* **2024**, *42*, 1405–1421.

Disclaimer/Publisher's Note: The statements, opinions and data contained in all publications are solely those of the individual author(s) and contributor(s) and not of MDPI and/or the editor(s). MDPI and/or the editor(s) disclaim responsibility for any injury to people or property resulting from any ideas, methods, instructions or products referred to in the content.

sensors

MDPI

Article

The Performance of an ML-Based Weigh-in-Motion System in the Context of a Network Arch Bridge Structural Specificity

Dawid Piotrowski *, Marcin Jasiński, Artur Nowoświat, Piotr Łaziński and Stefan Pradelok

Faculty of Civil Engineering, Silesian University of Technology, ul. Akademicka 5, 44-100 Gliwice, Poland; marcin.jasinski@polsl.pl (M.J.); artur.nowoswiat@polsl.pl (A.N.); piotr.lazinski@polsl.pl (P.Ł.); stefan.pradelok@polsl.pl (S.P.)

* Correspondence: dawid.piotrowski@polsl.pl

Abstract

Machine learning (ML)-based techniques have received significant attention in various fields of industry and science. In civil and bridge engineering, they can facilitate the identification of specific patterns through the analysis of data acquired from structural health monitoring (SHM) systems. To evaluate the prediction capabilities of ML, this study examines the performance of several ML algorithms in estimating the total weight and location of vehicles on a bridge using strain sensing. A novel framework based on a combined model and data-driven approach is described, consisting of the establishment of the finite element (FE) model, its updating according to load testing results, and data augmentation to facilitate the training of selected physics-informed regression models. The article discusses the design of the Fiber Bragg Grating (FBG) sensor-based Bridge Weigh-in-Motion (BWIM) system, specifically focusing on several supervised regression models of different architectures. The current work proposes the use of the updated FE model to generate training data and evaluate the accuracy of regression models with the possible exclusion of selected input features enabled by the structural specificity of a bridge. The data were sourced from the SHM system installed on a network arch bridge in Wolin, Poland. It confirmed the possibility of establishing the BWIM system based on strain measurements, characterized by a reduced number of sensors and a satisfactory level of accuracy in the estimation of loads, achieved by exploiting the network arch bridge structural specificity.

Keywords: artificial intelligence; machine learning; neural network; network arch bridge; structural health monitoring

1. Introduction

Structural health monitoring (SHM) comprises a network of interconnected sensors that are essential elements of the entire monitoring framework [1]. Its establishment may require the integration of various sensor types, each allowing the recording and analysis of specific parameters of structural response. One of the widely used types of sensors is fiber optic sensors, which have been successfully applied in many engineering fields, including civil engineering [2,3], geotechnology [4,5], aviation [6], energy [7], and material engineering [8]. They are resistant to corrosion, immune to electromagnetic interference, and versatile in geometric shape [9], and they are also able to detect small variations in measured values [10].

SHM systems have been increasingly used to estimate road [11–14] and railway traffic load [15–17]. This task, known as Weigh-in-Motion (WIM), or Bridge Weigh-In-Motion

(BWIM) specifically for bridge-level load recognition, may involve different methods and instrumentation [18]. The strain-based BWIM systems were developed and introduced for various types of railway bridges, including single-span [19], multi-span [20], and truss structures [21]. The use of specific fiber optic sensing technologies was reported by Yoon et al. [22] to analyze the response of a bridge superstructure under a train load, allowing for the identification of car types. Pimentel et al. [23] developed an influence line-based framework to estimate the static axle load, geometry, and speed of trains. Wang et al. [24] proposed the use of crossbeam strain measurement to assess load magnitude using Fiber Bragg Grating (FBG) sensors and the linear superposition algorithm. Although the use of fiber optic sensors in BWIM is apparent, the vast majority of applications involve the measurement of strains in directly loaded components of the railway, including rails, sleepers, and a subgrade [25]. For example, Zhou et al. [26] described the method used to estimate the magnitude and positions of the wheel–rail contact forces using fiber optic sensors mounted on the rails. Mishra et al. [27] designed an FBG-based WIM system to estimate train parameters, including the speed, weight, and axle count of cars. Similar characteristics were analyzed by Martincek et al. [28] who incorporated the interferometric optical fiber sensing, Lan et al. [29] who used the rail- and track slab-embedded sensors, and Mishra et al. [30] who analyzed the impact of train speed and weight on the optomechanical behavior of optical sensors.

In the context of road infrastructure, WIM proposals should address the issues associated with the non-deterministic nature, uncertain positioning, and variety of road traffic scenarios. Reported applications include systems based on the measurement of strains by sensors embedded in pavement [31–34] and subgrade layers [35]. Several studies documented the implementation of strain gauges in bridge-level WIM, especially for vehicle detection and classification [36], load magnitude estimation [37], and axle count obtainment [38]. Zhao et al. [39] proposed the framework for axle detection using strain measurement and wavelet transformations. Tan et al. [40] described the detection of vehicle configuration and speed using a strain-based BWIM approach enhanced of the regularization and iterative approach. Similar systems were evaluated considering thermal field effects [41] and the spatial variability of structural properties [42]. Heinen et al. [43] examined single-span bridge structures using shear force-based BWIM systems. Among various applications, the use of fiber optic sensing has also been reported. Alamandala et al. [44] proposed a BWIM system using Fiber Bragg Grating (FBG) sensors arranged at different angles. The authors measured wavelength shifts to produce a temporal response curve and predict vehicle parameters, including load and speed. Zhang et al. [45] described a method for assessing vehicle weight considering random traffic flow and using the advantages of long-gauge FBG sensors. Chaudhary et al. [46] proposed an influence line-free BWIM method based on spatiotemporal strain data from distributed fiber optic sensors (DFOS). The gross weight of the vehicles was identified by spline regression and structural mechanics relationships. Oskoui et al. [47] developed an FBG-based sensor to measure end rotations of a bridge girder for the purpose of estimating vehicle load.

Numerous studies describe the issues of optimizing the sensor layout to facilitate decisions about the number and location of sensors and to obtain the most adequate information on the actual behavior of a structure [48]. Several works focused on the analysis of sensor types, power consumption, and efficiency in data acquisition and transmission for different bridge structures [49]. Among various implementations, the use of automated optimization techniques was reported, including genetic algorithm (GA) [50], particle swarm optimization (PSO) [51], and bioinspired methods [52–54]. Capellari et al. [55] proposed a Bayesian experimental design approach to optimize sensor layout, including minimizing the number of sensors, selecting their type, and determining their spatial deployment. Gonen et al. [56] described a framework for determining optimal sensor

locations for the purpose of identifying modal properties, incorporating uncertainties in modal displacements and hierarchical clustering. Various other applications include the optimal sensor layout design for anomaly detection [57], damage detection [58], and damage identification [59,60]. The current study focuses on recognizing the impact of the structural specificity of a bridge on the potential layout of FBG sensors and accuracy of the BWIM application. Based on the example of a network arch bridge, it is assumed that the number and location of FBG sensors can be reduced while maintaining the performance and satisfactory accuracy of vehicle weight estimation by exploiting structural specifics of the bridge. The network arch, characterized by inclined hangers that cross each other at least twice, allows a significant reduction in the bending moments for both the arch ribs and the girders, a limitation of the load influence surface range, and a general improvement in structural efficacy compared to other types of arch bridges [61]. However, the difficulties in the interpretation of complex traffic conditions with conventional methods have led to an increasing interest in machine learning (ML)-based solutions.

Recent advances in computer science have significantly contributed to the enhancement of SHM systems through the integration of ML-based algorithms [62]. These techniques may be used in many areas of civil engineering, including damage detection [63,64], estimation of structural deformation [65], and dynamic analysis [66]. ML algorithms are also used in the BWIM approach, and their implementation can involve various tools and frameworks. Le et al. [67] proposed the classification approach to detect the structural overload in the railway bridge. Bosso et al. [68] described the regression tree approach to predict vehicle weight and identify the overload trucks. Except for traditional supervised learning, classification, and regression models, transfer learning is also often used with very good results. Yan et al. [69] proposed the transfer learning-enhanced CNN algorithm to identify the gross weight and axle weight of the vehicles passing the bridge. Their research also showed the possibility of reducing the training set using transfer learning. Computer vision is also often used in BWIM systems. Jian et al. [70] proposed a BWIM method with a focus on complicated traffic scenarios. Their method can identify strain influence surfaces of the bridge structure and vehicle weights.

The current research integrates the advantages of FBG sensors and ML algorithms for the purpose of SHM system deployment using a network arch bridge in Wolin, Poland, as an example. A novel combined model- and data-driven framework is proposed consisting of the establishment of the FE model, its validation and adjustment based on static and dynamic load testing, and data augmentation to facilitate the training of selected physics-informed regression ML models. The work analyzes the accuracy and performance of selected ML regression algorithms, namely linear regression (LR), random forest (RF), and neural networks (NN), showing the impact of the structural specificity of the network arch bridge on the performance of the proposed BWIM system.

The current research is structured as follows. Section 2 presents the bridge and SHM system overview, including details on the arrangement and characteristics of the installed FBG sensors, a description of the network arch-specific strain distribution, and the preparation of training data for the purpose of ML-based BWIM deployment. Section 3 discusses the performance and accuracy of selected ML algorithms in predicting vehicle weight and position for various sets of features. Section 4 contains conclusions, limitations, and perspectives of the developed framework.

2. Methodology

2.1. Bridge and SHM System Overview

The BWIM system, which involves weighing and locating vehicles passing through the structure, was implemented on a steel bridge in Wolin, Poland. The structure is a

single-span network arch bridge with a span of 165.0 m. The superstructure consists of two steel arches with a closed box cross section of 1.00 × 1.80 m, is connected by steel circular tube bracings with a diameter of 1.22 m, and is slightly inclined inward in relation to the vertical plane. The bridge deck was suspended to the arch ribs with inclined wire hangers arranged in a network layout. The deck has a form of a steel greed structure composed of two longitudinal tie beams and transverse crossbeams placed at a regular spacing of 6.00 m. The distance between the end and the closest middle crossbeams is set at 7.50 m. The cross section of the tie beams is a closed rectangular box measuring 0.75 m in width and 1.30 m in height. The axial spacing between the tie-beams, measured in the transverse cross section, is 16.15 m. The middle crossbeams have an I section of 0.45 m wide and a variable height ranging from 0.94 to 1.19 m. The end crossbeams are designed as closed box sections that are 2.58 m wide and vary in height from 0.88 to 1.20 m. The steel grid is integrally connected to a concrete deck slab, thus forming a composite superstructure. The slab consists of precast concrete slab members interconnected with a 14.0 cm cast in-place layer. The entire steel structure was made of S460N steel, while the bridge slab was made of C50/60 and C40/50 concrete, for precast and in situ layers, respectively.

To estimate the weight and position of the vehicles on the bridge, an SHM system was installed, consisting of optical sensors based on Giber Bragg Grating (FBG) technology. Three measuring gates were designated on the bridge, located at 1/4, 1/2, and 3/4 of the span, in which a total of 17 measuring points were distinguished, based on the response characteristics of the network structure. Each of the measuring gates consists of three points installed on the crossbeam (CB) and two points installed on the hangers (H), one located on the left and the other on the right hanger. The middle gate includes two additional measurement points in the tie-beams (TB), each on one side of the deck.

In the case of the crossbeams and tie-beams, the sensors are spot welded to the structure after the prior cleaning and grinding of the surface. In addition to strain sensors, temperature sensors are also installed near the strain measurement points for temperature compensation purposes. The crossbeam sensors are installed on the top surface of the bottom flanges, whereas those on the tie-beams are mounted on the underside of the section. Subsequently, they were protected against corrosion according to the HBK specification [71], including a high adhesion nonhardening masking sealant AK22, 0.05 mm thick aluminum foil coating, and a 3 mm thick layer of kneadable putty (ABM75). The arrangement and characteristics of the welded strain and temperature sensors in the elements of the deck grid are shown in Figure 1.

The hangers installed on the bridge are part of the full locked coil rope system by Teufelberger-Redaelli [72]. These include wire cables of high strength steel that preclude the use of welded strain measurement. Due to the characteristics of the hanger cross-section and the potential torsional effects that may arise in response to the change in tension force, dedicated clamps were fabricated and used for the installation of the strain sensors. They are arranged together with temperature measurement sensors that are attached to the surface of the hanger (Figure 2).

All sensors in the three gates are connected to the breakout cables. These cables extend along the bridge and transmit signals to an MXFS interrogator, with 8 inputs of 16 channels each. The interrogator is installed in a cabinet mounted on one of the bridge end supports. The cabinet is also equipped with an industrial computer for data acquisition, processing, and management, a permanent Internet connection, and an uninterruptible power supply (UPS), which ensures continuous operation in the event of a power outage. The system enables synchronous acquisition from all channels, allowing for time-correlated analysis managed by the Catman Easy v5.6.1 software. Using the software, it is possible to record

in real time the strain values at key points of the structure that serve as input data for ML-based BWIM algorithms.

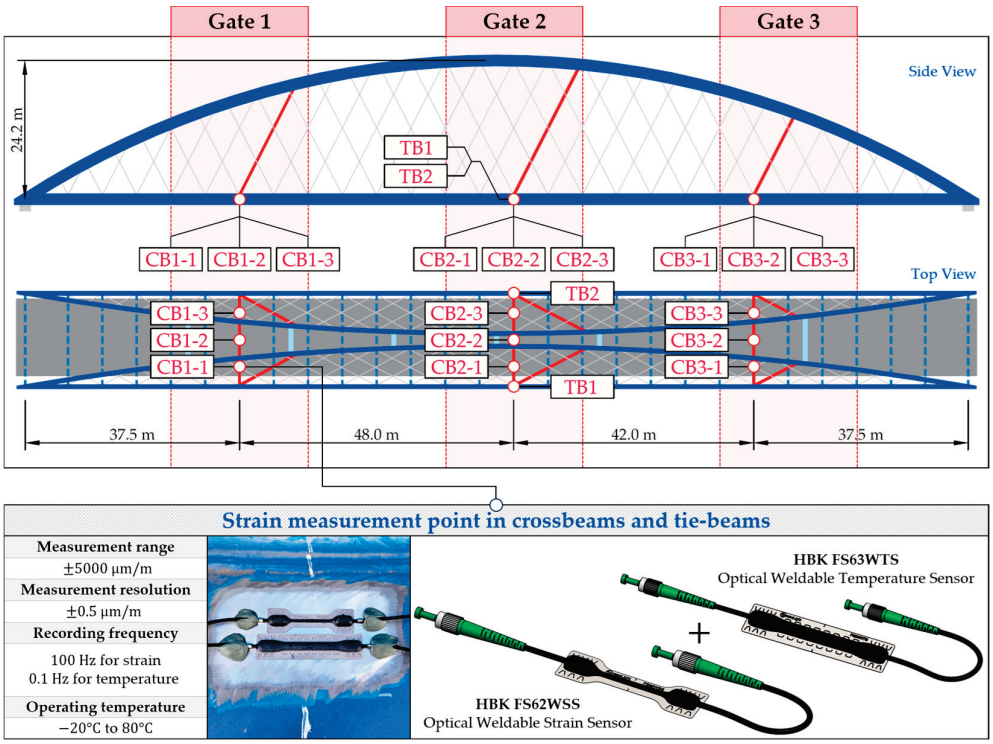


Figure 1. The measurement gates, arrangement, and characteristics of the welded FBG sensors in the crossbeams (CB) and tie-beams (TB).

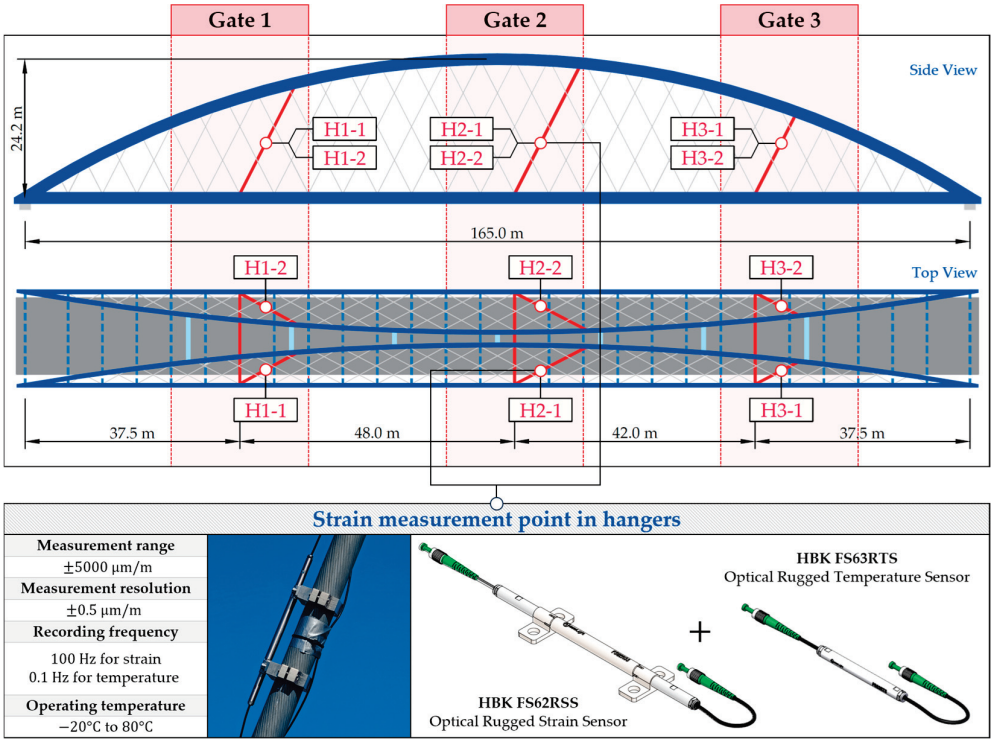


Figure 2. The measurement gates, arrangement, and characteristics of the bolted FBG sensors in the hangers (H).

2.2. Load Testing and Physics-Informed BWIM Design

After the installation of the sensor system and prior to training of the ML algorithms, load tests were carried out to verify the correct behavior of the structure. Load tests can be an element of the bridge acceptance procedure that confirms design assumptions and allows the estimation of the influence of additional factors on the stiffness and response of the structure. Finally, data obtained on this basis allow for the verification of the SHM system and calibration of the analytical finite element (FE) model, which will ultimately become a source of training data for the purpose of the ML-based BWIM.

The load testing procedure consists of static and dynamic tests. Five different static load schemes were assumed to generate maximum strain values at the selected measurement points. They include three symmetric schemes, one above each of the measurement gates, and two additional asymmetric cases to verify the transverse distribution of loads and the torsional stiffness of the span. The schemes consisted of nine trucks, each of them weighing between 27.8 and 41.5 t, that were introduced onto the bridge to yield the strain at a level of at least 60% of the theoretical strain values caused by the live load model assumed in the design. According to the established procedure, the load is kept on the bridge for a minimum duration of 30 min. The duration of the test is extended by successive 10 min intervals if strain stabilization has not been achieved. Stabilization is defined as no increase in strain values exceeding 2% between consecutive readings within the 10 min measurement interval. The response of the structure is also measured after unloading to observe residual strains and to assess the general ability of the structure to return to its initial state.

The data recorded by the SHM system were used to calibrate the numerical FE model, which was then used to generate a synthetic training set for the ML algorithms. Acquiring an appropriate data set solely through experimental studies would entail significant time and financial expenditure, which is why an approach using simulation data was adopted. The use of the FE model in the procedure allowed us to increase the variety of loads examined in relatively short time compared to the site experiments. It enabled the analysis of vehicular loads of varying magnitude, axle configuration, and placement, among which single- and multi-vehicle scenarios of different structure can be introduced. In addition to the increase in the size and diversity of datasets, the FE model enables analyzing the response of the structure in a controlled manner, with reduced uncertainties related to the actual placement and characteristics of the load. It is possible to design field tests in the early stage, ultimately selecting those scenarios that allow for the most robust verification and recognition of bridge structural specificity. The main challenge in generating such a set is to ensure its accuracy and reliability in relation to future data that are observable during the operation of the system in real conditions. This objective was achieved by updating the FE model by modifying the stiffness parameters of its individual components to ensure that the simulated strain values correspond to those observed during load tests. Using an uncalibrated FE model would introduce additional uncertainties into the procedure due to the discrepancies between the response of the actual structure and its simulations. On the other hand, relying solely on field test information, possibly extended by data obtained in the operational stage, would not be controlled and reliably labeled due to unknown weight, characteristics, and uncertain structure of real road traffic. Due to the extensiveness of this subject matter and the constraints on the length of this paper, the current study does not provide a detailed description of the FE model calibration.

In addition to the static load test, the examination of the bridge structure incorporated dynamic tests using a single truck of known weight and dimensions, moving along the bridge. The tests involved passages in different positions on the width of the road, at different speeds, and in different directions, including passing through an artificial obstacle

to intensify the vibrations and dynamic response of the bridge. Static and dynamic load tests allowed for the identification of the structural specificity of the bridge required for the adequate design of the SHM-based BWIM system. Figure 3 shows an exemplary change of strain measured by three sensors installed on the bottom flange of the crossbeam at the measurement gate no. 3, recorded during one of the dynamic load test passages. The test was carried out using a vehicle with a total weight of 33.0 t, moving at a constant speed of 10 ± 2 km/h. The figure illustrates the timestamps for the entry and exit of the load on the bridge, as well as the timespan that reveals the presence of the vehicle above the gate. The varied intensification of the strains is noticeable within each of the measurement points, which is directly dependent on the position of the vehicle on the width of the road. At the same time, the limited range of the influence surface for strains in the crossbeam is visible, which corresponds to an evident response only for the vehicle located in the immediate vicinity of the monitored beam. The sensors do not detect the presence of a vehicle if the distance is greater than 2 or 3 times the spacing of the intermediate crossbeams, here about 36.0 m. The limited range of the surface influence for crossbeams is an important feature of the network arch bridges compared to structures of different hanger layout. In the context of implementing the BWIM systems, it allows for reducing the impact of loads placed over a large part of the bridge, beyond the range of the influence surface. Measurement points on the crossbeams do not require additional processing or filtering to mitigate the influence of other loads in the weight detection procedure for a single vehicle within the gate. At the same time, the system in which weight detection is carried out independently by three successive gates becomes potentially useful, allowing for the averaging or cross-validation of results.

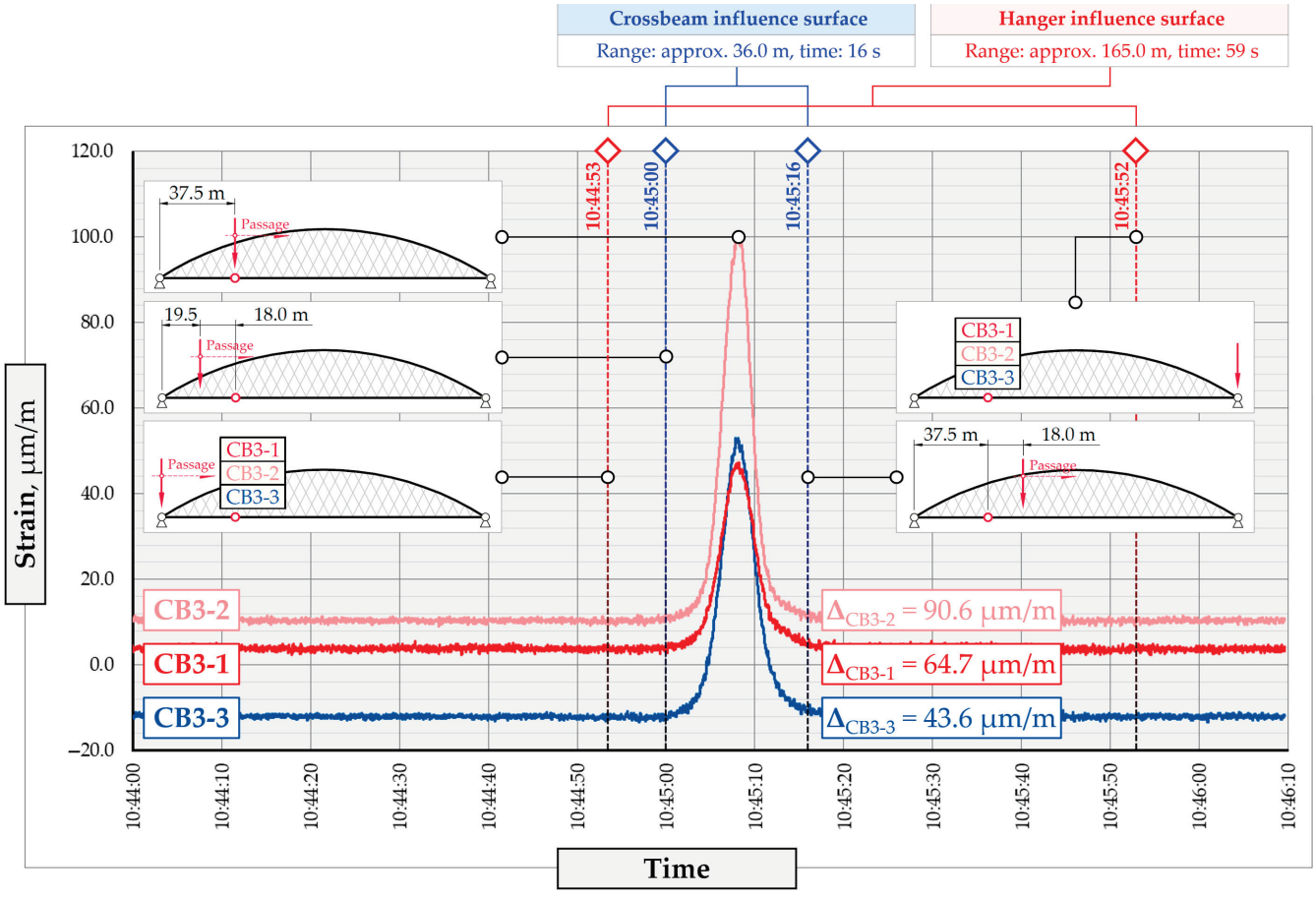


Figure 3. Strains in the crossbeam at gate no. 3 during the dynamic load test passage.

The hangers are characterized by a different shape and range of the influence surface and remain sensitive to the loads outside the gate (Figure 4). In this case, the strains in the hangers recorded during the same test indicate various scales of strain increase depending on the position of the vehicle on the bridge width. Although the timestamp of the maximum strains can also be clearly seen, corresponding to the load located right above the measurement gate, the strain values on the hangers can be affected by other vehicles passing the bridge at a given moment.

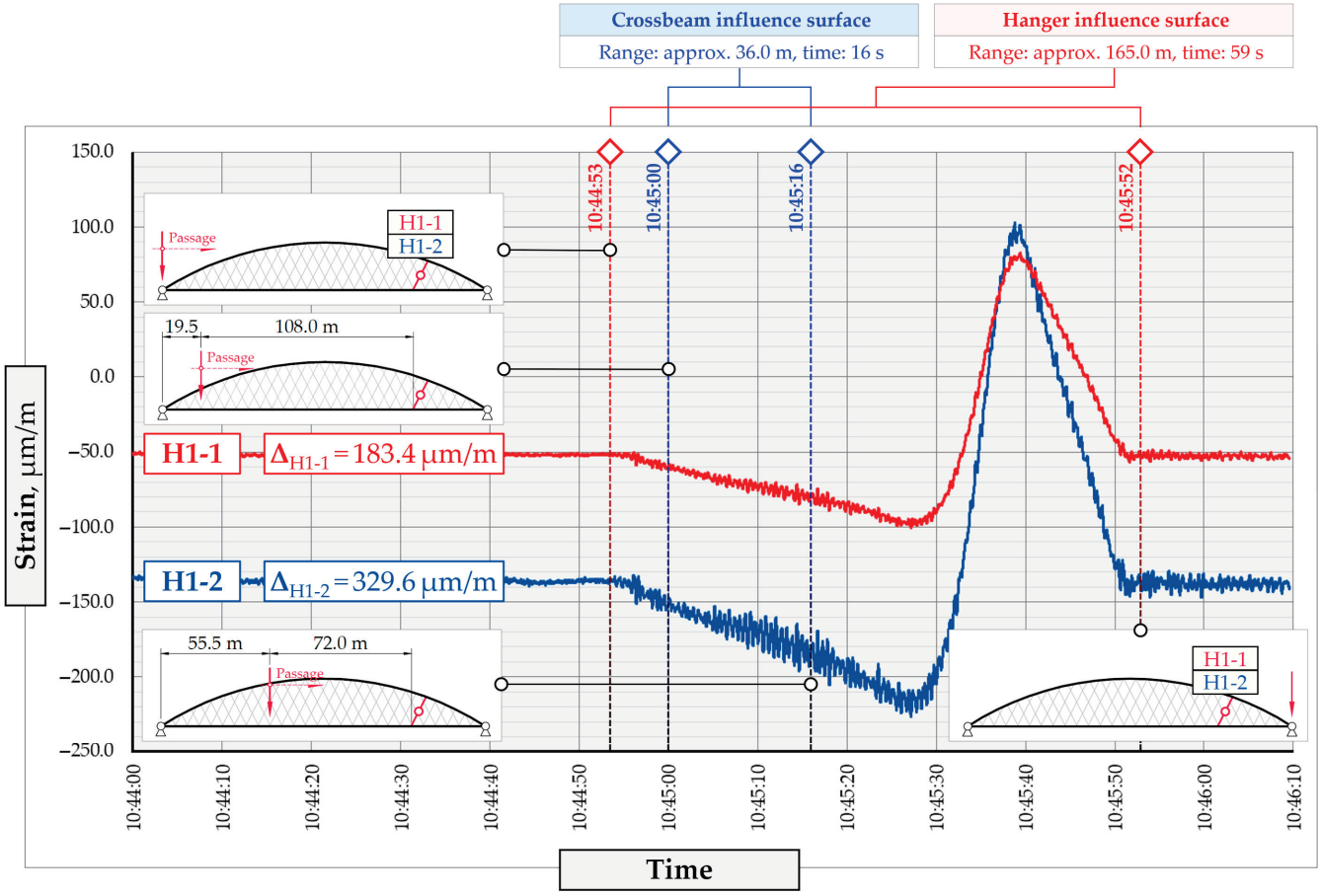


Figure 4. Strains in the hangers at gate no. 1 during the dynamic load test passage.

Similar characteristics of the influence range and the change in strain in time were confirmed at the other measuring points on the crossbeams, tie-beams, and hangers. The remaining tests involved different types and weights of vehicles passing the bridge in different positions related to the width of the road and at various speeds. The used vehicles, nine in total, including seven vehicles of different axle configurations, as well as an overview of the selected results obtained in the measurement gates, are given in Table 1. The other scenarios involved groups of vehicles passing the bridge in different groups and configurations. It can also be seen that relatively short vehicle-induced excitations are also not affected by loads of longer duration and significant inertia, including thermal and environmental actions. In the final implementation of the system, the differences between unloaded and loaded states are considered in the weight estimation procedure. Taking into account the specificity and structural behavior of the network arch bridge, the current research attempts to evaluate the performance of various ML algorithms for the purpose of BWIM systems, depending on the set of features considered in the input data.

Table 1. Overview of the vehicle and strain development during dynamic load tests.

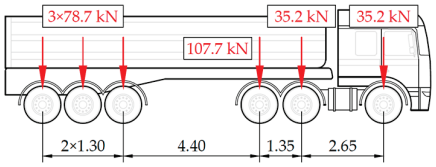
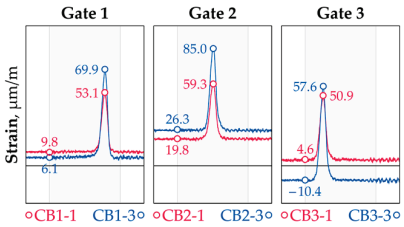
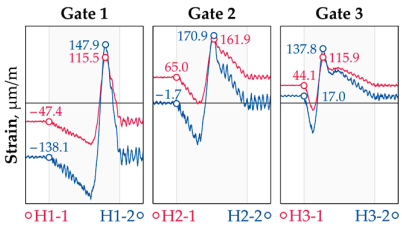
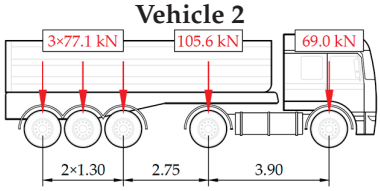
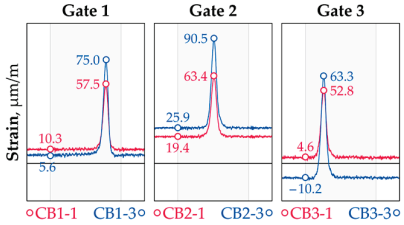
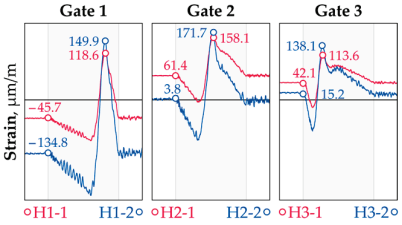
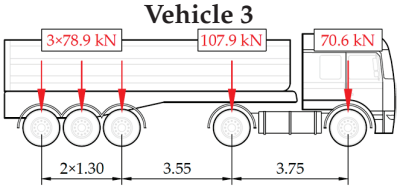
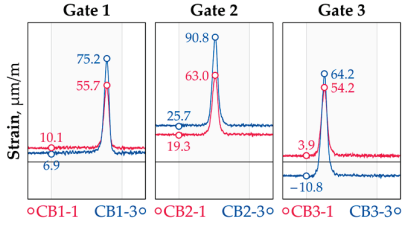
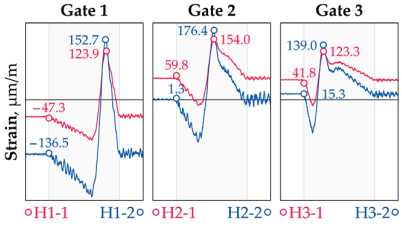
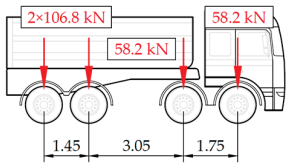
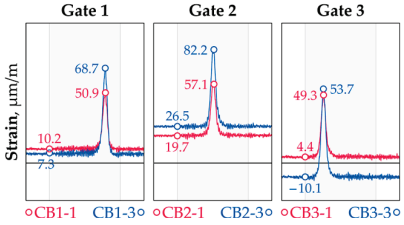
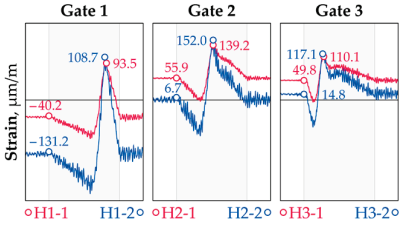
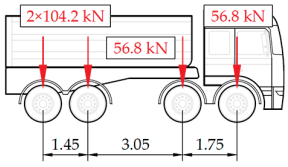
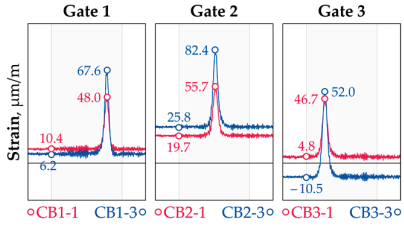
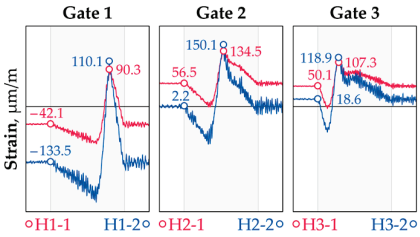
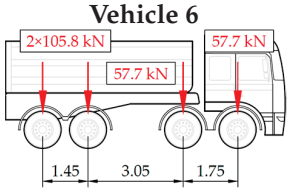
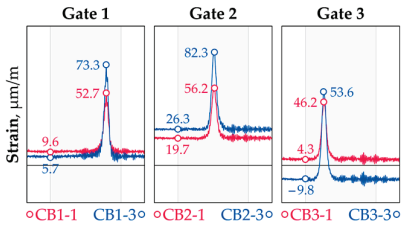
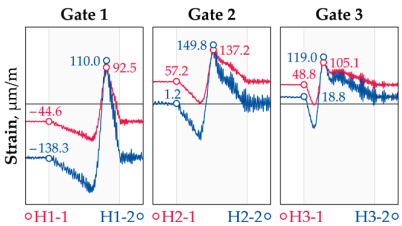
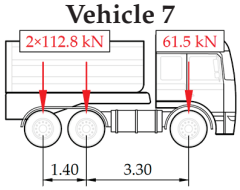
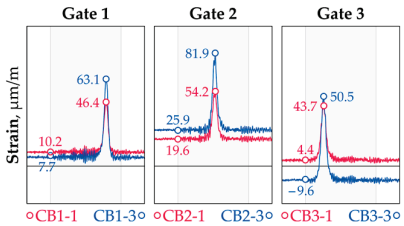
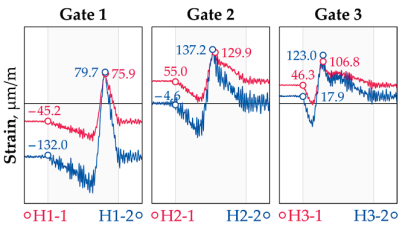
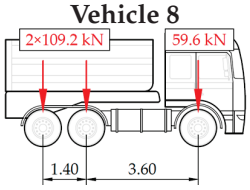
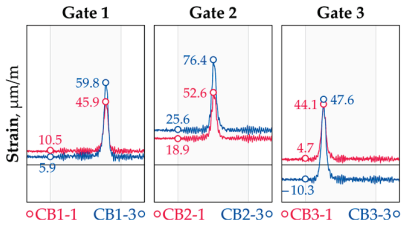
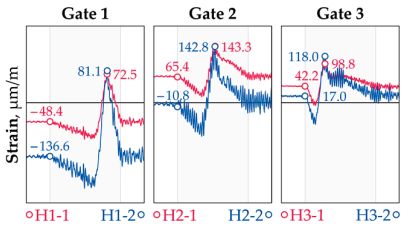
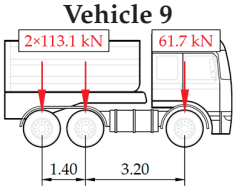
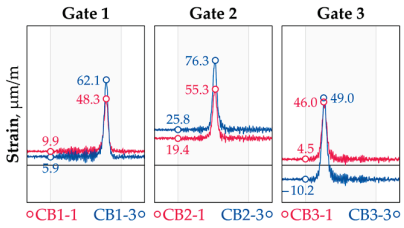
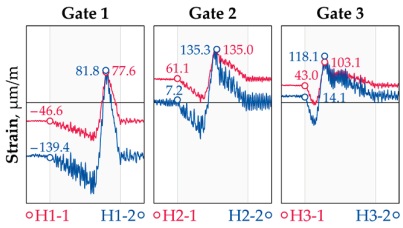
Vehicle Type, Dimensions, and Weight	Crossbeam Strains	Hanger Strains
Vehicle 1  Type: **1**—Total weight: 41.4 t	 	
Vehicle 2  Type: **2**—Total weight: 40.6 t	 	
Vehicle 3  Type: **3**—Total weight: 41.5 t	 	
Vehicle 4  Type: **4**—Total weight: 33.0 t	 	
Vehicle 5  Type: **4**—Total weight: 32.2 t	 	
Vehicle 6  Type: **4**—Total weight: 32.7 t	 	
Vehicle 7  Type: **5**—Total weight: 28.7 t	 	

Table 1. *Cont.*

Vehicle Type, Dimensions, and Weight	Crossbeam Strains	Hanger Strains
Vehicle 8  Type: **6**—Total weight: 27.8 t	 	
Vehicle 9  Type: **7**—Total weight: 28.8 t	 	

Single-vehicle dynamic tests included only, speed: 80 km/h ± 2 km/h. Transverse positions along the right lane, Szczecin → Wolin, 7.4 m ± 0.5 m from the tie-beam TB2 acc. to Figure 1.

2.3. Methods and Further Use

The objective of this study is to determine the ability of various ML algorithms to predict the position and weight of vehicles based on strain, formulating the framework of a multivariate regression. In the SHM and BWIM design stage, when not enough data may be collected prior to the operational stage, missing information can be gathered based on FE simulations. It also allows us to collect a more diverse response to a greater extent compared to real experiments conducted during the load test. The crucial requirement in this approach is to incorporate the calibrated FE model in accordance with the load test results.

The methods used in this research are as follows. Employing the updated FE model, synthetic datasets are generated. By simulating vehicles passing the bridge, each of their various weights, axis configurations, and transverse placements, the maximum strain increase is recorded in the sensors of a given gate, together with the associated strain change in the sensors assigned to the rest of the gates. The input vector includes values that are expected to be obtained from FBG sensors, with a maximum dimensionality corresponding to the number of measurement points, specifically 17 in this case. The size of the input vector is then reduced to assess the influence of the input configuration on the accuracy and reliability of the predicted output. The output values include the total weight of the vehicle and its transverse position.

Three ML models of various architectures and the number of inputs are trained and compared: linear regression (LR), random forest (RF), including its variant of the single-ensemble decision tree (DT), and neural networks (NN). A synthetic data set of 6000 samples was generated and divided into training and test sets of sizes 4800 and 1200, respectively. The input features consist of strain values, and the output includes the coordinates and weight of the vehicle. The accuracy of each regression model was evaluated using the root mean square error (RMSE) as the primary metric. The same input structure was used for all algorithms to compare their predictive accuracy. The equation is shown as follows:

$$\mathrm{RMSE}(\mathbf{X},\, h) = \sqrt{\frac{1}{m}\sum_{i=1}^{m}\left(h\left(\boldsymbol{x}^{(i)}\right) - y^{(i)}\right)^2} \tag{1}$$

where:

m—number of elements in the data set;
$\boldsymbol{X}$—matrix containing the values of all features (excluding target values) of all samples;
$\boldsymbol{x}^{(i)}$—vector of feature values (excluding target values) of the ith sample;
$y^{(i)}$—target value of the ith sample;
h—model's prediction function.

Three input configurations are tested for each of the ML regression methods. First, all 17 strain values are incorporated, assessing the accuracy of the weight and transverse placement estimation. In the next step, the reduction to 5 inputs is considered, consisting of measurement in a single gate, involving three points in the cross-beam and two points in the hangers. Finally, only 3 inputs are considered, corresponding to three measurement points in the gate-specific cross-beam. The purpose of this study is to confirm that the reduced number of inputs can still allow a reliable estimate of vehicle weight and placement, directly incorporating the specificity of the network arch bridge. The work also identifies potential risks associated with the use of synthetic data that, if no specific measures are introduced, are free of various distortion effects.

To automate the generation of data sets for the training and validation of regression ML algorithms, a dedicated framework was developed, allowing for the direct use of the updated FE model (Figure 5). It was created in SOFiSTiK 2023-1 software, a commercial structural analysis environment, using text batch files with the content defined in the internal CADINP language and the SOFiSTiK API adapted to the object-oriented C# programming language. The code includes methods responsible for reading the batch files with the definition of geometry, material, and load cases, calculation, and saving the strain results to an Excel workbook. In the loadings, sets of concentrated forces corresponding to the axle arrangement of seven typical truck vehicles were provided, including those used in the load tests. The vehicles were located in different positions on the bridge and assigned different total weights, while maintaining the proportion of load distribution on the individual axles. The diversity of vehicles allows for the assessment of the universality of the ML models in predicting the total weights of vehicles with different numbers and axle spacings.

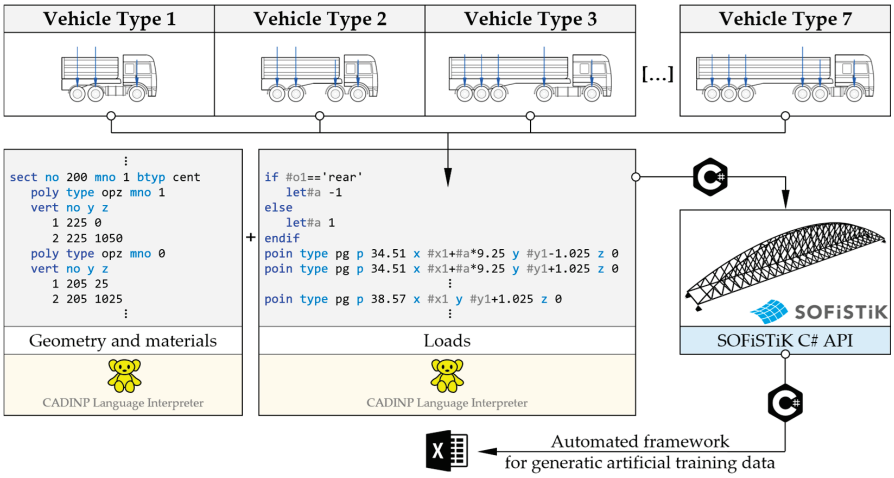


Figure 5. Automation of the data generation process for the purpose of training regression ML models.

To estimate the influence of measurement noise on the accuracy of weight prediction, the following procedure is incorporated. Regression models are trained on the noise-free data derived from the static analysis of the calibrated FE model. Unless otherwise stated in the text, the models are evaluated by calculating the RMSE on training and test sets and, in the latter case, allowing for the assessment of generalizability on samples that were

not incorporated in the training process. Both the training and test sets do not include the influence of noise at this stage. The evaluation of the ability to maintain the accuracy of the prediction is performed by calculating the RMSE on test data contaminated with standard noise, according to Figure 6. In this way, apart from the assessment of robustness to random disturbances, the overestimation of the performance on the noise-free data may potentially be highlighted.

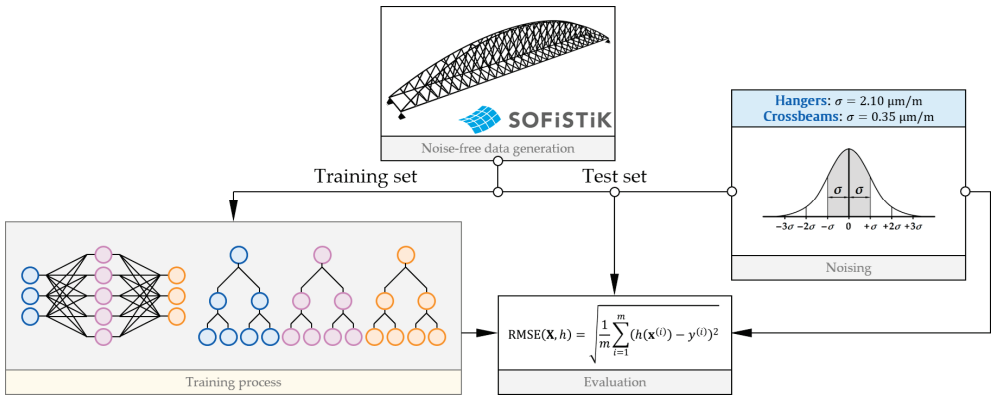


Figure 6. Training and performance evaluation procedure.

As a whole, the final implementation of the entire SHM system can be divided into the following four main stages: (1) structural monitoring, (2) training ML algorithms using the synthetic data, (3) data analysis and final predictions using ML algorithms, and (4) bridge management, as seen in Figure 7. In the first stage, fiber optic sensors record the strains in selected points of the structure in real time. Data obtained from these sensors during the load test were then used in the second stage to calibrate the FE model, based on which a set of synthetic data was generated. They served as the basis for training the ML algorithms, which were then used in the third stage for the final prediction of a vehicle's weight and position. The ML models are automatically executed on the incoming data, and their output is continuously fed into the management layer. The last stage includes the integration of results with infrastructure management systems, such as a digital twin, a dedicated website, and a notification system for exceeding permitted threshold values to enable quick and informed operational decisions. In addition to real-time alerts, all processed data are stored for historical analysis and can be used to assess traffic load trends and structural performance over time.

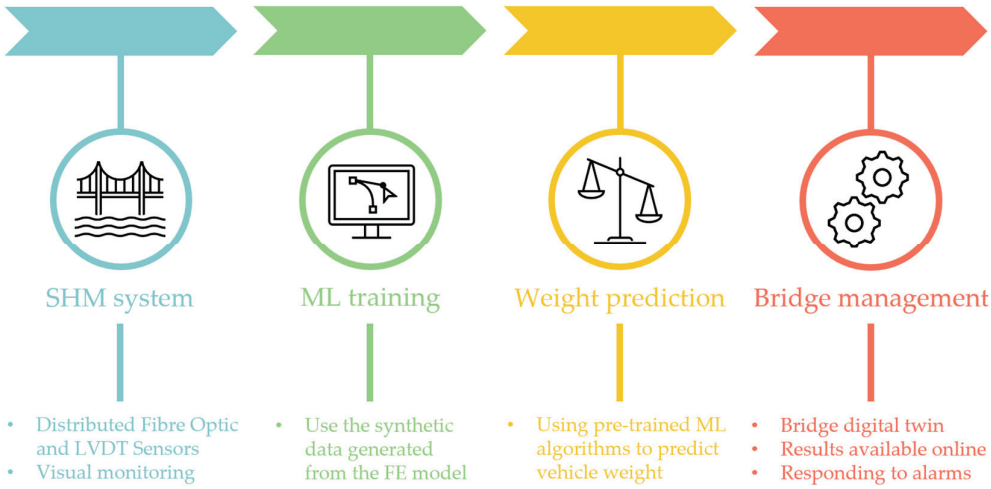


Figure 7. SHM system framework.

Figure 8 presents the data flow for the purpose of the ML-based approach incorporated into the SHM system. It consists of the real structure with the installed sensors and the digital FE model that reflects its structural behavior and specifics. The FE model, once updated in the calibration process, is used to generate the training data set. In the current framework, several regression ML algorithms of various architectures and number of inputs are evaluated and compared in terms of precision in predicting vehicle weight and coordinates. The best-performance model can be utilized to establish a BWIM module in the final system, wherein continuous sensor readings are used to collect information about road traffic and load magnitude on the bridge.

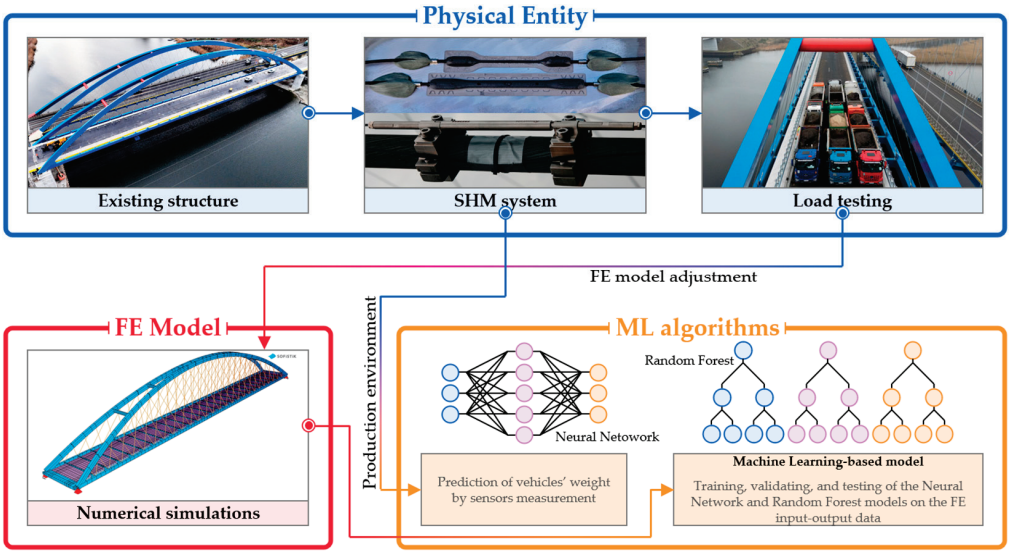


Figure 8. The procedure of establishing the BWIM module, including the SHM system, load testing, FE model adjustment, and ML regression algorithms.

3. Results

3.1. Linear Regression-Based Predictive Models

Linear regression (LR) is one of the basic regression models used to generalize the relationship between a dependent variable and a set of independent inputs by fitting a linear function to the observed data. In this research, the LR model is used as a baseline for further comparison with more sophisticated regression methods, allowing for the assessment of linearity in data obtained from linear FE models. At first, the LR predictor is trained on the strain values recorded by all sensors in the system at a specific timestamp. The performance of the regression model is analyzed by the RMSE value of the predictions on the weight and transverse position of the vehicle, Y. As seen in Figure 3 for the strains in the crossbeam, the exact timestamp that triggers the predictions, as well as the longitudinal placement of the load, X, can be clearly indicated by the peak values in the strain time series data.

Figure 9 shows the performance of the LR model depending on the set of input features. Providing strain values measured in all 17 points reduces the RMSE in the weight estimation procedure to negligible values, revealing a seemingly high accuracy. However, this performance should be interpreted in a broader context, examining the influence of data structure and their quality on the generalizability of the model. The current data include strain values recorded by all sensors at the timestamp of maximum excitations at a given gate. It turns out that, at this time, the strains in the distant crossbeams oscillate around relatively small values of low variance, caused by the limited range of their influence surface. At the same time, the training data reflect the results of the linear

static analysis performed on the calibrated FE model and do not include the noise that is common in real-world applications. Under these circumstances, the LR model assigns large weights to small strain values at distant crossbeams, attributing them to a significant influence on the model fit. Even a small deviation from the expected value, including that due to noise effects, causes a disproportionate change in the weight estimate and a significantly large RMSE value. Training non-regularized regression models, including LR, on the simulated data with no noise poses the risk of overestimating their performance and reducing robustness in the real-world environment. Limiting the input features to five and three inputs decreases the performance of the model, resulting in an RMSE of 407.7 kg and 2323.1 kg on the test set, respectively. The results reveal non-linear relationships between the explanatory variables and the output. At the same time, the vulnerability to noise effects is mitigated as the simplified linear function imposed on the non-linear dependencies and serves as a form of regularization. The prediction of Y coordinates is not affected by the complexity of the input features and achieves accuracies in the range between 1.016 and 1.096 m in the test set. It results from the absence of a linear relationship between the transverse position of the vehicle and the inputs as well as a very similar impact of the strain values in the closest crossbeam that are incorporated in all three models.

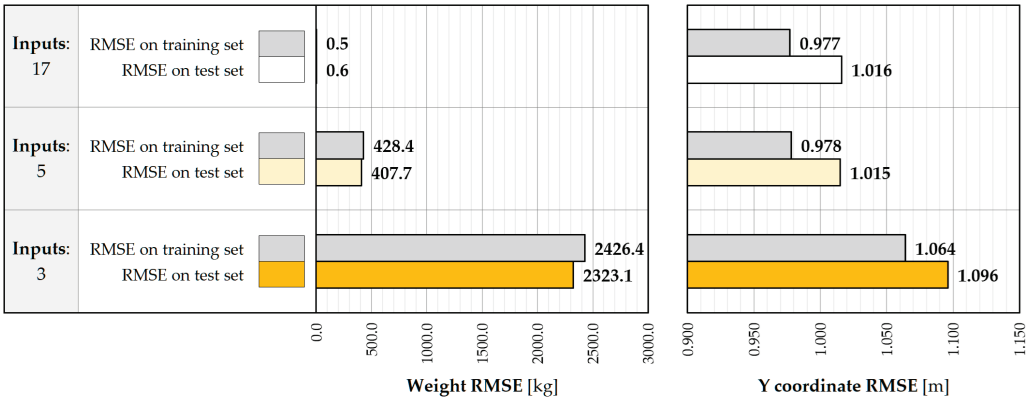


Figure 9. Weight and Y coordinate RMSE for LR model with 17, 5, and 3 inputs.

The sensitivity to noise can be analyzed following the procedure mentioned in Figure 8. As can be seen in Figure 10, the accuracy of the 17-input model decreased significantly, due to the overestimated weights assigned to the strain measurements in the distant crossbeams. This effect can be mitigated by excluding the measurement points from the input features. If no additional measures are used to reduce noise effects on the input values, then the vulnerability of the five- and three-input models becomes apparent through the increase in the RMSE value of about 150 kg, despite the relatively overall low performance of LR.

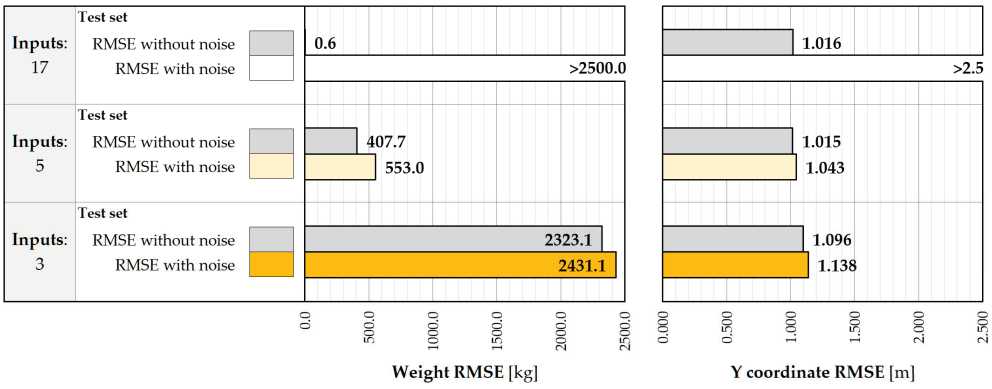


Figure 10. Weight and Y coordinate RMSE for LR model with 17, 5, and 3 inputs, with noise included.

The drawbacks of the LR model and its oversimplification for a reduced number of input features do not allow for achieving the required level of accuracy according to project specifications, 0.5 t. Performance in this context can be considered unsatisfactory and justifies the use of more sophisticated regression methods.

3.2. Random Forest-Based Predictive Models

Random forest (RF) is one of the ensemble ML algorithms used in various classification and regression tasks. For the latter, it consists of a given number of regression decision trees, each of which is independently trained on a specified group of samples from the training set. The training process consists of gradually expanding the tree by splitting the set into two nodes. Newly created nodes are progressively split into deeper subsets until a stop criterion is met, usually reaching the maximum tree depth or minimum number of samples in the node. In the current approach, the best split in the node is obtained by minimizing the average squared difference between the feature values of the samples assigned to the potential sub-nodes and their means. The splitting algorithm evaluates every possible split and selects the one that results in the greatest reduction in mean squared error in the resulting subsets. This process is repeated for given and subsequent nodes until a single element leaves at the end. A single RF consists of several decision trees, making the model more diverse and reducing the variance of the entire forest. The final prediction is calculated as the average of the outputs returned by each of the trees.

In the current study, RF models with different numbers of decision trees and different numbers of training samples in relation to the size of the whole dataset are considered and compared with the performance of the NN regression models. At first, different RF architectures are trained on the strain values recorded by all sensors in the system at a specific timestamp. The performance of the regression model is analyzed by the RMSE value of the predictions on the weight and transverse position of the vehicle, Y.

Figures 11 and 12 show the impact of the RF architecture on the prediction error for vehicle weight and its transverse position, Y, respectively. Five various numbers of trees are assumed, in turn 1, 10, 50, 100, and 500 trees. For each number, different relative sizes of the training subsets are analyzed, labeled as max samples, and range from 10.0 to 100.0%. The models are evaluated on training and test sets to estimate the variance and assess the ability of the model to generalize the results for inputs that did not participate in the learning process.

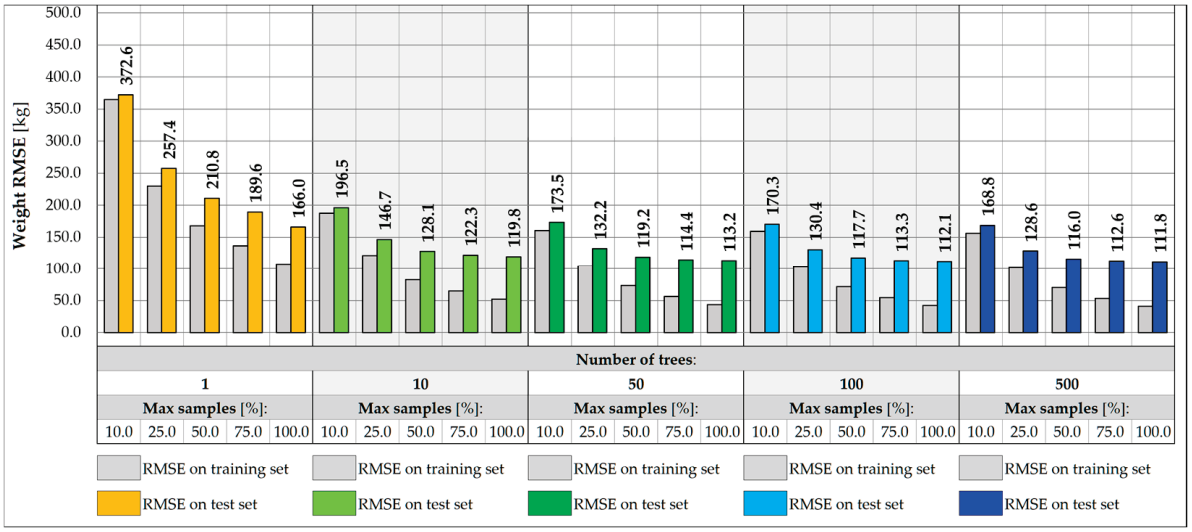


Figure 11. Weight RMSE for different RF architectures with 17 inputs.

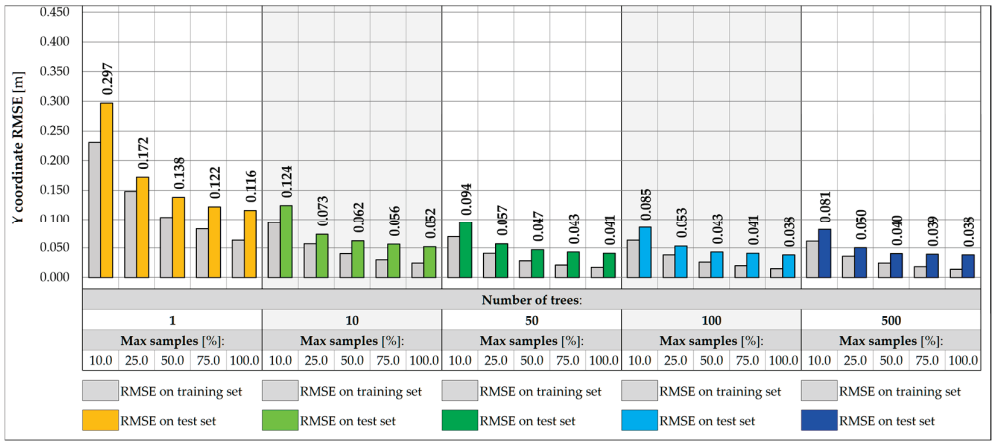


Figure 12. Coordinate Y RMSE for different RF architectures with 17 inputs.

For single-tree architectures, the RMSE values are in the range from 166.0 to 372.6 kg for weight and 0.116 to 0.297 m for coordinate Y. The variance of a single decision tree is regularized by the introduction of sampling with replacement, which allows for the repetitive occurrence of samples in the training subset, while keeping some of the samples out of the badge. In most cases, an effect of overfitting is observed, in which the error measured on the test set is higher than the error on the training set. The problem can potentially be solved by introducing more trees or using additional regularization techniques, including reducing the size of the training subsets. The overfitting effect is reduced only for drastically reduced subsets, at least 25.0.% of the initial set size. Despite the effect, the best performance model is usually chosen based on the error measured on the test set. Following this assumption, it can be seen that the higher the number of tress and the larger the size of the subset, the higher the accuracy of the RF model. For models consisting of at least 50 trees and trained on at least 75.0% of the initial set, the accuracy measured on the test samples lies in the range from 111.8 kg to 114.4 kg for total weight and 0.038 to 0.043 m for Y estimations. It is possible to achieve an accuracy of less than 50.0 kg for the training set.

Reducing the feature set by excluding the strains measured at the points outside the given measurement gate allows for limiting the potential impact of vehicles located in other parts of the bridge. In this case, a five-element input vector is considered, consisting of strain points on the crossbeams and two hangers on the left and right sides of the deck. In the example of gate no. 1, the accuracy of the weight and transverse position predictions decreases for all RF architectures considered, as shown in Figures 13 and 14. For the best model identified for the entire set of features, the RMSE value measured for the test set drops from 111.8 kg to 391.9 kg, which is still satisfactory, considering the expected traffic load range estimated up to 40 t. The achievable accuracy for the prediction of the transverse position reaches 0.070 m.

Further reduction of features in the input vector may involve excluding strains in hangers while maintaining the strain reading in the measurement gate crossbeam. In this case, due to the limited range of the surface influence, the RF input values depend only on the vehicles located within the gate and its closest vicinity. This approach allows for exclusion of the use of algorithms that filter the influence of distant loads, which, however, involves further reduction of the accuracy of predicting weight and transverse position. The RMSE values measured in the training and test set for the three-input vectors for the same RF architectures are shown in Figures 15 and 16. For the best model identified so far, the RMSE value measured for the test set drops to 1266.7 kg, which exceeds the required

level of accuracy assumed in the specification, 0.5 t. The RMSE for the transverse position is less than 0.130 m.

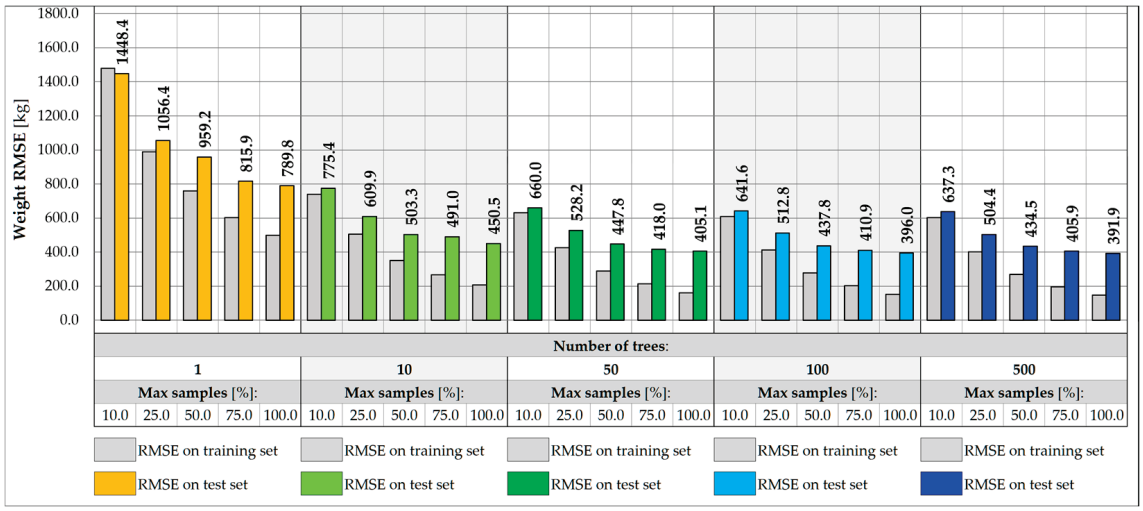


Figure 13. Weight RMSE for different RF architectures with 5 inputs.

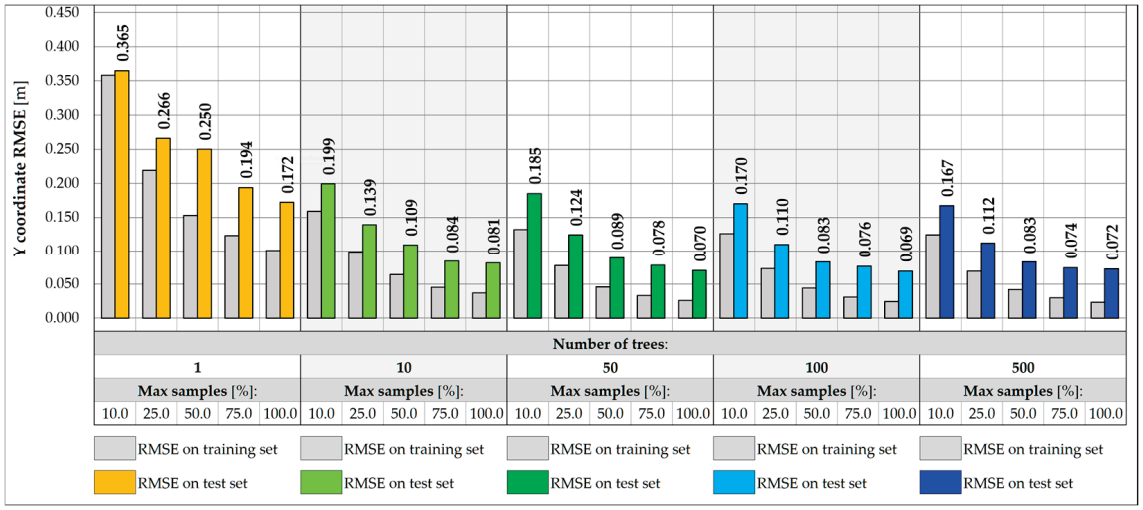


Figure 14. Coordinate Y RMSE for different RF architectures with 5 inputs.

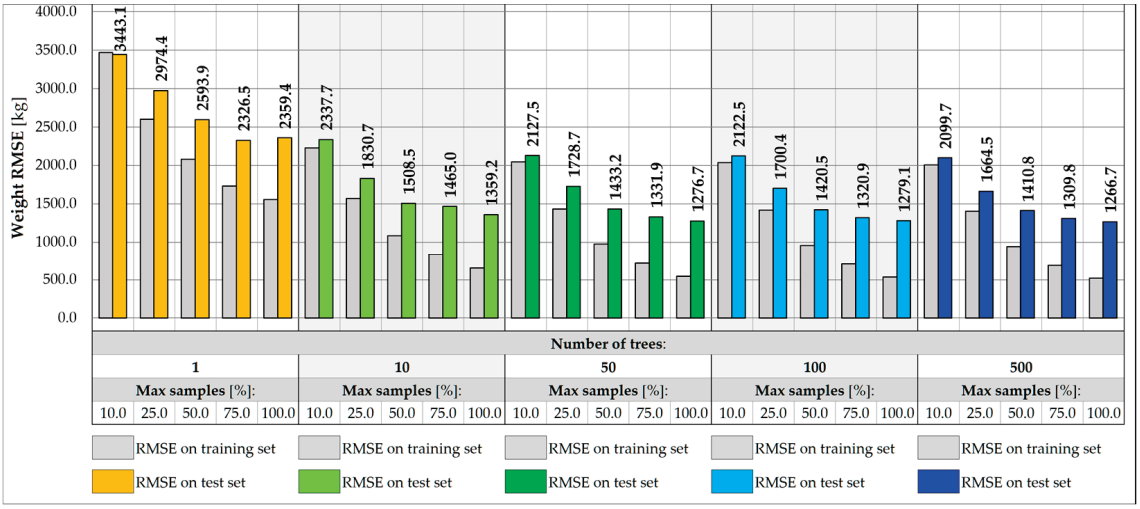


Figure 15. Weight RMSE for different RF architectures with 3 inputs.

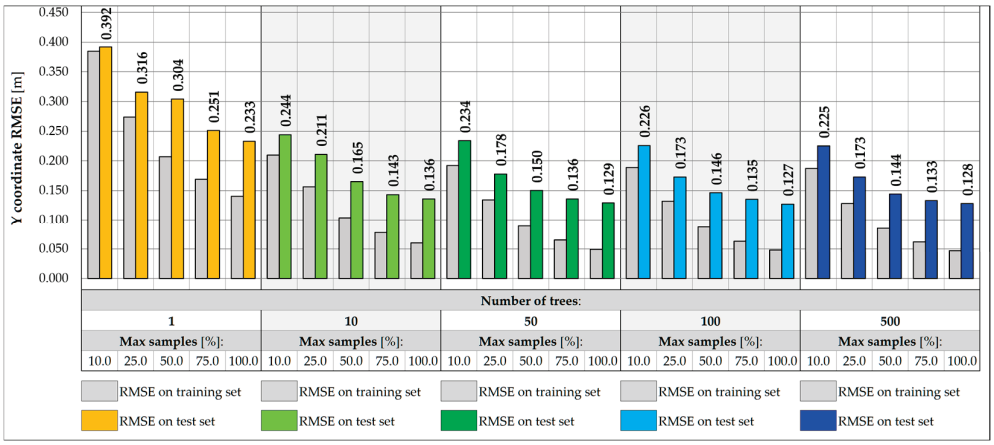


Figure 16. Coordinate Y RMSE for different RF architectures with 3 inputs.

It was also noted that the performance and accuracy of the RF models depend to a large extent on the size of the training set (Table 2). With 4800 samples in the training set, the learning time of a 500-tree three-input RF model was within 6 s, which is much shorter compared to the time required to train more advanced models, including neural networks. As seen in Table 2, a tenfold increase in the size of the training set allows for the reduction of the RMSE value in weight prediction to an acceptable level of 509.6 kg, with an increase in training time to 73.2 s.

Table 2. Comparison of accuracy and learning time for different sizes of the training set.

Random Forest Regression: Total weight estimation number of trees: 500, max samples: 100.0%			
Training Set Size	**Training Time** [1] **[s]**	**RMSE [kg]**	
		Training Set	**Test Set**
4800	5.5	518.1	1266.7
12,000	14.4	356.8	883.4
24,000	33.1	271.9	674.1
48,000	73.2	197.7	509.6

[1] Personal computer, processor: Intel Core i9-14900HX, 32.0 GB RAM, GPU 12 GB.

The influence of noise measured by an increase in the RMSE value for the noise-contaminated test set for the best-performance RF models was analyzed. In the case of the 17-input regression, the accuracy of the weight prediction was significantly reduced, exceeding the error of 3.5 t, which does not qualify the model for further development and deployment in the real structure. The reason for this effect is again the too high significance of the strain values in the distant crossbeams. Oscillating around relatively small values of a magnitude similar to that of noise disrupts the data flow in each of the decision trees, leading to incorrect inference about the weight of the vehicle. The models trained on a reduced number of features, excluding strains in the distant crossbeams, are able to mitigate the noise impact. The increase in RMSE is 124.6 kg and 60.0 kg for models with five and three inputs, respectively.

Based on the results obtained, the RF regression models of a reduced number of inputs are close to achieving the required level of accuracy of 0.5 t, according to project specifications, for both training and test sets. However, it requires models of higher complexity, involving at greater number decision trees, at least 500, and a data set of significant size, about 48,000 samples in the reported case. Although the latter legitimates the use of updated FE models and synthetic data in the evaluation of various ML architectures prior to their final deployment, several limitations may be observed in the context of use

on real data. First, the evaluation using synthetic data does not involve uncertainties that can exist in real-world applications, including noise, impact of environmental effects, diversity of traffic scenarios, and nonlinearity of structural response. Second, the RF models examined still exhibit the effect of overfitting. Although the overfitting could be addressed by introducing additional regularization, including reducing the depth of decision trees or imposing a minimum number of training samples in leaves required for the growth of each tree, it would require a further increase in dataset size to maintain the accuracy obtained. Consequently, it is desirable to develop models for which the accuracy achieved will be significantly below the required threshold, while mitigating the effect of overfitting.

3.3. Neural Network-Based Predictive Models

In this research, which consists of the prediction of the weight and location of the vehicles passing by the bridge, neural network (NN) models can also be used. This is an example of a regression problem, in which NNs have high accuracy and effectiveness. These models are used for complex predictions and the identification of dependencies between input and output data. Under their assumption, they constitute a network of interconnected neurons grouped into input, output, and intermediate hidden layers. All input data are transferred to the first layer of the network and then transformed into subsequent layers according to the assigned weights. The value stored in each neuron corresponds to the sum of the products of the values from neurons from the previous layer and the weights assigned to each connection. Then, it is modified by adding an additional deviation and is transformed using an activation function. In practice, the operation of NNs can be described using a matrix equation that transforms the input data. During the training phase, the NN adjusts the model weights for each connection to most closely represent the known output given the input.

When designing NNs, an important part is the selection of the appropriate architecture, in particular, the number of layers and neurons. In the presented study, a total of 25 different NN architectures were tested, including configurations with 1, 2, 3, 5, and 10 hidden layers and with 10, 50, 100, 150, and 200 neurons in each layer. The NNs were tasked with accurately predicting the location of the vehicle on the bridge in the transverse Y direction and its weight. Each of the networks was trained for a maximum of 1000 epochs, using an early stopping mechanism with the patience parameter set to 100 epochs. During NN training, the learning rate plays a very important role, defining the size of parameter changes in each iteration. Too high a value can lead to learning instability, where the model weights tend to infinity instead of stabilizing. On the other hand, too low a value leads to slow convergence and creates the risk of stopping the learning process at a local minimum. Therefore, different learning rate values were tested, and a value was chosen for which the best models were obtained. The values of 0.001, 0.005, 0.01, 0.05, and 0.1 were adopted. The loss function was the Huber function, which combines the features of the mean square error (MSE) and the mean absolute error (MAE). For small errors (below the threshold value), it has a quadratic character, making it learn faster and achieving convergence near the target values. However, above the threshold value, it takes a linear form, which makes it more resistant to outliers. The metric defining the accuracy of each architecture was the root mean square error (RMSE) calculated for the entire training and test set (Figures 17 and 18).

For vehicle weight prediction, the best accuracy is achieved by an NN of moderate depth consisting of two or three hidden layers. Shallower networks with one hidden layer are not able to correctly model the relationships between data, achieving significantly higher RMSE values. There is also a noticeable decrease in accuracy for deeper networks with five or ten layers, leading to higher RMSE values. The best accuracy was achieved for

an NN consisting of two hidden layers and 100 neurons, for which the RMSE is 19.9 kg. The predictions presented for 17 input data show that increasing the depth and number of network neurons does not necessarily lead to better accuracy. Choosing an architecture consisting of two or three hidden layers with at least 50 neurons is the best compromise between model accuracy and its complexity.

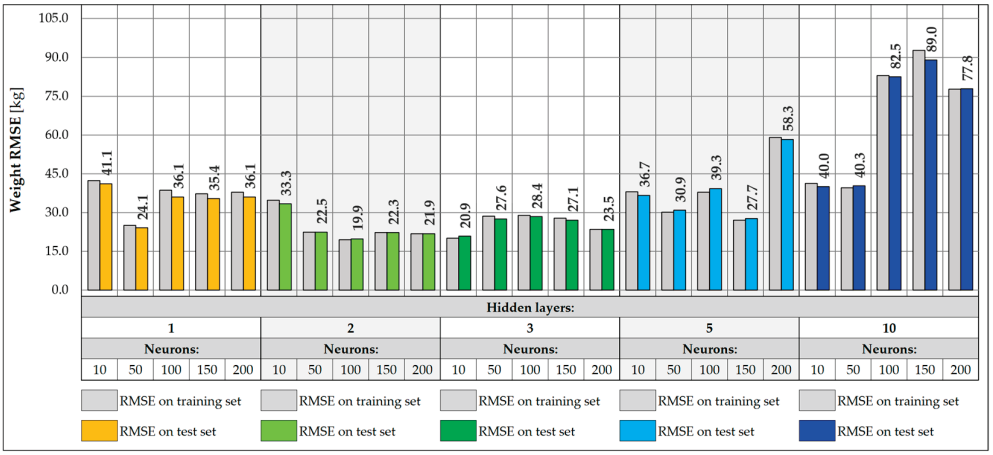


Figure 17. Weight RMSE for different NN architectures with 17 inputs.

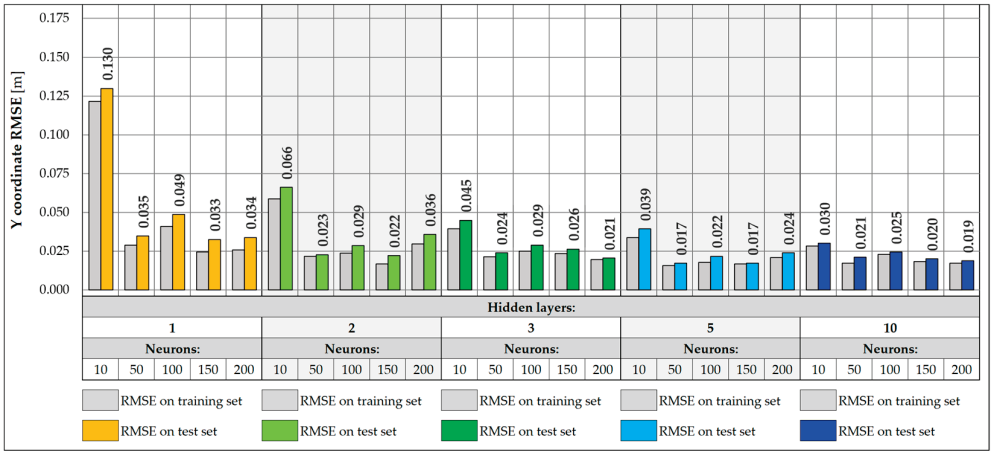


Figure 18. Coordinate Y RMSE for different NN architectures with 17 inputs.

For prediction of the Y coordinate of a vehicle on a bridge, the best results are achieved by NNs with a depth of two to ten hidden layers. Shallow networks or those containing a smaller number of neurons were characterized by greater overfitting, resulting in higher RMSE values in the test set compared to the training set. This indicates the inability of simpler models to capture complex dependencies between data. In turn, networks with a larger number of layers did not provide further improvement in accuracy and achieved RMSE values similar to those of simpler two- or three-layer networks. The best accuracy was obtained for a network consisting of five hidden layers and 150 neurons, achieving an RMSE of 0.017 m and the lowest degree of overfitting in relation to all architectures. However, two-layer networks with 50 or more neurons achieve satisfactory results and can be a good compromise between accuracy and model complexity.

In the case described above, the input data are the strains recorded on all 17 sensors. In such a system, it may be difficult for the NN to determine the location of the vehicle in the longitudinal direction X when there are more vehicles on the bridge at the same time. This results from the specificity of the operation of the arch structure with a network suspension, which is characterized by small areas of influence for the measurement points

located on the crossbeams. They cover only about two bands of crossbeams, which means that they record strains only when the vehicle is directly above a given measurement gate. Consequently, when there are more vehicles on the bridge, the NN may have difficulty accurately predicting the exact weight and location of each of them. For this reason, it was decided to use measurement gates as an effective method to determine the position of the vehicle along the length of the bridge because the results obtained are not disturbed by vehicles standing at a greater distance from a specific gate. Therefore, NN can predict the position Y and the weight of only one vehicle at a time, currently passing through the measurement gate. As a result, it can be assumed that the X coordinate of the vehicle position is equal to the position of the measuring gate along the bridge.

NNs were trained with input data collected from a single measurement gate consisting of five sensors, located on crossbeams and hangers. The same architectures were analyzed as for 17 input data, consisting of one, two, three, five, and ten hidden layers and 10, 50, 100, 150, and 200 neurons, respectively. Each network was trained for a maximum of 1000 epochs, assuming an early stopping mechanism with a patience factor of 100 and analyzing different values of the learning rate, 0.001, 0.005, 0.01, 0.05, and 0.1, respectively, choosing the value for which the model performed best. The RMSE values were then determined for the training and test sets (Figures 19 and 20).

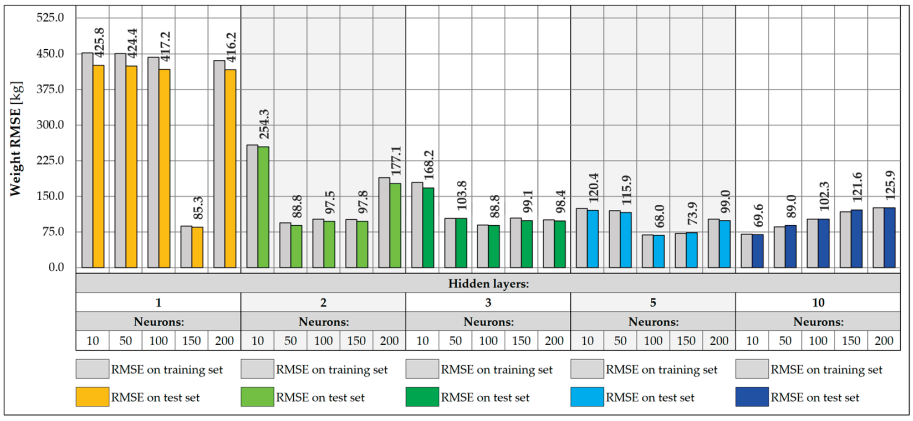


Figure 19. Weight RMSE for different NN architectures with 5 inputs.

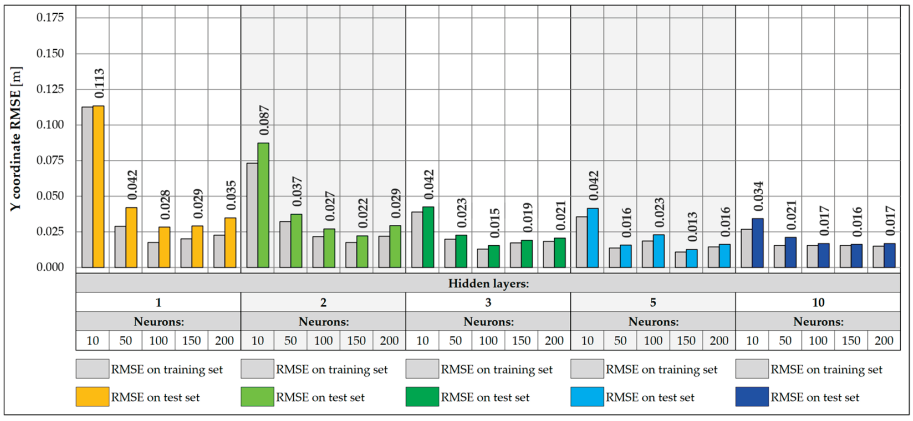


Figure 20. Coordinate Y RMSE for different NN architectures with 5 inputs.

In the case of weight prediction with five input data, networks with at least two hidden layers and 50 neurons perform very well, achieving RMSE values below 100.0 kg. On the other hand, the shallow network with one hidden layer is too simple and was unable to effectively model the appropriate relationship between data for any learning rate. These networks (except for the one with 150 neurons) stopped at a local minimum and were

unable to fully carry out the learning process. Their training was stopped already around the 300th epoch using the early stopping mechanism, which indicates that they did not improve their accuracy during the subsequent epochs. There is also a slight increase in the RMSE values for more complex architectures, including 10-layer networks, which achieve RMSE values exceeding 100.0 kg. The best accuracy was achieved by the NN with five hidden layers and 100 neurons, for which the RMSE is equal to 68.0 kg.

The best accuracy in determining the vehicle Y coordinate is achieved by networks with at least three hidden layers and 50 neurons. There is also a slight improvement in accuracy compared to networks using all 17 input data. Also in this case, increasing the depth of the network does not lead to achieving better accuracy, and networks with three or five hidden layers are good solutions, which are also not complex architectures. The best accuracy was achieved by a network with five hidden layers and 150 neurons, for which the RMSE value is 0.013 m.

The disadvantage of the models using five inputs is the consideration of strains from the hangers. Although the influence surface for the crossbeams is rather limited and covers a narrow range, for the hangers, it reaches much further along the bridge. As a result, with a larger number of vehicles, the effectiveness of these models can be disturbed by vehicles standing in front of or behind the measuring gate. Further data filtering and NN training show a greater influence of the model architecture on its accuracy. In this case, the RMSE values are larger than in the previous models, but they are not disturbed by other vehicles that are not located above the specific measuring gate. At the same time, the accuracy achieved by these networks is sufficient in the conducted study (Figures 21 and 22).

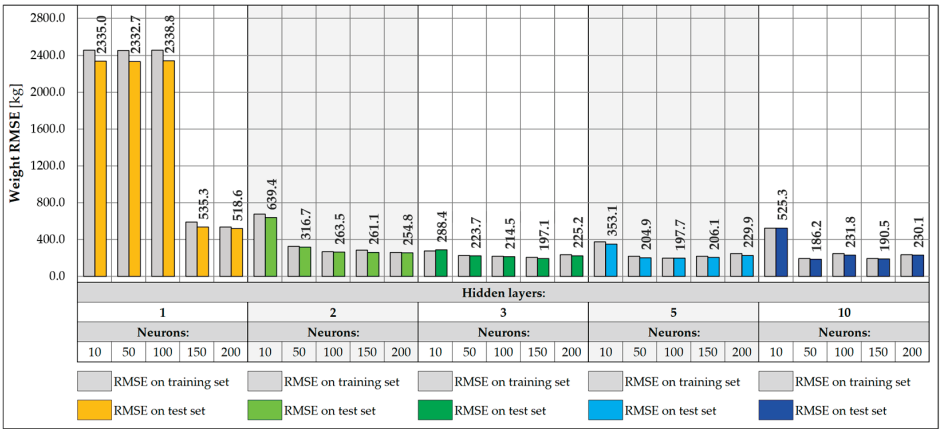


Figure 21. Weight RMSE for different NN architectures with 3 inputs.

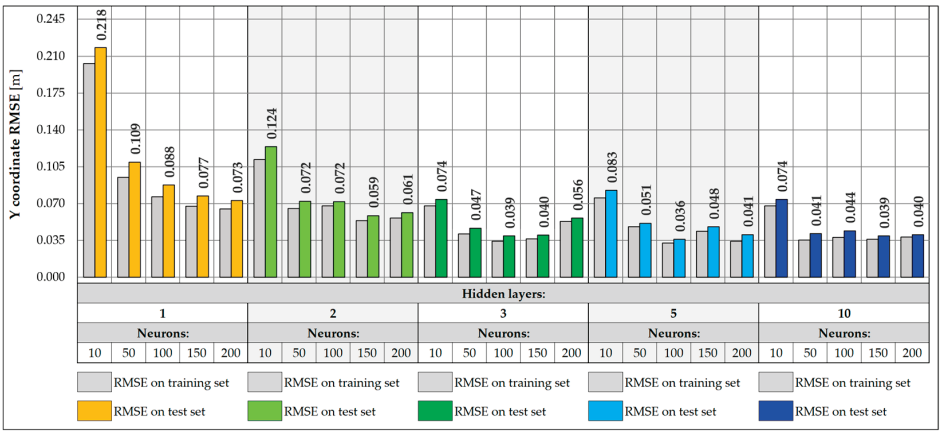


Figure 22. Coordinate Y RMSE for different NN architectures with 3 inputs.

In the case of vehicle weight prediction, NNs with at least two hidden layers and 50 neurons performed very well, being able to make predictions with an accuracy of about 200 kg, which is sufficient for vehicles weighing up to 40 t. Shallow networks with one hidden layer and a small number of neurons were too simple and were unable to correctly complete the learning process, stopping each time at a local minimum, while checking different variants of the learning rate. Three-layer networks provide a good compromise between accuracy and model complexity and can be successfully used in vehicle weight prediction. On the other hand, the best accuracy was achieved by an NN with 10 hidden layers and 50 neurons, for which the RMSE value is 186.2 kg.

The RMSE for predicting the Y coordinate of the vehicle's position decreases with the increase in the number of neurons in the network layers. However, for NNs with at least three hidden layers and 50 neurons, they already reach similar values that constitute good solutions, with not necessarily complicated architectures. On the other hand, shallower networks, especially those with one hidden layer, do not generalize new data well and perform much worse, achieving about twice as high RMSE values and being characterized by slight model overfitting. The best accuracy is characterized by a network with five hidden layers and 100 neurons, which reached an RMSE value of 0.036 m.

For each of the feature sets analyzed, the NN-based regression model is able to produce results with required accuracy, 0.5 t. However, by examining the performance of the models on a test set containing noise effects, a significant increase in the RMSE value for the 17-input vector is observed. Similarly to LR and RF regression models, the sensitivity to noise can be mitigated by incorporating models with a reduced number of features where the distant crossbeams are excluded from input features in a specific gate. In their case, the increase in RMSE values does not exceed 100.0 kg.

3.4. Model Accuracy

To check the accuracy of the ML algorithms, regression models were implemented. Perfect fitting occurs when the error is equal to 0.0, meaning the regression model takes the form $x = y$, where y is defined by the following Equation (2):

$$y = \beta_0 + \beta_1 x + \xi \tag{2}$$

where:

β_0, β_1—structural parameters of the function;

ξ—random component.

In this regression model, β_1 is a coefficient indicating the deviation of the predicted results from the measurement. The average difference (standard error of estimate) between measured and predicted values is the simulated error, where σ is the variance of the model residual.

Therefore, σ is a benchmark of model fit, based on the model residual, which means the discrepancies between the actual values of the dependent variable in the sample and the value of the convergent dependent variable calculated on the basis of the model. Therefore, the goal is to achieve a situation where the variance value tends to 0: $\sigma \to 0$. Figure 23 presents the regression models obtained from the best performing models predicting the vehicle weight based on three input data. These models are a linear regression (Figure 23a), an RF consisting of 100 trees with the tree size built by sampling with replacement and the size equal to the initial set (Figure 23b), and an NN with 10 hidden layers and 50 neurons per layer (Figure 23c).

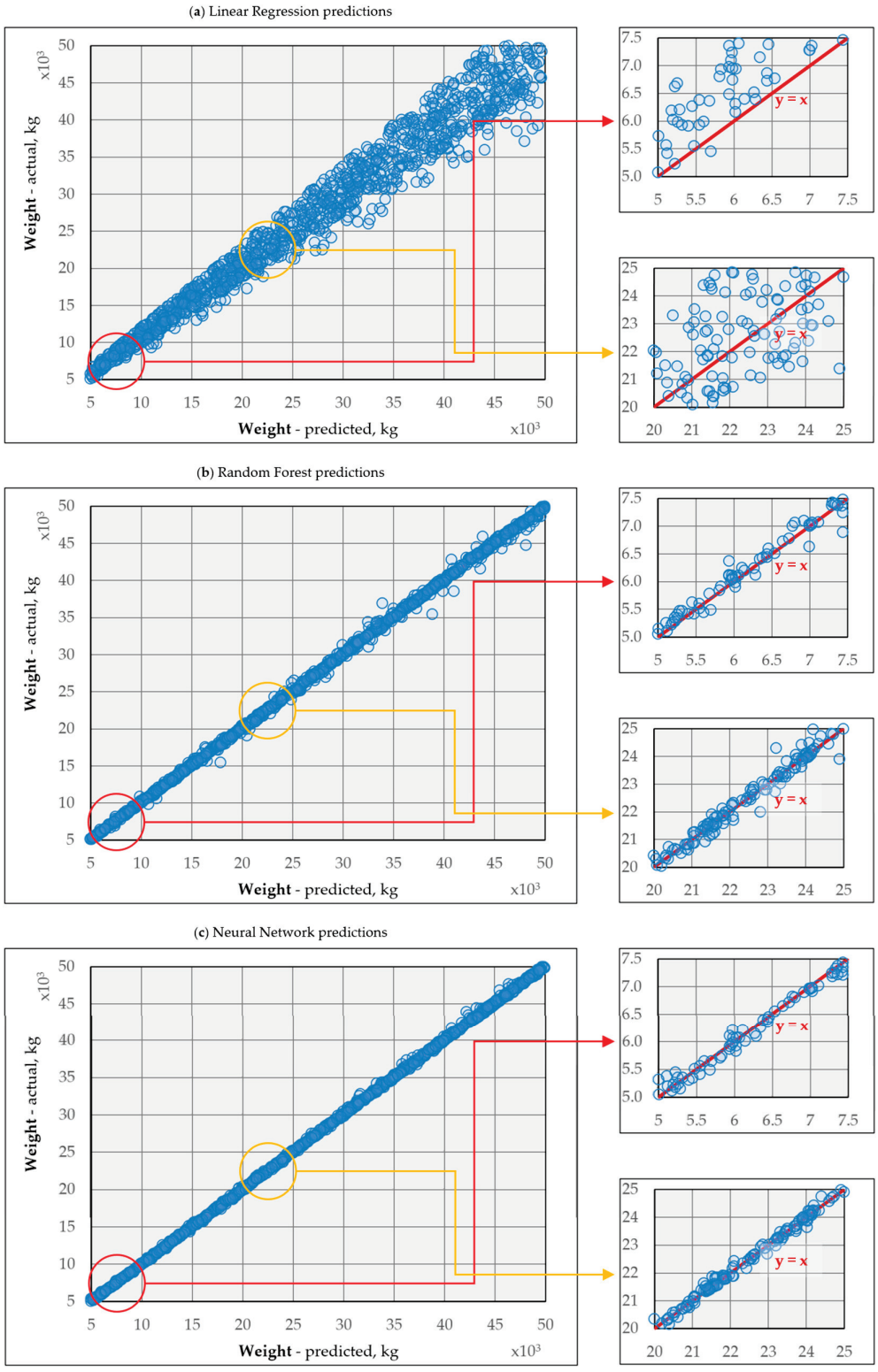


Figure 23. Model accuracy for predicting vehicle weight based on 3-input vector: (**a**) neural network regression model, (**b**) random forest regression model, (**c**) linear regression model.

The models presented in Table 3 were trained on data without noise. The best predictions of weight and Y position were achieved when using all sensors, i.e., 17 input data sets. The impact of noise was determined by introducing noise into the test set, not the training set, which allowed for an estimation of any potential degradation in the accuracy of the algorithms. This degradation occurred in each model, but for RF and NN, it did not exceed

124 kg and 100 kg, respectively, with appropriately selected architectures. It was also noted that unregularized models, such as LR, for which the RMSE value increased by more than 2.5 t, are the most sensitive to noise. Therefore, special care should be taken when training models on synthetic data, which do not incorporate various distortions, including noise. However, it is possible to train algorithms on noisy data or apply input filtering procedures to mitigate noise.

Table 3. Comparison of accuracy for different ML models.

Number of Inputs	Predictions	Linear Regression (LR)	Random Forest (RF)	Neural Network (NN)
17 Inputs	Weight [kg]	0.600	111.8	19.9
	Y Coordinate [m]	1.016	0.038	0.017
5 Inputs	Weight [kg]	407.7	391.9	68.0
	Y Coordinate [m]	1.015	0.069	0.013
3 Inputs	Weight [kg]	2323.1	1266.7	186.2
	Y Coordinate [m]	1.096	0.127	0.036

4. Conclusions

This article presents the implementation of the BWIM framework based on fiber optic sensors and FBG technology. Its design integrates the data obtained from the SHM system and ML algorithms to predict the total weight and position of vehicles on a network arch bridge. To generate a training set, a load test of the bridge was carried out, during which strains measured by the fiber optic sensors were recorded. The strain measurement points were placed at key points of the structure to ensure an accurate representation of its response and operation. Based on these load tests, the FE model updating procedure was performed, enabling training set generation and assessment of the specificity of the bridge structure on the final operation of the BWIM system.

The analysis showed that reducing the number of sensors and focusing on specific measurement gates eliminated the influence of other loads on the bridge due to limited influence surfaces. Each sensor records the impact of a vehicle located in close proximity to the measurement gate, and its indications are not disturbed by other loads and vehicles located at a further distance.

To predict the total weight and position of vehicles on the bridge, the accuracy achieved for the linear regression (LR), random forest (RF), and neural network (NN) models was compared with various hyperparameters and architectures. In this study, after reducing the number of sensors and training the model on three input features, the accuracy achieved for the RF with an architecture consisting of 500 trees was about 1.3 t and 0.5 t for 4800 samples and 48,000 samples in the training set, respectively. Increasing the number of decision trees, as well as increasing the size of the subsets used to train individual trees, improved performance, but led to overfitting.

To achieve better accuracy and reduce the effect of overfitting, NN models were introduced into the system with various architectures, including the number of layers and neurons. It was found that a deeper and more complex NN did not necessarily give better results, and often, good correspondences could be obtained for a moderate depth consisting of 2–3 hidden layers and about 50–100 neurons. This solution provides a good compromise between the accuracy of the model and its complexity, which significantly affects the computation time. Shallower networks consisting of only one hidden layer are often too simple to model complex dependencies in the data and are also susceptible to overfitting. In addition, a significant influence of the learning rate on the learning process

of NN was identified. Therefore, it was decided to analyze different values for each of the architectures. Similarly to RF, the best results were achieved when 17 sensors were used as input data. The gradual reduction of features slightly worsened the accuracy of the model, finally achieving about 200 kg for three input data. Despite the higher error value compared to the training models on the full set of input features, the accuracy was sufficient from the point of view of the target application, in which the expected load intensity reached the order of 30–40 t. When the number of features in the input data is reduced, the influence of other vehicles located outside the area of influence of the crossbeam gates is eliminated.

However, the methodology presented has certain limitations that require further research. Fiber optic sensors installed to the structural elements and hangers did not allow the axles to be distinguished from passing vehicles, making it impossible to determine the exact type of vehicle. Furthermore, the presented research focused on the occurrence of one vehicle within the measurement gate. The surface of influence for which the sensors register the vehicle is approximately twice the crossbeam spacing, i.e., approximately 12 m. A situation in which two or more vehicles are simultaneously in this area of the bridge, if it is relatively rare, requires appropriate preparation and calibration.

Future work includes generation of a digital twin (DT) based on sensors and the SHM system. Due to the prediction of vehicle weight and location determined on the basis of a limited number of sensors reading, it is possible to simulate load effects and compare them between the FE model and the remaining sensors. A system constructed in this way provides the possibility of full automation of the structural monitoring and an anomaly detection system, in which the basic elements, in addition to the ML algorithms, are installed fiber optic sensors.

Author Contributions: Conceptualization, D.P., M.J. and S.P.; methodology, D.P., M.J., A.N., P.Ł. and S.P.; software, D.P. and M.J.; validation, D.P. and M.J.; formal analysis, D.P. and M.J.; investigation, D.P., M.J., A.N., P.Ł. and S.P.; resources, P.Ł.; data curation, S.P.; writing—original draft preparation, D.P., M.J., A.N. and P.Ł.; writing—review and editing, D.P., M.J., A.N. and P.Ł.; visualization, D.P. and M.J.; supervision, A.N. and P.Ł.; project administration, A.N., P.Ł. and S.P.; funding acquisition, S.P. All authors have read and agreed to the published version of the manuscript.

Funding: This research received no external funding.

Institutional Review Board Statement: Not applicable.

Informed Consent Statement: Not applicable.

Data Availability Statement: Data are available upon request from the authors.

Conflicts of Interest: The authors declare no conflicts of interest.

References

1. Pozo, F.; Tibaduiza, D.A.; Vidal, Y. Sensors for Structural Health Monitoring and Condition Monitoring. *Sensors* **2021**, *21*, 1558. [CrossRef] [PubMed]
2. Moser, D.; Martin-Candilejo, A.; Cueto-Felgueroso, L.; Santillán, D. Use of Fiber-Optic Sensors to Monitor Concrete Dams: Recent Breakthroughs and New Opportunities. *Structures* **2024**, *67*, 106968. [CrossRef]
3. Richter, B.; Messerer, D.; Herbers, M.; Speck, K.; Laukner, J.; Gläser, C.; Jesse, F.; Marx, S. Monitoring of a Prestressed Bridge Girder with Integrated Distributed Fiber Optic Sensors. *Procedia Struct. Integr.* **2024**, *64*, 1208–1215. [CrossRef]
4. Li, H.-J.; Zhu, H.-H.; Wu, H.-Y.; Zhu, B.; Shi, B. Experimental Investigation on Pipe-Soil Interaction Due to Ground Subsidence via High-Resolution Fiber Optic Sensing. *Tunn. Undergr. Space Technol.* **2022**, *127*, 104586. [CrossRef]
5. Ren, B.; Zhu, H.; Shen, Y.; Zhou, X.; Zhao, T. Deformation Monitoring of Ultra-Deep Foundation Excavation Using Distributed Fiber Optic Sensors. *IOP Conf. Ser. Earth Env. Sci.* **2021**, *861*, 072057. [CrossRef]
6. García, I.; Zubia, J.; Durana, G.; Aldabaldetreku, G.; Illarramendi, M.; Villatoro, J. Optical Fiber Sensors for Aircraft Structural Health Monitoring. *Sensors* **2015**, *15*, 15494–15519. [CrossRef]

7. Bae, C.; Manandhar, A.; Kiesel, P.; Raghavan, A. Monitoring the Strain Evolution of Lithium-Ion Battery Electrodes Using an Optical Fiber Bragg Grating Sensor. *Energy Technol.* **2016**, *4*, 851–855. [CrossRef]
8. Ikeda, Y.; Takeda, S.; Hisada, S.; Ogasawara, T. Detection of Matrix Cracks in Composite Laminates Using Embedded Fiber-Optic Distributed Strain Sensing. *Sens. Actuators A Phys.* **2024**, *380*, 116039. [CrossRef]
9. Wang, H.; Jiang, L.; Xiang, P. Improving the Durability of the Optical Fiber Sensor Based on Strain Transfer Analysis. *Opt. Fiber Technol.* **2018**, *42*, 97–104. [CrossRef]
10. Khonina, S.N.; Kazanskiy, N.L.; Butt, M.A. Optical Fibre-Based Sensors—An Assessment of Current Innovations. *Biosensors* **2023**, *13*, 835. [CrossRef]
11. Al-Tarawneh, M.; Huang, Y.; Lu, P.; Bridgelall, R. Weigh-In-Motion System in Flexible Pavements Using Fiber Bragg Grating Sensors Part A: Concept. *IEEE Trans. Intell. Transp. Syst.* **2020**, *21*, 5136–5147. [CrossRef]
12. Kara De Maeijer, P.; Luyckx, G.; Vuye, C.; Voet, E.; Van den bergh, W.; Vanlanduit, S.; Braspenninckx, J.; Stevens, N.; De Wolf, J. Fiber Optics Sensors in Asphalt Pavement: State-of-the-Art Review. *Infrastructures* **2019**, *4*, 36. [CrossRef]
13. Sujon, M.; Dai, F. Application of Weigh-in-Motion Technologies for Pavement and Bridge Response Monitoring: State-of-the-Art Review. *Autom. Constr.* **2021**, *130*, 103844. [CrossRef]
14. Yang, X.; Wang, X.; Podolsky, J.; Huang, Y.; Lu, P. Assessing Vehicle Wandering Effects on the Accuracy of Weigh-in-Motion Measurement Based on In-Pavement Fiber Bragg Sensors through a Hybrid Sensor-Camera System. *Sensors* **2023**, *23*, 8707. [CrossRef] [PubMed]
15. Pau, A.; Vestroni, F. Weigh-in-motion of Train Loads Based on Measurements of Rail Strains. *Struct. Control Health Monit.* **2021**, *28*, e2818. [CrossRef]
16. Pintão, B.; Mosleh, A.; Vale, C.; Montenegro, P.; Costa, P. Development and Validation of a Weigh-in-Motion Methodology for Railway Tracks. *Sensors* **2022**, *22*, 1976. [CrossRef]
17. Zakharenko, M.; Frøseth, G.T.; Rönnquist, A. Train Classification Using a Weigh-in-Motion System and Associated Algorithms to Determine Fatigue Loads. *Sensors* **2022**, *22*, 1772. [CrossRef]
18. Paul, D.; Roy, K. Application of Bridge Weigh-in-Motion System in Bridge Health Monitoring: A State-of-the-Art Review. *Struct. Health Monit.* **2023**, *22*, 4194–4232. [CrossRef]
19. Hekič, D.; Kosič, M.; Kalin, J.; Žnidarič, A.; Anžlin, A. Challenges of Implementing Bridge Weigh-in-Motion on a Century-Old Steel-Riveted Railway Bridge. In *Bridge Maintenance, Safety, Management, Digitalization and Sustainability*; CRC Press: London, UK, 2024; pp. 1429–1436.
20. Breccolotti, M.; Natalicchi, M. Bridge Damage Detection Through Combined Quasi-Static Influence Lines and Weigh-in-Motion Devices. *Int. J. Civ. Eng.* **2022**, *20*, 487–500. [CrossRef]
21. Hajializadeh, D.; Žnidarič, A.; Kalin, J.; OBrien, E.J. Development and Testing of a Railway Bridge Weigh-in-Motion System. *Appl. Sci.* **2020**, *10*, 4708. [CrossRef]
22. Yoon, H.-J.; Song, K.-Y.; Choi, C.; Na, H.-S.; Kim, J.-S. Real-Time Distributed Strain Monitoring of a Railway Bridge during Train Passage by Using a Distributed Optical Fiber Sensor Based on Brillouin Optical Correlation Domain Analysis. *J. Sens.* **2016**, *2016*, 1–10. [CrossRef]
23. Pimentel, R.; Ribeiro, D.; Matos, L.; Mosleh, A.; Calçada, R. Bridge Weigh-in-Motion System for the Identification of Train Loads Using Fiber-Optic Technology. *Structures* **2021**, *30*, 1056–1070. [CrossRef]
24. Wang, S.; Cheng, Y.; Li, Z.; Zhang, L.; Zhang, F.; Sui, Q.; Jia, L.; Jiang, M. Load Identification of High-Speed Train Crossbeam Based on Bayesian Finite Element Model Updating and Load-Strain Linear Superposition Algorithm. *IEEE Sens. J.* **2023**, *23*, 13489–13498. [CrossRef]
25. Du, C.; Dutta, S.; Kurup, P.; Yu, T.; Wang, X. A Review of Railway Infrastructure Monitoring Using Fiber Optic Sensors. *Sens. Actuators A Phys.* **2020**, *303*, 111728. [CrossRef]
26. Zhou, W.; Abdulhakeem, S.; Fang, C.; Han, T.; Li, G.; Wu, Y.; Faisal, Y. A New Wayside Method for Measuring and Evaluating Wheel-Rail Contact Forces and Positions. *Measurement* **2020**, *166*, 108244. [CrossRef]
27. Mishra, S.; Sharan, P.; Alodhayb, A.N.; Alrebdi, T.A.; Upadhyaya, A.M. Design and Development of Wagon Load Monitoring System Using Fibre Bragg Grating Sensor. *Opt. Fiber Technol.* **2025**, *90*, 104149. [CrossRef]
28. Martincek, I.; Kacik, D.; Horak, J. Interferometric Optical Fiber Sensor for Monitoring of Dynamic Railway Traffic. *Opt. Laser Technol.* **2021**, *140*, 107069. [CrossRef]
29. Lan, C.; Yang, Z.; Liang, X.; Yang, R.; Li, P.; Liu, Z.; Li, Q.; Luo, W. Experimental Study on Wayside Monitoring Method of Train Dynamic Load Based on Strain of Ballastless Track Slab. *Constr. Build. Mater.* **2023**, *394*, 132084. [CrossRef]
30. Mishra, S.; Sharan, P.; Saara, K. Optomechanical Behaviour of Optical Sensor for Measurement of Wagon Weight at Different Speeds of the Train. *J. Opt.* **2023**, *52*, 751–762. [CrossRef]
31. Duong, N.S.; Blanc, J.; Hornych, P.; Bouveret, B.; Carroget, J.; Le feuvre, Y. Continuous Strain Monitoring of an Instrumented Pavement Section. *Int. J. Pavement Eng.* **2019**, *20*, 1435–1450. [CrossRef]

32. Haider, S.W.; Singh, R.R.; Wang, H. Impact of Surface Roughness, Speed, and Sensor Configuration on Weigh-in-Motion (WIM) System Accuracy. *Int. J. Pavement Res. Technol.* **2025**, 1–14. [CrossRef]
33. Jia, Z.; Fu, K.; Lin, M. Tire–Pavement Contact-Aware Weight Estimation for Multi-Sensor WIM Systems. *Sensors* **2019**, *19*, 2027. [CrossRef]
34. Kim, J.W.; Jung, Y.W.; Utebayeva, A.; Kamaliyeva, Z.; Collins, N.; Sarbassov, D.; Sagin, J.; Amanzhlova, R. High-Performance High-Speed WIM For Sustainable Road Load Monitoring Using GIS Technology. *Transp. Probl.* **2021**, *16*, 149–162. [CrossRef]
35. Wang, J.; Han, Y.; Cao, Z.; Xu, X.; Zhang, J.; Xiao, F. Applications of Optical Fiber Sensor in Pavement Engineering: A Review. *Constr. Build. Mater.* **2023**, *400*, 132713. [CrossRef]
36. Ma, R.; Zhang, Z.; Dong, Y.; Pan, Y. Deep Learning Based Vehicle Detection and Classification Methodology Using Strain Sensors under Bridge Deck. *Sensors* **2020**, *20*, 5051. [CrossRef] [PubMed]
37. Oliveira Rocheti, E.; Moreira Bacurau, R. Weigh-in-Motion Systems Review: Methods for Axle and Gross Vehicle Weight Estimation. *IEEE Access* **2024**, *12*, 134822–134836. [CrossRef]
38. Deng, L.; He, W.; Yu, Y.; Cai, C.S. Equivalent Shear Force Method for Detecting the Speed and Axles of Moving Vehicles on Bridges. *J. Bridge Eng.* **2018**, *23*, 04018057. [CrossRef]
39. Zhao, H.; Tan, C.; OBrien, E.J.; Uddin, N.; Zhang, B. Wavelet-Based Optimum Identification of Vehicle Axles Using Bridge Measurements. *Appl. Sci.* **2020**, *10*, 7485. [CrossRef]
40. Tan, C.; Zhang, B.; Zhao, H.; Uddin, N.; Guo, H.; Yan, B. An Extended Bridge Weigh-in-Motion System without Vehicular Axles and Speed Detectors Using Nonnegative LASSO Regularization. *J. Bridge Eng.* **2023**, *28*, 4023022. [CrossRef]
41. Chen, S.Z.; Chen, J.Q.; Zhao, M.X.; Zhong, Q.M.; Liu, J.; Wang, T. Performance of Bridge Weigh-in-Motion Methods Considering Environmental Temperature Field Effect. *Structures* **2025**, *76*, 108981. [CrossRef]
42. Chen, S.-Z.; Zhong, Q.-M.; Zhang, S.-Y.; Yang, G.; Feng, D.-C. Evaluation of Performance of Bridge Weigh-in-Motion Methods Considering Spatial Variability of Bridge Properties. *ASCE ASME J. Risk Uncertain. Eng. Syst. A Civ. Eng.* **2023**, *9*, 4023036. [CrossRef]
43. Heinen, S.K.; Lopez, R.H.; Miguel, L.F.F. A Shear-Force-Based Bridge Weigh-in Motion Approach for Simple Supported Structures. *Structures* **2024**, *70*, 107607. [CrossRef]
44. Alamandala, S.; Sai Prasad, R.L.N.; Pancharathi, R.K.; Pavan, V.D.R.; Kishore, P. Study on Bridge Weigh in Motion (BWIM) System for Measuring the Vehicle Parameters Based on Strain Measurement Using FBG Sensors. *Opt. Fiber Technol.* **2021**, *61*, 102440. [CrossRef]
45. Zhang, L.; Cheng, X.; Wu, G. A Bridge Weigh-in-Motion Method of Motorway Bridges Considering Random Traffic Flow Based on Long-Gauge Fibre Bragg Grating Sensors. *Measurement* **2021**, *186*, 110081. [CrossRef]
46. Chaudhary, M.T.A.; Morgese, M.; Taylor, T.; Ansari, F. Method and Application for Influence-Line-Free Distributed Detection of Gross Vehicle Weights in Bridges. *Structures* **2025**, *73*, 108298. [CrossRef]
47. Oskoui, E.A.; Taylor, T.; Ansari, F. Method and Sensor for Monitoring Weight of Trucks in Motion Based on Bridge Girder End Rotations. *Struct. Infrastruct. Eng.* **2020**, *16*, 481–494. [CrossRef]
48. Meo, M.; Zumpano, G. On the Optimal Sensor Placement Techniques for a Bridge Structure. *Eng. Struct.* **2005**, *27*, 1488–1497. [CrossRef]
49. Chen, G.; Shi, W.; Yu, L.; Huang, J.; Wei, J.; Wang, J. Wireless Sensor Placement Optimization for Bridge Health Monitoring: A Critical Review. *Buildings* **2024**, *14*, 856. [CrossRef]
50. Qin, X.; Zhan, P.; Yu, C.; Zhang, Q.; Sun, Y. Health Monitoring Sensor Placement Optimization Based on Initial Sensor Layout Using Improved Partheno-Genetic Algorithm. *Adv. Struct. Eng.* **2021**, *24*, 252–265. [CrossRef]
51. Li, X.; Niu, S.; Bao, H.; Hu, N. Improved Adaptive Multi-Objective Particle Swarm Optimization of Sensor Layout for Shape Sensing with Inverse Finite Element Method. *Sensors* **2022**, *22*, 5203. [CrossRef]
52. Yang, J.; Peng, Z. Improved ABC Algorithm Optimizing the Bridge Sensor Placement. *Sensors* **2018**, *18*, 2240. [CrossRef]
53. Yang, J.; Peng, Z. Beetle-Swarm Evolution Competitive Algorithm for Bridge Sensor Optimal Placement in SHM. *IEEE Sens. J.* **2020**, *20*, 8244–8255. [CrossRef]
54. Tan, Y.; Zhang, L. Computational Methodologies for Optimal Sensor Placement in Structural Health Monitoring: A Review. *Struct. Health Monit.* **2020**, *19*, 1287–1308. [CrossRef]
55. Capellari, G.; Chatzi, E.; Mariani, S.; Azam, S.E. Optimal Design of Sensor Networks for Damage Detection. *Procedia Eng.* **2017**, *199*, 1864–1869. [CrossRef]
56. Gonen, S.; Demirlioglu, K.; Erduran, E. Optimal Sensor Placement for Structural Parameter Identification of Bridges with Modeling Uncertainties. *Eng. Struct.* **2023**, *292*, 116561. [CrossRef]
57. Bigoni, C.; Zhang, Z.; Hesthaven, J.S. Systematic sensor placement for structural anomaly detection in the absence of damaged states. *Comput. Methods Appl. Mech. Eng.* **2020**, *371*, 113315. [CrossRef]
58. Liang, X. Enhancing Seismic Damage Detection and Assessment in Highway Bridge Systems: A Pattern Recognition Approach with Bayesian Optimization. *Sensors* **2024**, *24*, 611. [CrossRef]

59. Shi, Q.; Wang, X.; Chen, W.; Hu, K. Optimal Sensor Placement Method Considering the Importance of Structural Performance Degradation for the Allowable Loadings for Damage Identification. *Appl. Math. Model.* **2020**, *86*, 384–403. [CrossRef]
60. Sony, S. Bridge Damage Identification Using Deep Learning-Based Convolutional Neural Networks (CNNs). *Civ. Environ. Eng. Publ.* **2021**, *203*, 1–35.
61. Lai, Y.; Li, Y.; Huang, M.; Zhao, L.; Chen, J.; Xie, Y.M. Conceptual Design of Long Span Steel-UHPC Composite Network Arch Bridge. *Eng. Struct.* **2023**, *277*, 115434. [CrossRef]
62. Di Mucci, V.M.; Cardellicchio, A.; Ruggieri, S.; Nettis, A.; Renò, V.; Uva, G. Artificial Intelligence in Structural Health Management of Existing Bridges. *Autom. Constr.* **2024**, *167*, 105719. [CrossRef]
63. Bayane, I.; Leander, J.; Karoumi, R. An Unsupervised Machine Learning Approach for Real-Time Damage Detection in Bridges. *Eng. Struct.* **2024**, *308*, 117971. [CrossRef]
64. Song, L.; Cao, Z.; Sun, H.; Yu, Z.; Jiang, L. Transfer Learning for Structure Damage Detection of Bridges through Dynamic Distribution Adaptation. *Structures* **2024**, *67*, 106972. [CrossRef]
65. Chen, M.; Xin, J.; Tang, Q.; Hu, T.; Zhou, Y.; Zhou, J. Explainable Machine Learning Model for Load-Deformation Correlation in Long-Span Suspension Bridges Using XGBoost-SHAP. *Dev. Built Environ.* **2024**, *20*, 100569. [CrossRef]
66. Camara, A.; Reyes-Aldasoro, C.C. Dynamic Analysis of the Effects of Vehicle Movement over Bridges Observed with CCTV Images. *Eng. Struct.* **2024**, *317*, 118653. [CrossRef]
67. Le, N.T.; Keenan, M.; Nguyen, A.; Ghazvineh, S.; Yu, Y.; Li, J.; Manalo, A. A Supervised Machine Learning Approach for Structural Overload Classification in Railway Bridges Using Weigh-in-Motion Data. *Structures* **2025**, *71*, 108005. [CrossRef]
68. Bosso, M.; Vasconcelos, K.L.; Ho, L.L.; Bernucci, L.L.B. Use of Regression Trees to Predict Overweight Trucks from Historical Weigh-in-Motion Data. *J. Traffic Transp. Eng.* **2020**, *7*, 843–859. [CrossRef]
69. Yan, W.; Yang, J.; Luo, X. Quick Weighing of Passing Vehicles Using the Transfer-Learning-Enhanced Convolutional Neural Network. *Comput. Model. Eng. Sci.* **2024**, *139*, 2507–2524. [CrossRef]
70. Jian, X.; Xia, Y.; Sun, S.; Sun, L. Integrating Bridge Influence Surface and Computer Vision for Bridge Weigh-in-motion in Complicated Traffic Scenarios. *Struct. Control Health Monit.* **2022**, *29*, e3066. [CrossRef]
71. HBK—Hottinger Brüel & Kjær HBM. *FiberSensing: Optical Measurement Solutions–Brochure*; HBK: Vilar do Pinheiro, Portugal, 2025.
72. Teufelberger-Redaelli Cable System (FLC). *Technical Product Data*; Teufelberger-Redaelli Cable System (FLC): Milan, Italy, 2021.

Disclaimer/Publisher's Note: The statements, opinions and data contained in all publications are solely those of the individual author(s) and contributor(s) and not of MDPI and/or the editor(s). MDPI and/or the editor(s) disclaim responsibility for any injury to people or property resulting from any ideas, methods, instructions or products referred to in the content.

sensors

MDPI

Article

Digital Image Correlation-Based Bolt Preload Monitoring

Linsheng Huo *, Liukun Zhao, Aocheng Hu, Fanwei Meng and Hongnan Li

State Key Laboratory of Coastal and Offshore Engineering, Dalian University of Technology, Dalian 116024, China; z_duters@163.com (L.Z.); xiaocusuan@163.com (A.H.); fanwei@mail.dlut.edu.cn (F.M.); hnli@dlut.edu.cn (H.L.)
* Correspondence: lshuo@dlut.edu.cn

Abstract

Bolt connections are widely used in engineering structures but are susceptible to loosening during operation, which can result in significant safety concerns. Consequently, reliable bolt-loosening detection is of paramount importance. Conventional detection methodologies frequently exhibit deficiencies, including reduced efficiency, constrained accuracy, and the requirement for contact sensors. To overcome these limitations, this study proposes a novel non-contact approach for bolt preload monitoring based on Digital Image Correlation (DIC). In this method, an industrial camera captures speckle images of the bolt head before and after deformation, thereby enabling measurement of the surface strain. The DIC technique is employed to calculate the strain field on the bolt head surface, which exhibits a linear relationship with the bolt preload. The proposed method utilizes strain field tracking to facilitate effective and precise monitoring of bolt preload. Experimental results demonstrate that the method provides a precise, efficient, and user-friendly solution for bolt preload monitoring, showing great potential for applications in structural health monitoring.

Keywords: bolt preload; digital image correlation; structural health monitoring; bolt looseness monitoring

1. Introduction

Bolted connections are utilized extensively in a variety of engineering and industrial applications due to their convenience and versatility. However, their integrity may be compromised by several factors, including dynamic loading [1], overloading, and corrosion [2]. The integrity of a bolted connection is contingent upon the bolt preload, which is instrumental in ensuring the reliability and safety of the associated equipment or structure. Insufficient preload has been demonstrated to accelerate bolt loosening and may ultimately lead to structural failure. Therefore, continuous monitoring of bolt preload is of paramount importance [3]. Over the past few years, scholars have conducted extensive and innovative research, proposing numerous techniques for monitoring bolt loosening [4]. These techniques can generally be classified into two categories: contact and non-contact methods. The distinction between these categories depends on the necessity of direct contact with the surface of the measured object during monitoring.

Common contact-based approaches include the tapping method, electromechanical impedance (EMI) method, and ultrasonic method [5]. The tapping method utilizes the fact that bolted structures emit distinct acoustic responses when struck. By analyzing the frequency characteristics of these sounds under different preload conditions, the state of the bolted connection can be inferred [6–9]. However, this method necessitates a testing environment that is devoid of noise, and it is highly susceptible to interference from

environmental noise. This limitation compromises its accuracy in practical engineering applications. The EMI-based demonstrates consistent performance under diverse testing conditions and has emerged as a prevalent tool for damage assessment in various structures. This method involves attaching a piezoelectric sensor to the structure and evaluating the local health condition near the sensor [10–13]. The evaluation is achieved by measuring the coupled electromechanical impedance parameters of the structure and sensor under high-frequency sweep excitation. Nevertheless, one sensor is required for each bolt, making it difficult to assess the degree and location of loosening when multiple bolts are involved. The ultrasonic method can monitor the loosening of multiple bolts by attaching sensors to the connected structural components [14–16]. As ultrasonic waves propagate through the structure, their energy undergoes attenuation. Through meticulous analysis of this attenuation pattern, the condition of the bolt connection can be ascertained. Although this method has the capacity to can monitor multiple bolts simultaneously, its practical application is constrained by the elevated cost of sensors and associated equipment. In summary, the aforementioned bolt-loosening monitoring methods are contact-based and may introduce interference to the measured object during testing. Furthermore, the applicability of these methods is frequently constrained by environmental conditions, rendering them inadequate for specific bolt-monitoring scenarios.

The non-contact monitoring method eliminates the need to install sensors on the surface of the measured structure and imposes minimal constraints on the monitoring environment. In certain scenarios, non-contact approaches can effectively compensate for the limitations of traditional contact-based methods. Machine vision, often integrated with artificial intelligence (AI), has been widely adopted in non-contact monitoring and applied to bolt-loosening detection [17–19]. The general principle of this method is to compare digital images of bolts captured under different conditions to determine whether loosening has occurred. A commonly used vision-based technique involves quantifying the loosening angle. For instance, Park et al. [20–22] demonstrated a rotational-angle detection approach based on boundary detection and the Hough line transform. Similarly, Zhao et al. [18] proposed a deep learning–based method for calculating the loosening angle. Although the machine vision-based bolt-loosening monitoring is cost-effective and easy to implement, it lacks the sensitivity to detect early-stage bolt loosening and cannot accurately quantify bolt preload.

Digital Image Correlation (DIC) is an optical measurement technique that detects object deformation by analyzing digital images. Its extensive utilization in engineering practice is evident in its employment for measuring structural strain and deformation, as evidenced by numerous studies [23–26]. Chevalier et al. [27] employed DIC to analyze surface displacement fields of polymers under uniaxial and biaxial tensile loading, thereby obtaining non-uniform strain distributions of rubber-like materials under multi-axial conditions. Reder et al. [28] used laser irradiation to inscribe speckle patterns on the surfaces of ceramic and carbon fibers, enabling the acquisition of stress–strain curves in tensile experiments. Gencturk et al. [29] measured the full-scale deformation of prestressed concrete using DIC and compared the results with sensor-based measurements, thus validating the accuracy of DIC. These studies collectively demonstrated that DIC is a feasible, accurate, and highly sensitive technique capable of capturing even minute deformations. Jiménez Peña [30] further proposed a DIC-based approach for monitoring bolt preload by calculating bolt elongation. However, this approach is unsuitable for internal bolts or joints where the bolt head is embedded within the clamped material. Moreover, its measurement accuracy may be compromised for extended bolts due to a diminution in reduced spatial resolution.

In order to surmount the challenges of delayed detection, low accuracy, and high cost inherent in traditional bolt detection methods, this study proposes a Digital Image

https://doi.org/10.3390/s26030913

Correlation (DIC)-based approach for monitoring bolt preload. In this method, speckle patterns on the bolt surface are captured using an industrial camera before and after deformation. The acquired images are subsequently processed through DIC to compute the strain distribution on the bolt head surface. Consequently, experimental tests are performed to validate the effectiveness and accuracy of the proposed method.

2. Methodology

The methodology adopted in this study primarily consists of five stages: (1) preparation of a speckle pattern on the bolt head surface, (2) acquisition of speckle images, (3) calculation of strain fields, (4) analysis of the strain field distribution, and (5) estimation of bolt preload, as illustrated in Figure 1.

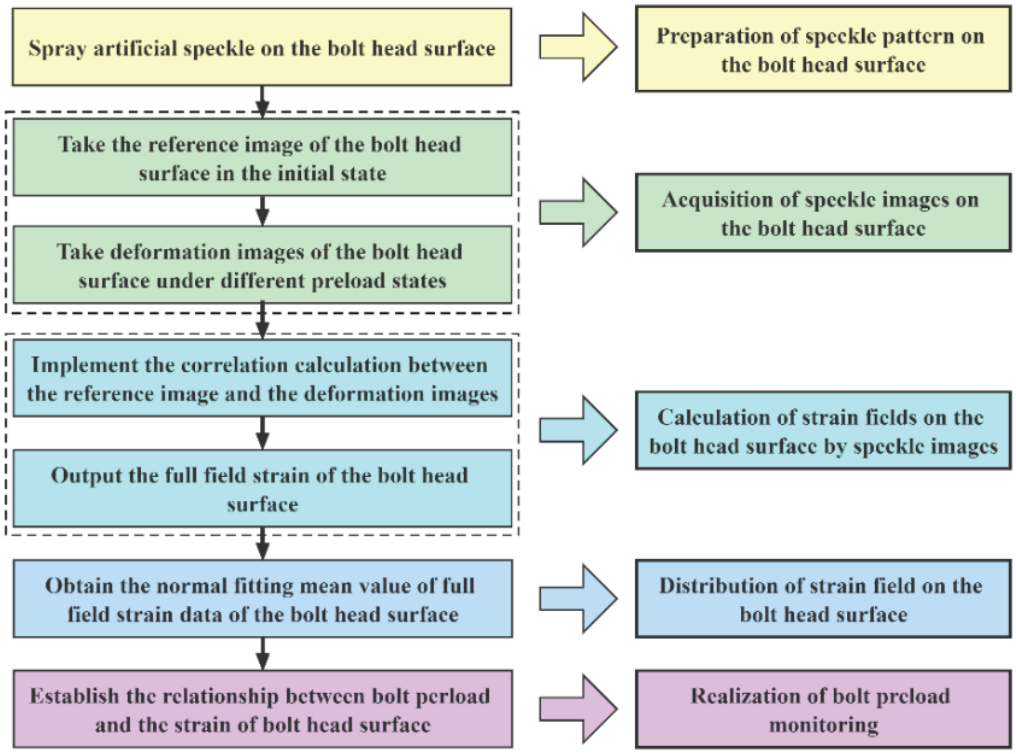


Figure 1. Basic implementation steps of the proposed method.

2.1. Preparation of Speckle Pattern on the Bolt Head Surface

For strain measurement using Digital Image Correlation (DIC), the quality of the speckle pattern on the bolt head surface is critical for accurately capturing deformation information. The standard approach for creating a speckle pattern typically involves manually applying matte black and white spray paint. To achieve a uniformly distributed pattern, a thin base coat of white primer is first sprayed onto the specimen surface. After the primer has solidified, a layer of black paint is randomly applied to form the speckle pattern.

In this study, prior to testing, the bolt head surface was polished with sandpaper to remove burrs and ensure smoothness. Subsequently, matte paint was manually applied following the polishing process. During spraying, it is essential not to aim the spray gun directly at the bolt surface, as this may produce overly dense speckle clusters and introduce unwanted directional texture, thereby compromising the accuracy of the subsequent DIC analysis. Instead, the spray nozzle was positioned at an oblique angle relative to the bolt head surface, as shown in Figure 2, to ensure the formation of a uniformly distributed speckle pattern suitable for DIC measurement.

https://doi.org/10.3390/s26030913



Figure 2. Method for spraying speckle patterns on the bolt head surface.

2.2. Computation of Strain Fields on the Bolt Head Surface Using Speckle Images

The Digital Image Correlation (DIC) method is an optical, non-contact technique for measuring displacement and strain. It provides full-field displacement and strain data by analyzing speckle patterns on the bolt surface captured in images taken before and after deformation, and by correlating the two images. The image acquired prior to deformation serves as the reference image, whereas the image captured after deformation is termed the deformed image.

The DIC algorithm determines the corresponding position of each subset in the deformed image by performing a cross-correlation analysis between the reference subset and the deformation subset, as illustrated in Figure 3. The successful matching of image subsets enables the calculation of displacement vectors and subsequent derivation of the strain field on the bolt head surface.

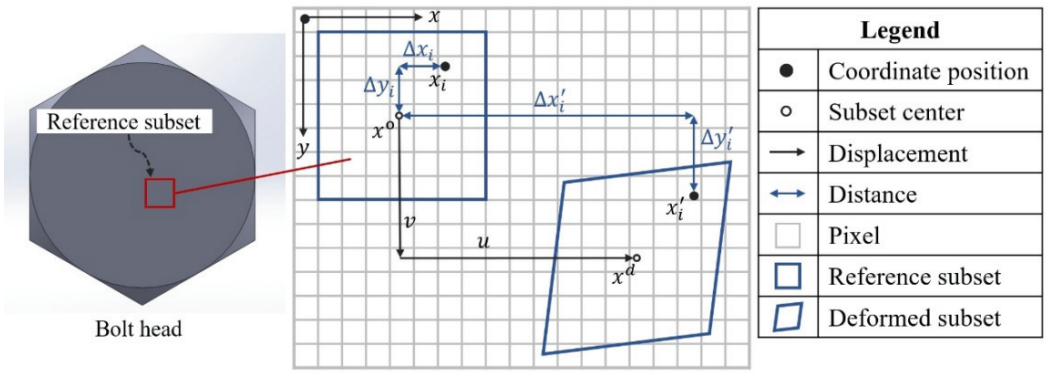


Figure 3. Schematic diagram of correlation calculation between reference subset and deformed subset.

By using the coordinates of the center point x_0 in the reference subset, the coordinates of any point x_i within the subset can be expressed as follows:

https://doi.org/10.3390/s26030913

$$\begin{bmatrix} x_i \\ y_i \end{bmatrix} = \begin{bmatrix} x_0 \\ y_0 \end{bmatrix} + \begin{bmatrix} \Delta x_i \\ \Delta y_i \end{bmatrix} \tag{1}$$

where x_i and y_i denote the coordinates of the points in the reference subset along the x and y axes, respectively; x_0 and y_0 represent the coordinates of the center point in the reference subset along the x and y axes, respectively; and Δx_i and Δy_i indicate the coordinate offsets of the points relative to the center point along the x and y axes in the reference subset.

After deformation, the original point x_i moves to a new location in the deformation subset, denoted as x_i', and its new coordinates can be expressed as:

$$\begin{bmatrix} x_i' \\ y_i' \end{bmatrix} = \begin{bmatrix} x_0 \\ y_0 \end{bmatrix} + \begin{bmatrix} \Delta x_i' \\ \Delta y_i' \end{bmatrix} \tag{2}$$

where x_i' and y_i' refer to the coordinates of the points in the deformation subset along the x and y axes, respectively; $\Delta x_i'$ and $\Delta y_i'$ represent the coordinate offsets of the points relative to the center of the reference subset along the x and y axes.

By calculating the values of $\Delta x_i'$ and $\Delta y_i'$ in Equation (2), the position of the reference subset within the deformed image can be determined. Owing to the non-rigid behavior of the bolts, the selected rectangular reference subset also undergoes deformation as the bolt preload changes. Therefore, a first-order shape function is utilized to describe the subset deformation, ensuring the accuracy of the subsequent subset-matching process, as illustrated in Equation (3).

$$\begin{bmatrix} \Delta x_i' \\ \Delta y_i' \end{bmatrix} = \begin{bmatrix} 1+u_x & u_y & u \\ v_x & 1+v_y & v \end{bmatrix} \begin{bmatrix} \Delta x_i \\ \Delta y_i \\ 1 \end{bmatrix} \tag{3}$$

where u, u_x, u_y, v, v_x and v_y are the parameters of the first-order shape function to be determined, and let $\boldsymbol{P} = [u, u_x, u_y, v, v_x, v_y]^{\mathrm{T}}$.

The two-dimensional digital image can be regarded as a sampling of light intensity, forming a matrix composed of the gray values of individual pixels. Let F and G denote the gray distribution functions of the reference subset and the deformed subset, respectively. Accordingly, the gray value at each pixel can be expressed as follows:

$$f_i = F(x_i, y_i) \tag{4}$$

$$g_i = G(x_i', y_i') \tag{5}$$

where f_i and g_i represent the gray values of individual pixels points in the reference subset and the deformed subset, respectively.

A correlation coefficient C is introduced to evaluate the similarity between corresponding points in the reference and deformed subsets. In this study, the zero-mean normalized cross-correlation (ZNCC) and zero-mean normalized sum of squared difference (ZNSSD) criteria are employed to perform the correlation analysis between the reference subset and the deformed subset,

$$C_{\mathrm{ZNCC}} = \sum_{i=1}^{I} \frac{(f_i - \bar{f})(g_i - \bar{g})}{\tilde{f}\tilde{g}} \tag{6}$$

$$C_{\mathrm{ZNSSD}} = \sum_{i=1}^{I} \left[\frac{f_i - \bar{f}}{\tilde{f}} - \frac{g_i - \bar{g}}{\tilde{g}} \right]^2 \tag{7}$$

where I represents the number of pixels within the subset; $\bar{f} = \sum_{i=1}^{I} f_i / I$ and $\bar{g} = \sum_{i=1}^{I} g_i / I$ de-

https://doi.org/10.3390/s26030913

note the average gray values of the reference subset and the deformed subset, respectively; and $\tilde{f} = \sqrt{\sum_{i=1}^{I}(f_i - \bar{f})^2}$ and $\tilde{g} = \sqrt{\sum_{i=1}^{I}(g_i - \bar{g})^2}$ are the normalized gray-value functions of the corresponding subsets.

Pan et al. [31] illustrated the relationship between these two correlation criteria as follows:

$$C_{\mathrm{ZNCC}} = 1 - \frac{C_{\mathrm{ZNSSD}}}{2} \tag{8}$$

A first-order shape function is used to characterize the deformation of the reference subset, while the shape of the deformed subset is continuously optimized through nonlinear optimization during the correlation process [32,33]. When CZNCC approaches 1 or CZNSSD approaches 0, the optimized subset closely matches the actual deformation state of the deformed subset. Once the matching process is completed, the deformation information at the center point of the subset can be obtained. Several search algorithms have been developed to determine the location of corresponding subsets in the deformed bolt images, among which the Newton-Raphson (NR) algorithm is the most commonly employed [34]. The NR algorithm is utilized to iteratively compute the deformation vector, and the solution is obtained as follows:

$$\boldsymbol{P} = \boldsymbol{P}_0 - \frac{\nabla C(\boldsymbol{P}_0)}{\nabla\nabla C(\boldsymbol{P}_0)} \tag{9}$$

where $\boldsymbol{P_0}$ denotes the initial value of the subset displacement vector; $\boldsymbol{P}$ represents the updated solution after each iteration; $\nabla C(\boldsymbol{P_0})$ is the gradient of the correlation criterion; and $\nabla\nabla C(\boldsymbol{P_0})$ is its second-order derivative, commonly referred to as the Hessian matrix.

The bicubic spline interpolation scheme is iteratively applied to determine the gray values at sub-pixel locations [35], as expressed in the following equation:

$$g(x, y) = \sum_{m=0}^{3}\sum_{n=0}^{3} a_{mn} x^m y^n \tag{10}$$

where the coefficient a_{mn} is determined by the gray values of the adjacent 4×4 pixel points centered on the interpolation point. The combination of NR algorithm with the bicubic spline interpolation scheme ensures high alignment accuracy and improved convergence stability. The sub-pixel displacement is obtained through the aforementioned iterative process. This procedure is repeated for multiple subsets to acquire the full-field displacement distribution of the component [36].

The full-field displacement data obtained from the previous calculations are utilized to compute the corresponding full-field strains through a specific strain evaluation method. Pan et al. [37] proposed a point-by-point local least squares fitting algorithm, which offers a practical and straightforward approach for strain computation with clear theoretical principles and simple implementation. To derive the full-field strains from the displacement field, a strain computation window with $(2M + 1) \times (2M + 1)$ data points is defined, with a specific data point selected as the widow center, as illustrated in Figure 4. The displacement data points within this window are then fitted using a two-dimensional polynomial, as expressed below:

$$\begin{aligned} u(x, y) &= a_0 + a_1 x + a_2 y \\ v(x, y) &= b_0 + b_1 x + b_2 y \end{aligned} \tag{11}$$

where x and y range from $-M$ to M; $u(x, y)$ and $v(x, y)$denote the displacement field data

https://doi.org/10.3390/s26030913

in the x and y directions obtained from the DIC analysis; and a_i and b_i (where i = 0, 1, 2) are the polynomial coefficients to be determined.

	x=-M	⋯	x=0	⋯	x=M
y=-M	u(-M,-M)	⋯	u(0,-M)	⋯	u(M,-M)
⋮	⋮	⋮	⋮	⋮	⋮
y=0	u(-M,0)	⋯	u(0,0)	⋯	u(M,0)
⋮	⋮	⋮	⋮	⋮	⋮
y=M	u(-M,-M)	⋯	u(0,M)	⋯	u(M,M)

Figure 4. Displacement data for local least-squares fitting.

The first equation in Equation (11) can be expressed in matrix form as follows.

$$\boldsymbol{u} = \boldsymbol{X}\boldsymbol{a} \implies \begin{bmatrix} u(-M,-M) \\ u(-M+1,-M) \\ \vdots \\ u(0,0) \\ \vdots \\ u(M-1,M) \\ u(M,M) \end{bmatrix} = \begin{bmatrix} 1 & -M & -M \\ 1 & -M+1 & -M \\ \vdots & \vdots & \vdots \\ 1 & 0 & 0 \\ \vdots & \vdots & \vdots \\ 1 & M-1 & M \\ 1 & M & M \end{bmatrix} \begin{pmatrix} a_0 \\ a_1 \\ a_2 \end{pmatrix} \tag{12}$$

By applying Equation (12), the coefficients can be obtained as $\boldsymbol{a} = \begin{bmatrix} a_0, & a_1, & a_2 \end{bmatrix}^{\mathrm{T}} = (\boldsymbol{X}^{\mathrm{T}}\boldsymbol{X})^{-1}\boldsymbol{X}^{\mathrm{T}}\boldsymbol{u}$, where $a_1 = \frac{\partial u}{\partial x}$ and $a_2 = \frac{\partial u}{\partial y}$. Similarly, the coefficients b_0, b_1 and b_2 can be determined, with $b_1 = \frac{\partial v}{\partial x}$ and $b_2 = \frac{\partial v}{\partial y}$. Consequently, Equation (13) yields the Lagrange strain component equations, in which E_{xx} and E_{yy} express the strain components in the x and y directions, respectively. This iterative procedure is performed point by point to obtain the full-field strain distribution.

$$\begin{aligned} E_{xx} &= \frac{1}{2}\left(2\frac{\partial u}{\partial x} + \left(\frac{\partial u}{\partial x}\right)^2 + \left(\frac{\partial v}{\partial x}\right)^2\right) = \frac{1}{2}\left(2a_1 + a_1^2 + b_1^2\right) \\ E_{yy} &= \frac{1}{2}\left(2\frac{\partial v}{\partial y} + \left(\frac{\partial u}{\partial y}\right)^2 + \left(\frac{\partial v}{\partial y}\right)^2\right) = \frac{1}{2}\left(2b_2 + a_2^2 + b_2^2\right) \end{aligned} \tag{13}$$

3. Experimental Verification

To validate the feasibility and effectiveness of the proposed method, experiments were conducted using an M20 bolt, and the resulting data were analyzed. One critical factor influencing the measurement results is the selection of the region of interest (ROI) in the DIC analysis; therefore, this aspect was examined in detail. The experimental data obtained from the M20 bolt were used to evaluate the effect of different ROIs on the strain distribution of the bolt head surface. Furthermore, to confirm that the experimental results for the M20 bolt were not coincidental, additional verification experiments were carried out using bolts of different sizes—specifically, M18 and M22—to compare and analyze the DIC results across bolts with varying dimensions.

https://doi.org/10.3390/s26030913

3.1. Instrumentation Setup

The experimental hardware primarily consisted of an industrial charge-coupled device (CCD) camera (6.3 MP; 3072 × 2048 resolution; Huagu Power WP-UC600, Shenzhen, China), a rock-bolt drawing dynamometer (0–300 kN; ML-300B; Cangzhou Zhaolong Zhongke Construction Equipment Co., Ltd., Cangzhou, China), a steel plate, a light source, a camera mount, and a laptop computer (Lenovo (Beijing) Co., Ltd., Beijing, China), as shown in Figure 5. To minimize interference from external illumination, the experimental setup was arranged in a low-light environment. A dedicated light source was used to ensure uniform illumination on the bolt-head surface, thereby enhancing image contrast and improving measurement accuracy by clearly defining the surface speckle patterns.

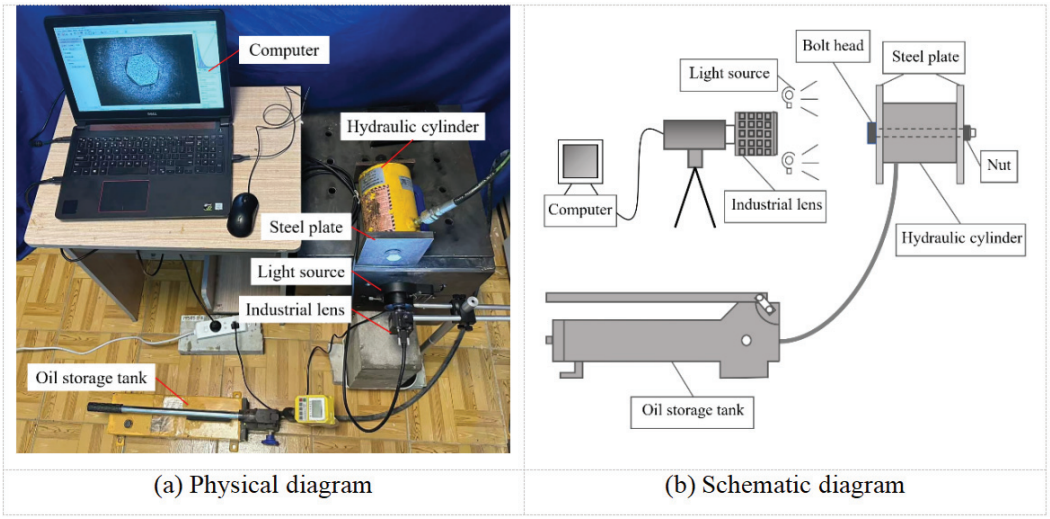


Figure 5. Experimental setup.

To establish the relationship between the bolt preload and the surface strain of the bolt head, a single-bolt axial loading experiment was conducted. Prior to testing, the surface of the M20 bolt head was preprocessed to generate a random speckle pattern, as illustrated in Figure 6. During the experiment, the hydraulic cylinder of the anchor puller was positioned horizontally on the workbench, and a square steel plate with pre-drilled holes was placed in front of it. The bolt screw was inserted through both the steel plate and the hydraulic cylinder, with the protruding end secured using an anchor tool. The bolt preload was applied by operating the handle of the anchor puller. To prevent bolt movement during the initial pre-tightening phase, the initial preload was set to 5 kN, after which the load was increased in increments of 1 kN. The total experimental preload range was thus set from 5 kN to 13 kN.

Subsequently, speckle images of the bolt head surface were captured at each 1 kN preload increment. Image acquisition was conducted by monitoring the liquid crystal display (LCD) while applying pressure to the handle of the anchor puller. The reference image (before deformation) and the deformed images (under various preload conditions) were then imported into the DIC analysis program to compute the strain field distribution on the bolt head surface corresponding to different preload levels.

3.2. Relationship Between Preload and Strain

The M20 bolt was employed to verify the effectiveness of the proposed DIC-based method for monitoring bolt preload, with the experimental results analyzed according to the methodology described in the previous sections. Figure 7 presents the strain fields on the surface of the M20 bolt head in the x and y directions under a preload of 10.03 kN. Examination of the strain contour maps indicates that a relatively large number of

https://doi.org/10.3390/s26030913

pixels are concentrated near the middle of the color scale, while fewer pixels appear at both extremes. This distribution pattern is consistent with the bell-shaped profile of a normal distribution, suggesting that the measured strain field exhibits reasonable uniformity and stability.



Figure 6. Surface of the M20 bolt head after preprocessing.

As illustrated in Figure 7, the surface strain distribution on the bolt head is theoretically expected to exhibit symmetry. In practice, however, the distribution at individual points lacks a discernible pattern, as actual loading conditions often induce non-uniformity. Nevertheless, the measured strain field data indicates that, after normalization, the overall dataset aligns well with a normal distribution.

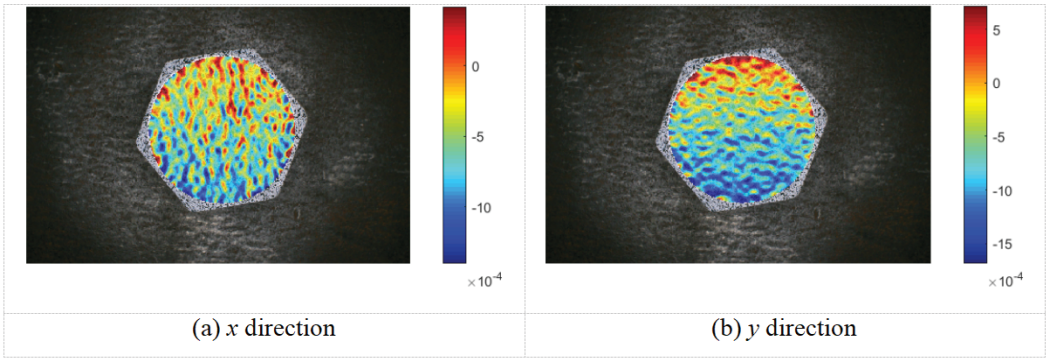


Figure 7. Strain field maps of the M20 bolt head surface in the x and y directions under a preload of 10.03 kN.

https://doi.org/10.3390/s26030913

The strain field on the surface of the bolt head was obtained using the DIC technique, which provides strain data for each pixel within the analyzed region. To establish the correlation between the applied bolt preload and the resulting surface strain, a data processing strategy was developed. This strategy employs the strain field data corresponding to each specific preload condition to determine the representative strain value of the bolt under that load. The strain at each pixel of the bolt head surface varies with the applied preload. If a correlation exists between the surface strain field and the bolt preload, then a consistent relationship should also be observed between the average surface strain and the corresponding preload. To provide a more intuitive representation of the strain distribution, the average value derived from the normal fitting curve of the strain field data is used to establish this correlation. The probability density function of the normal distribution is expressed as follows:

$$f(x) = \frac{1}{\sqrt{2\pi}\sigma} \exp\left\{-\frac{(x-\mu)^2}{2\sigma^2}\right\} \tag{14}$$

where $f(x)$ represents the probability density function of the normal distribution, and σ and μ denote the standard deviation and mean value of the strain field data on the surface of the bolt head, respectively.

The relationship between the surface strain field of the bolt head and the bolt preload was determined by averaging the strain field data points across the bolt head surface. The normal fitting curves of the strain field data in the x and y directions under a preload of 10.03 kN are presented in Figure 8. The frequency on the y-axis refers to the number of speckle points sharing the same strain value; that is, it represents the count of occurrences for each specific strain magnitude among all analyzed points. As shown in the figure, the histogram of the strain field data on the bolt head surface closely follows a normal distribution pattern. To facilitate efficient subsequent data processing, a normal fitting was applied to the strain field data of the bolt head surface, and the mean value obtained from this fitting was used to establish the correlation between the bolt preload and the surface strain field.

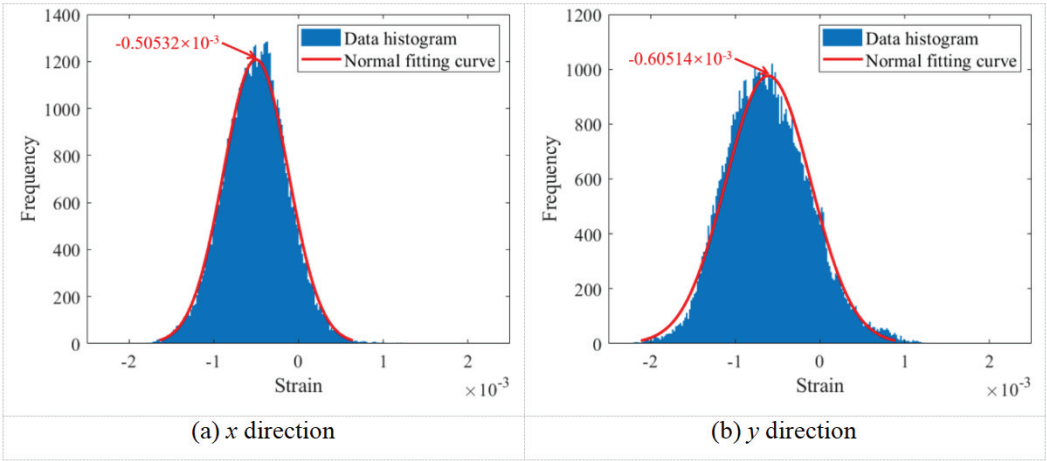


Figure 8. Normal fitting curves of strain field data in the x and y directions under a preload of 10.03 kN.

Figure 9 presents the normal distribution fittings of the strain field data obtained from the surface of the M20 bolt head under various preload levels. The figure also shows the variations in the mean values derived from these fittings for the strain field data in the x and y directions. It can be observed that the mean strain values on the bolt head surface vary consistently with changes in the applied bolt preload.

https://doi.org/10.3390/s26030913

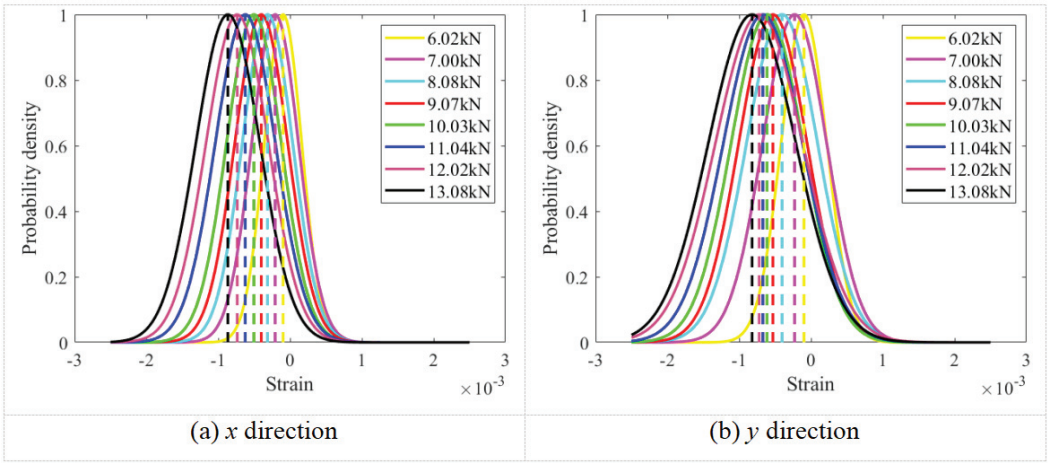


Figure 9. The change in the mean of the normal fitting for the strain field on the M20 bolt head surface in the x and y directions under different preloads.

A linear regression analysis was conducted to establish the relationship between the bolt preload and the surface strain of the M20 bolt head, as shown in Figure 10. The figure indicates that the correlation coefficient of the regression equation is close to 1, demonstrating a strong linear relationship between the bolt preload and the mean surface strain. Overall, the relationship between the bolt preload and the surface strain on the M20 bolt head exhibits a clear linear increasing trend.

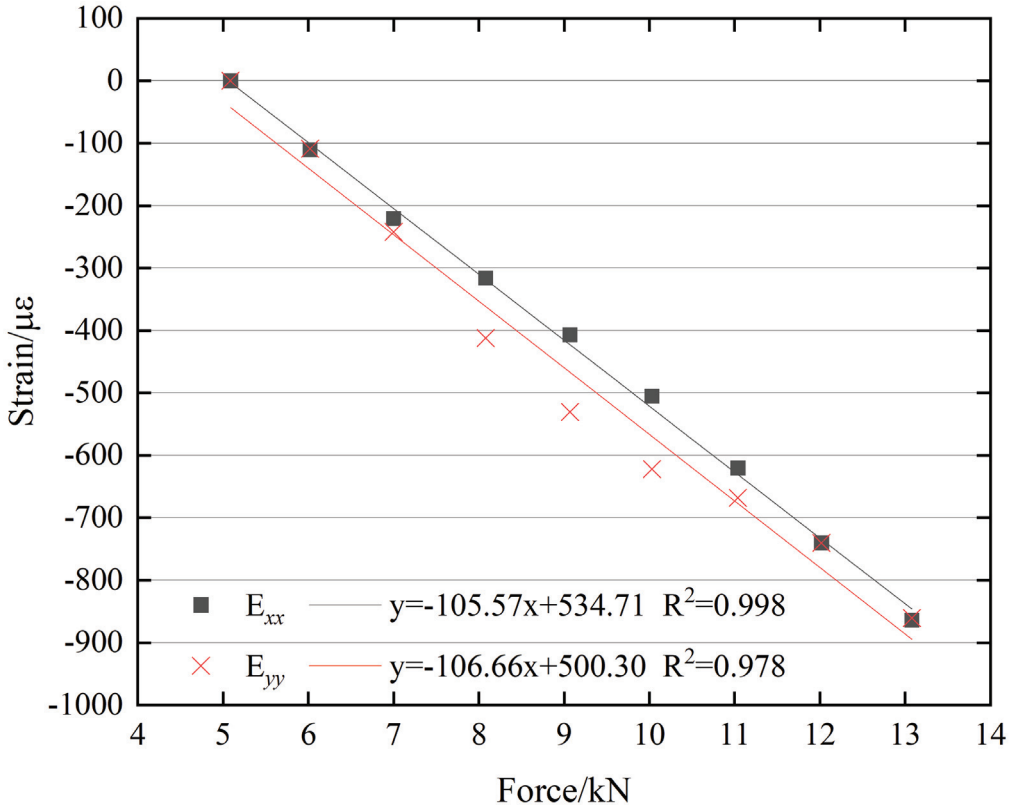


Figure 10. Linear relationship between bolt preload and surface strain of the M20 bolt head.

3.3. Influence of Region of Interest Selection

Prior to conducting the DIC analysis, it is imperative to define the specific computational area—designated as the region of interest (ROI)—on the bolt head surface. In this study, experimental data obtained from the M20 bolt were used to examine the influence of

https://doi.org/10.3390/s26030913

ROI selection. The diameter of the M20 bolt head was 30 mm. The ROI on the bolt head surface was configured as a circular region, centered at the midpoint of the bolt head. The diameter of the circular ROI was varied from 30 mm to 5 mm, in increments of 5 mm, as illustrated in Figure 11.

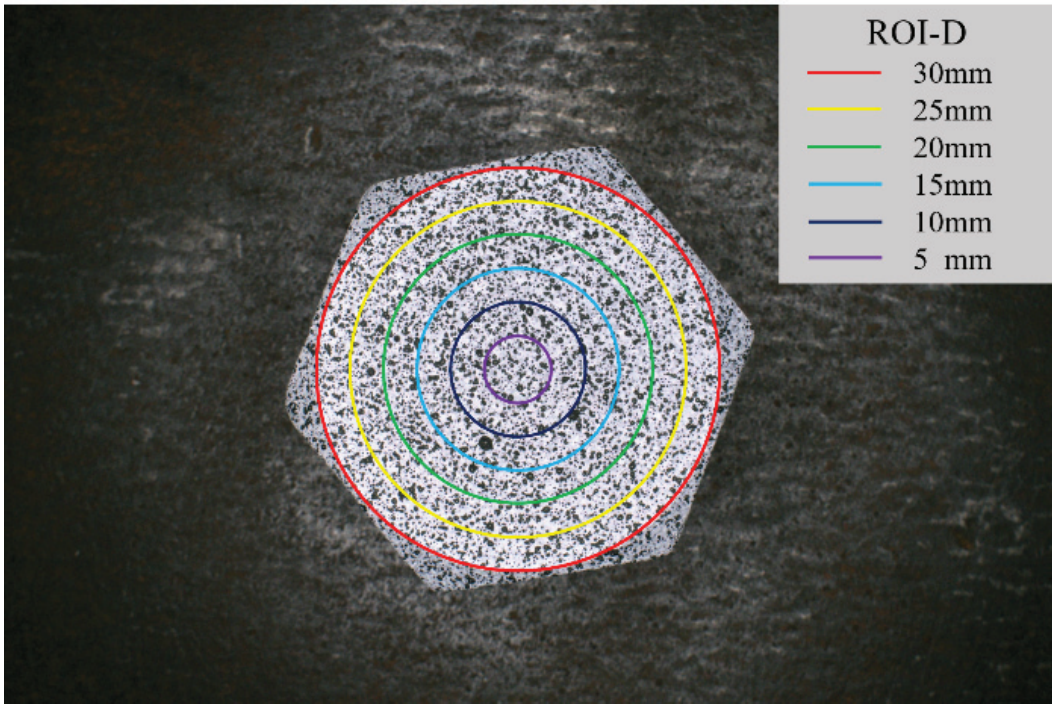


Figure 11. Regions of interest with different diameters on the surface of the bolt head.

The strain fields were computed using the experimental data obtained from six different ROIs, and normal fitting was applied to determine the mean strain values under each preload condition. The normal fitting curves of the strain field data within ROIs of varying diameters in the x and y directions under a preload of 10.03 kN are shown in Figure 12. As evident from the figure, the histograms of the strain field data corresponding to different ROIs on the bolt head surface in both the x and y directions follow a normal distribution, and the mean values obtained from the normal fittings in the same direction are approximately consistent.

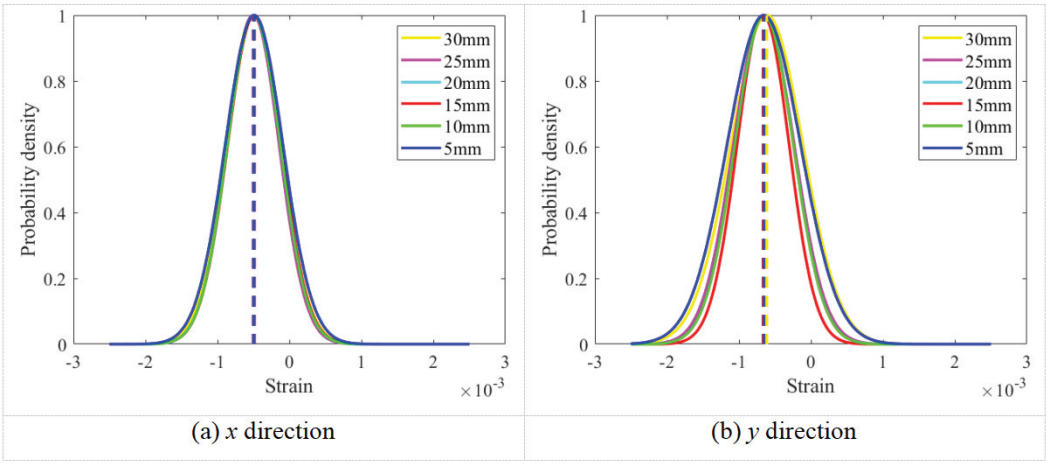


Figure 12. Normal fitting curves of the strain field data in regions of interest with different diameters in x and y directions under a preload of 10.03 kN.

https://doi.org/10.3390/s26030913

The tested bolt preload range (6–13 kN) was divided into eight discrete preload levels, and the corresponding sequence numbers for each preload are listed in Table 1.

Table 1. Sequence numbers corresponding to different preload levels.

Sequence Number	1	2	3	4	5	6	7	8
Preload (kN)	6.02	7.00	8.08	9.07	10.03	11.04	12.02	13.08

Figure 13 illustrates the relative error distribution of the surface strain values for the bolt under eight preload levels across six distinct ROIs in the x and y directions. As shown in the figure, the mean strain values obtained from different ROIs on the bolt surface under the same preload and in the same direction are nearly identical, with relative errors below 5%.

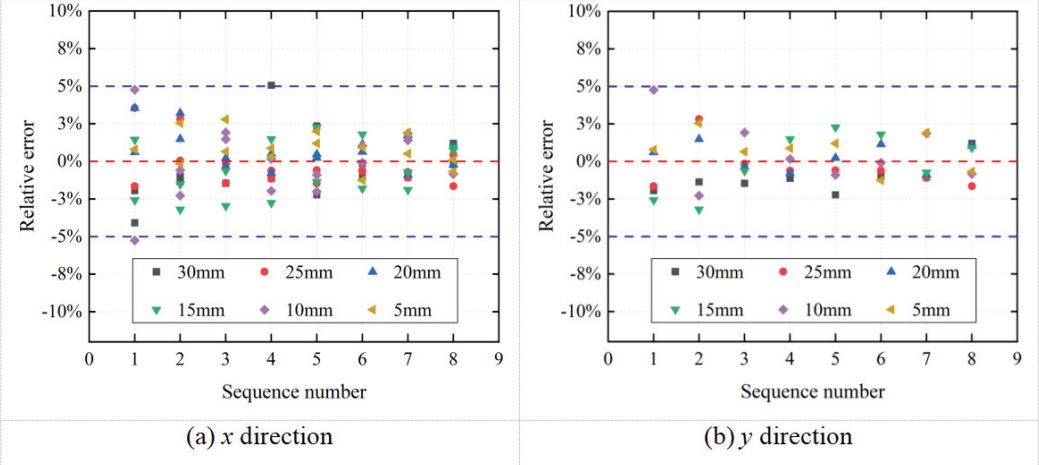


Figure 13. Relative error of bolt surface strain values under eight preload levels across six regions of interest in the x and y directions.

Figures 14 and 15 illustrate the correlation between the bolt preload and the surface strain of the bolt head across six distinct ROIs with varying diameters in both the x and y directions. The experimental results confirm a linear increase in the surface strain of the bolt head with increasing bolt preload. Furthermore, the slopes of the linear fitting curves for different ROIs are nearly identical, indicating that the selection of ROI has minimal influence on the correlation between the bolt preload and the surface strain.

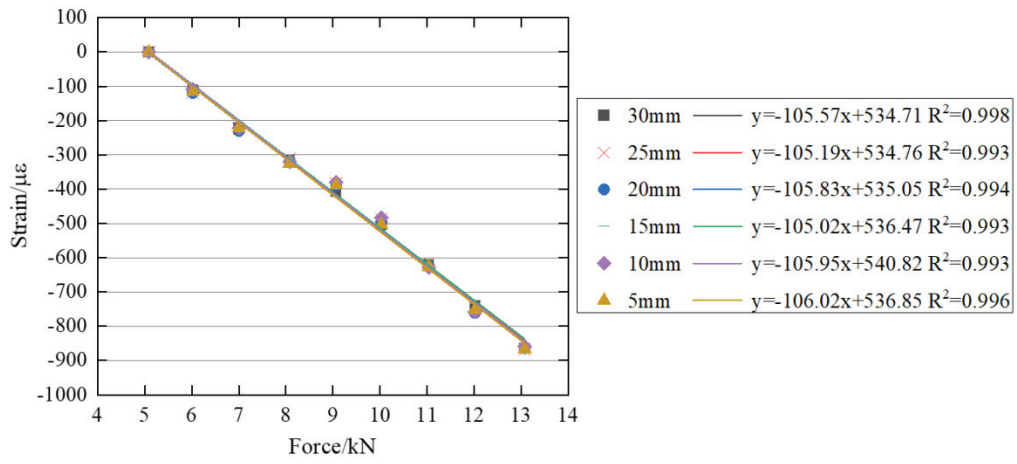


Figure 14. Relationship between bolt preload and surface strain of the bolt head in six regions of interest with different diameters in the x direction.

https://doi.org/10.3390/s26030913

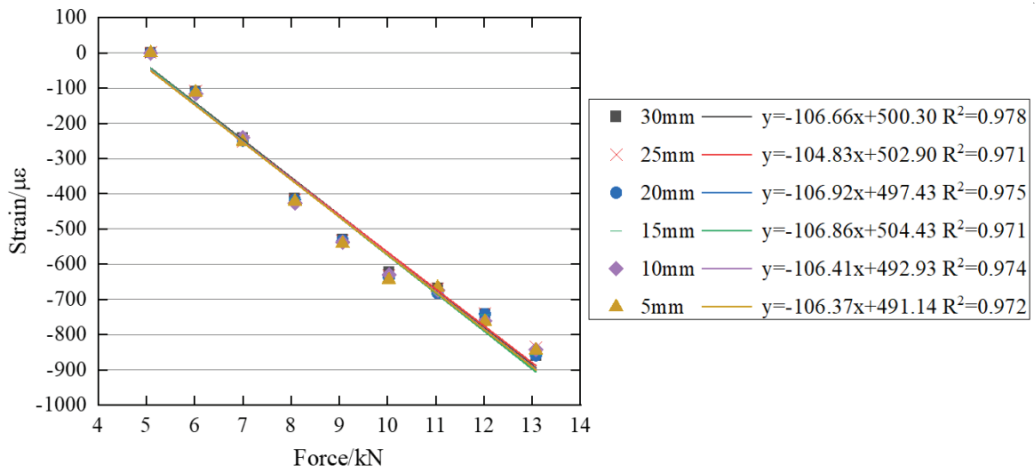
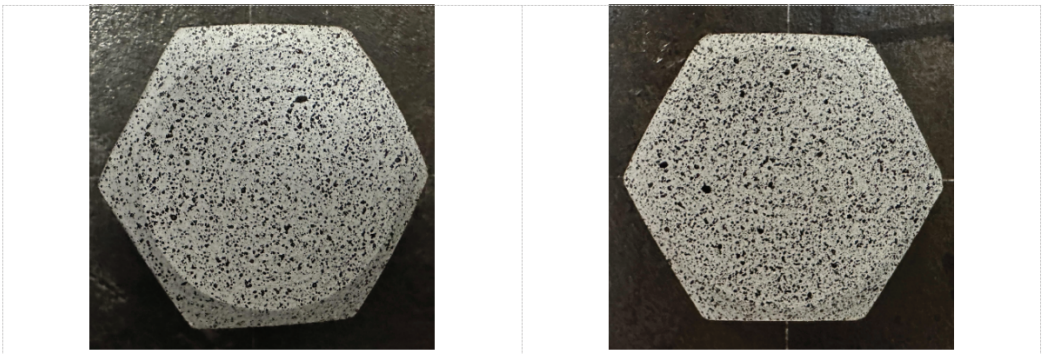


Figure 15. Relationship between bolt preload and surface strain of the bolt head in six regions of interest with different diameters in the *y* direction.

Experimental results suggest that choosing different ROIs does not notably impact the detected average strain value of the strain field on the surface of the bolt head. As a result, the relationship between the bolt preload and surface strain remains consistent regardless of the chosen ROI.

3.4. Verification Using Other Bolts Types

To further validate the experimental results, similar tests were performed on M18 and M22 bolts. The speckle patterns on the surfaces of these bolts are shown in Figure 16. The speckle preparation procedure described in the earlier sections was adopted to generate the speckle patterns on the bolt surfaces.



(a) M18 bolt (b) M22 bolt

Figure 16. Speckle patterns on the bolt head surfaces of the M18 and M22 bolts.

The correlations between bolt preload and surface strain for the M18 and M22 bolts are presented in Figures 17 and 18, respectively. The figures show that the correlation coefficients of the linear regression equations are close to 1, indicating a strong linear relationship between bolt preload and surface strain for both bolt types.

3.5. Correction of Bolt Rotation

To accurately address bolt deformation involving rotational movement, incorporating image rotation strategies during the pre-processing image registration phase is recommended. The specific workflow is as follows: During specimen preparation, geometric markers with distinct colors (e.g., rectangles or triangles) are placed on the bolt surface. For post-deformation images, integrating edge detection algorithms with color recognition

https://doi.org/10.3390/s26030913

technology yields optimal results for extracting the markers' edge features. Subsequently, Principal Component Analysis (PCA) [38] is utilized to determine the principal orientation (slope) of the markers. Based on this, the rotation angle of the test image relative to the reference image is calculated. Finally, a reverse rotational transformation is applied to the test image using this angle. The corrected image is then suitable for the quantitative calculation of bolt deformation. The rotation calibration flowchart is shown in Figure 19.

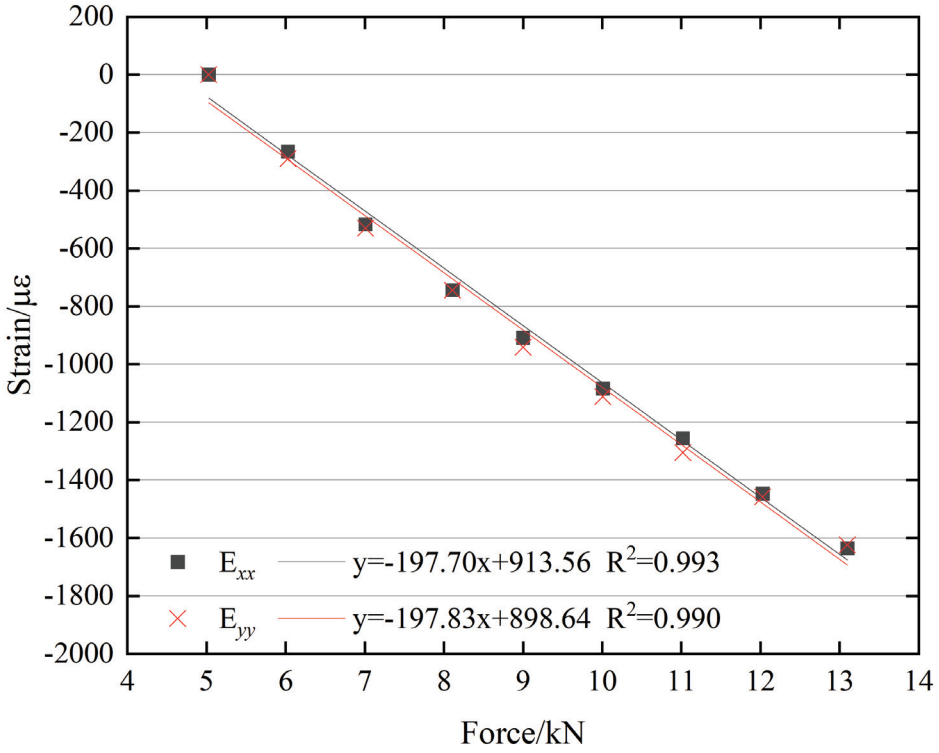


Figure 17. Relationship between the bolt preload and surface strain of the M18 bolt head.

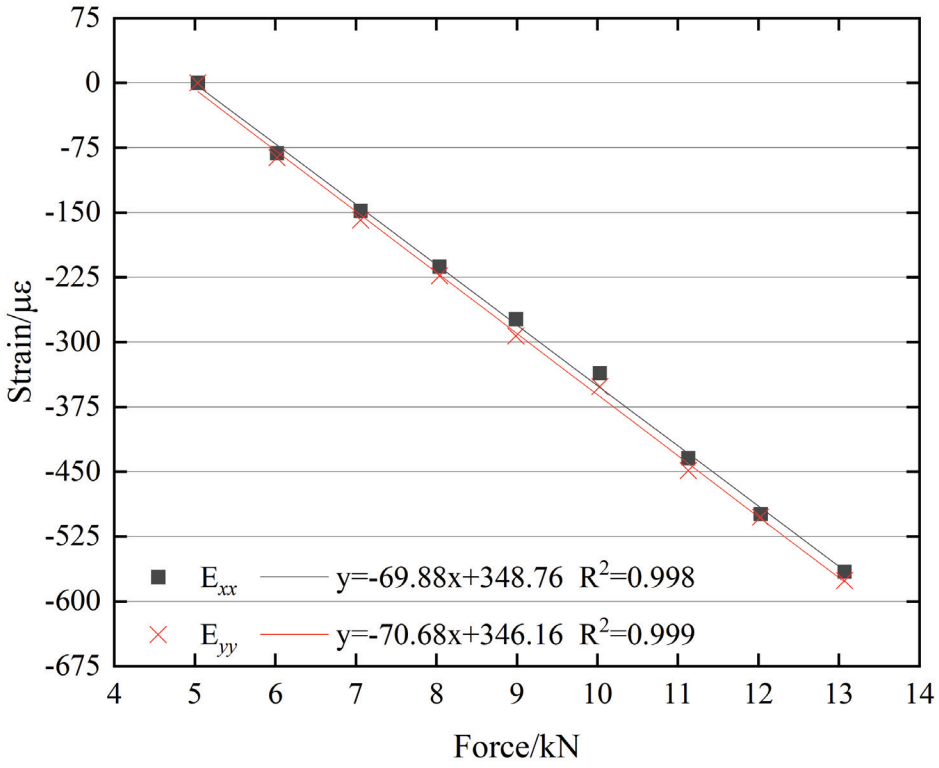


Figure 18. Relationship between the bolt preload and surface strain of the M22 bolt head.

https://doi.org/10.3390/s26030913

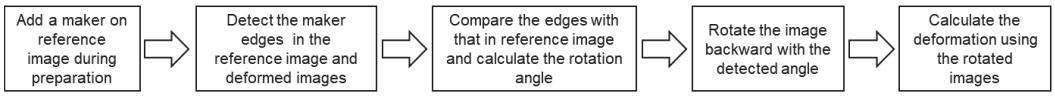


Figure 19. The flow chart of the rotation calibration.

To validate the rotational correction method, an image of an M20 bolt was selected and trapezoidal markers were superimposed on the original image, as illustrated in Figure 20. The image was subjected to a series of rotations at angles of 0.8°, 1.7°, 3.4°, 5.0° and 6.1°, after which corrected images were generated using the proposed method. Subsequently, strain calculations were performed by comparing the pre-rotation and post-correction images. The measurement regions are shown in Figure 20, and the results are presented in Table 2.

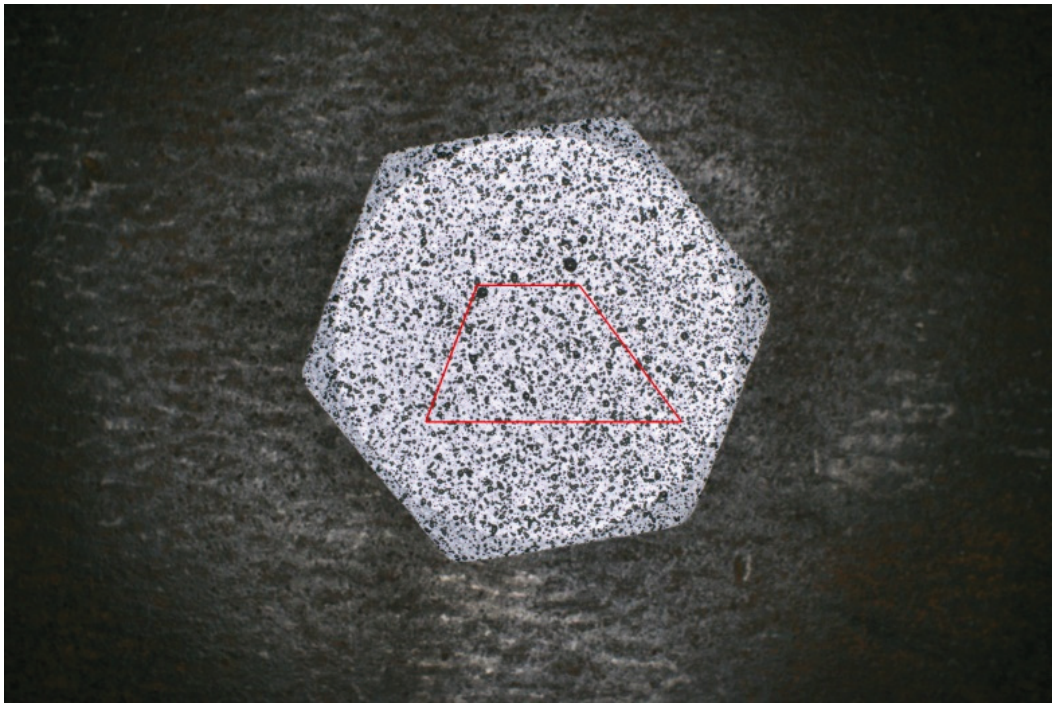
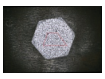
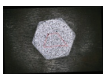
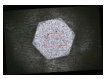
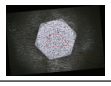
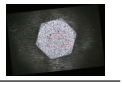
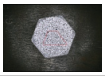
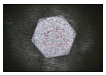
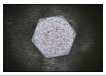


Figure 20. Selected M20 bolt image with trapezoid markings under a preload of 8.08 kN.

Table 2. Bolt rotation diagram and strain calculation results under a preload of 8.08 kN.

Rotation Angle	**0°**	**0.8°**	**1.7°**	**3.4°**	**5.0°**	**6.1°**
Before calibration						
After calibration						
Average strain in the x-direction/$\mu\epsilon$	−318	−314	−315	−313	−315	−314
Average strain in the y-direction/$\mu\epsilon$	−420	−411	−409	−409	−410	−410

Comparative experiments demonstrate that in the initial state without rotation, the measured strains in the x and y directions were -318 $\mu\epsilon$ and -420 $\mu\epsilon$, respectively. Following the implementation of the rotational correction scheme proposed in this study, the maximum errors in the x and y directions were limited to 5 $\mu\epsilon$ and 11 $\mu\epsilon$. These data

https://doi.org/10.3390/s26030913

confirm the validity and feasibility of the correction scheme, providing an effective solution for addressing measurement deviations caused by bolt rotation in practical applications.

4. Discussion

While the correction algorithm proposed in this study effectively mitigates errors caused by in-plane rotation, we acknowledge that out-of-plane displacement remains a critical factor affecting measurement accuracy in a single-camera 2D-DIC setup. Specifically, any displacement along the optical axis alters the object distance, leading to variations in magnification. This optical phenomenon causes the DIC algorithm to misinterpret the change in image scale as tensile or compressive deformation, thereby introducing significant fictitious strains. Consequently, to overcome this inherent limitation, our future work will transition to a stereoscopic 3D-DIC system. By utilizing binocular vision principles to reconstruct the three-dimensional coordinates of the bolt surface, we can effectively decouple out-of-plane motion from the actual surface strain.

In future applications, it will be feasible to establish specific linear relationships between preload and strain for various bolt models. By comparing the DIC-measured strain data from in situ bolts against these pre-calibrated linear curves (derived from identical bolts under controlled conditions), bolt loosening can be effectively detected.

5. Conclusions

This paper proposes a novel digital image correlation (DIC)-based method for monitoring bolt preload, and its feasibility has been verified through experimental studies. The main conclusions are summarized as follows:

(1) As the bolt preload increases, the strain on the bolt head surface also increases. The strain field on the bolt head surface follows a normal distribution, and a strong linear correlation exists between the mean strain value and the bolt preload, with a correlation coefficient close to 1. These results demonstrate the feasibility of using DIC for quantitative bolt preload monitoring.

(2) The relative error of the strain values obtained from different regions of interest (ROIs) under the same preload is within 5%, and the slopes of the linear fitting curves representing the relationship between bolt preload and surface strain remain consistent across ROIs. This indicates that ROI selection has little influence on the accuracy of the proposed method.

(3) A strong linear correlation is also observed between the bolt preload and the surface strain for various bolt types (M18, M20, and M22), with regression equations yielding correlation coefficients close to 1.

Compared with traditional bolt-loosening monitoring methods, the proposed approach offers simple implementation, fewer constraints, and good applicability, showing strong potential for further development.

Author Contributions: Conceptualization, L.H.; Investigation, L.Z.; Resources, F.M.; Data curation, F.M.; Writing—original draft, L.Z.; Writing—review & editing, L.H.; Visualization, A.H.; Supervision, L.H.; Project administration, H.L. All authors have read and agreed to the published version of the manuscript.

Funding: This research was supported by the National Natural Science Foundation of China (NSFC) under Grant No. 51778111.

Institutional Review Board Statement: Not applicable.

Informed Consent Statement: Not applicable.

https://doi.org/10.3390/s26030913

Data Availability Statement: The original contributions presented in this study are included in the article. Further inquiries can be directed to the corresponding author.

Conflicts of Interest: The authors declare that they have no known competing financial interests or personal relationships that could have appeared to influence the work reported in this paper.

References

1. Liu, J.; Ouyang, H.; Feng, Z.; Cai, Z.; Liu, X.; Zhu, M. Study on self-loosening of bolted joints excited by dynamic axial load. *Tribol. Int.* **2017**, *115*, 432–451. [CrossRef]
2. Kim, I.T.; Lee, J.M.; Huh, J.; Ahn, J.H. Tensile behaviors of friction bolt connection with bolt head corrosion damage: Experimental research B. *Eng. Fail. Anal.* **2016**, *59*, 526–543. [CrossRef]
3. Wang, F.; Chen, Z.; Song, G. Monitoring of multi-bolt connection looseness using entropy-based active sensing and genetic algorithm-based least square support vector machine. *Mech. Syst. Signal Process.* **2020**, *136*, 106507. [CrossRef]
4. Huang, J.; Liu, J.; Gong, H.; Deng, X. A comprehensive review of loosening detection methods for threaded fasteners. *Mech. Syst. Signal Process.* **2022**, *168*, 108652. [CrossRef]
5. Caccese, V.; Mewer, R.; Vel, S.S. Detection of bolt load loss in hybrid composite/metal bolted connections. *Eng. Struct.* **2004**, *26*, 895–906. [CrossRef]
6. Miao, R.; Shen, R.; Zhang, S.; Xue, S. A review of bolt tightening force measurement and loosening detection. *Sensors* **2020**, *20*, 3165. [CrossRef]
7. Zhang, Y.; Zhao, X.; Sun, X.; Su, W.; Xue, Z. Bolt loosening detection based on audio classification. *Adv. Struct. Eng.* **2019**, *22*, 2882–2891. [CrossRef]
8. Kong, Q.; Zhu, J.; Ho, S.C.M.; Song, G. Tapping and listening: A new approach to bolt looseness monitoring. *Smart Mater. Struct.* **2018**, *27*, 07LT02. [CrossRef]
9. Wang, F.; Song, G.; Mo, Y.L. Shear loading detection of through bolts in bridge structures using a percussion-based one-dimensional memory-augmented convolutional neural network. *Comput.-Aided Civ. Infrastruct. Eng.* **2021**, *36*, 289–301. [CrossRef]
10. Yuan, R.; Lv, Y.; Kong, Q.; Song, G. Percussion-based bolt looseness monitoring using intrinsic multiscale entropy analysis and BP neural network. *Smart Mater. Struct.* **2019**, *28*, 125001. [CrossRef]
11. Wang, F.; Ho, S.C.M.; Huo, L.; Song, G. A novel fractal contact-electromechanical impedance model for quantitative monitoring of bolted joint looseness. *IEEE Access* **2018**, *6*, 40212–40220. [CrossRef]
12. Ritdumrongkul, S.; Abe, M.; Fujino, Y.; Miyashita, T. Quantitative health monitoring of bolted joints using a piezoceramic actuator–sensor. *Smart Mater. Struct.* **2003**, *13*, 20. [CrossRef]
13. Qiu, H.; Li, F. Bolt looseness monitoring based on damping measurement by using a quantitative electro-mechanical impedance method. *Smart Mater. Struct.* **2022**, *31*, 095022. [CrossRef]
14. Wang, F.; Song, G. Bolt early looseness monitoring using modified vibro-acoustic modulation by time-reversal. *Mech. Syst. Signal Process.* **2019**, *130*, 349–360. [CrossRef]
15. Bhalla, S.; Vittal, P.A.; Veljkovic, M. Piezo-impedance transducers for residual fatigue life assessment of bolted steel joints. *Struct. Health Monit.* **2012**, *11*, 733–750. [CrossRef]
16. Li, N.; Wang, F.; Song, G. Monitoring of bolt looseness using piezoelectric transducers: Three-dimensional numerical modeling with experimental verification. *J. Intell. Mater. Syst. Struct.* **2020**, *31*, 911–918. [CrossRef]
17. Amerini, F.; Meo, M. Structural health monitoring of bolted joints using linear and nonlinear acoustic/ultrasound methods. *Struct. Health Monit.* **2011**, *10*, 659–672. [CrossRef]
18. Zhao, X.; Zhang, Y.; Wang, N. Bolt loosening angle detection technology using deep learning. *Struct. Control Health Monit.* **2019**, *26*, e2292. [CrossRef]
19. Huynh, T.C.; Park, J.H.; Jung, H.J.; Kim, J.T. Quasi-autonomous bolt-loosening detection method using vision-based deep learning and image processing. *Autom. Constr.* **2019**, *105*, 102844. [CrossRef]
20. Park, J.H.; Huynh, T.C.; Choi, S.H.; Kim, J.T. Vision-based technique for bolt-loosening detection in wind turbine tower. *Wind Struct.* **2015**, *21*, 709–726. [CrossRef]
21. Deng, X.; Liu, J.; Gong, H.; Huang, J. Detection of loosening angle for mark bolted joints with computer vision and geometric imaging. *Autom. Constr.* **2022**, *142*, 104517. [CrossRef]
22. Kong, X.; Li, J. Image registration-based bolt loosening detection of steel joints. *Sensors* **2018**, *18*, 1000. [CrossRef] [PubMed]
23. Godara, A.; Raabe, D. Microstrain localisation measurement in epoxy FRCs during plastic deformation using a digital image correlation technique coupled with scanning electron microscopy. *Nondestruct. Test. Eval.* **2008**, *23*, 229–240. [CrossRef]
24. Dong, Y. In-situ evaluation of C/SiC composites via an ultraviolet imaging system and microstructure based digital image correlation. *Nondestruct. Test. Eval.* **2018**, *33*, 427–437. [CrossRef]

https://doi.org/10.3390/s26030913

25. Chen, B.; Pan, B. Mirror-assisted panoramic-digital image correlation for full-surface 360-deg deformation measurement. *Measurement* **2019**, *132*, 350–358. [CrossRef]
26. Bharadwaj, K.; Sheidaei, A.; Afshar, A.; Baqersad, J. Full-field strain prediction using mode shapes measured with digital image correlation. *Measurement* **2019**, *139*, 326–333. [CrossRef]
27. Chevalier, L.; Calloch, S.; Hild, F.; Marco, Y. Digital image correlation used to analyze the multiaxial behavior of rubber-like materials. *Eur. J. Mech.-A/Solids* **2001**, *20*, 169–187. [CrossRef]
28. Reder, C.; Loidl, D.; Puchegger, S.; Gitschthaler, D.; Peterlik, H.; Kromp, K.; Khatibi, G.; Betzwar-Kotas, A.; Zimprich, P.; Weiss, B. Non-contacting strain measurements of ceramic and carbon single fibres by using the laser-speckle method. *Compos. Part A Appl. Sci. Manuf.* **2003**, *34*, 1029–1033. [CrossRef]
29. Gencturk, B.; Hossain, K.; Kapadia, A.; Labib, E.; Mo, Y.L. Use of digital image correlation technique in full-scale testing of prestressed concrete structures. *Measurement* **2014**, *47*, 505–515. [CrossRef]
30. Jiménez-Peña, C.; Lavatelli, A.; Balcaen, R.; Zappa, E.; Debruyne, D. A novel contactless bolt preload monitoring method using digital image correlation. *J. Nondestruct. Eval.* **2021**, *40*, 54. [CrossRef]
31. Pan, B.; Xie, H.; Wang, Z. Equivalence of digital image correlation criteria for pattern matching. *Appl. Opt.* **2010**, *49*, 5501–5509. [CrossRef] [PubMed]
32. Pan, B.; Li, K.; Tong, W. Fast, robust and accurate digital image correlation calculation without redundant computations. *Exp. Mech.* **2013**, *53*, 1277–1289. [CrossRef]
33. Yoo, J.C.; Han, T.H. Fast normalized cross-correlation. *Circuits Syst. Signal Process.* **2009**, *28*, 819–843. [CrossRef]
34. Pan, B.; Xie, H.; Xu, B.; Dai, F. Performance of sub-pixel registration algorithms in digital image correlation. *Meas. Sci. Technol.* **2006**, *17*, 1615–1621. [CrossRef]
35. Schreier, H.W.; Braasch, J.R.; Sutton, M.A. Systematic errors in digital image correlation caused by intensity interpolation. *Opt. Eng.* **2000**, *39*, 2915–2921. [CrossRef]
36. Pan, B. Reliability-guided digital image correlation for image deformation measurement. *Appl. Opt.* **2009**, *48*, 1535–1542. [CrossRef]
37. Pan, B.; Xie, H.; Guo, Z.; Hua, T. Full-field strain measurement using a two-dimensional Savitzky-Golay digital differentiator in digital image correlation. *Opt. Eng.* **2007**, *46*, 033601. [CrossRef]
38. Lee, Y.S.; Koo, H.S.; Jeong, C.S. A straight line detection using principal component analysis. *Pattern Recognit. Lett.* **2006**, *27*, 1744–1754. [CrossRef]

Disclaimer/Publisher's Note: The statements, opinions and data contained in all publications are solely those of the individual author(s) and contributor(s) and not of MDPI and/or the editor(s). MDPI and/or the editor(s) disclaim responsibility for any injury to people or property resulting from any ideas, methods, instructions or products referred to in the content.

https://doi.org/10.3390/s26030913

sensors

MDPI

Article

Machine Learning-Enhanced Evaluation of Handheld Laser-Induced Breakdown Spectroscopy (LIBS) Analytical Performance for Multi-Element Analysis of Rock Samples

Giorgio S. Senesi [1,*], Olga De Pascale [1], Ignazio Allegretta [2], Roberto Terzano [3] and Bruno Marangoni [4]

[1] CNR-Istituto per la Scienza e Tecnologia dei Plasmi (ISTP) Sede di Bari, Via Amendola, 122/D, 70126 Bari, Italy; olga.depascale@istp.cnr.it
[2] Dipartimento di Scienze e Tecnologie Biologiche ed Ambientali, Università del Salento, Via Monterioni 165, 73100 Lecce, Italy; ignazio.allegretta@unisalento.it
[3] Dipartimento di Scienze del Suolo, della Pianta e degli Alimenti, Università degli Studi di Bari, Via G. Amendola 165/A, 70126 Bari, Italy; roberto.terzano@uniba.it
[4] Programa de Pós-Graduação em Ciência dos Materiais, UFMS–Universidade Federal de Mato Grosso do Sul, Av. Costa e Silva, s/nº, Campo Grande 79070-900, Brazil; bruno.marangoni@ufms.br
* Correspondence: giorgio.senesi@cnr.it

Abstract

Handheld laser-induced breakdown spectroscopy (hLIBS) can be considered one of the most recent techniques for rock characterization in situ. Handheld LIBS devices are useful tools for providing "fit for purpose" qualitative and quantitative geochemical data. The analytical performance of hLIBS instruments varies significantly between similar instruments from different manufacturers. This study employed two commercial hLIBS instruments, both making use of noise reduction and multivariate partial-least-squares (PLS) calibration. Model validation was performed using the Leave-One-Out Cross-Validation (LOOCV) method. The Random Forest (RF) and Artificial Neural Network (ANN) algorithms were also employed as complementary approaches to PLS modeling, with the goal of exploring potential nonlinear relationships between spectral intensities and reference analyte concentrations. A comparison was also made with the most basic and commonly used approach, univariate analysis, demonstrating that multivariate methods achieve superior performances. To evaluate the predictive performance and quantification capability of the acquired LIBS spectra, the Pearson's coefficient (R^2) and root-mean-square error (RMSE) were employed in the analysis of 21 diverse certified geochemical reference materials (CRMs). The results achieved suggested that the spectral resolution was the key factor determining the performance of multivariate LIBS calibrations. The PLS model proved to be satisfactory for analyses performed by the higher-spectral-resolution instrument, whereas complementary algorithms were necessary to achieve better results with the lower-spectral-resolution instrument.

Keywords: handheld LIBS instruments; certified geochemical reference materials; PLS; RF; ANN

1. Introduction

In geoscience research, the need for chemical data has continuously expanded with regard to not only the type of elements and their concentration levels but also to the extension of applications to a wider and wider variety of geological materials. A persistent

requirement by the geoscience community is the availability of field-deployable instrumentation that can be used regularly outside the laboratory to perform in situ chemical analysis. The basic requisites of these instruments include ease portability, lightweightness to enable individual operation, durability and robustness for use in challenging environments, user friendliness, and the ability to detect the broadest spectrum of elements in a brief acquisition time [1,2].

Laser-induced breakdown spectroscopy (LIBS) and X-ray fluorescence spectrometry (XRF) are two analytical methods that meet the above-listed requisites for field use under current environmental conditions, enabling exploration geologists to acquire an immediate insight into the geochemistry of an ore prospect. In this way, field survey work can be optimized, and field-acquired data can assist in deciding which samples to gather for additional laboratory examination, thereby offering significant savings in both time and expense. Furthermore, data acquired in the field allow environmental geologists to quickly understand the existence of pollution by hazardous elements throughout an area and/or assess the effectiveness of a remediation effort to restore a contaminated site [1], identify the possible presence of precious or useful elements [2], and explore mine wastes on site in view of their possible recovery [3].

LIBS is one of the very few current analytical technologies suitable for routine use outside the laboratory and possesses a persuasive set of advantages that makes it ideally suited for chemical analysis in the field [2]. These include the possibility of using a compact and lightweight instrument operated by a single individual to analyze most types of natural materials under ambient environmental conditions in real time, and with little to no sample preparation [2]. Although portable LIBS instruments may not achieve the same levels of elemental detection and analytical accuracy as those of laboratory instruments, they still offer an effective and robust tool for the field investigator. Currently, LIBS is being extensively utilized in various geoscience sub-disciplines, including mineralogy, petrology, volcanology, sedimentology, the exploration and exploitation of natural resources, pedology, and geoarchaeology [4–6].

In the first decade of the current millennium, the progress in the analytical performances of small and compact LIBS analyzers has been significantly influenced by the choice of LIBS as one of the technologies incorporated into the NASA ChemCam system on the Curiosity rover to assess the elemental composition of Martian soils and rocks [7]. Subsequently, in 2013, the initial handheld (h) LIBS analyzer was launched in the commercial sector and was reported in the scientific literature soon after [8]. While the progress of portable LIBS equipment for geological use has advanced in research laboratories e.g., [9–11], commercial hLIBS analyzers have become the favored response to the ongoing demand for technology that enables quick chemical analysis in field settings.

The aim of this study was to analyze the reliability and precision of two commercial hLIBS instruments operating in different configurations (i.e., varying pulse energies and durations, acquisition geometries, spot sizes, raster grids, repetition rates, and spectral ranges) in analyzing 21 diverse certified geochemical reference materials (CRMs). Besides evaluating the general applicability of hLIBS for the geochemical analysis of rocks, the effect of multiple rock characteristics on the hLIBS performance was also investigated. In order to verify the performances of the two instruments, noise reduction and multivariate partial-least-squares (PLS) calibration and validation Leave-One-Out Cross-Validation (LOOCV) were used. For each test sample in the LOOCV, hyperparameter optimization was conducted using nested cross-validation (NCV) to avoid overfitting [12,13]. The Random Forest (RF) and Artificial Neural Network (ANN) algorithms were also employed as complementary approaches to PLS modeling, with the goal of exploring potential nonlinear relationships between spectral intensities and reference analyte concentrations [14–16].

https://doi.org/10.3390/s26031076

Univariate analysis was employed for quantitative purposes as a benchmark against the multivariate approaches, highlighting the performance achieved. The final aim of this work is to assess the robustness of hLIBS in general, and the intention is not to suggest the best instrument but rather the range of applicability of two types of common commercial instruments.

2. Materials and Methods

2.1. Certified Geochemical Reference Materials

A total of 21 homogenized rock samples originating from 10 different countries were examined in this study. The raw materials to obtain these CRMs originated from various deposits spread across the globe (Service d'Analyse des Roches et des Minéraux-SARM). The goal was to offer the scientific community CRMs adapted to geochemical analysis and necessary for the calibration of a device or the evaluation of a measurement method. An overview of the samples, along with their specific rock characteristics and elemental concentrations, can be found in the Supplementary Materials (Tables S1 and S2). The CRM samples were air-dried and ground to achieve particle sizes < 20 μm. The pellets to be used for the analysis were obtained by mixing 5.0 g of powdered sample with 2 mL of 2% (*w*/*v*) Elvacite® 2046 (PANalytical B.V., Almelo, The Netherlands) acetone solution in a mortar, stirring the slurry until the acetone evaporated, and finally pelletizing the powder placed in 30 mm open-ended aluminum cups by uniaxial pressing (25 tons).

2.2. Handheld LIBS Instruments Used and LIBS Spectrum Collection

In this work, a NanoLIBS hLIBS instrument (B&W Tek, Newark, DE, USA) described in detail by Senesi et al. [17] was used. The entire apparatus has dimensions of 26 × 10 × 30 cm, a weight of 1.8 kg, is powered by an onboard rechargeable Li-ion battery (8 h battery life) and operates at ambient atmosphere. The instrument employs a 1064 nm Nd:YAG miniature-diode-pumped solid-state short-pulsed laser that produces a focused beam of 20–30 μm that delivers a maximum pulse energy of 150 μJ to the sample at a pulse duration of 500 ps for a shot repetition frequency between 1 and 5 KHz.

The NanoLIBS hLIBS instrument allows for the scanning of a spectral range from 180 to 800 nm with an overall resolution of 0.4 nm (lower-spectral-resolution instrument). The emission light signal is collected and transferred via a fiber optic cable into a compact low-resolution spectrometer operating in non-gated mode. The system is equipped with a raster scan that provides spatial averaging. Measurements were performed by placing the instrument against the surface of the pellet, and the analysis was initiated via a trigger. Spectral data were collected at an integration time of 4 msec, which corresponded to twelve laser pulses for a 1 kHz laser. Five different positions on each pellet were analyzed, and five laser measurements were acquired at each position, which were then averaged to obtain a single spectrum for each position. The spectra were then analyzed qualitatively to identify and highlight the emission lines using the National Institute of Standards and Technology (NIST) Atomic Spectra Database [18].

The other instrument employed in this study was a Z-300 (SciAps, Inc., Woburn, MA, USA) LIBS device, measuring 21 × 29 × 11 cm, weighing 1.8 kg, and operating by an internal Li-ion battery. This device utilizes a Class 3 PULSARTM 1064 nm Nd:YAG diode-pumped solid-state pulsed laser, generating a 100 μm focused beam that fires a 5–6 mJ pulse to the sample with a 1 ns pulse duration at a repetition rate of 1 to 50 Hz. The analyzer operates in ambient air but can also perform gas purging by supplying an inert gas (Ar) from a canister in the instrument handle directly to the focusing area on the sample surface where LIBS plasma is formed, thereby enhancing plasma containment and emission signals.

https://doi.org/10.3390/s26031076

The Z-300 instrument captures a wide spectrum of plasma light emissions, spanning from 190 to 950 nm. The emission light signal is gathered and transmitted through a fiber optic cable to three internal spectrometers that use time-gated CCD detectors, which have spectral ranges and resolutions of 190–365 nm with a full width at half maximum (FWHM) of 0.18 nm, 365–620 nm with a FWHM of 0.24 nm, and 620–950 nm with a FWHM of 0.35 nm (higher-spectral-resolution instrument). Spectral data were gathered with a delay time of 650 ns over an integration period of 1 ms. The routine wavelength calibration of the spectrometers was conducted by examining an internal target composed of Grade 316 Mo-bearing stainless steel. For each spectrometer in the system, discrepancies in wavelengths between the chosen observed emission lines and the data obtained from the NIST database [18] were identified, and correction factors were utilized. The updated coefficients remained in use until the subsequent wavelength calibration occurred, and a stored record of all calibration spectra and adjustment values was maintained onboard. The analyzer is equipped with a video camera to observe the sample prior to analysis and a laser spot finder that indicates where the laser beam is hitting the sample. The instrument features a computer-controlled, onboard 3D translational stage that automates laser focusing on the sample site and allows for rastering the laser beam across the sample in the XY-direction at specific positions for targeted analysis or data averaging. The raster pattern was obtained at intervals of 12.5 μm across an area of up to 2 × 2 mm^2, with both the grid size and number of laser shots at each raster point fixed by the user. Furthermore, it was possible to use a number of non-analytical shots for surface "cleaning" before gathering the spectral data.

Obviously, the two hLIBS instruments feature different configurations that are reflected in the resulting spectra. The comparison in Table 1 reports an overview of the main characteristics of the two hLIBS instruments. LIBS analysis was undertaken averaging four spectra recorded after one cleaning shot at a laser-firing rate of 50 Hz over a 4 × 3 grid for each pellet. This array sampling was repeated five times on random positions on each pellet.

Table 1. Overview of the main characteristics, as reported by the manufacturers, of the two hLIBS instruments used in this study and some of their physical and operational parameters.

Brand	Laser Type	Laser Class	Laser Repetition Rate	Laser Energy Per Pulse	Wavelength Range (nm)	Spectral Resolution FWHM * (nm)
B&W Tek NanoLIBS	Nd:YAG 1064 nm	3B	5 kHz	150 μJ	180–800	0.38–0.5
SciAps *Z-300*	Nd:YAG 1064 nm	3B	50 Hz	5–6 mJ	190–950	0.18–0.35
Brand	**Detector Type**	**Laser Crater Diameter (μm)**	**Analysis Atmosphere**	**Dimensions L × H × W (cm)**	**Weight with Battery (kg)**	**Battery Type Operating Time**
B&W Tek NanoLIBS	CCD	300	Ambient	26.5 × 30.4 × 10	1.8	Li-ion >4 h
SciAps *Z-300*	CCD	100	Ambient or argon purge	21 × 29.2 × 11.4	1.8	Li-ion 4–7 h

* The exact value depends on the spectral region and application, so these numbers are approximate.

2.3. Pre-Analyses and Limit of Detection (LOD)

The raw spectra initially underwent a preprocessing pipeline. This sequence consisted in: (i) background removal using a polynomial fitting method; (ii) outlier detection via the Spectral Angle Mapper (SAM) algorithm; and (iii) normalization by Standard Normal Variate (SNV) [19]. Finally, the five-position spectra acquired for each pellet were averaged.

https://doi.org/10.3390/s26031076

In this specific study, the SAM analysis did not exclude any spectra as outliers, and thus all acquired data were retained for subsequent analysis.

An additional preprocessing step was applied prior to feeding the data to the machine learning routines. To reduce the number of initial variables (wavelengths) and improve the training efficiency, an automatic correlation-based variable selection procedure was implemented to retain the most informative spectral features. First, the Pearson's coefficient (R^2) between the intensity of each wavelength and the reference concentration of the constituent was calculated to exclude from the dataset the wavelengths exhibiting R^2 values lower than 0.3 [20]. This threshold was chosen based on the empirical observation that most of the uncorrelated transitions and background noise lay below this value. Subsequently, a second filtering routine was used to compare the selected spectral variables with a list of known atomic and ionic transitions for the element or oxide of interest. Wavelengths that were not located within a ± 1 nm window of a registered emission line for the corresponding element were removed from the analysis. The electronic transitions for each element were extracted from the NIST LIBS database [18], and the strongest transitions were selected, with a maximum of 30 transitions (atomic and ionic), considering a plasma condition at a temperature of 1 eV and an electron density of 10^{17} cm^{-3}.

The limit of detection (LOD) was determined using a univariate calibration curve that related the intensity variation of a specific spectral transition to the reference concentration of the analyte in the sample. A linear model was adjusted, and the slope of the regression line was obtained. The standard deviation of the background noise (std) was estimated from a clean spectral region with no corresponding emission line [21]. According to the criteria established by the International Union of Pure and Applied Chemistry (IUPAC), the LOD was calculated as:

$$\text{LOD} = 3\text{std}/\text{slope} \quad (1)$$

The LOD values obtained in this study were consistent with those reported in the literature for LIBS systems applied to geochemical standards with vast compositional variety that include unique natural (igneous, sedimentary, and metamorphic) samples [22]. Tables 2 and 3 present the figures of merit, R^2, standard deviation of the background (Std background) and slope of the regression line used for the calculation of the LOD. The corresponding univariate calibration and validation curves are provided in the Supplementary Materials (Figures S1–S8). After this stage, samples with concentrations below the LOD were excluded in order to ensure the statistical robustness of the models (PLS, RF and ANN). This criterion ensures that the model maintains adequate complexity to capture relevant relationships while minimizing the likelihood of overfitting to the calibration data.

Table 2. Data related to the processing and calculation of the LOD for the higher-spectral-resolution hLIBS instrument. The LOD and Std background have the same units as the corresponding compounds (wt% for oxides and mg/kg for elements), whereas R^2 is dimensionless.

	Analyte	Conc. Average	Conc. Range	LOD	R^2	Std Background	Slope	Emission Line (nm)
Oxides (wt%)	**SiO_2**	56.5	36.45–75.80	3.19	0.69	0.39	0.37	390.53
	Al_2O_3	18.6	2.9–59.2	0.83	0.94	0.39	1.41	394.53
	MgO	4.87	0.01–35.21	0.94	0.98	0.39	1.25	517.50
	CaO	3.53	0.04–15.9	1.01	0.97	0.39	1.15	865.43
	Na_2O	2.44	0.04–15.9	0.53	0.97	0.39	2.21	820.00
	K_2O	3.34	0.02–12.81	0.35	0.98	0.39	3.31	693.63
	TiO_2	0.77	0.01–2.61	0.12	0.72	0.39	9.40	375.33
	Fe_2O_3	5.95	0.075–19.6	1.57	0.88	0.39	0.74	254.17

https://doi.org/10.3390/s26031076

Table 2. *Cont.*

	Analyte	Conc. Average	Conc. Range	LOD	R^2	Std Background	Slope	Emission Line (nm)
Elements (mg/kg)	**Li**	40.79	1–110	1.27	0.84	0.43	1.01	670.43
	Ba	117.1	6–385	22.74	0.69	0.43	0.06	454.83
	V	91.3	0.2–340	33.34	0.85	0.41	0.04	322.20
	Cr	44.72	2–140	1.94	0.77	0.34	0.52	279.30
	Rb	76.07	1–238	16.05	0.99	0.48	0.089	779.63
	Sr	147.69	3–570	51.96	0.93	0.40	0.023	420.93

Table 3. Data related to the processing and calculation of the LOD for the lower-spectral-resolution hLIBS instrument. The LOD and Std background have the same units as the corresponding compounds (wt% for oxides and mg/kg for elements), whereas R^2 is dimensionless.

	Analyte	Conc. Average	Conc. Range	LOD	R^2	Std Background	Slope	Emission Line (nm)
Oxides (wt%)	**SiO_2**	56.5	36.45–75.80	1.62	0.80	0.13	0.24	250.00
	Al_2O_3	18.6	2.9–59.2	1.57	0.95	0.13	0.25	394.77
	MgO	4.87	0.01–35.21	1.76	0.92	0.13	0.22	293.91
	CaO	3.53	0.04–15.9	0.52	0.92	0.13	0.76	392.79
	Na_2O	2.44	0.04–15.9	0.23	0.94	0.13	1.69	590.08
	K_2O	3.34	0.02–12.81	2.21	0.84	0.13	0.18	767.07
	TiO_2	0.77	0.01–2.61	0.43	0.66	0.13	0.92	375.70
	Fe_2O_3	5.95	0.075–19.6	1.60	0.77	0.13	0.25	275.78
Elements (mg/kg)	**Be**	5.09	0.2–35	1.90	0.67	0.14	0.22	249.87
	Cr	44.72	2–140	3.04	0.73	0.10	0.10	277.76
	Pb	39.48	2–240	14.54	0.55	0.143	0.029	287.41

2.4. Multivariate Analysis

To assess the calibration and quantification performances of the two LIBS systems, three distinct analytical approaches were employed: PLS, ANN, and RF. The choice of these methods was based on their complementary characteristics. In particular, PLS is widely used in spectroscopy because it efficiently handles highly correlated and noisy data while exploiting the existing linear relationships between spectral intensities and analyte concentration variations [23]. This approach is particularly advantageous when the number of spectral variables exceeds the number of samples, as it enables dimensionality reduction without the significant loss of relevant chemical information.

Differently, the machine learning-based methods RF and ANN exhibit a superior capacity to model nonlinear relationships between spectral variables and concentrations. In particular, the RF algorithm is composed of an ensemble of decision trees; thus, it is robust to noise and less prone to overfitting. Furthermore, it provides metrics of variable importance that facilitate the interpretation and identification of the most relevant emission lines. In turn, ANNs offer high flexibility in capturing complex patterns and variable interactions, making them suitable for scenarios in which the spectral response exhibits nonlinear behavior as a function of the analyte concentration [24]. The combined use of these approaches allows for a comprehensive analysis, capable of capturing both linear and nonlinear trends in the data.

Univariate validation analysis was also performed using the same criteria established for the multivariate analysis. This approach was adopted as a benchmark against multivariate methods, enabling a direct comparison and allowing the effectiveness of applying multivariate analysis to this set of samples and experimental setup to be properly assessed.

https://doi.org/10.3390/s26031076

To evaluate the predictive performance and quantification capability of the acquired spectra, the R^2 and root-mean-square error (RMSE) were employed. Model validation was performed using the LOOCV method, from which the RMSE and R^2 values were extracted.

To ensure a robust and unbiased evaluation of the model performance while mitigating the risk of overfitting, a nested cross-validation (NCV) procedure within the LOOCV procedure was implemented and employed to perform the selection of hyperparameters for each model's training [25]. This approach is particularly advantageous for smaller datasets, as it provides a reliable estimate of a model's predictive capability on unseen data [26]. The methodology consists of two hierarchical loops: an external loop and an internal loop. The external loop employs LOOCV, where each individual sample in the dataset is sequentially held out as an independent test set. For each iteration of this external loop, the remaining N-1 samples form the training set. Within this training set, an inner 5- or 10-fold cross-validation loop is executed to perform the hyperparameter optimization. This internal loop conducts a grid search over a pre-defined parameter space to identify the optimal configuration that maximizes the model performance on the internal validation folds, ensuring that the model is adjusted without any information from the held-out test sample leaking into the training process. Once the optimal hyperparameters are identified, a final model is trained on the entire N-1 training set using these parameters, and then the model is used to predict the held-out test sample. The cycle described above is repeated until every sample has served as the test sample once [27]. The most frequently selected parameters are then chosen and used to perform a LOOCV procedure. The predictions from all LOOCV iterations are subsequently aggregated and compared against the reference values. A table detailing the optimal hyperparameter values selected for each classifier (PLS, RF, and ANN) during the LOOCV procedure is provided in the Supplementary Materials Table S3.

The overall performance of the modeling strategy was quantitatively assessed by constructing a validation plot of predicted versus real concentrations and by calculating the R^2 and RMSE. Although computationally demanding, this procedure is feasible with our sample size and effectively prevents overfitting by strictly separating the data used for model tuning from those used for performance assessment. In this work, the specific hyperparameters optimized using NCV were the number of latent variables for the PLS; the number of trees and number of leaf nodes for the RF; and, for the ANN, the number of neurons, number of hidden layers, and number of PCA latent variables used as input features. The ANN was performed with 100 epochs with a fixed learning rate of 0.01 (e.g., Figures S9 and S10 in the Supplementary Materials, where the RMSE for the calibration and validation curves for the CaO and MgO analyses in the lower-spectral-resolution instrument are shown).

The LOOCV approach consists of a cross-validation process in which, at each iteration, a single sample is excluded from the calibration set and used as a test sample. This procedure is repeated successively until every sample is used once for testing. The main advantage of LOOCV lies in its maximal utilization of available data, which is particularly beneficial for datasets with limited sample sizes, thereby providing a robust estimate of the model's generalization capability.

The RMSE represents the square root of the mean of the squared differences between the predicted values generated by the model and the experimental reference values. This parameter quantifies the predictive accuracy of the model, i.e., smaller RMSE values indicate a higher predictive capability and lower error dispersion. The coefficient of determination (R^2) complements this metric by quantifying the proportion of the variance in the reference data that is explained by the model. Higher R^2 values denote better agreement between predicted and measured values, reflecting the model's ability to capture the

https://doi.org/10.3390/s26031076

underlying data structure. However, the R^2 alone may overestimate the model performance, particularly in cases of model overfitting or when the variance of the target variable is high. While the RMSE directly measures the predictive error magnitude, the R^2 evaluates the explanatory power of the model. Thus, used together, the RMSE and R^2 provide a more comprehensive and reliable assessment of the model performance. Their combined use ensures a balanced interpretation between goodness of fit and predictive performance, reducing the likelihood of overestimating the model quality due to overfitting effects. All routines used in this work were developed by the authors using Matlab2016b.

2.5. Partial-Least-Squares (PLS) Modeling

The PLS regression approach was employed to correlate the spectral intensities with the reference concentrations of the analytes. PLS is a multivariate statistical method widely used in spectroscopy, as it combines dimensionality reduction and predictive modeling within a single framework [20]. The algorithm projects both the spectral variables (matrix X) and concentration variables (matrix Y) into a new space of latent variables to maximize the covariance between X and Y. These latent variables thus retain the most relevant information for prediction while minimizing noise and multicollinearity, which is a challenge in LIBS spectral datasets.

The final dataset, comprising 21 samples at maximum, was used for the initial model training. Samples with excessively high concentrations were excluded to avoid biasing the calibration and the dominance of extreme points (see the Supplementary Materials (Table S2)). The optimal number of latent variables was determined by maximizing the R^2 calibration in the NCV phase. The model performance was optimized using NCV and validated by the LOOCV procedure. As figures of merit, the R^2 and RMSE for LOOCV validation were computed to quantitatively assess the model performance.

2.6. Random Forest and Artificial Neural Network Modeling

The RF and ANN algorithms were employed as complementary approaches to PLS modeling, with the goal of exploring potential nonlinear relationships between spectral intensities and reference analyte concentrations. Both algorithms were implemented following a prior spectral selection of the most intense transitions, based on the NIST LIBS database, which provided reliable information on the strongest emission lines of each element [18].

The RF algorithm is an ensemble learning method that constructs multiple independent decision trees from random subsets of the calibration data and spectral variables. Each tree performs an individual prediction, and the final output is obtained as the average (in regression tasks) of all tree predictions. This ensemble approach reduces the risk of overfitting and enhances model robustness against experimental noise. The parameter optimization for the RF model was conducted by varying both the number of trees (estimators) and maximum leaf nodes.

ANNs are models inspired by the structure and functioning of the human brain; i.e., they are composed of multiple layers of interconnected artificial neurons. Each neuron applies a nonlinear activation function to its input data, allowing the model to capture complex and nonlinear dependencies between spectral variables and analyte concentrations [28].

For the ANN analyses, a Principal Component Analysis (PCA) preprocessing step was performed. PCA is a statistical technique that transforms the original set of correlated variables into a smaller number of uncorrelated components, known as principal components. This transformation preserves most of the variance in the dataset while reducing its dimensionality. The use of PCA is particularly important in spectroscopic and multivariate analysis because it removes redundant information, mitigates collinearity

https://doi.org/10.3390/s26031076

issues, and highlights the most prominent variance patterns. By reducing the number of variables while retaining the essential spectral features, PCA contributes to faster model training and can improve the overall stability and generalization ability of machine learning models. This step was essential for performing the ANN training, as using the raw wavelength intensities directly would have made the routine computationally prohibitive for the analysis.

The hyperparameter optimization and validation process applied to both the RF and ANN models was the same of that employed for the PLS, i.e., NCV and LOOCV. As figures of merit, the R^2 and RMSE obtained were calculated for the validation curves. The model parameters, which include the numbers of trees, leaves, neurons and hidden layers, were systematically adjusted to maximize the calibration R^2 while monitoring the RMSE in the NCV phase, thereby ensuring the stability, reproducibility, and statistical consistency of the models. Samples with concentrations below the LOD were excluded in order to ensure the statistical robustness of the model. A flowchart illustrating the data processing and analysis pipeline is presented in Figure 1.

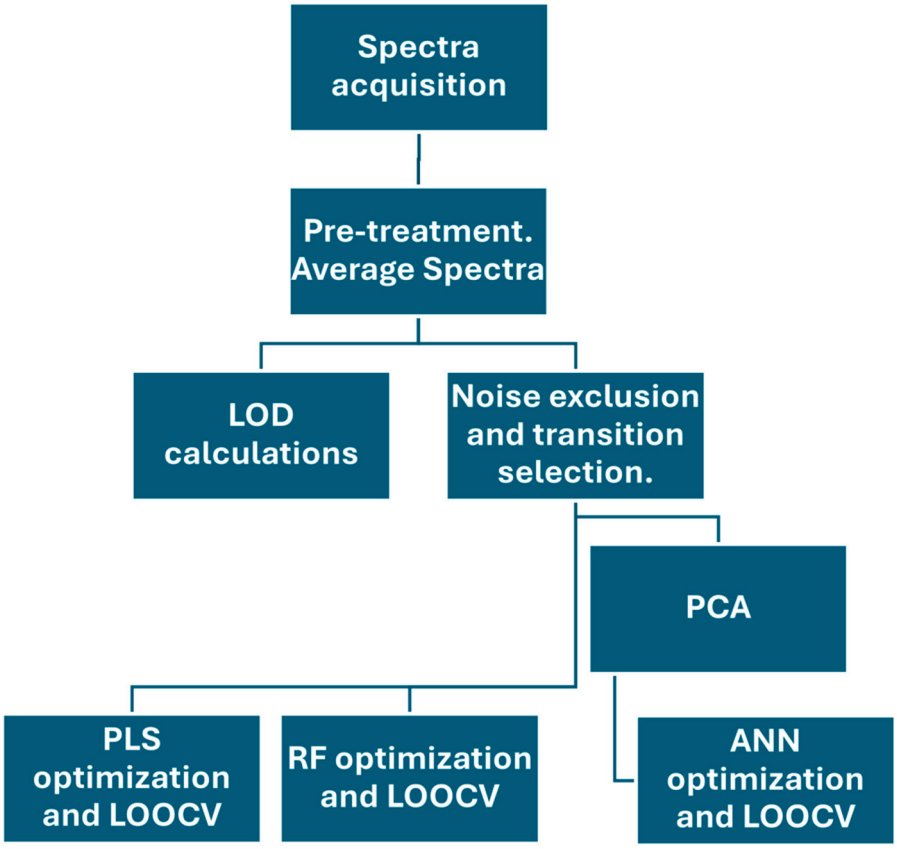


Figure 1. Schematic overview of data treatment and analysis sequence employed.

3. Results and Discussion

3.1. Results Achieved by the Higher-Spectral-Resolution Instrument

The processed spectra acquired by the higher-spectral-resolution instrument are shown in Figure 2. This figure provides a comparative visualization of selected atomic emission lines across different samples. The electronic transitions of Mg, Al, and Na are highlighted, clearly illustrating the variation in the signal intensities corresponding to the concentration differences among the samples.

https://doi.org/10.3390/s26031076

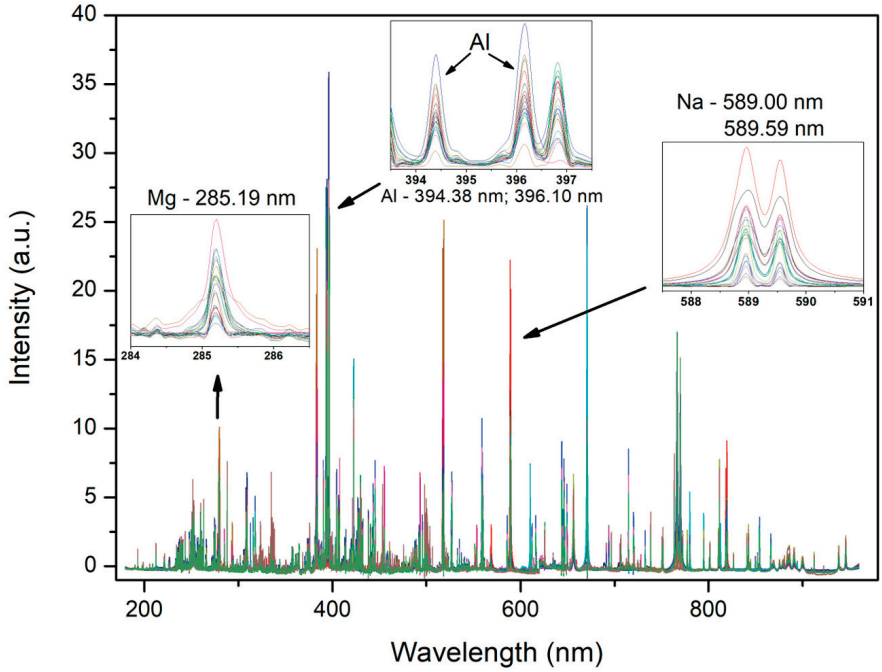


Figure 2. Averaged LIBS spectra acquired for all samples with the higher-spectral-resolution instrument.

The results summarized in Table 4 show that the higher-spectral-resolution hLIBS system exhibits a good analytical performance and was able to quantify 16 out of the 25 evaluated analytes in the samples, including most of the major oxides and several trace elements. Nine analytes presented non-trustable results (MnO, P_2O_5, CO_2, SO_3, F, Cl, Ni, Cu, Zn), which are excluded from Table 4, and could not be reliably characterized because their concentrations were below the LOD or their emission lines exhibited significant spectral interference that prevented a reliable calibration.

Table 4. The LOD, R^2 and RMSE values achieved by the application of the univariate analysis, PLS, RF and ANN algorithms to data acquired by the higher-spectral-resolution hLIBS instrument. The best-performing metrics from the validation are indicated in bold. The LOD and RMSE have the same units as the corresponding compounds (wt% for oxides and mg/kg for elements), whereas the R^2 is dimensionless.

				Univariate		PLS		RF		ANN	
	Analyte	**Conc. Range**	**LOD**	**R^2**	**RMSE**	**R^2**	**RMSE**	**R^2**	**RMSE**	**R^2**	**RMSE**
Oxides (wt%)	**SiO_2**	36.45–75.80	3.19	0.36	10.22	**0.70**	**7.52**	0.4	10.28	0.43	9.69
	Al_2O_3	2.9–59.2	0.83	0.79	5	**0.93**	**2.92**	0.75	7.26	0.83	5.30
	MgO	0.01–35.21	0.94	0.93	2.66	**0.95**	**2.22**	0.88	4.32	0.93	2.90
	CaO	0.04–15.9	1.01	0.91	1.66	0.92	1.78	**0.94**	**1.62**	0.93	1.71
	Na_2O	0.04–15.9	0.53	0.87	0.88	**0.89**	**0.86**	0.80	1.41	0.88	1.02
	K_2O	0.02–12.81	0.35	**0.96**	**0.71**	**0.92**	**0.99**	0.85	1.40	0.89	1.21
	TiO_2	0.01–2.61	0.12	0.01	0.72	0.42	0.58	0.44	**0.55**	0.40	0.71
	Fe_2O_3	0.075–19.6	1.57	0.62	3.08	**0.73**	**2.67**	0.71	3.02	0.70	3.10
Elements (mg/kg)	**Li**	1–110	1.25	0.59	21.46	**0.80**	**15.41**	0.58	22.54	0.75	17.46
	Ba	6–385	22.74	0.36	143.57	0.63	71.43	0.73	64.17	**0.76**	**62.36**
	V	0.2–340	33.34	0.54	61.75	**0.84**	**36.77**	0.79	49.40	0.81	47.10
	Cr	2–140	1.94	0.07	38.4	**0.69**	**23.51**	0.67	24.16	0.68	25.31
	Rb	1–238	16.05	0.92	20.88	**0.94**	**18.8**	0.92	24.55	0.93	23.85
	Sr	3–570	51.96	0.75	91.63	0.85	68.93	0.83	80.2	**0.92**	**47.20**

https://doi.org/10.3390/s26031076

Data in Table 4 also show that the achieved LOD values fall within the expected range for samples of similar composition [22], which confirms that the instrumentation employed is suitable for quantitative analyses of complex materials, such as rocks of different origins and compositions. Furthermore, high R^2 values and low RMSEs were achieved for most of the major oxides, with good performances for Al_2O_3, MgO, CaO, Na_2O, and K_2O, which exhibited a strong linear correlation between their spectral intensities and reference concentrations.

The three algorithms demonstrated distinct but complementary performances. In particular, the PLS algorithm provided a consistent performance across most analytes, thereby confirming its effectiveness in modeling predominantly linear relationships. Differently, the RF and ANN appeared to be more effective at capturing nonlinear dependencies, particularly for minor elements and analytes affected by multiple spectral interferences. This complementarity highlights the advantage of combined (multi-algorithm) modeling approaches in achieving more robust and generalizable LIBS calibrations.

In conclusion, the higher-spectral-resolution LIBS system demonstrated a broad and precise analytical capability, allowing for the identification of both major oxides and trace elements with high reliability.

Overall, the PLS model exhibited the best performance in the quantification of the investigated elements and oxides. For some analytes, i.e., CaO, TiO_2, Ba and Sr, PLS provided inferior but comparable results, although its predictive accuracy was nearly equivalent. Only for Ba and Sr did the ANN model demonstrate a clearly superior performance. This discrepancy might be attributed to electronic transition interferences or co-dependencies arising from fluctuations of other constituents, a phenomenon also reported in similar studies [22]. Moreover, the strategies adopted here for hyperparameter optimization and validation substantially minimize the risk of overfitting [26], thereby ensuring a more reliable estimation of the model's predictive capability. For the analysis of TiO_2, the results appear limited, indicating the need for more samples with a broader concentration range for further investigation.

Based on the optimal results achieved for each algorithm (PLS, RF, or ANN) from the validation in Table 4, scatter plots were constructed comparing the predicted analyte concentration against the actual measured concentration. For most measurements, the multivariate analyses yielded superior results when compared to the univariate approach. The only exception was K_2O, for which a slight improvement was observed using univariate analysis, with the R^2 increasing from 0.92 to 0.96 and the RMSE decreasing from 0.99 to 0.71 wt%. In this specific case, the selected emission line (693.63 nm; Table 2) effectively captured the concentration-dependent behavior. Additionally, the oxides MgO, CaO, and Na_2O, as well as the element Rb, also produced satisfactory results under univariate analysis, although their performances remained slightly inferior to those achieved with the multivariate methods. Figure 3 presents the validation plots for the oxides, while Figure 4 displays the corresponding plots for the elements.

3.2. Results Achieved by the Lower-Spectral-Resolution Instrument

Figure 5 presents the acquired averaged LIBS spectra for the lower-spectral-resolution instrument, highlighting the electronic transitions of Mg, Al, and Na. The intensity variations of these emission lines correspond to concentration differences among the samples.

https://doi.org/10.3390/s26031076

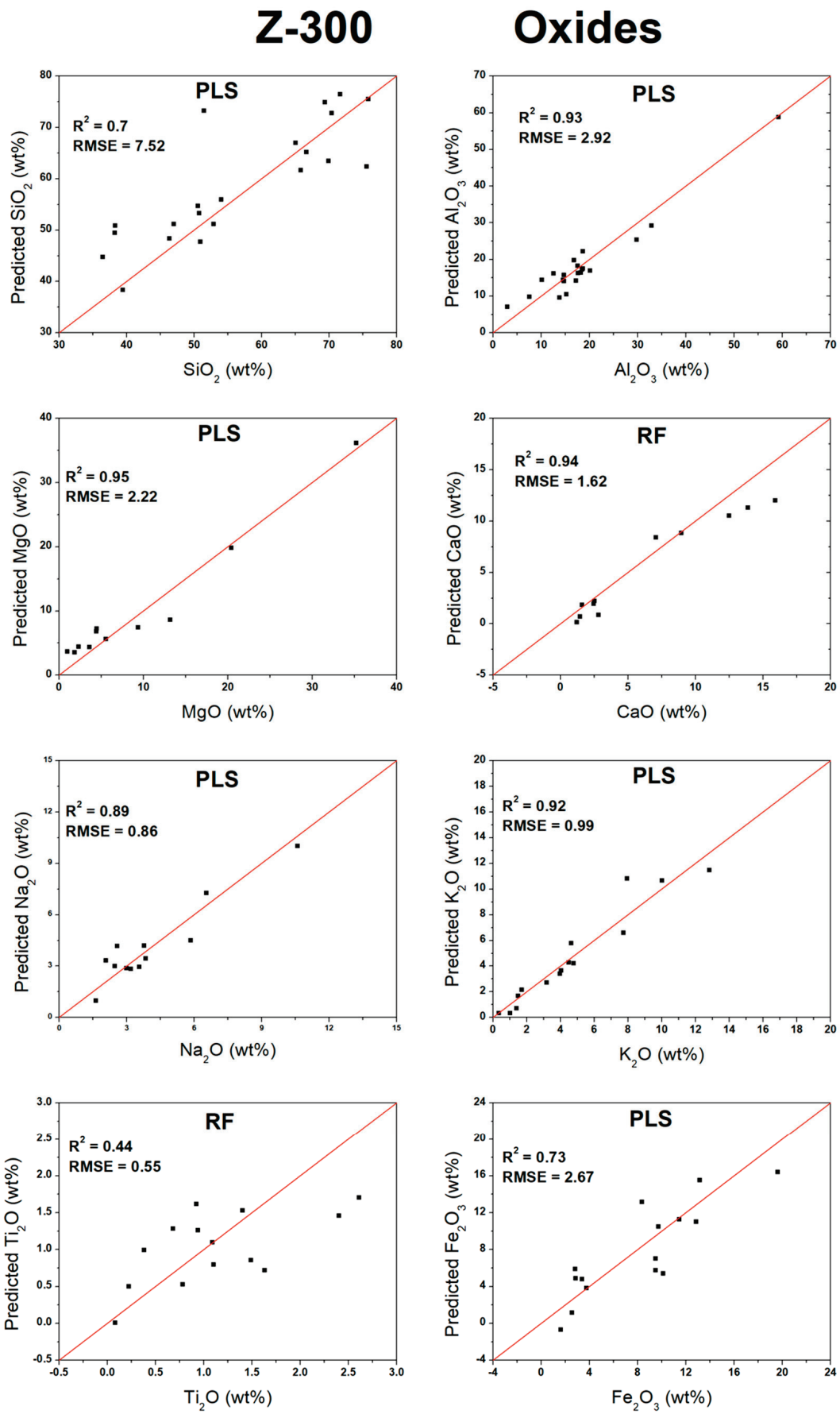


Figure 3. Validation curves for oxides measured by higher-spectral-resolution instrument.

https://doi.org/10.3390/s26031076

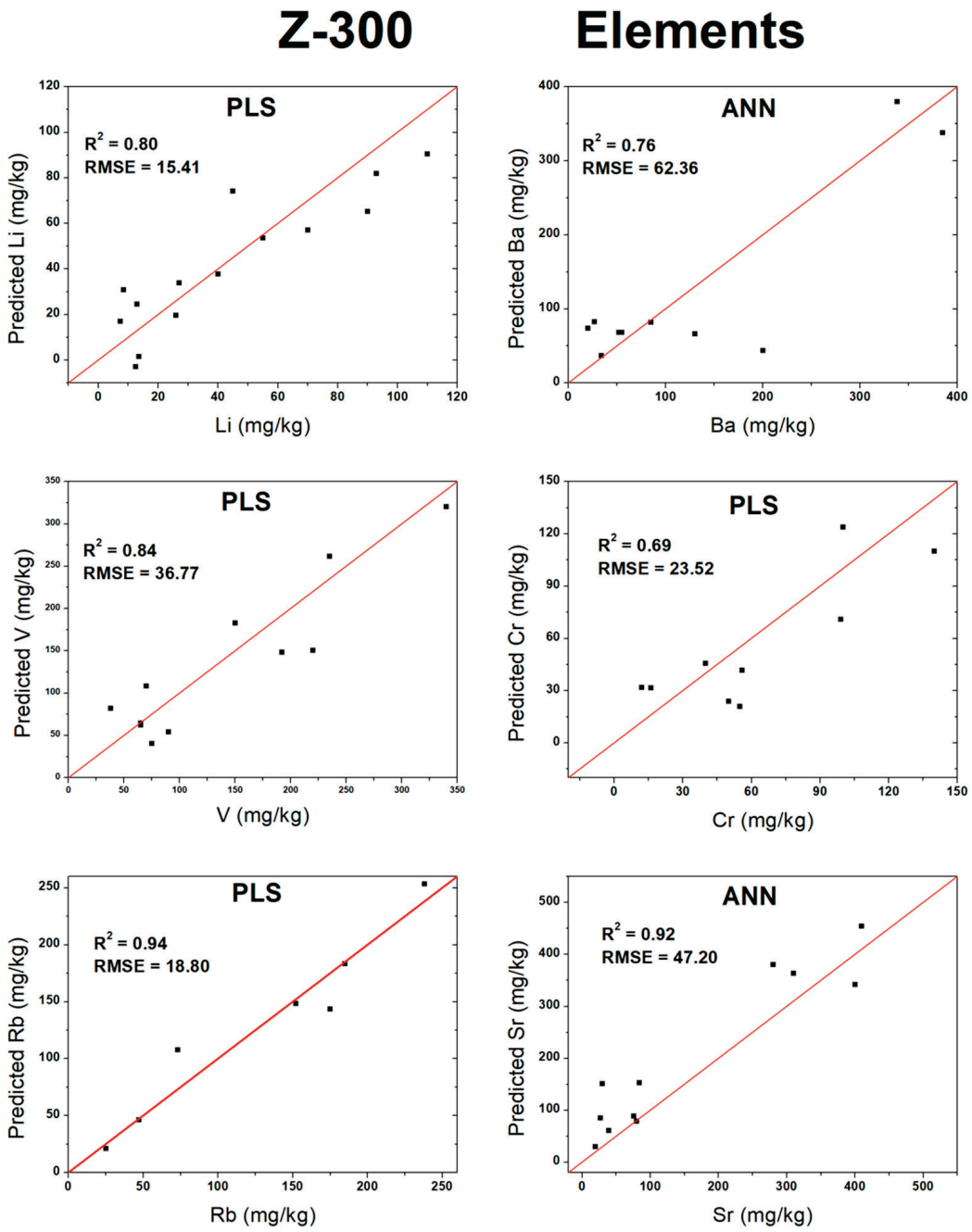


Figure 4. Validation curves for atomic elements measured by higher-spectral-resolution instrument.

The lower-spectral-resolution instrument was able to satisfactorily quantify only 11 out of the 25 analytes (Table 5), using the same calibration and validation criteria. Nevertheless, the lower-spectral-resolution instrument still provided very good results for Al_2O_3, MgO, CaO, and Na_2O, with R^2 values above 0.9, which indicates that, despite its optical limitations, the system can still be useful for process control applications or the rapid screening of homogeneous samples. In particular, the analyte K_2O showed a poorer performance for all models, likely because its main emission line (≈766 nm) lies near the upper end of the instrument's spectral range, where detector gain and sensitivity decrease. This effect is well known and reported in the literature as a common limitation of spectrometers equipped with short-range linear CCD detectors [29]. TiO_2, Fe_2O_3, and Cr show limited results, indicating that further studies are required to improve their performances. Be and Pb, although also limited, exhibited results that indicate potential

https://doi.org/10.3390/s26031076

for future measurements. Overall, the multivariate analyses once again outperformed the univariate approach. The only exception was Cr, for which the R^2 increased from 0.48 to 0.63 when using univariate analysis. Nevertheless, this improvement remains limited, indicating that the quantitative analysis for low-concentration elements is constrained when using a low-resolution spectrometer. Reasonable results were obtained with univariate analysis for the oxides Al_2O_3, MgO, and Na_2O, suggesting that univariate approaches may still be applicable for these specific cases.

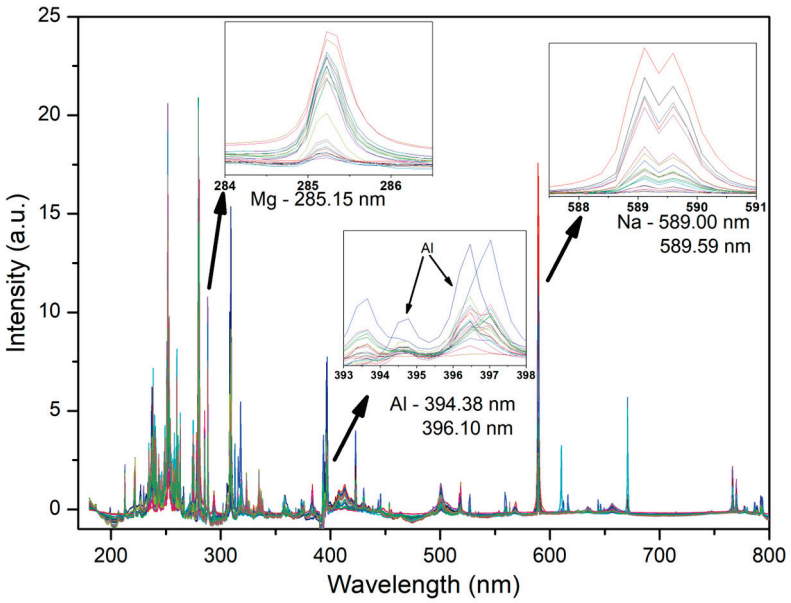


Figure 5. Averaged LIBS spectra for all samples acquired with lower-spectral-resolution instrument.

Table 5. The LOD, R^2 and RMSE values achieved by application of the univariate analysis, PLS, RF and ANN algorithms to data acquired by the lower-spectral-resolution instrument. The best-performing metrics from the validation are indicated in bold. The LOD and RMSE have the same units as the corresponding compounds (wt% for oxides and mg/kg for elements), whereas R^2 is dimensionless.

				Univariate		PLS		RF		ANN	
	Analyte	**Conc. Range**	**LOD**	**R^2**	**RMSE**	**R^2**	**RMSE**	**R^2**	**RMSE**	**R^2**	**RMSE**
Oxides (wt%)	**SiO_2**	36.45–75.80	1.62	0.58	8.29	**0.73**	**7**	0.65	7.58	0.58	8.40
	Al_2O_3	2.9–59.2	1.57	0.89	3.67	**0.94**	**2.9**	0.85	6.88	0.77	5.39
	MgO	0.01–35.21	1.76	0.82	4.25	0.72	4.48	0.82	4.23	**0.94**	**2.25**
	CaO	0.04–15.9	0.52	0.74	2.69	0.75	2.95	0.93	1.43	**0.94**	**1.34**
	Na_2O	0.04–15.9	0.23	0.82	1.08	**0.93**	**0.72**	0.79	1.41	0.89	0.93
	K_2O	0.02–12.81	2.21	0.20	3.28	**0.54**	**2.46**	0.48	2.76	0.44	3.02
	TiO_2	0.01–2.61	0.43	0.22	0.67	0.40	0.75	0.43	0.68	**0.44**	**0.54**
	Fe_2O_3	0.075–19.6	1.60	0.29	4.35	0.29	5.44	**0.38**	**4.11**	0.34	4.70
Elements (mg/kg)	**Be**	0.2–35	1.90	0.08	10.32	**0.94**	**5.21**	0.70	8.62	0.67	8.79
	Cr	2–140	3.04	**0.63**	**21.51**	**0.48**	**31.12**	0.45	35.2	0.43	39.7
	Pb	2–240	14.54	0.30	69.72	0.25	84.9	0.36	75.3	**0.81**	**44.21**

Based on the optimal results achieved for each algorithm (PLS, RF, or ANN) from the validation shown in Table 5, scatter plots were constructed comparing the predicted analyte concentrations against the measured concentrations. Figure 6 presents the validation plots for the oxides, while Figure 7 displays the corresponding plots for the elements.

https://doi.org/10.3390/s26031076

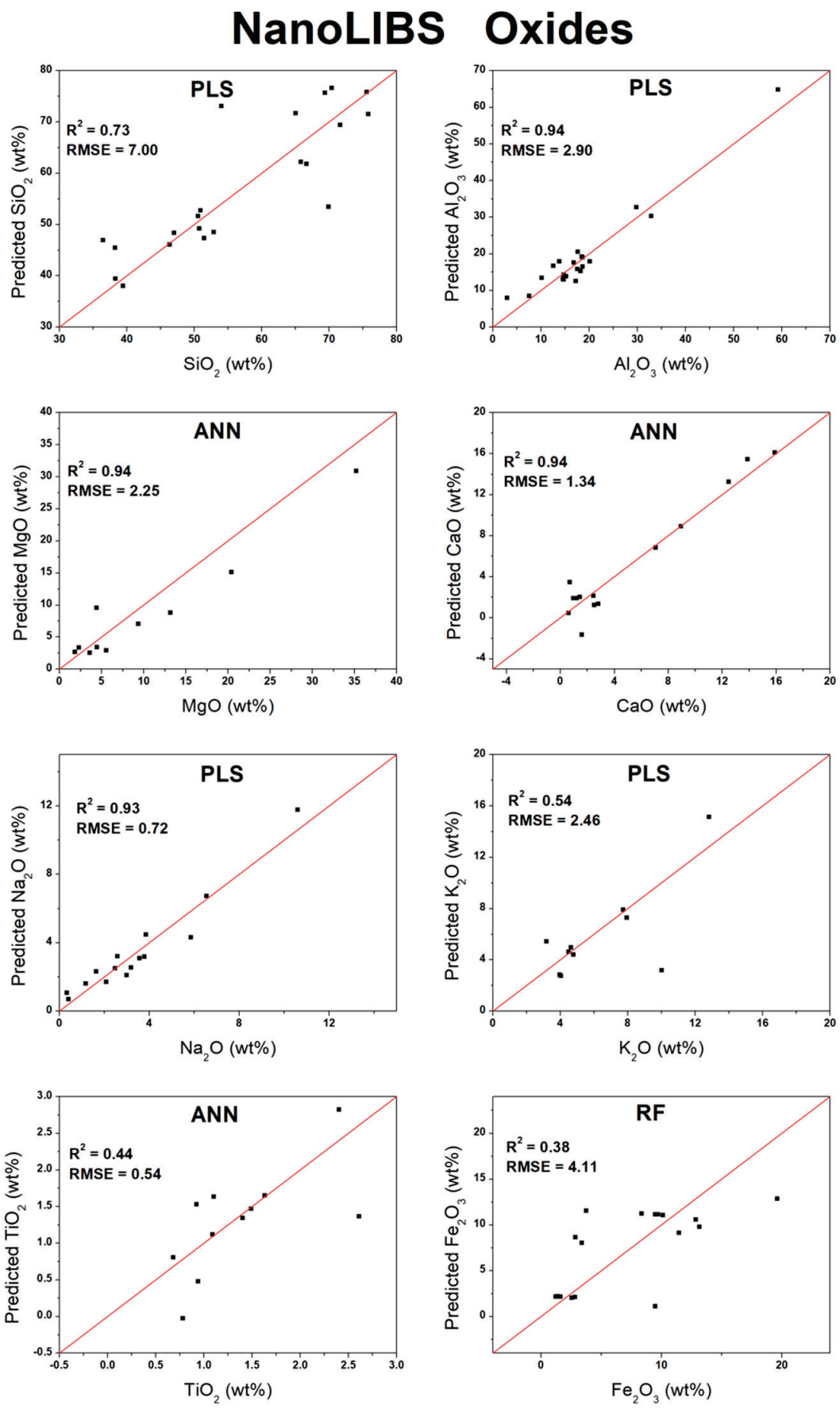


Figure 6. Validation curves for oxides measured by lower-spectral-resolution instrument.

https://doi.org/10.3390/s26031076

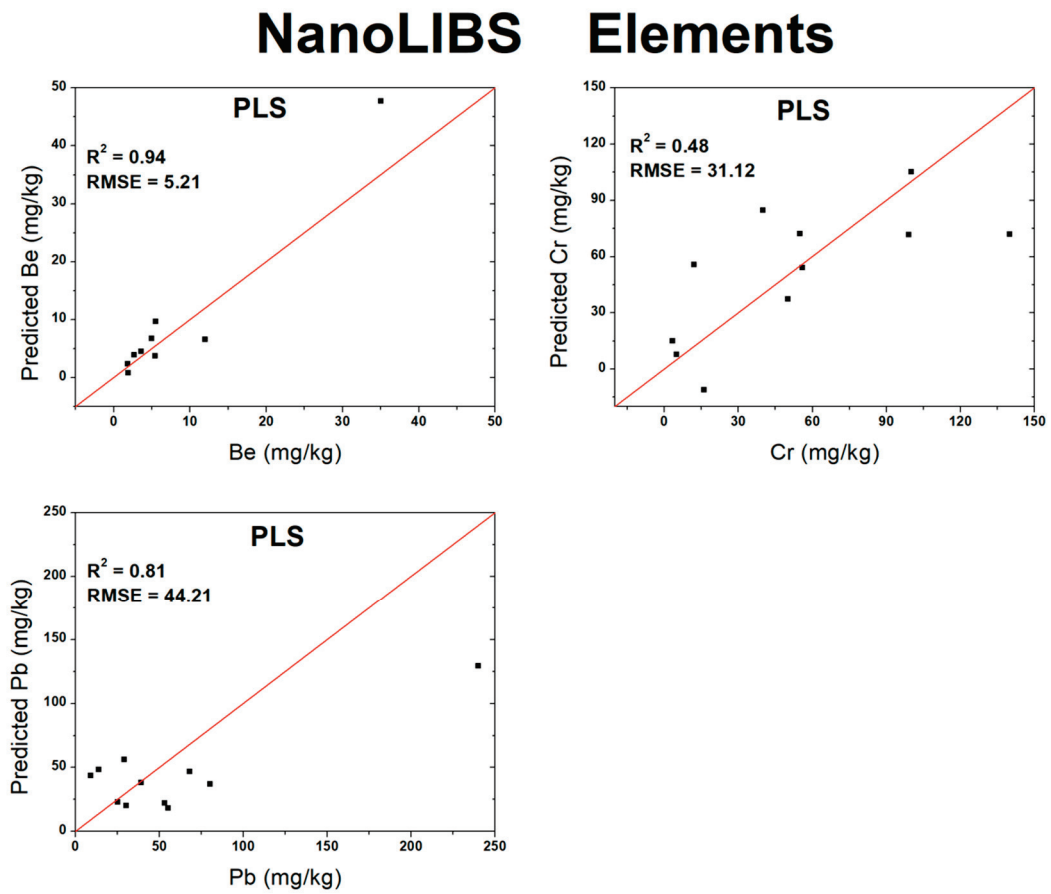


Figure 7. Validation curves for atomic elements measured by lower-spectral-resolution instrument.

3.3. Complementary Performances of the Two Instruments

The results obtained indicated that, as expected, the two instruments feature different analytical performances, which suggests that a higher spectral resolution and optical sensitivity are critical for improving the analytical accuracy and quantification capability. In particular, the spectral resolution was the key factor determining the performance of multivariate LIBS calibrations. A direct comparison of the spectra acquired with the two instruments (Figures 2 and 5) reveals a clear difference in the spectral resolutions between them, highlighting their different analytical capabilities. The main limitations were related to the lower spectral resolution and reduced signal-to-noise (SNR) ratio, which hinder the discrimination of closely spaced spectral lines and increase the overlap of transitions. These limitations directly affect the system's ability to perform automatic modeling and reduce the reliability of multivariate calibrations, mainly for trace elements. While one instrument was able to model both major oxides and trace elements with good stability, the other system exhibited some limitations in sensitivity and selectivity, especially for low-concentration analytes. However, one point that should be highlighted is the ability of the lower-resolution instrument to measure Pb and Be, with some limitations, which is an outcome that the higher-resolution system was unable to achieve. This difference may be associated with intrinsic factors, such as spectrometer gain settings or the greater ease of data processing under these conditions. It should also be noted that, in this case, fewer samples were analyzed and, specifically for Be and Pb, the concentration distributions were not homogeneous, which may have influenced the results. In this context, the findings indicate the potential for application; however, a larger number of samples must be included to ensure greater robustness.

https://doi.org/10.3390/s26031076

Another possible cause of the different performances of the two instruments can be attributed to the different laser raster grids used; i.e., while the one has a fixed grid, the other allows the user to modify the grid, thereby improving its number. However, the different spectral ranges of the two instruments appeared to not have affected their overall performances.

In particular, the LODs achieved with the higher-spectral-resolution system were systematically lower for most of the reported elements. For instance, the LOD for K_2O decreased from 2.21 wt% (lower-resolution system) to 0.35 wt% (higher-resolution system), and for TiO_2, these values decreased from 0.43 wt% to 0.12 wt%. Lower LODs are directly associated with improved SNRs, enabling the reliable detection of smaller concentrations, a critical factor for trace element analysis in geochemistry [30].

Furthermore, the higher-spectral-resolution instrument enabled the construction of good models ($R^2 \geq 0.7$) for a good number of elements, especially the trace elements Li, Ba, V, Rb, and Sr, whereas not-so-robust models were achieved by the lower-spectral-resolution instrument. In fact, the low-resolution spectrometer was only able to analyze three trace elements (Be, Cr and Pb), and even then, with limitations that need to be further investigated. This result reflects the greater spectral stability and reproducibility of the higher-spectral-resolution instrument, which can minimize pulse-to-pulse fluctuations that weaken the signal–concentration correlation.

The RMSE results achieved with the higher- and lower-spectral-resolution systems are compared in Table 6 with those of a previous study by Ytsma et al. [22], who used PLS on a similar sample set consisting of 2000 rock standards of the Mount Holyoke College (MHC) Mineral Spectroscopy Laboratory using the SciAps Z-300 (higher-resolution) instrument. However, these authors adopted a different protocol, including the collection of three spectra from each sample, each of which was the culmination of a 4×3 plasma grid. Despite the difference in the number nature and origin of the samples, the overall performance achieved in this work is surprisingly comparable and appears to capture the range of LIBS accuracies that can be achieved with these instruments for diverse geological samples and diverse modeling approaches. In particular, our work comprises a smaller sample set, incorporates an internal hyperparameter selection scheme (NCV), with LOOCV, and applies the PLS, RF and ANN modeling approaches.

Table 6. A comparison of the validation errors (RMSE) achieved with the higher-spectral-resolution and lower-spectral-resolution instruments and the literature data from Ytsma et al. [22].

Oxides	Higher Spectral Resolution (wt%)	Lower Spectral Resolution (wt%)	Ytsma et al. [22] (wt%)
SiO_2	7.52	7.00	8.61
Al_2O_3	2.95	2.90	3.38
MgO	2.22	2.25	4.41
CaO	1.62	1.34	3.08
Na_2O	0.86	0.72	1.09
K_2O	0.99	2.46	1.52
TiO_2	0.55	0.54	0.77
Fe_2O_3	2.67	4.11	3.84
Elements	**(mg/kg)**	**(mg/kg)**	**(mg/kg)**
Li	15.41	N/A	21
Be	N/A	5.21	N/A
Ba	62.36	N/A	565
V	36.77	N/A	N/A
Cr	23.51	31.12	239
Rb	18.80	N/A	N/A
Sr	47.20	N/A	N/A
Pb	N/A	44.21	19

N/A: No prediction (<LOD).

https://doi.org/10.3390/s26031076

Among the major oxides, there is strong agreement among the RMSE values, which are closely similar. For Li, the results from the higher-spectral-resolution instrument were very similar to those found by Ytsma et al. [22]. For Ba and Cr, the analysis performed in this work shows a superior performance, although the sample set featured substantially lower mean concentrations, which may have influenced the outcomes. In contrast, for Pb, the result was slightly inferior to the one achieved by the lower-spectral-resolution instrument.

Despite the superiority of the higher-spectral-resolution system, the lower-spectral-resolution instrument demonstrated a comparable performance for a few analytes that could be successfully modeled, i.e., the major oxides Al_2O_3, MgO, CaO and Na_2O with relatively high concentrations in the clay matrix (e.g., Al_2O_3: 18.6%wt; CaO: 3.53%wt). As the elements present at higher abundances produce sufficiently strong, stable, and prominent spectral lines to correlate with the concentration, the instrumental limitations of the lower-spectral-resolution system (e.g., spectral resolution or SNR) are not critical factors [31].

3.4. Synergy Among the Calibration Techniques (PLS, RF, and ANN)

The combined use of PLS, RF, and ANN proved to be a possible and complementary strategy for assessing LIBS data quality. The PLS algorithm consistently showed robustness, providing high-quality models ($R^2 > 0.9$) for most of the major-element data acquired by both instruments. The strength of this algorithm lies in its capacity for handling multicollinear spectral data through projection into latent variables, which makes it one of the most stable and interpretable methods [23]. The quantitative performance achieved for major elements deserves further discussion considering the intrinsic plasma-related effects in LIBS, particularly self-absorption (SA). The deviations from linearity observed for major elements can be partially attributed to plasma SA, a well-known phenomenon in LIBS analyses. SA occurs when atoms in the ground state, located in cooler and denser regions of the plasma, partially reabsorb the radiation emitted from hotter regions, which occurs especially for intense spectral lines of elements present at high concentrations. This effect leads to saturation, peak flattening, and line broadening, ultimately resulting in a loss of linearity between the emission intensity and elemental concentration, thereby degrading the quantitative calibration performance. In particular, SA is especially relevant for major elements such as Mg, Al, Ca, and Na, whose concentrations in geological matrices often exceed 1%wt. Consequently, the elevated RMSE values and reduced linear correlations that are achieved for these elements should be interpreted by considering them as intrinsic physical limitations of the LIBS plasma rather than as shortcomings of the modeling strategy. Thus, wavelength intensities rather than integrated peak areas were used in this work. For transitions affected by SA, the line wings often preserve good linearity, whereas the line core is more strongly affected by saturation, as was observed in our previous studies [32].

Differently, both the machine learning algorithms RF and ANN were able to capture complex nonlinear relationships, occasionally outperforming PLS. For example, the ANN achieved an R^2 of 0.94 for MgO data acquired with the lower-spectral-resolution instrument, which suggests a good predictive power.

The complementarity among the methods used is thus evident; i.e., when one algorithm fails to model an element effectively, the other is often successful. For instance, for TiO_2 data acquired by the higher-spectral-resolution instrument, all algorithms achieved limited performances ($R^2 \approx 0.42$–0.44), with the RF being more accurate. Yet the consistency across them confirms that Ti transitions possibly suffer from spectral interferences or matrix effects. This multi-algorithm approach adds robustness to the study, allowing for the selection of the best model for each element and enabling cross-validation [33].

https://doi.org/10.3390/s26031076

One aspect that deserves attention is, however, the limited performance for SiO_2 data. Although SiO_2 represented the major constituent of the sample (56.5%wt), it exhibited a limited calibration performance by the higher-spectral-resolution instrument (best $R^2 = 0.72$ with PLS) and lower-spectral-resolution instrument (best $R^2 = 0.73$ with PLS). As Si features numerous strong spectral lines, a higher R^2 value is expected; thus, signal saturation of the most intense Si lines might occur, which restricts the analytical sensitivity or matrix effects [34]. Future experiments should address this issue by using a lower laser power.

4. Conclusions

In summary, the results of this study confirm the superior performance of the higher-resolution system in terms of sensitivity (lower LODs), versatility (a greater number of calibrated elements), and reliability (higher R^2 values). Nonetheless, this study also demonstrates that the lower-resolution instrument remains a practically valuable and economically viable tool for the routine quantification of major elements in rocks. Furthermore, the use of multiple calibration algorithms is strongly recommended to account for complex or nonlinear analytical behaviors that may influence LIBS systems.

The implementation of a complementary multi-algorithm approach based on the use of PLS, RFs, and ANNs for the quantitative determination of oxides and major, minor, and trace elements in a set of geochemical reference materials proved to be a powerful and complementary strategy for assessing the LIBS data quality in hLIBS instruments. In particular, PLS consistently represents a robust and interpretable model for linearly correlated data, while the machine learning techniques (RF and ANN) capture complex and nonlinear relationships. This synergy allows for the selection of the most appropriate model for each specific element-instrument combination, enhancing the overall robustness and reliability of the LIBS analytical technique. The results were also compared with those obtained from univariate analysis, demonstrating that the multivariate methods achieved superior performances.

The results of this work demonstrate evidently different performances between the two instruments, primarily attributable to their distinct configurations. The instrument with a higher spectral resolution, broader wavelength range, variable raster grid, and higher pulse energy achieved superior analytical capabilities, enabling the development of calibration models for 16 out of 25 analytes, and exhibited lower average LODs and greater predictive accuracy for both major oxides and trace elements. The other system was effective for the quantitative analysis of 11 analytes out of 25, with a limited performance in trace elements, showing, however, a good performance primarily for major oxides (e.g., Al_2O_3, MgO, CaO), the high concentration and strong emission lines of which mitigated its limitations in terms of the spectral resolution and SNR ratio.

In conclusion, the choice between the two types of hLIBS instruments depends heavily on the specific application requirements. For applications demanding high sensitivity, broader elemental coverage, and higher quantification accuracy for trace elements, the higher-spectral-resolution instrument shows a superior performance; however, the lower-spectral-resolution instrument remains a viable and cost-effective option for the rapid field screening and quantification of major elements.

Finally, the results of this work underscore the maturity of hLIBS as a powerful tool for in situ geochemical analysis and highlight the critical importance of instrumental specifications and robust data processing in achieving optimal analytical results. Furthermore, in the future, the algorithm and hyperparameter selection used in this work will be trained by an automated (AI-driven) system and will hopefully be incorporated directly into the software of the handheld instruments to allow for the achievement of a direct in situ response, making their use easier even for non-trained people.

https://doi.org/10.3390/s26031076

Supplementary Materials: The following supporting information can be downloaded at: https://www.mdpi.com/article/10.3390/s26031076/s1, Figure S1: Calibration curves–Z300 LIBS–oxides; Figure S2: Calibration curves–Z300 LIBS–elements; Figure S3: Calibration curves–NanoLIBS–oxides; Figure S4: Calibration curves–NanoLIBS–elements; Figure S5: Validation curves–Z300 LIBS–oxides; Figure S6: Validation curves–Z300 LIBS–elements; Figure S7: Validation curves–NanoLIBS–oxides; Figure S8: Validation curves–NanoLIBS–elements; Figure S9: Evolution of the root-mean-square error (RMSE) for calibration and validation datasets as a function of the number of training epochs for MgO measured in the lower-spectral-resolution instrument. The convergence of both curves, together with the analysis of the LOOCV results (R^2 = 0.94), indicates a low likelihood of overfitting and the high generalization capability of the model for predicting external samples; Figure S10: Evolution of the root-mean-square error (RMSE) for calibration and validation datasets as a function of the number of training epochs for CaO measured in the lower-spectral-resolution instrument. The convergence of both curves, together with the analysis of the LOOCV results (R^2 = 0.94), indicates a low likelihood of overfitting and the high generalization capability of the model for predicting external samples. Table S1: List of the 21 Certified Reference Materials and their origin; Table S2: Oxides and elements chemical composition for the 21 Certified Reference Materials; Table S3: Optimal hyperparameter values selected for each classifier (PLS, RF, and ANN) during the LOOCV procedure.

Author Contributions: Conceptualization, G.S.S. and B.M.; Methodology, G.S.S. and B.M.; Formal Analysis, G.S.S. and B.M.; Investigation, G.S.S. and B.M.; Resources, G.S.S., B.M., O.D.P., R.T. and I.A.; Machine Learning Design, B.M. and G.S.S.; Writing—Original Draft Preparation, G.S.S. and B.M.; Writing—Review and Editing, G.S.S., B.M., O.D.P., R.T. and I.A.; Supervision, G.S.S. and B.M. All authors have read and agreed to the published version of the manuscript.

Funding: Marangoni thanks Conselho Nacional de Desenvolvimento Cientifico e Tecnologico-CNPq (310376/2023-8; 402863/2024-0, and 200560/2025-5).

Data Availability Statement: All data analyzed during this study are included in this published article for any further request you're welcome to get in touch.

Conflicts of Interest: The authors declare no conflict of interest.

References

1. Lemière, B.; Harmon, R.S. XRF and LIBS for field geology. In *Portable Spectroscopy and Spectrometry*; Crocombe, R., Leary, P., Kammrath, B., Eds.; JohnWiley and Sons: Hoboken, NJ, USA, 2021; pp. 455–497.
2. Senesi, G.S.; Harmon, R.S.; Hark, R.R. Field-portable and handheld laser-induced breakdown spectroscopy: Historical review, current status, and future prospects. *Spectrochim. Acta Part B At. Spectrosc.* **2021**, *175*, 106013. [CrossRef]
3. Senesi, G.S. Handheld Laser-Induced Breakdown Spectroscopy (hLIBS) Applied to On-Site Mine Waste Analysis/Evaluation in View of Its Recycling/Reuse. *Chemosensors* **2025**, *13*, 41. [CrossRef]
4. Senesi, G.S. Laser-Induced Breakdown Spectroscopy (LIBS) applied to terrestrial and extraterrestrial analogue geomaterials with emphasis to minerals and rocks. *Earth Sci. Rev.* **2014**, *139*, 231–267. [CrossRef]
5. Harmon, R.S.; Senesi, G.S. Laser-Induced Breakdown Spectroscopy-A geochemical tool for the 21st century. *Appl. Geochem.* **2021**, *128*, 104929. [CrossRef]
6. Harmon, R.S.; Fabre, C.; Senesi, G.S. Laser-induced breakdown spectroscopy. In *Treatise on Geochemistry*, 3rd ed.; Anbar, A., Weis, D., Eds.; Elsevier: Amsterdam, The Netherlands, 2025; pp. 607–644.
7. Wiens, R.C.; Maurice, S.; Lasue, J.; Forni, O.; Anderson, R.B.; Clegg, S.; Bender, S.; Blaney, D.; Barraclough, B.L.; Cousin, A.; et al. Pre-flight calibration and initial data processing for the ChemCam laser-induced breakdown spectroscopy instrument on the Mars Science Laboratory rover. *Spectrochim. Acta Part B At. Spectrosc.* **2013**, *82*, 1–27. [CrossRef]
8. Connors, B.; Somers, A.; Day, D. Application of handheld laser-induced breakdown spectroscopy (LIBS) to geochemical analysis. *Appl. Spectrosc.* **2016**, *70*, 810–815. [CrossRef]
9. Guo, G.; Niu, G.; Lin, Q.; Wang, S.; Tian, D.; Duan, Y. Compact instrumentation and (analytical) performance evaluation for laser-induced breakdown spectroscopy. *Instrum. Sci. Technol.* **2019**, *47*, 70–89. [CrossRef]

https://doi.org/10.3390/s26031076

10. Kumar, N.; Lan, Y.-J.; Lu, Y.; Li, Y.-D.; Geng, Y.-J.; Zheng, R.-E. Development of a micro-joule portable LIBS system and the preliminary results for mineral recognition. *Optoelectron. Lett.* **2018**, *14*, 401–404. [CrossRef]
11. Meng, D.; Zhao, N.; Ma, M.; Fang, L.; Gu, Y.; Jia, Y.; Liu, J.; Liu, W. Application of a mobile laser-induced breakdown spectroscopy system to detect heavy metal elements in soil. *Appl. Opt.* **2017**, *56*, 5204–5210. [CrossRef]
12. Pahikkala, T.; Airola, A.; Pietilä, S.; Shakyawar, S.; Szwajda, A.; Tang, J.; Aittokallio, T. Toward more realistic drug–target interaction predictions. *Brief. Bioinform.* **2015**, *16*, 325–337.
13. Fortunati, S.; Giannetto, M.; Rozzi, A.; Corradini, R.; Careri, M. PNA-functionalized magnetic microbeads as substrates for enzyme-labelled voltammetric genoassay for DNA sensing applied to identification of GMO in food. *Anal. Chim. Acta* **2021**, *1153*, 338297. [CrossRef] [PubMed]
14. PereiraNaves, S.D.; Fernandes, V.F.; Ribeiro, M.C.; França, T.; Senesi, G.S.; Sanches, S.; Galvaõ, C.; Mantovani, C.; Cena, C.; Marangoni, B. Early and noninvasive bird Ggender identification by ATR-FTIR spectra coupled with a randon forest algorithm. *ACS Omega* **2025**, *10*, 49118–49125. [CrossRef]
15. Sreenivasulu, G.; Rao, R.R.; Babu, B.S.; Swathantra, A.; Srinivasulu, A. Predictive modeling of mean residence time in bubble column reactors: A machine learning approach using linear regression, random forest, and neural networks. *Biotech. Res. Asia* **2025**, *22*, 763–778. [CrossRef]
16. Zhou, W.; Yan, Z.; Zhang, L. A comparative study of 11 non-linear regression models highlighting autoencoder, DBN, and SVR, enhanced by SHAP importance analysis in soybean branching prediction. *Sci. Rep.* **2024**, *14*, 5905. [CrossRef]
17. Senesi, G.S.; Allegretta, I.; Marangoni, B.S.; Ribeiro, M.C.S.; Porfido, C.; Terzano, R.; De Pascale, O.; Eramo, G. Geochemical identification and classification of cherts using handheld laser induced breakdown spectroscopy (LIBS) supported by supervised machine learning algorithms. *Appl. Geochem.* **2023**, *151*, 105625. [CrossRef]
18. NIST Database. 2025. Available online: https://physics.nist.gov/PhysRefData/ASD/LIBS/libs-form.html (accessed on 10 September 2025).
19. Barnes, R.J.; Dhanoa, M.S.; Lister, S.J. Standard Normal Variate Transformation and De-Trending of Near-Infrared Diffuse Reflectance Spectra. *Appl. Spectrosc.* **1989**, *43*, 772–777. [CrossRef]
20. Kabir, M.H.; Guindo, M.L.; Chen, R.; Sanaeifar, A.; Liu, F. Application of Laser-Induced Breakdown Spectroscopy and chemometrics for the quality evaluation of foods with medicinal properties: A review. *Foods* **2022**, *11*, 2051. [CrossRef]
21. Casanova, L.; Beldjilali, S.A.; Bilge, G.; Sezer, B.; Motto-Ros, V.; Pelascini, F.; Bănaru, D.; Hermann, J. Evaluation of limits of detection in laser-induced breakdown spectroscopy: Demonstration for food. *Spectrochim. Acta Part B At. Spectrosc.* **2023**, *207*, 106760. [CrossRef]
22. Ytsma, C.R.; Knudson, C.A.; Dyar, M.D.; McAdam, A.C.; Michaud, D.D.; Rollosson, L.M. Accuracies and detection limits of major, minor, and trace element quantification in rocks by portable laser-induced breakdown spectroscopy. *Spectrochim. Acta Part B At. Spectrosc.* **2020**, *171*, 105946. [CrossRef]
23. Wold, S.; Sjöström, M.; Eriksson, L. PLS-regression: A basic tool of chemometrics. *Chemom. Intell. Lab. Syst.* **2001**, *58*, 109–130. [CrossRef]
24. D'Andrea, E.; Pagnotta, S.; Grifoni, E.; Lorenzetti, G.; Legnaioli, S.; Palleschi, V.; Lazzerini, B. An artificial neural network approach to laser-induced breakdown spectroscopy quantitative analysis. *Spectrochim. Acta Part B At. Spectrosc.* **2014**, *99*, 52–58. [CrossRef]
25. Guo, S.; Bocklitz, T.; Neugebauer, U.; Popp, J. Common mistakes in cross-validating classification models. *Anal. Methods* **2017**, *9*, 4410–4417. [CrossRef]
26. Vabalas, A.; Gowen, E.; Poliakoff, E.; Casson, A.J. Machine learning algorithm validation with a limited sample size. *PLoS ONE* **2019**, *14*, e0224365. [CrossRef]
27. Scheda, R.; Diciotti, S. Explanations of Machine Learning Models in Repeated Nested Cross-Validation: An Application in Age Prediction Using Brain Complexity Features. *Appl. Sci.* **2022**, *12*, 6681. [CrossRef]
28. Motto-Ros, V.; Koujelev, A.S.; Osinski, G.R.; Dudelzak, A.E. Quantitative multi-elemental laser-induced breakdown spectroscopy using artificial neural networks. *J. Eur. Opt. Soc. Rapid Publ.* **2008**, *3*, 08011. [CrossRef]
29. Limbeck, A.; Brunnbauer, L.; Lohninger, H.; Pořízka, P.; Modlitbová, P.; Kaiser, J.; Janovszky, P.; Kéri, A.; Galbács, G. Methodology and applications of elemental mapping by laser induced breakdown spectroscopy. *Anal. Chim. Acta* **2021**, *1147*, 72–98. [CrossRef]
30. Khan, Z.H.; Ullah, M.H.; Rahman, B.; Talukder, A.I.; Wahadoszamen Md Abedin, K.M.; Haider, A.F.M.Y. Laser-Induced Breakdown Spectroscopy (LIBS) for trace element detection: A review. *J. Spectrosc.* **2022**, *2022*, 3887038. [CrossRef]
31. Zhang, P.; Sun, L.; Yu, H.; Zeng, P. Quantitative analysis of the main components in ceramic raw materials based on the desktop LIBS analyzer. *Plasma Sci. Technol.* **2022**, *24*, 084006. [CrossRef]

https://doi.org/10.3390/s26031076

32. Cervantes, C.; Marangoni, B.S.; Nicolodelli, G.; Senesi, G.S.; Villas-Boas, P.R.; Silva, C.S.; Nogueira, A.R.A.; Benites, V.M.; Milori, D.M.B.P. Laser-Induced Breakdown Spectroscopy Applied to the Quantification of K, Ca, Mg and Mn Nutrients in Organo-Mineral, Mineral P Fertilizers and Rock Fertilizers. *Minerals* **2024**, *14*, 1109. [CrossRef]
33. Moros, J.; Cabalín, L.M.; Laserna, J.J. Refractory residues classification strategy using emission spectroscopy of laser-induced plasmas in tandem with a decision tree-based algorithm. *Anal. Chim. Acta* **2022**, *1191*, 339294. [CrossRef] [PubMed]
34. Wangeci, A.; Knadel, M.; De Pascale, O.; Greve, M.H.; Senesi, G.S. Assessing the performance of handheld LIBS for predicting soil organic carbon and texture in European soils. *J. Anal. At. Spectrom.* **2024**, *39*, 2903–2916. [CrossRef]

Disclaimer/Publisher's Note: The statements, opinions and data contained in all publications are solely those of the individual author(s) and contributor(s) and not of MDPI and/or the editor(s). MDPI and/or the editor(s) disclaim responsibility for any injury to people or property resulting from any ideas, methods, instructions or products referred to in the content.

https://doi.org/10.3390/s26031076

sensors

MDPI

Article

Experimental Accuracy Evaluation of UAV-Based Homography for Static and Dynamic Displacement Monitoring of Structures

Ante Marendić [1,*], Dubravko Gajski [1], Ivan Duvnjak [2] and Ana Kosor [1]

[1] Faculty of Geodesy, University of Zagreb, 10000 Zagreb, Croatia; dubravko.gajski@geof.unizg.hr (D.G.); ana.kosor@geof.unizg.hr (A.K.)
[2] Faculty of Civil Engineering, University of Zagreb, 10000 Zagreb, Croatia; ivan.duvnjak@grad.unizg.hr
* Correspondence: ante.marendic@geof.unizg.hr

Abstract

Structural displacement monitoring is an essential component of structural health monitoring of bridges, providing valuable information for performance evaluation, numerical model validation, and damage detection. While conventional contact-based sensors provide high accuracy, their installation is often complex, costly, and disruptive to traffic. Recent developments in unmanned aerial vehicle (UAV) platforms and vision-based measurement techniques offer a flexible, non-contact alternative; however, platform motion remains a major source of uncertainty. This study evaluates the accuracy and operational feasibility of UAV-based homography for static and dynamic displacement monitoring. The proposed approach is validated through three complementary experimental campaigns: a controlled calibration field test, a beam static load test, and bridge monitoring under traffic loading, with direct comparison to LVDT and RTS measurements. Under controlled conditions, sub-millimetre vertical precision was achieved, with RMSE values below 0.3 mm. In full-scale bridge applications, the method captured traffic-induced displacement trends with errors generally within 1–2 mm compared to LVDT data and with RMSE values below 1.4 mm. The results demonstrate that, when appropriate reference point configuration and imaging geometry are ensured, UAV-based homography provides a practical and sufficiently accurate solution for bridge displacement monitoring which is especially important in applications where sensor installation is difficult or unsafe.

Keywords: UAV; homography; photogrammetry; displacement measurement; static displacements; dynamic displacements; LVDT; RTS

1. Introduction

The maintenance and preservation of structural integrity across the construction phases and the service life of critical infrastructure—such as bridges, high-rise buildings, and industrial facilities—is a cornerstone of modern structural engineering. Given the inevitable degradation of materials, escalating traffic loads, and the intensifying impact of climate change [1,2], the implementation of systematic Structural Health Monitoring (SHM) has transitioned from a recommendation to a technical imperative to ensure quality, safety, and serviceability. Among various response parameters, structural displacements provide one of the most direct indicators of global structural behaviour, supporting performance evaluation, numerical model validation, damage detection, and long-term condition assessment [3–5].

Conventional displacement measurement techniques, including Linear Variable Differential Transformers (LVDTs) [6], robotic total stations [7,8], GNSS-based positioning [9],

precise levelling [10], and terrestrial laser scanning [11,12], are capable of achieving high accuracy. Their application in field conditions, however, is frequently constrained by demanding installation procedures, the requirement for stable reference points, limited accessibility, and, in many cases, disruption to traffic flow [13,14].

Recent developments in vision-based measurement techniques, together with rapid advances in unmanned aerial vehicle (UAV) platforms, have enabled new possibilities for non-contact displacement monitoring [15]. UAV-based systems provide rapid deployment, flexible sensor positioning, and high spatial resolution, making them particularly attractive for bridge inspection and structural testing. Nevertheless, reliable displacement measurement from UAV imagery remains challenging, primarily due to unavoidable platform motion. Camera vibrations, rotations, and translational movements introduce apparent displacements into image sequences, which can significantly obscure the true structural response [16–18].

Displacement estimation from UAV imagery relies on a range of vision-based techniques, including three-dimensional reconstruction using structure-from-motion (SfM), planar motion compensation through homography-based correction, digital image correlation (DIC), and feature-based tracking of image sequences [19–22]. These approaches differ in computational complexity, robustness to platform motion, and suitability for field deployment, particularly under real-world environmental and operational constraints. While SfM and multi-image based methods enable full three-dimensional reconstruction, they often require dense image acquisition and significant computational effort, whereas homography-based techniques provide an efficient alternative for planar displacement monitoring in scenarios dominated by in-plane structural motion.

To mitigate UAV-induced motion effects, homography-based image stabilization techniques have been increasingly adopted. By estimating planar projective transformations between consecutive frames using stable reference points, homography allows effective compensation of camera motion without the need for explicit camera calibration or full three-dimensional reconstruction [16,23,24]. Despite encouraging results reported in previous studies, several practical challenges remain, particularly regarding reference point availability, geometric sensitivity, and robustness under real-world operating conditions.

This study investigates the accuracy and operational feasibility of UAV-based homography for monitoring static and dynamic structural displacements. Particular emphasis is placed on systematically investigating the influence of reference point configuration and their number on measurement accuracy, aspects that have received limited attention in previous studies [25,26]. The importance of measurement point configuration has also been recognized more broadly in structural health monitoring research, particularly in studies addressing optimal sensor placement and sensitivity analysis for damage identification in bridge structures [27]. Although these studies focus on different monitoring objectives, they similarly demonstrate that the spatial distribution of measurement points significantly influences identification reliability and overall system performance. This broader perspective further supports the need to systematically examine reference point configuration effects within homography-based displacement monitoring. The proposed method is evaluated through three complementary experimental campaigns, encompassing a controlled calibration test field, a static load test of the beam, and full-scale monitoring of a bridge subjected to traffic-induced dynamic deformations which enabled assessment of the method under both controlled and realistic operating conditions. The main contributions of this study can be summarized as follows:

- Experimental validation of UAV-based homography across three different campaigns.
- Systematic investigation of the influence of reference point number and spatial configuration on displacement accuracy.

https://doi.org/10.3390/s26051593

- Direct quantitative comparison with high-precision LVDT and RTS measurements under both controlled and operational conditions.
- Practical evaluation of methodological limitations and operational constraints relevant to real-world bridge monitoring.

The paper is structured as follows. Section 2 presents the experimental setup and measurement methodology, including the homography-based displacement estimation framework. Section 3 describes the three experimental campaigns and corresponding results. Section 4 discusses the accuracy, reference point configuration effects, and practical limitations of the proposed approach. Finally, Section 5 summarizes the main conclusions and outlines directions for future research.

2. Materials and Methods

2.1. Experimental Test Fields

This section describes the experimental setups used to evaluate the accuracy and applicability of the UAV-based homography method under controlled and real-world conditions. First, a controlled calibration field experiment was used to assess the influence of reference point configuration on homography stability. Second, a beam static load test enabled a direct comparison between UAV-derived displacements and high-accuracy LVDT measurements. Finally, a dynamic bridge test was conducted under real traffic loading to evaluate performance in field conditions with uncontrolled dynamic influences.

2.1.1. Calibration Field Test

The first part of the testing was done at the Institute for Photogrammetry's photogrammetric calibration field in Zagreb. This facility was used to calibrate all sensors used in this study. The calibration field is in a covered garage area, providing a stable geometric configuration and lighting conditions during taking images. There were 36 targets mounted on the walls and columns placed along the bisectors of the load-bearing columns (shown by red marks in Figure 1) and the rear walls (shown by white marks in Figure 1). There were three height levels for the targets: 0.5 m, 2.0 m, and 3.5 m arranged in a regular grid. This setup made sure that all images will have uniform image coverage and favourable photogrammetric geometry.



Figure 1. Calibration field—position of 36 targets.

The coordinates of all targets were determined using a high-precision total station (Leica TPS1201) (Leica Geosystems AG, Heerbrugg, Switzerland) through repeated observations, achieving a positional accuracy of less than 1 mm. This level of accuracy

https://doi.org/10.3390/s26051593

fully meets the requirements for high-precision photogrammetric calibration and lens distortion assessment.

In this phase, three imaging systems were utilized: a Nikon D800E camera (Nikon Corporation, Tokyo, Japan) mounted on a tripod with a SIGMA RF20/1.8 lens, a DJI Matrice 300 RTK UAV (DJI, Shenzhen, China) equipped with a DJI Zenmuse P1 camera, and a DJI Phantom 4 UAV (DJI, Shenzhen, China) featuring an FC330 camera. The significant difference in horizontal Field of View (FOV_h) between the Zenmuse P1 camera (FOV_h = 54.30°) and the other two (NIKON D800E FOV_h = 83.81°; DJI Phantom 4 FC330 FOV_h = 81.03°) leads to a significant difference in object-to-camera distance (see Table 1). Following the calibration, each sensor was tested in the same test field to evaluate the precision of displacement determination from images and video sequences by applying homography transformation. The controlled environment of the calibration field allowed for the isolation of the effects of camera calibration quality and the distribution of reference points on the precision of the coordinates derived from homography.

Table 1. Overview of sensors and imaging parameters used for displacements determination at the calibration field test.

Sensor	Mode	Resolution	Frame Rate	Distance to Object	Pixel Size on the Object	Sensor Stability
Nikon D800E + SIGMA RF20	Photo Video	7360 × 4912 1920 × 1080	- 29.97	~13.0 m ~15.3 m	3.2 mm 12.7 mm	Tripod-mounted
DJI Matrice 300 RTK + Zenmuse P1	Photo Video	8192 × 5460 1920 × 1080	- 59.94	~22.2 m ~23.6 m	2.8 mm 11.9 mm	UAV hovering
DJI Phantom 4 + FC330	Photo Video	4000 × 3000 3840 × 2160	- 29.97	~13.9 m ~13.5 m	5.9 mm 6.0 mm	UAV hovering

2.1.2. Beam Static Load Test

The second part of the experimental investigation was conducted on a simply supported reinforced concrete beam with a length of 36 m. UAV photogrammetric measurements were conducted during the static load test of the beam in five different loading phases. Phase 1 was unloaded initial phase, in Phase 2 the beam was loaded with 14.88 tons (25% of total load), in Phase 3 with 29.76 tons (50% of total load), in Phase 4 with 44.64 tons (75% of total load) and in Phase 5 with 59.52 tons (100% of total load). A total of 24 pallets, each weighing 2.48 tons, were used for the loading (Figure 2).

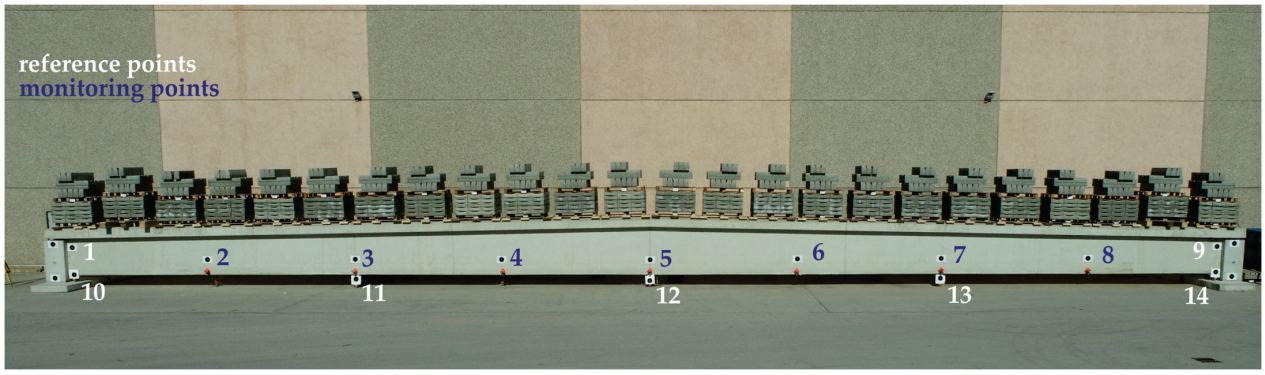


Figure 2. Position of the UAV and LVDT monitoring points on the beam and reference points.

Beam deflections during the load testing were tracked by the photogrammetric measurements at 7 signalized monitoring points (points 2–8 in Figure 2). Homography transformations were computed using a selected subset of reference points, including points located on the beam (points 1 and 9) and nominally stable points located beneath the

https://doi.org/10.3390/s26051593

beam (points 10–14). The same physical reference targets were used throughout all loading phases. As reference points are, in principle, required to remain stationary, their stability was continuously assessed during the experiment. Points 1 and 9 exhibited small but measurable displacements during loading; therefore, their object-space coordinates were updated using the corresponding LVDT measurements before homography transformation. Reference points 10–14 were considered stable throughout most of the loading process. However, during the final loading phase (Phase 5), minor vertical movements were detected at points 12 and 13 because of the beam settlement under the load. In order to preserve the geometric consistency of the homography transformation, their object-space coordinates were updated in Phase 5 based on simultaneous robotic total station (RTS) measurements. The homography matrix was subsequently recalculated using these corrected object coordinates, while the image coordinates remained unchanged.

In contrast to previous studies employing a static ground-based camera setup [20], the present experiment utilized a UAV platform for data acquisition. A DJI Phantom 4 Pro equipped with a 20-megapixel camera (focal length 8.8 mm, pixel size 2.4 μm) was operated at a hovering altitude of approximately 2 m and 22.5 m distance from the beam, maintaining a camera view oriented towards the centre of the concrete beam. The UAV was positioned to capture the entire beam and surrounding reference frame within a single field of view.

Images were captured at discrete loading phases corresponding to 0%, 25%, 50%, 75%, and 100% of the design load.

In each loading phase, ten consecutive photographs were captured (resolution 5472 × 3648 px). Because the load was static and the beam remained motionless within each phase, the repeated images enabled an assessment of the measurement repeatability. For every signalized point, the dispersion of image coordinates across the 10 images was used to quantify precision, while the averaged values provided a more robust estimate of the points displacements in each loading phase.

To provide an independent and high-accuracy reference for displacement validation, six LVDT sensors were installed in monitoring points 1–5 and 9 as shown in Figure 3. The sensors were mounted on a rigid steel reference frame anchored to the ground and on the beam supports, ensuring that measured displacements were not affected by structural movement of the beam. The LVDT sensors (HBM, model type WA) continuously measured the vertical displacement with a resolution of 0.01 mm in all loading phases. Additionally, to LVDT the UAV displacements were compared to the displacements determined using a robotic total station Leica TPS1201, with a direction measurement accuracy of 1″ and a distance measurement accuracy of 2 mm + 2 ppm. By RTS, displacements were measured in seven monitoring points (points 2–8) identical to those from UAV measurements.

2.1.3. Dynamic Bridge Test

The third set of measurements were performed in real conditions during exploitation on the Podsused bridge in Zagreb, Croatia, where the traffic load that took place over the bridge was used for the dynamic load.

The new Podsused Bridge (Figure 4) was constructed on the piers of the former railway-road bridge. It features a continuous static system with a constant superstructure height across nine spans of 37.15 m each. The bridge has a total length of 334.35 m and a width of 14.7 m. The load-bearing structure consists of two steel box girders connected by transverse beams, while the deck is a steel orthotropic slab. Following damage caused by strong water currents, the bridge piers were reinforced and repaired between 2016 and 2018.

The measurements were carried out by monitoring ambient traffic flow specifically capturing the passage of heavy vehicles (trucks and buses) at speeds ranging from 40 km/h

https://doi.org/10.3390/s26051593

to 70 km/h. Measurements were carried out in the second span of the bridge from the direction of city of Samobor.



(**a**) (**b**)

Figure 3. Setup of the LVDT sensor beneath the beam in measuring point 3 (**a**) and on the beam support in measuring point 1 (**b**).

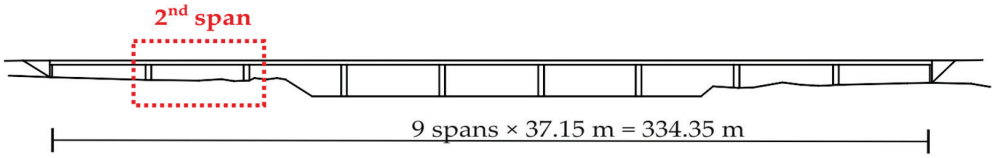


Figure 4. Longitudinal section of the new Podsused bridge.

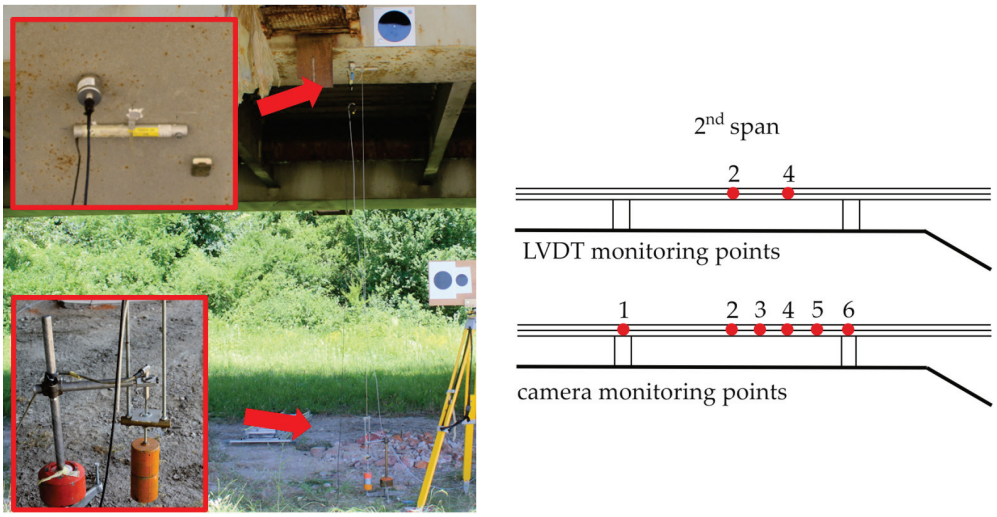
Six measuring points were stabilized on the bridge structure using 27 cm diameter circular targets marked in Figure 5 with numbers from 1 to 6. At these points, the dynamic displacements of the structure were determined from video captured from UAV platform and ground-based camera. Points 7 and 10 were placed on the pillars of the bridge and points 8 and 9 were placed on a tripod on the ground below the point stabilized in the middle of the span (point 2) and served as additional reference points (in addition to points 7 and 8) for homography transformation. Those points were stabilized using 15 cm diameter circles.



Figure 5. Position of the measuring points in the 2nd span of the bridge.

https://doi.org/10.3390/s26051593

To validate the results, reference measurements were conducted via direct displacement sensing using LVDT sensors, which were installed in measuring point 2 and point 4 (Figure 6). Since the measurement accuracy of LVDT sensors significantly exceeds the accuracy of camera used in this study, displacements obtained by LVDT sensors were used as a reference.



(**a**) (**b**)

Figure 6. LVDT sensor in measuring point 2 (**a**), location of UAV measuring points (points 1–6) on bridge (**b**).

The dynamic displacements of the bridge at different measuring points signalized within 2nd span were measured with Nikon D800E camera and UAV Phantom 4 (see Table 2).

Table 2. Imaging parameters for the bridge measurement campaign.

Sensor	Mode	Resolution	Frame Rate	Distance to Object	Pixel Size on the Object	Sensor Stability
Nikon D800E + SIGMA RF20	Video	1920 × 1080	29.97	~18 m	20.6 mm	Tripod-mounted
DJI Phantom 4 + FC330	Video	3840 × 2160	29.97	~24 m	13.3 mm	UAV hovering

Both systems recorded video sequences, later decomposed into individual frames for displacement extraction.

2.2. Displacement Measurement Methodology

While Section 2.1 describes the experimental setups, this section presents the methodology used to derive structural displacements from UAV imagery using homography-based transformation.

2.2.1. Methodology of the Homography-Based Displacement Measuring

Prior to acquiring photographs and video sequences to track the deformation of the observed object, all cameras used in this research were calibrated on the test field, as it is explained in Section 2.1. These calibration data, in particular the parameters of radial and tangential distortion, were used to remove their impact on further measurements by reprojecting them to distortion-free ones. Signalized targets placed in reference and monitoring points were tracked in successive image frames using sub-pixel feature detection using a custom Python 3.12. implementation based on the OpenCV 4.8.0 library. Initial target localization was performed using multi-scale template matching to ensure scale invariance under varying UAV-to-object distances. The detected target positions

https://doi.org/10.3390/s26051593

were subsequently refined to sub-pixel accuracy using an iterative Least Squares Matching (LSM) algorithm, optimizing translation and scale parameters. Image preprocessing steps, including grayscale conversion and contrast enhancement, were applied to improve robustness under varying illumination conditions. From video sequences, image coordinates were extracted independently for each frame, forming time series of image-space displacements prior to homography transformation. The frame rate (29.97 fps) of video sequences was fixed during individual measurement campaigns and chosen to ensure sufficient temporal resolution for capturing traffic-induced displacement responses dominated by low-frequency components. Since the focus of this study was on displacement amplitude accuracy rather than detailed spectral analysis, higher frame rates were not required. In one configuration, a higher frame rate was additionally tested to evaluate potential accuracy degradation; however, this was not observed in the processed results. Acquired images were projected onto the monitored object's plane by homography transformation using image coordinates measured by DIC and object coordinates measured manually by robotic total station. Finally, structural displacements were obtained by computing frame-to-frame differences in transformed object-plane coordinates relative to the initial reference frame. The resulting displacement time histories were evaluated using mean absolute displacement, maximum displacement, and Root Mean Square Error (RMSE), depending on the test scenario. The main steps of deformation measuring on the structural objects are shown in the following flowchart (Figure 7).

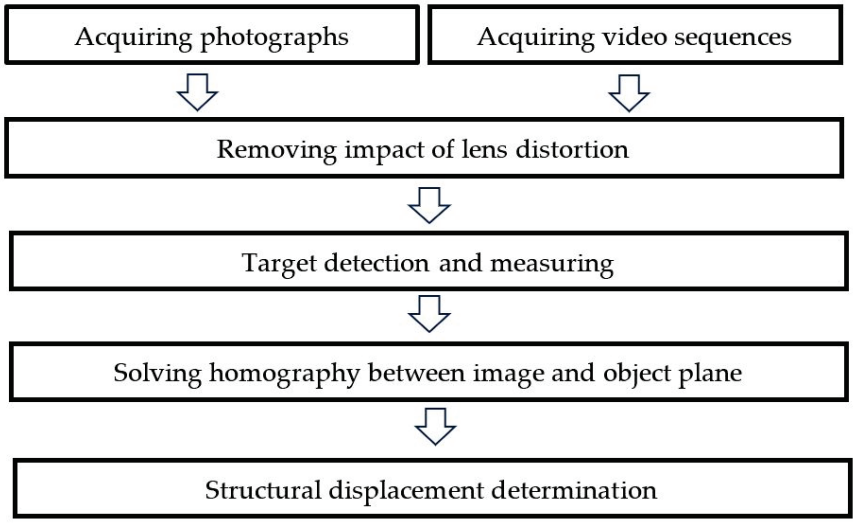


Figure 7. Image processing flowchart.

2.2.2. Principle of the Homography Based Displacement Measurement

A comprehensive review of the use of the homography-based displacement measurement method can be found in [28], where points measured on images are projected to the reference image by homography. To have displacement properly scaled, we suggest using homography to transfer points from every image to the object plane. The key assumption of the method is that both reference points and the points of interest on the monitored structure lie approximately in the same plane. In UAV-based monitoring, camera motion and vibration during flight introduce false apparent displacements. To remove this effect, the image pairs are geometrically aligned to the plane, where lies the monitored structure, using the homography matrix derived from fixed reference points. After alignment, the residual movement of the signalized points corresponds exclusively to the true structural deformation.

Homography transformation of images is typically characterized as the projection mapping relationship between photographs of an identical planar object captured from var-

https://doi.org/10.3390/s26051593

ious positions by two distortion-free cameras. It delineates the transformation relationship between two planes. In our case, it represents the homographic transformation between the image and the object plane (Figure 8).

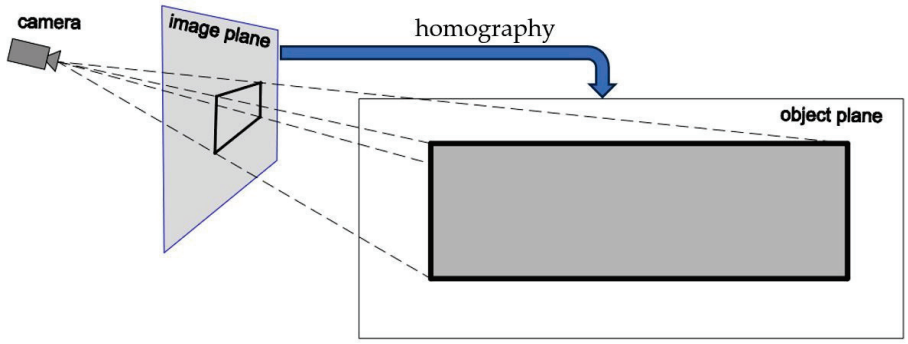


Figure 8. The principle of homographic transformation from image to object plane.

This coordinate transformation can be expressed as:

$$\begin{bmatrix} X \\ Y \\ 1 \end{bmatrix} = H \begin{bmatrix} x \\ y \\ 1 \end{bmatrix}, \tag{1}$$

where

X, Y are coordinates of the object in the object plane
x, y are image coordinates of the object
H is the homography matrix

$$H = \begin{bmatrix} h_{11} & h_{12} & h_{13} \\ h_{21} & h_{22} & h_{23} \\ h_{31} & h_{32} & h_{33} \end{bmatrix}. \tag{2}$$

Expanding Equation (1) we can get:

$$X = \frac{h_{11}x + h_{12}y + h_{13}}{h_{31}x + h_{32}y + h_{33}} \quad Y = \frac{h_{21}x + h_{22}y + h_{23}}{h_{31}x + h_{32}y + h_{33}}. \tag{3}$$

Finally, by multiplying the denominator of both equations to their left and moving the left side of the equation over the right side, we get:

$$0 = (h_{11}x + h_{12}y + h_{13}) - (h_{31}Xx + h_{32}Xy + h_{33}X), \tag{4}$$

$$0 = (h_{21}x + h_{22}y + h_{23}) - (h_{31}Yx + h_{32}Yy + h_{33}Y), \tag{5}$$

or in matrix form:

$$0 = Ah = \begin{bmatrix} x & y & 1 & 0 & 0 & 0 & -Xx & -Xy & -X \\ 0 & 0 & 0 & x & y & 1 & -Yx & -Yy & -Y \end{bmatrix} \begin{bmatrix} h_{11} \\ h_{12} \\ h_{13} \\ h_{21} \\ h_{22} \\ h_{23} \\ h_{31} \\ h_{32} \\ h_{33} \end{bmatrix}. \tag{6}$$

https://doi.org/10.3390/s26051593

where h is a nine-dimensional vector consisting of coefficients of the homography matrix H. Because the homography matrix is a 3 × 3 homogeneous matrix, its h_{33} element is normalized to 1 so that it has only 8 degrees of freedom. To find the solution for the homography matrix, a minimum of four pairs of corresponding points on the object and the image are needed. If there are more than four pairs of corresponding points, the final solution is obtained by Direct Linear Transformation (DLT) [29] or Singular Value Decomposition (SVD), minimizing the errors in determination of the homography coefficients caused by measuring noise present in object and image coordinates.

3. Results

This section presents the results obtained from three experimental setups: the calibration test field, the static load beam test, and the dynamic bridge test. Each setup was designed to analyze specific aspects of the UAV-based homography approach. The calibration field experiment focused on evaluating the influence of reference point configuration and camera stability on the accuracy of homography-based transformations. The beam test verified the method's performance under controlled static load, while the bridge test extended the assessment to dynamic displacements induced by real traffic loads.

3.1. Influence of Reference Point Configuration on Homography Accuracy—Calibration Field Test

To evaluate the accuracy of the homography transformation in relation to the number and spatial distribution of reference points, a detailed test was performed using a static calibration field (Figure 9). The test was conducted at the same test site used for the interior calibration of all imaging sensors included in this study. Ten monitoring points were signalized within the calibration field using circular targets with a diameter of 16 cm, as illustrated in Figure 9. These points were selected to represent typical object points monitored in structural applications, while ensuring a well-defined and repeatable image geometry.

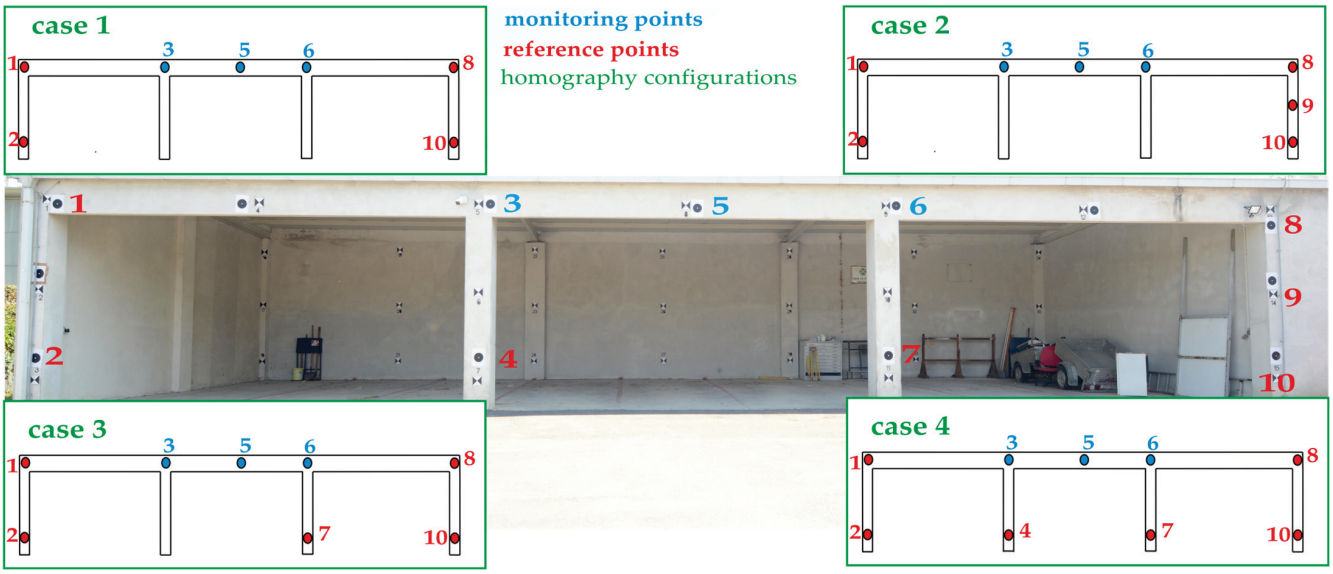


Figure 9. Calibration field with signalized points and a schematic representation of four different homography configurations.

Three different imaging systems were employed: (i) a DJI Phantom 4 UAV, (ii) a DJI Matrice 300 RTK UAV equipped with a Zenmuse P1 camera, and (iii) a Nikon D800E ground-based camera mounted on a rigid tripod. For each sensor, 15 still images and one video sequence were acquired under static conditions, ensuring that all detected

https://doi.org/10.3390/s26051593

displacements originate exclusively from image measurement noise and homography estimation errors rather than from actual object motion.

The accuracy evaluation was performed on three monitoring points (3, 5 and 6). For each image, the coordinates of these points were transformed using four different homography configurations (Figure 9):

1. Case 1—edge-only configuration (points 1, 2, 8, 10):

Represents the most common scenario in field measurements of structures such as bridges, where reference signals can only be installed near image boundaries (e.g., bridge abutments or piers).

2. Case 2—edge configuration + one additional edge point (points 1, 2, 8, 10 + 9)

Used to evaluate whether an additional reference point near the image boundary improves geometric stability.

3. Case 3—edge configuration + one central point (points 1, 2, 8, 10 + 7):

Assesses whether introducing a single interior point reduces perspective distortion and improves overall transformation accuracy.

4. Case 4—edge configuration + two central points (points 1, 2, 8, 10 + 4 and 7):

Represents an optimized layout with improved spatial coverage.

For each sensor and homography configuration, the RMSE was computed based on the apparent displacements of monitoring points 3, 5, and 6. Since no actual structural motion occurred during image acquisition, the true displacement of all monitoring points was zero. Consequently, the apparent displacements obtained from successive images represent measurement errors resulting from image noise, subpixel localization uncertainty, and imperfections in the homography transformation.

The RMSE values were calculated from the displacement time series derived from image coordinates relative to the initial reference position. Any deviation from zero displacement was therefore interpreted as a measurement error, allowing the RMSE to serve as a direct indicator of the internal precision and stability of the homography-based displacement estimation.

The maximum RMSE values obtained for the Nikon D800E camera were 0.12 pixels (Case 2), while for the DJI Phantom 4 and DJI Matrice 300 RTK systems the maximum RMSE values reached 0.25 pixels and 0.28 pixels, respectively, observed in both Case 1 and Case 2 (Table 3). When considering the corresponding object-space pixel sizes listed in Table 1, these values indicate that the achieved displacement accuracy is in the order of a few tenths of a millimetre for the ground-based system and within a millimetres for the UAV-based systems.

Table 3. RMSE (pixels) of homography transformation for different reference point configurations.

Case	Reference Points	Nikon D800E		DJI Phantom 4		DJI Matrice 300 RTK	
		RMSE X	**RMSE Y**	**RMSE X**	**RMSE Y**	**RMSE X**	**RMSE Y**
1	1–2–8–10	0.11	0.01	0.25	0.04	0.28	0.08
2	1–2–8–10–9	0.12	0.01	0.25	0.04	0.28	0.07
3	1–2–8–10–7	0.03	0.02	0.12	0.04	0.13	0.07
4	1–2–8–10–4–7	0.04	0.02	0.09	0.04	0.12	0.07

These results confirm that homography-based correction enables subpixel-level displacement precision even under UAV hovering conditions, provided that a sufficient number of well-distributed reference points is available.

Also, the results clearly show that configurations including one or more central points (Cases 3 and 4) reduce RMSE values compared to edge-only configurations (Cases 1 and 2).

https://doi.org/10.3390/s26051593

The inclusion of centrally located reference points minimizes perspective-induced warping and provides better geometric control, particularly along the X-axis, while the Y-axis results remain largely stable regardless of configuration. The reduced sensitivity observed in the Y-direction can be attributed to a more favourable vertical distribution of reference points within the image, providing sufficient geometric control even in edge-only configurations.

Analysis of Video Sequences

To further evaluate the applicability of the homography transformation method for dynamic monitoring, the same analysis procedure was extended to video recordings. The video sequences were decomposed into individual frames, each processed independently using homography transformation based on the defined set of reference points.

The analyzed video datasets consisted of (1) 920 frames recorded with the DJI Phantom 4 (3840 × 2160 px resolution and 29.97 fps), (2) 460 frames recorded with DJI Matrice P1 (1920 × 1080 px resolution and 59.94 fps) and (3) 920 frames recorded with Canon D800E camera (1920 × 1080 px resolution and 29.97 fps). Since no load was applied to the observed object, all apparent displacements represent measurement noise caused by UAV motion, image stabilization imperfections, and subpixel localization uncertainty and residual homography estimation errors.

The computed displacements of monitoring points 3, 5 and 6 are illustrated in Figure 10 for the Phantom 4 video sequence. The figure presents both horizontal and vertical coordinate variations obtained from the video sequence before and after applying homography transformation. For the monitoring point, the corrected trajectory is nearly linear, confirming that homography successfully compensates UAV-induced camera motion.

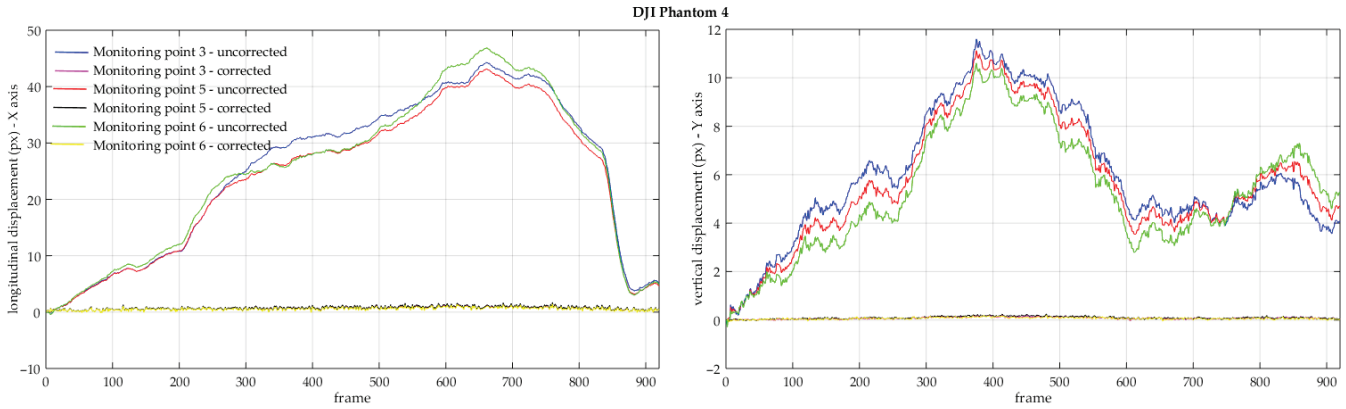


Figure 10. Displacements of monitoring points 3, 5 and 6 before (uncorrected) and after (corrected) applying homography correction in DJI Phantom 4 video.

The computed apparent displacements for monitoring points 3, 5 and 6 after applying homography transformation are illustrated in Figure 11 (DJI Phantom 4), Figure 12 (DJI Matrice 300 RTK) and in Figure 13 (Nikon D800E camera). Each figure presents both horizontal and vertical coordinate variations obtained from the video sequence for Case 1 and Case 3 homography configurations. Only Case 1 and Case 3 configurations are presented in the figures, since Cases 1 and 2 as well as Cases 3 and 4 produced nearly identical results, indicating that the inclusion of additional reference points did not further improve transformation stability.

https://doi.org/10.3390/s26051593

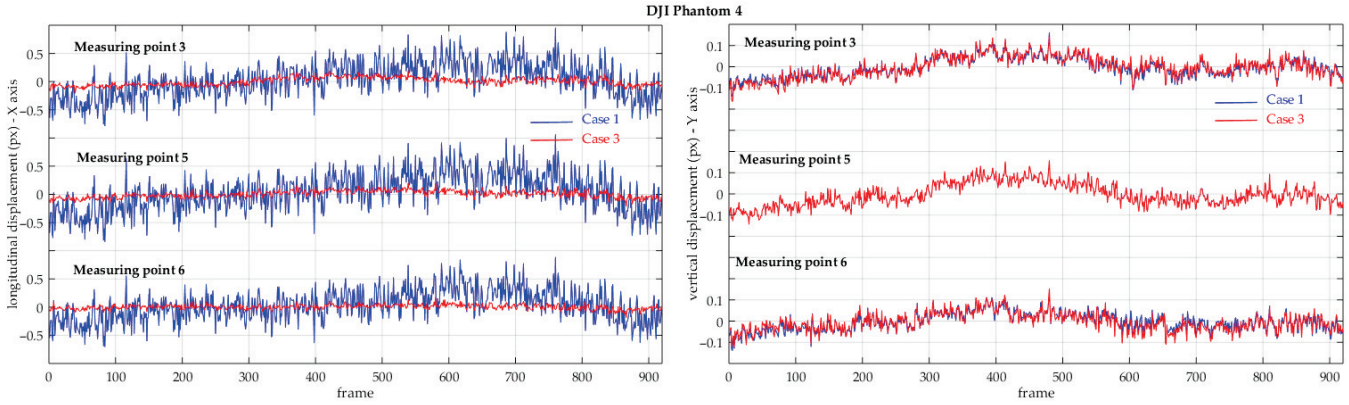


Figure 11. Longitudinal and vertical displacements of measuring points 3, 5 and 6 derived from DJI Phantom 4 video after homography transformation (Case 1 and Case 3).

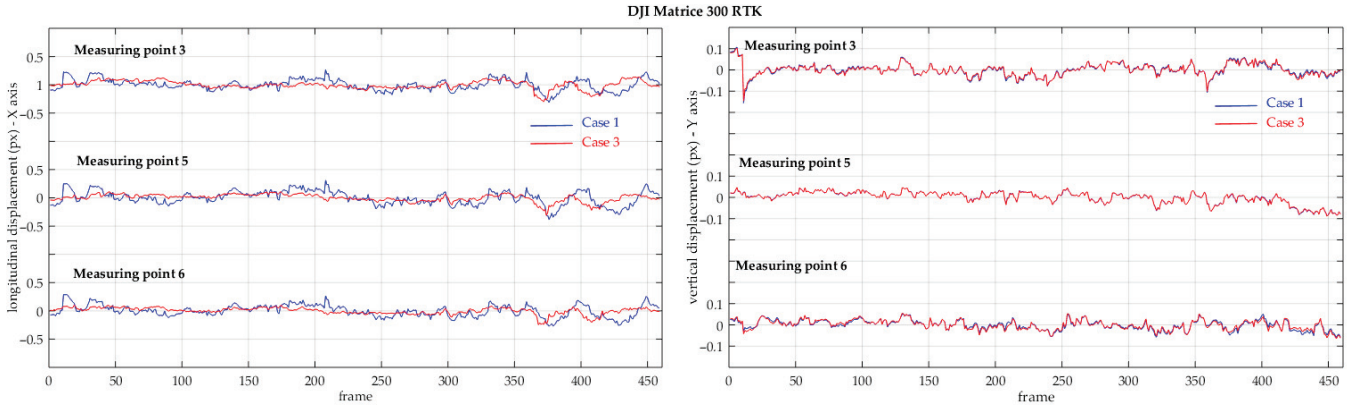


Figure 12. Longitudinal and vertical displacements of measuring points 3, 5 and 6 derived from DJI Matrice 300 RTK video after homography transformation (Case 1 and Case 3).

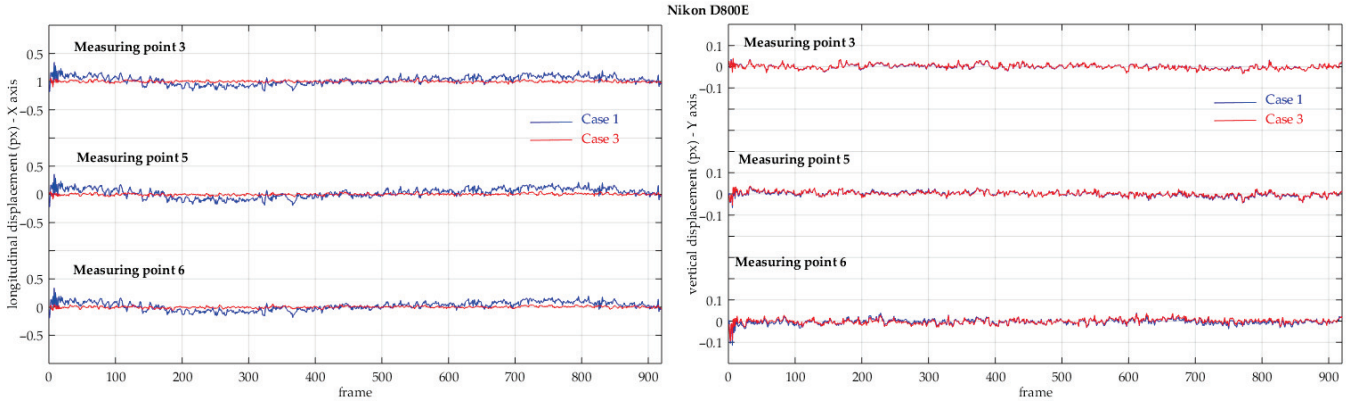


Figure 13. Longitudinal and vertical displacements of measuring points 3, 5 and 6 derived from Nikon D800E video after homography transformation (Case 1 and Case 3).

The results presented in Table 4 summarize the displacements obtained from video sequences for three monitoring points (points 3, 5, and 6) and four homography configurations. For each camera system and homography case, three statistical indicators are reported for both the longitudinal (X) and vertical (Y) directions: the mean of the absolute displacement values, the maximum absolute displacement, and the RMSE. The results allow a quantitative comparison between different homography configurations as well as between the UAV-based camera systems and the tripod mounted camera.

https://doi.org/10.3390/s26051593

Table 4. Comparison of apparent displacement statistics obtained from UAV-based and ground-based camera systems under static conditions (pixels).

Case	Monitoring Point	Axis	DJI Phantom 4 (920 Frames)			DJI Matrice 300 RTK (460 Frames)			Nikon D800E (920 Frames)		
			Mean	Max	RMSE	Mean	Max	RMSE	Mean	Max	RMSE
1	3	X	0.24	0.96	0.30	0.08	0.32	0.10	0.06	0.35	0.08
		Y	0.04	0.16	0.05	0.02	0.16	0.03	0.01	0.04	0.01
	5	X	0.27	1.03	0.32	0.10	0.39	0.12	0.07	0.36	0.09
		Y	0.04	0.16	0.05	0.02	0.09	0.03	0.01	0.07	0.01
	6	X	0.22	0.88	0.28	0.09	0.29	0.11	0.06	0.34	0.08
		Y	0.04	0.14	0.04	0.02	0.06	0.02	0.01	0.11	0.01
2	3	X	0.25	0.95	0.30	0.08	0.32	0.10	0.06	0.35	0.08
		Y	0.04	0.16	0.05	0.02	0.16	0.03	0.01	0.04	0.01
	5	X	0.27	1.05	0.33	0.10	0.40	0.12	0.08	0.37	0.09
		Y	0.04	0.15	0.05	0.02	0.09	0.03	0.01	0.07	0.01
	6	X	0.22	0.88	0.27	0.08	0.31	0.10	0.07	0.34	0.08
		Y	0.03	0.16	0.04	0.02	0.06	0.02	0.01	0.12	0.02
3	3	X	0.06	0.21	0.07	0.06	0.30	0.07	0.01	0.10	0.02
		Y	0.04	0.17	0.05	0.02	0.15	0.03	0.01	0.04	0.01
	5	X	0.05	0.22	0.06	0.05	0.32	0.07	0.01	0.09	0.02
		Y	0.04	0.16	0.05	0.02	0.09	0.03	0.01	0.05	0.01
	6	X	0.03	0.19	0.04	0.05	0.25	0.06	0.01	0.06	0.02
		Y	0.03	0.15	0.04	0.02	0.07	0.02	0.01	0.10	0.01
4	3	X	0.06	0.21	0.07	0.07	0.27	0.08	0.01	0.08	0.02
		Y	0.04	0.18	0.05	0.02	0.15	0.03	0.01	0.04	0.01
	5	X	0.05	0.22	0.06	0.05	0.24	0.06	0.01	0.06	0.02
		Y	0.04	0.16	0.05	0.02	0.09	0.03	0.01	0.05	0.01
	6	X	0.03	0.19	0.04	0.05	0.23	0.06	0.01	0.07	0.02
		Y	0.03	0.15	0.04	0.02	0.06	0.02	0.01	0.09	0.01

The results presented in Table 4 confirm the trends observed in the still-image experiment. For all three imaging systems, homography configurations including centrally located reference points (Cases 3 and 4) yield substantially lower mean, maximum, and RMSE displacement values compared to edge-only configurations (Cases 1 and 2) in the longitudinal (X) direction. Also, results in the Y-direction remained stable in all four homography configurations, indicating that the vertical geometry of reference points already provides sufficient control even in simplified layouts.

Results presented in this section indicate that, under controlled geometric conditions, the homography-based approach achieves sub-millimetre precision. The stability observed across different reference point configurations confirms the robustness of the transformation when adequate spatial distribution is ensured.

3.2. Static Load Test of the Reinforced Concrete Beam

This section presents the results obtained from the static load test of a reinforced concrete beam. The aim of this experiment was to evaluate the accuracy of UAV-based homography photogrammetry under controlled static loading conditions and to compare the UAV-derived displacements with reference measurements obtained using LVDTs and RTS.

The beam was loaded in four incremental loading phases corresponding to 25%, 50%, 75%, and 100% of the design load. For each loading phase, displacements were measured independently using UAV photogrammetry, LVDTs, and RTS observations. Three different homography reference point configurations (Figure 14) were applied, analogous to those used in the calibration field experiment, in order to assess the influence of reference point selection on displacement accuracy.

Figure 15 presents the measured displacements for all monitoring points in the fifth loading phase, corresponding to the maximum applied load, using the edge-only homography configuration (Case 1).

https://doi.org/10.3390/s26051593

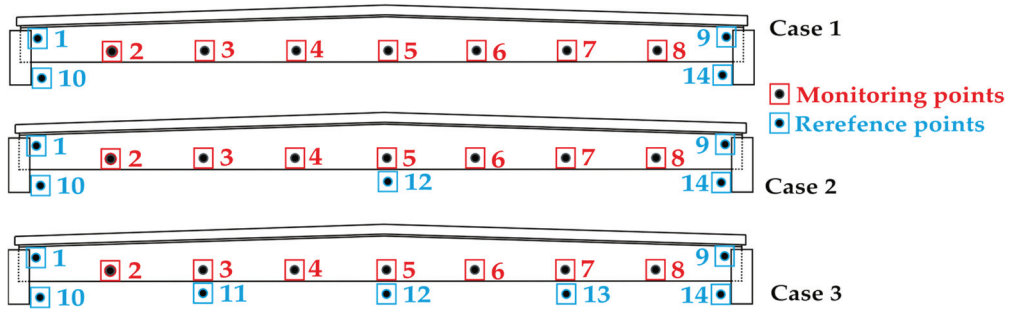


Figure 14. A reinforced concrete beam with positions of signalized points and three different homography configurations.

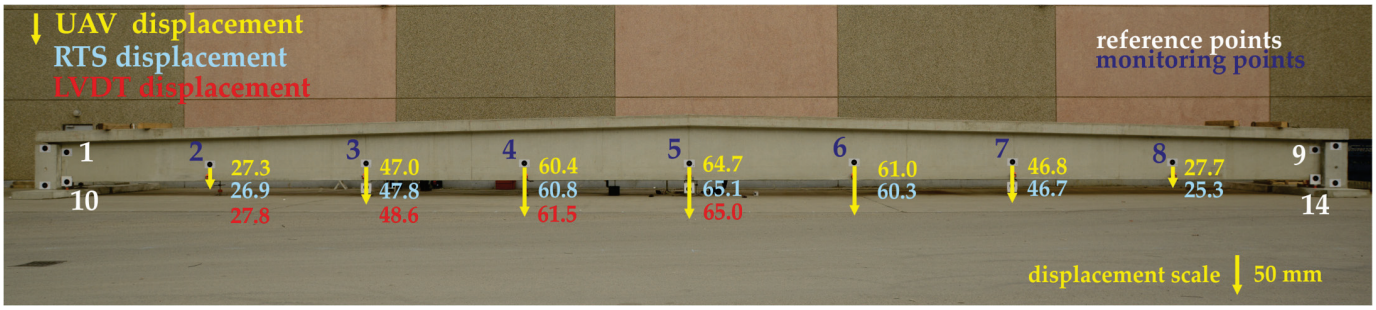


Figure 15. Measured vertical displacements (mm) by UAV, LVDT and RTS in Phase 5.

The results show a consistent deformation shape obtained by all three measurement systems. The displacement differences between the UAV-derived measurements and the reference RTS and LVDT measurements for all loading phases are summarized in Table 5. The results show no systematic increase in discrepancies with increasing load level. Instead, the differences remain relatively consistent across all loading phases, indicating stable homography performance even at higher displacement amplitudes.

Table 5. The displacement differences between the UAV-derived measurements and the reference RTS and LVDT measurements for Case 1 (mm).

Reference Measurement	Loading Phase	Monitoring Point						
		2	3	4	5	6	7	8
RTS	F2	−2.8	−3.7	−3.1	−1.8	−2.2	−3.6	−0.5
	F3	1.6	−0.6	0.0	0.4	−0.4	−1.2	0.4
	F4	−1.4	−2.9	−3.5	−2.7	−1.9	−2.6	0.5
	F5	−0.5	0.8	0.4	0.4	−0.6	−0.1	1.6
LVDT	F2	−2.6	−4.0	−3.5	−2.3	-	-	-
	F3	2.0	0.0	0.3	−0.1	-	-	-
	F4	−0.7	−2.3	−3.1	−3.1	-	-	-
	F5	0.5	1.6	1.0	0.3	-	-	-

A statistical accuracy evaluation was performed for all three homography configurations by comparing UAV-derived displacements against both RTS and LVDT reference measurements. The results are summarized in Table 6.

The analysis shows a gradual improvement in measurement accuracy with increasing number and spatial coverage of reference points. Case 3 achieved the lowest RMSE values for both RTS and LVDT comparisons, confirming that the inclusion of additional reference points improves homography stability. However, the observed differences between configurations remain relatively small, indicating that even simplified reference point layouts can provide acceptable accuracy under controlled static loading conditions.

https://doi.org/10.3390/s26051593

Table 6. The UAV displacement differences statistics for a different homography reference point configurations (mm).

Case	Reference Measurement	No of Displacements	Mean	Max.	St. dev.	RMSE	
						mm	px
1	RTS	28	1.5	3.7	1.6	1.9	0.26
	LVDT	16	1.7	4.0	2.0	2.1	0.28
2	RTS	28	1.3	3.2	1.5	1.7	0.23
	LVDT	16	1.5	3.5	1.8	1.9	0.26
3	RTS	28	1.3	3.1	1.4	1.6	0.22
	LVDT	16	1.4	3.3	1.7	1.8	0.24

From the results, we can conclude that observed agreement with LVDT measurements demonstrates that the method remains reliable under controlled static loading conditions, although minor deviations become more noticeable with less favourable reference point configurations.

3.3. Influence of Reference Point Configuration on Homography Accuracy—Podsused Bridge

Two UAV video sequences acquired using the DJI Phantom 4 were analyzed to evaluate the applicability of homography-based displacement correction under real traffic loading conditions on the Podsused bridge. The first video sequence (Video 1), with a duration of 83 s, captured three distinct traffic-induced loading events, clearly visible in the UAV-derived displacement records. The second video sequence (Video 2), lasting 25 s, recorded the passage of a heavy truck with a trailer. All detected events are illustrated in Figure 16.



Figure 16. Traffic-induced loading events in recorded videos.

Each video was decomposed into individual frames and processed using a DIC-based tracking approach. For each frame, the image coordinates of all ten signalized points were determined. Subsequently, homography transformations based on the selected set of stable reference points were applied independently to each frame in order to remove false displacements caused by UAV motion.

Figure 17 presents the longitudinal (X-direction) and vertical (Y-direction) displacements of four monitoring points on the bridge (points 2, 3, 4 and 5), both before and after homography transformation in Video 1. Prior to correction, the displacement signals exhibit significant apparent motion dominated by UAV instability. After applying homography transformation, the false global trends are removed, and the remaining displacement patterns clearly correspond to traffic-induced dynamic structural behaviour.

To assess the measurement accuracy, UAV-derived vertical displacement were compared against reference measurements obtained using an LVDT sensor installed at measuring points 2 and 4. Since the UAV and LVDT records were neither synchronized nor sampled at the same rate, an event-based time alignment was applied by matching the maximum absolute displacement values corresponding to the same loading event. This event-based alignment approach is straightforward and well suited to low-frequency dynamic response. However, it may introduce minor temporal uncertainties, particularly

https://doi.org/10.3390/s26051593

due to measurement noise present in the UAV-derived signal and the limited temporal resolution of visually identified peak values. For applications involving higher-frequency dynamic response, more advanced synchronization techniques (e.g., cross-correlation-based alignment) could provide improved temporal accuracy. In the present study, given the predominantly low-frequency dynamic response of the loading events, the adopted procedure was considered adequate for comparative accuracy assessment. The records were then truncated to a common time interval, vertical offsets were removed by equalizing the mean displacement in the unloaded state, and the LVDT signal was linearly interpolated to the UAV time stamps. The displacement differences were subsequently used to quantify the measurement accuracy.

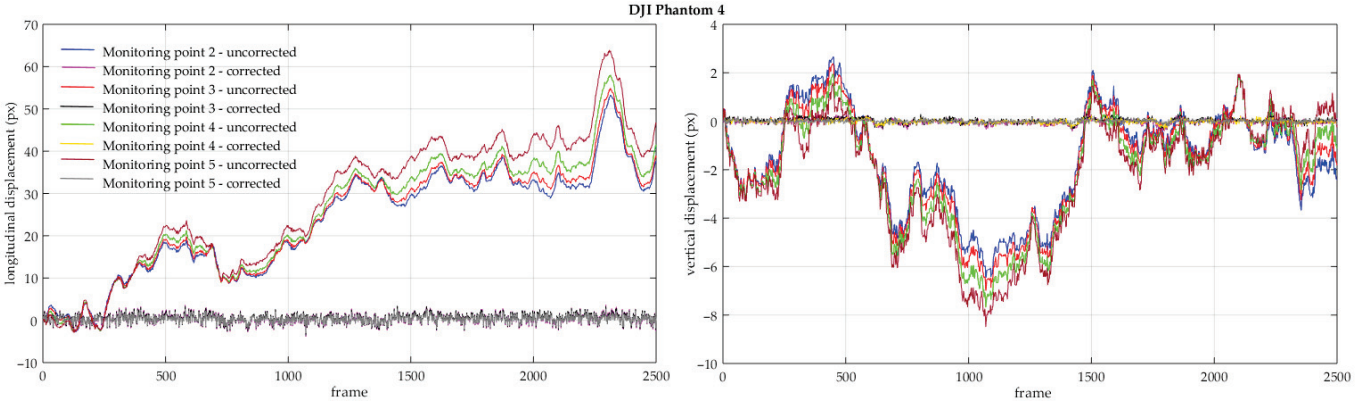


Figure 17. Displacements of monitoring points on the bridge before (uncorrected) and after (corrected) applying homography correction in Video 1.

Due to differences in acquisition start times and sampling rates between the UAV video and LVDT recordings, only the overlapping portions of both signals were used for accuracy analysis. Consequently, although Video 1 had a total duration of 83 s, the comparison was performed over a 60 s interval corresponding to the common time window with available LVDT data, while for Video 2 the overlapping interval was limited to 20 s.

Figures 18 and 19 illustrates the comparison between UAV and LVDT-derived vertical displacements at measuring points 2 and 4 for both video sequences. A very good agreement in displacement trends and peak values is observed for both loading scenarios, confirming the ability of the UAV–homography approach to capture dynamic bridge displacements under real traffic conditions.

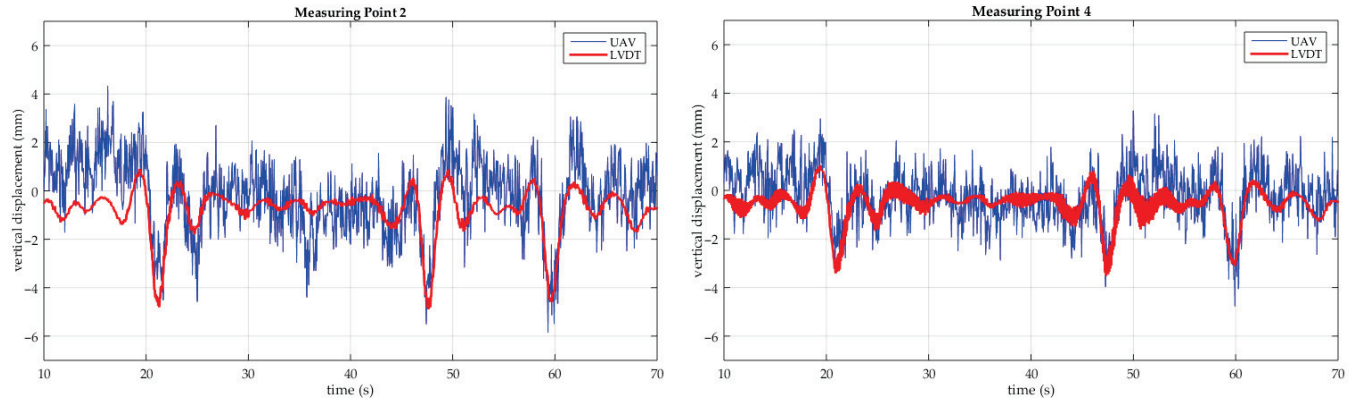


Figure 18. Vertical displacements of measuring point 2 and measuring point 4 derived from Phantom 4 UAV Video 1 and from LVDT sensor.

https://doi.org/10.3390/s26051593

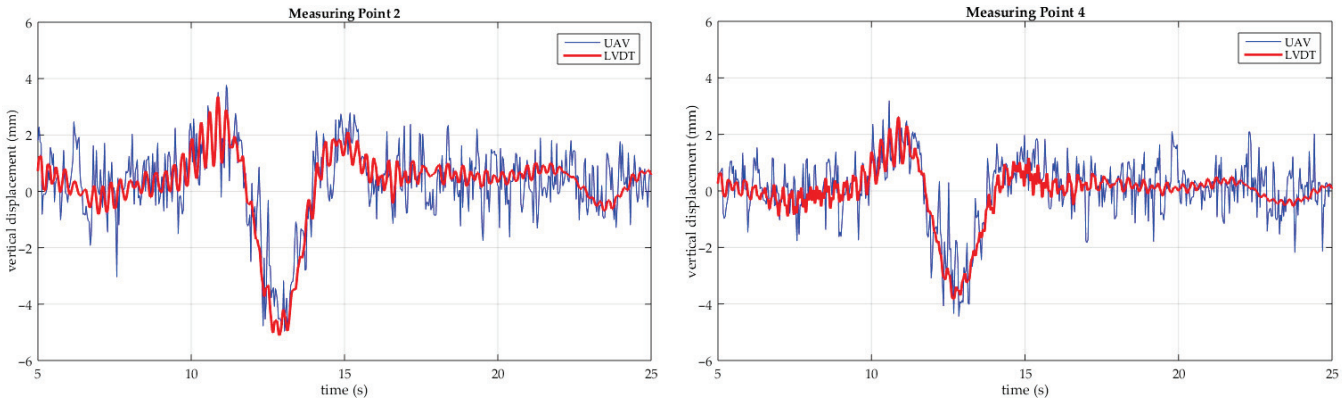


Figure 19. Vertical displacements of measuring point 2 and measuring point 4 derived from Phantom 4 UAV Video 2 and from LVDT sensor.

Table 7 summarizes the statistical indicators computed from the displacement differences relative to the LVDT reference values for both video sequences. The results show RMSE of 1.38 mm and 1.01 mm for monitoring points 2 and 4 in Video 1 and 0.88 mm and 0.76 mm in Video 2. When expressed in image space, these values correspond to subpixel-level accuracy, with RMSE values at approximately 0.1 pixels, considering that one pixel represents approximately 13.3 mm in object space.

Table 7. Accuracy analysis of UAV displacement measurements compared to LVDT values (mm).

	Measuring Point	Frames	Mean	Max.	St. dev.	RMSE	
						mm	px
Video 1	2	1856	1.10	4.66	1.24	1.38	0.10
	4		0.80	3.83	0.94	1.01	0.08
Video 2	2	634	0.70	3.03	0.88	0.88	0.07
	4		0.57	3.23	0.75	0.76	0.06

Despite the fact that the maximum traffic-induced displacements observed in both video sequences reached values of less than half a pixel in image space, the UAV-based measurements were able to reliably capture and reproduce these small-amplitude structural responses. All characteristic loading events identified visually in the recorded videos, including the passages of heavy vehicles illustrated in Figure 16, are clearly recognizable in the corresponding displacement time histories. This confirms the high sensitivity of the homography-corrected photogrammetric approach and demonstrates its capability to detect dynamic bridge displacements of very small magnitude under real traffic conditions.

In accordance with the findings from the calibration field and beam experiments, the homography transformation in the bridge test was not limited to the minimum number of four reference points. In addition to the primary reference points 1, 6, 7, and 10 (Figure 5), two additional centrally located reference points (points 8 and 9) were introduced for Video 2, resulting in a six-point homography configuration. The UAV-derived displacement results obtained using both four-point and six-point configurations are shown in Figure 20.

https://doi.org/10.3390/s26051593

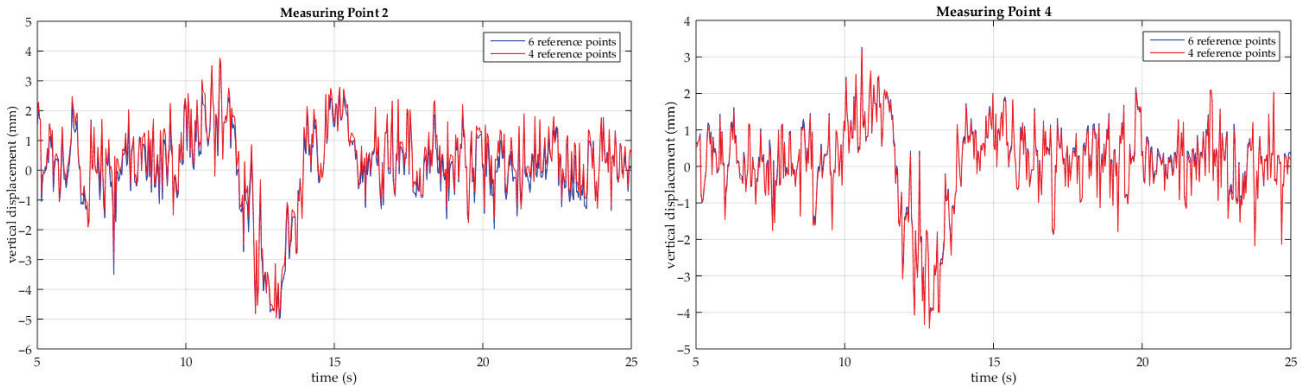


Figure 20. Vertical dispacements of measuring points 2 and 4 from Video 2 after homography transformation by 6 reference points and 4 reference points.

The comparison reveals that the inclusion of additional central reference points did not lead to a significant improvement in vertical displacement accuracy. The displacement time histories obtained using four and six reference points are nearly identical, and the resulting accuracy metrics remain at the same level for both configurations. This indicates that, under favourable geometric conditions and with well-distributed boundary reference points, a minimal homography configuration can already provide sufficient stability for reliable displacement monitoring. These findings are consistent with the results obtained in the calibration field and beam experiments, where additional reference points improved robustness but did not always yield substantial accuracy gains.

In addition to UAV measurements, bridge deformations were also measured with a Nikon D800E camera mounted on a solid and stable tripod. Figure 21 illustrates the comparison between camera and LVDT-derived vertical displacements at measuring points 2 and 4.

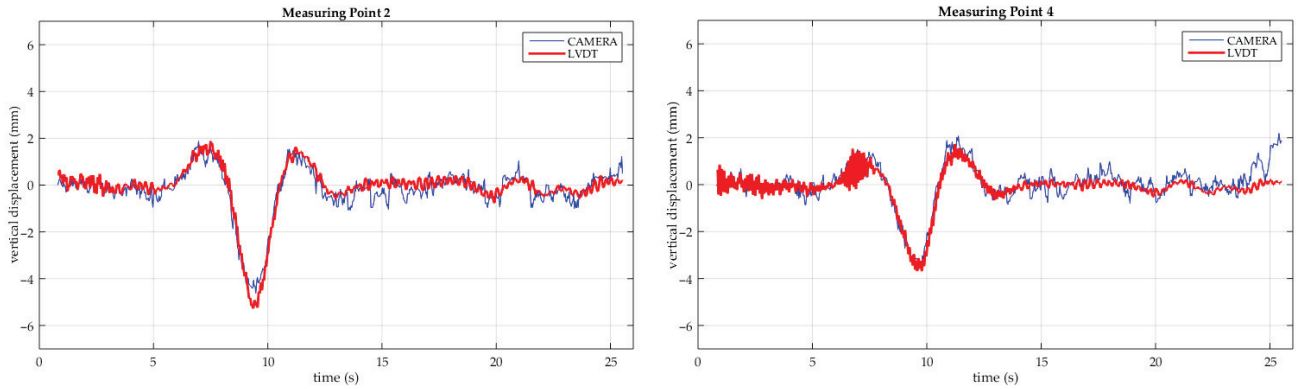


Figure 21. Vertical displacements of measuring point 2 and measuring point 4 derived from Nikon D800E video sequence and from LVDT sensor.

Due to the superior recording quality, longer focal length, and complete elimination of camera movement, the tripod mounted camera achieved significantly higher accuracy compared to UAV measurements. The resulting RMSE values were below 0.5 mm, confirming the potential of vision-based displacement measurement under ideal imaging conditions (Table 8).

These outcomes establish a benchmark for evaluating UAV-based measurements, highlighting the impact of camera stability and image geometry on achievable accuracy. The tripod mounted camera is more precise; however, it is impractical for actual bridge monitoring scenarios due to its inability to access appropriate locations or operate under suitable conditions. Conversely, UAV-based systems offer numerous practical advantages.

https://doi.org/10.3390/s26051593

Table 8. Accuracy analysis of camera displacement measurements compared to LVDT values (mm).

	Measuring Point	Frames	Mean	Max.	St. dev.	RMSE	
						mm	px
Video 1	2	742	0.30	1.29	0.37	0.38	0.02
	4		0.33	2.12	0.42	0.45	0.02

From the UAV results, we can conclude that although environmental variability and UAV platform motion introduce additional noise, the overall displacement trends show satisfactory agreement with reference sensors, confirming the practical applicability of the approach in field conditions.

4. Discussion

4.1. Accuracy and Consistency of UAV–Homography Displacement Measurements

The experimental results obtained from the three performed tests demonstrated that UAV-based homography can provide precise measurements of static and dynamic structural displacements in monitoring projects with different spatial scales and operational conditions.

At the calibration test field, very high internal precision was achieved. The maximum RMSE values of the vertical displacements were below 0.08 pixels, corresponding to approximately 0.25 mm in object space for the UAV-based systems and about 0.10 mm for the ground-based camera system. Lower accuracy was observed in the longitudinal direction, which can be attributed to less favourable imaging geometry and reduced geometric sensitivity along this axis. In this direction, RMSE values remained on the order of a few tenths of a millimetre for the ground-based system and within one millimeter for the UAV-based measurements. Since vertical displacements are typically of primary interest in bridge load testing and serviceability assessments, the achieved accuracy is considered highly satisfactory. These results confirm that homography-based correction successfully compensates UAV-induced camera motion and enables subpixel-level displacement precision, provided that a sufficient number of well-distributed reference points is available.

The measurements during the static load test of the beam validated the accuracy of the proposed approach through direct comparison with high-precision LVDT measurements. The close agreement observed between UAV-derived and reference displacement confirms the capability of the method to capture vertical static displacements with an accuracy of approximately 2 mm. Compared to the calibration test field measurement results, a reduction in accuracy was observed, which can primarily be attributed to less favourable imaging geometry and reference point configuration. Additional factors included longer observation distances and variable illumination conditions. Nevertheless, considering that the maximum displacements during the final loading stage reached 27.3 mm at the beam edges and up to 64.7 mm at midspan, the achieved accuracy corresponds to relative errors of approximately 7% at the supports and 3% at midspan. This level of accuracy is particularly suitable for long-span and flexible structures, where expected displacements align with the precision thresholds necessary for reliable structural assessment. Moreover, in comparison with conventional contact-based sensors, the UAV-based approach enables significantly simpler deployment and provides full-field displacement information along the entire beam length.

In the third test, measurements were performed on a full-scale bridge during regular traffic operation in order to capture dynamic displacement response induced by heavy vehicle loading. The UAV-based measurements successfully reproduced the characteristic displacement patterns, with RMSE values of approximately 0.1 pixels, corresponding to up to 1.38 mm in object space. Although the absolute accuracy was reduced compared to the calibration test field, the temporal evolution and magnitude of the measured displacements

https://doi.org/10.3390/s26051593

showed good agreement with the LVDT reference data, and all characteristic loading events were clearly identified. This confirms the operational feasibility of the proposed approach for real-world bridge monitoring, where operational constraints inevitably affect measurement quality (further discussed in Section 4.3). A direct comparison between UAV-based and ground-based camera measurements in this test further highlights the importance of camera stability and quality. The ground-based system achieved significantly higher accuracy, with RMSE values below 0.5 mm, confirming that camera stability and image geometry play a critical role in achieving higher displacement measurement precision.

4.2. Influence of Homography Reference Point Configuration

Additionally, in this study, the systematic investigation of the influence of reference point number and spatial configuration on homography-based displacement accuracy was done. The calibration test field measurements clearly indicate that both the number and geometric distribution of reference points affect the stability and precision of the estimated displacements.

Based on the conducted experiments, several practical principles for reference point selection and arrangement can be summarized. First, reference points should be located on geometrically stable parts of the structure or on externally stable elements whenever possible. Any movement of reference points directly affects homography stability and may require coordinate correction.

Second, reference points should be (as much as possible but reasonable) uniformly distributed across the image. Concentrated or nearly collinear arrangements decrease the reliability and accuracy of homography. Furthermore, the inclusion of centrally located reference point compared to edge-only configurations, minimizes perspective-induced warping and provides better geometric control along the X-axis, while the Y-axis results remain largely stable regardless of configuration. At all three measurement locations we had a more favourable vertical distribution of reference points within the image, which provided sufficient geometric control even in edge-only configurations.

Third, an adequate number of reference points should be used to provide redundancy and improve robustness against individual point tracking errors. However, increasing the number of points does not automatically guarantee higher accuracy if their spatial distribution is unfavourable.

These findings highlight a limitation of homography-based displacement monitoring in practical field applications, where the availability of suitable stationary reference features is often constrained. Unlike controlled environments, real-world bridge sites rarely offer ideally distributed reference points within the camera field of view. Consequently, careful planning of UAV positioning, camera orientation, and reference points selection becomes essential to achieve reliable displacement estimation.

4.3. Practical Limitations and Operational Considerations

Several practical aspects constrain the performance of UAV-based homography displacement monitoring in real-world applications. In particular, the method is sensitive to UAV drift, wind-induced platform instability, illumination variability, camera calibration errors, and motion blur. Platform instability may introduce geometric inconsistencies that affect homography estimation accuracy, while reduced illumination or strong shadows can decrease image contrast and the number of reliably detectable features, increasing susceptibility to matching errors. Uncorrected lens distortion and calibration inaccuracies may further introduce spatially varying errors across the image domain.

In the present study, these effects were mitigated by performing measurements under favourable weather and lighting conditions, applying prior camera calibration, and ensur-

https://doi.org/10.3390/s26051593

ing stable hovering during image acquisition. Nevertheless, such operational factors remain critical when evaluating the robustness and reliability of UAV-based displacement monitoring in practical bridge applications. Beyond these environmental and platform-related influences, the method assumes predominantly planar structural motion, and significant out-of-plane displacements may introduce projection-related errors. Measurement accuracy also strongly depends on imaging geometry, camera resolution, and flight stability, emphasizing the importance of careful mission planning and flight control.

Moreover, the requirement for stationary reference points remains a major operational challenge, especially for long-span bridges or complex structural layouts. However, this challenge can be addressed by employing aerial manipulators designed to mount targets and sensors directly onto the structure, a process that eliminates the need for specialized inspection trucks and costly road closures [30]. Also, recent advances in reference-free vision-based methods, including feature tracking and digital image correlation techniques, show promising potential. However, such approaches are often more sensitive to illumination variability, texture quality, and environmental disturbances. Therefore, the use of controlled reference targets currently provides improved geometric stability and measurement robustness in field applications. Although the proposed UAV-based approach requires the placement of reference and monitoring targets, the installation effort remains significantly lower compared to traditional contact sensors such as LVDTs. In bridge load testing scenarios, LVDTs typically require stable external supports, mounting frames, wiring, and physical access beneath the structure, which can be time-consuming and sometimes impractical for large spans or over-water crossings. In contrast, the installation of lightweight photogrammetric targets can be performed rapidly and without the need for heavy supporting equipment. Nevertheless, for very large-scale infrastructure or structures with restricted access, the installation of artificial targets may still present logistical challenges. Taking into account the above, future developments may involve the integration of multi-camera UAV platforms, onboard inertial measurement units, and hybrid photogrammetric–inertial correction frameworks to further enhance robustness and reduce reliance on external reference points. Such advancements could significantly extend the applicability of UAV-based displacement monitoring for routine structural health assessment and long-term monitoring campaigns.

5. Conclusions

This study investigated the accuracy and operational feasibility of UAV-based homography photogrammetry for monitoring static and dynamic displacements of civil engineering structures. The results demonstrated that sub-millimetre precision was achievable under controlled conditions, while full-scale bridge monitoring showed displacement errors generally within 1–2 mm compared to LVDT measurements. The results confirmed that reference point number, spatial distribution, and stability significantly influence homography-based displacement accuracy. Importantly, the vertical displacement accuracy remained largely insensitive to reference point configuration, which is particularly relevant for bridge load testing, where vertical deflections are typically of primary interest and the identification of suitable stationary reference features often represents a practical challenge.

Despite the encouraging results, several challenges remain. Measurement accuracy is still affected by environmental conditions, illumination variability, and UAV platform stability. Moreover, the assumption of predominantly planar structural behaviour limits the direct applicability of the method in scenarios involving complex three-dimensional deformations. Future research will therefore focus on extending the proposed framework toward multi-camera UAV configurations, enhanced real-time stabilization strategies, and

https://doi.org/10.3390/s26051593

the integration of advanced computer vision and machine learning techniques to improve robustness under demanding field conditions. While the present study focused primarily on displacement reconstruction accuracy in the time domain, future work will also extend the validation framework toward frequency-domain analysis and potentially modal parameter identification, further assessing the applicability of UAV-based methods in structural dynamics monitoring. Overall, the findings demonstrated that UAV-based homography provides a flexible, contactless, and sufficiently accurate alternative to conventional displacement sensors, particularly in applications where sensor installation is complex or access is limited.

Author Contributions: Conceptualization, A.M. and I.D.; methodology, A.M. and D.G.; software, A.M. and D.G.; validation, A.M., D.G. and I.D.; formal analysis, D.G. and A.K.; investigation, A.M., A.K. and D.G.; resources, A.M. and I.D.; data curation, A.M.; writing—original draft preparation, A.M. and D.G.; writing—review and editing, A.M. and D.G.; visualization, A.K.; supervision, A.K. and I.D.; project administration, A.M. and A.K. All authors have read and agreed to the published version of the manuscript.

Funding: This research received no external funding.

Institutional Review Board Statement: Not applicable.

Informed Consent Statement: Not applicable.

Data Availability Statement: The data presented in this study are available on reasonable request from the corresponding author.

Acknowledgments: The authors wish to express their gratitude to the Institute for Photogrammetry, Zagreb for enabling the measurements to be carried out on the calibration field, and to Croatian Geological Survey, Department of Hydrogeology and Engineering Geology for providing access to a DJI Matrice 300 RTK.

Conflicts of Interest: The authors declare no conflicts of interest.

Abbreviations

The following abbreviations are used in this manuscript:

UAV	Unmanned Aerial Vehicle
LVDT	Linear Variable Differential Transformers
SHM	Structural Health Monitoring
RTS	Robotic Total Station
DIC	Digital Image Correlation
SfM	Structure-from-Motion

References

1. Golovastikov, N.V.; Kazanskiy, N.L.; Khonina, S.N. Optical Fiber-Based Structural Health Monitoring: Advancements, Applications, and Integration with Artificial Intelligence for Civil and Urban Infrastructure. *Photonics* **2025**, *12*, 615. [CrossRef]
2. Sonbul, O.S.; Rashid, M. Bridge Structural Health Monitoring: A Multi-Dimensional Taxonomy and Evaluation of Anomaly Detection Methods. *Buildings* **2025**, *15*, 3603. [CrossRef]
3. Wang, G.; Ke, J. Literature Review on the Structural Health Monitoring (SHM) of Sustainable Civil Infrastructure: An Analysis of Influencing Factors in the Implementation. *Buildings* **2024**, *14*, 402. [CrossRef]
4. Lydon, D.; Lydon, M.; Kromanis, R.; Dong, C.-Z.; Catbas, N.; Taylor, S. Bridge Damage Detection Approach Using a Roving Camera Technique. *Sensors* **2021**, *21*, 1246. [CrossRef] [PubMed]
5. Gharehbaghi, V.R.; Noroozinejad Farsangi, E.; Noori, M.; Yang, T.Y.; Li, S.; Nguyen, A.; Málaga-Chuquitaype, C.; Gardoni, P.; Mirjalili, S. A Critical Review on Structural Health Monitoring: Definitions, Methods, and Perspectives. *Arch. Comput. Methods Eng.* **2022**, *29*, 2209–2235. [CrossRef]
6. Zhang, S.; Liu, H.; Darwish, E.; Mosalam, K.M.; DeJong, M.J. Distributed Fiber-Optic Strain Sensing of an Innovative Reinforced Concrete Beam–Column Connection. *Sensors* **2022**, *22*, 3957. [CrossRef]

https://doi.org/10.3390/s26051593

7. Kovačič, B.; Motoh, T. Determination of Static and Dynamic Response of Structures with Geodetic Methods in Loading Tests. *Acta Geod. Geophys.* **2019**, *54*, 243–261. [CrossRef]
8. Lienhart, W.; Ehrhart, M.; Grick, M. High Frequent Total Station Measurements for the Monitoring of Bridge Vibrations. *J. Appl. Geod.* **2017**, *11*, 1–8. [CrossRef]
9. Meng, X.; Nguyen, D.T.; Xie, Y.; Owen, J.S.; Psimoulis, P.; Ince, S.; Chen, Q.; Ye, J.; Bhatia, P. Design and Implementation of a New System for Large Bridge Monitoring—Geoshm. *Sensors* **2018**, *18*, 775. [CrossRef] [PubMed]
10. Wagner, A.; Wiedemann, W.; Wunderlich, T. TS 6-New Technologies in Engineering Geodesy and Multisensor Systems Using IATS to Read and Analyze Digital Leveling Staffs. In *Proceedings of the International Symposiun on Engineering Geodesy-SIG 2016, Varazdin, Croatia, 20–22 May 2016*; Paar, R., Marendić, A., Zrinjski, M., Eds.; Croatian Geodetic Society: Zagreb, Croatia, 2016.
11. Tan, D.; Li, W.; Tao, Y.; Ji, B. Bridge Deformation Monitoring Combining 3D Laser Scanning with Multi-Scale Algorithms. *Sensors* **2025**, *25*, 3869. [CrossRef]
12. Liu, X.; Wang, P.; Lu, Z.; Gao, K.; Wang, H.; Jiao, C.; Zhang, X. Damage Detection and Analysis of Urban Bridges Using Terrestrial Laser Scanning (TLS), Ground-Based Microwave Interferometry, and Permanent Scatterer Interferometry Synthetic Aperture Radar (PS-InSAR). *Remote Sens.* **2019**, *11*, 580. [CrossRef]
13. Won, J.; Park, J.-W.; Park, J.; Shin, J.; Park, M. Development of a Reference-Free Indirect Bridge Displacement Sensing System. *Sensors* **2021**, *21*, 5647. [CrossRef]
14. Zhou, Y.; Zhu, J.; Zhao, L.; Hu, G.; Xin, J.; Zhang, H.; Yang, J. High-Precision Monitoring Method for Bridge Deformation Measurement and Error Analysis Based on Terrestrial Laser Scanning. *Remote Sens.* **2024**, *16*, 2263. [CrossRef]
15. Goricanec, J.; Ereiz, S.; Orsag, M.; Duvnjak, I. Identification of the Dynamic Parameters of Bridge Elements Using Unmanned Aerial Vehicle. *J. Sound Vib.* **2023**, *566*, 117901. [CrossRef]
16. Wu, Z.; Chen, G.; Ding, Q.; Yuan, B.; Yang, X. Three-Dimensional Reconstruction-Based Vibration Measurement of Bridge Model Using UAVs. *Appl. Sci.* **2021**, *11*, 5111. [CrossRef]
17. Yoon, H.; Shin, J.; Spencer, B.F., Jr. Structural Displacement Measurement Using an Unmanned Aerial System. *Comput.-Aided Civ. Infrastruct. Eng.* **2018**, *33*, 183–192. [CrossRef]
18. Dong, C.-Z.; Celik, O.; Catbas, F.N.; OBrien, E.; Taylor, S. A Robust Vision-Based Method for Displacement Measurement under Adverse Environmental Factors Using Spatio-Temporal Context Learning and Taylor Approximation. *Sensors* **2019**, *19*, 3197. [CrossRef]
19. Maboudi, M.; Backhaus, J.; Mai, I.; Ghassoun, Y.; Khedar, Y.; Lowke, D.; Riedel, B.; Bestmann, U.; Gerke, M. Very High Resolution Bridge Deformation Monitoring Using UAV-Based Photogrammetry. *J. Civ. Struct. Health Monit.* **2025**, *15*, 3489–3508. [CrossRef]
20. Marendić, A.; Gajski, D.; Duvnjak, I.; Paar, R. Evaluation of Photogrammetric Methods for Displacement Measurement During Structural Load Testing. *Remote Sens.* **2025**, *17*, 2569. [CrossRef]
21. Reagan, D.; Sabato, A.; Niezrecki, C. Feasibility of Using Digital Image Correlation for Unmanned Aerial Vehicle Structural Health Monitoring of Bridges. *Struct. Health Monit.* **2018**, *17*, 1056–1072. [CrossRef]
22. Zhang, J.; Wu, Z.; Chen, G.; Liang, Q. Comparisons of Differential Filtering and Homography Transformation in Modal Parameter Identification from UAV Measurement. *Sensors* **2021**, *21*, 5664. [CrossRef]
23. Habeenzu, H.; McGetrick, P.; Hester, D.; Taylor, S. UAS Displacement Measurement Using a Three Point Homography Method with Potential Bridge Monitoring Applications. *Measurement* **2024**, *232*, 114718. [CrossRef]
24. Weng, Y.; Shan, J.; Lu, Z.; Lu, X.; Spencer, B.F., Jr. Homography-Based Structural Displacement Measurement for Large Structures Using Unmanned Aerial Vehicles. *Comput.-Aided Civ. Infrastruct. Eng.* **2021**, *36*, 1114–1128. [CrossRef]
25. Chen, P.; Suter, D. Error Analysis in Homography Estimation by First Order Approximation Tools: A General Technique. *J. Math. Imaging Vis.* **2009**, *33*, 281–295. [CrossRef]
26. Acuna, R.; Willert, V. Insights into the robustness of control point configurations for homography and planar pose estimation. *arXiv* **2018**, arXiv:1803.03025.
27. Mao, Y.; Xiao, F.; Tian, G.; Xiang, Y. Sensitivity Analysis and Sensor Placement for Damage Identification of Steel Truss Bridge. *Structures* **2025**, *73*, 108310. [CrossRef]
28. Luo, Y.; Wang, X.; Liao, Y.; Fu, Q.; Shu, C.; Wu, Y.; He, Y. A Review of Homography Estimation: Advances and Challenges. *Electronics* **2023**, *12*, 4977. [CrossRef]
29. Agarwal, A.; Jawahar, C.V.; Narayanan, P.J. *A Survey of Planar Homography Estimation Techniques*; Technical Report; International Institute of Information Technology: Hyderabad, India, 2005.
30. Ivanovic, A.; Markovic, L.; Car, M.; Duvnjak, I.; Orsag, M. Towards Autonomous Bridge Inspection: Sensor Mounting Using Aerial Manipulators. *Appl. Sci.* **2021**, *11*, 8279. [CrossRef]

Disclaimer/Publisher's Note: The statements, opinions and data contained in all publications are solely those of the individual author(s) and contributor(s) and not of MDPI and/or the editor(s). MDPI and/or the editor(s) disclaim responsibility for any injury to people or property resulting from any ideas, methods, instructions or products referred to in the content.

https://doi.org/10.3390/s26051593

sensors

MDPI

Article

Concrete Crack Detection and Classification Methods Based on Machine Vision and Deep Learning

Weibin Chen [1,2,3,4], Zhijie Peng [5], Xiangsheng Chen [1,2,3,4], Linshuang Zhao [5,*], Tao Xu [1,2,3,4], Qiang Li [1,2,3,4], Xianwen Huang [6] and K. K. Pabodha M. Kannangara [7]

1 College of Civil and Transportation Engineering, Shenzhen University, Shenzhen 518060, China; wbchen@szu.edu.cn (W.C.); xschen@szu.edu.cn (X.C.); taoxu@szu.edu.cn (T.X.); parkli@szu.edu.cn (Q.L.)
2 Underground Polis of Academy, Shenzhen University, Shenzhen 518060, China
3 Key Laboratory of Coastal Urban Resilience Infrastructure, Ministry of Education, Shenzhen University, Shenzhen 518060, China
4 National Engineering Research Center of Deep Shaft Construction, Shenzhen 518060, China
5 College of Engineering, Shantou University, Shantou 515063, China; 24zjpeng@stu.edu.cn
6 School of Civil Engineering, Suzhou University of Science and Technology, 1701 Riverside Road, Suzhou 215009, China; huangxianwen194@usts.edu.cn
7 Construction and Quality Management, Hong Kong Metropolitan University, Hong Kong SAR, China; kkpmkann@hkmu.edu.hk
* Correspondence: lshzhao@stu.edu.cn

Abstract

With the rapid development of underground space, structural crack monitoring has become increasingly critical. This study proposes a unified framework integrating image preprocessing, feature extraction, model training, and safety assessment for crack analysis. An improved OTSU threshold segmentation algorithm based on sliding windows and local statistical analysis is developed to enhance noise suppression and detail preservation under complex backgrounds and varying resolutions. For crack identification and orientation classification, SVM, CNN, ResNet-18, and K-means clustering are systematically compared. The results show that the improved OTSU method outperforms the classical approach in both high- and low-resolution images. In classification tasks, SVM achieves the best performance under limited data conditions, with accuracy exceeding 96% and reaching 97% after outlier removal, outperforming CNN, K-means, and ResNet-18. Although ResNet-18 demonstrates strong overall performance with high prediction confidence across crack categories, it remains slightly inferior to SVM when training data are limited. Experimental validation using full-scale loading tests of metro shield tunnel segments further confirms the robustness of the proposed approach, with SVM achieving an accuracy of 95.45% in real-world conditions. This study provides an efficient and reliable solution for automated crack detection and classification in metro tunnel infrastructure and similar underground segment-based systems.

Keywords: machine vision; crack detection; OTSU algorithm; Support Vector Machine; classification

1. Introduction

As underground space development continues, the potential impact of subsurface constructions on adjacent buildings has become more pronounced, particularly regarding issues such as foundation settlement and structural displacement [1–3]. These problems may not only hinder normal building operations but also pose risks to urban safety [4–7].

Monitoring of cracks in underground structures holds substantial practical significance and engineering value. Real-time monitoring and analysis of cracks enable the prediction of structural failure modes and facilitate the assessment of impacts on neighboring structures, thereby supporting the scientific planning and safe management of urban underground spaces [8].

Over the past few decades, manual visual inspection, a traditional way to identify and assess cracks, has shown clear flaws in practice: it is inefficient, takes too much time, and results are subjective [9]. Although conventional manual inspection is widely used for concrete crack detection, it remains labor-intensive, time-consuming, and subjective due to heavy reliance on the experience of inspectors. It is also unsuitable for large-scale continuous monitoring and cannot precisely quantify cracks, which may affect the efficiency and reliability of structural assessment. Differences in inspector skills and experience also make results inconsistent and unstable. In monitoring the health of concrete structures, accurately identifying and assessing cracks is key to ensuring safety and durability [10]. But manual inspection, though widely used, has become increasingly problematic for these reasons. To fix these issues, digital image processing has become a better option. It automatically gets key info like whether a crack exists, where it is, and how wide it is by analyzing images of concrete surfaces. Today, main image processing methods fall into three types: Intensity threshold methods, like the OTSU algorithm, use image binarization—turning grayscale images into black and white—to separate cracks (usually darker) from the background (usually brighter) [11–13], yet in uneven light or with complex backgrounds (like stains or shadows), they often mistake dark spots for cracks. Edge detection methods find cracks by their edges but are sensitive to noise, creating fake edges in complex backgrounds [14,15]. Mathematical morphology, used as a helper tool, changes crack shapes with operations like dilation and erosion to improve connections or remove noise [13,16]. But choosing the right parameters depends on the situation, or else the original crack shape might get damaged.

Although the aforementioned image processing methods have demonstrated great potential in crack identification, their underlying shared assumption—that the given images contain actual cracks—severely limits the realization of fully automated monitoring. In practical engineering, concrete surface images captured by digital cameras or unmanned aerial vehicles often contain both cracked and non-cracked regions (such as dark stains, shadows, dust, and lumps), and these "crack-like" features are visually indistinguishable from real cracks [17,18]. For instance, image binarization may misclassify dark stains as cracks, directly leading to an increase in the false detection rate. Therefore, accurately distinguishing real cracks from crack-like features in complex backgrounds has become a critical bottleneck in achieving fully automated crack monitoring. In recent years, the introduction of machine learning techniques has provided new insights for solving this problem; in particular, the integration of supervised learning and computer vision has significantly improved the intelligence level of crack identification. Examples include: Nyathi et al.'s [19] proposed method combining deep learning and laser calibration, which exhibited excellent performance in crack classification, segmentation, and parameter measurement accuracy, but the generalization ability of the model is limited by the scale of the training dataset; Oh et al. [20] adopted a BP neural network to realize crack extraction and detection through nonlinear classification algorithms, providing a reference for nonlinear feature modeling; Long et al. [21] proposed an algorithm combining grayscale correction and adaptive minimum error threshold segmentation, which can effectively extract cracks but lacks classification and evaluation capabilities; Nishikawa et al. [22] combined image processing with genetic programming, verifying its effectiveness under complex surface textures, though there remains room for improvement in accuracy;

https://doi.org/10.3390/s26082381

Han et al. [23] improved the calculation accuracy of geometric parameters by identifying crack edges and correcting parameters using an interactive genetic algorithm, yet the method involves large computational costs and performs poorly when the grayscale difference between cracks and the background is small; Li et al. [24] proposed a CNN-based classifier that achieves high-accuracy detection on large databases without manual feature extraction, highlighting the advantages of deep learning in automatic feature learning. Deep learning-based methods such as YOLO and U-Net have been widely applied to crack detection tasks. A lightweight YOLOv8-seg framework was proposed to achieve crack segmentation and quantification, improving computational efficiency while maintaining high detection accuracy [25]. Zhang et al. [26] utilized a U-Net-based fully convolutional network to perform pixel-level crack segmentation, demonstrating strong detection accuracy. Shamsabadi et al. [27] employed a Vision Transformer (ViT)-based framework for crack detection, achieving improved segmentation performance, especially for small and multi-scale cracks. However, such methods rely on dense pixel-level annotations and are therefore less suitable for data-constrained engineering scenarios. He et al. [28] proposed the ResNet architecture, which introduces residual connections to facilitate the training of deep neural networks and improve feature representation. This approach effectively alleviates the vanishing gradient problem and has become a widely used backbone in computer vision tasks. A comparison of the aforementioned crack detection methods is summarized in Figure 1.

In summary, while the evolution from traditional image processing to machine learning has gradually enhanced the automation and accuracy of crack identification, multiple technical bottlenecks persist. For traditional OTSU methods, in uneven light or with complex backgrounds (like stains or shadows), they often mistake dark spots for cracks. At a broader level, future research must address core challenges: balancing algorithm robustness with adaptability to complex scenarios, reducing reliance on large annotated datasets, and achieving full-process automation from existence detection to accurate classification.

In this study, a novel integrated framework encompassing image preprocessing, feature extraction, model training, and safety assessment was established for the comprehensive analysis of cracks in tunnel structures. To address the issues of noise interference and detail loss inherent in the traditional OTSU threshold segmentation algorithm under conditions of complex backgrounds and variable resolutions, an improved OTSU algorithm incorporating a sliding window mechanism and local statistical analysis is proposed. Subsequently, three methods—Support Vector Machine (SVM), Convolutional Neural Network (CNN), K-Means clustering and ResNet—were adopted for crack identification and orientation classification (i.e., Horizontal, Vertical, and Inclined), with a systematic comparison of their performance metrics conducted. Finally, case verification was carried out on shield tunnel segment loading tests to validate the practical applicability of the developed framework.

The main research gaps can be summarized as follows:

- Global thresholding methods lack robustness under uneven illumination and complex underground backgrounds;
- Crack-like features such as stains and shadows are difficult to distinguish from real cracks;
- Data-driven approaches rely on large annotated datasets, limiting practical applicability;
- Existing studies lack integrated frameworks for crack detection and classification.

The main contributions of this study are as follows:

- An improved OTSU algorithm incorporating sliding window and local statistical analysis is proposed;

https://doi.org/10.3390/s26082381

- A comparative study of SVM, CNN, K-Means and Resnet for crack identification and orientation classification is conducted;
- A feature-based approach is proposed for accurate crack orientation recognition;
- The proposed method is validated through full-scale metro shield tunnel segment loading tests.

Method	Type	Advantages	Limitations	Annotation Requirement	Computational Cost	Applicability
Image Processing (e.g., Otsu, edge detection)	Traditional	Simple, fast, no training required; low computational cost; easy to implement	Sensitive to noise, illumination, and complex backgrounds; poor generalization	None	Very low	Suitable for simple environments
K-Means Clustering	Unsupervised learning	No labeled data required; simple implementation; useful for coarse segmentation	Sensitive to initialization; limited feature representation; poor performance in complex scenes	None	Low	Basic segmentation tasks
SVM + Image Processing	Machine learning	Good performance with small datasets; low annotation cost; fast training and inference; robust classification with handcrafted features	Depends on feature quality; limited ability to learn complex patterns; may struggle with highly irregular cracks	Low (image-level labels)	Low	Suitable for real-time and data-scarce scenarios
CNN	Deep learning	Automatic feature extraction; high accuracy; strong representation ability	Requires large labeled datasets; high computational cost; prone to overfitting on small datasets	High	High	Suitable for large-scale datasets
YOLO	Object detection	Real-time detection; end-to-end framework; strong generalization ability	Requires bounding box annotation; limited precision for thin cracks	Medium–High	Medium–High	Real-time detection tasks
U-Net	Semantic segmentation	Pixel-level segmentation; excellent performance for thin cracks	Requires pixel-level annotation (very labor-intensive); high training cost	Very High	High	High-precision crack segmentation
ResNet (e.g., ResNet-18)	Deep CNN	Deeper architecture; improved feature representation via residual learning; strong baseline performance	Requires sufficient data; still computationally expensive	Medium-High	High	Transfer learning; feature extraction
Vision Transformer (ViT)	Transformer-based	Captures global contextual information; strong performance in complex scenes	Requires large datasets and high computational cost; complex training	Very High	Very High	Large-scale, high-complexity tasks

Figure 1. Comparison of Crack Detection and Classification Methods.

2. Methodology

In crack detection tasks, accuracy and robustness are strongly influenced by image preprocessing, feature extraction, and the choice of classification methods. In this study, the OTSU algorithm is employed for image threshold segmentation, and an improved version is further developed to enhance crack region extraction. SVM, CNN, ResNet-18, and K-means clustering are then utilized as classification models to systematically compare their performance in terms of recognition accuracy and generalization capability.

2.1. OTSU Threshold Segmentation Algorithm

The OTSU algorithm was proposed in 1979 by Otsu [29]. This method determines the optimal threshold by maximizing the between-class variance and has been widely applied in the field of image processing for binarization tasks. It is particularly suitable for

https://doi.org/10.3390/s26082381

images where there is a clear difference in grayscale distribution between the target and the background. However, its widespread use is limited in complex crack images. Relying on global gray level statistics, it falters with highly heterogeneous backgrounds—such as uneven illumination, varying textures, or noise. Unable to adapt to local gray variations, it often over-segments (misidentifying non-cracks) or under-segments (missing faint/narrow cracks) and lacks dynamic threshold adjustment for local crack features, reducing accuracy in complex surroundings [30].

2.2. Improved OTSU Threshold Segmentation Algorithm

To address these limitations, an improved locally adaptive thresholding method is proposed by integrating a sliding window mechanism with local statistical analysis. The method combines global thresholding with local adaptive adjustment to enhance crack detection under complex conditions. The main procedure is as follows:

(1) The classical OTSU algorithm is applied to compute the global optimal threshold T_1, which maximizes the between-class variance $\sigma_B^2(T)$ to separate the foreground and background:

$$T_1 = argmax\ \sigma_B^2(T) \tag{1}$$

(2) Local statistical computation: The image is divided into windows of size $N \times N$, and the local mean $\overline{I}$ and variance D within each window are calculated as:

$$\overline{I} = \frac{1}{N^2}\sum_{(x,y)\in W} I(x,y) \tag{2}$$

$$D = \frac{1}{N^2}\sum_{(x,y)\in W} (I(x,y) - \overline{I})^2 \tag{3}$$

where $I(x,y)$ denotes the grayscale value of pixel (x,y) in window W, and N^2 is the total number of pixels in the window. The variance D reflects local intensity variations.

(3) Adaptive segmentation strategy: The local variance D is used to evaluate the complexity of each region. If $D < \tau$, where τ is a predefined variance threshold, the region is considered homogeneous and segmented using the global threshold:

$$T = T_1 \tag{4}$$

Otherwise, the region is regarded as containing cracks or complex background, and a locally adaptive threshold is applied.

(4) Threshold adjustment: The local threshold is defined as:

$$T_2 = \alpha T_1 + (1-\alpha)\overline{I} \tag{5}$$

where $I(x,y)$ denotes the grayscale value of pixel (x,y) in window W, and N^2 is the total number of pixels in the window.

Here, α acts as a weighting coefficient that balances global information and local features, allowing the threshold to adaptively adjust for improved detection of low-contrast cracks. The global threshold T_1 describes the overall intensity distribution, whereas $\overline{I}$ characterizes local brightness. A larger α improves stability under uniform illumination, while a smaller α enhances sensitivity to local variations under uneven lighting and low-contrast conditions.

2.3. Crack Identification and Classification Using SVM

SVM is a classification algorithm based on statistical learning theory, proposed by Vapnik [31]. In this study, SVM is applied to distinguish between "crack" and "non-crack" images by constructing an optimal hyperplane, thereby enabling accurate crack

https://doi.org/10.3390/s26082381

identification. Due to its strong generalization ability in high-dimensional spaces, SVM is capable of effectively handling nonlinearly distributed data, making it well-suited for complex image analysis tasks such as crack detection.

In linearly separable cases, SVM constructs an optimal hyperplane to perform crack classification. The primary objective is to maximize the margin between two classes, expressed as $2/|\mathrm{w}|$. The corresponding optimization framework can be described as the hard margin model:

- Objective function:

$$\min_{w,b} \frac{1}{2}\|w\|^2 \tag{6}$$

- Constraint condition:

$$y_i\left(w^T x_i + b\right) \geq 1, \forall i \tag{7}$$

where w denotes the weight vector, b is the bias term, and (x_i, y_i) represents the training samples with $y_i \in \{+1,-1\}$, indicating crack and non-crack categories. The model requires that all samples strictly satisfy the classification constraint, and the optimal solution is determined by the support vectors that meet the condition $y_i(\mathrm{w}^{\mathrm{T}} x_i + b) = 1$.

To handle noisy or non-linearly separable data, a soft margin model is introduced by incorporating slack variables $\xi_i \geq 0$ and a regularization parameter C:

- Objective function:

$$\min_{w,b} \frac{1}{2}\|w\|^2 + C\sum_{i=1}^{N} \xi_i \tag{8}$$

- Constraint condition:

$$y_i\left(\mathrm{w}^{\mathrm{T}} x_i + b\right) \geq 1 - \xi_i,\ \xi_i \geq 0, \forall i \tag{9}$$

The parameter C balances the trade-off between maximizing the margin and tolerating misclassification. A larger C imposes a heavier penalty on misclassification, while a smaller C promotes better generalization.

When crack features are not linearly separable in the original space, a kernel function mapping mechanism is employed to project the data into a higher-dimensional space. Common kernel functions include the linear kernel, Gaussian (RBF) kernel, and polynomial kernel, with respective formulations:

- Linear kernel:

$$K(x_i, x_j) = x_i^T x_j \tag{10}$$

- Gaussian kernel:

$$K(x_i, x_j) = exp\left(-\frac{\left|x_i - x_j\right|^2}{2\sigma^2}\right) \tag{11}$$

- Polynomial kernel:

$$K(x_i, x_j) = \left(x_i^{\mathrm{T}} x_j + c\right)^d \tag{12}$$

For the linearly separable scenario, the classification function is defined as:

$$f(x) = sign\left(w^T x + b\right) \tag{13}$$

https://doi.org/10.3390/s26082381

For kernel-based scenarios, it is formulated as:

$$f(x) = sign\left(\sum_{i=1}^{N} \alpha_i y_i K(x_i, x) + b\right) \tag{14}$$

where α_i denotes the Lagrange multiplier, and sign$(\cdot)$ indicates the predicted class label (+1 for crack, −1 for non-crack). The kernel mapping mechanism enhances the nonlinear classification capability and effectively addresses the challenge of classifying cracks when there is significant overlap with background features.

2.4. Crack Identification and Classification Using CNN

CNN consists of convolutional layers, pooling layers, fully connected layers, and activation functions. The convolutional layers extract local features using convolution kernels, while pooling layers down sample the feature maps to reduce dimensionality and computational complexity. Fully connected layers integrate the extracted features to perform final classification, and activation functions introduce nonlinearity, enhancing the network's representational capacity [32].

The key components of CNNs can be described mathematically. In the convolutional layer, the input image is convolved with a kernel, expressed as:

$$y(i,j) = (x \cdot w)(i,j) = \sum_M \sum_N x(i+m, j+n) \cdot w(m,n) \tag{15}$$

where $x(i,j)$ denotes the input image or feature map, $w(m,n)$ represents the convolution kernel of size $m \times n$, and $y(i,j)$ is the output of the convolution operation. The max pooling operation is defined as:

$$y(i,j) = max\{x(p,q) : p \in [i, i+k], q \in [j, j+k]\} \tag{16}$$

In fully connected layers, each neuron is connected to all neurons in the previous layer. The mathematical representation is:

$$y = f(Wx + b) \tag{17}$$

where W is the weight matrix, x is the output from the preceding layer, b is the bias term, and f denotes the activation function. Activation functions such as ReLU (Rectified Linear Unit), Sigmoid, and Softmax are commonly used to introduce nonlinearity and compute class probabilities. Their formulations are as follows:

$$ReLU(x) = max(0, \mathrm{x}) \tag{18}$$

$$\sigma(x) = \frac{1}{1+_e{}^{-x}} \tag{19}$$

$$Softmax(x_i) = \frac{{}^{e^{x_i}}}{\sum_j {}^{e^{x_j}}} \tag{20}$$

In classification tasks, the cross-entropy loss function is typically applied, defined by:

$$\mathrm{L} = -\sum_{i=1}^{C} y_i log(\hat{y}_i) \tag{21}$$

where C denotes the number of classes, y_i is the one-hot encoded ground truth label, and $\hat{y}_i$ represents the predicted probability.

Through its multilayer convolutional structure, a CNN is capable of extracting features progressively, ranging from edge textures to high-level semantic information,

https://doi.org/10.3390/s26082381

thereby achieving superior performance in tasks such as image classification and object detection.

2.5. Fundamental Principles of Morphological Operations

Morphological operations are grounded in the theory of mathematical morphology and are designed to extract and refine shape-related features within an image [33]. In crack detection, they effectively suppress noise, enhance crack connectivity, and improve the structural integrity of segmented regions, playing an important role in both preprocessing and feature extraction stages. For crack images segmented by the OTSU method, this study applies a series of morphological operations, including dilation, erosion, opening, closing, as well as bridging and filling, to improve detection accuracy. Dilation expands crack regions to enhance connectivity and repair fragmented structures, while erosion removes isolated noise and refines edges. Opening (erosion followed by dilation) is used to eliminate small-scale noise and smooth contours, whereas closing (dilation followed by erosion) bridges discontinuities and strengthens connectivity. These operations collectively improve the quality of crack regions and provide a reliable basis for subsequent analysis [34].

In addition, morphological filling is employed to restore enclosed holes within crack regions. By improving pixel connectivity and smoothing boundaries, this operation compensates for discontinuities caused by noise, shadows, or resolution limitations, thereby enhancing the accuracy of crack skeleton extraction and ensuring stability in subsequent classification tasks.

3. A Novel Framework for Crack Recognition and Classification

This study proposes a novel framework for crack recognition and classification, as illustrated in Figures 2 and 3. As shown in Figure 2, the key image processing steps and training set construction process are presented, including the transformation from the original image to the binarized result, skeletonized representation, and the extraction of features for model training. The framework begins with the acquisition of images via detection equipment, which are aggregated into an image library. These images first undergo processing using an improved OTSU algorithm to generate a labeled dataset, distinguishing between cracked and non-cracked regions. For crack presence detection, two models are trained in parallel on the labeled dataset: a CNN model, which is trained directly on a labeled dataset consisting of two image groups—crack and non-crack—to classify images as cracked or non-cracked, and an SVM model trained on handcrafted features—including gray area and gray histogram information. A test set is then used to evaluate the performance of both models; if the validation is successful, the process proceeds, otherwise, model training is refined accordingly. Subsequently, images identified as containing cracks undergo binarization and skeletonization. Grayscale projections along the X-axis and Y-axis are performed on the skeletonized cracks to classify them into Horizontal, Vertical, or Inclined types. Finally, based on these classification results, a structural safety prevention plan is formulated, thereby completing a comprehensive loop from detection and identification to classification and application, which supports effective management of structural safety related to cracks.

https://doi.org/10.3390/s26082381

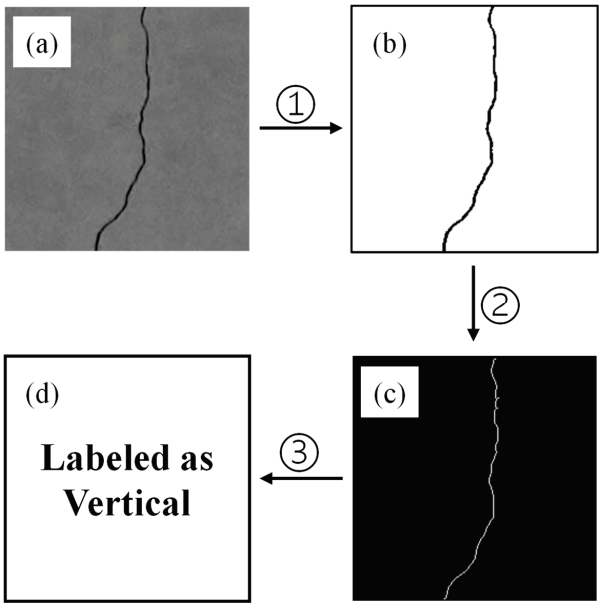


Figure 2. Key Image Processing and Training Set Construction: (**a**) original image, (**b**) binary segmentation image, (**c**) single-pixel image, and (**d**) Training Set; (1) improved OTSU processing, (2) morphological processing and skeletonization and (3) construct SVM training set using X, Y projection pixel histogram distribution.

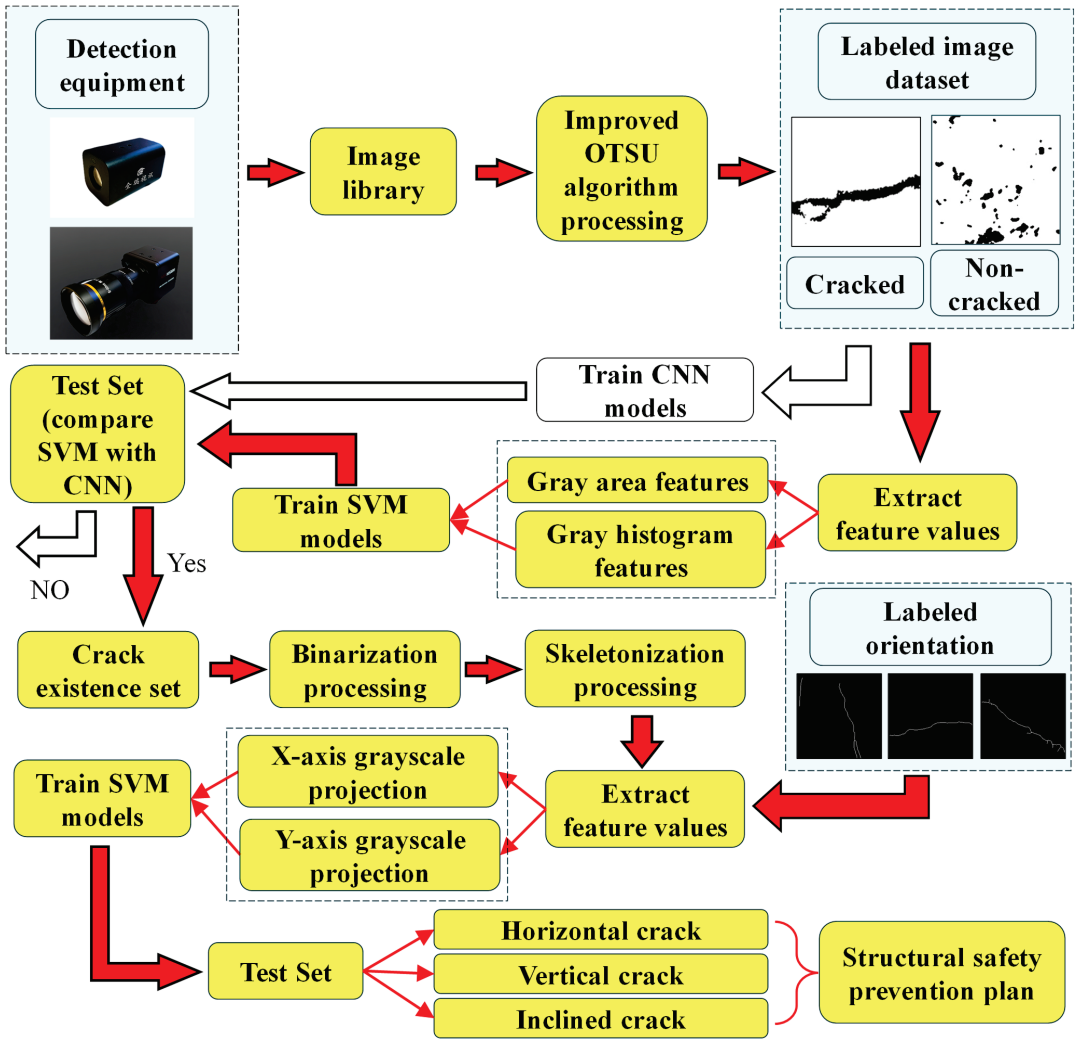


Figure 3. Workflow of Crack Detection and Classification Using Improved OTSU and SVM. Red arrows and yellow boxes represent the main workflow.

https://doi.org/10.3390/s26082381

4. Crack Detection and Classification

In this section, all experiments were conducted on a workstation equipped with an Intel Core i5-13400F CPU, 16 GB RAM, and an NVIDIA GeForce RTX 3070 Ti GPU. This unified hardware configuration ensures consistency, reproducibility, and fair comparison across all evaluated methods. The concrete crack images used in this study are sourced from the dataset available at https://www.kaggle.com/thesighsrikar/concrete-crack-images-for-classification (accessed on 9 April 2026).

4.1. Performance Comparison Between Classical and Improved OTSU Algorithms on Images with Different Resolutions

Figure 4 presents a comparison between the classical and improved OTSU algorithms applied to high-resolution images, including the original image, the result from the classical OTSU algorithm, and the result from the improved version. In high-resolution scenarios, the classical algorithm is prone to threshold deviation due to gray-level distortion caused by increased noise and complex background textures, resulting in significant noise in the processed image (Figure 4b). In contrast, the improved algorithm is more adaptable to complex scenes and effectively suppresses noise. Figure 4c shows that the improved OTSU algorithm significantly reduces noise and achieves higher segmentation accuracy.

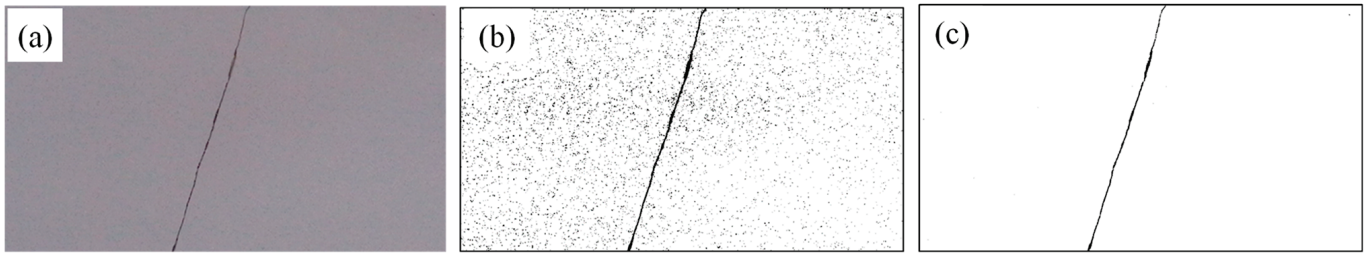


Figure 4. Classical OTSU and improved OTSU applied to high-resolution images: (**a**) original image, (**b**) result of classical OTSU, and (**c**) result of improved OTSU.

Figure 5 illustrates the performance of both algorithms on low-resolution images, including the original image, the result from the classical algorithm, and the result from the improved one. While the classical algorithm demonstrates reasonable noise suppression in low-resolution cases, it tends to lose fine crack features due to pre-denoising procedures. This issue arises because the algorithm typically applies a denoising step prior to segmentation, which enhances contrast between foreground and background but may weaken or even eliminate subtle crack structures. As a result, certain fine details are not preserved. The improved OTSU algorithm, by contrast, processes images directly without requiring pre-denoising, thereby achieving significant improvements in the preservation of crack details (Figure 5c). These results indicate that the improved OTSU algorithm, through optimized threshold selection, effectively addresses the noise interference problem in high-resolution images and overcomes the detail loss issue in low-resolution scenarios, thus demonstrating comprehensive advantages in high-precision crack extraction tasks.

https://doi.org/10.3390/s26082381

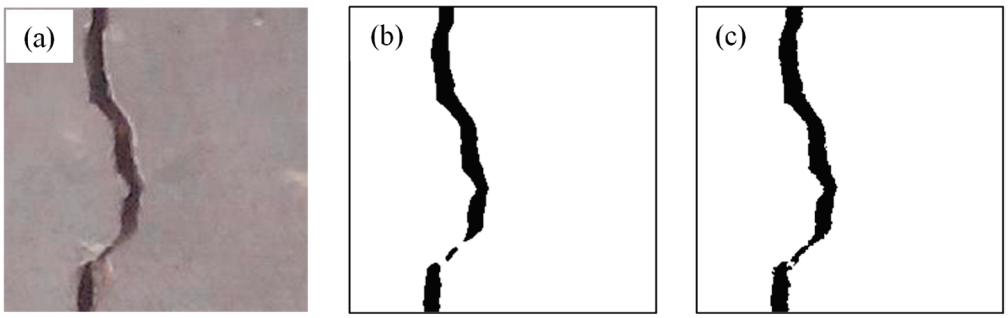


Figure 5. Classical OTSU and improved OTSU applied to low-resolution images: (**a**) original image, (**b**) result of classical OTSU, and (**c**) result of improved OTSU.

4.2. Performance Analysis of Crack Detection Based on SVM and CNN

In the task of crack detection, the primary function of the SVM lies in classifying images based on extracted features, aiming to accurately distinguish crack regions from background or non-crack areas. Given the diverse morphological characteristics of cracks (e.g., linear, tortuous, branched), the effectiveness of feature extraction methods directly affects the classification performance of SVM. In this study, an improved OTSU algorithm is applied as a unified preprocessing step for all monitoring images to enhance contrast between crack regions and the background. This preprocessing enhances the clarity of crack features and improves the reliability of subsequent SVM training. As illustrated in Figure 6 (Unified processing results using improved OTSU algorithm), the visual distinction between crack and non-crack images becomes more pronounced after preprocessing. For feature selection, the SVM model employs crack area (a morphological feature) and grayscale histogram features as key discriminative indicators. A representative training set is constructed using both crack and non-crack images, and performance is validated on the constructed dataset. The experimental results indicate an overall classification accuracy exceeding 95%, demonstrating effective differentiation between crack and background in most scenarios. However, the model shows limitations when the grayscale contrast between cracks and background is low. Some low-contrast cracks are misclassified as non-crack regions, while certain background textures or noise are incorrectly identified as cracks. Typical misclassification cases are shown in Figure 7a,b, highlighting the adverse impact of background similarity on detection accuracy.

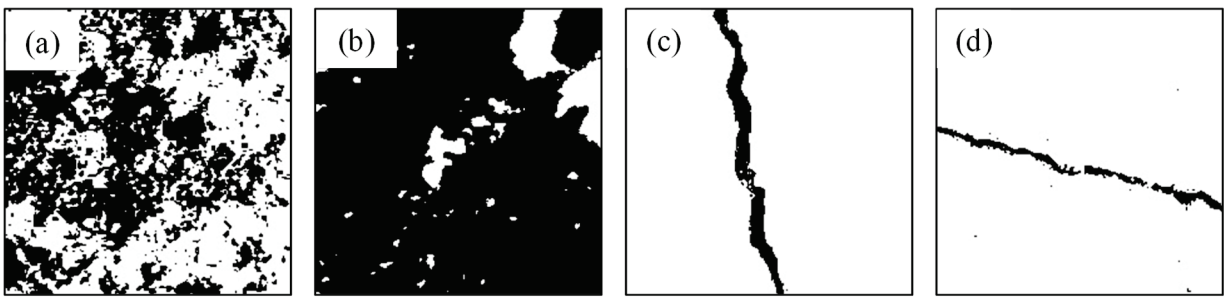


Figure 6. Unified processing results using improved OTSU Algorithm: (**a**,**b**) Processed images without cracks; (**c**,**d**) Processed images with cracks.

Following the SVM-based classification process, morphological operations are utilized to connect fragmented crack regions and extract complete contours, thereby providing a solid foundation for subsequent morphological analysis and structural assessment of cracks.

To comprehensively evaluate the performance of the algorithms, a comparative analysis was conducted between SVM and CNN for crack recognition under two preprocessing schemes, namely the improved OTSU algorithm and a combination of nonlinear denoising

https://doi.org/10.3390/s26082381

with the classical OTSU algorithm. All experiments were conducted on a unified dataset, which was randomly divided into training and testing sets with an approximate ratio of 80:20. The test set consists of 684 images, and the same data partition was used across all methods to ensure a fair comparison. Under the improved OTSU preprocessing, the SVM model achieved an accuracy of 97.92% for non-crack regions and 95.05% for crack regions, resulting in an overall accuracy of 96.05%. In comparison, the CNN model reached a non-crack recognition accuracy of 98.33% and a crack recognition accuracy of 94.02%, yielding an overall accuracy of 95.76%. The corresponding probability distributions are shown in Figure 8.

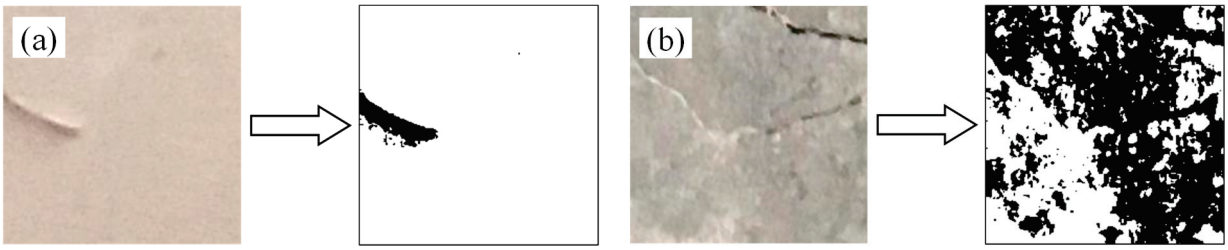


Figure 7. Examples of low grayscale contrast between cracks and background: (**a**) Improved OTSU processed image of a non-crack image; (**b**) improved OTSU processed image of a faint crack.

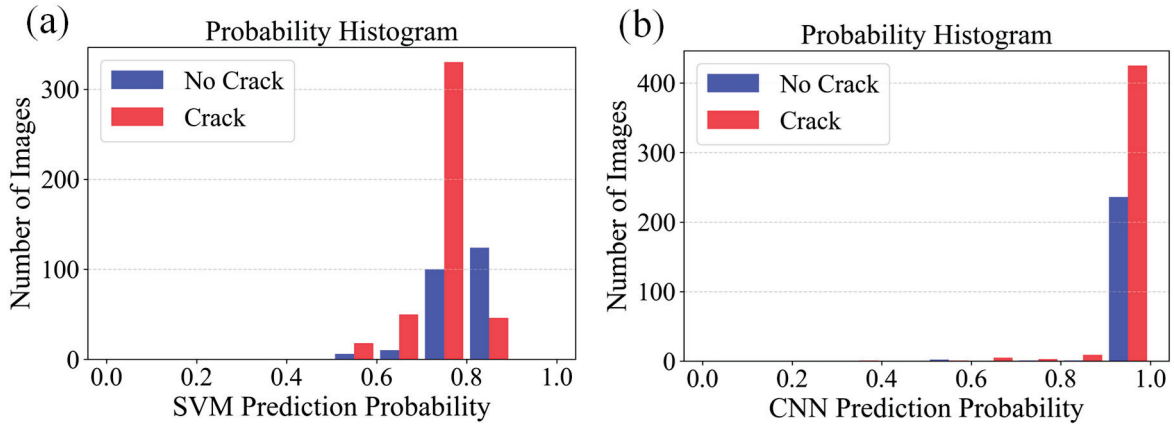


Figure 8. Prediction probability histograms based on improved OTSU-preprocessed images: (**a**) SVM and (**b**) CNN.

Under the preprocessing scheme combining nonlinear denoising with the classical OTSU algorithm, the performance of both models was further evaluated on the same dataset. The results are presented in Figure 9. For the SVM model, the non-crack recognition accuracy decreased to 92.50%, with a crack recognition accuracy of 86.71%, resulting in an overall accuracy of 88.74%. The CNN model, under the same conditions, achieved a non-crack recognition accuracy of 99.17%, a crack recognition accuracy of 94.37%, and an overall accuracy of 96.05%.

The results indicate that the improved OTSU preprocessing significantly enhances the performance of the SVM model, primarily due to its reliance on handcrafted features that are highly sensitive to feature quality. By improving the separation between crack and background regions, the proposed method produces more discriminative grayscale and morphological features, which directly benefits the SVM classifier. In contrast, the CNN model demonstrates relatively stable performance under different preprocessing schemes, as it is capable of automatically learning feature representations from raw image data and is therefore less sensitive to variations in preprocessing quality.

https://doi.org/10.3390/s26082381

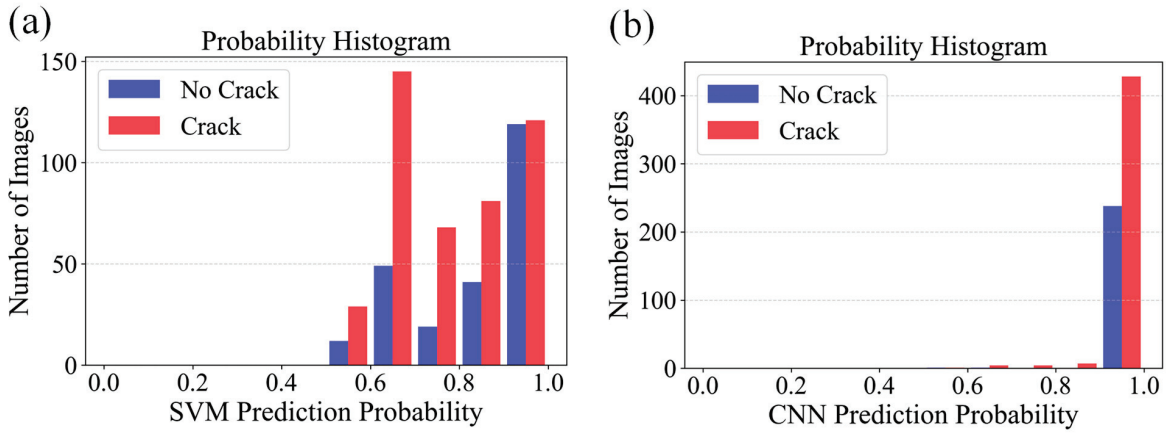


Figure 9. Prediction probability histograms based on classical OTSU-preprocessed images: (**a**) SVM and (**b**) CNN.

Furthermore, it is worth noting that, under the limited training data conditions considered in this study, the SVM model achieves performance comparable to that of the CNN model. This observation suggests that, when only a small number of labeled images are available-as is often the case in practical engineering scenarios-the combination of improved preprocessing and feature-based classification can provide a more efficient and robust solution. The enhanced binarization effect of the improved OTSU algorithm contributes to clearer structural representation of cracks, thereby reinforcing the effectiveness of SVM in small-sample conditions.

4.3. Optimization and Classification of Crack Detection Based on Skeletonization and Morphological Processing

Skeletonization, as a key morphological operation, aims to iteratively remove peripheral pixels of the target object, reducing the foreground region of an image to its central axis. This process effectively eliminates redundant details while preserving the geometric shape and topological connectivity of the object, thereby providing concise and essential morphological information for subsequent feature analysis, such as the extraction of crack length and branching structures. In the present study, skeleton extraction is primarily conducted using the Zhang-Suen algorithm.

The Zhang-Suen algorithm is a classical iterative method widely adopted in the field of skeletonization. Its core concept involves progressively removing non-essential boundary pixels through multiple iterations, ultimately preserving the skeletal structure that represents the medial axis of the object [35]. The algorithm operates on binary images, where a pixel set S is defined such that pixels with a value of 1 represent the foreground (e.g., crack regions), while those with a value of 0 correspond to the background. The algorithm follows a logical sequence in which edge pixels eligible for removal are identified and eliminated. In each iteration, isolated edge pixels—defined as pixels with all eight neighboring pixels equal to zero—are removed first. The remaining edge pixels are then evaluated for deletion based on specific criteria, such as the preservation of connectivity and the protection of terminal points. Pixels meeting all deletion conditions are removed, and this process continues until a stable skeleton structure is obtained. The iterative procedure relies on strict pixel deletion rules to ensure the continuity and topological consistency of the skeleton, making it well-suited for extracting the medial axes of elongated structures such as cracks.

$$Delete(S(x,y)) \Leftrightarrow (Condition\ 1) \wedge (Condition\ 2) \tag{22}$$

https://doi.org/10.3390/s26082381

Here, *Condition* 1 and *Condition* 2 refer to specific configurations of neighboring pixels required to maintain structural integrity during the deletion process.

Based on the above morphological methods, this study establishes an optimized structural processing workflow for crack images, with the following steps: First, an improved OTSU algorithm is applied for binarization to extract the initial crack regions. Morphological bridging is then employed to enhance crack connectivity. This operation combines dilation and erosion (expressed as $B = E(D(I, S), S)$, where I denotes the input binarized crack image, S represents the structuring element—typically a linear or elliptical kernel—$D(I, S)$ and $E(\cdot)$ indicate the dilation and erosion operations, respectively, and B corresponds to the crack region after bridging). This approach enhances connectivity while minimizing edge blurring caused by dilation.

Subsequently, morphological hole-filling is applied to eliminate internal voids and improve crack integrity. This step is realized through morphological reconstruction (expressed as $F = R(B, S)$, where $R(B, S)$ denotes the reconstruction operation, and in practical computation, closing operation $F = E(D(B, S), S)$, may be used). Skeletonization is then performed to extract the crack centerlines. Finally, morphological features and grayscale histogram features are integrated, and SVM is employed to classify crack types. The effectiveness of skeletonization and morphological bridging at fracture locations is illustrated in Figure 10.

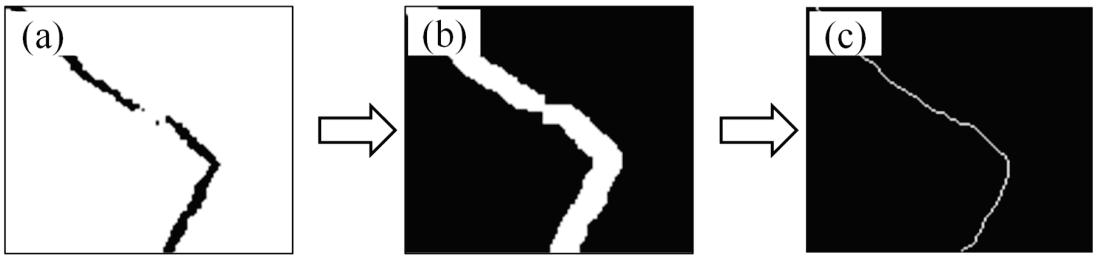


Figure 10. Morphological Processing for Crack Fracture Connection: (**a**) Original image processed with improved OTSU method; (**b**) Morphological connection of fracture openings; (**c**) Skeletonization through single-pixel refinement.

In crack detection, dilation is used to fill voids, followed by erosion to restore the basic crack shape. The combined use of morphological bridging and filling is critical for improving crack extraction, as it enhances both connectivity and integrity, thereby contributing to more accurate feature extraction and classification. Appropriate selection of kernel size and shape enables the effective connection of discontinuities, background compression, and emphasis of crack features. However, dilation may also lead to thickened edges, burr-like artifacts, and grayscale distribution shifts [36], potentially affecting the accuracy of subsequent feature extraction and classification, as shown in Figure 11.

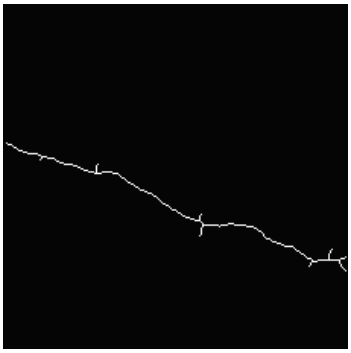


Figure 11. "Burr" effect after crack refinement.

https://doi.org/10.3390/s26082381

4.4. SVM-Based Classification of Crack Orientation

4.4.1. Feature Extraction and Training Set Construction

Following the skeletonization process, grayscale projection techniques are applied to conduct in-depth analysis of crack morphology. By summing grayscale values along the X-axis or Y-axis of an image, the projection distribution of cracks in horizontal and vertical directions is obtained, revealing their geometric characteristics and spatial patterns. The X-axis projection represents the sum of pixel values in each column, while the Y-axis projection represents the sum in each row:

$$P_x(j) = \sum_{j=1}^{H} I(i \cdot j),\ j = 1, 2, \cdots, W \tag{23}$$

$$P_y(i) = \sum_{i=1}^{W} I(i \cdot j),\ i = 1, 2, \cdots, H \tag{24}$$

where $I(i \cdot j)$ denotes the grayscale value at the i-th row and j-th column of the image; H and W represent the image height and width, respectively; $P_x(j)$ and $P_y(i)$ are the grayscale projection values for the j-th column and i-th row, respectively.

Analysis of grayscale projections along the X and Y axes enables the automatic identification of crack orientation. For Vertically oriented cracks, most grayscale values in the X-axis projection approach zero, with significant peaks only at crack positions, while the Y-axis projection typically presents a single sharp peak. In contrast, horizontally oriented cracks produce the opposite pattern. Irregular or Y-shaped cracks result in multiphasic distributions on both axes, without clear zero-grayscale regions. Based on these characteristics, a grayscale trend-based classification criterion is proposed: vertical cracks are indicated by extensive zero-grayscale regions along the X-axis with a single peak on the Y-axis; horizontal cracks exhibit the inverse; Inclined cracks display no dominant peak in either axis. Taking a single-pixel-width crack as an example (see Figure 12), the X-axis projection shows near-zero values across most regions, with a sharp peak at the crack location, while the Y-axis projection contains a single prominent peak. This pattern aligns with the vertical crack criterion: extensive zero grayscale along the X-axis and a single peak along the Y-axis.

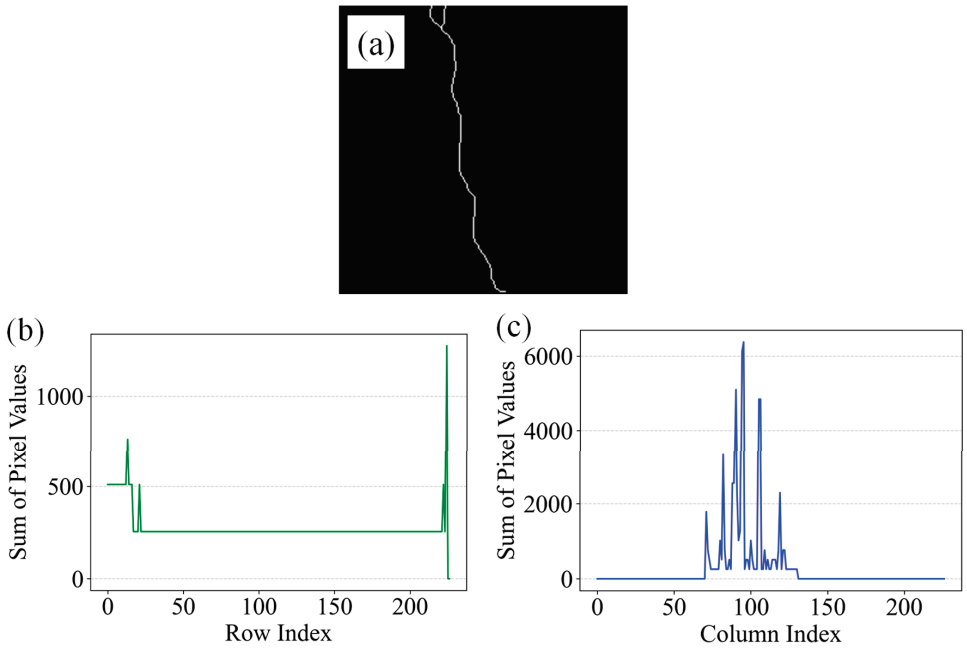


Figure 12. Grayscale distribution of a single-pixel crack: (**a**) crack image, (**b**) Y-axis projection, (**c**) X-axis projection.

https://doi.org/10.3390/s26082381

To evaluate the performance of an SVM in classifying crack morphology and leverage its high accuracy in small-sample settings, a tailored classification approach is constructed:

- Feature extraction: Based on the skeletonized crack image, grayscale projection features along the X and Y axes are extracted. The X-axis projection reflects grayscale distribution in the horizontal direction, while the Y-axis projection corresponds to the vertical direction. The distinction between the two is used to differentiate Horizontal, Vertical, and Inclined cracks.
- Dataset construction: A total of 319 binarized crack images—derived from the improved OTSU algorithm—are used as the dataset, covering three representative crack types (as shown in Figure 13):

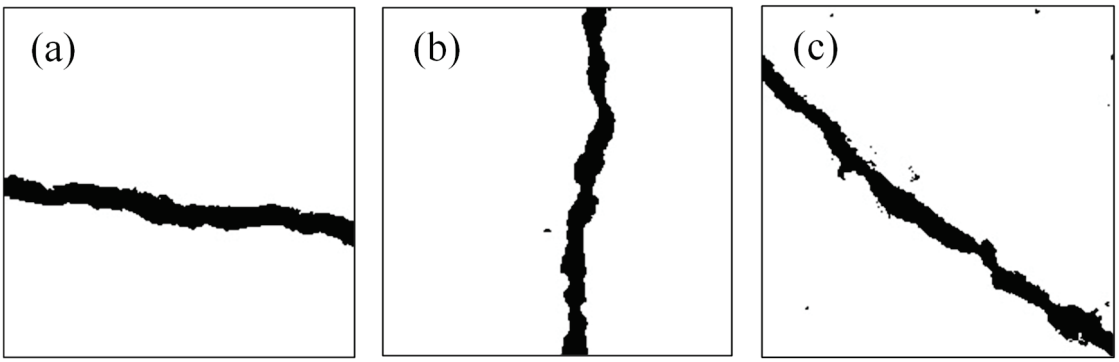


Figure 13. Crack types: (**a**) Horizontal crack, (**b**) Vertical crack, (**c**) Inclined crack.

Figure 13a: Horizontal cracks extending along the horizontal axis, characterized by concentrated Y-axis projections and elongated X-axis distributions; 98 samples (30.72%);

Figure 13b: Vertical cracks developing along the vertical axis, characterized by concentrated X-axis projections and elongated Y-axis distributions; 109 samples (34.17%);

Figure 13c: Inclined cracks forming an angle with the coordinate axes, with both X and Y projections showing dispersed and continuous multiphasic features; 112 samples (35.11%).

- Model training: Based on the extracted features and labeled samples, an SVM classification model is constructed. By leveraging the generalization capability of SVM in small-sample scenarios, the model achieves the accurate classification of the three crack orientations, providing foundational support for subsequent quantitative crack analysis.

4.4.2. SVM-Based Crack Classification Results

The SVM classifier employed in this study adopts a radial basis function (RBF) kernel with parameters C and γ. The input feature space is constructed based on the grayscale projection characteristics described in the previous section, from which statistical descriptors (i.e., mean and variance along both the horizontal (X) and vertical (Y) directions) are extracted to form a low-dimensional feature representation. This design enables the model to effectively capture orientation-related characteristics of cracks while maintaining robustness under limited data conditions.

Using these features, the SVM classifier was trained on the constructed dataset and subsequently evaluated on a validation set consisting of crack images processed by the improved OTSU method. This validation set covers a wide range of crack morphologies representative of practical structural conditions.

The updated classification results, summarized in Table 1 and visualized through the confidence histograms in Figure 14, indicate that the model exhibits strong discriminative capability across the three crack categories. The mean predicted probabilities achieved

https://doi.org/10.3390/s26082381

97.25% for Vertical cracks, 96.08% for Inclined cracks, and 96.94% for Horizontal cracks, respectively. These values are reflected in the corresponding histogram distributions: for example, the Vertical crack category (Figure 14b) shows a pronounced aggregation of samples in the high-confidence region (approaching 1.0), demonstrating the stability and reliability of the predictions. A comparable pattern is observed for Horizontal cracks (Figure 14a), whereas Inclined cracks (Figure 14c) display a slightly broader confidence distribution, consistent with their marginally lower average probability.

Table 1. Crack Classification Results Using the SVM Algorithm.

Category	Quantity	Proportion	Average Predicted Probability	Overall Accuracy
Vertical crack	109	34.17%	97.25%	
Inclined crack	112	35.11%	96.08%	96.76%
Horizontal crack	98	30.72%	96.94%	

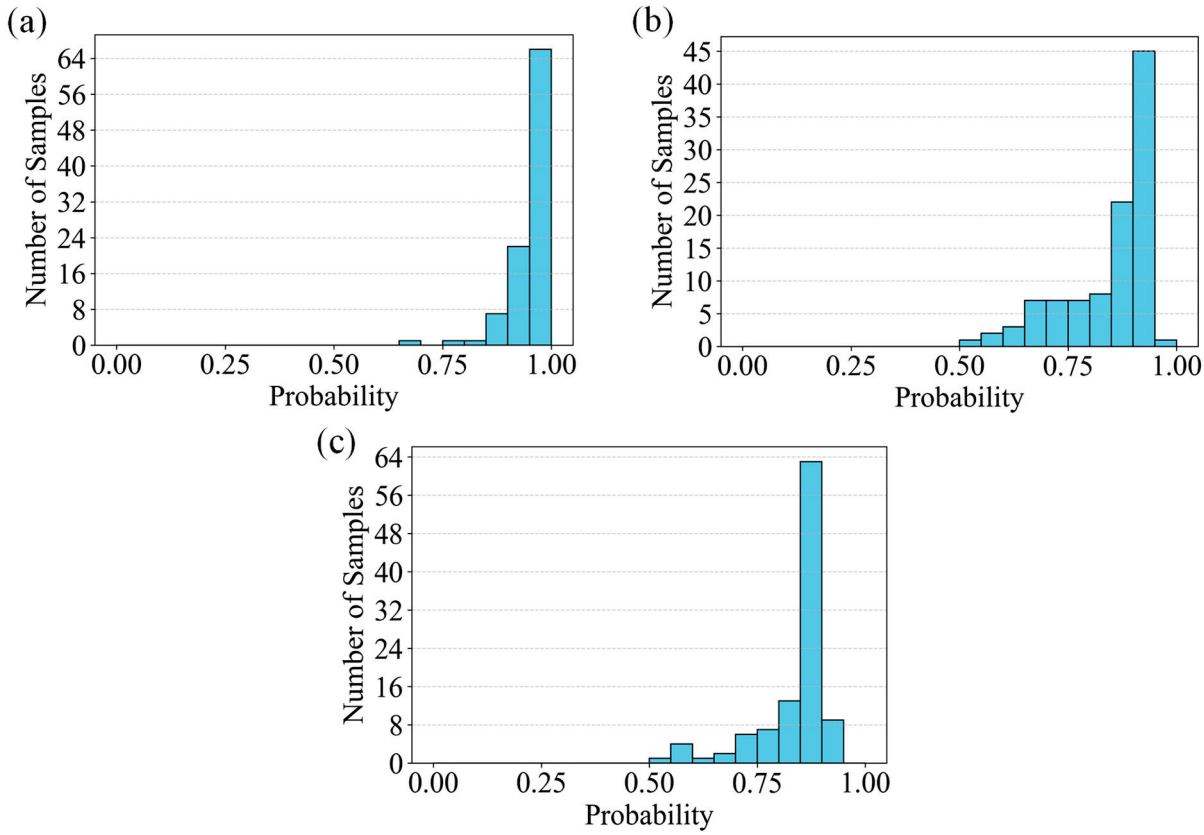


Figure 14. Confidence histograms of SVM classification results: (**a**) Horizontal cracks, (**b**) Vertical cracks, (**c**) Inclined cracks.

The model achieves an overall classification accuracy exceeding 96%, with category-specific accuracies of 97.25%, 96.08%, and 96.94% for Vertical, Inclined, and Horizontal cracks, respectively. The predominance of high-confidence predictions across all categories confirms the robustness of the trained SVM model and validates its ability to effectively capture grayscale projection features and structural characteristics that differentiate crack orientations.

Further analysis of the misclassified and lower-confidence samples reveals that prediction uncertainty primarily arises from complex crack morphologies—such as branching, intersections, or irregular spatial distributions—and environmental interferences, including illumination variations and background texture noise. These factors are directly mani-

https://doi.org/10.3390/s26082381

fested in the histograms through the presence of samples distributed in the medium-to-low confidence ranges, indicating increased feature ambiguity under such conditions.

In summary, the combined tabular and graphical evidence demonstrates that the proposed SVM-based approach effectively distinguishes Vertical, Horizontal, and Inclined cracks with high accuracy and strong confidence consistency. The confidence histograms quantitatively capture the separability of the three categories within the feature space, while the updated metrics further substantiate the classifiers generalization capability. These findings highlight both the accuracy and interpretability of the method and provide a foundation for future enhancements aimed at improving robustness under complex crack geometries and challenging imaging environments.

4.4.3. Performance Comparison Between SVM and CNN in Crack Classification

To further validate the effectiveness of the classification approach, CNN is employed for comparative analysis. A CNN model is designed and trained to perform automatic classification of crack orientation. Specifically, the CNN architecture consists of three convolutional layers followed by three max-pooling layers and one fully connected hidden layer. The convolutional layers use 3×3 kernels with ReLU activation functions, and the numbers of filters are set to 32, 64, and 128, respectively. Each convolutional layer is followed by a 2×2 max-pooling operation for spatial down sampling. After feature extraction, the feature maps are flattened and connected to a fully connected layer with 128 neurons, followed by a dropout layer with a rate of 0.5 to reduce overfitting. The output layer adopts a Softmax activation function with three neurons corresponding to Horizontal, Vertical, and Inclined crack categories. In terms of hyperparameters, the input images are uniformly resized to 227×227 pixels to ensure consistency with the SVM-based method, which is trained using the Adam optimizer with a learning rate of 0.001, a batch size of 32, and 20 training epochs.

Table 2 presents the classification results of the CNN model, while Figure 15 provides corresponding confidence histograms, forming a multi-dimensional framework for evaluating model performance. The average confidence for Horizontal cracks reaches 94.90%, with the histogram in Figure 15a showing a concentration of samples in the high-probability interval (approaching 1.0), indicating strong classification confidence. For Vertical cracks, the average confidence is 87.16%, and Figure 15b reveals a distribution consistent with this value, though the presence of medium- and low-confidence samples contributes to a lower mean. For Inclined cracks, the average confidence is only 25.00%, as Figure 15c indicates a predominance of samples in the medium-to-low confidence intervals, visually reflecting the increased classification difficulty.

Table 2. Crack classification results using the CNN algorithm.

Category	Quantity	Proportion	Average Predicted Probability	Overall Accuracy
Vertical Crack	109	34.17%	87.16%	
Inclined Crack	112	35.11%	25.00%	67.71%
Horizontal Crack	98	30.72%	94.90%	

Compared with the SVM model, CNN shows slightly lower performance in Horizontal crack recognition, with 94.90% compared with 97.25%. The difference is more significant for Vertical cracks, where CNN achieves 87.16% compared with 96.94%, and especially for Inclined cracks, where CNN achieves 25.00% compared with 96.08%. These results indicate that CNN struggles to learn discriminative features under limited training data, particularly for cracks with subtle angular variations and ambiguous boundaries. This limitation is reflected in the larger proportion of medium- and low-confidence predictions. In contrast,

https://doi.org/10.3390/s26082381

the SVM model maintains robust performance by leveraging discriminative handcrafted features to construct an effective feature space. The dominance of high-confidence predictions demonstrates its strong generalization capability under small-sample conditions. Moreover, SVM provides better interpretability, as the extracted features, such as grayscale projection and morphological characteristics, have clear physical meanings and can be directly associated with crack geometry. In comparison, CNN features are learned automatically and are more abstract, making physical interpretation less straightforward. Both models demonstrate high computational efficiency, with inference time well below 0.1 s per image and negligible differences between them, indicating suitability for real-time tunnel inspection.

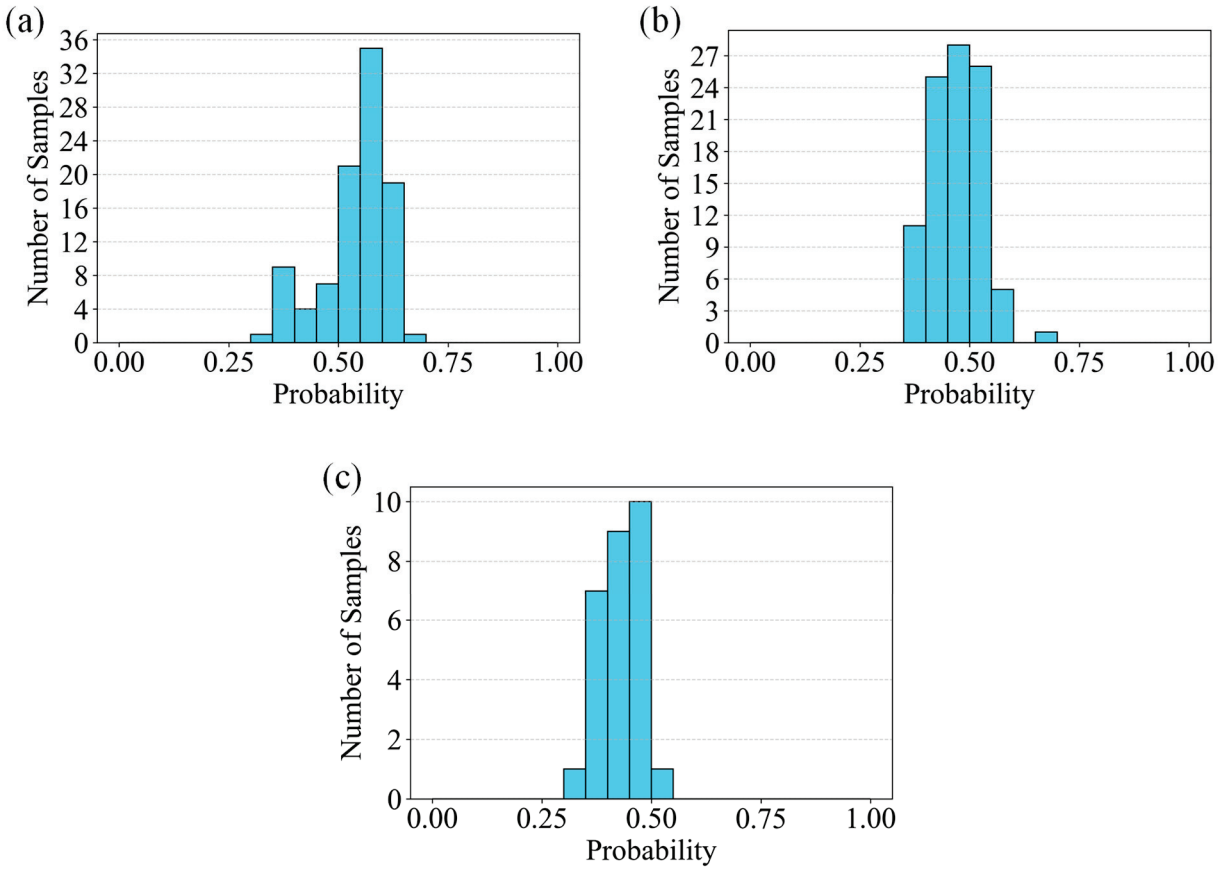


Figure 15. Confidence histograms of CNN classification results: (**a**) Horizontal cracks, (**b**) Vertical cracks, (**c**) Inclined cracks.

In summary, although CNN can achieve competitive performance in certain cases, its generalization is limited under small-sample conditions. SVM demonstrates greater stability and reliability in scenarios with limited data and clear feature representations, making it more suitable for practical crack classification tasks.

4.4.4. Performance Comparison Between SVM and K-Means Clustering in Crack Classification

In the task of crack orientation classification, unsupervised learning methods such as clustering are widely applied in addition to supervised algorithms. Clustering identifies underlying data patterns by grouping samples based on feature similarity without requiring labeled information. K-Means, a commonly used clustering algorithm, partitions data by iteratively optimizing cluster centroids until convergence is achieved. This section

https://doi.org/10.3390/s26082381

compares the methodological differences between K-Means and SVM in the context of crack classification. The fundamental principle of K-Means clustering is defined as:

$$J = \sum_{i=1} \sum_{x_i \in C_i} \|x_i - u_i\|^2 \quad (25)$$

where k is the number of clusters, C_i represents the i-th cluster, u_i denotes the centroid of cluster C_i, and x_i is a data point within cluster C_i [37].

This study applies an unsupervised K-Means clustering approach to crack image recognition. A 456-dimensional feature vector is constructed based on grayscale image features. First, each image is resized to 227 × 227 pixels and converted to grayscale. Grayscale projection features are then extracted in both the Horizontal and vertical directions, along with the grayscale mean and variance. All feature vectors are subsequently standardized to eliminate the impact of differences in dimensional units. During training, the K-Means algorithm is applied to cluster three types of crack images: Horizontal, Inclined, and Vertical. The results of K-Means clustering after dimensionality reduction are shown in Figure 16. In the clustering outcome, Cluster 1 corresponds to the "Vertical Crack" category, Cluster 2 to the "Horizontal Crack" category, and Cluster 0 to the "Inclined Crack" category. In the prediction phase, the same features are extracted and standardized for the target image. The trained model is then used to predict the crack category, and the prediction confidence is estimated based on the inverse distance between the sample and the corresponding cluster center.

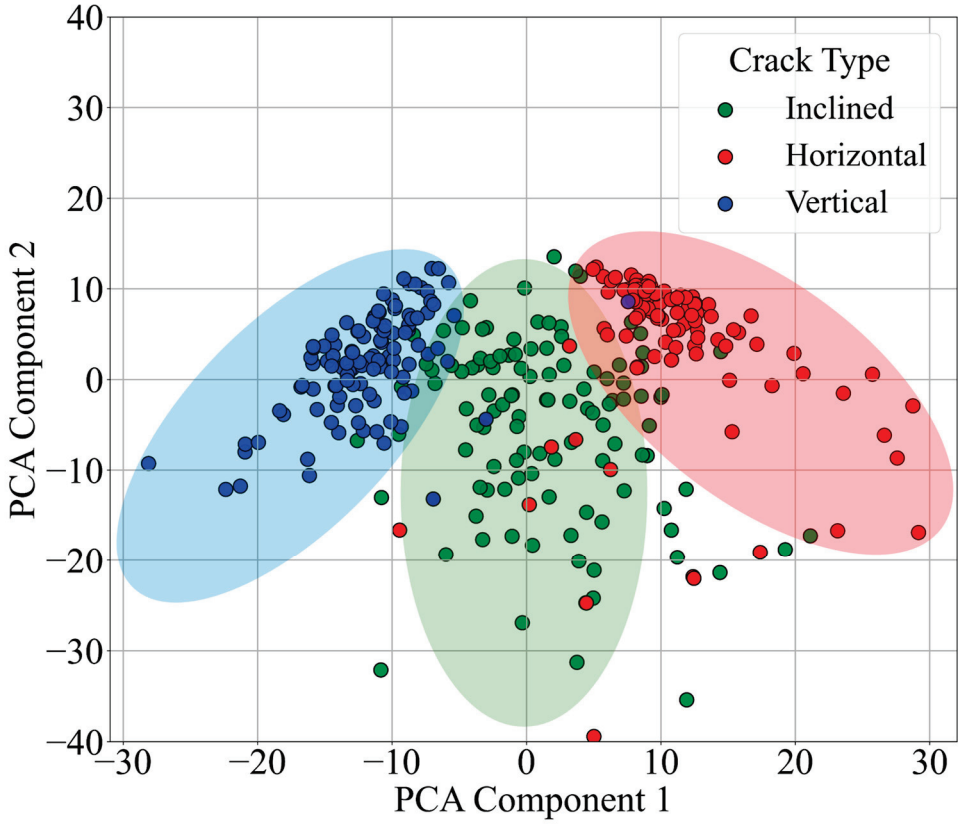


Figure 16. K-means dimensionality reduction clustering distribution map. Green, red and blue points/ellipses denote Inclined, Horizontal and Vertical cracks, respectively. Overlaps reflect spatial correlations in the feature space.

The intra-cluster distance distribution histograms in Figure 17, along with the classification outcomes presented in Table 3, jointly validate the crack recognition characteristics of the K-Means clustering method. The degree of dispersion in the histograms reflects

https://doi.org/10.3390/s26082381

the varying clustering difficulties among different crack types. Specifically, samples of Horizontal cracks (Cluster 2) and Vertical cracks (Cluster 1) exhibit short distances to their respective centroids and relatively concentrated distributions (Figure 17a,b). These patterns correspond to the high average prediction probabilities of 98.17% and 88.78% in Table 3, indicating that grayscale projection features of regular-shaped cracks form clearly distinguishable clusters.

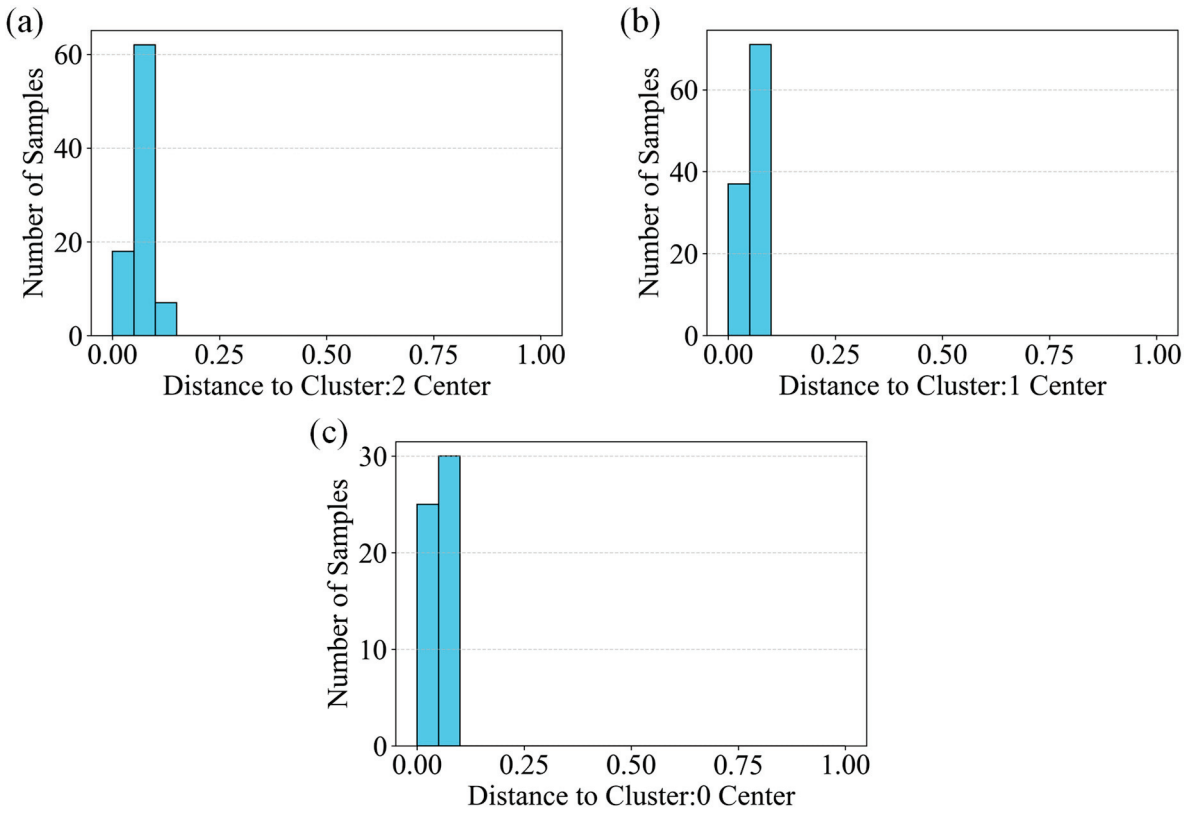


Figure 17. K-means Intra-cluster Distance Distribution Histograms: (**a**) Distance distribution from cluster center for Cluster 2 (Horizontal cracks), (**b**) Distance distribution from cluster center for Cluster 1 (Vertical cracks), (**c**) Distance distribution from cluster center for Cluster 0 (Inclined cracks).

Table 3. K-Means Clustering Results for Crack Classification.

Category	Quantity	Proportion	Average Prediction Probability	Overall Accuracy
Vertical Crack	109	34.17%	98.17%	
Inclined Crack	112	35.11%	49.11%	78.05%
Horizontal Crack	98	30.72%	88.78%	

In contrast, Inclined cracks (Cluster 0) show larger and more scattered distances from the cluster center (Figure 17c), corresponding to a lower average prediction probability of 49.11%. This suggests that the inherent complexity of inclined crack orientations results in less cohesive grayscale feature distributions, complicating the clustering process.

In comparison to the SVM model, while K-Means can distinguish between distinctly shaped Horizontal and Vertical cracks, its reliance on unsupervised grayscale projection features limits its performance in classifying complex forms such as Inclined cracks. For instance, Inclined cracks with smaller angles may share similar grayscale features with Horizontal or Vertical cracks, leading to misclassification. The SVM model, by contrast, leverages supervised learning to target critical features, achieving an overall accuracy exceeding 96% (rising to 97% after excluding exceptional cases). Its average confidence

https://doi.org/10.3390/s26082381

level for Inclined cracks (96.08%) significantly outperforms that of K-Means (49.11%), demonstrating superior adaptability to crack shape diversity.

In summary, K-Means clustering is suitable for the preliminary differentiation of regular-shaped cracks. However, for more complex categories such as Inclined cracks, the SVM model—based on supervised learning and focused feature extraction—offers irreplaceable advantages in both precision and robustness. These findings provide empirical support and methodological guidance for model selection and optimization in intelligent crack recognition tasks.

4.4.5. Performance Comparison Between SVM and ResNet in Crack Classification

To further evaluate the performance of deep learning methods in crack classification tasks, the ResNet-18 model was introduced for comparative analysis. The ResNet-18 model pre-trained on ImageNet was adopted as the deep learning baseline. To ensure a fair comparison with the SVM-based method, all input images were uniformly resized to 227 × 227 pixels. The model was fine-tuned using a cross-entropy loss function and optimized with the Adam optimizer, with an initial learning rate of 1×10^{-4}, a batch size of 16, and a total of 20 training epochs. All experiments were implemented in PyCharm (version 2024.2.4) and conducted on a GPU to ensure computational efficiency. The final fully connected layer was modified to output three classes corresponding to Horizontal, Vertical, and Inclined cracks.

Table 4 presents the classification results of the ResNet-18 model, while Figure 18 provides the corresponding prediction probability histograms, forming a multi-dimensional framework for evaluating model performance. In terms of average prediction probability, the model achieves 96.94% for Horizontal cracks, with Figure 18a showing a clear concentration of samples in the high-probability interval (close to 1.0), reflecting high classification stability. For Vertical cracks, the average prediction probability is 96.33%, and Figure 18b reveals a distribution aligned with this value, demonstrating consistent confidence across most samples. For Inclined cracks, the average prediction probability is 92.88%, and Figure 18c indicates a slight shift toward medium-probability intervals compared to the other two categories, visually confirming the greater challenge of feature extraction for this type of crack. The overall classification accuracy of the model reaches 95.38%, further verifying its reliable performance in crack orientation classification.

Table 4. ResNet Results for Crack Classification.

Category	Quantity	Proportion	Average Prediction Probability	Overall Accuracy
Vertical Crack	109	34.17%	96.33%	
Inclined Crack	112	35.11%	92.88%	95.38%
Horizontal Crack	98	30.72%	96.94%	

Compared with the SVM model, ResNet-18 shows slightly lower performance in recognizing Horizontal cracks (96.94% vs. 97.25%) and Vertical cracks (96.33% vs. 96.94%), although the differences are relatively small. This indicates that deep learning models can achieve strong discriminative capability for categories with clear structural features. However, for Inclined cracks, ResNet-18 (92.88% vs. 96.08%) still underperforms compared to SVM, suggesting reduced stability when dealing with samples exhibiting subtle angular variations and indistinct boundaries.

The prediction confidence of the ResNet-18 model is generally above 90%, indicating that the model has learned relatively stable feature representations. However, despite the high confidence, its classification accuracy—especially for Inclined cracks—remains lower than that of SVM. This suggests that deep learning models may struggle to effectively

https://doi.org/10.3390/s26082381

generalize fine-grained orientation features under limited data conditions. In contrast, the SVM model, based on discriminative handcrafted features, is less sensitive to data scale and can better capture subtle differences, resulting in more stable performance in small-sample scenarios.

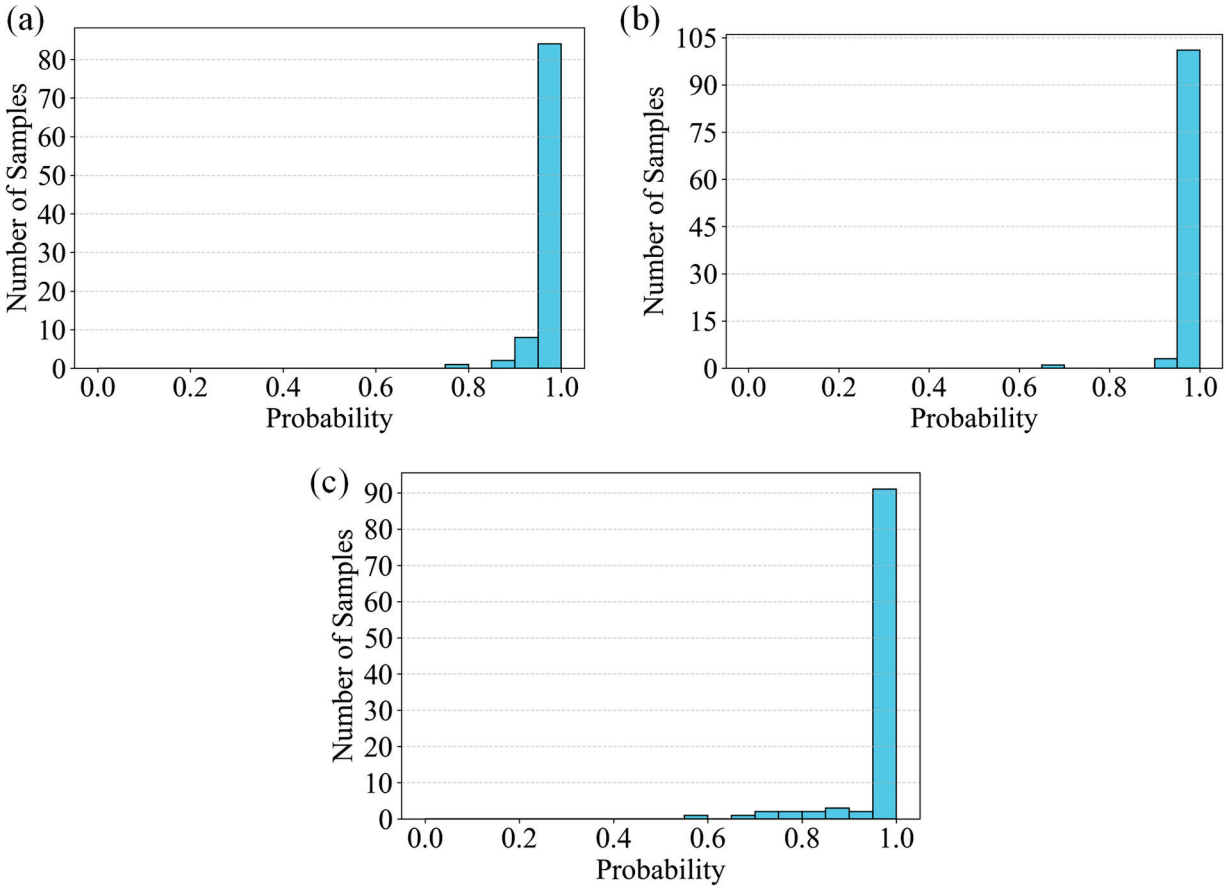


Figure 18. Confidence histograms of ResNet classification results: (**a**) Horizontal cracks, (**b**) Vertical cracks, (**c**) Inclined cracks.

In summary, ResNet-18 exhibits strong overall performance in crack classification tasks and achieves results comparable to SVM in most categories. However, under small-sample and complex-feature scenarios, its performance remains slightly inferior to that of SVM. These findings further indicate that, when the dataset size is limited, traditional machine learning methods based on discriminative feature engineering, such as SVM, still hold significant advantages, whereas deep learning approaches demonstrate greater potential when sufficient training data are available.

5. Example Validation

Crack orientation emerges as a key morphological feature that directly encodes the underlying mechanical response of the lining structure. Unlike crack width or length, which only reflect the severity of damage, orientation reveals the specific stress states that initiate and drive crack development in segments. In this context, full-scale laboratory segment loading tests were conducted, and synchronous imaging of cracks was performed to facilitate subsequent quantitative analysis. This experimental investigation is centered on the conventional shield tunnel employed in Metro tunnel, characterized by an outer diameter of 6.7 m, with its constituent segments featuring a thickness of 0.35 m. Throughout the experiment, external loading was imparted to the segment assembly (illustrated in the schematic layout of Figure 19a and the physical test setup of Figure 19b), while a camera

https://doi.org/10.3390/s26082381

system was deployed to acquire surface crack images of the segments. A total of 22 crack image samples were collected, which were subsequently utilized to evaluate the practical performance of SVM-based crack orientation classification framework.

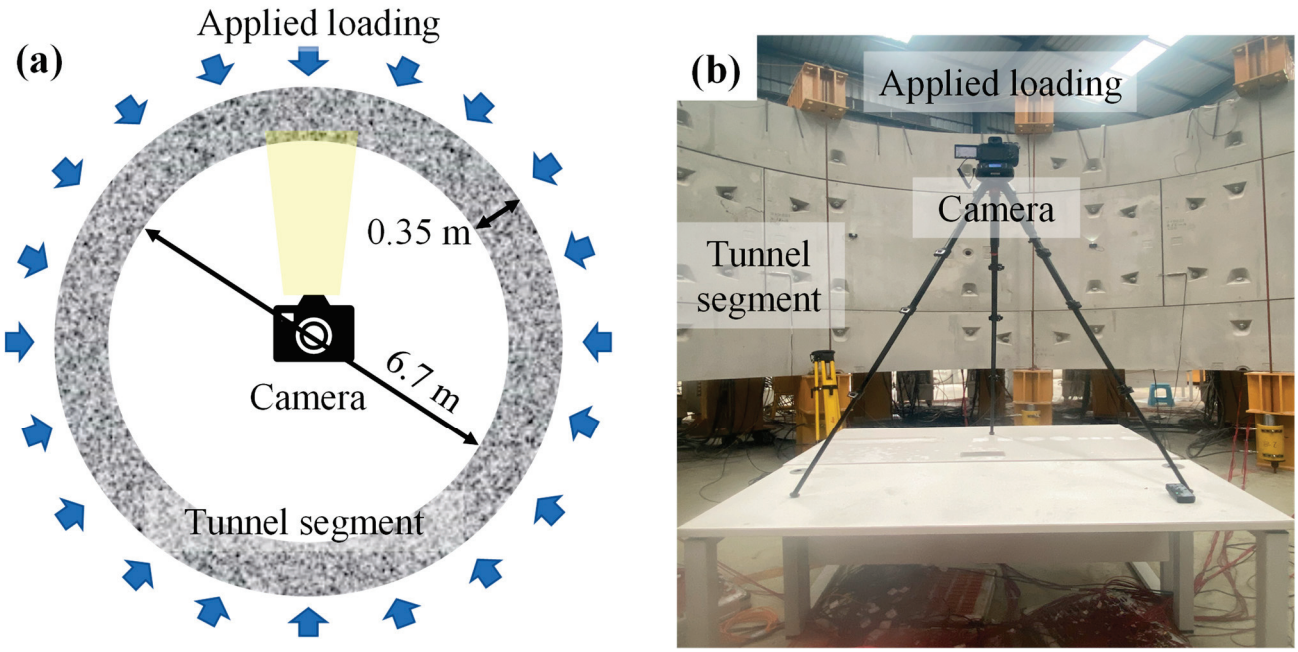


Figure 19. Schematic diagram and physical test setup of (**a**) tunnel segment loading and (**b**) crack image acquisition system.

Table 5 presents the crack classification results under real-world conditions, covering three typical crack categories: Vertical, Inclined, and Horizontal. Specifically, vertical cracks account for the largest proportion of the test samples (54.54%, n = 12), with an average prediction probability of 91.67%. By contrast, inclined cracks (n = 5, 22.73%) and horizontal cracks (n = 5, 22.73%) both achieve a 100% average prediction probability, indicating high model confidence in identifying these two crack types. Overall, the proposed method yields an excellent classification accuracy of 95.45% in practical scenarios, which verifies its strong robustness and applicability for on-site crack detection tasks.

Table 5. Real-world conditions Results for Crack Classification.

Category	Quantity	Proportion	Average Prediction Probability	Overall Accuracy
Vertical Crack	12	54.54%	91.67%	
Inclined Crack	5	22.73%	100%	95.45%
Horizontal Crack	5	22.73%	100%	

To intuitively evaluate the classification performance of the SVM model under real-world conditions, Figure 20 plots the confidence histograms of the SVM classification results, which are further divided into three subgraphs based on crack types: (a) Horizontal cracks, (b) Vertical cracks, and (c) Inclined cracks. These histograms clearly reflect the distribution characteristics of the classification confidence scores output by the model across different crack categories, providing a quantitative basis for subsequent model accuracy assessment and optimization.

https://doi.org/10.3390/s26082381

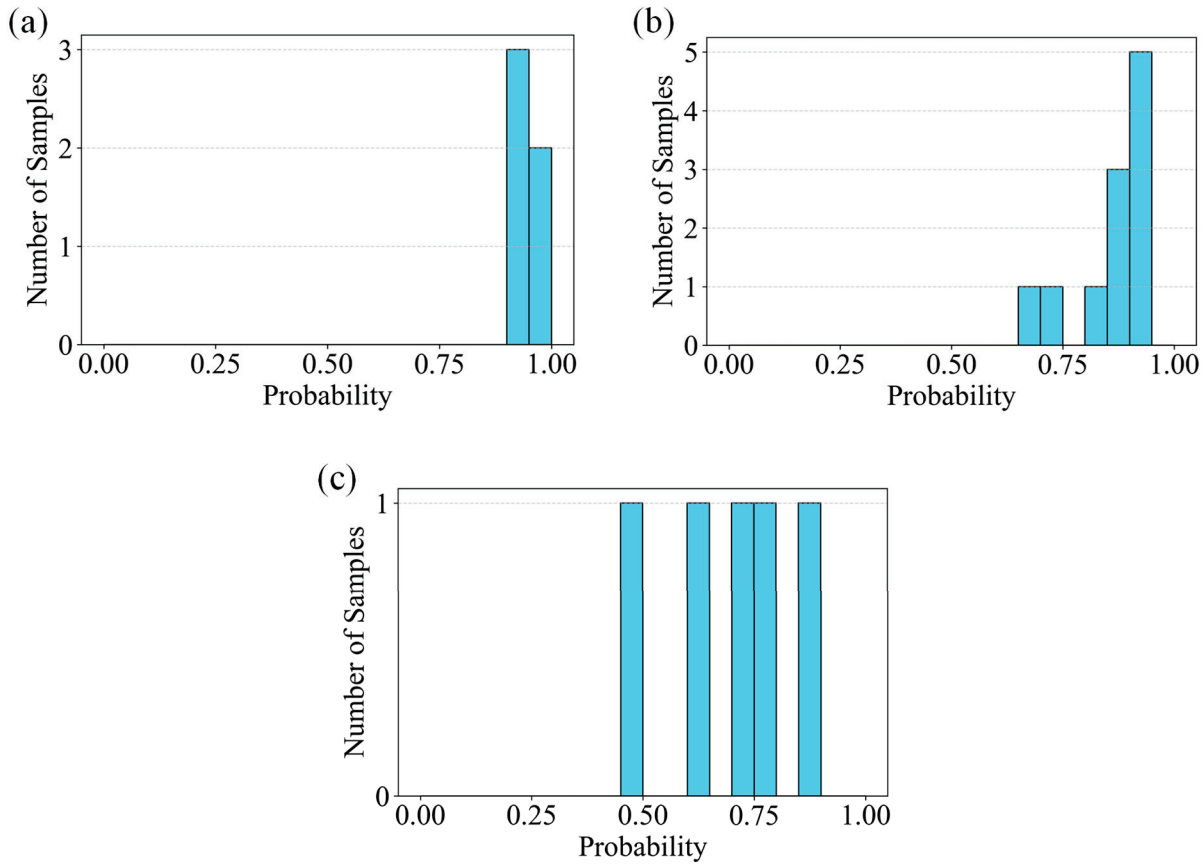


Figure 20. Confidence Histograms of SVM Classification Results Under Real-World Conditions: (**a**) Horizontal Cracks, (**b**) Vertical Cracks, (**c**) Inclined Cracks.

The images obtained after applying skeletonization and other morphological processing techniques to the field crack photographs are shown in Figure 21. These operations simplify the crack contours into single-pixel-width skeletons while preserving the geometric features (e.g., direction, branching) of the original cracks, providing a streamlined representation for subsequent orientation classification tasks. The dataset covers diverse crack patterns (vertical, inclined, and irregular forms), which align with the real-world crack distribution characteristics of tunnel segments in the test.

To further evaluate the robustness of the proposed method in complex scenarios, additional experiments were conducted on images containing crack-like objects, such as joints, construction marks, bolt holes, drill holes, and segment seams. These objects are commonly found in tunnel linings and may introduce interference in crack detection tasks. As shown in Figure 22, the improved OTSU algorithm is first applied to these images to obtain binarized results. Although some structures exhibit visual similarity to cracks, their morphological characteristics differ from actual crack patterns. Subsequently, the processed images are fed into the SVM model for classification.

The corresponding prediction results are presented in Figure 23. It can be observed that the SVM model correctly classifies these crack-like objects as non-crack images with high confidence values (close to 1.0). This demonstrates that the proposed framework is capable of filtering out certain types of interference and reducing false positives in crack detection. However, it should be noted that the number of such samples in this study is relatively limited. Further investigation with a more diverse dataset is necessary to comprehensively evaluate the generalization ability of the model in more complex real-world environments.

https://doi.org/10.3390/s26082381

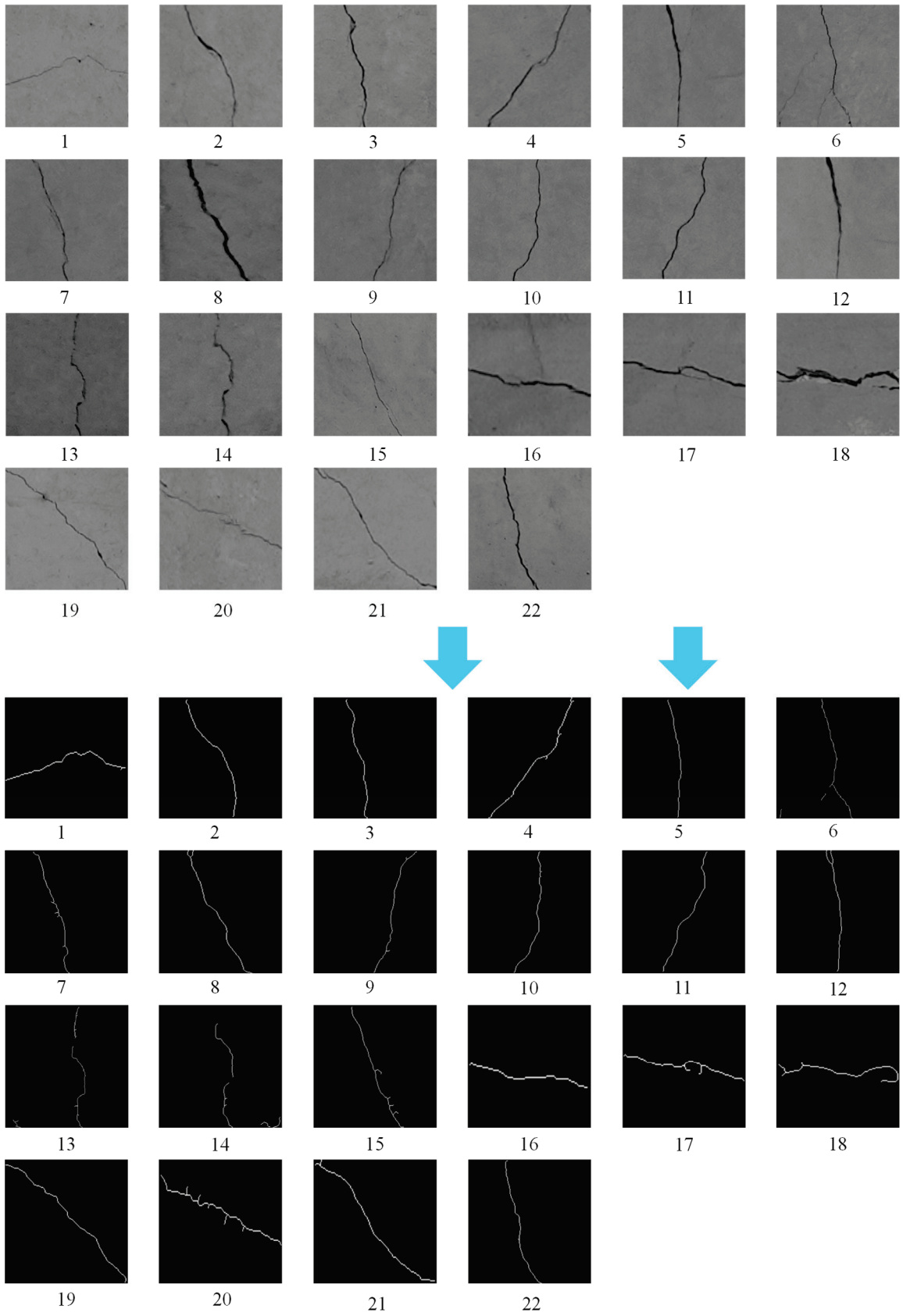


Figure 21. Collection of 22 in situ crack images acquired during field testing for orientation recognition. Numbers denote sample indices; arrows mark representative samples. Upper row: original images; lower row: segmented binary images.

https://doi.org/10.3390/s26082381

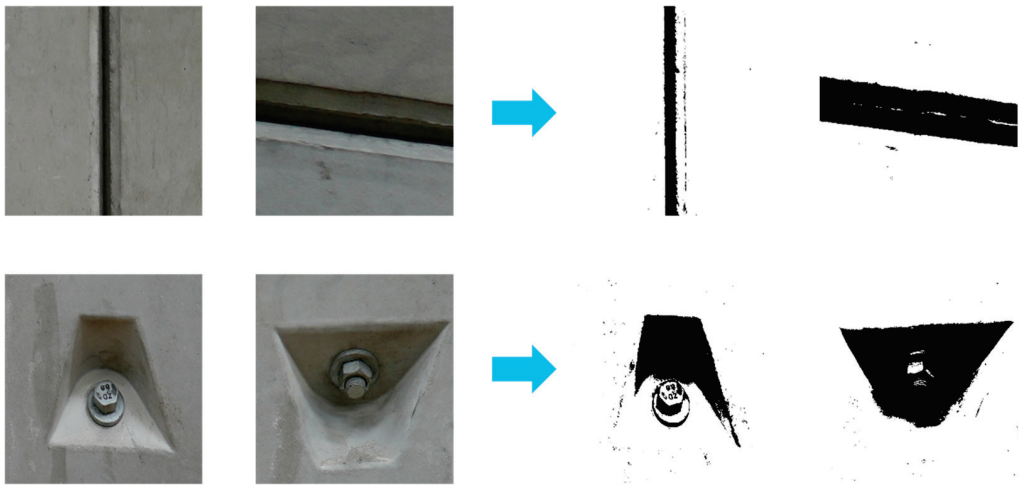


Figure 22. Binarization results of representative crack-like objects after improved OTSU processing.

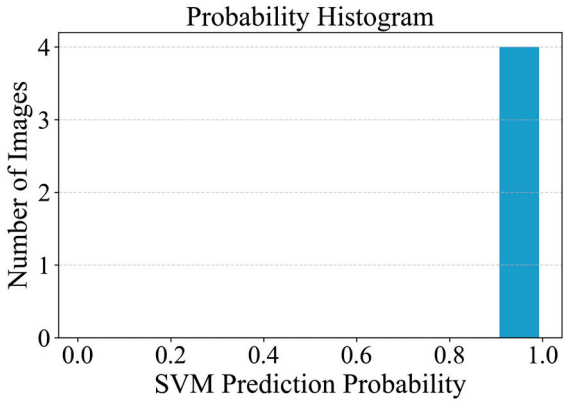


Figure 23. SVM prediction confidence for crack-like object images classified as non-crack.

6. Conclusions

This study systematically explores crack detection and classification methods based on machine vision and deep learning. Through in-depth research on image preprocessing algorithms, classification models, and engineering applications, the following key conclusions are drawn:

(1) By integrating global threshold calculation with local grayscale variance analysis and dynamic threshold adjustment, the algorithm achieves superior performance in both high and low-resolution crack images. It not only suppresses noise interference in high-resolution images with complex backgrounds but also avoids the loss of fine crack details in low-resolution images caused by pre-denoising, laying a reliable foundation for subsequent crack feature extraction and classification. In this study, a 5×5 sliding window is adopted for 227×227 pixel images, which achieves a good balance between segmentation performance and computational efficiency.

(2) In the comparative analysis of crack classification models, the SVM model demonstrates clear advantages under small-sample conditions, achieving an overall accuracy above 96% based on grayscale projection and morphological features. In contrast, deep learning models show performance degradation with limited training data. The CNN model performs poorly for Inclined cracks, with confidence dropping to 25.00%, while ResNet-18 achieves relatively stable performance with an overall accuracy of 95.38% but remains less effective than SVM for complex crack orientations. The K-means algorithm exhibits the lowest accuracy of 78.05% due to its inability to

https://doi.org/10.3390/s26082381

capture discriminative features without supervision. Overall, SVM proves to be more suitable for engineering scenarios with limited labeled data, whereas deep learning methods show greater potential when sufficient data are available.

(3) Verification in shield tunnel segment loading tests shows that the framework achieves an overall classification accuracy of 95.45% in real-world conditions, with 100% average prediction confidence for Horizontal and Inclined cracks. This verifies the framework's strong robustness and practical applicability, providing effective technical support for analyzing the mechanical response of tunnel segments through crack orientation features. In addition, validation on crack-like objects (e.g., joints, bolt holes, and segment seams) shows that the proposed method can effectively distinguish them from actual cracks, demonstrating its ability to reduce false positives in complex tunnel environments.

Despite the promising results, several limitations remain. The relatively small dataset may restrict generalization under more complex real-world conditions, and the classification performance still depends on handcrafted features, limiting adaptability to irregular patterns. In addition, the current framework focuses on crack orientation classification and does not include pixel-level segmentation or multi-scale analysis. Future work will focus on expanding the dataset, improving robustness in complex environments, and integrating deep learning or hybrid approaches to enhance feature representation and generalization. Extending the method to more comprehensive crack characterization, such as width estimation and severity assessment, will also be explored.

Author Contributions: Conceptualization, W.C., X.C., L.Z. and Q.L.; Methodology, W.C., Z.P., X.C. and L.Z.; Software, Z.P.; Validation, W.C., Z.P. and T.X.; Formal analysis, Z.P.; Investigation, Z.P.; Resources, X.C., L.Z., X.H. and K.K.P.M.K.; Data curation, Z.P.; Writing—original draft, Z.P.; Writing—review & editing, W.C., Z.P., X.C., L.Z., T.X., Q.L., X.H. and K.K.P.M.K.; Visualization, W.C. and Z.P.; Supervision, W.C., X.C., L.Z., T.X., Q.L. and K.K.P.M.K.; Project administration, X.C.; Funding acquisition, W.C., X.C. and L.Z. All authors have read and agreed to the published version of the manuscript.

Funding: This research was funded by the National Key Research and Development Program of China (grant number: 2023YFC3009303 and 2023YFC3807502), Shenzhen Startup Fund for Newly Introduced High-End and Shortage Talents (grant number: 827-0001170), Science and Technology Strategic Consulting Project of the Chinese Academy of Engineering (grant number: 2025-XZ-65), National Natural Science Foundation of China (grant number: 52308361), and Talent Program of Guangdong Province, China (grant number: 0202202300033).

Data Availability Statement: The source code and figures presented in this paper are available from the corresponding author upon reasonable request.

Acknowledgments: Financial support from the National Key Research and Development Program of China (2023YFC3009303 and 2023YFC3807502), Shenzhen Startup Fund for Newly Introduced High-End and Shortage Talents (827-0001170), Science and Technology Strategic Consulting Project of the Chinese Academy of Engineering (2025-XZ-65), National Natural Science Foundation of China (52308361), and Talent Program of Guangdong Province, China (0202202300033) are greatly acknowledged.

Conflicts of Interest: The authors declare no conflict of interest.

References

1. Ren, D.; Kang, C.; Peng, T.; Li, Y.; Wang, J. Deformation behavior of a Large-Scale excavation and the effect of an adjacent foundation pit on the excavation. *Int. J. Civ. Eng.* **2024**, *22*, 1493–1505. [CrossRef]
2. Zeng, C.-F.; Zheng, G.; Zhou, X.-F.; Xue, X.-L.; Zhou, H.-Z. Behaviours of wall and soil during pre-excavation dewatering under different foundation pit widths. *Comput. Geotech.* **2019**, *115*, 103169. [CrossRef]

https://doi.org/10.3390/s26082381

3. Zheng, G.; Lei, Y.; Cheng, X.; Li, X.; Wang, R. Experimental study on progressive collapse mechanism in braced and tied-back retaining systems of deep excavations. *Can. Geotech. J.* **2021**, *58*, 540–564. [CrossRef]
4. Zheng, G.; Wei, S.-W. Numerical analyses of influence of overlying pit excavation on existing tunnels. *J. Cent. South Univ. Technol.* **2008**, *15*, 69–75. [CrossRef]
5. Liu, J.; Xue, B.; Wang, H.; Zhang, X.; Zhang, Y. Numerical study on the behavior of an existing tunnel during excavating adjacent deep foundation pit. *Sustainability* **2023**, *15*, 9740. [CrossRef]
6. Ye, S.; Zhao, Z.; Wang, D. Deformation analysis and safety assessment of existing metro tunnels affected by excavation of a foundation pit. *Undergr. Space* **2021**, *6*, 421–431. [CrossRef]
7. Goel, R. Status of tunnelling and underground construction activities and technologies in India. *Tunn. Undergr. Space Technol.* **2001**, *16*, 63–75. [CrossRef]
8. O'Brien, D.; Osborne, J.A.; Perez-Duenas, E.; Cunningham, R.; Li, Z. Automated crack classification for the CERN underground tunnel infrastructure using deep learning. *Tunn. Undergr. Space Technol.* **2023**, *131*, 104668.
9. Rao, A.S.; Nguyen, T.; Palaniswami, M.; Ngo, T. Vision-based automated crack detection using convolutional neural networks for condition assessment of infrastructure. *Struct. Health Monit.* **2021**, *20*, 2124–2142. [CrossRef]
10. Gharehbaghi, V.R.; Noroozinejad Farsangi, E.; Noori, M.; Yang, T.; Li, S.; Nguyen, A.; Málaga-Chuquitaype, C.; Gardoni, P.; Mirjalili, S. A critical review on structural health monitoring: Definitions, methods, and perspectives. *Arch. Comput. Methods Eng.* **2022**, *29*, 2209–2235. [CrossRef]
11. Liu, Y.; Cho, S.; Spencer, B.F., Jr.; Fan, J. Automated assessment of cracks on concrete surfaces using adaptive digital image processing. *Smart Struct. Syst.* **2014**, *14*, 719–741. [CrossRef]
12. Kamaliardakani, M.; Sun, L.; Ardakani, M.K. Sealed-crack detection algorithm using heuristic thresholding approach. *J. Comput. Civ. Eng.* **2016**, *30*, 04014110. [CrossRef]
13. Attard, L.; Debono, C.J.; Valentino, G.; Di Castro, M. Tunnel inspection using photogrammetric techniques and image processing: A review. *ISPRS J. Photogramm. Remote Sens.* **2018**, *144*, 180–188. [CrossRef]
14. Abdel-Qader, I.; Abudayyeh, O.; Kelly, M.E. Analysis of edge-detection techniques for crack identification in bridges. *J. Comput. Civ. Eng.* **2003**, *17*, 255–263. [CrossRef]
15. Wang, G.; Peter, W.T.; Yuan, M. Automatic internal crack detection from a sequence of infrared images with a triple-threshold Canny edge detector. *Meas. Sci. Technol.* **2018**, *29*, 025403. [CrossRef]
16. Jahanshahi, M.R.; Masri, S.F.; Padgett, C.W.; Sukhatme, G.S. An innovative methodology for detection and quantification of cracks through incorporation of depth perception. *Mach. Vis. Appl.* **2013**, *24*, 227–241. [CrossRef]
17. Yamaguchi, T.; Hashimoto, S. Fast crack detection method for large-size concrete surface images using percolation-based image processing. *Mach. Vis. Appl.* **2010**, *21*, 797–809. [CrossRef]
18. Lattanzi, D.; Miller, G.R. Robust automated concrete damage detection algorithms for field applications. *J. Comput. Civ. Eng.* **2014**, *28*, 253–262. [CrossRef]
19. Nyathi, M.A.; Bai, J.; Wilson, I.D. Deep learning for concrete crack detection and measurement. *Metrology* **2024**, *4*, 66–81. [CrossRef]
20. Oh, J.-K.; Jang, G.; Oh, S.; Lee, J.H.; Yi, B.-J.; Moon, Y.S.; Lee, J.S.; Choi, Y. Bridge inspection robot system with machine vision. *Autom. Constr.* **2009**, *18*, 929–941. [CrossRef]
21. Long, J.; Shen, X.; Chen, H. Interactive document images thresholding segmentation algorithm based on image regions. *J. Comput. Res. Dev.* **2012**, *49*, 1420–1431.
22. Nishikawa, T.; Yoshida, J.; Sugiyama, T.; Fujino, Y. Concrete crack detection by multiple sequential image filtering. *Comput. Aided Civ. Infrastruct. Eng.* **2012**, *27*, 29–47. [CrossRef]
23. Han, F.; Zhao, S.; Zhang, L.; Wu, J. Survey of strategies for switching off base stations in heterogeneous networks for greener 5G systems. *IEEE Access* **2016**, *4*, 4959–4973. [CrossRef]
24. Li, X.; Li, C.; Rahaman, M.M.; Sun, H.; Li, X.; Wu, J.; Yao, Y.; Grzegorzek, M. A comprehensive review of computer-aided whole-slide image analysis: From datasets to feature extraction, segmentation, classification and detection approaches. *Artif. Intell. Rev.* **2022**, *55*, 4809–4878. [CrossRef]
25. Xu, J.; Wang, S.; Han, R.; Wu, X.; Zhao, D.; Zeng, X. Crack segmentation and quantification in concrete structures using a lightweight YOLO model based on pruning and knowledge distillation. *Expert Syst. Appl.* **2025**, *283*, 127834. [CrossRef]
26. Liu, Z.; Cao, Y.; Wang, Y.; Wang, W. Computer vision-based concrete crack detection using U-net fully convolutional networks. *Autom. Constr.* **2019**, *104*, 129–139. [CrossRef]
27. Asadi Shamsabadi, E.; Xu, C.; Rao, A.S.; Nguyen, T.; Ngo, T.; Dias-da-Costa, D. Vision transformer-based autonomous crack detection on asphalt and concrete surfaces. *Autom. Constr.* **2022**, *140*, 104316. [CrossRef]
28. He, K.; Zhang, X.; Ren, S.; Sun, J. Deep residual learning for image recognition. In Proceedings of the IEEE Conference on Computer Vision and Pattern Recognition, Denver, CO, USA, 3–7 June 2016; pp. 770–778.
29. Otsu, N. A Threshold Selection Method from Gray-Level Histograms. *IEEE Trans. Syst. Man Cybern.* **1979**, *9*, 62–66. [CrossRef]

https://doi.org/10.3390/s26082381

30. Liang, S.; Jianchun, X.; Xun, Z. An Extraction and Classification Algorithm for Concrete Cracks Based on Machine Vision. *IEEE Access* **2018**, *6*, 45051–45061. [CrossRef]
31. Vapnik, V. *The Nature of Statistical Learning Theory*; Springer Science & Business Media: Berlin/Heidelberg, Germany, 2013.
32. Goodfellow, I.; Bengio, Y.; Courville, A.; Bengio, Y. *Deep Learning*; MIT Press: Cambridge, MA, USA, 2016; Volume 1.
33. Moghbel, M.; Ooi, C.Y.; Ismail, N.; Hau, Y.W.; Memari, N. A review of breast boundary and pectoral muscle segmentation methods in computer-aided detection/diagnosis of breast mammography. *Artif. Intell. Rev.* **2020**, *53*, 1873–1918. [CrossRef]
34. Haralick, R.M.; Sternberg, S.R.; Zhuang, X. Image analysis using mathematical morphology. *IEEE Trans. Pattern Anal. Mach. Intell.* **1987**, *9*, 532–550. [CrossRef] [PubMed]
35. Song, T.; Pang, S.; Hao, S.; Rodriguez-Paton, A.; Zheng, P. A parallel image skeletonizing method using spiking neural P systems with weights. *Neural Process. Lett.* **2019**, *50*, 1485–1502. [CrossRef]
36. Meng, Q.; Hu, L.; Wan, D.; Li, M.; Wu, H.; Qi, X.; Tian, Y. Image-based concrete cracks identification under complex background with lightweight convolutional neural network. *KSCE J. Civ. Eng.* **2023**, *27*, 5231–5242. [CrossRef]
37. McQueen, J.B. Some methods of classification and analysis of multivariate observations. In Proceedings of the 5th Berkeley Symposium on Mathematical Statistics and Probability, Berkeley, CA, USA, 21 June–18 July 1965; pp. 281–297.

Disclaimer/Publisher's Note: The statements, opinions and data contained in all publications are solely those of the individual author(s) and contributor(s) and not of MDPI and/or the editor(s). MDPI and/or the editor(s) disclaim responsibility for any injury to people or property resulting from any ideas, methods, instructions or products referred to in the content.

https://doi.org/10.3390/s26082381

sensors

MDPI

Article

Piezoresistive Sensing Performance of Smart Layer in Multi-Material 3D-Printed Reinforced Cementitious Beams

Han Liu [1], Israel Sousa [2], Shelby E. Doyle [3], Antonella D'Alessandro [2], Filippo Ubertini [2] and Simon Laflamme [1,4,*]

[1] Department of Civil, Construction, and Environmental Engineering, Iowa State University, Ames, IA 50010, USA
[2] Department of Civil and Environmental Engineering, University of Perugia, Via G. Duranti, 93, 06125 Perugia, Italy; antonella.dalessandro@unipg.it (A.D.); filippo.ubertini@unipg.it (F.U.)
[3] Department of Architecture, Iowa State University, Ames, IA 50010, USA
[4] Department of Electrical and Computer Engineering, Iowa State University, Ames, IA 50010, USA
* Correspondence: laflamme@iastate.edu

Abstract

3D concrete printing (3DP) enables automated construction with reduced material waste and enhanced geometric flexibility. However, its structural performance remains sensitive to anisotropy, mix design, and printing parameters, thereby complicating quality control. Self-sensing cementitious materials provide a promising approach by enabling intrinsic strain monitoring during fabrication and service. In this study, a hybrid multi-material printing strategy was developed using a conductive cement-based mix incorporating graphite (G), milled carbon microfibers (MCMF), and chopped carbon microfibers (CCMF), alongside a plain cement-based matrix. Based on percolation analysis, an optimal composition of 2 wt.% G, 0.25 wt.% MCMF, and 0.0625 wt.% CCMF was selected. Reinforced beam specimens were fabricated with the conductive material embedded in either the tensile (bottom) or compressive (top) region, combined with two internal architectures: diagonal infill and solid-base configuration. Four configurations were defined: Pattern 1 (bottom/diagonal), Pattern 2 (bottom/solid-base), Pattern 3 (top/diagonal), and Pattern 4 (top/solid-base). Cyclic three-point bending tests with spatially distributed electrical measurements were conducted to evaluate the electromechanical response in the elastic range. Specimens with the conductive layer located in the tensile region (Patterns 1 and 2) consistently exhibited higher gauge factors than those in the compressive region (Patterns 3 and 4). Pattern 2 exhibited the best sensing performance, with an average gauge factor of 556 and SNR of 31. Across all configurations, SNR decreased with increasing electrode spacing, with reductions of up to 31.0%, demonstrating the effect of current path length on sensing performance.

Keywords: 3D printed concrete; self-sensing; structural health monitoring; smart concrete; hybrid printing; piezoresistive properties

1. Introduction

Additive manufacturing, particularly extrusion-based three-dimensional printing (3DP) of cementitious materials, has emerged as a promising construction technology due to its ability to reduce the amount of required formwork, minimize material waste, accelerate construction, enable the fabrication of complex geometries with improved design flexibility [1–3]. Despite these advantages, the structural performance of 3D printed

components remains highly dependent on the layering quality that is affected by interlayer bonding, printing path, infill topology, and material variability [4–6]. These factors can introduce inherent anisotropy and heterogeneity, which significantly affect load transfer mechanisms and structural reliability, thereby posing challenges for large-scale implementation in civil infrastructure [7–9].

To address these challenges, one can implement structural health monitoring (SHM) to provide real-time assessment of structural performance during and after fabrication [10–12]. Conventional sensing approaches, including strain gauges [13], fiber-optic sensors [14], acoustic emission [15], and piezoelectric transducers [16], have demonstrated effectiveness in evaluating the condition of concrete elements. However, the deployment of conventional SHM technologies in 3DP applications remains limited due to issues related to sensor integration, durability, wiring complexity, and compatibility with the printing process [17]. These limitations motivate the interest in 3DP self-sensing cementitious materials.

Piezoresistive cement-based composites consist of regular cementitious materials mixed with conductive fillers used to increase the piezoresistive effect that creates measurable changes in electrical resistance upon mechanical strain [18–20]. Several types of conductive fillers have been studied, including graphite (G) [21,22], carbon microfibers (CMF) [23,24], carbon nanotubes [25,26], and carbon black [27,28] to form percolating conductive networks within the material. Among these, hybrid systems combining particulate fillers and fibrous inclusions have shown particular promise, as they can leverage multiple conduction mechanisms. For example, G primarily contributes to particle-based conduction and tunneling effects, while carbon microfibers enhance network connectivity through bridging across microcracks and microscale gaps within the heterogeneous conductive network [29,30]. As a result, hybrid conductive systems can improve both sensitivity and stability of the electromechanical response.

Existing research on self-sensing cementitious materials can be broadly categorized into two groups. The first focuses on material-level investigations, including material composition, conductive mechanisms, percolation behavior, and electromechanical response in cast or small-scale laboratory specimens [31]. The second includes emerging studies on additive manufacturing of self-sensing systems, which primarily address printability and basic sensing functionality [24,32,33]. Research efforts in this second group remain largely limited to simplified geometries or non-structural components, and do not fully capture the complexity of load-bearing 3D-printed elements. In particular, the combined effects of printing-induced anisotropy, internal architecture, and sensing-layer placement on the electromechanical response remain insufficiently explored.

While the integration of self-sensing functionality into structurally relevant 3D printed components could accelerate the transition of 3DP elements through monitoring and ultimately quality control and assessment, existing studies remain limited in several key aspects, including the integration of sensing functionality within load-bearing printed elements, the influence of printing-induced anisotropy and internal architecture on electromechanical response, and the spatial variability of sensing performance across structural-scale components [34–38]. Our prior study has demonstrated that 3D printed self-sensing cementitious composites can be embedded within structural components to enable integrated strain monitoring [39]. However, in such systems, the sensing response is governed not only by the intrinsic properties of the conductive material, but also by the location of the sensing material relative to the neutral axis, the printing path, infill topology, the presence of reinforcement, and the spatial distribution of strain under loading. These factors introduce additional complexity in interpreting electrical signals, making it challenging to establish a direct and consistently quantifiable relationship between measured resistance changes and structural response.

https://doi.org/10.3390/s26103204

This study investigates the integration of self-sensing cementitious layers within 3D-printed reinforced beam specimens, termed smart beams, to enable embedded sensing functionality in load-bearing elements. A conductive Sikacrete-based composite incorporating G, MCMF, and CCMF is optimized through percolation analysis and selectively embedded within either the tensile or compressive regions using a multi-material printing approach. Two internal configurations, including a diagonal infill and a solid-base design, are implemented to assess the effect of structural topology on sensing performance. Cyclic three-point bending tests, combined with spatially distributed electrical measurements and an electromechanical model, are used to characterize the piezoresistive response. The novelty of this study lies in three aspects. First, it advances self-sensing cementitious materials from material-scale demonstrations to structurally integrated, load-bearing 3D-printed elements. Second, it quantifies the coupled effects of sensing-layer placement and printing-induced internal architecture on electromechanical response. Third, it introduces a spatially distributed sensing configuration that enables direct evaluation of sensing performance along the beam length, providing new insights into the relationship between structural behavior and electrical response in additively manufactured cementitious components.

The rest of the paper is organized as follows. Section 2 provides the background on 3D printed self-sensing cementitious specimens including the material properties, the fabrication process, and the derivation of the electromechanical model. Section 3 describes the experimental methodology. Section 4 presents and discusses results from the experimental investigation. Section 5 concludes the paper.

2. Background

2.1. Materials

Self-sensing cement-based composites are fabricated through the incorporation of conductive fillers into the cementitious matrix. The addition of these fillers imparts piezoresistive properties to the composite, enabling it to function as an intrinsic sensing material capable of transducing mechanical stimuli into measurable electrical signals. In this study, a hybrid conductive network was established using G (Thermo Scientific Chemicals, Milwaukee, WI, USA, APS 7–11 μm, 99%) in combination with MCMF (SGL Carbon C M150-4.0/240-UN)) and CCMF (SGL Carbon C M150-4.0/240-G100).

Both types of CMFs exhibited favorable feedability (i.e., the ability of the fresh cementitious mixture to be continuously and reliably transported into the extrusion system without blockage, segregation, or interruption), uniform dispersion within the matrix, and good compatibility with the cementitious matrix [40]. Morphological observations indicate that both fiber types possess relatively smooth surfaces, occasionally featuring longitudinal grooves characteristic of polyacrylonitrile-derived carbon fibers that are produced through the stabilization and carbonization of polyacrylonitrile precursors. A representative scanning electron microscopy (SEM) image of the CMFs is provided in [40], and their detailed material properties are summarized in Table 1. CCMF is received coated with a glycerin-based sizing, which primarily facilitates fiber dispersion and workability with minimal influence on interfacial bonding. The parameter "filament resistivity" denotes the intrinsic electrical resistivity of a single carbon fiber filament as provided by the manufacturer (SGL Carbon GmbH, Arkadelphia, AR, USA). This property is independent of fiber length, as both CCMF and MCMF are derived from the same precursor material and possess identical filament diameters.

https://doi.org/10.3390/s26103204

Table 1. Material properties for the Fisher Chemical, APS 7–11 μm, 99% G powder and SGL milled and chopped CMF, adapted from [41].

Properties	G	MCMF	CCMF
density (g/cm^3)	1.06	1.80	1.80
mean fiber length (μm)	-	150	6000
filament diameter (μm)	37	7	7
tensile strength (GPa)	-	4.0	4.0
tensile modulus (GPa)	-	240	240
elongation at break (%)	-	1.7	1.7
filament resistivity (μΩm)	40	15	15
bulk density (g/L)	800	250	-
sizing type	unsized	unsized	glycerin
sizing mass content (%)	-	-	4.0

2.2. Composite Mixtures

Sikacrete 752-3D, a commercially available one-part micro-concrete composed of Portland cement, fine aggregates, and functional admixtures, was adopted as the binder matrix. Its rheology, tailored for extrusion-based 3D printing, exhibits shear-thinning behavior, rapid structural build-up, and adequate open time, enabling stable filament deposition, interlayer bonding, and compatibility with conductive fillers.

The mixture proportions for each set of specimens are summarized in Table 2, and specimens were labeled using the following convention. The numerical prefix denotes the filler content (wt.%) relative to the Sikacrete mass. To investigate the percolation behavior and strain sensitivity of the conductive system, G was first introduced at contents ranging from 0 to 16 wt.%, following a stepwise doubling sequence (1, 2, 4, 8, and 16 wt.%) to capture the evolution of conductive behavior across the percolation regime. The water-to-binder (w/b) ratio was assigned as 0.21, 0.23, 0.26, 0.29, 0.34, and 0.44 for the 0 G, 1 G, 2 G, 4 G, 8 G, and 16 G mixtures, respectively, which were determined through preliminary mixture optimization [39]. Increasing the w/b ratio with increasing G content was necessary to compensate for its high specific surface area, which increases water demand and alters rheological behavior. This adjustment ensured sufficient flowability for extrusion while maintaining adequate structural build-up after deposition [42].

Based on the percolation analysis of the G system, discussed further in Section 4, the 2 wt.% G mixture was identified as being within the percolation zone, providing a balance between electrical sensitivity and printability, and was therefore selected as the reference composition (2G0CMF). MCMF and CCMF were subsequently incorporated over a range of 0.03125 wt.% to 0.25 wt.% following a similar stepwise scaling approach, as presented in Table 2. For mixtures containing CMFs, a constant w/b ratio of 0.26 was adopted, consistent with the 2G reference mixture, in order to eliminate the effect of fiber incorporation. Plain specimens without conductive fillers (0G0CMF) were also prepared for benchmarking results.

A hybrid composition consisting of 2 wt.% G, 0.25 wt.% MCMF, and 0.0625 wt.% CCMF (denoted as 2G250M62CCMF) was selected as the mixture design for 3D printing in this study. This mixture lies near the percolation threshold of each filler, enabling a stable and well-connected conductive network with enhanced sensitivity, while maintaining sufficient workability and buildability for extrusion-based 3D printing. Higher CCMF contents were not considered, as previous studies have shown that excessive fiber loading can lead to nozzle blockage and compromised printability [24,43].

https://doi.org/10.3390/s26103204

Table 2. Mixture proportions for each type of 3DP conductive concrete specimens, with G/S (%) denoting the mass fraction of graphite relative to the Sikacrete binder.

Specimen	G (g)	G/S (%)	MCMF (g)	MCMF/S (%)	CCMF (g)	CCMF/S (%)	w/b (%)
0G0CMF	0	0	-	-	-	-	0.21
1G0CMF	3	1	-	-	-	-	0.23
2G0CMF	6	2	-	-	-	-	0.26
4G0CMF	12	4	-	-	-	-	0.29
8G0CMF	24	8	-	-	-	-	0.34
16G0CMF	48	16	-	-	-	-	0.44
2G31MCMF	6	2	0.09375	0.03125	-	-	0.26
2G62MCMF	6	2	0.1875	0.0625	-	-	0.26
2G125MCMF	6	2	0.375	0.125	-	-	0.26
2G250MCMF	6	2	0.75	0.250	-	-	0.26
2G31CCMF	6	2	-	-	0.09375	0.03125	0.26
2G62CCMF	6	2	-	-	0.1875	0.0625	0.26
2G125CCMF	6	2	-	-	0.375	0.125	0.26
2G250CCMF	6	2	-	-	0.75	0.250	0.26

2.3. Fabrication Process

A standardized mixing protocol was adopted to ensure consistent rheological behavior and material dispersion. Two types of mixtures, namely a conductive Sikacrete composite and a normal Sikacrete composite, were prepared as illustrated in Figure 1. For the conductive composite, Sikacrete powder was combined with G, MCMF, and CCMF according to the mix design. All dry constituents were first premixed for 2 min to mitigate particle agglomeration. Subsequently, 50 wt.% of the total mixing water was added, and the mixture was blended using a handheld mixer at 200 rpm for 2 min. The remaining 50 wt.% of water was then introduced to achieve a designed water-to-binder (w/b) ratio, as presented in Table 2, followed by an additional 3 min of mixing at the same speed to ensure adequate homogenization and printability. The normal Sikacrete composite was prepared following the same procedure, excluding the addition of conductive fillers, and using a w/b ratio of 0.21 to account for the absence of high-surface-area additives.

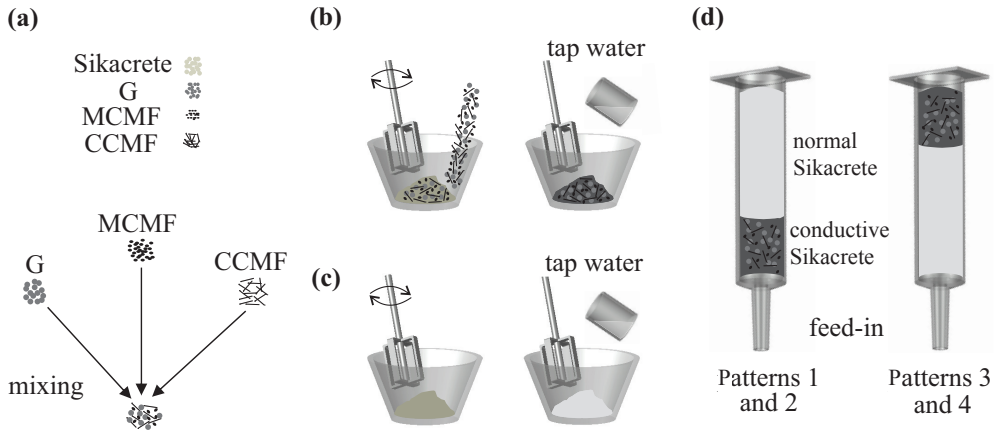


Figure 1. Fabrication process of the cement-based composites: (**a**) conductive fillers; (**b**) preparation of the conductive mix; (**c**) preparation of the normal mix; and (**d**) extrusion cylinder filled with feed-in composite mixtures in two different configurations.

A series of cubic specimens ($50 \times 50 \times 50$ mm^3, illustrated in Figure 2a) were fabricated to investigate the percolation behavior and strain sensitivity of the conductive system using

https://doi.org/10.3390/s26103204

the mixture proportions summarized in Table 2. All specimens were produced using a mold-casting approach to allow for the controlled evaluation of the conductive network prior to printing. Each specimen was fabricated using 300 g of normal Sikacrete by placing the mixtures into pre-oiled cubic molds in two stages, with light tamping applied after the first pour to release entrapped air and ensure uniform compaction. Conductive electrodes were embedded during casting, consisting of two parallel copper mesh layers positioned with a fixed spacing interval D of approximately 38 mm across the specimen. Sets of three specimens were fabricated under 14 different mix designs for a total of 42 cast specimens.

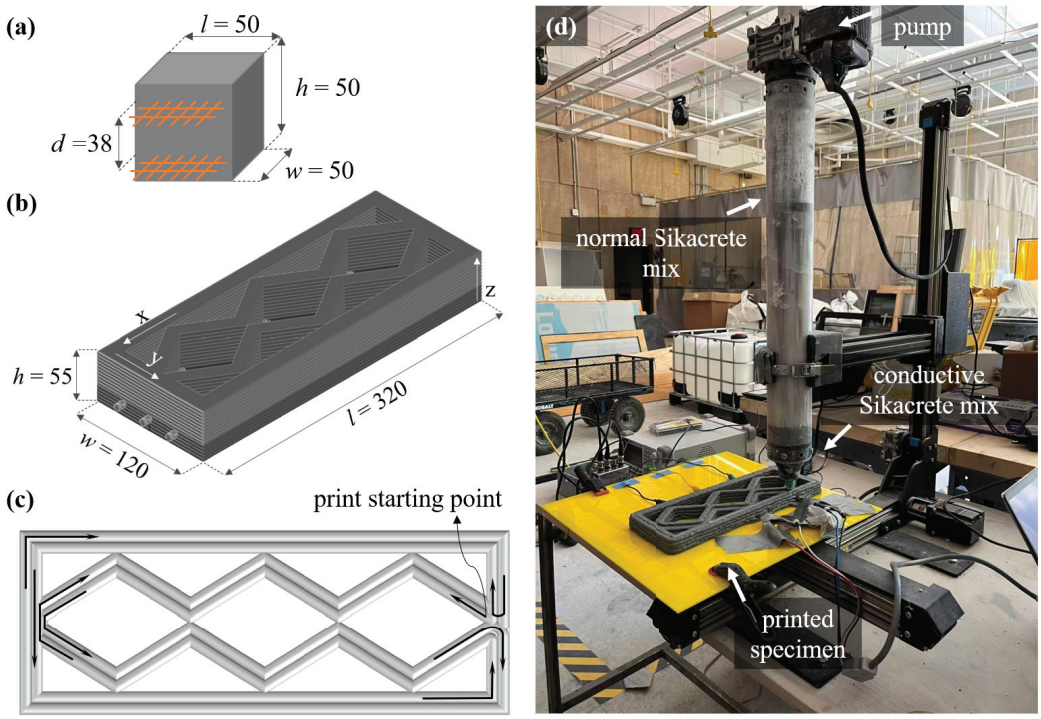


Figure 2. Fabrication of specimens: (**a**) geometry of the cast cubic specimens; (**b**) geometry of the smart beams; (**c**) printing path; and (**d**) overall printing configuration.

An extrusion-based commercial 3D clay printer (3D Potter 7) was used for fabricating the smart beams using the selected mix design (2G250M62CCMF). The printer has a resolution in the X and Y axes of 0.15 mm, and a resolution in the Z axis of 0.7 mm. Beam specimens with overall dimensions of $320 \times 120 \times 55$ mm^3 were designed and sliced in Cura into 15 layers with a uniform layer height of 3.66 mm, as shown in Figure 2b. It should be noted that layer height may influence the electromechanical response by affecting interlayer cohesion, internal pore structure, and anisotropy in printed cementitious elements [44–46]. The selection of layer height is also governed by factors such as specimen scale, nozzle diameter, and the configuration of the 3D printing system, which affect extrusion stability and geometric fidelity [47,48]. In this study, the adopted layer height was determined based on preliminary trial prints to ensure consistent filament deposition, adequate interlayer bonding, and stable buildability throughout the fabrication process.

The freshly mixed materials were manually loaded into the extrusion cylinder in three consecutive pours, with the loading sequence adjusted to control the placement of the conductive layer. Each pour consisted of approximately 1500 g of fresh material, corresponding to the deposition of five printed layers. Thus, three pours (4500 g in total) were used to complete the 15-layer specimens. For specimens with a bottom conductive layer, the conductive Sikacrete composite was introduced first, followed by two pours of normal Sikacrete. The loading sequence was reversed for specimens designed with the

https://doi.org/10.3390/s26103204

conductive layer at the top, with normal Sikacrete introduced first and the conductive mixture placed in the final pour, as shown in Figure 1d.

A circular nozzle with a diameter of 8 mm was used, and the stand-off distance between the nozzle and the printing platform was maintained at approximately 4 mm. The nozzle movement path is illustrated in Figure 2c. Printing initiates at a predefined corner of the specimen, from which the nozzle first traverses the outer boundary to complete the perimeter of the layer. Subsequently, the nozzle follows a continuous deposition path to construct the internal pattern, advancing along each filament path and translating laterally by approximately one filament width to the adjacent path without interrupting extrusion. This sequence is repeated until all filaments within the layer are completed, with smooth directional transitions at turning points to maintain geometric consistency. Printing was conducted at a constant extrusion rate of 320 mm^3/s and a platform movement speed of 120 mm/s to ensure stable and uniform material deposition. An image of the printing setup is shown in Figure 2d. The printability of the hybrid conductive mixture was evaluated based on its extrusion stability, filament formation, and buildability during the printing process. Deposited filaments maintained their geometry with minimal deformation, indicating adequate yield stress and structural build-up. The multi-material deposition process was also successfully achieved without notable interfacial instability between the conductive and non-conductive phases. The selected mixture exhibited continuous and uniform extrusion without observable nozzle blockage, filament collapse, or material segregation during the printing process, confirming the proposed mixture design is compatible with extrusion-based multi-material 3D printing and suitable for fabricating structurally relevant components.

Four smart beam configurations were designed by combining two internal pattern types with two conductive layer placements. The internal patterns consisted of a diagonal pattern along the height of the beam, and of a partially solid configuration in which the first six layers were printed with a 100% infill followed by a diagonal pattern for the remaining height (layers 7 to 15). The introduction of a solid base was intended to provide a more uniform and continuous load-transfer region near the bottom of the specimen, thereby reducing geometric-induced variability and enabling assessment of the effect of internal architecture on both structural response and sensing performance.

For each internal pattern, two conductive layer arrangements were implemented. In the first arrangement, the conductive material was placed in the bottom six layers (layers 1 to 6), whereas in the second arrangement it was positioned in the top five layers (layers 11 to 15). Accordingly, Pattern 1 corresponds to the diagonal pattern with the conductive layer at the bottom (Figure 3a), Pattern 2 corresponds to the partially solid internal pattern with the conductive layer at the bottom (Figure 3b), Pattern 3 corresponds to the diagonal internal pattern with the conductive layer at the top (Figure 3c). Pattern 4 corresponds to the partially solid internal pattern with the conductive layer at the top (Figure 3d). These four patterns were selected for the independent assessment of the effects of infill topology (diagonal vs. solid base) and sensing-layer location (tension vs. compression) under bending. These designs correspond to a 2×2 factorial design, in which the effects of sensing-layer placement relative to the neutral axis and internal structural topology are independently evaluated.

Six steel drop-in anchors were embedded as electrodes at equal spacing along the beam length and labeled sequentially as A–F (as shown in Figure 3a). For specimens with bottom conductive layers (Patterns 1 and 2), the electrodes were positioned in the third layer, whereas for specimens with top conductive layers (Patterns 3 and 4), the electrodes were embedded in the twelfth layer to align with the conductive region. In addition, three #2 steel reinforcement rebars (diameter 6.35 mm) were placed longitudinally after deposition

https://doi.org/10.3390/s26103204

of the fifth layer to provide a more realistic structural configuration and to ensure elastic behavior under bending during testing. A center-to-center spacing of 30 mm between the longitudinal reinforcement bars was adopted, measured from the center of each bar, to prevent direct contact between the reinforcement and the embedded electrodes. The beam specimens were designed to represent structurally relevant elements, incorporating longitudinal reinforcement and beam-scale geometry to approximate realistic load-bearing conditions. The inclusion of reinforcement and controlled geometry ensures that the measured electromechanical response reflects behavior under representative flexural loading rather than material-scale testing. Following fabrication, all specimens were cured under laboratory conditions for 28 days to promote hydration and ensure stable mechanical and electrical performance.

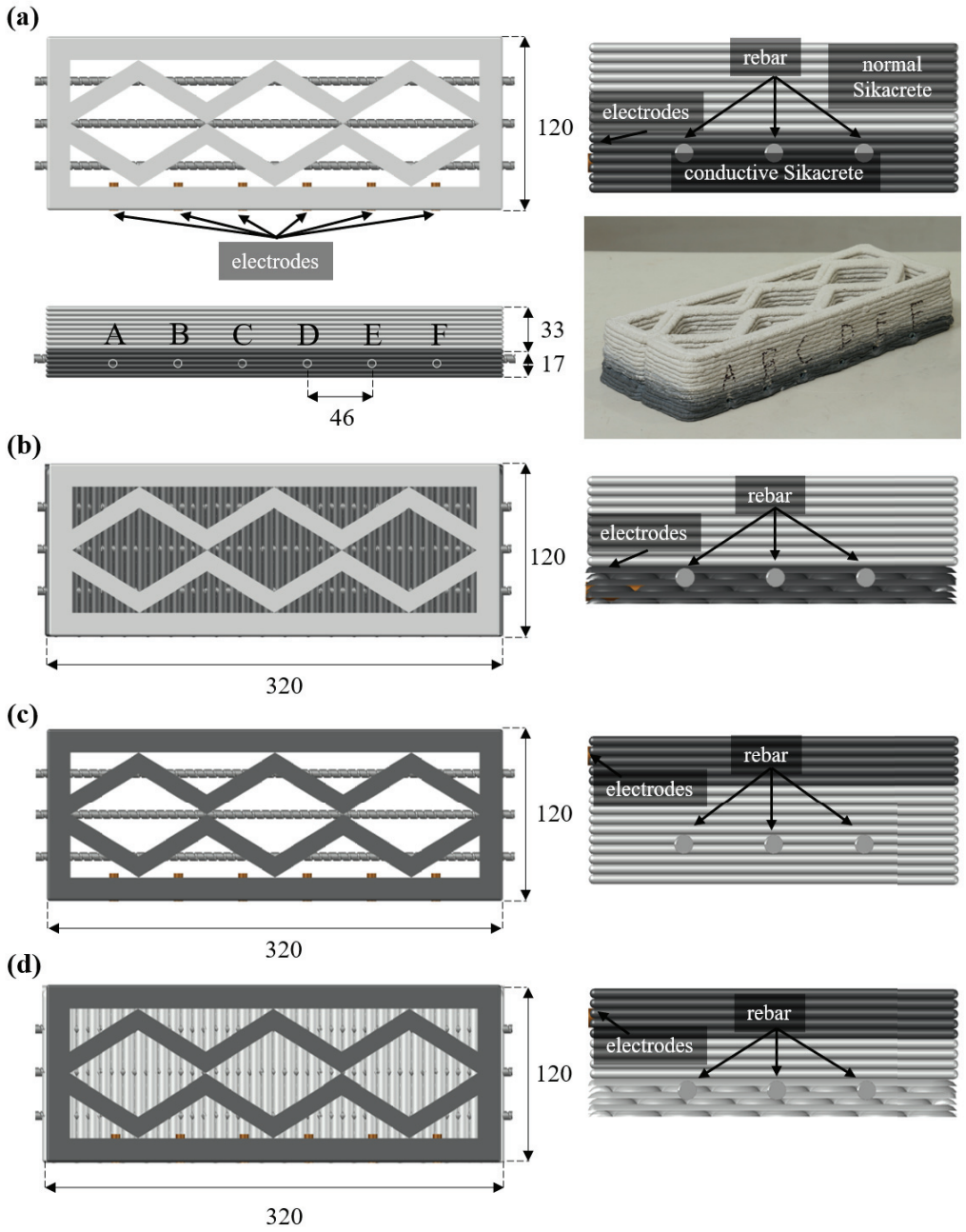


Figure 3. Schematic illustrations of the four sample configurations: (**a**) Pattern 1, including top, side, front, and 3D views; (**b**) Pattern 2, showing top and front views; (**c**) Pattern 3, showing top and front views; and (**d**) Pattern 4, showing top and front views. Units are in mm.

https://doi.org/10.3390/s26103204

2.4. Electromechanical Model

The electromechanical response of self-sensing cement-based materials is commonly described through their piezoresistive behavior, whereby mechanical deformation induces a measurable change in electrical resistance. For the conductive region between the embedded electrodes, the nominal electrical resistance can be expressed as

$$R_0 = \rho \frac{D}{A} \tag{1}$$

where ρ is the bulk electrical resistivity of the conductive cementitious composite, D is the electrode spacing, and A is the effective cross-sectional area normal to the current path. For the present 3D-printed beam specimen, the conductive paths are non-uniform due to the heterogeneous, percolated conductive network and the effect of internal architecture. As such, A does not correspond to a strictly geometric cross-section, but is treated as a parameter that is constant for a given pattern configuration in the undeformed state. Under mechanical loading, its incremental variation due to deformation is captured through the differential term $\mathrm{d}A/A$. While this assumption limits direct physical interpretation, it enables a tractable formulation for comparative analysis. Taking the natural logarithm of Equation (1) gives

$$\ln R = \ln \rho + \ln D - \ln A \tag{2}$$

Differentiating Equation (2) yields

$$\frac{\mathrm{d}R}{R} = \frac{\mathrm{d}\rho}{\rho} + \frac{\mathrm{d}D}{D} - \frac{\mathrm{d}A}{A} \tag{3}$$

Assuming that the conductive region undergoes uniform longitudinal deformation, isotropic lateral contraction is considered for the transverse dimensions due to Poisson's effect. Let b and t denote the width and thickness of the conductive region between the electrodes, respectively. The corresponding transverse strain components are expressed as

$$\frac{\mathrm{d}b}{b} = \frac{\mathrm{d}t}{t} = -\nu \frac{\mathrm{d}D}{D} \tag{4}$$

where ν is the Poisson's ratio of the conductive cementitious material. The cross-sectional area therefore varies with deformation, and its relative change can be written as

$$\frac{\mathrm{d}A}{A} = \frac{\mathrm{d}b}{b} + \frac{\mathrm{d}t}{t} = -2\nu \frac{\mathrm{d}D}{D} \tag{5}$$

Substituting Equation (5) into Equation (3) gives

$$\frac{\mathrm{d}R}{R} = \frac{\mathrm{d}\rho}{\rho} + (1 + 2\nu)\frac{\mathrm{d}D}{D} \tag{6}$$

which shows that the change in resistance arises from both intrinsic resistivity variation and geometrical effects associated with deformation. For small deformations, the infinitesimal form may be approximated by finite increments

$$\frac{\Delta R}{R_0} = \frac{\Delta \rho}{\rho} + (1 + 2\nu)\frac{\Delta D}{D} = \frac{\Delta \rho}{\rho} + (1 + 2\nu)\varepsilon \tag{7}$$

and the fractional change in resistance (FCR) becomes

$$\mathrm{FCR} = \frac{\Delta R}{R_0} = \frac{\Delta \rho}{\rho} + (1 + 2\nu)\varepsilon \tag{8}$$

https://doi.org/10.3390/s26103204

Equation (8) represents the local electromechanical constitutive relation of the sensing material. However, for the beam specimens printed in this study, the strain in the sensing region is pattern-dependent because the four configurations differ in the infill topologies, conductive-layer location, and reinforcement layout.

At a first-order approximation, the printed elements are modeled as Euler–Bernoulli elastic beams for interpreting the results. This is a simplification, given the geometry of the specimens—characterized by varying cross-sections along their length and widths comparable to their lengths—as well as the anisotropic behavior of printed cement-based materials. This assumption neglects the effects of material heterogeneity, anisotropy, and printing paths inherent to 3D-printed cementitious specimens. Nevertheless, it provides a consistent framework for capturing the global bending behavior and estimating the average strain in the sensing layer across different configurations, and is therefore sufficient to describe the main physical phenomena. Under three-point bending, the mid-span deflection δ of a simply supported beam subjected to a central point load P is given by

$$\delta = \frac{PL^3}{48EI} \tag{9}$$

where L is the span length, E is the effective elastic modulus, assumed to be constant along the beam length as a first-order approximation, and I is the effective moment of inertia of the transformed section. The maximum bending moment at mid-span is $M_{\max} = PL/4$, and the curvature (κ) at mid-span is defined as

$$\kappa = \frac{M_{\max}}{EI} = \frac{1}{EI} \cdot \frac{PL}{4} = \frac{1}{EI} \cdot \frac{48EI\delta}{L^3} \cdot \frac{L}{4} = \frac{12\delta}{L^2} \tag{10}$$

Let z denote the vertical coordinate measured from the bottom surface of the beam, $z_{\mathrm{NA}}^{(p)}$ the neutral-axis location for pattern p, and $z_s^{(p)}$ the centroid of the conductive sensing region. The bending strain in the sensing layer is then written

$$\varepsilon_s^{(p)} = \kappa\left(z_{\mathrm{NA}}^{(p)} - z_s^{(p)}\right) = \frac{12\delta}{L^2}\left(z_{\mathrm{NA}}^{(p)} - z_s^{(p)}\right) \tag{11}$$

where $p = 1, 2, 3, 4$ denotes the beam pattern. For the smart beams Patterns 1 and 2, the centroid of the bottom conductive layer is located at $z_b = 10.98$ mm, and for Patterns 3 and 4, the centroid of the top conductive layer is located at $z_t = 45.75$ mm, giving

$$\varepsilon_s^{(1)} = \frac{12\delta}{L^2}\left(z_{\mathrm{NA}}^{(1)} - z_b\right) \tag{12}$$

$$\varepsilon_s^{(2)} = \frac{12\delta}{L^2}\left(z_{\mathrm{NA}}^{(2)} - z_b\right) \tag{13}$$

$$\varepsilon_s^{(3)} = \frac{12\delta}{L^2}\left(z_{\mathrm{NA}}^{(3)} - z_t\right) \tag{14}$$

$$\varepsilon_s^{(4)} = \frac{12\delta}{L^2}\left(z_{\mathrm{NA}}^{(4)} - z_t\right) \tag{15}$$

Under three-point bending, the bottom region of the beam is subjected to tension and the top region to compression. Accordingly, the sensing layer experiences tensile strain in Patterns 1 and 2 ($\varepsilon_s^{(1)}, \varepsilon_s^{(2)} > 0$), and compressive strain in Patterns 3 and 4 ($\varepsilon_s^{(3)}, \varepsilon_s^{(4)} < 0$), following the sign convention adopted herein.

The neutral-axis location $z_{\mathrm{NA}}^{(p)}$ varies among the four patterns due to differences in internal architecture and the presence of longitudinal reinforcement. It is determined using

https://doi.org/10.3390/s26103204

a transformed-section approach that accounts for both the cementitious matrix and the steel reinforcement. In general form,

$$z_{\mathrm{NA}}^{(p)} = \frac{\sum_i E_i A_i z_i + \sum_j E_s A_{s,j} z_{s,j}}{\sum_i E_i A_i + \sum_j E_s A_{s,j}} \tag{16}$$

where A_i and z_i are the area and centroid of the ith printed subregion, $A_{s,j}$ and $z_{s,j}$ are the area and centroid of the jth reinforcing bar, and E_i and E_s denote the elastic moduli of the cementitious material and steel, respectively.

Substituting the pattern-dependent sensing strain into Equation (8) gives

$$\mathrm{FCR}^{(p)} = \frac{\Delta R}{R_0} = \frac{\Delta \rho}{\rho} + (1 + 2\nu)\varepsilon_s^{(p)} \tag{17}$$

The bending gauge factor for each pattern is then defined as

$$\lambda^{(p)} = \frac{d(\mathrm{FCR}^{(p)})}{d(\varepsilon_s^{(p)})} \tag{18}$$

2.5. Pattern- and Electrode-Pair-Dependent Bending Strain

When the electrical response is measured between different electrode pairs, the strain input to the electromechanical model is not unique, because it depends on both the beam pattern and the spanwise location of the selected electrode pair. The strain used for electromechanical analysis is therefore defined as the average bending strain over the conductive region between any electrodes I, and J under pattern p.

Let $x_A < x_B < x_C < x_D < x_E < x_F$ denote the longitudinal coordinates of electrodes A-F, measured from the left support, and let $x_{IJ} = x_J - x_I$ denote the gauge length between electrodes I and J. Here, the six electrodes are equally spaced at 46 mm intervals and are assumed to be symmetrically arranged about the beam mid-span, independent of the pattern configuration. With $s = 46$ mm, their coordinates are written as

$$x_A = \frac{L-5s}{2}, \quad x_B = \frac{L-3s}{2}, \quad x_C = \frac{L-s}{2}, \quad x_D = \frac{L+s}{2}, \quad x_E = \frac{L+3s}{2}, \quad x_F = \frac{L+5s}{2} \tag{19}$$

Under three-point bending, the curvature distribution along the beam is

$$\kappa(x) = \begin{cases} \dfrac{24\delta}{L^3} x, & 0 \le x \le \dfrac{L}{2} \\ \dfrac{24\delta}{L^3}(L-x), & \dfrac{L}{2} \le x \le L \end{cases} \tag{20}$$

where δ is the mid-span deflection and L is the support span. This formulation assumes a perfect bond between the reinforcement and the surrounding cementitious matrix. Possible bond-slip behaviors, especially near the beam ends, are neglected. The average curvature over the sensing length between electrodes I and J is then

$$\bar{\kappa}_{IJ} = \frac{1}{x_{IJ}} \int_{x_I}^{x_J} \kappa(x)\, dx \tag{21}$$

where the bar in $(\bar{\kappa})$ denotes the spatial average over the electrode gauge length between x_I and x_J. The corresponding average bending strain between electrodes I and J $(\bar{\varepsilon})$ in the conductive sensing layer for pattern p is written as

$$\bar{\varepsilon}_{IJ}^{(p)} = c_p \bar{\kappa}_{IJ} \tag{22}$$

https://doi.org/10.3390/s26103204

where c_p is the signed distance between the neutral axis and the centroid of the conductive sensing layer for pattern p:

$$c_p = z_{\mathrm{NA}}^{(p)} - z_s^{(p)} \tag{23}$$

Thus,

$$c_1 = z_{\mathrm{NA}}^{(1)} - z_b, \qquad c_2 = z_{\mathrm{NA}}^{(2)} - z_b, \qquad c_3 = z_{\mathrm{NA}}^{(3)} - z_t, \qquad c_4 = z_{\mathrm{NA}}^{(4)} - z_t \tag{24}$$

Substituting Equation (19) into Equations (20)–(22), the average bending strains for the electrode pairs are obtained as follows.

For adjacent electrode pairs,

$$\bar{\varepsilon}_{AB}^{(p)} = \bar{\varepsilon}_{EF}^{(p)} = c_p \frac{\delta}{L^3}(12L - 48s) = c_p \frac{\delta}{L^3}(12L - 2208) \tag{25}$$

$$\bar{\varepsilon}_{BC}^{(p)} = \bar{\varepsilon}_{DE}^{(p)} = c_p \frac{\delta}{L^3}(12L - 24s) = c_p \frac{\delta}{L^3}(12L - 1104) \tag{26}$$

$$\bar{\varepsilon}_{CD}^{(p)} = c_p \frac{\delta}{L^3}(12L - 6s) = c_p \frac{\delta}{L^3}(12L - 276) \tag{27}$$

For non-adjacent electrode pairs,

$$\bar{\varepsilon}_{AC}^{(p)} = \bar{\varepsilon}_{DF}^{(p)} = c_p \frac{\delta}{L^3}(12L - 36s) = c_p \frac{\delta}{L^3}(12L - 1656) \tag{28}$$

$$\bar{\varepsilon}_{AD}^{(p)} = \bar{\varepsilon}_{CF}^{(p)} = c_p \frac{\delta}{L^3}(12L - 26s) = c_p \frac{\delta}{L^3}(12L - 1196) \tag{29}$$

$$\bar{\varepsilon}_{AE}^{(p)} = \bar{\varepsilon}_{BF}^{(p)} = c_p \frac{\delta}{L^3}\left(12L - \frac{51}{2}s\right) = c_p \frac{\delta}{L^3}(12L - 1173) \tag{30}$$

$$\bar{\varepsilon}_{AF}^{(p)} = c_p \frac{\delta}{L^3}(12L - 30s) = c_p \frac{\delta}{L^3}(12L - 1380) \tag{31}$$

$$\bar{\varepsilon}_{BD}^{(p)} = \bar{\varepsilon}_{CE}^{(p)} = c_p \frac{\delta}{L^3}(12L - 15s) = c_p \frac{\delta}{L^3}(12L - 690) \tag{32}$$

$$\bar{\varepsilon}_{BE}^{(p)} = c_p \frac{\delta}{L^3}(12L - 18s) = c_p \frac{\delta}{L^3}(12L - 828) \tag{33}$$

These expressions show that the strain input to the electromechanical model depends on both the beam pattern, through c_p, and the selected electrode pair, through its spanwise position relative to the curvature distribution. Accordingly, the pair-dependent fractional change in resistance is written as

$$\mathrm{FCR}_{IJ}^{(p)} = \frac{\Delta R_{IJ}^{(p)}}{R_{0,IJ}^{(p)}} = \frac{\Delta \rho_{IJ}^{(p)}}{\rho_{IJ}^{(p)}} + (1 + 2\nu)\bar{\varepsilon}_{IJ}^{(p)} \tag{34}$$

and the corresponding pair-dependent gauge factor is defined as

$$\lambda_{IJ}^{(p)} = \frac{\mathrm{FCR}_{IJ}^{(p)}}{\bar{\varepsilon}_{IJ}^{(p)}} \tag{35}$$

The magnitude of the average bending strain for different electrode pairs is determined solely by their spanwise position relative to the curvature distribution. Therefore,

https://doi.org/10.3390/s26103204

the theoretical ranking of the bending strain magnitude is given by

$$\begin{aligned} |\bar{\varepsilon}_{CD}| > |\bar{\varepsilon}_{BD}| = |\bar{\varepsilon}_{CE}| > |\bar{\varepsilon}_{BE}| > |\bar{\varepsilon}_{BC}| = |\bar{\varepsilon}_{DE}| \\ > |\bar{\varepsilon}_{AE}| = |\bar{\varepsilon}_{BF}| > |\bar{\varepsilon}_{AD}| = |\bar{\varepsilon}_{CF}| \\ > |\bar{\varepsilon}_{AF}| > |\bar{\varepsilon}_{AC}| = |\bar{\varepsilon}_{DF}| > |\bar{\varepsilon}_{AB}| = |\bar{\varepsilon}_{EF}| \end{aligned} \tag{36}$$

To further quantify this relationship, the bending strain is normalized with respect to the CD segment, i.e., $|\bar{\varepsilon}_{CD}| = 1$. The corresponding normalized strain magnitudes for all electrode pairs are then expressed as

$$\begin{aligned} |\bar{\varepsilon}_{CD}| &= 1.000 \\ |\bar{\varepsilon}_{BD}| = |\bar{\varepsilon}_{CE}| &= 0.884 \\ |\bar{\varepsilon}_{BE}| &= 0.845 \\ |\bar{\varepsilon}_{BC}| = |\bar{\varepsilon}_{DE}| &= 0.768 \\ |\bar{\varepsilon}_{AE}| = |\bar{\varepsilon}_{BF}| &= 0.748 \\ |\bar{\varepsilon}_{AD}| = |\bar{\varepsilon}_{CF}| &= 0.742 \\ |\bar{\varepsilon}_{AF}| &= 0.690 \\ |\bar{\varepsilon}_{AC}| = |\bar{\varepsilon}_{DF}| &= 0.613 \\ |\bar{\varepsilon}_{AB}| = |\bar{\varepsilon}_{EF}| &= 0.458 \end{aligned} \tag{37}$$

The proposed formulation is intended to establish the relationship between the change in resistance and bending strain and to interpret the spatial variations of the electromechanical response. The consistency between the theoretical strain distribution and the experimentally observed FCR trends across electrode pairs indicates that the model captures the dominant behavior, as discussed in detail in Section 4.

The signal-to-noise ratio (SNR) was employed to quantitatively evaluate signal quality. The SNR measures the relative energy of the signal with respect to the noise and computed as:

$$\mathrm{SNR}_{\mathrm{dB}} = 10 \log_{10} \left(\frac{P_{\mathrm{signal}}}{P_{\mathrm{noise}}} \right) \tag{38}$$

where P_{signal} and P_{noise} denote the powers of the signal and noise, respectively.

3. Experiments

3.1. Measurements

Impedance spectra were measured using an LCR meter (Agilent 4263B, 100 Hz–100 kHz sweep, resistance–reactance mode) under two AC excitation amplitudes (0.1 V and 1.0 V) to evaluate the quality of conductive filler dispersion. The frequency range is selected for the response to be dominated by bulk conductive behavior and less by capacitive and interfacial effects [49,50]. Measurements were taken at 28 days of curing to ensure a stabilized hydration state. An AC two-probe configuration was adopted, which is suitable for highly resistive cementitious systems where direct current measurements may be affected by polarization effects [50,51]. Based on the selected measurement configuration and previous research works, embedded copper mesh electrodes were used to improve electrical contact at the electrode–matrix interface and to reduce contact resistance [52].

The obtained impedance spectra were analyzed in two ways. First, the full frequency-dependent response (100 Hz–100 kHz) was examined to assess dispersion quality, frequency stability, and conductive network formation. Second, a characteristic frequency of 1 kHz was selected for quantitative comparison across mixtures, as it provides a balance between

https://doi.org/10.3390/s26103204

minimizing electrode polarization effects and capturing the bulk conductive response associated with the percolated filler network [49,50]. Data acquisition was performed using LabVIEW to monitor potential polarization drift during testing, which may arise from dielectric responses of the cement-based matrix [53,54] or possible piezoelectric effects [55,56]. All measurements were conducted under controlled laboratory conditions with consistent temperature and humidity.

3.2. Flexural Tests

The electromechanical response of the self-sensing Sikacrete beam was evaluated under controlled flexural loading using a three-point bending configuration. Figure 4a shows the overall experimental setup. Testing was performed using an Instron 5944 universal testing frame equipped with a 1 kN (Series 2580) load cell. The testing machine utilized here has been extensively calibrated and validated for strain measurements, and given the small size of specimens and the axial loading configuration, it was assumed that the strain or force applied by the testing machine was that experienced by the materials. Beam specimens were supported over a 200 mm span, and a concentrated load was applied at midspan through the loading nose. To prevent electrical shorting during simultaneous mechanical and resistance measurements, fiberglass insulating plates were inserted between the specimen and both the loading nose and the support rollers, as shown in Figure 4b.

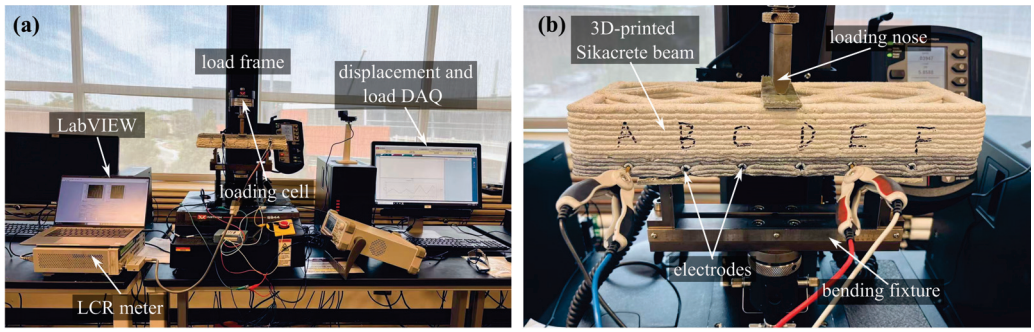


Figure 4. Experimental setup showing: (**a**) overall experimental configuration; and (**b**) close-up view of the flexural bending setup.

Loading was applied in a cyclic triangular waveform with progressively increasing amplitude. Two initial cycles were conducted up to 150 N at a loading rate of 30 N/s, followed by two cycles reaching 300 N at 60 N/s. The final two cycles were conducted at a peak load of 600 N at 120 N/s. This loading protocol was designed to remain within the elastic regime to ensure repeatability and to isolate the intrinsic piezoresistive response of the conductive network. While microcracking can significantly influence conductive pathways and enhance sensitivity, it also introduces irreversible and path-dependent effects that complicate interpretation. The present results therefore represent baseline sensing behavior independent of damage-related effects.

Prior to the cyclic protocol, a preload of 20 N was applied to ensure stable contact conditions and eliminate seating-related compliance effects in the fixture assembly. The mechanical response was acquired continuously at 100 samples/second (S/s), including both applied load and mid-span displacement. In parallel, spatially distributed electrical measurements were obtained at 10 S/s across adjacent electrode pairs (AB, BC, CD, DE, and EF). Electrical resistance was measured independently for each segment using an LCR meter operating in resistance–reactance (R–X) mode, with data acquisition automated through a LabVIEW interface. This synchronized measurement scheme enabled direct correlation between flexural deformation and localized resistance variation along the beam length.

https://doi.org/10.3390/s26103204

4. Results and Discussion

4.1. Particle Distribution

The impedance magnitude and phase angle spectra obtained from a representative electrode pair (e.g., C–D) in the cast cubic specimens under two excitation amplitudes are presented in Figure 5a,b. The responses exhibit near-complete overlap across the entire frequency range from 100 Hz to 10 kHz, indicating negligible amplitude-dependent variation. The impedance magnitude remains in the low-kΩ range (approximately 4 to 4.5 kΩ at low frequency) and decreases gradually with increasing frequency, while the phase angle decreases from near-resistive behavior to a modest capacitive response (approximately 0 to −15°), associated with interfacial polarization and dielectric effects within the cementitious matrix [50,57]. No measurable amplitude-dependent distortion or nonlinear behavior is observed within experimental uncertainty, confirming that the conductive network operates within a stable linear regime.

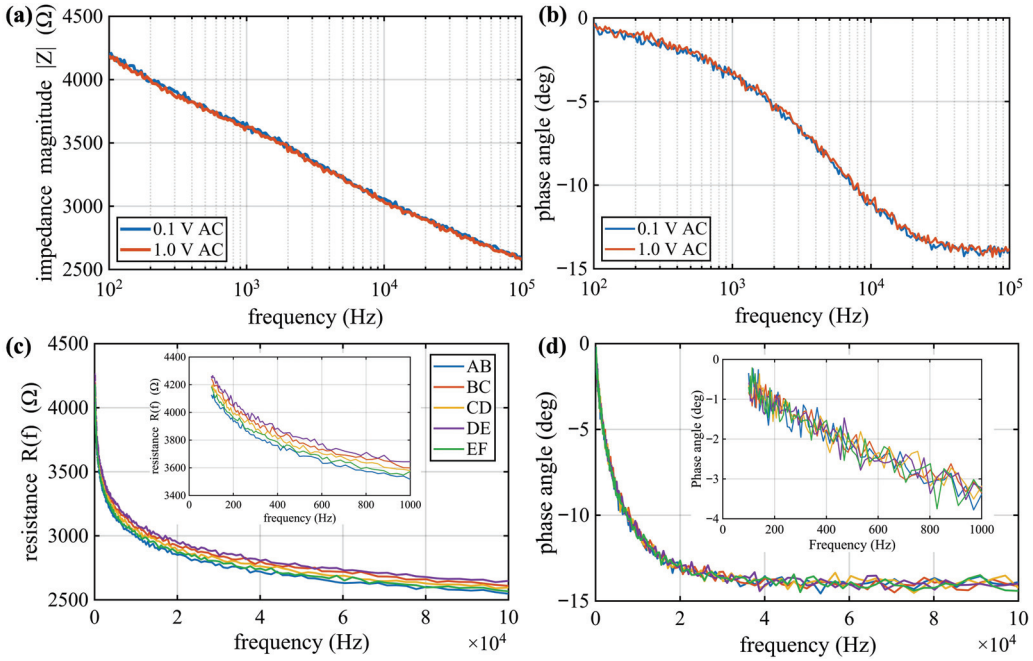


Figure 5. Impedance-based evaluation of conductive filler dispersion: (**a**) impedance magnitude under 0.1 V and 1.0 V excitation; (**b**) phase angle spectra showing negligible amplitude dependence; (**c**) resistance $R(f)$; and (**d**) phase spectra cross adjacent segments (AB–EF).

More importantly, impedance responses measured across adjacent electrode segments (AB, BC, CD, DE, and EF) exhibit low spatial variability in both resistance magnitude and frequency-dependent characteristics, as shown in Figure 5c,d. The resistance spectra $R(f)$ across different segments remain closely clustered, with only minor variations in magnitude (within approximately 5 to 10%), while the spectral slope and phase evolution show consistent trends. The characteristic transition behavior in the phase response also exhibits minimal deviation among segments. Such spatial consistency indicates that conductive fillers are well dispersed along the beam length, forming a continuous and homogeneous percolated network. The high repeatability observed across repeated frequency sweeps further supports reliable electrode embedment and stable electrical contact throughout the specimen.

4.2. Percolation

Figure 6a presents the 28-day electrical resistance of G-filled specimens as a function of G content, with error bars representing the full range of values obtained from three

https://doi.org/10.3390/s26103204

replicate specimens. The results show that the electrical resistance decreases markedly with increasing G content, with the most pronounced reduction occurring between 2 wt.% and 4 wt.%. In this range, the resistance decreases from approximately 9.0×10^4 Ω to 1.5×10^4 Ω, corresponding to a reduction of about 83%. Beyond this transition region, further increases in G content result in a more gradual decrease in resistance, indicating that a conductive network has largely been established. A content of 2 wt.% was selected to balance electrical performance and printability in this study. Increased G content raises water demand and reduces flowability, which can adversely affect extrusion stability and print quality.

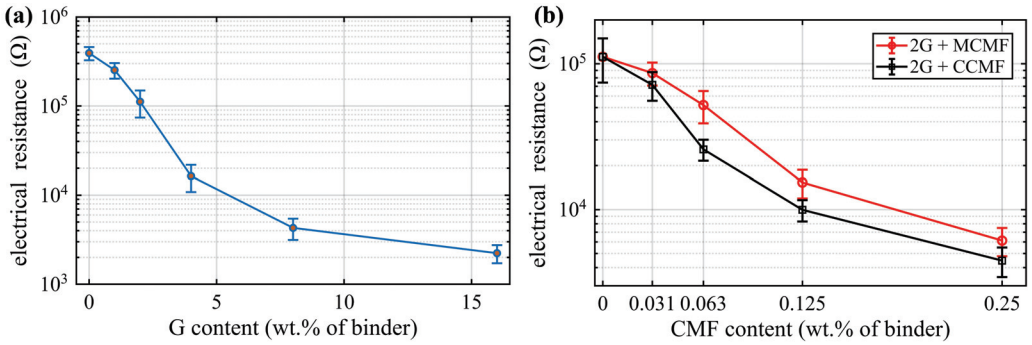


Figure 6. Percolation behavior at 28 days: (**a**) electrical resistance as a function of G content; and (**b**) electrical resistance as a function of MCMF and CCMF content (with 2 wt.% G).

The percolation behavior of mixtures containing 2 wt.% G combined with MCMF or CCMF is shown in Figure 6b. The addition of both CMF types further reduces the electrical resistance with respect to the 2G0CMF reference, confirming their effectiveness in enhancing conductive network formation. The CCMF-based mixtures exhibit a more pronounced reduction in resistance at low dosages, particularly between 0.03125 wt.% and 0.0625 wt.%, whereas the MCMF-based mixtures show a more gradual decrease across the investigated range. This difference is attributed to variations in fiber morphology and dispersion affecting conductive path formation. From these results, a combination of 2 wt.% G with 0.25 wt.% MCMF and 0.0625 wt.% CCMF was selected as the final mix design for printing the beam specimens among the investigated mixes, as higher CCMF contents increased viscosity and induce fiber entanglement resulting in nozzle blockage or unstable extrusion.

4.3. Mechanical Properties

The mechanical response of the four beam configurations was evaluated based on the strain data obtained during cyclic three-point bending, and results are presented in Figure 7. All specimens exhibited largely linear and repeatable load–displacement behavior across loading cycles, with minimal residual deformation upon unloading, indicating that the tests remained within the elastic regime, as shown in Figures 8–10.

The average strain magnitudes of Patterns 1 to 4, obtained by averaging the bending strain across all electrode pairs, were 2873 με, 1925 με, 3513 με, and 2461 με, respectively. Patterns 3 and 4 exhibited 22.2% and 27.8% higher average strain compared to Patterns 1 and 2, respectively. This difference is attributed to the downward shift of the neutral axis caused by the bottom reinforcement and section geometry, which increases the distance between the neutral axis and the top conductive layer.

In addition to the average response, the peak strain values observed at the maximum loading level reached approximately 3982 με and 5071 με for Patterns 1 and 3, respectively, and 2731 με and 3701 με for Patterns 2 and 4, as shown in Figure 7a. These results further confirm that top-layer configurations (Patterns 3 and 4) experience

https://doi.org/10.3390/s26103204

higher strain amplitudes than bottom-layer configurations, while the inclusion of a solid-base region (Patterns 2 and 4) reduces overall deformation compared to their diagonal infill counterparts.

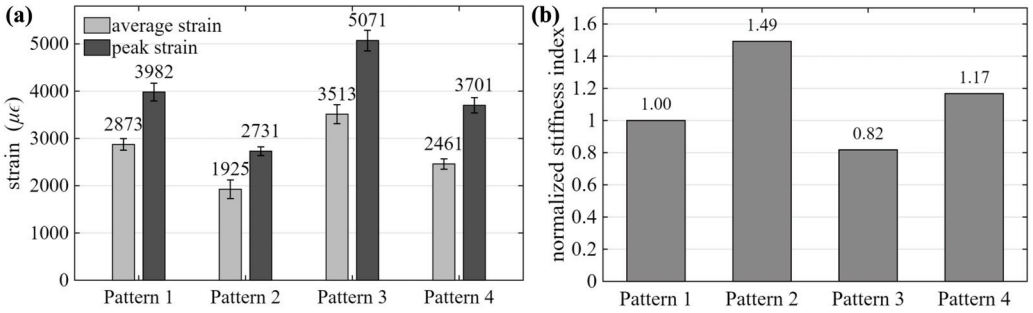


Figure 7. Comparison of (**a**) average strain and peak strain; and (**b**) normalized relative flexural stiffness index for the four beam configurations under cyclic three-point bending.

To further compare mechanical behaviors, a relative flexural stiffness index was defined based on the inverse relationship between bending strain and flexural rigidity under identical loading conditions. The index was computed using the average strain response obtained from the last three loading cycle (maximum load level) for each configuration. Specifically, the stiffness index for each configuration p is expressed as

$$K^{(p)} \propto \frac{1}{\bar{\varepsilon}^{(p)}} \tag{39}$$

where $\bar{\varepsilon}^{(p)}$ denotes the average bending strain across all electrode pairs for pattern p. For comparison, the stiffness is normalized with respect to Pattern 1, yielding

$$\tilde{K}^{(p)} = \frac{\bar{\varepsilon}^{(1)}}{\bar{\varepsilon}^{(p)}} \tag{40}$$

The normalized stiffness values for Patterns 1 to 4 are 1.00, 1.49, 0.82, and 1.17, respectively, as shown in Figure 7b. This corresponds to increases of approximately 49.2% and 42.8% for Patterns 2 and 4 relative to their diagonal counterparts (Patterns 1 and 3), respectively, demonstrating that the incorporation of a solid-base region enhances load distribution and reduces deformation.

4.4. Strain Sensing

Figure 8 presents the time-series FCR responses measured between different electrode pairs for the beam specimen configured with Pattern 1, compared against the average bending strain computed from Equation (28) to Equation (33), during the dynamic test. Subplots show the electrode pair labeled at the top-left corner of each subplot. Black solid lines indicate the FCR response, while red dashed lines represent the corresponding strain input. The presented datasets are taken from the best-performing specimen, determined using the dynamic gauge factor (λ_{dyn}). The presented data were post-processed using a Savitzky–Golay filter (first-order polynomial, window size of 100) to correct baseline drift associated with intrinsic polarization effects, which may otherwise affect the linearity of the FCR response. The window length was determined based on the sampling rate (10 S/s) and loading frequency (0.1 Hz), corresponding to approximately a full loading cycle. This configuration enabled effective noise reduction while preserving the amplitude and phase characteristics of the cyclic strain signal. Additional tests using window sizes of 80 and 120 resulted in variations in peak amplitude and gauge factor of less than 5%,

https://doi.org/10.3390/s26103204

indicating that the selected filtering parameters did not significantly influence the measured strain response.

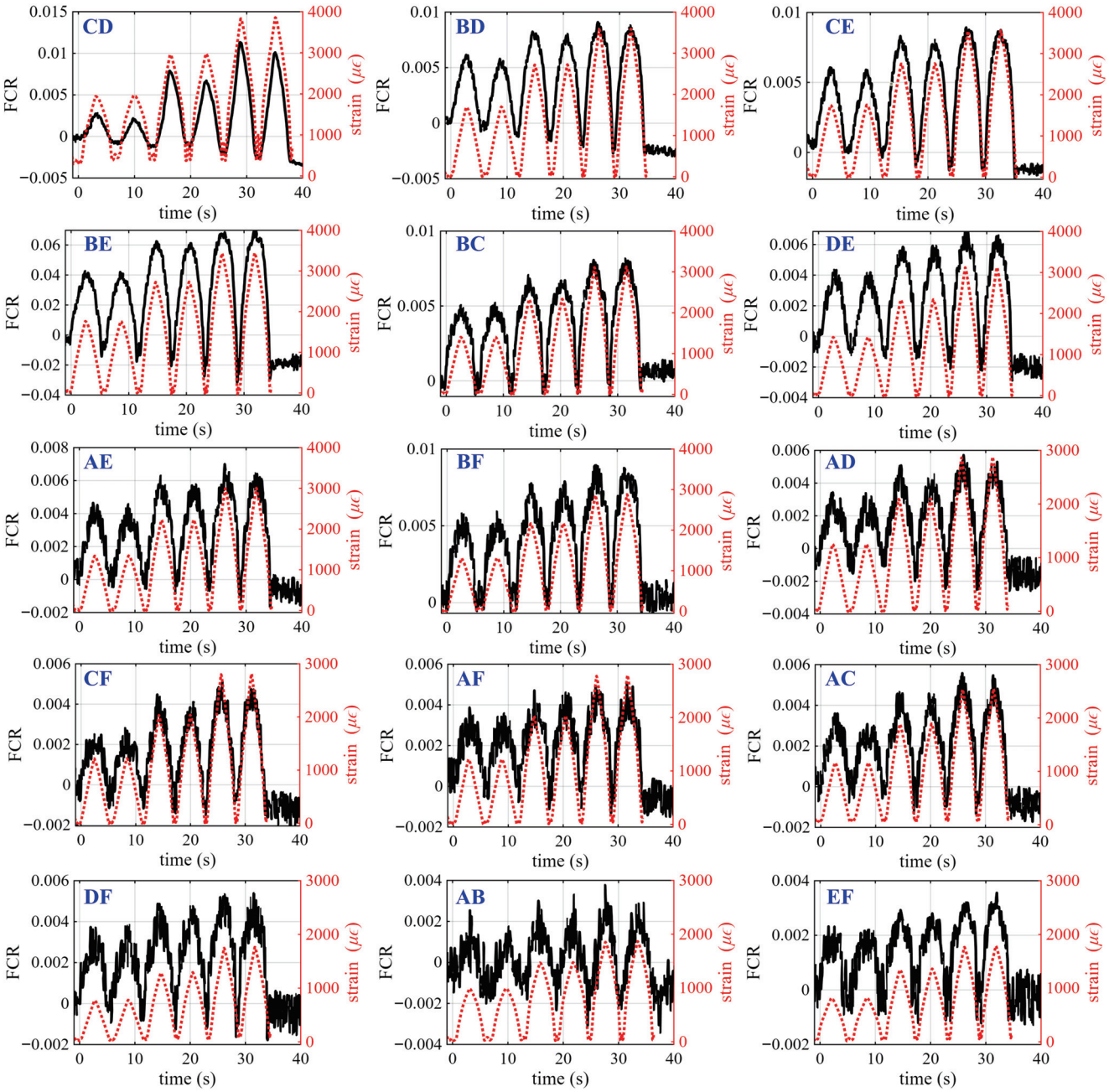


Figure 8. Time-series of FCR measured across electrode pairs for smart beam specimens—Pattern 1.

The results show a close match between the electrical signal and strain time histories, with all electrode pairs exhibiting periodic FCR variations synchronized with the loading cycles. The amplitude of the FCR response varies almost systematically among electrode pairs, indicating the non-uniform bending strain distribution along the beam. In particular, electrode pairs located near the mid-span (e.g., CD, BD, and CE) exhibit the largest response amplitudes, whereas those located closer to the supports (e.g., AB and EF) show significantly smaller variations. This trend is consistent with the theoretical bending strain distribution (Equation (35)), in which the curvature, and thus strain, is maximized at the mid-span and decreases toward the supports. Intermediate electrode pairs (e.g., BC,

https://doi.org/10.3390/s26103204

DE, AE, and BF) exhibit responses of moderate amplitude, following the expected spatial variation in curvature.

Minor deviations from the ideal theoretical ranking (Equation (36)) are observed for certain electrode pairs, which can be attributed to localized variations in the conductive network at the mesoscale, slight variations in electrode contact conditions, and the inherent variability associated with additively manufactured cementitious materials. In addition, a certain degree of baseline drift and asymmetry between loading and unloading cycles is present in several signals, likely attributed to residual polarization effects (i.e., the time-dependent charge accumulation and relaxation at the electrode–matrix interface and within the cementitious matrix) and potential microstructural rearrangement under repeated loading. Additionally, extrusion-based 3D printing of cementitious materials may introduce interlayer defects and weak interfaces, which can influence both mechanical behavior and electrical response. In particular, interlayer bonding imperfections and shrinkage-induced microcracking may locally disrupt conductive pathways or alter strain transfer within the printed structure. In this study, all specimens were tested within the elastic regime, and no visible cracking or interlayer delamination was observed during loading. The consistent and repeatable piezoresistive responses across electrode pairs indicate that the conductive network remained stable under the applied conditions. However, the effects of printing-induced defects, including interlayer bonding imperfections and shrinkage-related cracking, as well as long-term performance and damage evolution, remain to be investigated in future work.

Figure 9 shows the corresponding FCR responses for the beam specimen configured with Pattern 2. Similary to Pattern 1, all electrode pairs exhibit cyclic variations that closely follow the applied strain, with response amplitudes varying along the beam length in accordance with the theoretical bending strain distribution (Equation (36)). This indicates that the relative distribution of bending strain along the beam is preserved regardless of internal pattern configuration. Compared to Pattern 1, the responses in Pattern 2 exhibit more uniform waveform shapes and reduced signal noise among cycles. This behavior is attributed to the presence of the solid base in Pattern 2, which enhances load transfer and promotes a more homogeneous strain field within the specimen. As a result, the electrical response becomes more stable and consistent across electrode pairs.

Figure 10 presents the time-series -FCR responses measured across representative electrode pairs for Patterns 3 and 4, where symmetric pairs are omitted for clarity. For these configurations, the conductive layer is located near the top of the beam and is therefore subjected to compressive strain under three-point bending. In contrast to the tensile configurations, the -FCR increases with increasing load, as compression promotes densification of the conductive network and enhances inter-particle contact. Despite the sign reversal, the spatial variation among electrode pairs remains consistent with the bending strain distribution, with signal amplitudes decreasing from the mid-span toward the supports.

4.5. Sensing Performance Metrics

Figure 11 presents the gauge factor and SNR across different electrode pair configurations for the four sensing patterns. The gauge factor was determined from cyclic loading data by analyzing the average power spectral density and calculated as the ratio between resistance variation and the corresponding strain response, while the SNR was computed using Equation (38). It is found that both metrics exhibit consistent spatial trends across electrode pairs, while clear differences arise from the electrode configurations and the placement of the conductive layers.

https://doi.org/10.3390/s26103204

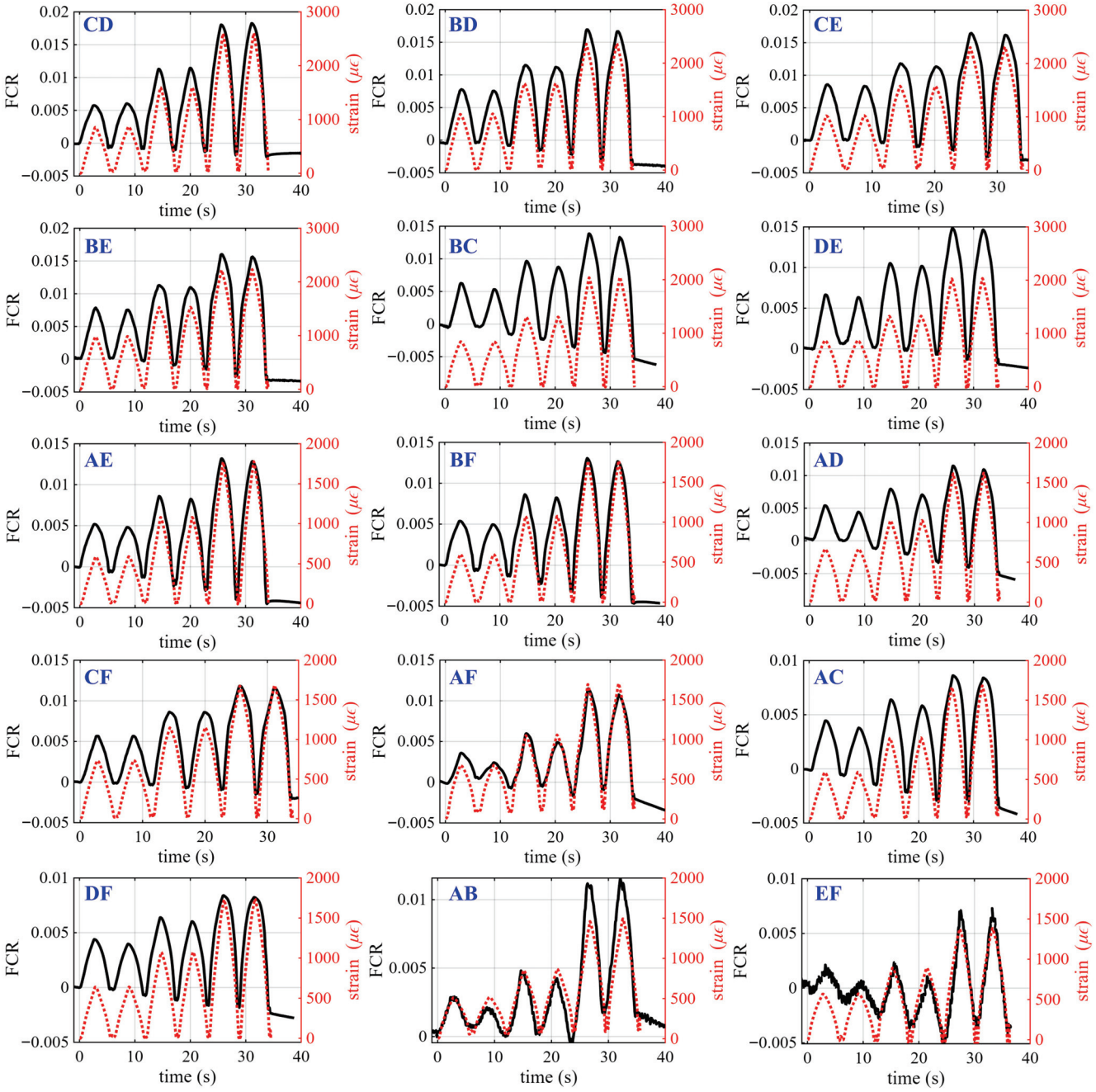


Figure 9. Time-series of FCR measured across electrode pairs for smart beam specimens—Pattern 2.

As shown in Figure 11a, the gauge factor remains relatively uniform across electrode pairs within each pattern, indicating the formation of a stable percolated conductive network. The corresponding standard deviations are 8.4, 10.9, 8.5, and 9.1 for Patterns 1 to 4, respectively. The average gauge factors are 355, 556, 244, and 443 for Patterns 1 to 4, respectively, which are significantly higher than typical values reported for graphite-based cementitious composites (generally below 200) [26,58]. This suggests enhanced electromechanical sensitivity, likely resulting from improved conductive network connectivity and the tailored structural configurations.

https://doi.org/10.3390/s26103204

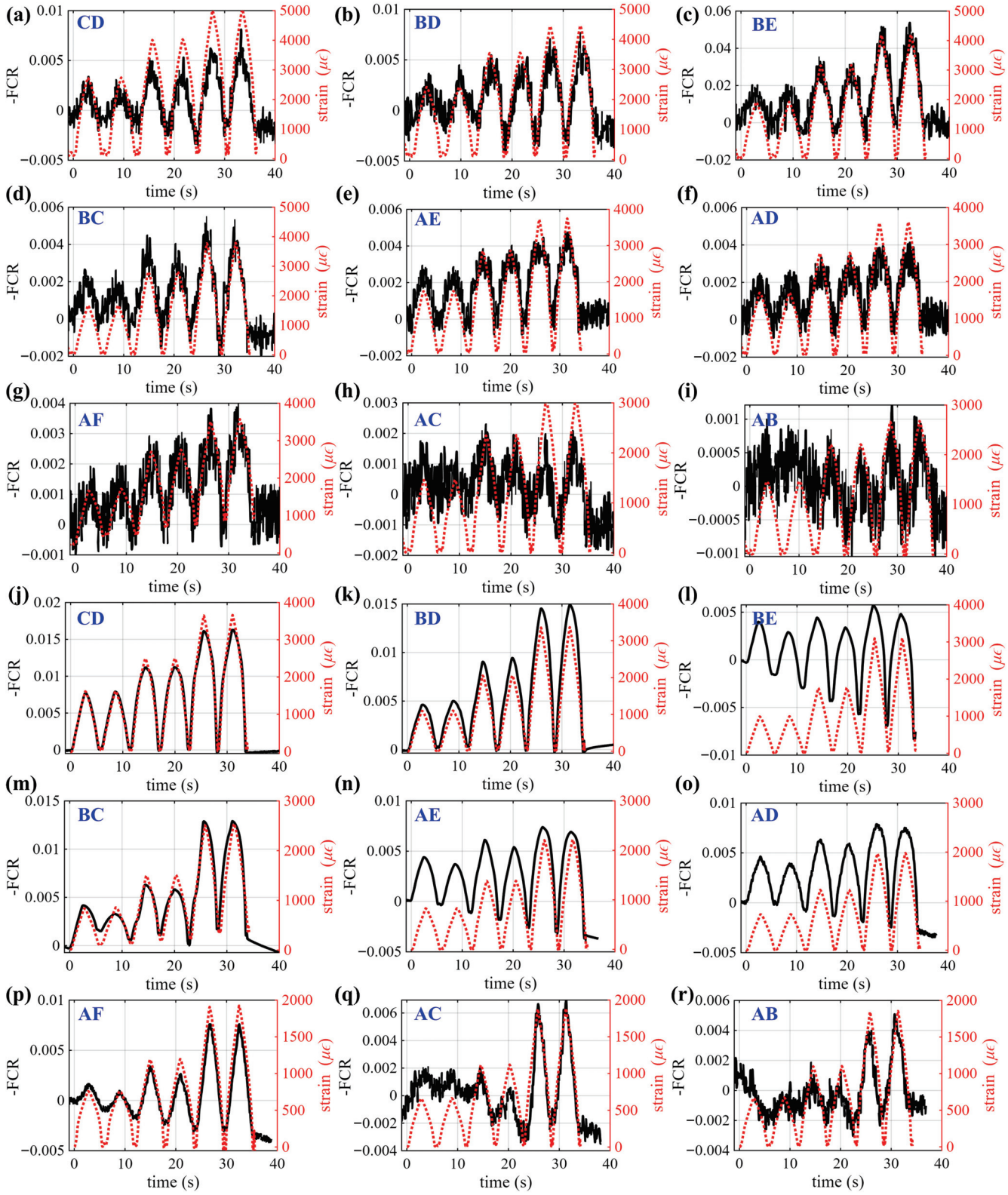


Figure 10. Time-series of -FCR measured across electrode pairs for smart beam specimens: (**a**–**i**) Pattern 3; and (**j**–**r**) Pattern 4. For symmetric electrode pairs (e.g., BD and CE), only one representative pair is shown.

https://doi.org/10.3390/s26103204

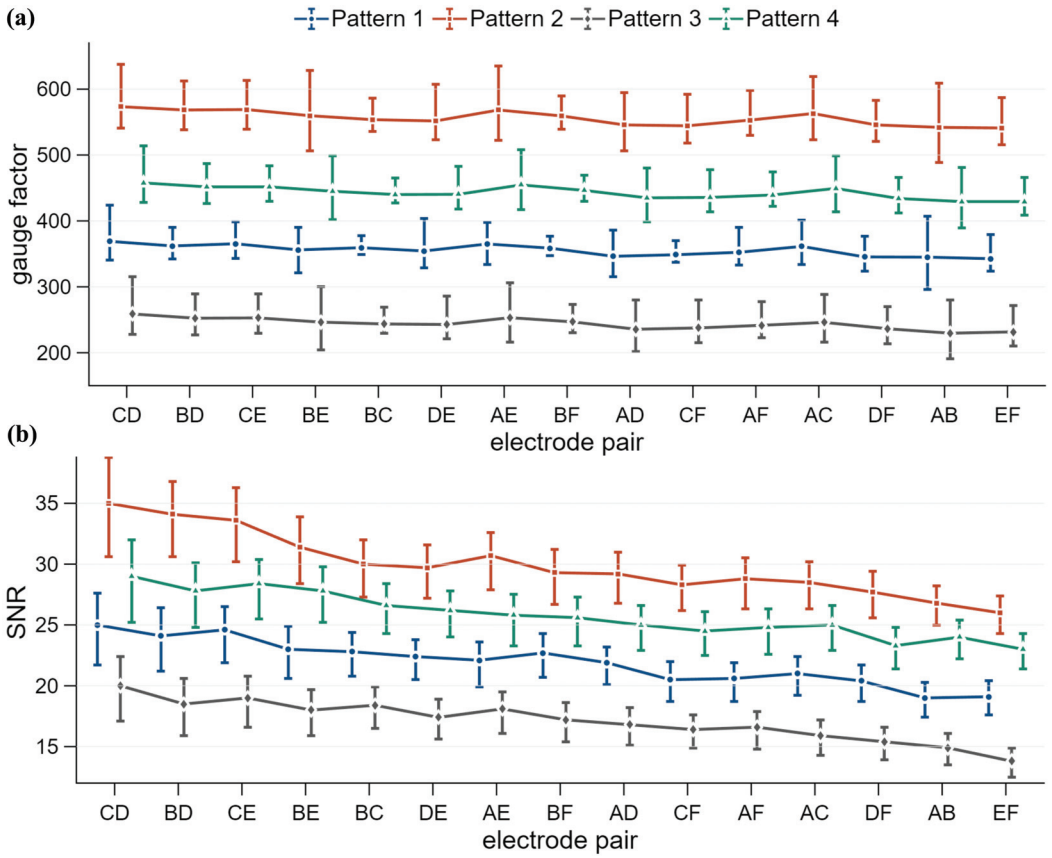


Figure 11. Comparison of three-specimen averaged sensing metrics: (**a**) gauge factor and (**b**) SNR, computed across electrode pairs for specimens under different configuration patterns.

Among the four patterns, Pattern 2 exhibits the highest gauge factor, followed by Patterns 4, 1, and 3. In relative terms, Pattern 2 shows higher sensitivity than Patterns 1, 4, and 3 by 56.6%, 25.6%, and 128.1%, respectively. This enhanced response can be attributed to two primary factors. First, the conductive layer is located in the tensile region, where strain is maximized under bending, leading to greater perturbation of the conductive network. Second, the solid-base configuration promotes more continuous conductive pathways aligned with the current flow, enabling efficient translation of strain-induced changes in interparticle contacts into electrical signals. In contrast, Pattern 3 yields the lowest gauge factor due to less effective engagement of the conductive network.

A similar trend is observed when comparing patterns with an identical conductive-layer placement. Between Patterns 1 and 2 (bottom layer), Pattern 2 exhibits a 56.6% higher gauge factor, while between Patterns 3 and 4 (top layer), Pattern 4 shows a 97.8% increase over Pattern 3. This indicates that the presence of a solid base enhances sensing performance regardless of whether the conductive layer is in tension or compression. This effect is attributed to improved load transfer and a more homogeneous strain field, which stabilize the conductive network and reduce variability in the electrical response.

Comparing Patterns 1 and 3, which share the same diagonal infill but differ in conductive-layer placement, Pattern 1 exhibits a gauge factor approximately 45.5% higher than Pattern 3. This difference reflects the distinct electromechanical response under tension and compression. Under tensile loading, microcrack initiation and interparticle separation lead to more pronounced disruption of conductive pathways, resulting in larger resistance changes. In contrast, compressive loading tends to densify the conductive network and enhance particle contact, producing a more gradual response. Similar tension–compression asymmetry has been widely reported in self-sensing cementitious materials [26,59,60].

https://doi.org/10.3390/s26103204

In addition to intrinsic material behavior, the presence of reinforcement may also influence the measured response by altering stress distribution and strain localization within the beam. Although not explicitly modeled in this study, this effect may contribute to the observed differences among configurations and is left for future investigation.

Figure 11b shows that the SNR consistently decreases from electrode pair CD to EF, which is associated with increasing current path length and accumulated electrical noise. Longer conduction paths result in higher resistance, reducing signal amplitude, while simultaneously increasing the influence of accumulated electrical noise and material heterogeneity. The reduction from CD to EF is about 25.7%, 20.7%, 23.6%, and 31.0% for Patterns 2, 4, 1, and 3, respectively. The SNR ranking follows the same order as the gauge factor (Figure 11a), indicating that sensitivity and signal stability are likely governed by the same mechanism. In particular, the average SNR of Pattern 2, which incorporates a solid base, is about 36.4% higher than that of Pattern 1, while Pattern 4, also featuring a solid base, exhibits an approximately 50.9% increase compared to Pattern 3. The results provides an insight that configurations with continuous conductive networks and stable structural support not only enhance resistance change but also reduce noise by stabilizing current distribution in additively manufactured components. The sensing performance, in terms of gauge factor, standard deviation, and SNR across different pattern configurations are summarized in Table 3.

Table 3. Summary of sensing performance, variability, and structural characteristics across different pattern configurations. Arrows indicate relative increasing (↑) or decreasing (↓) trends among the evaluated configurations.

Pattern	Configuration	$\bar{\lambda}$	Std	SNR Trend	Relative Performance
P1	bottom layer	355	8.4	↓ (23.6%)	baseline
P2	bottom + solid base	556	10.9	↓ (25.7%)	+56.4% $\bar{\lambda}$ vs. P1; +36.4% SNR
P3	top layer	244	8.5	↓ (31.0%)	lowest $\bar{\lambda}$
P4	top + solid base	443	9.1	↓ (20.7%)	+81.6% $\bar{\lambda}$ vs. P3; +50.9% SNR

5. Conclusions

This study investigated the performance of smart beam elements capable of self-sensing, demonstrating the feasibility of localizing sensing nodes within 3D-printed cementitious components for condition assessment and quality control. A Sikacrete-based composite incorporating G, MCMF, and CCMF was developed to achieve electrical percolation and a stable piezoresistive response, and implemented through a controlled multi-material printing strategy. The relative sensing performance of different structural configurations was investigated.

Electrical percolation analysis identified an optimal composition of 2 wt.% G, 0.25 wt.% MCMF, and 0.0625 wt.% CCMF, balancing conductivity and printability. This mixture was embedded within beam specimens in either tensile or compressive regions, combined with diagonal infill and solid-base configurations. Two internal structural configurations were considered, consisting of a fully patterned diagonal infill and a partially solid configuration with a 100% infill base. An electromechanical model was formulated to relate the fractional change in resistance to bending strain, accounting for variations in neutral-axis location, sensing-layer position, and electrode spacing, and enabling interpretation of the spatially distributed electrical measurements obtained during cyclic three-point bending.

Results show that all configurations exhibited consistent and repeatable piezoresistive responses, with electrical signals closely following the applied strain. The gauge factor remained relatively uniform within each configuration, while clear differences were observed among patterns. Specimens with sensing layers in the tensile region (Patterns 1

https://doi.org/10.3390/s26103204

and 2) exhibited higher sensitivity than those in compression (Patterns 3 and 4). Pattern 2 exhibited the highest gauge factor ($\bar{\lambda} = 556$), followed by Patterns 4, 1, and 3. The spatial variation of the response was consistent with the theoretical strain distribution along the beam, with normalized strain magnitudes ranging from 1.000 at the mid-span segment (CD), used as the reference, to 0.458 near the supports (e.g., AB and EF). Signal quality followed a similar pattern-level trend. Pattern 2 showed a 36.4% higher SNR than Pattern 1, while Pattern 4 exceeded Pattern 3 by 50.9%. In addition, SNR decreased with increasing electrode spacing, with reductions of 25.7%, 20.7%, 23.6%, and 31.0% for Patterns 2, 4, 1, and 3, respectively. Mechanical analysis indicated consistent elastic behavior across all configurations. The average strain values for Patterns 1 to 4 were 2873, 1925, 3513, and 2461 $\mu\varepsilon$, respectively.

Overall, this study demonstrated the feasibility of embedding self-sensing cementitious layers within structurally relevant 3D-printed elements using hybrid conductive composites. The proposed approach provided a practical pathway for integrating strain-sensing functionality directly into additively manufactured structures, enabling simultaneous in-print and in-operation structural health monitoring. The effect of damage evolution, long-term performance, environmental effects, and reinforcement effects on sensing behavior, as well as scalability to larger structural components, will be investigated in future work.

Author Contributions: Conceptualization, H.L. and S.L.; methodology, H.L., I.S. and S.L.; software, H.L. and I.S.; validation, H.L., I.S. and S.L.; formal analysis, H.L.; investigation, H.L. and I.S.; resources, H.L., S.L. and I.S.; data curation, H.L.; writing—original draft preparation, H.L. and I.S.; writing—review and editing, H.L., I.S., S.L., S.E.D., A.D. and F.U.; visualization, H.L. and I.S.; supervision, S.L., S.E.D., A.D. and F.U.; project administration, S.L.; funding acquisition, S.L., S.E.D., A.D. and F.U. All authors have read and agreed to the published version of the manuscript.

Funding: This material is partly supported by the National Science Foundation under Grants No. 2349792 and 2431765, and by the Italian Ministry of University and Research (MUR) via the FIS2021 Advanced Grant "SMS-SAFEST—Smart Masonry enabling SAFEty-assessing STructures after earthquakes" (FIS00001797). Any opinions, findings, and conclusions or recommendations expressed in this material are those of the author(s) and do not necessarily reflect the views of the National Science Foundation and the MUR.

Institutional Review Board Statement: Not applicable.

Informed Consent Statement: Not applicable.

Data Availability Statement: The data are available in a publicly accessible repository at the following link: https://www.dropbox.com/scl/fo/9lqctuls6xagyy2lm1dgb/APHe2cS5ESMJHpV6KTocFhM?rlkey=qz0ee0s7cggdkybuosp5idxbo&st=e27ty8ls&dl=0 (accessed on 2 May 2026).

Acknowledgments: The authors would like to acknowledge Moneef Mohamed Elobaid Musa and Pushp Raj Poudel at the Department of Civil, Construction and Environmental Engineering of Iowa State University for their assistance with experimental tests.

Conflicts of Interest: The authors declare no conflicts of interest.

Abbreviations

The following abbreviations are used in this manuscript:

3DP	Three-dimensional printing
SHM	Structural health monitoring
G	Graphite
CMF	Carbon microfibers
MCMF	Milled carbon microfibers

https://doi.org/10.3390/s26103204

CCMF	Chopped carbon microfibers
SEM	Scanning electron microscopy
w/b	Water-to-binder ratio
FCR	Fractional change in resistance
GF	Gauge factor
SNR	Signal-to-noise ratio
PSD	Power spectral density
LCR	Inductance-capacitance-resistance (meter)
R-X	Resistance-reactance (measurement mode)
AC	Alternating current
LVDT	Linear variable differential transformer

References

1. Zhang, J.; Wang, J.; Dong, S.; Yu, X.; Han, B. A review of the current progress and application of 3D printed concrete. *Compos. Part A Appl. Sci. Manuf.* **2019**, *125*, 105533. [CrossRef]
2. Xiao, J.; Ji, G.; Zhang, Y.; Ma, G.; Mechtcherine, V.; Pan, J.; Wang, L.; Ding, T.; Duan, Z.; Du, S. Large-scale 3D printing concrete technology: Current status and future opportunities. *Cem. Concr. Compos.* **2021**, *122*, 104115. [CrossRef]
3. Liu, D.; Zhang, Z.; Zhang, X.; Chen, Z. 3D printing concrete structures: State of the art, challenges, and opportunities. *Constr. Build. Mater.* **2023**, *405*, 133364. [CrossRef]
4. Ahmed, W.; Zaneldin, E.; El Hassan, A. Investigating the Integrity and Failure Characteristics of Deteriorated Polymeric 3D-Printed Components as Candidates for Structural and Construction Applications. *Buildings* **2023**, *13*, 2402. [CrossRef]
5. Cao, J.; Shengzhao, E.; Yang, Y.; Shi, Y.; Chai, J.; Xu, Z. A strategy for the improvement of the bonding performance of 3D-printed concrete interlayer interfaces. *J. Build. Eng.* **2024**, *97*, 110675. [CrossRef]
6. Skripkiunas, G.; Tolegenova, A.; Rishko, L.; Akmalaiuly, K.; Baltuškiene, D. Durability and Cracking Defects in 3D-Printed Concrete. *Adv. Civ. Eng.* **2025**, *2025*. [CrossRef]
7. Bayrak, A.T.; Shaban, N.; Saritas, A.; Meral Akgul, C. A semi-empirical framework for modeling anisotropy, spatial variation and failure mechanisms in 3D printed concrete. *Constr. Build. Mater.* **2025**, *491*, 142648. [CrossRef]
8. Aminpour, N.; Memari, A. Analysis of anisotropic behavior in 3D concrete printing for mechanical property evaluation. *J. Build. Eng.* **2025**, *99*, 111652. [CrossRef]
9. Xing, W.; Li, Z. Quantifying the heterogeneous anisotropic thermal performance of extrusion-based 3D printed structures: A multiscale computational approach. *Constr. Build. Mater.* **2025**, *494*, 143501. [CrossRef]
10. Ubertini, F.; D'Alessandro, A.; Downey, A.; García-Macías, E.; Laflamme, S.; Castro-Triguero, R. Recent Advances on SHM of Reinforced Concrete and Masonry Structures Enabled by Self-Sensing Structural Materials. *Proceedings* **2017**, *2*, 119. [CrossRef]
11. Parida, L.; Moharana, S. Structural health monitoring for 3D-printed civil infrastructures: A review of challenges, applications and future directions. *Smart Mater. Struct.* **2024**, *33*, 103001. [CrossRef]
12. Laflamme, S.; Blasch, E.; Ubertini, F.; Liu, Z.; Wertz, J.; Knott, C.; Cherry, M.; Lindgren, E.; Chang, F.K.; Kumar, A.; et al. Roadmap: Integrating artificial intelligence in structural health monitoring systems. *Meas. Sci. Technol.* **2026**, *37*, 103001. [CrossRef]
13. Bachofner, W.; Kollegger, J. Monitoring the Evolution of Concrete Strain Using Vibrating Wire Strain Gauges. In *Building for the Future: Durable, Sustainable, Resilient*; Springer Nature: Cham, Switzerland, 2023; pp. 1173–1180. [CrossRef]
14. Casas, J.R. Bridging the gap between research and practice: The case of distributed fiber optic sensors for SHM of concrete structures. *Struct. Infrastruct. Eng.* **2025**, *21*, 1883–1897. [CrossRef]
15. Van Steen, C.; Pahlavan, L.; Verstrynge, E. Smart aggregates for acoustic emission monitoring of concrete cracking and reinforcement corrosion. *Constr. Build. Mater.* **2024**, *443*, 137644. [CrossRef]
16. Gomasa, R.; Talakokula, V.; Kalyana Rama Jyosyula, S.; Bansal, T. A review on health monitoring of concrete structures using embedded piezoelectric sensor. *Constr. Build. Mater.* **2023**, *405*, 133179. [CrossRef]
17. Al Agha, W.; Pal, S.; Dev, N. Challenges for structural health monitoring of concrete curing using piezoelectric sensor and electromechanical impedance (EMI) technique: A critical review. *Mater. Today Proc.* 2023, *in press*. [CrossRef]
18. Laflamme, S.; Ubertini, F. Self-Sensing Materials for Nondestructive Evaluation. *Mater. Eval.* **2020**, *78*, 526–536. [CrossRef]
19. Wang, L.; Aslani, F. Structural performance of reinforced concrete beams with 3D printed cement-based sensor embedded and self-sensing cementitious composites. *Eng. Struct.* **2023**, *275*, 115266. [CrossRef]
20. Dinesh, A.; Indhumathi, S.; Pichumani, M. Self-sensing cement composites for structural health monitoring: From know-how to do-how. *Autom. Constr.* **2024**, *160*, 105304. [CrossRef]
21. Wang, X.; Cao, B.; Vlachakis, C.; Al-Tabbaa, A.; Haigh, S.K. Characterization and piezo-resistivity studies on graphite-enabled self-sensing cementitious composites with high stress and strain sensitivity. *Cem. Concr. Compos.* **2023**, *142*, 105187. [CrossRef]

https://doi.org/10.3390/s26103204

22. Abebe, T.N.; Woo, B.H.; Kim, H.G.; Ryou, J.S. Real-time monitoring of self-sensing cementitious composite incorporating hybrid silicon carbide and graphite for enhanced structural health monitoring. *Cem. Concr. Compos.* **2024**, *146*, 105404. [CrossRef]
23. Birgin, H.B.; D'Alessandro, A.; Ubertini, F. A new smart sustainable earth-cement composite doped by carbon microfibers with self-sensing properties. *Dev. Built Environ.* **2023**, *14*, 100168. [CrossRef]
24. Liu, H.; Laflamme, S.; D'Alessandro, A.; Ubertini, F. 3D printed self-sensing cementitious composites using graphite and carbon microfibers. *Meas. Sci. Technol.* **2024**, *35*, 085105. [CrossRef]
25. Ding, S.; Xiang, Y.; Ni, Y.Q.; Thakur, V.K.; Wang, X.; Han, B.; Ou, J. In-situ synthesizing carbon nanotubes on cement to develop self-sensing cementitious composites for smart high-speed rail infrastructures. *Nano Today* **2022**, *43*, 101438. [CrossRef]
26. Li, X.; Feng, Z.G.; Cui, Q.; Wang, Z.; Du, W.; Li, X. Piezoresistive behaviors of self-sensing cementitious composite with well-dispersed carbon nanotube. *Constr. Build. Mater.* **2025**, *474*, 141123. [CrossRef]
27. Dinesh, A.; Saravanakumar, P.; Rahul Prasad, B.; Kilbert Raj, S. Carbon black based self-sensing cement composite for structural health monitoring—A review on strength and conductive characteristics. *Mater. Today Proc.* 2023, *in press*. [CrossRef]
28. Kang, Z.; Zhang, J.; Li, N.; Yang, Y.; Lv, T.; Lu, J. Development of self-sensing cement composites by incorporating hybrid biochar and nano carbon black. *Cem. Concr. Compos.* **2024**, *153*, 105708. [CrossRef]
29. Luo, T.; Wang, Q.; Fang, Z. Effect of graphite on the self-sensing properties of cement and alkali-activated fly ash/slag based composite cementitious materials. *J. Build. Eng.* **2023**, *77*, 107493. [CrossRef]
30. Wang, Y.; Liu, S.; Zhang, L.; Sun, S.; Song, H.; Fan, X.; Zhao, C. Intrinsic self-sensing cementitious composites with hybrid nanofillers exhibiting excellent piezoresistivity. *Nanotechnol. Rev.* **2025**, *14*, 20250209. [CrossRef]
31. Bekzhanova, Z.; Memon, S.A.; Kim, J.R. Self-Sensing Cementitious Composites: Review and Perspective. *Nanomaterials* **2021**, *11*, 2355. [CrossRef]
32. Wang, L.; Aslani, F.; Mukherjee, A. Development of 3D printable self-sensing cementitious composites. *Constr. Build. Mater.* **2022**, *337*, 127601. [CrossRef]
33. Atkinson, C.D.; Aslani, F. Performance of 3D printed columns using self-sensing cementitious composites. *Constr. Build. Mater.* **2023**, *375*, 130961. [CrossRef]
34. Dong, W.; Li, W.; Tao, Z.; Wang, K. Piezoresistive properties of cement-based sensors: Review and perspective. *Constr. Build. Mater.* **2019**, *203*, 146–163. [CrossRef]
35. Heidarnezhad, F.; Zhang, Q. Shotcrete based 3D concrete printing: State of art, challenges, and opportunities. *Constr. Build. Mater.* **2022**, *323*, 126545. [CrossRef]
36. Strohle, M.; Sadique, M.; Dulaimi, A.; Kadhim, M.A. Prospect and barrier of 3D concrete: A systematic review. *Innov. Infrastruct. Solut.* **2022**, *8*, 21. [CrossRef]
37. Sousa, I.; D'Alessandro, A.; Mesquita, E.; Laflamme, S.; Ubertini, F. Comprehensive review of 3D printed cementitious composites with carbon inclusions: Current Status and perspective for self-sensing capabilities. *J. Build. Eng.* **2024**, *98*, 111192. [CrossRef]
38. Vlachakis, C.; Su, Y.F.; Rengaraju, S.; Wang, X.; Milone, G.; Taj, K.; Al-Tabbaa, A. Self-Sensing concrete: A data-driven approach to comprehensive analysis and review. *Int. Mater. Rev.* **2025**, *71*, 09506608251391873. [CrossRef]
39. Liu, H.; Sousa, I.; Laflamme, S.; Doyle, S.E.; D'Alessandro, A.; Ubertini, F. Embedment of 3D Printed Self-Sensing Composites for Smart Cementitious Components. *Sensors* **2025**, *25*, 6005. [CrossRef] [PubMed]
40. Birgin, H.B.; D'Alessandro, A.; Laflamme, S.; Ubertini, F. Hybrid Carbon Microfibers-Graphite Fillers for Piezoresistive Cementitious Composites. *Sensors* **2021**, *21*, 518. [CrossRef]
41. Carbon, S. Sigrafil Short Carbon Fibers. SGL. 2025. Available online: https://www.sglcarbon.com/en/markets-solutions/material/sigrafil-short-carbon-fibers (accessed on 2 May 2026).
42. Razzaghian Ghadikolaee, M.; Cerro-Prada, E.; Pan, Z.; Habibnejad Korayem, A. Nanomaterials as Promising Additives for High-Performance 3D-Printed Concrete: A Critical Review. *Nanomaterials* **2023**, *13*, 1440. [CrossRef]
43. Liu, H.; Laflamme, S.; Cai, B.; Lyu, P.; Sritharan, S.; Wang, K. Investigation of 3D Printed Self-Sensing UHPC Composites Using Graphite and Hybrid Carbon Microfibers. *Sensors* **2024**, *24*, 7638. [CrossRef]
44. Wolfs, R.; Salet, T.; Roussel, N. Filament geometry control in extrusion-based additive manufacturing of concrete: The good, the bad and the ugly. *Cem. Concr. Res.* **2021**, *150*, 106615. [CrossRef]
45. Surehali, S.; Tripathi, A.; Nimbalkar, A.S.; Neithalath, N. Anisotropic chloride transport in 3D printed concrete and its dependence on layer height and interface types. *Addit. Manuf.* **2023**, *62*, 103405. [CrossRef]
46. Lin, Y.; Yan, J.; Sun, M.; Han, X.; Tang, B. Interlayer cohesion in 3D printed concrete: The role of width-to-height ratio in modulating transport properties and pore structure. *J. Build. Eng.* **2024**, *98*, 111009. [CrossRef]
47. Nair, S.A.; Tripathi, A.; Neithalath, N. Examining layer height effects on the flexural and fracture response of plain and fiber-reinforced 3D-printed beams. *Cem. Concr. Compos.* **2021**, *124*, 104254. [CrossRef]
48. Huang, X.; Yang, W.; Song, F.; Zou, J. Study on the mechanical properties of 3D printing concrete layers and the mechanism of influence of printing parameters. *Constr. Build. Mater.* **2022**, *335*, 127496. [CrossRef]

https://doi.org/10.3390/s26103204

49. Sassani, A.; Ceylan, H.; Kim, S.; Gopalakrishnan, K.; Arabzadeh, A.; Taylor, P.C. Influence of mix design variables on engineering properties of carbon fiber-modified electrically conductive concrete. *Constr. Build. Mater.* **2017**, *152*, 168–181. [CrossRef]
50. Hou, Y.y.; Sun, M.q.; Chen, J.z. Electrical resistance and capacitance responses of smart ultra-high performance concrete with compressive strain by DC and AC measurements. *Constr. Build. Mater.* **2022**, *327*, 127007. [CrossRef]
51. Piro, N.S.; Mohammed, A.S.; Jalil, P.J.; Hamad, S.M. Comparison between Four-Probe and Two-Probe Electrical Resistivity Measurement to Monitor the Curing and Piezoresistivity Behavior of Smart Cement Paste Modified with Waste Steel Slag and Green Nano-magnetite. *J. Test. Eval.* **2023**, *52*, 873–896. [CrossRef]
52. McCarter, W.J.; Taha, H.M.; Suryanto, B.; Starrs, G. Two-point concrete resistivity measurements: Interfacial phenomena at the electrode–concrete contact zone. *Meas. Sci. Technol.* **2015**, *26*, 085007. [CrossRef]
53. Wen, S.; Chung, D. Cement-based materials for stress sensing by dielectric measurement. *Cem. Concr. Res.* **2002**, *32*, 1429–1433. [CrossRef]
54. Corral-Higuera, R.; Arredondo-Rea, S.P.; Neri Flores, M.A.; Orozco-Carmona, V.; Gómez-Soberón, J.M.; Almeraya Calderon, F.; Almaral-Sánchez, J.L. Dielectric and Electrochemical Properties of Sustainable Concrete. *ECS Trans.* **2010**, *29*, 115–124. [CrossRef]
55. Sun, M.; Liu, Q.; Li, Z.; Hu, Y. A study of piezoelectric properties of carbon fiber reinforced concrete and plain cement paste during dynamic loading. *Cem. Concr. Res.* **2000**, *30*, 1593–1595. [CrossRef]
56. Chung, D.D.L. Piezoresistive Cement-Based Materials for Strain Sensing. *J. Intell. Mater. Syst. Struct.* **2002**, *13*, 599–609. [CrossRef]
57. Robles, K.P.V.; Yee, J.J.; Kee, S.H. Electrical Resistivity Measurements for Nondestructive Evaluation of Chloride-Induced Deterioration of Reinforced Concrete—A Review. *Materials* **2022**, *15*, 2725. [CrossRef]
58. Yoo, D.Y.; You, I.; Lee, S.J. Electrical Properties of Cement-Based Composites with Carbon Nanotubes, Graphene, and Graphite Nanofibers. *Sensors* **2017**, *17*, 1064. [CrossRef]
59. Deng, Z.; Mahmood, A.H.; Nguyen, Q.D.; Li, W.; Sheng, D. Piezoresistivity and mechanical performance of self-sensing cement-based sensors under the influence of seawater. *Constr. Build. Mater.* **2025**, *502*, 144246. [CrossRef]
60. Dong, W.; Peng, S.; Wang, K.; Huang, Y.; Shi, L.; Wu, F.; Li, W. Integrated triboelectric self-powering and piezoresistive self-sensing cementitious composites for intelligent civil infrastructure. *Nano Energy* **2025**, *135*, 110656. [CrossRef]

Disclaimer/Publisher's Note: The statements, opinions and data contained in all publications are solely those of the individual author(s) and contributor(s) and not of MDPI and/or the editor(s). MDPI and/or the editor(s) disclaim responsibility for any injury to people or property resulting from any ideas, methods, instructions or products referred to in the content.

https://doi.org/10.3390/s26103204

MDPI AG
Grosspeteranlage 5
4052 Basel
Switzerland
Tel.: +41 61 683 77 34

Sensors Editorial Office
E-mail: sensors@mdpi.com
www.mdpi.com/journal/sensors



Disclaimer/Publisher's Note: The title and front matter of this reprint are at the discretion of the Guest Editor. The publisher is not responsible for their content or any associated concerns. The statements, opinions and data contained in all individual articles are solely those of the individual Editor and contributors and not of MDPI. MDPI disclaims responsibility for any injury to people or property resulting from any ideas, methods, instructions or products referred to in the content.





Academic Open
Access Publishing

mdpi.com

ISBN 978-3-7258-9142-9